



energies

Selected Papers from PRES'19

The 22nd Conference
on Process Integration,
Modelling and Optimisation
for Energy Saving and
Pollution Reduction

Edited by

Jiří Jaromír Klemeš, Yee Van Fan and Zorka Novak Pintarič

Printed Edition of the Special Issue Published in *Energies*

Selected Papers from PRES'19

Selected Papers from PRES'19

The 22nd Conference on Process Integration, Modelling and Optimisation for Energy Saving and Pollution Reduction

Editors

Jiří Jaromír Klemeš

Yee Van Fan

Zorka Novak Pintarič

MDPI • Basel • Beijing • Wuhan • Barcelona • Belgrade • Manchester • Tokyo • Cluj • Tianjin



Editors

Jiří Jaromír Klemeš
Brno University of Technology
Czech Republic

Yee Van Fan
Brno University of Technology
Czech Republic

Zorka Novak Pintarič
University of Maribor
Slovenia

Editorial Office

MDPI
St. Alban-Anlage 66
4052 Basel, Switzerland

This is a reprint of articles from the Special Issue published online in the open access journal *Energies* (ISSN 1996-1073) (available at: https://www.mdpi.com/journal/energies/special_issues/PRES_2019).

For citation purposes, cite each article independently as indicated on the article page online and as indicated below:

LastName, A.A.; LastName, B.B.; LastName, C.C. Article Title. <i>Journal Name</i> Year , Article Number, Page Range.

ISBN 978-3-03943-120-5 (Hbk)

ISBN 978-3-03943-121-2 (PDF)

© 2020 by the authors. Articles in this book are Open Access and distributed under the Creative Commons Attribution (CC BY) license, which allows users to download, copy and build upon published articles, as long as the author and publisher are properly credited, which ensures maximum dissemination and a wider impact of our publications.

The book as a whole is distributed by MDPI under the terms and conditions of the Creative Commons license CC BY-NC-ND.

Contents

About the Editors	vii
Yee Van Fan, Zorka Novak Pintarič and Jiří Jaromír Klemeš Emerging Tools for Energy System Design Increasing Economic and Environmental Sustainability Reprinted from: <i>Energies</i> 2020 , <i>13</i> , 4062, doi:10.3390/en13164062	1
Poh Ying Hoo, Cassandra Phun Chien Bong and Yee Van Fan Operational Management Implemented in Biofuel Upstream Supply Chain and Downstream International Trading: Current Issues in Southeast Asia Reprinted from: <i>Energies</i> 2020 , <i>13</i> , 1799, doi:10.3390/en13071799	27
Leonid Tovazhnyanskyy, Jiří Jaromír Klemeš, Petro Kapustenko, Olga Arsenyeva, Olexandr Perevertaylenko and Pavlo Arsenyev Optimal Design of Welded Plate Heat Exchanger for Ammonia Synthesis Column: An Experimental Study with Mathematical Optimisation Reprinted from: <i>Energies</i> 2020 , <i>13</i> , 2847, doi:10.3390/en13112847	53
Rok Gomilšek, Lidija Čuček, Marko Homšak, Raymond R. Tan and Zdravko Kravanja Carbon Emissions Constrained Energy Planning for Aluminum Products Reprinted from: <i>Energies</i> 2020 , <i>13</i> , 2753, doi:10.3390/en13112753	71
Bohong Wang, Jiří Jaromír Klemeš, Petar Sabev Varbanov and Min Zeng An Extended Grid Diagram for Heat Exchanger Network Retrofit Considering Heat Exchanger Types Reprinted from: <i>Energies</i> 2020 , <i>13</i> , 2656, doi:10.3390/en13102656	89
Ron-Hendrik Hechelmann, Jan-Peter Seevers, Alexander Otte, Jan Sponer and Matthias Stark Renewable Energy Integration for Steam Supply of Industrial Processes—A Food Processing Case Study Reprinted from: <i>Energies</i> 2020 , <i>13</i> , 2532, doi:10.3390/en13102532	103
Robert Hren, Aleksandra Petrovič, Lidija Čuček and Marjana Simonič Determination of Various Parameters during Thermal and Biological Pretreatment of Waste Materials Reprinted from: <i>Energies</i> 2020 , <i>13</i> , 2262, doi:10.3390/en13092262	123
Michael Castro, Myron Alcanzare, Eugene Esparcia Jr. and Joey Ocon A Comparative Techno-Economic Analysis of Different Desalination Technologies in Off-Grid Islands Reprinted from: <i>Energies</i> 2020 , <i>13</i> , 2261, doi:10.3390/en13092261	139
Petar Sabev Varbanov, Hon Huin Chin, Alexandra-Elena Plesu Popescu and Stanislav Boldryev Thermodynamics-Based Process Sustainability Evaluation Reprinted from: <i>Energies</i> 2020 , <i>13</i> , 2132, doi:10.3390/en13092132	165
Honghua Yang, Linwei Ma and Zheng Li A Method for Analyzing Energy-Related Carbon Emissions and the Structural Changes: A Case Study of China from 2005 to 2015 Reprinted from: <i>Energies</i> 2020 , <i>13</i> , 2076, doi:10.3390/en13082076	193

Martin Pavlas, Jan Dvořáček, Thorsten Pitschke and René Peche Biowaste Treatment and Waste-To-Energy—Environmental Benefits Reprinted from: <i>Energies</i> 2020, 13, 1994, doi:10.3390/en13081994	217
Kiara Capreece Premllal and David Lokhat Reducing Energy Requirements in the Production of Acrylic Acid: Simulation and Design of a Multitubular Reactor Train Reprinted from: <i>Energies</i> 2020, 13, 1971, doi:10.3390/en13081971	235
Xing Tian, Jian Yang, Zhigang Guo, Qiuwang Wang and Bengt Sundén Numerical Study of Heat Transfer in Gravity-Driven Particle Flow around Tubes with Different Shapes Reprinted from: <i>Energies</i> 2020, 13, 1961, doi:10.3390/en13081961	249
Piotr Józwiak, Jarosław Herczeg, Aleksandra Kiedrzyńska, Krzysztof Badyda and Daniela Olevano Thermal Effects of Natural Gas and Syngas Co-Firing System on Heat Treatment Process in the Preheating Furnace Reprinted from: <i>Energies</i> 2020, 13, 1698, doi:10.3390/en13071698	265
Jenő Hancsók, Tamás Kasza and Olivér Visnyei Isomerization of n-C ₅ /C ₆ Bioparaffins to Gasoline Components with High Octane Number Reprinted from: <i>Energies</i> 2020, 13, 1672, doi:10.3390/en13071672	281
Tomáš Létal, Vojtěch Turek, Dominika Babička Fialová and Zdeněk Jegla Nonlinear Finite Element Analysis-Based Flow Distribution and Heat Transfer Model Reprinted from: <i>Energies</i> 2020, 13, 1664, doi:10.3390/en13071664	295
Christian Langner, Elin Svensson and Simon Harvey A Framework for Flexible and Cost-Efficient Retrofit Measures of Heat Exchanger Networks Reprinted from: <i>Energies</i> 2020, 13, 1472, doi:10.3390/en13061472	315
Yao Sheng, Linlin Liu, Yu Zhuang, Lei Zhang and Jian Du Simultaneous Synthesis of Heat Exchanger Networks Considering Steam Supply and Various Steam Heater Locations Reprinted from: <i>Energies</i> 2020, 13, 1467, doi:10.3390/en13061467	339
Ana-Maria Cormos, Simion Dragan, Letitia Petrescu, Vlad Sandu and Calin-Cristian Cormos Techno-Economic and Environmental Evaluations of Decarbonized Fossil-Intensive Industrial Processes by Reactive Absorption & Adsorption CO ₂ Capture Systems Reprinted from: <i>Energies</i> 2020, 13, 1268, doi:10.3390/en13051268	357
Weiyu Tang, David John Kukulka, Wei Li and Rick Smith Comparison of the Evaporation and Condensation Heat Transfer Coefficients on the External Surface of Tubes in the Annulus of a Tube-in-Tube Heat Exchanger Reprinted from: <i>Energies</i> 2020, 13, 952, doi:10.3390/en13040952	373
Limei Gai, Petar Sabev Varbanov, Timothy Gordon Walmsley and Jiří Jaromír Klemesš Critical Analysis of Process Integration Options for Joule-Cycle and Conventional Heat Pumps Reprinted from: <i>Energies</i> 2020, 13, 635, doi:10.3390/en13030635	393

About the Editors

Jiří Jaromír Klemeš (Prof., Dr., DSc., Dr. h.c. (mult.)). Jiří Jaromír Klemeš is now Head of the Laboratory and Key Foreign Scientist at the Sustainable Process Integration Laboratory (SPIL). Previously, he was Project Director, Senior Project Officer and Hon. Reader at the Department of Process Integration at UMIST, the University of Manchester and the University of Edinburgh, UK. He was awarded with the Marie Curie Chair of Excellence (EXC) by the EC and has a track record of managing and coordinating 96 major EC, NATO, bilateral and UK know-how projects, with research that has attracted over 37 MC in funding. He is Co-Editor-in-Chief of top journals *Journal of Cleaner Production* (IF 7.246) and *Chemical Engineering Transactions* (SciScore), Subject Editor of *Energy* (IF 6.082), Managing Guest Editor of *Renewable and Sustainable Energy Reviews* (IF 12.11) and Emeritus Executive Editor of *Applied Thermal Engineering* (IF 4.725). He is the founder of the Process Integration for Energy Saving and Pollution Reduction (PRES) conference, and has been President for 23 years. He has been Chair of the CAPE-WP of the European Federation of Chemical Engineering (EFCE) for 7 years, and is a member of the Sustainability Platform and Process Intensification WP. In 2015, he was awarded with the EFCE Life-Time Achievements Award. PUBLONS Highly Cited Author.

Yee Van Fan (Dr, MPhil). Yee Van Fan is currently a key researcher at the Sustainable Process Integration Laboratory (SPIL), NETME Centre, Faculty of Mechanical Engineering, Brno University of Technology, Czech Republic. She graduated from the Brno University of Technology in Design and Process Engineering and obtained her MPhil from Universiti Teknologi Malaysia in Bioprocess Engineering. Her research expertise and interests are in solid waste treatment (composting, waste to energy–anaerobic digestion, etc.) and management (optimisation, decision-making tool, supply chain, etc.), with the extension to environmental sustainability assessment. She received three outstanding reviewing awards from different international journals and received two Awards from Publons (first reviewer for *JCLEPRO* and top 1% reviewers in *Engineering*). She was a member of the Junior Editorial Board for *Journal of Cleaner Production* (*JCLEPRO*), and is currently the Associate Editor of *JCLEPRO* and Editorial Advisory Board of *Energy Sources, Part A: Recover, Utilisation, and Environmental Effect*, Taylor & Francis Online.

Zorka Novak Pintarič (Prof, Dr). Zorka Novak Pintarič is a full professor of chemical engineering at the University of Maribor and Vice-Dean of Education at the Faculty of Chemistry and Chemical Engineering. She graduated in Chemical Engineering at the University of Maribor. She became the Head of the MSc study program Chemical Engineering at the Faculty of Chemistry and Chemical Engineering at the University of Maribor, where she teaches several courses in undergrad and postgrad studies. She is a member of the Faculty Senate, member of the working group on Loss Prevention and Safety Promotion at the European Federation of Chemical Engineering and the EURECHA for the promotion of the use of Computers in Chemical Engineering. She has been a frequent reviewer. Her research expertise and interests lie in the areas of design, integration, optimization and synthesis of chemical processes and supply chains, as well as process safety and engineering economics. She has carried out several R&D projects for industrial companies.

Review

Emerging Tools for Energy System Design Increasing Economic and Environmental Sustainability

Yee Van Fan ¹, Zorka Novak Pintarič ² and Jiří Jaromír Klemeš ^{1,*}

¹ Sustainable Process Integration Laboratory—SPIL, NETME Centre, Faculty of Mechanical Engineering, Brno University of Technology—VUT Brno, Technická 2896/2, 616 69 Brno, Czech Republic; fan@fme.vutbr.cz

² Faculty of Chemistry and Chemical Engineering, University of Maribor - UM FKKT, Smetanova ulica 17, 2000 Maribor, Slovenia; zorka.novak@um.si

* Correspondence: klemes@fme.vutbr.cz

Received: 12 June 2020; Accepted: 30 July 2020; Published: 5 August 2020

Abstract: Energy is a fundamental element supporting societal development, particularly with the increasing dependency on the Internet of Things. It is also the main contributor to environmental impacts and subsequently, a potential sector for mitigation. Sustainable energy system design considers energy savings and energy efficiency, waste and consumption reduction, process efficiency enhancement, waste heat recovery, and integration of renewable energy. Emerging tools range from advanced Process Integration, modelling, simulation, and optimisation, to system analysis and assessment. This review covers selected emerging studies promoting sustainable system design, including the recent developments reported in the Special Issue (SI) of the 22nd Conference on Process Integration, Modelling and Optimisation for Energy Saving and Pollution Reduction (PRES'19). The primary emphasis was to enhance the economic and environmental performance. However, social factors were also highlighted as essential for future sustainable development. The discussion and analysis in this review focus on the most recent developments of (a) heat integration and heat transfer; (b) integrated and newly developed heat exchangers, (c) integration of renewables, and (d) roles in economic and environmental sustainability. The key results are highlighted, and future research ideas are suggested according to their links to a broader context.

Keywords: energy system; environmental sustainability; heat integration; economic sustainability; optimisation and modelling tools

1. Introduction

Energy is a fundamental social need and plays an essential role in driving economic growth. The emerging economy requires the support of a reliable, affordable, and energy system with low carbon emissions and air pollutants. Energy transition [1], process optimisation [2], efficiency enhancement, [3] and waste heat recovery [4] are the keys to support a sustainable energy system, especially when increasing energy consumption is unavoidable. There is no straightforward and absolute answer to sustainable design as various temporal [5], and spatial [6] factors have to be considered. The trade-off between the economic, environmental, and social factors remains an active research subject. The recently reported share of global renewable electricity generation by International Energy Agency (IEA) [7] is 26%, dominated by solar photovoltaic (PV) followed by onshore wind and hydropower. Table 1 shows the greenhouse gas (GHG) and the water footprint of different energy sources. Some of the sources of renewable energy having a lower GHG footprint but a higher water footprint. The environmental performance of renewable energy cannot be concluded merely by the GHG or water footprint. The priority—GHG or water footprint reduction—and the selection of renewable energy is highly dependent on local conditions (e.g., resources). Involving the water–energy nexus complicates the issue further [8] because the water footprint consists of embodied energy. A more comprehensive sustainability assessment of different renewable energy

sources is still needed to facilitate appropriate decision making. Non-renewable energy generally has a higher GHG and water footprint than that of renewable energy. However, it should also be noted that this footprint can be varied according to the technology, operation, and even the assessed life cycle boundary. Some of the most frequently implemented examples are biomass, where a large variation is reported [9], and biogenic carbon, which can significantly affect the estimated footprint [10].

The development of sustainable systems remains a challenge in reality due to the extensive range of economic, environmental, and social factors that have to be included during the system life cycle. It is important to ensure that sustainable system design is not transforming one problem into another problem. Comprehensive tools, methodologies, and assessment frameworks remain an on-going topic of research. Figure 1 shows the GHG and air pollutant performance related to the increased share of renewable energy in the European Union (EU). Although the GHG, NO_x and SO₂, have decreased in line with reduced fossil fuel consumption, particulate matter (PM) and volatile organic compound (VOC) emissions have increased. More effort is required for a sustainable system design rather than focusing on solely questions of mitigating climate change or air pollution. Table 2 shows the levelized energy cost with and without subsidies and the changes in cost. The price of renewable energy has fallen significantly, particularly wind and solar energy, which are cheaper than non-renewable sources even without financial assistance. However, wind and solar are intermittent energy sources, which are not continuously available for conversion and available at every location. Lithium-ion batteries are the most competitive option with the highest potential for lifetime cost reduction [11], with the exception of long discharge applications. Based on a report by Lazard [12] considering the levelized cost of storage, solar PV with a storage system is economically attractive for short-duration wholesale and commercial use (102–139 USD/MWh) but remains a challenge for residential and longer-duration wholesale use (457–663 USD/MWh). Direct displacement of dispatchable energy sources by variable renewable energy can lead to cascade failures in the grid (blackouts) without consideration of flexible energy system design [13].

Table 1. The Greenhouse Gas (GHG) and water footprints of different energy sources.

Energy Sources	GHG Footprint (kg/MWh) [14]	Water Footprint (L/MWh) [15]	Share of Water Footprint [16]
Biomass	45	85,100	0.26% Operation; negligible Construction; 99.73% Fuel supply
Hydropower	26	4961	100% Operation; negligible Construction; 0% Fuel supply
PV	85	330	35.71% Operation; 64.29% Construction; 0% Fuel supply ^c
Wind	26	43	15.38% Operation; 84.62% Construction; 0% Fuel supply
CSP	108.6 ^a [17]	1250	35.71% Operation; 64.29% Construction; 0% Fuel supply ^c
Geothermal	53 ^b [18]	1022	99.39% Operation; 0.61% Construction; 0% Fuel supply
Oil	735	3220	88.70% Operation; negligible Construction; 11.1% Fuel supply
Nuclear	28	2290	89.93% Operation; negligible Construction; 10.03% Fuel supply
Coal	888	2220	89.93% Operation; negligible Construction; 10.03% Fuel supply
Natural Gas	500	598	97.13% Operation; 0.45% Construction; 2.43% Fuel supply

PV = photovoltaic; CSP = concentrated solar power. The GHG footprint is based on the reported study in [14] except for CSP^a and geothermal^b. ^c The share of water footprint reported in [16] for solar power is not specified by the type of technology.

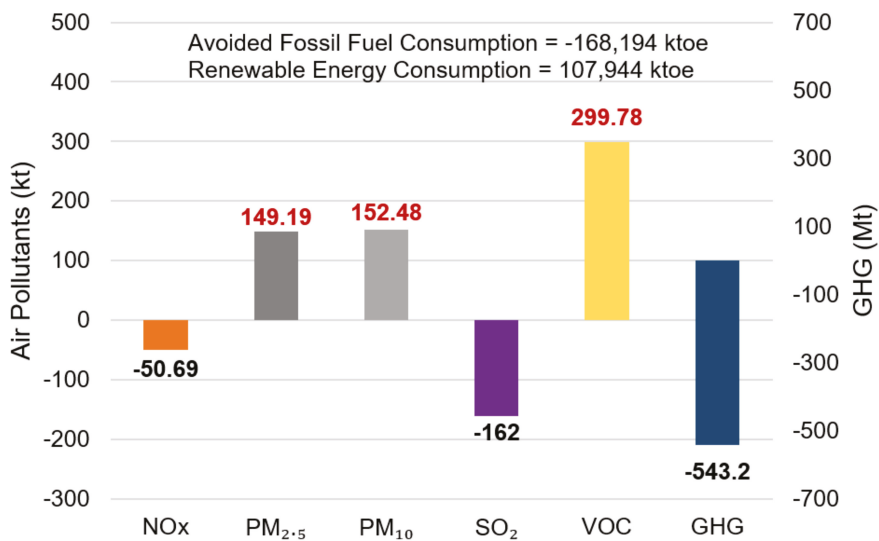


Figure 1. The changes in GHG and air pollutant performance with an increasing share of renewable energy (comparison between 2005 and 2018). Data extracted from [19].

Table 2. The levelized energy cost of different sources. ^a The considered subsidies are based on US federal tax subsidies which can vary from country to country. ^b Biomass is based on the analysis of Version 11.0 [20] because there is no related information in Version 12.0 [21].

Energy Sources	Levelized Energy Cost (USD/MWh) [21]	Without Subsidies (USD/MWh) [21]	Changes in Cost (%) [22] Global Weighted-Average LCOE
Solar PV	32–245	36–267	−77% (0.085 USD/kWh)
CSP	96–169	98–181	−45.75% (0.185 USD/kWh)
Geothermal	67–110	71–111	+50% (0.072 USD/kWh)
Wind	14–47	29–56	−20–34% (0.127 ^a –0.045 USD/kWh)
Biomass	40–112 ^b	55–114 ^b	−17.33% (0.062 USD/kWh)
Nuclear	112–189	NA	NA
Coal	60–143	NA	NA

Fikse et al. [23] stated that traditional system engineering practices attempt to anticipate disruptions; however, they may be susceptible to unforeseen factors. This is particularly reflected in the unexpected outbreak and impact of COVID-19. The disease threatens human life while also serving to highlight existing or potential vulnerabilities of emergency responses and various system designs (i.e., capacity, allocation, and flexibility). A sustainable system design with inherent resilience would likely be valuable in future research. One of the apparent crises during COVID-19 is the shortage of personal protective equipment, particularly in countries reliant on international production. Global value chains may be reconsidered after the COVID-19 outbreak, as suggested by Kambhampati [24], due to the profound risk they pose. COVID-19 has also had an influence on the energy system. Figure 2 shows the supplies of minerals that support energy production. In addition to Cu, Li, Co, and Ni, renewable energy used Si, Zn, Mo, and rare earth minerals, which are non-renewables. It has been reported that electric cars use five times more minerals than a conventional car, and onshore wind plants require eight times more minerals compared to gas-fired plants [25]. As shown in Figure 2, the production

of Si, Zn, Mo, and rare earth minerals is dominated by China. The reliability, security, and price fluctuations of mineral supplies is an under-analysed global challenge in the promotion of a 100% renewable energy future.

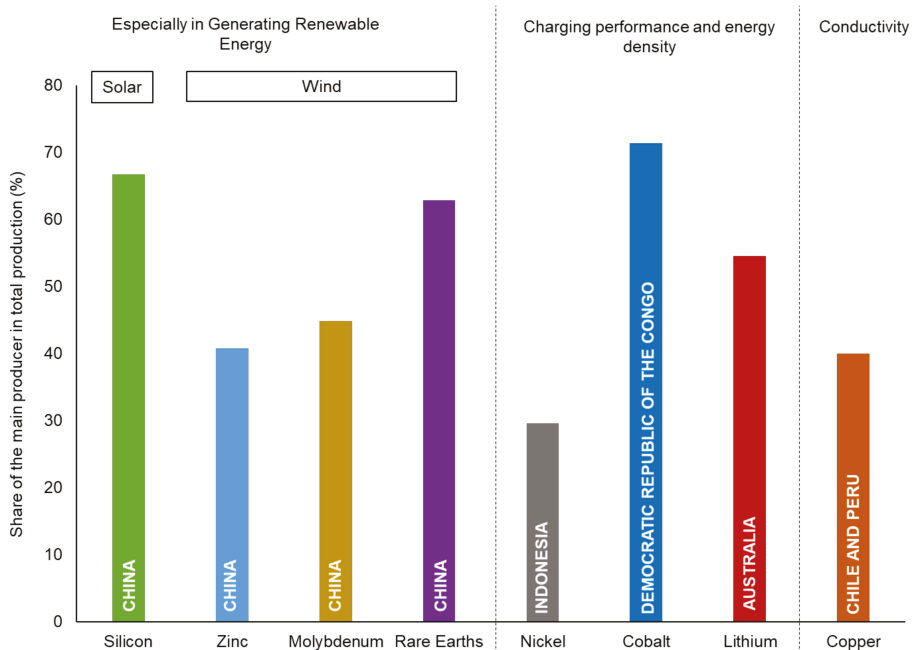


Figure 2. Supplies of minerals that support energy production. Information collected from [25], except for zinc [26] and silicon [27].

Figure 3 shows the structural changes and impacts of energy demand during movement restriction. Domestic electricity demand has generally increased, and there has been a shift in the timing of peak demand during the middle of the day. The reduction of electricity demand in selected countries has also been reported by IEA [28]. The fall in overall electricity consumption is due mainly to the shutdown of industry, and the share of renewable energy has been reported to have increased. The temporary impacts are generally favourable where the consumption and environmental footprint is reduced. However, IEA [29] highlighted that the energy industry that emerges from COVID-19 would change significantly, particularly given an expectation of a reduction in investment. This could inhibit sustainable development because energy is likely to be affected first. In Germany, the pandemic has led to a decrease in power demand and negative electricity prices. Amelang [30] highlighted that negative rates have no benefit to consumers as the difference between negative power prices and the feed-in tariffs ultimately have to be paid. Oversupply reflects inefficiency and highlights a need for a better demand response and flexible renewables design. Positively, however, this crisis has highlighted a weakness and represents an opportunity to steer system design research onto a more resilient, secure, and sustainable path.

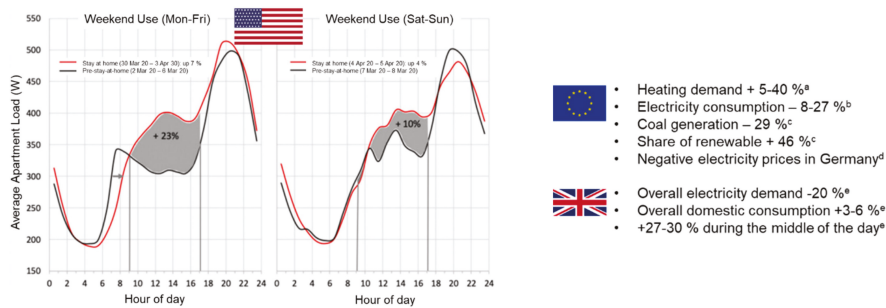


Figure 3. The structural changes and impacts of energy demand during movement restriction of COVID-19 in New York City [31], the European Union [32] ^a [33] ^b [34] ^c [30] ^d, and the UK [35] ^e.

The circular economy approach has undergone substantial development and increasingly used as a framework for system energy design, assessment, and implementation at various levels, beginning with production plants, through municipal and governmental strategic plans. Korhonen et al. [36] is one contributor who highlighted the need for scientific research into the quantification of actual environmental impacts. This is because a highly implemented circular economy progresses toward sustainability features. However, some of the circularity features (e.g., reprocessing waste) can be energy-intensive. Another work by Kirchherr et al. [37] emphasised that a potential variety of the circular economy concept which is complemented with a lack of quantification, if not fully based on a footprint strategy, can result in a conceptual deadlock. Table 3 summarises the six circular strategies consisting of the 9Rs (Refuse, Rethink, Reduce, Reuse, Refurbish, Remanufacture, Repurpose, Recycle, Recovery) practices with quantitative/qualitative indicators. A set of indicators comprising scale indicators and the circularity rate (%), and covering socioeconomic cycling, ecological cycling potential, and non-circularity, has also been proposed by Mayer et al. [38] for the EU. The proposed indicators can be considered to be relatively comprehensive. However, they serve mainly as a monitoring framework (system assessment tools) rather than a system engineering model.

Table 3. Circular economy strategy and its indicators. Extracted from [39].

Circular Strategies	Example	Indicators
1. Preserve the function of products/services	Refuse, Rethink, Reduce	eDiM, TRP, Longevity, MCI, EVR,
2. Preserve the product	Reuse, Refurbish, Remanufacture	PLCM, SCI
3. Preserve components of the products	Reuse, Repurpose	eDiM, TRP, PLCM
4. Preserve the materials	Recycle, downcycle	CR, RR, EOL-RR, RIR, OSR, NTUM, Longevity, MCI, CIRC, LMA, PLCM, SCI, GRI, CEI, CPI, VRE
5. Preserve the embodied energy	Energy Recovery	MCI, CPI, SCI
6. Measure the reference scenario	Compare to the linear economy	MCI, Longevity, SCI

eDiM = Ease of disassembly metric, TRP = Total restored product, MCI = Material circularity metric, EVR = Eco-cost value ratio, PLCM = Product-level circularity metric, SCI = Sustainable circular index, CR = Old scrap collection rate, RR = Recycling process efficiency rate, EOL-RR = End of life recycling rate, RIR = Recycling input rate, OSR = Old scrap ratio, NTUM = Number of times use of a materials, CIRC = Material circularity indicator, LMA = Lifetime of materials in anthroposphere, GRI = Global resource indicator, CEI = Circular economy index, CPI = Circular economy performance indicator, VRE = Value-based resource efficiency.

System design is important in facilitating sustainable development. Various works that aspire to promote sustainable system design by addressing the issues of enhancing energy and environmental performance were presented in the Special Issue (SI) of the 22nd Conference on Process Integration, Modelling and Optimisation for Energy Saving and Pollution Reduction (PRES'19). The aim of this

study is to review the emerging tools for sustainable system design, including the recent developments reported in the Special Issue (SI) of PRES 2019. The energy system design tools that are considered in this study are summarised in Figure 4, including modelling, simulation, optimisation, and analysis or assessment.

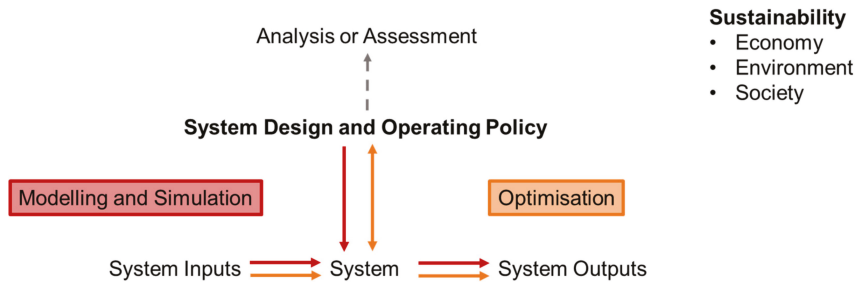


Figure 4. The research direction of sustainable system design. Modified based on Loucks [40]. The considered tools reviewed in this study include those used for modelling and simulation, optimisation, and analysis or assessment, that can contribute to energy system design. Red arrows represent modelling and simulation. Orange arrows represent optimisation. The grey arrow represents analysis or assessment. For example, modelling and simulation utilise system inputs and the available system design and operating policy to identify the system outputs. Analysis or assessment is conducted to determine the performance of an existing system.

The papers are categorised into four topics in Section 3, focused on modelling, simulation, optimisation, and assessment studies on the topics of:

- a. Heat Integration and heat transfer.
- b. Integrated and newly developed heat exchangers.
- c. Integration of renewables.
- d. Roles in economic and environmental sustainability.

2. Emerging Tools

This section discusses the modelling, simulation, optimisation, and assessment studies aimed at improving heat integration and heat transfer, integrated and newly developed heat exchangers, integration of renewables, and economic and environmental sustainability. One-third of energy is lost in the form of waste heat, as reported by [41]. According to the analysis by Papapetrou et al. [42], the total waste heat potential in EU is about 300 TWh/y, of which one-third is low-temperature waste heat, 25% occurs between 200–500 °C, and the remainder occurs above 500 °C. Bianchi et al. [43] suggested the theoretical potential of the EU's thermal energy waste was 920 TWh/y and 279 TWh of Carnot potential. This highlights the important roles of waste heat recovery in enhancing energy efficiency and emission reduction.

Heat integration [44] and heat transfer intensification [45] are long-standing tools for reducing energy consumption. However, they are continuing to be valuably extended. They have supported a significant issue, namely the reduction of the cost of energy transmitted to the cost of products and services. A substantial amount of effort has been made in making energy cleaner. However, the cleanest energy is that saved and consequently not produced [46]. These issues are closely related to environmental footprints, particularly carbon footprints. These should more precisely be named carbon emissions footprints and, more comprehensively, greenhouse gas footprints, including other greenhouse gases in addition to CO₂ [47]. The most important is, in addition to CO₂, CH₄ and water vapour. To a lesser extent, but still significant, are surface-level ozone, NO_x, and fluorinated gases, because all of these also involve infrared radiation [48].

However, all of the mentioned tools would not be possible without heat exchangers [49]. Heat exchangers are an important component in most plants, and they are also used in motor vehicles and airplanes. Their efficiency and cost-to-energy-saved ratio are important for their value to modern design. They have been continuously developed from their advent during the industrial revolution until the highly sophisticated pieces of equipment of the present [50]. A notable development comprises a modern plate and compact heat exchangers performing at low ΔT_{min} , which are able to reduce low potential waste heat. In Northern China, for example, this amounts to 100 Mt standard coal equivalents (Mtce, 2.93 EJ) and throughout steel mills in Hebei province it reaches 44,268 MW and in cement factories 2155 MW [51]. These issues were addressed by several papers in the SI, e.g., [52].

Renewables implementation remains a challenge despite the fact that their economic feasibility is reported to be improving (see Section 1). The technical challenges encountered arise mainly from the reliability of supply, facilities for transmission and distribution networks, connectivity to the existing grid, and storage. Modelling and simulation studies facilitate the understanding of the energy system (time profile scale and uncertainty, conditions, limitations) and predict performance in the real world for a more reliable integrated design. Different methods exist to address renewable uncertainty, for example, stochastic programming, fuzzy theory, robust programming, chance-constrained programming [53] and point estimate method [54]. Mehrjerdi and Rakhshani [55] modelled the correlation of time scale and uncertainty in an energy management system and incorporated load and wind energy uncertainties using mixed-integer stochastic programming. Talaat et al. [56] integrated wave, solar, and wind energy in a study in which the change of different environmental conditions was considered via simulation using Simulink. Baum et al. [57] assessed the intermittency mitigation potential of a dynamic, active demand response method in a smart grid using Monte Carlo simulation. Simulation software for a power system using intermittent energy sources was demonstrated by Fiedler [58] based on weather data in Australia. The advantages of diversification compared to dependence on a mono-system were highlighted. Draycott et al. [59] reviewed approaches to replicating the ocean environment, which is relatively complex, for an offshore renewable energy simulation (physical and numerical). Conducting such simulations is important prior to costly full-scale wave, tidal energy development. Long-range energy alternatives planning system (LEAP) and MARKAL simulations have also been used as forecasting models in various energy planning studies [60].

Optimisation studies of renewable energy are relatively broad, and coverage can range from micro (efficiency, material) to macro (regional planning, distribution design) aspects. An example of optimisation studies from a micro perspective is the optimisation of biomass blends for syngas production [61]. To enhance the energy efficiency of solar PV panels, Peng et al. [62] optimised their cooling performance and suggested the efficiency enhancement is up to 47%. Bravo et al. [63] assessed the integration of the calcium looping process as a thermochemical energy storage system in hybrid solar power plants. Macro-level optimisation focuses on distribution planning or design. For example, Zheng et al. [64] optimised the design of a biomass integrated microgrid with demand-side management under uncertainty. Nowdeh et al. [65] proposed a method based on a multi-objective evolutionary algorithm to optimise the placement and sizing of photovoltaic panels and wind turbines in a distribution network. A similar study was conducted by Jafari et al. [66], but the objective function was to minimise pollution, financial, and reliability issues rather than to reduce loss and improve reliability. Rinaldi et al. [67], in contrast, optimised the allocation of PV and storage capacity considering consumer types and urban settings for Switzerland. Another stochastic mathematical model was proposed by Santibañez-Aguilar et al. [68] to specifically support PV manufacturing supply chain development. It is crucial to support overall sustainability by considering the potential to locally produce different PV elements. Because flexibility is an important element of an integrated renewable energy system, stochastic optimisation algorithms are one of the most commonly applied methods [69]. The Fuzzy-graph is another method that can be applied to optimise renewable energy utility systems, as used by Aviso [70] for the abnormal operation of an off-grid system. Various software tools for the planning of hybrid renewable energy systems, including HOMER, Calliope, RETScreen, DER-CAM, Compose, iHOGA, and EnergyPRO,

were recently reviewed by Cuesta et al. [71]. Akhtari et al. [72] optimised hybrid renewable earth–air heat exchanger with an electric boiler, wind, PV, and hydrogen configuration and Amin Razmjoo et al. [73] optimised a distributed generation-based photovoltaic system using HOMER. The inclusion of social factors in software tools is suggested to further enhance the capability of the software packages in optimising design.

Analysis and assessment studies can act as monitoring tools to determine the current performance quantitatively for comparison between alternatives and identify possible improvements in design. Life cycle assessment (LCA) based on environmental impacts or environmental footprints [47] and techno-economic assessment [74] are among the common approaches. Khoshnevisan et al. [75] performed a consequential life cycle assessment to compare the conversion of the organic fraction of municipal solid waste to bioenergy and high-value bioproducts (e.g., microbial protein, lactic, and succinic acid). The environmental impact of energy production through anaerobic digestion of pig manure was quantified by Ramírez-Islas [76]. Eutrophication was identified as the most negative effect which required further attention. To simplify the LCA of solar heating and cooling technologies, Longo et al. [77] developed an Environmental Lifecycle Impacts of Solar Air-conditioning System (ELISA) tool to account for the energy and environmental impacts. The PV-assisted system was identified as having a better life cycle performance compared to thermal-driven solar heating and cooling and a conventional system (electric heat pump). Wang et al. (2020) identified the geothermal gradient as the key factor of environmental impacts, in which acidification, eutrophication, and global warming potential can be reduced by a large geothermal gradient. Life cycle sustainability assessment [78] has received increasing attention in recent years. This is similar to LCA, but more comprehensively represents sustainability, including consideration of social life cycle assessment and life cycle costing. Because of increasing concern regarding interrelationships, nexus analysis has been conducted to further understand sustainability, particularly relating to the water-energy nexus, as conducted by Duan and Chen [79]. Fan et al. [80] proposed a graphical analysis tool considering the emission–cost nexus for sustainable biomass utilisation. Various sustainability indicators have also been developed for decision making, e.g., sustainable energy development index [81] and other sustainability indicators for renewable energy systems reviewed by Liu [82].

3. Issues Developed and Extended in this Special Volume

3.1. Heat Integration and Heat Transfer

The first paper on this subject, entitled “Thermal Effects of Natural Gas and Syngas Co-Firing System on Heat Treatment Process in the Preheating Furnace” and authored by Józwiak et al. [83], examined the possibilities of partially replacing natural gas with synthesis gas derived from biomass. The system under study was a preheating furnace in the steel industry, for which the authors investigated how the air volume, the distribution of burner power, and the share of bio-based gas influenced heat transfer, temperature, and gas flow in the furnace. The modelling was performed with a computational fluid dynamics tool. Computational fluid dynamics (CFD) tools are widely used to simulate and optimise the processes of heat transfer [84] and energy release from various fuels [85]. The results showed that up to 40% of the natural gas could be replaced by syngas of biogenic origin, while still achieving satisfactory thermal efficiency and temperature characteristics. The authors claimed that GHG emissions could be reduced by 40%. The results showed that the replacement of fossil fuels by renewable fuels needs to be promoted, especially in heat-intensive industrial plants, as satisfactory operational performance can be achieved with significantly lower emissions. However, the economic performance also needs to be analysed and taken into account because renewable fuel production processes are not yet necessarily economically viable; see You et al. [86].

The next paper, “Isomerisation of n-C5/C6 Bioparaffins to Gasoline Components with High Octane Number”, authored by Hancsók et al. [87], addresses the challenges of producing fuels from alternative sources such as waste and biomass. These fuels often contain by-products, e.g., light hydrocarbons,

especially n-alkanes C5-C7, which reduce the quality and negatively affect the safety properties of the fuel. Light hydrocarbons are formed in the production of bio-gasoline from rice straw biomass [88], Fischer-Tropsch synthesis of syngas from wood chips [89], and in various chemical reactions involving sorbitol [90] and simple sugars [91]. Catalytic reactions of isomerisation and aromatisation were carried out in the experimental device, in which light hydrocarbons were converted into iso-alkanes with a higher octane number. The authors claimed that the yield of liquid products could exceed 98%, and the research octane number could reach 92. Improved reaction pathways and optimised operating conditions for high quality, affordable, and safe end products could facilitate the success of fossil fuel replacements.

One of the measures to increase energy efficiency is to improve heat transfer between fluids in heat exchanger units. The authors of the next paper, Tian et al. [92], entitled “Numerical Study of Heat Transfer in Gravity-Driven Particle Flow around Tubes with Different Shapes”, investigated the mechanism of heat transfer in moving bed heat exchangers, in which heat transfer takes place between the solid particle stream and the fluid. This type of heat exchanger is widely used in energy-intensive industries. The influence of tube shape, particle outlet velocity, and diameter on particle movement and heat transfer efficiency were investigated. Modelling was performed for five different geometric tube shapes, such as circular, elliptical, and flat elliptical, using the discrete element method [93]. The model was validated by comparing the authors’ results with experimental results from the literature [94]. The main contribution of the research was the visualisation of heat transfer parameters and solid particle motion for different tube shapes. The particle velocity distribution around the tubes, the contact time of the particles with the tube, and the heat transfer coefficient as a function of the output velocity of the particles were presented. The heat transfer coefficient was also influenced by the particle size; the smaller the particles, the higher the value of the coefficient. The authors concluded that the elliptical tube was best suited for use in moving bed heat exchangers as it demonstrated the best particle motion and heat transfer properties.

The next article, authored by Létal et al. [95] and entitled “Nonlinear Finite Element Analysis-Based Flow Distribution and Heat Transfer Model”, also dealt with fluid flow and heat transfer in large heat exchangers in the process and energy industry. The CFD method, which can be very computationally intensive, is most often used to model various types of heat transfer units, such as compact heat exchangers [96], cross-flow heat exchangers with elliptical tubes [97], or plate solar collectors [98]. In this paper, a simplified model using the finite element method was developed. The model calculated outlet temperatures and pressure drops on the pipe side and the shell side. It was able to handle the laminar and turbulent flow. The model was used for two types of heat exchangers. The results were compared with data from the literature [99], with the results of a commercial computer program [100] and with data from an existing energy plant. Visualisations of temperature profiles for hot and cold streams, in addition to fluid velocities within the exchanger, were presented. The authors argued that their program was easier to use than the commercial program and provided comparable results with less computational effort. They noted that the model still needs to be validated and improved to predict the mechanical stresses that could occur due to uneven thermal loads, which could also result in mechanical failures.

In the next paper, “Comparison of the Evaporation and Condensation Heat Transfer Coefficients on the External Surface of Tubes in the Annulus of a Tube-in-Tube Heat Exchanger”, the authors, Tang et al. [101], investigated the influence of the tube surface in a heat exchanger on the efficiency of heat transfer. They compared a tube with a smooth surface and a tube in which the dimples were arranged along the surface in a certain pattern. Several studies conducted in the past have shown that dimpled tubes provide better heat transfer than smooth tubes [102]. However, it was also observed that heat transfer in smooth tubes was better when the refrigerant was condensed on horizontal tubes [103]. Investigations were conducted using an experimental unit with a double-pipe heat exchanger, in which the evaporation and condensation of the refrigerant took place in the intermediate space (the so-called annulus). The influence of mass velocity, annulus width, and steam quality on the heat transfer

coefficient was measured. The results showed that the heat transfer coefficient increases with mass velocity in both types of tubes. Compared to a smooth tube, the tube with a modified surface showed significantly improved heat transfer during fluid condensation. A slight improvement was also observed in the case of boiling under certain conditions, while under other conditions a smooth tube proved to be better. It was concluded that the modified surface used in the study could be suitable to improve heat transfer during condensation of fluid, but not to enhance the wave-like stratified flow during boiling.

In the last paper on this topic, the authors Gai et al. [104] reported on the “Critical Analysis of Process Integration Options for Joule-Cycle and Conventional Heat Pumps”. They examined different types of heat pumps and their heat integration into the process. The analysis included traditional heat pumps, such as the vapour compression heat pump (VCHP) [105] and the transcritical heat pump (TCHP) [106], in addition to a newer Joule cycle heat pump (JCHP) [107]. The aim was to determine which type of heat pump was more suitable for a specific process. The operation of heat pumps was simulated with the Petro-SIM program. To investigate the integration of the heat pump into the process, the authors used the pinch method, in particular the Grand Composite Curve. Four case studies from the food and chemical industry were analysed. The results demonstrated that the slopes of the source and sink curves in the temperature–heat flow diagram were most important for the selection of the most suitable heat pump. If the source and sink process curves are steep, it is advantageous to choose a JCHP that has a low average temperature difference of the working fluid and the source/sink. Its Coefficient of Performance (COP) is consequently higher. For processes with flat sink and source process curves, VCHP is more favourable. The smaller the difference between the inlet temperatures of the sink and the source, the higher is COP with this type of heat pump. The use of TCHP is limited to processes where the slope of the source is relatively small, and the slope of the sink is relatively large. The advantage of the approach proposed is that it allows a quick selection of a suitable heat pump based on the temperature–enthalpy diagram for a particular process.

3.2. Integrated and Newly Developed Heat Exchangers

Wang et al. [108], in their paper entitled “An Extended Grid Diagram for Heat Exchanger Network Retrofit Considering Heat Exchanger Types”, developed a new approach to heat exchanger network retrofit that determines the retrofit design and selects the most cost-effective heat exchanger types. It targeted some specific features, as noted in a recent review [49]. The approach is based on the pinch method and uses the visualisation of an extended grid diagram previously developed by Yong et al. [109] to identify possible alternatives for improving the network. The method developed for this Special Issue allows choosing between six common industrial types of heat exchangers and estimates their capital cost. In addition to graphical methods, mathematical programming (MP) can also be used for a similar purpose, as shown by Soršak and Kravanja [110], who developed a mathematical model for network synthesis including the selection of heat exchanger types. However, as the presented paper demonstrated, selection of heat exchanger types for the retrofit should consider that the temperatures of the process streams should be within the temperature ranges applicable for each of the six types of heat exchangers. For this reason, the calculated heat transfer area is required to be within the recommended area range of the specific exchanger type. For the identified alternative retrofit plans, the investment in heat exchangers and the utility cost were assessed, and the optimum retrofit design was selected. The implementation of the proposed methodology to a network with six hot and one cold streams was presented based on the problem presented by Yong et al. [111]. The SRIGD-STR (Shifted Retrofit Thermodynamic Grid Diagram with the Shifted Temperature Range of Heat Exchangers) appears to provide valuable visualisation, representing a considerable advantage compared to MP for retrofitting heat exchanger networks (HENs). A reduction in utility cost was achieved, while the right choice of heat exchanger type enabled relatively low investment cost.

In the next article, written by Langner et al. [112] and entitled “A Framework for Flexible and Cost-Efficient Retrofit Measures of Heat Exchanger Networks”, the design of a retrofitted heat exchanger

network was discussed, taking into account uncertain input data. Uncertainty is an important aspect that influences the flexibility of the network, which should operate optimally even with fluctuating input data. The design of processes under uncertainty conditions is a significant challenge because a process model must be solved for several scenarios at the same time [113]. The presented model was extensive, and the computational effort for its solution can be high. Langner et al. [112] proposed a multi-step methodology in which they reduced the complexity of the problems they addressed in each step. The application of the methodology was demonstrated using the example of a network with two hot and two cold streams and eight uncertain parameters, i.e., related to inlet temperatures and heat capacity flow rates. The procedure started with the initial structure of the network, for which several reconstruction proposals were derived using graphical methods, with the aim of reducing the consumption of the hot utility. The flexibility of the given retrofit proposals was checked, and alternatives that did not reach the required value of the flexibility index were rejected. For feasible alternatives, critical points were determined using methods from the literature [114]. By considering critical points, a multi-period optimisation mixed-integer nonlinear programming (MINLP) problem that selects the network retrofit proposal with the lowest total annual cost was solved. Finally, the flexibility of the selected solution was reviewed. In the proposed methodology, graphical methods to generate alternative retrofit proposals and mathematical programming methods to select an optimal design of heat exchanger network were combined. They improved and automated the procedure for determining critical points. The authors suggested that their methodology could be suitable for retrofitting larger industrial networks.

The synthesis of heat exchanger networks (HENs) is usually performed separately from utility system design. The authors of the third article within this topic, Sheng et al. [115], pointed out the advantage of simultaneous synthesis of a heat exchanger network and a steam generation system in their paper entitled “Simultaneous Synthesis of Heat Exchanger Networks Considering Steam Supply and Various Steam Heater Locations”. The steam generation system was based on the Rankine cycle, which generates multi-level saturated and superheated steam, and the power [116]. The authors of this SI paper chose a multi-stage superstructure of a HEN as a basis, which they combined with a utility system. The mathematical model of a composite system corresponded to the MINLP optimisation model, which contained mass and energy balances, feasibility constraints for the temperature and utility system, and an objective function based on the total annual cost. Binary variables were used to select the heat matches; continuous variables represented temperatures, heat flows, surface areas of heat exchangers, amounts of generated steam, and power. The developed model was illustrated using a case study with four hot and four cold streams connected to a Rankine steam system. The selection of multi-level steams and their use at the end of the streams and/or between the stages allowed greater flexibility in optimising steam distribution, power generation, and fuel consumption. Better economic parameters of the overall system can be achieved. The simultaneous synthesis of the network and the utility system makes it possible to establish interactions between the investments, the fuel cost, and the revenues from the electricity generated, leading to better solutions than if the two systems were considered separately.

Haber–Bosch ammonia synthesis is a well-established mature technology, but is still a challenge due to the demanding operating conditions and the highly exothermic reaction that requires an efficient heat transfer system. Processes for the synthesis of ammonia under milder conditions and through more environmentally friendly reaction paths are under development [117]. Reactors with built-in heat recovery systems are most commonly used for traditional ammonia synthesis [118], in which hot reaction products heat the reactants to the required temperature. The authors of the final paper in this theme, Tovazhnyanskyy et al. [52], reported on “Optimal Design of Welded Plate Heat Exchanger for Ammonia Synthesis Column: An Experimental Study with Mathematical Optimisation”. They investigated heat transfer in a plate heat exchanger with a specially welded construction for use in ammonia synthesis. Plate heat exchangers (PHEs) are one of the high-efficiency types of compact heat exchangers with intensified heat transfer [119]. The main construction features and principles of

operation and design for PHE have been well discussed in publications (see, e.g., Klemeš et al. [120]). The exchanger consists of round, corrugated plates on which criss-cross channels are arranged to allow cross-flow of streams. The authors carried out an experiment in a laboratory to determine the correlations between heat transfer and pressure drop in a single-pass heat exchanger at high temperature and high pressure. With this data, they were able to develop a mathematical model for the design and optimisation of individual parts of the heat exchanger with a multiple-pass flow regime. The model was validated on an industrial device that confirmed better heat transfer properties than the tubular heat exchanger commonly used in ammonia synthesis. They carried out an optimisation of the exchanger surface, in which the height of a rib and the number of passes were optimisation variables. The validity of this model was confirmed by the results of industrial tests performed with the prototype WPHE (Welded Plate Heat Exchanger) installed in the operating column of ammonia synthesis at temperatures of about 500 °C and pressure of about 32 MPa. The tests confirmed the reliability of WPHE and its efficiency compared to a tubular heat exchanger. It has a significantly lower weight and occupies a smaller volume, which increases the ammonia production capacity by up to 15%. In addition, it has a higher heat transfer efficiency. The developed optimisation model allows for the optimal design of the exchanger plates and flow regime for specific operating conditions in an ammonia synthesis reactor.

3.3. Integration of Renewables

Many companies have sought replacements for fossil fuels from renewable sources in steam production to reduce CO₂ emissions. It has been shown that in powdered milk production, almost 100% of energy could be supplied from renewables [121]. In the first article on this theme, entitled “Renewable Energy Integration for Steam Supply of Industrial Processes—A Food Processing Case Study”, Hechelmann et al. [122] presented in detail several alternative technologies for steam generation using renewable sources, e.g., biogas and biomethane boilers, solid biomass boilers, fuel cells, micro gas turbine, solar panels, and heat pumps. The research was conducted for a plant producing wet animal food. Most of the steam was used for sterilisation. Batch production with large fluctuations in steam consumption is typical for such plants, so a dynamic simulation was performed for each technology using the MATLAB/Simulink program. Steam production with two natural gas boilers was considered as a reference case. Authors designed alternative renewable technologies; assessed the capital cost, energy cost, and CO₂ emissions; and compared them to a reference case. The results of the analysis showed that the highest reduction of CO₂ emissions (approx. 64%) compared to the reference case would be achieved with a biomass boiler in combination with a biogas backup boiler to cover peak steam demands. Biomass has a low carbon footprint, and a low price; the increase in energy costs, in this case, was about 28%. The smallest increase in energy costs (6.6%) compared to the reference case was achieved with the use of solar collectors, but the reduction in emissions was very small. The use of fuel cells was associated with the largest increase in energy costs due to high investment and low thermal efficiency. The authors concluded that a biomass boiler, in combination with a steam storage tank, represents a reasonable compromise between the reduction of CO₂ emissions and the increase in energy production cost.

The next article on this topic was a review paper, “Operational Management Implemented in Biofuel Upstream Supply Chain and Downstream International Trading: Current Issues in Southeast Asia”, written by Hoo et al. [123]. The authors provided an overview of methods for strategic, tactical, and operational decision making in biofuel supply chain planning. On the upstream side, important decisions include biomass cultivation, availability, harvesting, the modes of transport, pretreatment and processing, product storage, distribution and inventories, and selection of locations. The methods considered in the literature use mathematical programming [124], heuristic approaches [125], and multi-objective optimisation [126] to optimise the biofuel supply chain. The downstream side includes, in particular, international trade in biomass and biofuels, in which there is considerable uncertainty, especially regarding prices and demand. Analyses of various scenarios, including pessimistic and

optimistic situations, are common. It is important to include the impact of different policy instruments and measures on the international flow of biofuels, in addition to the barriers and drivers, in the optimisation models of regional and global biomass and biofuel supply chains. The goal is usually to maximise economic efficiency, but it is also necessary to optimise the overall footprint, which takes into account not only economic but also environmental and social impacts. The authors analysed the bioenergy situation in Malaysia, Indonesia, and Thailand in more detail. These countries have various sources of biomass (palm oil, cassava, sugar cane), and their governments employ several measures to encourage the increased use of biofuels in transportation, industry, electricity, and commercial uses. The authors concluded that sustainable biofuel supply chain planning requires a comprehensive approach and interdisciplinary research that enable appropriate policy decisions for sustainable resource use, reduced environmental impact, improved energy security, and economic growth.

In the article entitled “Determination of Various Parameters during Thermal and Biological Pretreatment of Waste Materials”, the authors Hren et al. [127] examined how the pretreatment of waste materials affects their further conversion into useful products, such as biofuels and biofertilisers. With a suitable pretreatment, it is possible to increase the efficiency of waste recycling and improve the circular use of resources [128]. Two waste materials—sewage sludge and riverbank grass—and their mixtures were examined by applying thermal pretreatment at lower and higher temperatures, and biological pretreatment with the addition of cattle rumen enzyme at a lower temperature. Various parameters in the liquid phase (e.g., the content of nutrients N, P, and K) before and after pretreatment were measured, in addition to the concentrations of CH₄, CO₂, and H₂S in the gas phase after pretreatment. The results of the experiments showed that thermal and biological pretreatment were most favourable at a lower temperature of 38.6 °C. The potassium and phosphorus concentrations increased in all substrates after pretreatment. The pretreatment of the grass and sludge mixture showed the highest concentrations of potassium compounds. The highest concentration of phosphorus was found in the pre-treated sludge. The total nitrogen content also increased in most cases during pretreatment, with the highest total nitrogen content found in the samples of sludge and its mixtures with grass. Analyses of the obtained gas phase show that the biological pretreatment of the sludge was most favourable at a temperature of 38.6 °C because it results in the highest concentration of methane and the lowest concentration of H₂S. The study suggested that the choice of the pretreatment process for waste material depends on the intended further use because the pretreatment influences the quality of the product made from waste material.

In the final paper on this topic, “Biowaste Treatment and Waste-To-Energy—Environmental Benefits”, the authors Pavlas et al. [129] compared the environmental impacts of three well-developed biowaste processing technologies—composting [130], fermentation [131], and incineration of biowaste combined with residual municipal solid wastes [132]. Global Warming Potential (GWP) was used as a criterion for assessing the environmental impact [133]. The results showed that all of the studied technologies reduced greenhouse gas emissions, which means that the overall change in GWP for each technology was negative. The smallest reduction in GWP was shown for composting technology, which was the least costly and investment intensive. By fermenting biowaste, an almost four-fold reduction in greenhouse gas emissions was achieved compared to composting. The result of the incineration of bio-waste as a component of the residual municipal waste depends on the ratio of heat and electricity generated in the cogeneration unit because heat generation entails a greater reduction in GWP than electricity generation. If the incineration plant mainly produces heat for district heating, the reduction in GWP would be greater than for fermentation. If the primary production were electricity, the reduction in GWP would be smaller than for fermentation. The authors concluded that if heat utilisation is ensured, it is best to incinerate biowaste as a part of the residual municipal solid waste. Otherwise, from a greenhouse gas emissions perspective, it is better to collect biowaste separately and process it by fermentation.

3.4. Roles in Economic and Environmental Sustainability

In energy-intensive plants that run on fossil fuels, it is essential to reduce greenhouse gas emissions. This can be achieved by introducing technologies for capture, utilisation, and storage of CO₂ for such plants. In the first article on this topic, entitled “Techno-Economic and Environmental Evaluations of Decarbonized Fossil-Intensive Industrial Processes by Reactive Absorption and Adsorption CO₂ Capture Systems”, the authors Cormos et al. [134] analysed two technologies. The first was a well-known reactive gas-liquid absorption, where CO₂ is absorbed in a solvent such as Methyl-DiEthanol-Amine (MDEA) [135]. Another technology was a newer reactive gas–solid adsorption system, in which CO₂ is adsorbed onto solid calcium oxide, followed by thermal decomposition of the resulting calcium carbonate [136]. The authors conducted an analysis of techno-economic and environmental indicators for the integration of decarbonisation technologies into various processes, such as coal-based power generation, and steel and cement production. They compared several indicators, e.g., specific capital investment; production costs of electricity, steel, or cement; plant emissions; power consumption; power output; and avoided CO₂ cost. The results showed that by integrating so-called decarbonisation technologies (more correctly decarbonisation emissions technologies), CO₂ emissions were reduced by up to 90% compared to conventional plants without decarbonisation. However, the investment was higher, the efficiency lower, and the cost of produced electricity, steel, or cement higher. According to economic indicators, the use of pre-combustion capture technology is more favourable than post-combustion capture. Life Cycle Analysis showed that decarbonisation reduces the value of the Global Warming Potential, while other environmental indicators can increase, e.g., acidification, eutrophication, and toxicity. In the industrial processes studied in this paper, the technology of capturing CO₂ by adsorption on solid calcium sorbent proved to be technologically and economically more favourable than the gas–liquid carbon capture system.

In the next article, Castor et al. [137] conducted “A Comparative Techno-Economic Analysis of Different Desalination Technologies in Off-Grid Islands”. The authors compared the technical and economic properties of four desalination technologies to produce drinking water from seawater. These are multi-effect distillation, multi-stage flash, mechanical vapour compression, and reverse osmosis. These processes need a reliable energy source, and it is appropriate to integrate them with the energy production system, particularly on islands that are not connected to the power grid. The use of diesel generators is widespread on islands, but the use of renewable sources for water desalination, such as a combination of solar photovoltaic and reverse osmosis, is encouraged [138]. The authors used a system that combines a renewable source (photovoltaic) and a fossil source (diesel) while using a battery-based energy storage system. Using computer programs, the authors of this SI paper optimised the integrated energy–water system for a period of one year, taking into account hourly fluctuations in water and energy consumption. The cost of power, the cost of water, and the net present value of the costs of the various desalination technologies were calculated. The uncertainty in energy and water consumption was taken into account with a stochastic Monte Carlo simulation. The results show that diesel-based power production would dominate on smaller islands because of lower capital cost. At low fuel prices, distillation and flash desalination technologies would be suitable. If the fuel price is high, and a renewable source is preferred, the use of reverse osmosis could be preferred. This is especially true for large islands, where energy and water requirements are higher and high investment costs are offset by lower fuel consumption in reverse osmosis. Forecasts for 30 y ahead indicate that the cost of water produced by reverse osmosis would be the lowest of all of the technologies studied, while energy costs are expected to remain comparable for all technologies.

Aluminium production is an important energy consumer and emitter of CO₂ emissions, although the energy efficiency of this process has improved significantly [139]. Gomilšek et al. [140], in their article entitled “Carbon Emissions Constrained Energy Planning for Aluminum Products”, conducted planning and optimisation for various sources of electricity used in the production of aluminium products, such as slugs and evaporator panels. Fossil fuel, renewable, and nuclear energy sources were considered in their study. Electricity mixes should be derived from different sources that do not exceed

the CO₂ emission values required by the legal framework. The first technique for CO₂ Constrained Energy Planning (CCEP) is the insight-based graphical targeting approach referred to as CEPA (Carbon Emission Pinch Analysis) and developed in 2007 by Tan and Foo [141]. CEPA uses a graphical approach based on the principles of traditional PA [142]. The numerical targeting approach with the cascade analysis methodology was originally developed for resource conservation networks [143] and had its roots in the Problem Table Algorithm, and the Heat Cascade developed for Maximum Heat Recovery networks [144]. The numerical targeting approach was further extended to determine the amount of low-carbon-emissions energy required to achieve the specified emission limits. In the case of the production of specific aluminium products, the authors found that about 20% of the energy should be replaced by sources with zero or low CO₂ emissions to achieve the prescribed target emission. Optimal source mixes for power generation that would ensure emission target values at minimum cost were identified using an optimisation approach. In the studies of different scenarios, fossil fuel sources and nuclear energy were selected. The renewable sources were not beneficial due to the still higher price of renewable energy. The cost of power generated from an optimal mix of resources would be 26% higher than for the current power mix. However, the prescribed CO₂ emission targets would be met. Finally, the authors summarised the advantages and disadvantages of the approaches used and recommended the development of combined methods that exploit the advantages of each approach.

Yang et al. [145], the authors of the article entitled “A Method for Analysing Energy-Related Carbon Emissions and the Structural Changes: A Case Study of China from 2005 to 2015”, used Sankey diagrams to show the structure of energy consumption and carbon emissions resulting from the consumption of fossil fuels in China. Sankey diagrams were used to analyse China’s energy consumption in 2005 [146]. However, calculating the components of the TRO indicator as proposed by the authors allowed trends to be identified, such as changes in total carbon emissions for individual sectors (T), relative growth in carbon emissions (R), and changes in the ratio of carbon emissions from a particular sector to total emissions (O). The visualisation of energy consumption and the resulting carbon emissions shows that coal is the predominant energy source and accounts for the largest share of emissions. Calculations of the individual components of the TRO index show that the share of coal in China’s energy structure has decreased and natural gas has become an important energy source. The use of renewable resources, particularly wind energy, is developing. This paper concluded that the boom in the industry, the construction of infrastructure, and the rise in living standards are slowing the decline in coal consumption and the decarbonisation of the country. The methodology developed by the authors analyses the responsibility of the individual sectors for carbon emissions by visualisation and evaluates changes and trends using the TRO indicator. Thus, decision-makers can design more effective measures and solutions to reduce emissions.

Acrylic acid is an important chemical intermediate, used in particular by the polymer and textile industries to produce various end products. Premllal and Lokhat [147] report on simulation and design of acrylic acid production with a focus on its reactor system in an article entitled “Reducing Energy Requirements in the Production of Acrylic Acid: Simulation and Design of a Multitubular Reactor Train”. The main objectives were more detailed design and optimisation of the reactor train and reduction of energy consumption. Two reaction steps were considered: the oxidation of propylene to acrolein and the oxidation of acrolein to acrylic acid. A plug-flow reactor model was used in Aspen Plus to simulate multitubular reactors with appropriate reaction kinetics for propylene oxidation [148] and for acrolein oxidation [149]. Side reactions produce CO₂ and acetic acid, and it is important to select a catalyst with high selectivity. Bismuth molybdate and vanadium molybdate proved to be the most efficient catalysts for this application [150]. Authors of this SI paper determined the operating and design parameters of the reactor system, such as the number of tubes, the length of the reactor, the flow and temperature of the heat transfer fluid, the pressure drop, and the heat transfer area. To reduce energy consumption, the authors introduced an inert pre-heating zone into the first reactor. The heating medium used is molten salt, which absorbs the heat of the exothermic reaction and cools down again when the feed stream is preheated. Cold air is introduced into the outlet stream of the first

reactor, which lowers the inlet temperature in the second reactor and increases the heat absorption capacity in this reactor. The authors concluded that it is possible to reduce energy consumption by about 7 MW with the measures and optimisations they proposed.

A new idea based on the exergy concept was developed in the article “Thermodynamics-Based Process Sustainability Evaluation” by Varbanov et al. [151], who proposed the concepts of Exergy Profit and Footprint. All industrial and other human activities involve non-spontaneous processes and exergy is necessary to drive them. The authors developed the framework based on the concepts of exergy assets and liabilities for driving the processes. The formulated Exergy Profit criterion was demonstrated as an appropriate quantitative indicator of the sustainability contribution of the assessed processes. The concept of exergy is not as widespread as deserved because it is more abstract and often more difficult to understand, even for engineers, although it can be efficiently combined with energy and economic methods to comprehensively evaluate process systems [152]. The difficulty in its application can be seen from [153], who used exergy in their model but with a focus on the techno-economic optimisation of embedded multiple criteria, including environmental. Exergy assets are associated with the ability of process streams to extract useful work and drive the processes, including energy generation. Exergy liabilities represent the demands and deficits of exergy that have to be supplied to the processes. Exergy Profit and Footprint are calculated by balancing the assets and liabilities. The surplus of the assets over the liabilities results in the Exergy Profit whereas, in the case of deficit, an Exergy Footprint results. The sustainability contribution is higher for a higher value of the Exergy Profit. The concepts were illustrated with two examples from different problem domains. These were acetic acid waste recovery and reuse, in addition to the evaluation of municipal solid waste treatment options. This clearly demonstrated the applicability of the method to a wide range of systems.

4. Suggestions for Research Focus and Development

4.1. Social Impact of Novel and Fast-Developing Methodologies

Although sustainability is a critical element of advanced system design, the consideration of social factors remains limited compared to economic and environmental factors. Design with optimised economic and environmental performance would be too idealised to be fully accomplished without regard for social impacts that could overturn the situation. The importance of social dimensions and socio-technical aspects for the broader achievement of climate and energy targets at the local level were also discussed by Balest et al. [154]. Garcia-Casals et al. [155] stated that energy–economy transitions do not occur in isolation; they are embedded in the wider economy, which, in turn, is embedded in social and environmental systems. The overall system is complex and involves many sources of feedback between the subsystems leading to the final outcome. In addition to advanced technological solutions, future research should concentrate on social aspects, as a fuller understanding could enhance the effectiveness of system design.

4.2. Energy Storage

A crucial issue for both the deeper penetration of renewables with fluctuating performance, such as PV and wind and resolving peak and off-peak demands, is energy storage. Recently numerous interesting ideas have been published. Researchers from the Massachusetts Institute of Technology presented a noteworthy study [156] that analysed economic and environmental variability of the reuse of e-car batteries as stationary batteries for power storage. Similar contributions to circular economies should be the subject of future design development and implementation. The rapid development of advanced batteries is also taking place [157], for example, the development of nanographene batteries. Improving and reducing the cost of batteries represents a major research challenge that has attracted significant investment.

4.3. Implementation of IoT and Advanced Technologies

IoT and other advanced technologies have made numerous important contributions. As an example, in addition to wasting a source of energy, leaked natural gas—mostly CH₄—is a powerful GHG and a significant contributor to climate change [158]. A number of options have been proposed by leading oil companies [159] as next-generation detection devices, deployed from space orbit, from traditional high-altitude planes, and, most recently, from low-cost drones operating close to the ground; these latter devices are able to perform for long periods in self-managed automatic mode. Artificial intelligence, connected sensors, and data analytics will play an increasingly significant role in energy system design [160], renewable energy integration [161], predictive maintenance [162], and policy formulation. These approaches are currently being implemented in renewable energy technology companies [160].

4.4. Non-Traditional Engineering Solutions

As an example of non-tradition engineering solutions, used landfills have emerged as promising battery storage sites to back up renewable energy. Similar to solar panels, batteries may present a new revenue stream for closed landfills. This has been reported by Bandyk [163], with projects underway at several sites in the USA.

5. Conclusions

This review targeted novel developments in a rapidly developing field and was helpfully supported by a special topical issue presented in 2019 at the PRES 19 conference (Process Integration, Modelling and Optimisation for Energy Saving and Pollution Reduction), from which we selected 20 important papers. This conference was held at a venue on the Greek Island of Crete, benefiting from a clean island environment and serving as an intensive cross-fertilisation meeting of leading scientists from more than 50 countries. As an important extension to reviewing the selected Special Issue papers, this review article also provided a wider overview of a number of the most recent developments in heat integration and heat transfer; integrated and newly developed heat exchangers; integration of renewables; and roles in economic and environmental sustainability. Topics relating to emerging tools for the design of energy systems to increase economic and environmental sustainability were considered in the selection of the contributions. A wide variety of system design tools have been proposed and targeted for different energy-related issues. This review suggested that the achievement of a sustainable energy system design relies on social aspects receiving greater research attention, thus placing them on a level equal to that of economic and environmental concerns. The consideration of social impacts, including behaviour analysis, could further enhance the practicality of the tools for system design.

Author Contributions: Conceptualisation, Y.V.F. and J.J.K.; methodology, J.J.K. and Y.V.F.; formal analysis, Z.N.P., Y.V.F., J.J.K.; resources, Y.V.F., J.J.K., Z.N.P.; writing—original draft preparation, Y.V.F., Z.N.P., J.J.K.; writing—review and editing, Y.V.F., J.J.K., Z.N.P.; visualisation, Y.V.F., J.J.K.; supervision, project administration, funding acquisition J.J.K. All authors have read and agreed to the published version of the manuscript.

Funding: This research was funded by the EC supported project Sustainable Process Integration Laboratory – SPIL, grant number CZ.02.1.01/0.0/0.0/15_003/0000456 by Czech Republic Operational Programme Research, Development, and Education, Priority 1: Strengthening capacity for quality research under the collaboration agreement with the University of Maribor, Slovenia.

Conflicts of Interest: The authors declare no conflict of interest.

References

1. Hong, J.H.; Kim, J.; Son, W.; Shin, H.; Kim, N.; Lee, W.K.; Kim, J. Long-term energy strategy scenarios for South Korea: Transition to a sustainable energy system. *Energy Policy* **2019**, *127*, 425–437. [[CrossRef](#)]
2. Qin, J.; Liu, Y.; Grosvenor, R.; Lacan, F.; Jiang, Z. Deep learning-driven particle swarm optimisation for additive manufacturing energy optimisation. *J. Clean. Prod.* **2020**, *245*, 118702. [[CrossRef](#)]

3. Liu, S.; Yuan, J.; Deng, W.; Luo, M.; Xie, Y.; Liang, Q.; Zou, Y.; He, Z.; Wu, H.; Cao, Y. High-efficiency organic solar cells with low non-radiative recombination loss and low energetic disorder. *Nat. Photonics* **2020**, *14*, 300–305. [CrossRef]
4. Ochoa, G.V.; Rojas, J.P.; Forero, J.D. Advance Exergo-Economic Analysis of a Waste Heat Recovery System Using ORC for a Bottoming Natural Gas Engine. *Energies* **2020**, *13*, 267. [CrossRef]
5. Marquand, J.F.; Mavromatidis, G.; Evins, R.; Carmeliet, J. Comparing different temporal dimension representations in distributed energy system design models. *Energy Proc.* **2017**, *122*, 907–912. [CrossRef]
6. Weinand, J.M.; McKenna, R.; Mainzer, K. Spatial high-resolution socio-energetic data for municipal energy system analyses. *Sci. Data* **2019**, *6*, 1–6. [CrossRef]
7. IEA. Renewables. 2020. Available online: www.iea.org/fuels-and-technologies/renewables (accessed on 4 June 2020).
8. Larsen, M.A.D.; Drews, M. Water use in electricity generation for water-energy nexus analyses: The European case. *Sci. Total Environ.* **2019**, *651*, 2044–2058. [CrossRef]
9. UCSUSA. Benefits of Renewable Energy Use. 2017. Available online: www.ucsusa.org/resources/benefits-renewable-energy-use (accessed on 2 June 2020).
10. Fan, Y.V.; Klemeš, J.J.; Ko, C.H. Bioenergy carbon emissions footprint considering the biogenic carbon and secondary effects. *Int. J. Energy Res.* **2020**. [CrossRef]
11. Schmidt, O.; Melchior, S.; Hawkes, A.; Staffell, I. Projecting the future levelized cost of electricity storage technologies. *Joule* **2019**, *3*, 81–100. [CrossRef]
12. Lazard. Levelized Cost of Energy and Levelized Cost Of Storage 2019. 2019. Available online: www.lazard.com/perspective/lcoe2019 (accessed on 1 June 2020).
13. Perera, A.T.D.; Nik, V.M.; Wickramasinghe, P.U.; Scartezzini, J.L. Redefining energy system flexibility for distributed energy system design. *Appl. Energy* **2019**, *253*, 113572. [CrossRef]
14. WNA (World Nuclear Association). Comparison of Lifecycle Greenhouse Gas Emissions of Various Electricity Generation Sources. 2011. Available online: www.world-nuclear.org/uploadedFiles/org/WNA/Publications/Working_Group_Reports/comparison_of_lifecycle.pdf (accessed on 4 June 2020).
15. Jin, Y.; Behrens, P.; Tukker, A.; Scherer, L. Water use of electricity technologies: A global meta-analysis. *Renew. Sustain. Energy Rev.* **2019**, *115*, 109391. [CrossRef]
16. Mekonnen, M.M.; Gerbens-Leenes, P.W.; Hoekstra, A.Y. The consumptive water footprint of electricity and heat: A global assessment. *Environ. Sci. Water Res. Technol.* **2015**, *1*, 285–297. [CrossRef]
17. Asdrubali, F.; Baldinelli, G.; D’Alessandro, F.; Scrucca, F. Life cycle assessment of electricity production from renewable energies: Review and results harmonisation. *Renew. Sustain. Energy Rev.* **2015**, *42*, 1113–1122. [CrossRef]
18. Amponsah, N.Y.; Troldborg, M.; Kington, B.; Aalders, I.; Hough, R.L. Greenhouse gas emissions from renewable energy sources: A review of lifecycle considerations. *Renew. Sustain. Energy Rev.* **2014**, *39*, 461–475. [CrossRef]
19. EEA. Renewable Energy Impacts Dashboard. 2019. Available online: www.eea.europa.eu/themes/energy/renewable-energy/renewables-crucial-for-eu-decarbonisation (accessed on 4 June 2020).
20. Lazard. Lazard’s Levelised Cost of Energy Analysis—Version 11.0. 2019. Available online: www.lazard.com/media/450337/lazard-levelized-cost-of-energy-version-110.pdf (accessed on 2 June 2020).
21. Lazard. Lazard’s Levelised Cost of Energy Analysis—Version 12.0. 2019. Available online: www.lazard.com/media/450784/lazards-levelized-cost-of-energy-version-120-vfinal.pdf (accessed on 2 June 2020).
22. Taylor, M. Cheaper than coal: IRENA’s Comprehensive Report on Cost Declines all Renewables Categories. 2019. Available online: energypost.eu/cheaper-than-coal-irenas-comprehensive-report-on-cost-declines-all-renewables-categories/ (accessed on 2 June 2020).
23. Fiksel, J. Designing resilient, sustainable systems. *Environ. Sci. Technol.* **2003**, *37*, 5330–5339. [CrossRef] [PubMed]
24. Kambhampati, U.S. The Whole Idea of Global Value Chains will be Reconsidered After Coronavirus. 2020. Available online: theconversation.com/the-whole-idea-of-global-value-chains-will-be-reconsidered-after-coronavirus-137132 (accessed on 4 June 2020).
25. IEA. Clean Energy Progress after the Covid-19 Crisis will need Reliable Supplies of Critical Minerals. 2020. Available online: www.iea.org/articles/clean-energy-progress-after-the-covid-19-crisis-will-need-reliable-supplies-of-critical-minerals#reference-4 (accessed on 4 June 2020).

26. Statista. Major Countries in Worldwide Zinc Mine Production from 2010–2019. 2020. Available online: www.statista.com/statistics/264634/zinc-production-by-country/ (accessed on 4 June 2020).
27. Statista. Major Countries Silicon Production from 2014–2019. 2020. Available online: www.statista.com/statistics/268108/world-silicon-production-by-country// (accessed on 4 June 2020).
28. IEA. Reductions of Electricity Demand after Implementing Lockdown Measures in Selected Countries, Weather Corrected, 0 to 68 Days. 2020. Available online: www.iea.org/data-and-statistics/charts/reductions-of-electricity-demand-after-implementing-lockdown-measures-in-selected-countries-weather-corrected-0-to-68-days/ (accessed on 4 June 2020).
29. IEA. Energy Investment is Set to Fall by One Fifty in 2020 due to the Covid-19 Pandemic. 2020. Available online: www.iea.org/reports/world-energy-investment-2020/key-findings#abstract (accessed on 4 June 2020).
30. Amelang, S. Negative Electricity Prices: Lockdown’s Demand Slump Exposes Inflexibility of German Power. 2020. Available online: energypost.eu/negative-electricity-prices-lockdowns-demand-slump-exposes-inflexibility-of-german-power/ (accessed on 4 June 2020).
31. Meinrenken, C.; Modi, V.; Mckeown, K.; Culligan, P. New data suggest COVID-19 is shifting the burden of energy cost to households. 2020. Available online: blogs.ei.columbia.edu/2020/04/21/covid-19-energy-costs-households// (accessed on 4 June 2020).
32. Amelang, S. Coronavirus Lockdown Pushes Up Heating Demand Across Europe—Report. 2020. Available online: www.cleanenergywire.org/news/coronavirus-lockdown-pushes-heating-demand-across-europe-report/ (accessed on 4 June 2020).
33. Kortenhorst, J. Here’s What we Know and Don’t Know about the Energy Transition. 2020. Available online: www.weforum.org/agenda/2020/04/heres-what-the-pandemic-means-for-the-energy-transition// (accessed on 4 June 2020.).
34. WARTSILA. European Responses to Covid-19 Accelerate the Electricity System Transition by a Decade. 2020. Available online: news.cision.com/wartsila-corporation/r/european-responses-to-covid-19-accelerate-the-electricity-system-transition-by-a-decade--according-t,c3090780/ (accessed on 4 June 2020).
35. BBC. Coronavirus: Domestic Electricity use up During Day as Nation Works From Home. 2020. Available online: www.bbc.com/news/technology-52331534/ (accessed on 4 June 2020).
36. Korhonen, J.; Honkasalo, A.; Seppälä, J. Circular economy: The concept and its limitations. *Ecol. Econ.* **2018**, *143*, 37–46. [CrossRef]
37. Kirchherr, J.; Reike, D.; Hekkert, M. Conceptualising the circular economy: An analysis of 114 definitions. *Resour. Conserv. Recycl.* **2017**, *127*, 221–232. [CrossRef]
38. Mayer, A.; Haas, W.; Wiedenhofer, D.; Krausmann, F.; Nuss, P.; Blengini, G.A. Measuring Progress towards a Circular Economy: A Monitoring Framework for Economy-wide Material Loop Closing in the EU28. *J. Ind. Ecol.* **2019**, *23*, 62–76. [CrossRef]
39. Moraga, G.; Huysveld, S.; Mathieux, F.; Blengini, G.A.; Alaerts, L.; Van Acker, K.; de Meester, S.; Dewulf, J. Circular economy indicators: What do they measure? *Resour. Conserv. Recycl.* **2019**, *146*, 452–461. [CrossRef]
40. Loucks, D.P.; van Beek, E. Models for Identifying and Evaluating Alternatives. In *Water Resource Systems Planning and Management*; Springer: Cham, Switzerland, 2017; pp. 73–91.
41. LLNL (Lawrence Livermore National Laboratory). Energy Flow Chart. Available online: flowcharts.llnl.gov/ (accessed on 4 June 2020).
42. Papapetrou, M.; Kosmadakis, G.; Cipollina, A.; La Commare, U.; Micale, G. Industrial waste heat: Estimation of the technically available resource in the EU per industrial sector, temperature level and country. *Appl. Therm. Eng.* **2018**, *138*, 207–216. [CrossRef]
43. Bianchi, G.; Panayiotou, G.P.; Aresti, L.; Kalogirou, S.A.; Florides, G.A.; Tsamos, K.; Christodoulides, P. Estimating the waste heat recovery in the European Union Industry. *Energy Ecol. Environ.* **2019**, *4*, 211–221. [CrossRef]
44. Klemeš, J.J.; Varbanov, P.V.; Walmsley, T.G.; Jia, X.X. New directions in the implementation of Pinch Methodology (PM). *Renew. Sustain. Energy Rev.* **2018**, *98*, 439–468. [CrossRef]
45. Klemeš, J.J.; Varbanov, P.S. Process Intensification and Integration: An assessment. *Clean Technol. Environ. Policy* **2013**, *15*, 417–422. [CrossRef]
46. Klemeš, J.J. (Ed.) *Assessing and Measuring Environmental Impact and Sustainability*; Elsevier/Butterworth-Heinemann: Oxford, UK, 2015; 559p, ISBN 978-0-12-799968-5.

47. Čuček, L.; Klemeš, J.J.; Kravanja, Z. A Review of Footprint Analysis Tools for Monitoring Impacts on Sustainability. *J. Clean. Prod.* **2012**, *34*, 9–20. [[CrossRef](#)]
48. Mann, M.E. Greenhouse Gas. 2019. Available online: www.britannica.com/science/greenhouse-gas#ref280534 (accessed on 1 June 2020).
49. Klemeš, J.J.; Wang, Q.W.; Varbanov, P.S.; Zeng, M.; Chin, H.H.; Lal, N.S.; Li, N.Q.; Wang, B.; Wang, X.C.; Walmsley, T.G. Heat transfer enhancement, intensification and optimisation in heat exchanger network retrofit and operation. *Renew. Sustain. Energy Rev.* **2020**, *120*, 109644. [[CrossRef](#)]
50. Forsberg, C.H. *Heat Transfer Principles and Applications*; Academic Press/Elsevier: Cambridge, MA, USA, 2020. [[CrossRef](#)]
51. Luo, A.; Fang, H.; Xia, J.; Lin, B.; Yiang, Y. Mapping potentials of low-grade industrial waste heat in Northern China. *Resour. Conserv. Recycl.* **2017**, *125*, 335–348. [[CrossRef](#)]
52. Tovazhnyanskyy, L.; Klemeš, J.J.; Kapustenko, P.; Arsenyeva, O.; Perevertaylenk, O.; Arsenyev, P. Optimal Design of Welded Plate Heat Exchanger for Ammonia Synthesis Column: An Experimental Study with Mathematical Optimisation. *Energies* **2020**, *13*, 2847. [[CrossRef](#)]
53. Vergara-Dietrich, J.D.; Morato, M.M.; Mendes, P.R.; Cani, A.A.; Normey-Rico, J.E.; Bordons, C. Advanced chance-constrained predictive control for the efficient energy management of renewable power systems. *J. Process Control* **2019**, *74*, 120–132. [[CrossRef](#)]
54. Alavi, S.A.; Ahmadian, A.; Aliakbar-Golkar, M. Optimal probabilistic energy management in a typical micro-grid based-on robust optimisation and point estimate method. *Energy Convers. Manag.* **2015**, *95*, 314–325. [[CrossRef](#)]
55. Mehrjerdi, H.; Rakhshani, E. Correlation of multiple time-scale and uncertainty modelling for renewable energy-load profiles in wind powered system. *J. Clean. Prod.* **2019**, *236*, 117644. [[CrossRef](#)]
56. Talaat, M.; Farahat, M.A.; Elkholy, M.H. Renewable power integration: Experimental and simulation study to investigate the ability of integrating wave, solar and wind energies. *Energy* **2019**, *170*, 668–682. [[CrossRef](#)]
57. Baum, Z.; Palatnik, R.R.; Ayalon, O.; Elmakis, D.; Frant, S. Harnessing households to mitigate renewables intermittency in the smart grid. *Renew. Energy* **2019**, *132*, 1216–1229. [[CrossRef](#)]
58. Fiedler, T. Simulation of a power system with large renewable penetration. *Renew. Energy* **2019**, *130*, 319–328. [[CrossRef](#)]
59. Draycott, S.; Sellar, B.; Davey, T.; Noble, D.R.; Venugopal, V.; Ingram, D.M. Capture and simulation of the ocean environment for offshore renewable energy. *Renew. Sustain. Energy Rev.* **2019**, *104*, 15–29. [[CrossRef](#)]
60. Wagh, M.M.; Kulkarni, V.V. Modeling and optimisation of integration of Renewable Energy Resources (RER) for minimum energy cost, minimum CO₂ Emissions and sustainable development, in recent years: A review. *Mater. Today Proc.* **2018**, *5*, 11–21. [[CrossRef](#)]
61. Al Nouss, A.; McKay, G.; Al-Ansari, T. Production of syngas via gasification using optimum blends of biomass. *J. Clean. Prod.* **2020**, *242*, 118499. [[CrossRef](#)]
62. Peng, Z.; Herfatmanesh, M.R.; Liu, Y. Cooled solar PV panels for output energy efficiency optimisation. *Energy Convers. Manag.* **2017**, *150*, 949–955. [[CrossRef](#)]
63. Bravo, R.; Ortiz, C.; Chacartegui, R.; Friedrich, D. Hybrid solar power plant with thermochemical energy storage: A multi-objective operational optimisation. *Energy Convers. Manag.* **2020**, *205*, 112421. [[CrossRef](#)]
64. Zheng, Y.; Jenkins, B.M.; Kornbluth, K.; Kendall, A.; Træholt, C. Optimisation of a biomass-integrated renewable energy microgrid with demand side management under uncertainty. *Appl. Energy* **2018**, *230*, 836–844. [[CrossRef](#)]
65. Nowdeh, S.A.; Davoudkhani, I.F.; Moghaddam, M.H.; Najmi, E.S.; Abdelaziz, A.Y.; Ahmadi, A.; Gandoman, F.H. Fuzzy multi-objective placement of renewable energy sources in distribution system with objective of loss reduction and reliability improvement using a novel hybrid method. *Appl. Soft Comput.* **2019**, *77*, 761–779. [[CrossRef](#)]
66. Jafari, A.; Khalili, T.; Ganjehlou, H.G.; Bidram, A. Optimal integration of renewable energy sources, diesel generators, and demand response program from pollution, financial, and reliability viewpoints: A multi-objective approach. *J. Clean. Prod.* **2020**, *247*, 119100. [[CrossRef](#)]
67. Rinaldi, A.; Soini, M.C.; Patel, M.K.; Parra, D. Optimised allocation of PV and storage capacity among different consumer types and urban settings: A prospective analysis for Switzerland. *J. Clean. Prod.* **2020**, *259*, 120762. [[CrossRef](#)]

68. Santibañez-Aguilar, J.E.; Castellanos, S.; Flores-Tlacuahuac, A.; Shapiro, B.B.; Powell, D.M.; Buonassisi, T.; Kammen, D.M. Design of domestic photovoltaics manufacturing systems under global constraints and uncertainty. *Renew. Energy* **2020**, *148*, 1174–1189. [[CrossRef](#)]
69. Zakaria, A.; Ismail, F.B.; Lipu, M.H.; Hannan, M.A. Uncertainty models for stochastic optimisation in renewable energy applications. *Renew. Energy* **2020**, *145*, 1543–1571. [[CrossRef](#)]
70. Aviso, K.B.; Marfori, I.A.V.; Tan, R.R.; Ubando, A.T. Optimising abnormal operations of off-grid community utility systems with fuzzy P-graph. *Energy* **2020**, *202*, 117725. [[CrossRef](#)]
71. Cuesta, M.A.; Castillo-Calzadilla, T.; Borges, C.E. A critical analysis on hybrid renewable energy modeling tools: An emerging opportunity to include social indicators to optimise systems in small communities. *Renew. Sustain. Energy Rev.* **2020**, *122*, 109691. [[CrossRef](#)]
72. Akhtari, M.R.; Shayegh, I.; Karimi, N. Techno-economic assessment and optimisation of a hybrid renewable earth-air heat exchanger coupled with electric boiler, hydrogen, wind and PV configurations. *Renew. Energy* **2020**, *148*, 839–851. [[CrossRef](#)]
73. Armin Razmjoo, A.; Sumper, A.; Davarpanah, A. Energy sustainability analysis based on SDGs for developing countries. *Energy Sources Part A Recovery Util. Environ. Eff.* **2020**, *42*, 1041–1056. [[CrossRef](#)]
74. Baldasso, E.; Mondejar, M.E.; Larsen, U.; Haglind, F. Regression Models for the Evaluation of the Techno-Economic Potential of Organic Rankine Cycle-Based Waste Heat Recovery Systems on Board Ships Using Low Sulfur Fuels. *Energies* **2020**, *13*, 1378. [[CrossRef](#)]
75. Khoshnevisan, B.; Tabatabaei, M.; Tsapekos, P.; Rafiee, S.; Aghbashlo, M.; Lindeneg, S.; Angelidaki, I. Environmental life cycle assessment of different biorefinery platforms valorising municipal solid waste to bioenergy, microbial protein, lactic and succinic acid. *Renew. Sustain. Energy Rev.* **2020**, *117*, 109493. [[CrossRef](#)]
76. Ramirez-Islas, M.E.; Güereca, L.P.; Sosa-Rodriguez, F.S.; Cobos-Peralta, M.A. Environmental assessment of energy production from anaerobic digestion of pig manure at medium-scale using life cycle assessment. *Waste Manag.* **2020**, *102*, 85–96. [[CrossRef](#)] [[PubMed](#)]
77. Longo, S.; Beccali, M.; Cellura, M.; Guarino, F. Energy and environmental life-cycle impacts of solar-assisted systems: The application of the tool “ELISA”. *Renew. Energy* **2020**, *145*, 29–40. [[CrossRef](#)]
78. Stamford, L. Life cycle sustainability assessment in the energy sector. In *Biofuels for a More Sustainable Future*; Elsevier: Amsterdam, The Netherlands; Oxford, UK; Cambridge, MA, USA, 2020; pp. 115–163.
79. Duan, C.; Chen, B. Driving factors of water-energy nexus in China. *Appl. Energy* **2020**, *257*, 113984. [[CrossRef](#)]
80. Fan, Y.V.; Tan, R.R.; Klemeš, J.J. A system analysis tool for sustainable biomass utilisation considering the Emissions-Cost Nexus. *Energy Convers. Manag.* **2020**, *210*, 112701. [[CrossRef](#)]
81. Razmjoo, A.A.; Sumper, A.; Davarpanah, A. Development of sustainable energy indexes by the utilisation of new indicators: A comparative study. *Energy Rep.* **2019**, *5*, 375–383. [[CrossRef](#)]
82. Liu, G. Development of a general sustainability indicator for renewable energy systems: A review. *Renew. Sustain. Energy Rev.* **2014**, *31*, 611–621. [[CrossRef](#)]
83. Józwiak, P.; Hercog, J.; Kiedrzyńska, A.; Badyda, K.; Olevano, D. Thermal Effects of Natural Gas and Syngas Co-Firing System on Heat Treatment Process in the Preheating Furnace. *Energies* **2020**, *13*, 1698. [[CrossRef](#)]
84. Echi, S.; Bouabidi, A.; Driss, Z.; Abid, M.S. CFD simulation and optimisation of industrial boiler. *Energy* **2019**, *169*, 105–114. [[CrossRef](#)]
85. Silva, J.; Teixeira, J.; Teixeira, S.; Preziati, S.; Cassiano, J. CFD Modeling of Combustion in Biomass Furnace. *Energy Proc.* **2017**, *120*, 665–672. [[CrossRef](#)]
86. You, S.; Ok, Y.S.; Tsang, D.C.W.; Kwon, E.; Wang, C.-H. Towards practical application of gasification: A critical review from syngas and biochar perspectives. *Crit. Rev. Environ. Sci. Technol.* **2018**, *48*, 1165–1213. [[CrossRef](#)]
87. Hancsók, J.; Kasza, T.; Visnyei, O. Isomerisation of n-C5/C6 Bioparaffins to Gasoline Components with High Octane Number. *Energies* **2020**, *13*, 1672. [[CrossRef](#)]
88. Wang, T.; Zhang, Q.; Ding, M.; Wang, C.; Li, Y.; Zhang, Q.; Ma, L. Bio-gasoline production by coupling of biomass catalytic pyrolysis and oligomerisation. *Energy Proc.* **2017**, *105*, 858–863. [[CrossRef](#)]
89. Sauciu, A.; Abosteif, Z.; Weber, G.; Potetz, A.; Rauch, R.; Hofbauer, H.; Schaub, G.; Dumitrescu, L. Influence of operating conditions on the performance of biomass-based Fischer-Tropsch synthesis. *Biomass Convers. Biorefin.* **2012**, *2*, 253–263. [[CrossRef](#)]

90. Kwon, E.E.; Kim, Y.T.; Kim, H.J.; Lin, K.Y.L.; Kim, K.H.; Lee, J.; Huber, G.W. Production of high-octane gasoline via hydrodeoxygenation of sorbitol over palladium-based bimetallic catalysts. *J. Environ. Manag.* **2018**, *227*, 329–334. [[CrossRef](#)]
91. Huber, G.W.; Chedda, J.N.; Barre, C.J.; Dumestic, J.A. Production of liquid alkanes by aqueous-phase processing of biomass-derived carbohydrates. *Science* **2005**, *308*, 1446–1450. [[CrossRef](#)] [[PubMed](#)]
92. Tian, X.; Yang, J.; Guo, Z.; Wang, Q.; Sundén, B. Numerical Study of Heat Transfer in Gravity-Driven Particle Flow around Tubes with Different Shapes. *Energies* **2020**, *13*, 1961. [[CrossRef](#)]
93. Bartsch, P.; Zunft, S. Granular flow around the horizontal tubes of a particle heat exchanger: DEM-simulation and experimental validation. *Solar Energy* **2019**, *182*, 48–56. [[CrossRef](#)]
94. Liu, J.; Yu, Q.; Peng, J.; Hu, X.; Duan, W. Thermal energy recovery from high-temperature blast furnace slag particles. *Int. Commun. Heat Mass Transfer* **2015**, *69*, 23–28. [[CrossRef](#)]
95. Létal, T.; Turek, V.; Babička Fialová, D.; Jegla, Z. Nonlinear Finite Element Analysis-Based Flow Distribution and Heat Transfer Model. *Energies* **2020**, *13*, 1664. [[CrossRef](#)]
96. Zhou, J.; Ding, M.; Bian, H.; Zhang, Y.; Sun, Z. Characteristics of flow distribution in central-type compact parallel-flow heat exchangers with modified inlet and header. *Appl. Therm. Eng.* **2020**, *166*, 114636. [[CrossRef](#)]
97. Łopata, S.; Ocloń, P.; Stelmach, T. Investigation of flow non-uniformities in the cross-flow heat exchanger with elliptical tubes. *E3S Web Conf.* **2019**, *108*, 01009. [[CrossRef](#)]
98. Karvounis, P.; Koubogiannis, D.; Hontzopoulos, E.; Hatziapostolou, A. Numerical and experimental study of flow characteristics in solar collector manifolds. *Energies* **2019**, *12*, 1431. [[CrossRef](#)]
99. Pismennyi, E.; Polupan, G.; Carvajal-Mariscal, I.; Sanchez-Silva, F.; Piore, I. Examples of calculations. In *Handbook for Transversely Finned Tube Heat Exchanger Design*; Academic Press: Cambridge, MA, USA, 2016; Chapter 7; pp. 83–106.
100. ANSYS, Inc. *ANSYS Fluent User's Guide, Version 2019 R3*; ANSYS, Inc.: Canonsburgh, PA, USA, 2019.
101. Tang, W.; Kukulka, D.; Li, W.; Smith, R. Comparison of the Evaporation and Condensation Heat Transfer Coefficients on the External Surface of Tubes in the Annulus of a Tube-in-Tube Heat Exchanger. *Energies* **2020**, *13*, 952. [[CrossRef](#)]
102. Shafae, M.; Mashouf, H.; Sarmadian, A.; Mohseni, S.G. Evaporation heat transfer and pressure drop characteristics of R-600a in horizontal smooth and helically dimpled tubes. *Appl. Eng.* **2016**, *107*, 28–36. [[CrossRef](#)]
103. Li, W.; Chen, X.; Chen, J.-X.; Sun, Z.-C.; Simon, T.W. Shell-Side Flow Condensation of R410A on Horizontal Tubes at Low-Mass Fluxes. *J. Heat Transf.* **2016**, *139*, 011501. [[CrossRef](#)]
104. Gai, L.; Varbanov, P.; Walmsley, T.; Klemeš, J. Critical Analysis of Process Integration Options for Joule-Cycle and Conventional Heat Pumps. *Energies* **2020**, *13*, 635. [[CrossRef](#)]
105. Radermacher, R.; Hwang, Y. *Vapor Compression Heat Pumps with Refrigerant Mixes*; Taylor & Francis: Boca Raton, FL, USA, 2005.
106. Lorentzen, G. Trans-Critical Vapour Compression Cycle. Device. Patent Application No. WO1990007683A1, 12 July 1990.
107. Fu, C.; Gundersen, T. A Novel Sensible Heat Pump Scheme for Industrial Heat Recovery. *Ind. Eng. Chem. Res.* **2016**, *55*, 967–977. [[CrossRef](#)]
108. Wang, B.; Klemeš, J.; Varbanov, P.; Zeng, M. An Extended Grid Diagram for Heat Exchanger Network Retrofit Considering Heat Exchanger Types. *Energies* **2020**, *13*, 2656. [[CrossRef](#)]
109. Yong, J.Y.; Varbanov, P.S.; Klemeš, J.J. Heat exchanger network retrofit supported by extended Grid Diagram and heat path development. *Appl. Therm. Eng.* **2015**, *89*, 1033–1045. [[CrossRef](#)]
110. Soršak, A.; Kravanja, Z. Simultaneous MINLP synthesis of heat exchanger networks comprising different exchanger types. *Comput. Chem. Eng.* **2002**, *26*, 599–615. [[CrossRef](#)]
111. Yong, J.Y.; Varbanov, P.S.; Klemeš, J.J. Shifted retrofit thermodynamic diagram: A modified tool for retrofitting heat exchanger networks. *Chem. Eng. Trans.* **2014**, *39*, 97–102.
112. Langner, C.; Svensson, E.; Harvey, S.A. Framework for Flexible and Cost-Efficient Retrofit Measures of Heat Exchanger Networks. *Energies* **2020**, *13*, 1472. [[CrossRef](#)]
113. Short, M.; Isafiade, A.J.; Fraser, D.M.; Kravanja, Z. Two-step hybrid approach for the synthesis of multi-period heat exchanger networks with detailed exchanger design. *Appl. Therm. Eng.* **2016**, *105*, 807–821. [[CrossRef](#)]
114. Pintarič, Z.N.; Kravanja, Z.A. Methodology for the synthesis of heat exchanger networks having large numbers of uncertain parameters. *Energy* **2015**, *92*, 373–382. [[CrossRef](#)]

115. Sheng, Y.; Liu, L.; Zhuang, Y.; Zhang, L.; Du, J. Simultaneous Synthesis of Heat Exchanger Networks Considering Steam Supply and Various Steam Heater Locations. *Energies* **2020**, *13*, 1467. [[CrossRef](#)]
116. Elsidio, C.; Martelli, E.; Grossmann, I.E. A Bilevel Decomposition Method for the Simultaneous Synthesis of Utility Systems, Rankine Cycles and Heat Exchanger Networks. *Comp. Aided Process Eng.* **2018**, *43*, 373–378.
117. Wang, Q.; Guo, J.; Chen, P. Recent progress towards mild-condition ammonia synthesis. *J. Energy Chem.* **2019**, *36*, 25–36. [[CrossRef](#)]
118. Khademi, M.H.; Sabbaghi, R.S. Comparison between three types of ammonia synthesis reactor configurations in terms of cooling methods. *Chem. Eng. Res. Des.* **2017**, *128*, 306–317. [[CrossRef](#)]
119. Arsenyev, P.Y.; Tovazhnyansky, L.; Klemeš, J.J.; Arsenyeva, O.P.; Perevertaylenko, O.Y.; Kapustenko, P.O. The Optimal Design of Welded Plate Heat Exchanger with Intensified Heat Transfer for Ammonia Synthesis Column. *Chem. Eng. Trans.* **2019**, *76*, 61–66.
120. Klemeš, J.J.; Arsenyeva, O.; Kapustenko, P.; Tovazhnyanskyy, L. *Compact Heat Exchangers for Energy Transfer Intensification*; CRC Press/Taylor & Francis Company: New York, NY, USA, 2015; Volume 372, pp. 54–65, ISBN-13: 978-1482232592.
121. Walmsley, M.R.; Walmsley, T.G.; Atkins, M.J.; Neale, J.R. Sustainable Milk Powder Production using Enhanced Process Integration and 100% Renewable Energy. *Chem. Eng. Trans.* **2016**, *2016*, 559–564.
122. Hechelmann, R.; SeEVERS, J.; Otte, A.; Sponer, J.; Stark, M. Renewable Energy Integration for Steam Supply of Industrial Processes—A Food Processing Case Study. *Energies* **2020**, *13*, 253. [[CrossRef](#)]
123. Hoo, P.Y.; Phun Chien, C.; Fan, Y.V. Operational Management Implemented in Biofuel Upstream Supply Chain and Downstream International Trading: Current Issues in Southeast Asia. *Energies* **2020**, *13*, 1799.
124. Čuček, L.; Martín, M.; Grossmann, I.E.; Kravanja, Z. Multi-Period Synthesis of Optimally Integrated Biomass and Bioenergy Supply Network. *Comput. Chem. Eng.* **2014**, *66*, 57–70. [[CrossRef](#)]
125. Asadi, E.; Habibi, F.; Nickel, S.; Sahebi, H.A. Bi-Objective Stochastic Location-Inventory-Routing Model for Microalgae-Based Biofuel Supply Chain. *Appl. Energy* **2018**, *228*, 2235–2261. [[CrossRef](#)]
126. How, B.S.; Lam, H.L. Integrated Palm Biomass Supply Chain toward Sustainable Management. *Chem. Prod. Process Model.* **2017**, *12*, 1–19. [[CrossRef](#)]
127. Hren, R.; Petrovič, A.; Čuček, L.; Simonič, M. Determination of Various Parameters during Thermal and Biological Pretreatment of Waste Materials. *Energies* **2020**, *13*, 2262. [[CrossRef](#)]
128. Seidl, P.R.; Goulart, A.K. Pretreatment processes for lignocellulosic biomass conversion to biofuels and bioproducts. *Curr. Opin. Green Sustain. Chem.* **2016**, *2*, 48–53. [[CrossRef](#)]
129. Pavlas, M.; Dvořáček, J.; Pitschke, T.; Peche, R. Biowaste Treatment and Waste-To-Energy—Environmental Benefits. *Energies* **2020**, *13*, 1994. [[CrossRef](#)]
130. Reyes-Torres, M.; Oviedo-Ocaña, E.R.; Dominguez, I.; Komilis, D.; Sánchez, A.A. Systematic review on the composting of green waste: Feedstock quality and optimisation strategies. *Waste Manag.* **2018**, *77*, 486–499. [[CrossRef](#)]
131. Fan, Y.V.; Klemeš, J.J.; Lee, C.T.; Perry, S. Anaerobic digestion of municipal solid waste: Energy and carbon emission footprint. *J. Environ. Manag.* **2018**, *223*, 888–897. [[CrossRef](#)]
132. Ferdan, T.; Pavlas, M.; Nevrlý, V.; Šomplák, R. Greenhouse Gas Emissions from Thermal Treatment of Non-Recyclable Municipal Waste. *Front. Chem. Sci. Eng.* **2018**, *12*, 815–831. [[CrossRef](#)]
133. Jensen, M.B.; Møller, J.; Scheutz, C. Comparison of the organic waste management systems in the Danish-German border region using life cycle assessment (LCA). *Waste Manag.* **2016**, *49*, 491–504. [[CrossRef](#)] [[PubMed](#)]
134. Cormos, A.; Dragan, S.; Petrescu, L.; Sandu, V.; Cormos, C. Techno-Economic and Environmental Evaluations of Decarbonized Fossil-Intensive Industrial Processes by Reactive Absorption CO₂ Capture Systems. *Energies* **2020**, *13*, 1268. [[CrossRef](#)]
135. Fang, M.; Yi, N.; Di, W.; Wang, T.; Wang, Q. Emission and control of flue gas pollutants in CO₂ chemical absorption system—A review. *Int. J. Greenh. Gas Control* **2020**, *93*, 102904. [[CrossRef](#)]
136. Fan, L.S. *Chemical Looping Systems for Fossil Energy Conversions*; Wiley-AIChE: Hoboken, NJ, USA, 2010.
137. Castro, M.; Alcanzare, M.; Esparcia, E.; Ocon, J.A. Comparative Techno-Economic Analysis of Different Desalination Technologies in Off-Grid Islands. *Energies* **2020**, *13*, 2261. [[CrossRef](#)]
138. Tafech, A.; Milani, D.; Abbas, A. Water storage instead of energy storage for desalination powered by renewable energy—King Island case study. *Energies* **2016**, *9*, 839. [[CrossRef](#)]

139. Haraldsson, J.; Johansson, M.T. Energy efficiency in the supply chains of the aluminium industry: The cases of five products made in Sweden. *Energies* **2019**, *12*, 245. [[CrossRef](#)]
140. Gomilšek, R.; Čuček, L.; Homšak, M.; Tan, R.; Kravanja, Z. Carbon Emissions Constrained Energy Planning for Aluminum Products. *Energies* **2020**, *13*, 2753. [[CrossRef](#)]
141. Tan, R.R.; Foo, D.C. Pinch analysis approach to carbon-constrained energy sector planning. *Energy* **2007**, *562*, 1422–1429. [[CrossRef](#)]
142. Foo, D.C.; Tan, R.R.; Ng, D.K. Carbon and footprint-constrained energy planning using cascade analysis technique. *Energy* **2008**, *33*, 1480–1488. [[CrossRef](#)]
143. Manan, Z.A.; Tan, Y.L.; Foo, D.C.Y. Targeting the minimum water flow rate using water cascade analysis technique. *AIChE J.* **2004**, *50*, 3169–3183. [[CrossRef](#)]
144. Klemeš, J.J.; Varbanov, P.S.; Kravanja, Z. Recent Developments in Process Integration. *Chem. Eng. Res. Des.* **2013**, *91*, 2037–2053. [[CrossRef](#)]
145. Yang, H.; Ma, L.; Li, Z.A. Method for Analysing Energy-Related Carbon Emissions and the Structural Changes: A Case Study of China from 2005 to 2015. *Energies* **2020**, *13*, 2076. [[CrossRef](#)]
146. Ma, L.; Allwood, J.M.; Cullen, J.M.; Li, Z. The use of energy in China: Tracing the flow of energy from a primary source to demand drivers. *Energy* **2012**, *40*, 174–188. [[CrossRef](#)]
147. Premllal, K.; Lokhat, D. Reducing Energy Requirements in the Production of Acrylic Acid: Simulation and Design of a Multitubular Reactor Train. *Energies* **2020**, *13*, 1971. [[CrossRef](#)]
148. Redlingshofer, H.; Fischer, A.; Weckbecker, K.H.; Emig, G. Kinetic modelling of the heterogeneously catalysed oxidation of propene to acrolein in a catalytic wall reactor. *Ind. Eng. Chem. Res.* **2003**, *42*, 5482–5488. [[CrossRef](#)]
149. Estenfelder, M.; Lintz, H.G. Simultaneous determination of reaction kinetics and oxygen activity in single-phase oxidic catalysts and their mixture during partial oxidations. *J. Catal.* **2002**, *209*, 177–185. [[CrossRef](#)]
150. Snyder, T.P.; Hill, C.G. The mechanism for the partial oxidation of propylene over bismuth molybdate catalysts. *Catal. Rev.* **1989**, *31*, 43–95. [[CrossRef](#)]
151. Varbanov, P.S.; Chin, H.H.; Popescu, A.-E.P.; Boldyryev, S. Thermodynamics-Based Process Sustainability Evaluation. *Energies* **2020**, *13*, 2132. [[CrossRef](#)]
152. Ehyaei, M.A.; Ahmadi, A.; Rosen, M.A. Energy, exergy, economic and advanced and extended exergy analyses of a wind turbine. *Energy Convers. Manag.* **2019**, *183*, 369–381. [[CrossRef](#)]
153. Quiroz-Ramírez, J.J.; Sánchez-Ramírez, E.; Segovia-Hernández, J.G. Energy, exergy and techno-economic analysis for biobutanol production: A multi-objective optimisation approach based on economic and environmental criteria. *Clean Technol. Environ. Policy* **2018**, *20*, 1663–1684. [[CrossRef](#)]
154. Balest, J.; Secco, L.; Pisani, E.; Garegnani, G. Municipal transitions: The social, energy, and spatial dynamics of sociotechnical change in South Tyrol, Italy. *Energy Res. Soc. Sci.* **2019**, *54*, 211–223. [[CrossRef](#)]
155. Garcia-Casals, X.; Ferroukhi, R.; Parajuli, B. Measuring the socioeconomic footprint of the energy transition. *Energy Transit.* **2019**, *3*, 105–118. [[CrossRef](#)]
156. Chandler, D.L. Battery Reuse Systems Could Be Profitable for Electric Vehicle Companies and Grid Scale Solar Operations. 2020. Available online: techxplore.com/news/2020-05-battery-reuse-profitable-electric-vehicle.html (accessed on 2 June 2020).
157. Hanley, S. Nanotech Energy Claims its Graphene Lithium Battery Will Charge 18 Times Faster than Conventional Li-Ion Battery. Clean Technica. 2020. Available online: cleantechnica.com/2020/05/25/nanotech-energy-claims-its-graphene-lithium-battery-will-charge-18-times-faster-than-conventional-li-ion-battery/ (accessed on 2 June 2020).
158. EDF Environmental Defence Fund. Why Are Natural Gas Leaks a Problem. 2020. Available online: www.edf.org/climate/methanemaps/leaks-problem (accessed on 2 June 2020).
159. Exxon Mobil Corporation. Using New Technologies to Reduce Methane Emissions. 2020. Available online: energyfactor.exxonmobil.com/news/tech-reducing-methane-emissions/ (accessed on 2 June 2020).
160. Georgiou, M. The Role of AI Technology in Improving the Renewable Energy Sector. 2019. Available online: [primary%20goal%20of%20AI,current%20energy%20consumption%20and%20demands](https://www.pwccleanenergy.com/primary-goal-of-20AI,current-20energy-20consumption-20and-20demands) (accessed on 4 June 2020).
161. Kosovic, B.; Haupt, S.E.; Adriaansen, D.; Alessandrini, S.; Wiener, G.; Delle Monache, L.; Liu, Y.; Linden, S.; Jensen, T.; Cheng, W.; et al. Comprehensive Wind Power Forecasting System Integrating Artificial Intelligence and Numerical Weather Prediction. *Energies* **2020**, *13*, 1372. [[CrossRef](#)]

162. Ho, L.T.T.; Dubus, L.; De Felice, M.; Troccoli, A. Reconstruction of Multidecadal Country-Aggregated Hydro Power Generation in Europe Based on a Random Forest Model. *Energies* **2020**, *13*, 1786. [[CrossRef](#)]
163. Bandyk, M. Landfills Emerge as Promising Battery Storage Sites to Back Up Renewable Energy. 2020. Available online: www.utilitydive.com/news/landfills-promising-sites-battery-storage-solar-renewable-energy/578582/ (accessed on 2 June 2020).



© 2020 by the authors. Licensee MDPI, Basel, Switzerland. This article is an open access article distributed under the terms and conditions of the Creative Commons Attribution (CC BY) license (<http://creativecommons.org/licenses/by/4.0/>).

Review

Operational Management Implemented in Biofuel Upstream Supply Chain and Downstream International Trading: Current Issues in Southeast Asia

Poh Ying Hoo ^{1,*}, Cassandra Phun Chien Bong ² and Yee Van Fan ³

¹ Energy Studies Institute (ESI), National University of Singapore (NUS), Singapore 119620, Singapore

² Faculty of Chemical and Energy Engineering, Universiti Teknologi Malaysia, Johor Bahru 81300, Malaysia; nitecass@gmail.com

³ Sustainable Process Integration Laboratory—SPIL, NETME Centre, Faculty of Mechanical Engineering, Brno University of Technology—VUT Brno, 616 69 Brno, Czech Republic; fan@fme.vutbr.cz

* Correspondence: esihpy@nus.edu.sg

Received: 26 February 2020; Accepted: 1 April 2020; Published: 8 April 2020

Abstract: Bioenergy is one of the alternatives to secure energy demand, despite increasing debate on the sustainability of using bioenergy as a renewable source. As the source is disseminated over a large area and affected by seasonality, the potential benefit is highly dependent on other cost and benefit trade-offs along the supply chain. This review paper aims to assess operational management research methods used in biofuel supply chain planning, including both upstream production and international downstream trading. There have been considerable operational management studies done on upstream processes in biofuel production based on different strategic and tactical decision making of a single or multiple feedstocks, considering economic and environmental factor. However, the environmental consideration is often limited to carbon emission where the other environmental impact such as land-use change, biodiversity loss, irrigation and fertilisation are often being overlooked. Biofuel supply chain and trading at international level remain as an apparent research potential where only limited numbers of global energy models explicitly simulate international bioenergy trade. The leading biofuel producing countries in Southeast Asia: Malaysia, Indonesia and Thailand, are selected as a case study to investigate further on how the supply chain management model could be applied considering the existing biofuel support policies. This study is expected to contribute to the selection of operational management research methods used for decision making under robust policy context, followed by several recommendations.

Keywords: biofuel; bioenergy; supply chain; Malaysia; Indonesia; Thailand; interdisciplinary; integrated assessment

1. Introduction and Problem Statement

The International Energy Agency (IEA) reported [1] that biofuel production for the transportation sector needs to triple by 2030 to 280 Mtoe to be on track with the Sustainable Development Scenario (SDS). This is equivalent to 10% of the global transport fuel demand, as compared to 3% global demand [1]. Table 1 shows the forecast annual production growth vs required production growth to meet SDS demand in 2030. Among the six countries/regions presented, China and ASEAN are among those with production growth that will possibly meet required biofuel production by 2030 under SDS. In 2017, the Chinese government announced to roll out the mandatory blending of 10% ethanol in gasoline nationwide by 2020 [2]. Significant development of new ethanol production capacity is currently underway in order to meet the target, which is equivalent to 15 Mt of biofuel annually,

or around 45 Mt of corn. In ASEAN, biofuel policy is robust as domestic biofuel consumption is a means for energy security while promoting socio-economic development through ensuring demand for strategically critical agricultural commodities (Table 2). Among the 10 ASEAN member states, Indonesia, Malaysia, Philippines, Thailand and Vietnam are those with existing comprehensive policies on biofuel.

Table 1. Forecast growth vs required growth to meet the year 2030 target under SDS [1].

Country/Region	Forecast Annual Production Growth in 2019–24 (%)	Required Production Growth Needed to Meet SDS in 2019–30 (%)
USA	1	6
EU	0.5	8
Brazil	3.5	6
India	11	22
China	16	17
ASEAN	9	8

Table 2. ASEAN countries with comprehensive biofuel policy.

Country	Policy/Strategy	The Biofuel Production Target for the Transportation Sector	Government Ministries/Agencies
Indonesia	Indonesia National Energy Plan (Ministerial Regulation No. 22/2017) [3]	30% biodiesel plan by 2025 (update: the government has announced B30 blending recently to start in January 2020 [4])	Ministry of Energy and Mineral Resources (MEMR)
Malaysia	National Biofuels Policy 2006 [5]	B5 programme was launched in 2011 to encourage 5% biofuels blend (update: the government has announced the B10 biodiesel program starting December 2018 [6])	Ministry of Plantation Industries and Commodities (MPIC) (renamed: Ministry of Primary Industries)
Philippines	National Biofuels Program (NBP) [7]	1% ethanol blend by 2007, 2% by 2008, 5% by 2009, 10% blend by 2011 and increasing to 20% by 2020. Meanwhile, 5% biodiesel blend by 2015 and 20% by 2025 (update: current biodiesel blend is at 2% [8])	Department of Energy
Thailand	Alternative Energy Development Plan (AEDP) 2015–2036 [9]	25% RE share in the transportation sector by 2036	Department of Renewable Energy Development and Energy Efficiency (2015), Ministry of Energy
Vietnam	The scheme on Development of Biofuels up to 2015 with the Vision to 2025 (Decision No. 177/2007QD-TTg); National Strategy on Renewable Energy [10]	Aims to produce 1.8×10^6 tons of biofuels per year by 2025; to supply 5% of total transport fuel demand by 2020 and to raise to 13% by 2030. (update: the government announced 5% mix of ethanol starting December 2014, however, was postponed to January 2018 [11])	Ministry of Industry and Trade

It is noted that Indonesia is the only ASEAN country with a target for a bioavtur (biojet fuel) mix of 5% by 2025 and 10% by 2050. The feedstocks used for biofuel production in ASEAN countries are palm oil (Indonesia, Malaysia, Thailand), coconut oil (the Philippines), sugarcane (Thailand, the Philippines) and cassava (Thailand, Indonesia). With Indonesia and Malaysia being the world top two producers of palm oil, Thailand being the world's second producer of sugarcane after Brazil, Indonesia and Thailand being the world's top second and third cassava producers, Indonesia and the Philippines being the top world producers of coconut oil, it is not an exaggeration to call Southeast Asia a rice bowl with

huge regional potential for bioenergy production. Since biofuel carries a sustainable label as vehicle fuel when compared to conventional fossil fuels like gasoline or diesel, sustainability governance and a biofuel supply chain framework are essential to ensure that large scale biofuel consumption achieve its environmental benefits while delivering tangible economic and social benefits. Besides land-based vehicles, scaling up of biofuel consumption is also expected in the maritime and aviation sectors in the form of drop-in fuels, before more advanced alternative fuels like a solar jet, or hydrogen, become commercially viable. A decision-making level supply chain management is essential when formulating policies that sustainably promote biofuel production while providing investor confidence through financial de-risking measures or market instruments. De Meyer et al. [12] reviewed existing optimisation methods or models for optimisation in the field of biomass supply chain design and management. Most of the models reviewed had a case study in the EU, US and Brazil, with some case studies in China appearing in recent publications. Atashbar et al. [13] carried out a similar review on the modelling and optimisation of biomass supply chains. Most review articles are surrounding either solely on the methods of biomass supply chain management models, or solely on the potential, targets and current status of bioenergy in certain countries.

There has been a gap between how these supply chain management models could be used to plan for more sustainable biofuel production, considering the robust policy context of each biofuel producing countries. This is especially important for policymakers when it comes to decision making based on evidence. For ASEAN countries that possess significant feedstock resources, this is especially important so that food security and environmental sustainability are not compromised. This paper aims to first review the existing operational methods used to optimise the bioenergy supply chain, from upstream decision-making operational management optimisation model to downstream bioenergy trade model; then followed by a review on biofuel policy in ASEAN countries and challenges faced when implementing the policy. Only biofuel targets, policies and status of Indonesia, Malaysia and Thailand have been reviewed as there is existing comprehensive biofuel policy with similar bioenergy crops. The discussion will be made based on how the existing operational methods used in managing biomass supply chain at decision-making level could be used to tackle the challenges faced, or what are the research gap/blind spot/assumption made in existing methods that overlooks the consideration at the decision-making level. Most ASEAN countries that have biofuel mixes in the early days are motivated by energy security to reduce fuel imports and socio-economic factors as it creates jobs for their local communities. With increasing motivation towards carbon mitigation potential of biofuel in achieving sustainability target, it will be interesting to look into this matter and how each factor interact with each other when it comes to bioenergy planning.

2. Biofuel Supply Chain Planning and Management

The biofuel supply chain consists of biomass production, pre-treatment, storage and biofuel conversion. Each operation either takes place at the biomass production sites, or at another facility that is being connected to the biomass production site through different transportation mode. Figure 1 shows the flow chart of the biofuel supply chain. The biofuel supply chain is distinguished into two segments: upstream and downstream, with the segment bioenergy conversion placed interchangeably between the two, depending on whether biomass feedstock or the final product biofuel is traded. In this section, methods used in biofuel supply chain planning will be presented based on two categories: the upstream supply chain decision-making model and the downstream trade model. It is noted that not all bioenergy produced is traded; in some cases, bioenergy is utilised locally. To distinguish between supply chain management model used in this study downstream generally refers to traded bioenergy with some publications considering local consumption too.

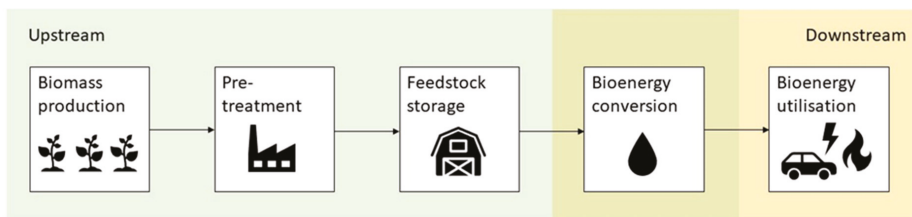


Figure 1. An example of a biofuel supply chain.

2.1. Methods Used in Biofuels Upstream Supply Chain Planning

The biofuel supply chain planning and management are influenced by various factors, among which are included biomass availability, choice of biomass cultivation type, harvesting, transport mode of the biomass, pre-treatment facility, biomass conversion technology type, conversion facility location and capacity, product storage facility, product distribution, routing and inventory. There are many decisions, of major and minor, to be made across the whole supply chain planning starting from crop selection to final product as covered in a review conducted by De Meyer et al. [12] and Atashbar et al. [13], in this case, biofuel consumption. There are three primary decision-making levels in supply chain planning and management: strategic, tactical and operational level (Figure 2). The strategic decision-making level refers to a decision where long-term investment is involved [12], for instance, location, capacity and type of storage, pre-processing, conversion facility, transportation mode (investment in ownership of the vehicle), crop selection. Tactical decision-making level refers to medium-term decision decisions, usually monthly or weekly and are within the constraint of a strategic decision [12]. Some examples of tactical decisions are harvest planning, inventory planning, transport routing and shipment capacity. Operational decision-making level usually refers to a decision over a short time frame, ranging from hourly to weekly that is within the limit of a tactical decision [12]. For instance, inventory planning and transport scheduling that ensures uninterrupted and efficient operations of plants and processes at another facility through the supply chain.

Under each decision-making level, three main approaches are applied in solving the supply chain problem: mathematical programming, heuristic approaches, multicriteria decision analysis. Mathematical programming refers to mathematical models that represent real-world problems. The model is solved by optimising the objective function. For instance:

1. To maximise profit or to minimise the overall cost for an economic purpose.
2. To minimise greenhouse gas (GHG) emission for environmental purpose.
3. To maximise job creation for social purpose, while satisfying the limit of the constraints formulated in the model.

While the mathematical programming method aims to identify the optimal solution by solving the equations simultaneously, the heuristic approach looks for an optimal point to a defined problem through a stepwise approach. According to a review conducted by De Meyer [12], three different heuristics algorithms are observed: genetic algorithm, particle swarm optimisation and binary honeybee foraging for upstream biomass planning and management optimisation. Multicriteria decision analysis is also one of the methods used for decision making in supply chain generally. According to Roy [14], multicriteria decision analysis is defined as 'a decision aid and a mathematical tool allowing the comparison of different alternatives or scenarios according to many criteria, often conflicting, in order to guide the decision-maker towards a judicious choice.

Thirty-two scientific publications could be found between 2014–2019 reviews the methods used for decision making at strategic and tactical levels under respective problem statement of the biofuel supply chain, with some exceptions for publications before 2014 for its method development related to recent publications. It shows a summary of recent scientific publications on decision making of

biofuel supply chain (Table 3) It is observed that most biofuel supply chain planning and management problems are formulated as a Mixed Integer Linear Programming (MILP) problem, covering 21 papers out of 32 articles. Aguayo et al. [15] present a MILP model to address a static and dynamic corn-stover harvest scheduling problem in cellulosic ethanol production by minimising system cost. Ahn et al. [16] developed a mathematical programming model for strategic planning and design of microalgae biomass-to-biodiesel supply chain which minimise the total cost of the supply chain by taking resource constraints, demand constraints and technology into accounts. The model is then applied in a case study of the biodiesel market in South Korea.

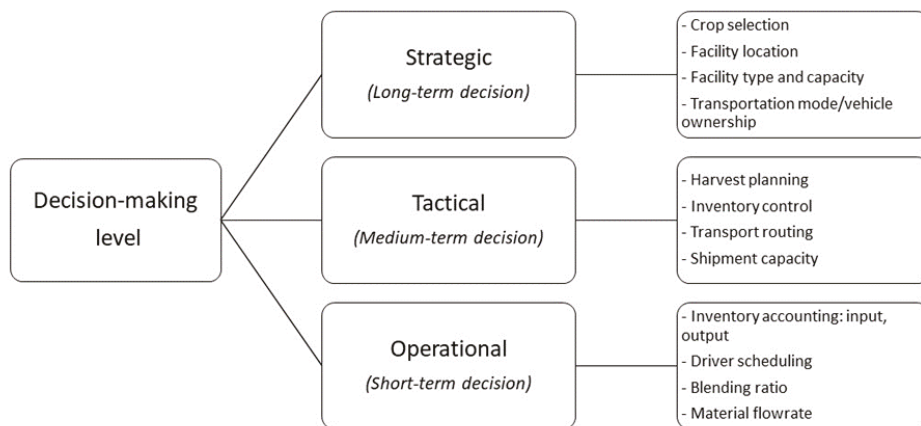


Figure 2. Decision-making levels of biofuel supply chain.

Čuček et al. [17] presented a multi-period MILP model for regional bioenergy supply network optimisation with sources of biomass from first, second and third generations of biofuels. The model enables strategic decision on raw material sourcing, conversion technology selection by maximising economic performance. Foo et al. [18] developed a linear programming (LP) model to identify optimal feedstock allocation of a direct biomass source-sink allocation. The model is extended to a MILP model for pragmatic decision planning in biomass supply chain logistics, where a minimum threshold quantity is met in an optimal network. Miret et al. [19] developed a multi-period MILP model that proposes optimal bioethanol supply chain design with the account to facility location, process selection and inventory policy. This study compared the economic, environment and social aspect of bioethanol production from first and second-generation biomass. Ng and Maravelias [20] presented a multi-period MILP model for biofuel supply chain design, taking a case study in Wisconsin. Ng et al. [21] developed a MILP model which maximises biomass utilisation of rubber seed oil to produce biodiesel that considers centralised and decentralised rubber seed processing facilities. Rabbani et al. [22] developed a MILP model that selects optimal biomass pre-processing plant, biofuel plant and biofuel storage warehouse. Santibañez et al. [23] presented a multi-objective, multi-period MILP model that seeks to optimise the biorefinery supply chain in fulfilling ethanol and biodiesel demands in Mexico with consideration of economic, environmental and social criteria.

Other than MILP, some problems have been formulated as a mixed-integer non-linear programming (MINLP) model and then linearised to form the MILP model. López et al. [24] developed a MINLP optimisation model for biorefinery system design while taking the interactions of the biorefinery system with the surrounding watershed into account. The non-linear term came from the exponent to represent the economy of scale of biorefinery plant. The model is then solved as MILP by fixing the exponent as one. How et al. [25] developed a MINLP model that solves biomass supply chain synthesis problem by maximising overall profit and minimising CO₂ emission through introduced CO₂ penalty. Santibañez et al. [26] developed an MINLP model to identify the optimal configuration

of a distributed biorefineries system, where the model can decide utilised raw materials, processing technologies, processing facilities and manufactured products.

It is observed that most supply chain optimisation problems are solely focused on optimising the economic benefits. Environmental, energetic and social factors deserve more attention in optimisation as these factors weight significantly when it comes to strategic decision making; this is especially true for the biofuel policymaker. To address this limitation, some authors used Pareto optimisation approach to obtain an optimal solution under the multi-objective situation. Liu et al. [27] present a multi-objective MILP model of biofuel conversion pathways with accounts to economic, energy and environmental criteria. Economic criteria are measured by total annual profit, energetic criteria are measured by fossil energy input per MJ biofuel, while environmental criteria are measured by GHG emissions per MJ biofuel. Pareto optimal surfaced is obtained to study the trade-offs between the three criteria. Miret et al. [19] applied the same approach through the epsilon-constraint method to study the multi-objective bioethanol supply chain model with a case study in France. Orjuela et al. [28] developed a multi-objective LP model that analyses biodiesel supply chain taking into consideration of economic, environment and social aspect, where the social aspect is taken from the perspective of food security concern. The epsilon-constraint method is then used to study the trade-off between multiple criteria. Osmani and Zhang [29] used an augmented epsilon-constraint method to solve multiple objective models with more than two objectives. Pareto optimal solution is also obtained in Santibañez et al. [23] multi-objective study.

It is undeniable that in the biofuel supply chain, which has a complex upstream supply chain, there are many uncertainties that could affect the performance of the supply chain, among which are included crop yield, potential disruption situations like pest attacks, floods or droughts, and biofuel price uncertainties. In order to address these uncertainties, a number of publications are found to have taken these factors into account. Azadeh et al. [30] present a stochastic multi-period MILP model that maximise the profit of a biofuel supply chain with prices of biofuels assumed to be stochastic. A case study is then conducted for the biofuel supply chain in Iran. Bairamzadeh et al. [31] proposes a hybrid robust MILP model for bioethanol supply chain design and planning with considerations of different types of uncertainties which included randomness, epistemic and deep uncertainties. Ghelichi et al. [32] developed a two-stage multi-period stochastic MILP model for biodiesel supply chain design with *Jatropha curcas* as feedstock, under consideration of feedstock supply and product demand uncertainties. Maheshwari et al. [33] developed biofuel supply chain resiliency optimisation model that consider no disruption and disruption scenarios during the flood, drought, pest attack, equipment failure, each weighted by their probability of occurrence. Mohseni and Pishvae [34] present a robust supply chain optimisation model that manages complexities in strategic and tactical planning of microalgae-based biofuel production. The supply chain is designed based on batch and continuous production system. Optimal scale for the batch system is determined by a trade-off between the cost of biofuel production, transportation and risk mitigation. Osmani and Zhang [29] presents a multi-objective, multi-period optimisation model of a second-generation biofuel supply chain under switchgrass yield, bioethanol demand and bioethanol sale price uncertainties. Santibañez et al. [35] presented a stochastic multi-period optimisation model that identifies optimal biorefinery supply chain planning under raw material price uncertainty considering environmental and economic aspects. A multi-scale multi-period MILP model is developed by Sharifzadeh et al. [36] to identify the optimal supply chain design of biofuel production using fast pyrolysis under consumer demands and biomass availability uncertainty.

Some authors integrated graphical approaches with mathematical programming in solving a biomass supply chain problem. Fan et al. [37] developed a novel graphical decision-making tool that allows the selection of transportation mode with lower environmental burden and energy consumption. Lam et al. [38] proposed a two-level graphical strategy for optimal regional-level biomass energy supply chain networks synthesis that minimises total carbon emissions footprint followed by optimal

biomass supply chain network synthesis within the region. The graphical approach was then applied to a case study at the Central European region.

Some authors integrated GIS functions to characterise the related biofuel supply chain when formulating the problem, especially in determining facility location. Harahap et al. [39] present a policy analysis using a spatially-explicit MILP model to optimise the overall palm oil supply chain—not just solely on palm oil biofuel supply chain in Sumatra, Indonesia. Hoo et al. [40] presented a spatial-economic optimisation MILP model to identify biomethane production plants with the aid of GIS network analysis. Zhang et al. [41] developed a GIS integrated optimisation model in designing a bioethanol feedstock supply chain, which allows the selection of facility location by minimising total system cost. The model is then applied on a case study in the northern part of Michigan’s Lower Peninsula, in the US.

Other than mathematical programming, a heuristic approach is also used by some authors to solve complex biofuel supply chain models. Note that the heuristic approach looks for satisfactory solutions, not necessarily an optimal solution and often presents reduced runtimes in solving models [12]. Asadi et al. [42] developed a multi-objective metaheuristic algorithm for algae biofuel supply chain design with an integrated formulation of inventory, routing and location decision under demand uncertainties. Marufuzzaman et al. [43] developed a two-staged (strategic level decision making followed by tactical decision making) stochastic model that assists the design and management of biodiesel supply chain by taking feedstock and technology uncertainties into account. The problem is then solved using an algorithm that combines Lagrangian relaxation and L-shaped solution methods. Poudel et al. [44] present a hybrid decomposition algorithm in solving an optimisation problem when studying the impact of disruption and congestion at the facility of a biofuel supply chain. While for multicriteria decision analysis, Nana et al. present a spatial explicit biodiesel supply chain optimisation model that was solved using an analytical hierarchy process (AHP). How and Lam [45] proposed a multi-objective optimisation (MOO) solution of biomass supply chain management (SBSCM) through AHP that integrates both economic and environmental factors. Among which the environmental factors included abiotic depletion potential (ADP), acidification potential (AP), aquatic toxicity potential (ATP), global warming potential (GWP), land footprint, nutrification potential (NP), ozone depletion potential (ODP), photochemical ozone creation potential (POCP), terrestrial toxicity potential (TTP), water footprint. A general method is also observed in Ng and Maravelias [46] study on the biofuel supply chain. The authors applied a systematic method to compare and investigate the economic performance and energy efficiency of the biofuel supply chain under various configurations and transportation modes. The author introduced hybrid configurations that can potentially improve economic performance and energy efficiency of different supply chain configuration. The findings of the result form the basis for larger-scale biofuel supply chain optimisation model in a future study.

It is observed that there is increasing research and publications on operational biofuel supply chain methods in China and Iran, especially for second-generation and third-generation biofuel production. Waste cooking oil as a feedstock for biofuel production is found in China biofuel supply chain planning (Table 4). Waste cooking oil can be converted into biofuel through hydro-processed esters and fatty acids (HEFA) conversion process. Advanced biofuel produced from waste cooking oil through HEFA process is also considered as Carbon Offsetting and Reduction Scheme for International Aviation (CORSIA)-eligible fuels, which it can be used as sustainable aviation fuel for aircraft. A number of supply chain planning involving microalgae are also found in recent literature. While crop selection in different continents varies geographically, seasonality also affects feedstock supply, as indicated in the most multi-period mathematical models. This is especially true for the northern hemisphere. Despite being primary world producers of biofuel [1], there are minimal scientific publications on supply chain planning from countries in Southeast Asia region found in the literature, except for [38] who have done extensive operational supply chain research on biomass in Malaysia. However, publication solely focusing on biofuel supply chain with case study characterising biofuel production in this region is missing.

Table 3. Recent scientific publications on state-of-art of decision making for the biofuel supply chain.

Source	Decision Level	Obj.	Decision Variables	Method	Case Study
Aguayo et al. [15]	T	EC	Tactical: - minimum number of balers required - harvest and routing decision	MP - MILP	USA
Ahn et al. [16]	S + T	EC	Strategic: - refineries facility location and capacity Tactical: - feedstock sourcing location and amount	MP - MILP	South Korea
Asadi et al. [42]	S + T	EC + EN	Strategic: - number and location of distribution facility - allocation of extraction sites to these facilities Tactical: - minimum inventory level - routing of extraction sites	H - algorithm	Iran
Azadeh et al. [30]	S	EC	Strategic: - facility locations and capacities- technology and material flows	MP - MILP	Iran
Bairamzadeh et al. [31]	S + T	EC	Strategic: - facilities location & capacity - technology type Tactical: - biomass allocation - inventory levels - production amounts - transportation among network	MP - MILP	Iran
Fan et al. [37]	T	EC + EN	Tactical: - transportation mode selection	MP - LP + P-graph	Rotterdam to Antwerp, Netherlands and Genova, Italy
Foo et al. [18]	T	EN	Tactical: - plant capacity - feedstock capacity	MP - LP + MILP	Malaysia
Čuček et al. [17]	S	EC	Strategic: - raw materials sourcing - conversion technologies - intermediate & final product flows	MP - MILP	EU
Gheltchi et al. [32]	S + T	EC	Strategic: - numbers, locations and capacities of cultivation and facility Tactical: - transportation mode allocation - number of purchased and rented trucks	MP - MILP	Iran

Table 3. *Cont.*

Source	Decision Level	Obj.	Decision Variables	Method	Case Study
Harahap et al. [39]	S	EC	- technology selection for biomass conversion Strategic: - biomass allocation - biomass transportation mode	MP - MILP + GIS	Sumatra, Indonesia
Hoo et al. [40]	S + T	EC	Strategic: - facility location - biomethane plant size Tactical: - transportation mode	MP - MILP + GIS	Johor, Malaysia
How and Lam [45]	T	EC + EN	Tactical: - biomass allocation - biomass transportation mode	MP - MILP	Johor, Malaysia
How et al. [25]	S + T	EC	Strategic: - processing hub selection Tactical: - biomass allocation - transportation mode selection	MP - MINLP	Johor, Malaysia
Lam et al. [38]	S	EN	Strategic: - biomass supply chain network design	MP - LP + P-graph	Central European region
Liu et al. [27]	S	EC + EN + SO	Strategic: - optimal conversion pathway - biomass type, locations - facility locations - network topology structure	MP - MILP	China
López et al. [24]	S	EC + EN	Strategic: - feedstocks type - location of cultivation sites - location of biomass facilities - biomass conversion technologies	MP - MINLP	Central-west part of Mexico
Maheshwari et al. [33]	S	EC	Strategic: - locations and capacities of pre-processing facility & biorefinery plant - biomass and intermediate product flows	MP - MILP	Southern Illinois, USA

Table 3. *Cont.*

Source	Decision Level	Obj.	Decision Variables	Method	Case Study
Marufuzzaman et al. [43]	S + T	EC + EN	Strategic: - transportation mode - facility location Tactical: - inventory control	H - algorithm	Mississippi, USA
Miret et al. [19]	S + T	EC + EN + SO	Strategic: - facilities location - process selection Tactical: - inventory	MP - MILP	France
Mohseni and Pishvaei [34]	S + T	EC	Strategic: - optimal production scale Tactical: - intermediate product and product flows - amount of fertiliser needed	MP - MILP	Iran
Nana et al. [47]	S	EC + EN	Strategic: - facility location & capacity	MCDA - AHP + GIS	Jiangsu, China
Ng and Maravelias [20]	S + T	EC	Strategic: - biomass selection and allocation - technology selection - regional depots and biorefineries locations and capacity Tactical: - production, inventory and shipment	MP - MILP	South Central, South of Wisconsin, USA
Ng and Maravelias [46]	-	EC + ENE	-	General method	NA
Ng et al. [21]	T + O	EC	Tactical + operational: - optimal blending ratio	MP - MILP	Malaysia
Orjuela et al. [28]	S	EC + EN + SO	Strategic: - strategy/solution selection	MP - LP	Columbia
Osmani and Zhang [29]	S	EC + EN + SO	Strategic: - land allocation for switchgrass cultivation - locations and capacities of facility - conversion technology	MP - MILP	Midwestern USA
Poudeh et al. [44]	S + T	EC	Strategic: - facility location Tactical:- production & storage - routing plan	MP - MINLP; H - algorithm	Mississippi and Alabama, USA

Table 3. *Cont.*

Source	Decision Level	Obj.	Decision Variables	Method	Case Study
Rabbani et al. [22]	S	EC	Tactical: - whether to purchase or rent the warehouses and plants - selection of pre-processing centre - selection of biofuel plants - selection of warehouses to store biofuels	MP - MILP	NA
Sanitibañez et al. [23]	T	EC + EN + SO	Tactical: - feedstock produced - feedstock transported - feedstock arrived/accumulated - product arrived/accumulated	MP - MILP	Mexico
Sanitibañez et al. [26]	T	EC	Strategic: - processing facility and technology Tactical: - material flow - inventory level	MP - MINLP	Mexico
Sanitibañez et al. [35]	S + T	EC + EN	Strategic: - facility location technology type Tactical: - raw materials and products - market	MP - MILP	Mexico
Sharifzadeh et al. [36]	S + T + O	EC	Strategic: - number, type, location and size of processing plants and mobile pyrolyser Tactical + operational: - materials flow/rates	MP - MILP	London, Liverpool, UK
Zhang et al. [41]	S + T	EC	Strategic: - facility location Tactical: - inventory level	MP - MILP + GIS	Northern part of Michigan's Lower Peninsula, USA

S—Strategic; T—Tactical; O—Operational; EC—Economic; EN—Environment; SO—Social; MP—Mathematical programming; H—Heuristic; MCDA—Multicriteria Decision Analysis

Table 4. *Cont.*

	Agricultural Residues	Industrial Wastewater	Energy Crops	Microalgae
[47]		x		
[20]	x			x
[46]	x			
[21]			x	
[28]		x		
[29]	x			x
[44]	x			x
[22]				x
[23]	x		x	x
[26]	x		x	x
[35]	x		x	x
[36]		x		x
[41]				x

CS—corn stover; MR—mill residues; WS—wheat straw; RS—rice straw; CR—cotton residues; BS—barley straw; WR—wood residues; PR—palm residues; SR—sugarcane residues; MSW—municipal solid waste; WS—wastewater sludge; WCO—waste cooking oil; C—corn; W—wheat; S—sugarcane; PO—palm oil; RO—rapeseed oil; RSO—rubber seed oil; SF—sunflower; J—Jatropha; SG—sorghum; WB—woody biomass; SCS—switchgrass; M—Miscanthus; SFR—safflower; MA—microalgae; NF—not specified.

2.2. Methods Used in Biofuel Downstream Supply Chain Planning

Bioenergy plays an essential role in promoting clean energy and securing the future energy supply. This rationale leads to increase global trade of biomass or energy carriers from biomass which has been reported by Schlamadinger et al. [48]. Welfle [49] highlighted that the bioenergy strategies of many countries highly depends on future imported resources to balance the demands. Biomass is unevenly distributed in the view of demand and resources availability. Developed countries and the energy policies drive the increasing reliance on bioenergy pathways to meet the energy demand. Some of the countries are facing insufficient biomass stock to meet the demand, but there are also countries with the potential supply that significantly exceeds the demand. An international biomass supply chain is vital to promote natural symbiosis. Junginger et al. [50] provide a comprehensive discussion on international bioenergy trade, including the drivers and barriers as well as developments in liquid biofuel trade. Europe is one of the prime markets for the trade of biomass for energy generation, with wood pellet as the main substrate (see Figure 3). Lamers et al. [51] show that Brazil is the leading exporter of bioethanol while the United States, Argentina, Indonesia and Malaysia are the major exporters of biodiesel. Based on the forecast by IEA [1], biofuel output is anticipated to reach 1.9×10^{11} L (+24%) by 2024, owing to better market prospects in Brazil, the United States and China. Asia is expected to lead to biofuel production growth.

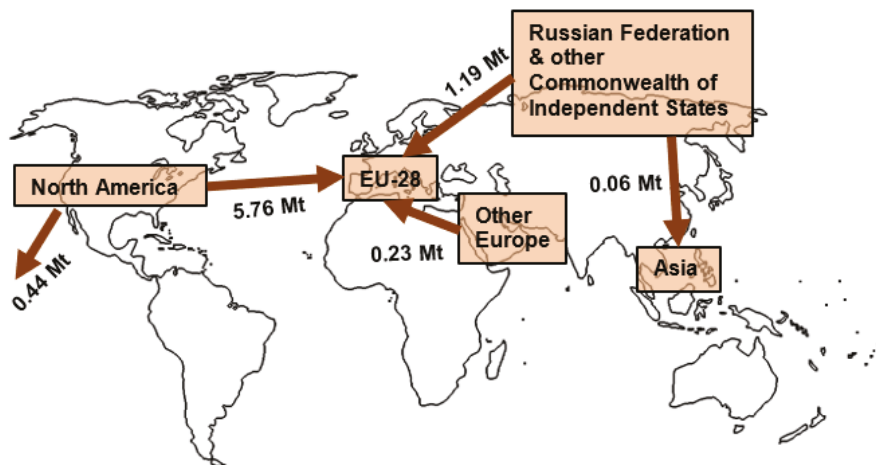


Figure 3. Wood pellet trade flows, adapted from World Bioenergy Association [52].

Downstream biofuel supply chain planning and management are subjected to a higher level of uncertainty, especially when it involves international trading. The objective function is generally the same as the upstream assessment, where economic and/or environmental aspect is optimised. Physical trade of biomass is not always the optimal solution due to international logistics, which increase the cost and environmental footprints. Laurijssena and Faaij [53], however, suggest that trading biomass is preferential than trading GHG emission credits. Other than the transporting distance, which is the main supply chain issue, the international trade (macro perspective) is affected by incentive-policy (e.g., the EU's Renewable Energy Directive) context and trade tariffs (both import and export tariffs) [54]. The reliability of the assessment results is relying on the accurateness of projection/ prediction as well as the assumptions. The assessment model is usually supported by a range of scenarios representing the optimistic and pessimistic situation. Welfle [49] applied the biomass resource model to evaluate the biomass potential in Brazil. The trading possibility is determined by the availability of the resource, considering the remaining land area, the potential of resource collection, competing for a market of biomass utilisation as well as the conversion pathway. Deng et al. [55] conducted similar research to

identify the potential of trading (import and export) based on resource availability but covering a more extensive range of feedstock and countries. The yield gradient, land-use change and technology development are varying to identify the biofuel potential. The estimation potential for the global scale ranges from 40 to 190 EJ final energy in 2070 where Brazil and Russia are recognised as the prominent exporters, while India and Nigeria are substantial importers. The forecasts mainly identifying the biomass potential rather than the biomass allocation, which considering the detailed costing, travel distance and available market. Lamers et al. [56] assess the potential import streams and supply costs under different sustainability constraints based on a bottom-up global trade model. Figure 4 shows the modelling framework which combining the biomass transport model and biomass allocation model. This modelling considered temporal and logistical determinants without neglecting the market development and time aspects (e.g., delay), where the biomass allocation is suggested.

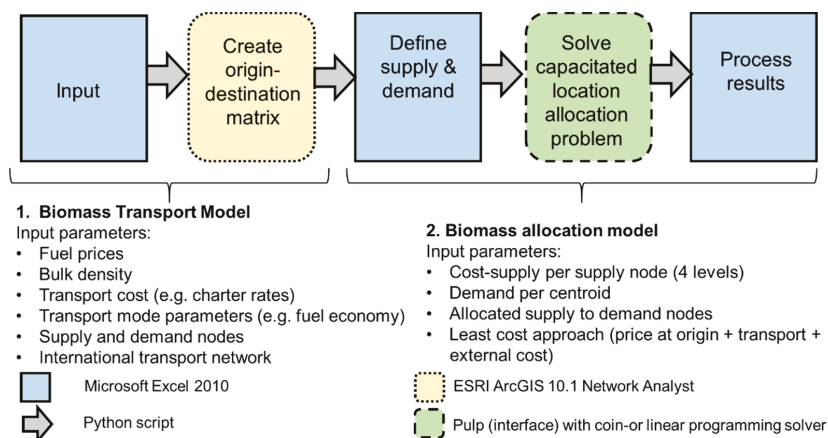


Figure 4. The integrated modelling framework for international biomass (to energy) trade adapted from by Lamers et al. [56].

The review by Diesenreiter and Kranzl [57] suggested that no customised models are available for incorporating global import/export potentials and international trade. The evaluated approaches in the review study are divided into basic modelling approaches for analysing the macroeconomic effect of international trade, computable general equilibrium models and geographic information system. A similar conclusion has been drawn by Solberg et al. [58] in a study for IEA bioenergy task 40 where none of the existing models is capable of performing good analyses of international trade of biomass and bioenergy products. Figure 5 summarises the assessed models in both studies in identifying the weakness and strengths. There is a common characteristic where all the presented models are customised more to the case of the EU. Green-X model [59], which allows the consideration of different energy policy instruments is also for the application of the European level. The gravity model of trade [60] is among the standard model in predicting bilateral trade flows according to the economic sizes and distance between two units despite the argument on the identified results [61]. Röttgers et al. [62] analyse the effect the EU imposes on the trade of the biofuel commodities and identify the drives (e.g., trade regulation or bioenergy regulation) of biofuel trade. The assessment suggests that EU trade integration has no enabling effect on canola oil trade where the import from outside of the EU is preferable. The result warrants a closer look at the political measures and its effectiveness, especially the green investment subsidy. However, other factors such as economies of scale, resource scarcity and value chain structure have to be taken into account as well for a conclusive picture.

Rentizelas et al. [63] stressed the need for a decision support tool to facilitate the supply chain design rather than assessing the supply chain of specific origin and destination location. A multicriteria tool based on data envelopment analysis which considers the environmental impact and cost is conducted to identify the efficiency of alternative pathways (Up to 56 pathways between Brazil and the UK) of international biomass supply chains are developed. Three models for bioenergy trade analysis, include TIMER (dynamic energy system model), GFPM (spatial partial equilibrium model based on price endogenous linear programming) and POLES (dynamic partial equilibrium model), have been reviewed by Matzenberger et al. [64]. It was concluded that further integration of international bioenergy trade, emerging barriers and drivers into the existing models is essential for a more realistic answer regarding the future role of the bioenergy system.

Basic Trade Models	Market Equilibrium Models	GIS Models
<ul style="list-style-type: none"> • Ricardian model [57] • Specific factors model [57] • Heckscher-Ohlin model [57] • Gravity model of trade [57] • BIOTRANS [58] 	<ul style="list-style-type: none"> • MERGE [57] • GREEN [57] • NEWAGE [57] • GEM-E3 [57] • GTAP/GTAP-E Model [57] • GRACE [58] • CAPRI [57] • EFI-GTM [57] 	<ul style="list-style-type: none"> • GIS-TIMES [58] • SDSS [57] • EDSS [57]

Figure 5. Model for international trade of biomass for energy. Please refer to Diesenreiter and Kranzl [57] and Solberg et al. [58] for the detailed discussion on each approach.

Maximising the economic performance is the common objective function in most of the models. However, the trade-offs between economic and environmental performance as well as the other factors have to be also considered. Total footprints-based multi-criteria optimisation is proposed by Čuček et al. [65] to consider the economic performance, environmental footprint as well as the social footprint in determining an optimal regional biomass energy supply chain. Jonkman et al. [66] propose a decision support tools with the advantages that it can take into account the goals of individual actors of the supply chain than only optimising the economic and environmental performance. This is a significant development and beneficial for supply chain with the involvement of different countries. The multicriteria approach is potential to adapted for global supply chain problem, although it is demonstrated through a case study in the Netherlands. Lee et al. [67] proposed a global supply chain optimisation framework supported by two-stage stochastic linear programming model (TRMISP) to identify the supply chain design (Southeast Asia to Europe and North America) under the price and demand uncertainty. This is important as uncertainties are one of the main challenges in modelling and optimisation of the international supply chain. Transfer pricing, currency exchange and taxation rates have to consider in the global supply chain planning. The studies which include one or more of the factors include de Matta and Miller [68] (Transfer price- generalised Benders decomposition approach), and Gonela et al. [69] (Tax-credit- stochastic mixed-integer linear programming model). Razm et al. [70] proposed a multi-objective mathematical model with the aids of GIS to design a global sustainable bioenergy supply network. This is a comparatively comprehensive model which considered all the crucial components at the international level.

The methodological challenges such as uncertainties of international statistics, inconsistent data on trade volumes and final use of traded products [71] persist despite advancing. It is expected to enhance the development of IoT and big data in the near future. Fingermaier et al. [72] assessed the opportunities and risks for sustainable biomass export, particularly to Europe from the South-Eastern

of United States. The long-term strategies assessment by Pelkmans et al. [73] for European bioenergy markets considered North America, South America, East Europe, Africa and Southeast Asia as the potential sourcing regions. It is concluded that policies should be stable and consistent within a long-term vision. Macro perspective assessments specifically done for Asia countries are generally lesser, especially compared to EU and South America. It deserves more research attention by adapted to the localised condition and forecast towards a close to the optimal global solution. Different approaches can be fitted for solving the problem related to international biofuel trade by integrating to the existing energy models. However, the considered variables are not consistent for a robust solution, and data availability for modelling is still one of the critical issues.

3. Case Study: Malaysia, Indonesia, Thailand

3.1. Existing Policy and Current Status

ASEAN is facing energy challenges in supplying sustainable and secure energy due to its increasing growth and depleting natural oil reserves. The rapid economic growth comes with a 50% increment in the regional energy demand within a decade [74]. The case studies are discussed in two sections. The first section looks into several essential policies in facilitating the installation and progression of the biofuel industry among the three Southeast Asian countries, namely Malaysia, Indonesia and Thailand. The second section discusses the challenges and the shift of attention on the upstream and downstream process of the biofuel supply chain following the progression of the biofuel industry.

3.1.1. Malaysia

In 2000, Malaysia included RE (small-scale hydro, solar, geothermal, wind and biomass) as its fifth energy source under the Fifth Fuel Diversification policy. Palm oil is the primary source of biofuel in Malaysia, with its available biomass from the 4.69×10^6 ha of oil palm plantations [75]. Crude palm oil is the primary feedstock to produce biodiesel or palm methyl ester (PME) [76]. In 2006, Malaysia announced the National Biofuel Policy (NBP) with the aim to improve energy security, environmental performance, and increasing the domestic consumption of surplus palm oil [77].

Malaysia has been actively promoting the use of biodiesel for its transportation sector and subsidised sector. The Biofuels Industry Act 666 was enacted in 2008 for the licensing and the regulation of the biofuel's industry and the mandate B5 blend was introduced for transport and industrial use progressively to all states from 2011–2014 [78]. In November 2014, the B7 biodiesel was introduced nationwide to increase the use of biodiesel by 47.5%, up to 575,000 t/y [79]. Subsequently, under the year 2019 Malaysian budget, the government implemented the B10 biodiesel program for the transportation sector and B7 for the industrial sector [80]. The consumption of palm oil was expected to reach 700,00–800,000 t palm oil annually under the B10 program, which is 50% higher under the B7 programme in 2018 [81]. Malaysia's government presently aims to raise its biodiesel mandate blend from the current B10 to B20 for the transport sector and from the present B7 to B10 for the industrial sector by 2020 [82].

Bioethanol is less utilised in Malaysia despite the high biomass production and availability [83], with 15.8–17 Mt/y of empty fruit bunches produced that can be converted to bioethanol through pre-treatment, hydrolysis and fermentation [84]. There is currently no mandate blend of bioethanol under the NBP. The Malaysian market for bioethanol is potentially much larger than the market for biodiesel because a much more significant proportion of the vehicle fleet runs on gasoline [83]. Abdulrazik et al. [85] identified a profit of around \$710 M/y, assuming single ownership from different bio-products derived from empty fruit bunch.

3.1.2. Indonesia

Indonesia is abundant in biomass, typically oil palm and *Jatropha* for biodiesel as well as cassava and sugar cane for bioethanol [86]. In 2006, the government of Indonesia announced the Indonesia

Presidential Regulation no.5, also known as the National Energy Policy (NEP), to include biofuel as one of its RE sources. The NEP aimed to have biofuel contributing more than 5% to the national energy consumption by the year 2025 [87]. The Indonesia government also introduced volumetric utilisation target to have 10–20% of diesel and petrol consumption to be replaced by biodiesel and bioethanol [86]. In 2008, the Ministry of Energy and Mineral Resource Regulation (MEMR) No.32 introduced mandatory biofuel utilisation in transportation, industry, commercial and electricity. In 2013, the MEMR No.25 expanded the biodiesel utilisation to public service obligation (PSO), non-PSO, industry and electricity [87]. Based on the Government Regulation No 70/2014 on National Energy Policy and the Presidential Regulation No 22/2017 on General Plan of National Energy, Indonesia is aiming to increase the biofuel share up to 23% of its RE mix by 2025 [88].

For the use of biodiesel, the government has expanded the use of B20 to all sectors, including both PSO and non-PSO. The Indonesia government has launched the highest mandate blend of B30 around the globe in December 2019, where it is expected to save USD 4.5×10^6 annually on fossil fuel import for the country [89]. The government is currently on its way to implement B30 by 2020 for the transportation sector and B40 for large sectors such as railways. For bioethanol, the government targets to have a mandated blend of E5 for PSO and E10 for non-PSO from the current E2 in 2020 then expand to E20 for all sectors in 2025 [88].

3.1.3. Thailand

Comparing the biofuel policies of Thailand with its neighbouring countries like Malaysia and Indonesia, the Thai government places more significant emphasis on its bioethanol industry. The Thai government has released a series of revised energy plans towards their transition into Thailand 4.0 with emphasis on the use of RE to achieve a low carbon society. In 2012, Thailand introduced the Alternative Energy Development Plan (AEDP) from 2012–2021 to increase its bioethanol production from 1.2 to 9×10^6 L from sugarcane and cassava as well as the oil palm plantation for biodiesel from 2.3 to 6×10^6 L [90]. The AEDP also aims to increase the mix of RE to 30% by 2036 into the energy mix, with a 25% target of substitution of fuel with biofuel [91]. In 2014, the new power development plan (PDP) was announced with five integration master plans, including the revised PDP and AEDP. The PDP 2015, which covers from 2015–2036, focuses on energy security and fuel diversification, cost of power generation, and lessening CO₂ emission of power generation [91]. The AEDP 2015 aimed to achieve 30% of RE in the energy mix in 2036, with 20–25% to be contributed by biofuel [92]. In 2018, the government of Thailand also announced its updated PDP for 2018–2037 to increase RE share up to 35% on the national energy mix [93].

The bioethanol policy of Thailand has been promoting high consumption of the ethanol fuel as the government provides incentives and tax reductions, where the price of gasohol can be 20–40% cheaper than regular gasoline for cars compatible with E20 and E85 gasohol [92]. The government of Thailand implemented public sales of B10 in 2019 and to replace the current B7 by 2021 [94], followed by the possible implementation of B20 on buses and trucks [95]. In its AEDP 2012–2021, the Thai's government has also looked into the production of advanced biodiesel fuel derived from algae and jatropha with a 1.95×10^9 L production target [96].

3.2. Discussion

As depicted in Figure 1, the biofuel supply chain contains the upstream (biomass production, pre-treatment, feedstock storage) and downstream (conversion and bioenergy utilisation) processes. Following the increasing volume of the biofuel blend and the expansion of the industries practising such mandatory blend, there will be increasing pressure in securing the biomass availability for the upstream process. For example, in Malaysia, the implementation of the B10 program will consume up to 750 kt of oil palm annually [81]. For Indonesia, the government has to secure a biofuel supply of 9.59×10^9 L for the implementation of the mandated blend of B30 [89]. The study also pointed out the need for more infrastructure support on the fuelling stations to supply the increasing blend.

For Thailand, 15% of extra land for plantation is required in order to achieve its B10 target [97]. This is also complicated where oil palm requires 24 years till maturation [77]. Abdul-Manan et al. [77] identified four major elements for improving the upstream performance, namely improving the fresh fruit bunch yield, improving worker productivity, increasing oil extraction rate and developing biogas plant for oil palm yield. The increasing production of the biomass also requires a parallel installation and upgrading of pre-treatment and storage facilities.

In terms of environmental performance for the upstream processes in securing the biomass availability, the palm oil industry will need to demonstrate better sustainability performance towards a greener environment and a broader market acceptance. [98]. There is still a lack of detailed assessment framework from the NBP. Abdul-Manan et al. [99] discussed the significant variation in the environmental performances from the differences in land use, deforestation, N fertilisers and fertilisation management practice of different palm-based biofuel refinery. Čuček et al. [100] also highlighted that footprints used to monitor sustainability usually vary and expressed ambiguously. For environmental footprints, there are carbon emission footprint, water footprint, energy footprint, emission footprint, nitrogen footprint, land footprint and biodiversity footprint [100]. Nitrogen footprint attributed to fertiliser, pesticide and final combustion of biofuel/biomass is often neglected when quantifying the environmental impact of the increasing use of bioenergy. In Indonesia, it was reported that 25% of the oil palm plantations were on peat soils, which can lead to the release of stored carbon and contribute to global warming [101]. From the economic perspective, there are concerns over the financial cost in importing and subsidising petroleum-based fuel [102] which can contribute to a significant expenditure of the government [98]. There is also increasing reluctance of the EU in importing palm oil and palm-derived products [103]. In addition, in the case of Malaysia where the biofuel industry is largely based on palm oil and FAME, Abdul-Manan et al. [77] also pointed out this may limit the technology innovation and the selection of best available techniques, especially in times when there is a change in the government policy or market preferences.

The greatest challenge in achieving its biofuel target is the amount of feedstock which is then associated with uncertain impact on the environmental sustainability due to land-use change, water consumption and net fossil energy savings [86]. With increasing population and rising projection of consumption, Kraxner et al. [104] reported that there would not be enough land to stop deforestation while switching to 100% renewables and conserve natural areas completely, especially in the tropical regions. There is still in need of assessment or optimisation on the sustainability performance for the designing or optimisation of the upstream process as pointed out by [77]. In addition to the environmental sustainability performance such as GHG and C change, some additional aspects of being considered for designing the upstream process include:

1. The time needed for maturation and the decreasing yield of oil palm following maturation.
2. Economic performances involving local and export demand.
3. Involvement of the installation of biofuel plants and blending facilities.
4. The utilisation of readily available biomass residual to produce 2nd generation biofuel or other bioproducts, e.g., utilisation of biogas produced from agroindustry wastewater.

The downstream process of the biofuel supply chain involves the conversion and the bioenergy utilisation aspects. Chanthawong et al. [105] identified three major factors affecting the long-term demand for biofuel, which includes the price of biofuels, real gross domestic production and the number of vehicles. Putrasari et al. [87] also pointed out that the biofuel program is limitedly applied to a specific area by the central Indonesia government with low social acceptance and limited research into the development of flexi fuel vehicle. Moreover, there is also competition in the allocation of the bioenergy utilisation. For example, Malaysia has 40% of its palm oil being used to produce biofuel and limiting the supply for vegetable oil demand [106]. Following the tighter environmental regulation, the palm oil biodiesel is also required to perform greener to secure its demand. For example, under the US Renewable Fuel Standards, cellulosic biofuel and biomass-based diesel are required to reduced

lifecycle GHG of at least 60% and 50% [107]. In addition to the improved environmental management during the upstream process, the downstream process could be optimised following the upgrading of conversion technology with a higher extraction rate, less emission to air and more. The installation of anaerobic digestion plant can contribute to GHG reduction through the utilisation of biogas as renewable energy [77]. The diversification of more value-added products from the downstream such as oleochemical derivatives and the utilisation of waste and biomass residuals for 2nd generation biofuels are attractive for improving both the environmental and economic performances [108], briquette and phytonutrients from crude palm oil [109].

In terms of the supply chain design for the downstream process, it is recommended to take into the environmental and social considerations of several aspects on the biofuel consumption that include:

1. The increasing mandate blend and the optimal mandate blend
2. Expanded consumption of biofuel to other sectors
3. Diversification of the product spectrum of the biomass
4. The different conversion rate of biomass to the biofuel.

4. Conclusions

This study reviewed the operational research methods used in biofuel supply chain planning. For the upstream supply chain optimisation, most optimisation focuses on either economic performance or environmental and social factors. For the downstream bioenergy trading optimisation, price and demand uncertainties are of the significant challenges for regional and international trading, which can be influenced by the policy or industry target of all trading partners involved. Following the increment in the mandate biofuel blend imposed by the three mentioned countries—Malaysia, Indonesia and Thailand—and the global demand for cleaner biofuel, the integration of the environmental and social factors to the supply chain design would offer better decision making on optimising the sustainability. The sustainability of bioenergy upstream supply chain can come to the negative environmental impact of bioenergy feedstock plantation due to land-use change, fertilisation and irrigation. Stricter qualification of advanced and greener biofuel for international downstream trading through the development of sustainability criteria and certification is crucial, especially the trade-offs of environmental and social footprints.

There is a consideration of the industry or policy's characteristic, such as a biofuel industry based on single biomass, the flexibility of other conversion technologies and the utilisation routes of the interested biomass. A more holistic approach that took sustainability criteria like land-use change, biodiversity loss, the impact of irrigation and fertilisation, carbon emission footprint, nitrogen footprint and other emission footprints into consideration is vital to assist a more informed policy decision. Good governance and coordination of different policy areas: an integrated assessment should support energy, land-use change, climate and rural socio-economic development. There is an urgent need for interdisciplinary research in this field, especially for the Southeast Asian countries which have a high forecasted annual biofuel production growth rate in years to come. While biofuel enables countries to meet their energy goals, established interdisciplinary research done in this field will lead to more sustainable resource use, improved environmental performance, strengthened energy security and enhanced economic development.

Author Contributions: Conceptualization, H.P.Y. and F.Y.V.; methodology, H.P.Y. and F.Y.V.; formal analysis, H.P.Y., C.B.P.C. and F.Y.V.; resources, H.P.Y., C.B.P.C. and F.Y.V.; writing—original draft preparation, H.P.Y., C.B.P.C. and F.Y.V.; writing—review and editing, H.P.Y., C.B.P.C. and F.Y.V.; visualization, H.P.Y. and F.Y.V.; supervision, H.P.Y. All authors have read and agreed to the published version of the manuscript.

Funding: This research was funded by the Energy Studies Institute and the EU project “Sustainable Process Integration Laboratory—SPIL”, project No. CZ.02.1.01/0.0/0.0/15_003/0000456 by EU “CZ Operational Programme Research, Development and Education”.

Acknowledgments: Energy Studies Institute is acknowledged for core funding this piece of work. The EU project Sustainable Process Integration Laboratory—SPIL, funded as project No. CZ.02.1.01/0.0/0.0/15 003/0000456, by Czech Republic Operational Programme Research and Development, Education under the collaboration agreement with the Universiti Teknologi Malaysia is gratefully acknowledged.

Conflicts of Interest: The authors declare no conflict of interest.

References

1. IEA (International Energy Agency). *Renewables 2019*; IEA: Paris, France, 2019.
2. REUTERS. China Sets 2020 Target for Nationwide Ethanol to Cut Corn Stocks. Available online: www.reuters.com/article/us-china-biofuels/china-sets-2020-target-for-nationwide-ethanol-use-to-cut-corn-stocks-idUSKCN1BO03R (accessed on 29 November 2019).
3. National Energy Council. *National Blueprint of Energy in Indonesia*; The Ministry of Energy and Mineral Resources of Indonesia: Jakarta, Indonesia, 2017.
4. REUTERS. Indonesia President Wants B30 in Use by Jan 2020: Cabinet Secretary. Available online: www.reuters.com/article/us-indonesia-biodiesel/indonesia-president-wants-b30-in-use-by-january-2020-cabinet-secretary-idUSKCN1V20VR (accessed on 29 November 2019).
5. Ministry of Plantation Industries and Commodities Malaysia. *The National Biofuel Policy*; Ministry of Plantation Industries and Commodities Malaysia: Putrajaya, Malaysia, 2006.
6. REUTERS. Malaysia to Implement B10 Biodiesel Programme from Dec. 1. Available online: www.reuters.com/article/malaysia-palmoil-biodiesel/malaysia-to-implement-b10-biodiesel-programme-from-dec-1-idUSL4N1XY24I (accessed on 29 November 2019).
7. Department of Energy Philippines. *Biofuels Act of 2006*; 13th Congress of the Philippines: Taguig, Philippines, 2007.
8. Ison, L. Biofuels Industry Bats for B5 in Diesel by 2021. Available online: www.pna.gov.ph/articles/1074753 (accessed on 29 November 2019).
9. Department of Alternative Energy Development and Efficiency Thailand. *Alternative Energy Development Plan: AEDP 2015*; Department of Alternative Energy Development and Efficiency Thailand: Bangkok, Thailand, 2015; p. 22.
10. Trinh, T.A.; Linh Le, T.P. Biofuels Potential for Transportation Fuels in Vietnam: A Status Quo and SWOT Analysis. In Proceedings of the IOP Conference Series: Earth and Environmental Science, Ho Chi Minh City, Vietnam, 17–19 April 2018; Volume 143, pp. 1–18.
11. F+L Daily. Vietnam to Mandate 5% Ethanol Blends by January 2018. Available online: www.fuelsandlubers.com/vietnam-to-mandate-5-ethanol-blends-by-january-2018/ (accessed on 29 November 2019).
12. De Meyer, A.; Cattrysse, D.; Rasinmäki, J.; Van Orshoven, J. Methods to Optimise the Design and Management of Biomass-for-Bioenergy Supply Chains: A Review. *Renew. Sustain. Energy Rev.* **2014**, *31*, 657–670. [CrossRef]
13. Zandi Atashbar, N.; Labadie, N.; Prins, C. Modelling and Optimisation of Biomass Supply Chains: A Review. *Int. J. Prod. Res.* **2018**, *56*, 3482–3506. [CrossRef]
14. Roy, B. *Multicriteria Methodology for Decision Aiding*; Springer US: Dordrecht, The Netherlands, 1996.
15. Aguayo, M.M.; Sarin, S.C.; Cundiff, J.S.; Comer, K.; Clark, T. A Corn-Stover Harvest Scheduling Problem Arising in Cellulosic Ethanol Production. *Biomass Bioenergy* **2017**, *107*, 102–112. [CrossRef]
16. Ahn, Y.C.; Lee, I.B.; Lee, K.H.; Han, J.H. Strategic Planning Design of Microalgae Biomass-to-Biodiesel Supply Chain Network: Multi-Period Deterministic Model. *Appl. Energy* **2015**, *154*, 528–542. [CrossRef]
17. Čuček, L.; Martín, M.; Grossmann, I.E.; Kravanja, Z. Multi-Period Synthesis of Optimally Integrated Biomass and Bioenergy Supply Network. *Comput. Chem. Eng.* **2014**, *66*, 57–70. [CrossRef]
18. Foo, D.C.Y.; Tan, R.R.; Lam, H.L.; Abdul Aziz, M.K.; Klemeš, J.J. Robust Models for the Synthesis of Flexible Palm Oil-Based Regional Bioenergy Supply Chain. *Energy* **2013**, *55*, 68–73. [CrossRef]
19. Miret, C.; Chazara, P.; Montastruc, L.; Negny, S.; Domenech, S. Design of Bioethanol Green Supply Chain: Comparison between First and Second Generation Biomass Concerning Economic, Environmental and Social Criteria. *Comput. Chem. Eng.* **2016**, *85*, 16–35. [CrossRef]
20. Ng, R.T.L.; Maravelias, C.T. Design of Biofuel Supply Chains with Variable Regional Depot and Biorefinery Locations. *Renew. Energy* **2017**, *100*, 90–102. [CrossRef]

21. Ng, W.P.Q.; Lam, H.L.; Yusup, S. Supply Network Synthesis on Rubber Seed Oil Utilisation as Potential Biofuel Feedstock. *Energy* **2013**, *55*, 82–88. [[CrossRef](#)]
22. Rabbani, M.; Ramezankhani, F.; Giahi, R.; Farshbaf-Geranmayeh, A. Biofuel Supply Chain Considering Depreciation Cost of Installed Plants. *J. Ind. Eng. Int.* **2016**, *12*, 221–235. [[CrossRef](#)]
23. Santibañez-Aguilar, J.E.; González-Campos, J.B.; Ponce-Ortega, J.M.; Serna-González, M.; El-Halwagi, M.M. Optimal Planning and Site Selection for Distributed Multiproduct Biorefineries Involving Economic, Environmental and Social Objectives. *J. Clean. Prod.* **2014**, *65*, 270–294. [[CrossRef](#)]
24. López-Díaz, D.C.; Lira-Barragán, L.F.; Rubio-Castro, E.; Ponce-Ortega, J.M.; El-Halwagi, M.M. Optimal Location of Biorefineries Considering Sustainable Integration with the Environment. *Renew. Energy* **2017**, *100*, 65–77. [[CrossRef](#)]
25. How, B.S.; Tan, K.Y.; Lam, H.L. Transportation Decision Tool for Optimisation of Integrated Biomass Flow with Vehicle Capacity Constraints. *J. Clean. Prod.* **2016**, *136*, 197–223. [[CrossRef](#)]
26. Santibañez-Aguilar, J.E.; Rivera-Toledo, M.; Flores-Tlacuahuac, A.; Ponce-Ortega, J.M. A Mixed-Integer Dynamic Optimization Approach for the Optimal Planning of Distributed Biorefineries. *Comput. Chem. Eng.* **2015**, *80*, 37–62. [[CrossRef](#)]
27. Liu, Z.; Qiu, T.; Chen, B. A Study of the LCA Based Biofuel Supply Chain Multi-Objective Optimization Model with Multi-Conversion Paths in China. *Appl. Energy* **2014**, *126*, 221–234. [[CrossRef](#)]
28. Orjuela-Castro, J.A.; Aranda-Pinilla, J.A.; Moreno-Mantilla, C.E. Identifying Trade-Offs between Sustainability Dimensions in the Supply Chain of Biodiesel in Colombia. *Comput. Electron. Agric.* **2019**, *161*, 162–169. [[CrossRef](#)]
29. Osmani, A.; Zhang, J. Multi-Period Stochastic Optimization of a Sustainable Multi-Feedstock Second Generation Bioethanol Supply Chain—A Logistic Case Study in Midwestern United States. *Land Use Policy* **2017**, *61*, 420–450. [[CrossRef](#)]
30. Azadeh, A.; Vafa Arani, H.; Dashti, H. A Stochastic Programming Approach towards Optimization of Biofuel Supply Chain. *Energy* **2014**, *76*, 513–525. [[CrossRef](#)]
31. Bairamzadeh, S.; Saidi-Mehrabad, M.; Pishvae, M.S. Modelling Different Types of Uncertainty in Biofuel Supply Network Design and Planning: A Robust Optimization Approach. *Renew. Energy* **2018**, *116*, 500–517. [[CrossRef](#)]
32. Ghelichi, Z.; Saidi-Mehrabad, M.; Pishvae, M.S. A Stochastic Programming Approach toward Optimal Design and Planning of an Integrated Green Biodiesel Supply Chain Network under Uncertainty: A Case Study. *Energy* **2018**, *156*, 661–687. [[CrossRef](#)]
33. Maheshwari, P.; Singla, S.; Shastri, Y. Resiliency Optimization of Biomass to Biofuel Supply Chain Incorporating Regional Biomass Pre-Processing Depots. *Biomass Bioenergy* **2017**, *97*, 116–131. [[CrossRef](#)]
34. Mohseni, S.; Pishvae, M.S. A Robust Programming Approach towards Design and Optimization of Microalgae-Based Biofuel Supply Chain. *Comput. Ind. Eng.* **2016**, *100*, 58–71. [[CrossRef](#)]
35. Santibañez-Aguilar, J.E.; Morales-Rodriguez, R.; González-Campos, J.B.; Ponce-Ortega, J.M. Stochastic Design of Biorefinery Supply Chains Considering Economic and Environmental Objectives. *J. Clean. Prod.* **2016**, *136*, 224–245. [[CrossRef](#)]
36. Sharifzadeh, M.; Garcia, M.C.; Shah, N. Supply Chain Network Design and Operation: Systematic Decision-Making for Centralized, Distributed, and Mobile Biofuel Production Using Mixed Integer Linear Programming (MILP) under Uncertainty. *Biomass Bioenergy* **2015**, *81*, 401–414. [[CrossRef](#)]
37. Van Fan, Y.; Klemeš, J.J.; Walmsley, T.G.; Perry, S. Minimising Energy Consumption and Environmental Burden of Freight Transport Using a Novel Graphical Decision-Making Tool. *Renew. Sustain. Energy Rev.* **2019**, *114*, 1. [[CrossRef](#)]
38. Lam, H.L.; Varbanov, P.S.; Klemeš, J.J. Optimisation of Regional Energy Supply Chains Utilising Renewables: P-Graph Approach. *Comput. Chem. Eng.* **2010**, *34*, 782–792. [[CrossRef](#)]
39. Harahap, F.; Leduc, S.; Mesfun, S.; Khatiwada, D.; Kraxner, F.; Silveira, S. Opportunities to Optimize the Palm Oil Supply Chain in Sumatra, Indonesia. *Energies* **2019**, *12*, 420. [[CrossRef](#)]
40. Hoo, P.Y.; Hashim, H.; Ho, W.S.; Yunus, N.A. Spatial-Economic Optimisation of Biomethane Injection into Natural Gas Grid: The Case at Southern Malaysia. *J. Environ. Manag.* **2019**, *241*, 603–611. [[CrossRef](#)]
41. Zhang, F.; Wang, J.; Liu, S.; Zhang, S.; Sutherland, J.W. Integrating GIS with Optimization Method for a Biofuel Feedstock Supply Chain. *Biomass Bioenergy* **2017**, *98*, 194–205. [[CrossRef](#)]

42. Asadi, E.; Habibi, F.; Nickel, S.; Sahebi, H. A Bi-Objective Stochastic Location-Inventory-Routing Model for Microalgae-Based Biofuel Supply Chain. *Appl. Energy* **2018**, *228*, 2235–2261. [[CrossRef](#)]
43. Marufuzzaman, M.; Eksioğlu, S.D.; Huang, Y. Two-Stage Stochastic Programming Supply Chain Model for Biodiesel Production via Wastewater Treatment. *Comput. Oper. Res.* **2014**, *49*, 1–17. [[CrossRef](#)]
44. Poudel, S.; Marufuzzaman, M.; Quddus, M.A.; Chowdhury, S.; Bian, L.; Smith, B. Designing a Reliable and Congested Multi-Modal Facility Location Problem for Biofuel Supply Chain Network. *Energies* **2018**, *11*, 1682. [[CrossRef](#)]
45. How, B.S.; Lam, H.L. Integrated Palm Biomass Supply Chain toward Sustainable Management. *Chem. Prod. Process Model.* **2017**, *12*, 1–19. [[CrossRef](#)]
46. Ng, R.T.L.; Maravelias, C.T. Economic and Energetic Analysis of Biofuel Supply Chains. *Appl. Energy* **2017**, *205*, 1571–1582. [[CrossRef](#)]
47. Geng, N.; Zhang, Y.; Sun, Y.; Geng, S. Optimization of Biodiesel Supply Chain Produced from Waste Cooking Oil: A Case Study in China. In *IOP Conference Series: Earth and Environmental Science*; IOP Publishing: Bristol, UK, 2019; Volume 264.
48. Schlamadinger, B.; Faaij, A.P.C.; Daugherty, E. Should We Trade Biomass, Electricity, Renewable Certificates, or CO₂ Credits? In *IEA Bioenergy Task 38 40*; IEA: Paris, France, 2004.
49. Welfle, A. Balancing Growing Global Bioenergy Resource Demands—Brazil’s Biomass Potential and the Availability of Resource for Trade. *Biomass Bioenergy* **2017**, *105*, 83–95. [[CrossRef](#)]
50. Junginger, M.; Goh, C.S.; Faaij, A. *International Bioenergy Trade*; Lect. Notes Energy; Springer: Berlin/Heidelberg, Germany, 2014.
51. Lamers, P.; Hamelinck, C.; Junginger, M.; Faaij, A. International Bioenergy Trade—A Review of Past Developments in the Liquid Biofuel Market. *Renew. Sustain. Energy Rev.* **2011**, *15*, 2655–2676. [[CrossRef](#)]
52. WBA (World Bioenergy Association). *Biomass Supply Chains—Harvesting & Collection, Pre-Treatment & Upgrading, Storage, Transportation & Handling*; World Bioenergy Association: Stockholm, Sweden, 2018.
53. Laurijssen, J.; Faaij, A.P.C. Trading Biomass or GHG Emission Credits? *Clim. Chang.* **2009**, *94*, 287. [[CrossRef](#)]
54. NREL (National Renewable Energy Laboratory). *International Trade of Biofuels*; NREL: Golden, CO, USA, 2013.
55. Deng, Y.Y.; Koper, M.; Haigh, M.; Dornburg, V. Country-Level Assessment of Long-Term Global Bioenergy Potential. *Biomass Bioenergy* **2015**, *74*, 253–267. [[CrossRef](#)]
56. Lamers, P.; Hoefnagels, R.; Junginger, M.; Hamelinck, C.; Faaij, A. Global Solid Biomass Trade for Energy by 2020: An Assessment of Potential Import Streams and Supply Costs to North-West Europe under Different Sustainability Constraints. *GCB Bioenergy* **2015**, *7*, 618–634. [[CrossRef](#)]
57. Diesenreiter, F.; Kranzl, L. Approaches for Modelling the International Trade of Biomass for Bioenergy (to Evaluate Its Impacts on Bioenergy Markets). Available online: www.researchgate.net/publication/228558774_Approaches_for_modelling_the_international_trade_of_Biomass_for_Bioenergy_to_evaluate_its_impacts_on_bioenergy_markets (accessed on 11 February 2020).
58. Solberg, B.; Dornburg, V.; Bolkesjø, T.F.; Faaij, A.; Junginger, M.; Trømborg, E. *Bioenergy and Biomass Trade: Evaluation of Models’ Suitability for Analysing International Trade of Biomass and Bioenergy Products*; Norwegian University of Life Sciences: Aas, Norway; Copernicus Institute, Utrecht University: Utrecht, The Netherlands, 2007.
59. Hoefnagels, R.; Kluts, I.; Junginger, M.; Visser, L.; Resch, G.; Mantau, U.; Pelkmans, L.; Devriendt, N. *Sustainable and Optimal Use of Biomass for Energy in the EU beyond 2020*; European Commission: Brussels, Belgium, 2017.
60. Van Bergeijk, P.A.G.; Brakman, S. *The Gravity Model in International Trade: Advances and Applications*; Van Bergeijk, P.A.G., Brakman, S., Eds.; Cambridge University Press: Cambridge, UK, 2010.
61. Baldwin, R.; Taglioni, D. *Gravity Chains Estimating Bilateral Trade Flows When Parts and Components Trade Is Important*; ECB (European Central Bank): Frankfurt, Germany, 2011.
62. Röttgers, D.; Faße, A.; Ulrike, G. The Canola Oil Industry and EU Trade Integration: A Gravity Model Approach. In *Proceedings of the German Development Economics Conference 2010*, Hannover, Germany, 18–19 June 2010; p. 32.
63. Rentizelas, A.; Melo, I.C.; Alves Junior, P.N.; Campoli, J.S.; Aparecida do Nascimento Rebelatto, D. Multi-Criteria Efficiency Assessment of International Biomass Supply Chain Pathways Using Data Envelopment Analysis. *J. Clean. Prod.* **2019**, *237*, 117690. [[CrossRef](#)]

64. Matzenberger, J.; Kranzl, L.; Tromborg, E.; Junginger, M.; Daioglou, V.; Sheng Goh, C.; Keramidis, K. Future Perspectives of International Bioenergy Trade. *Renew. Sustain. Energy Rev.* **2015**, *43*, 926–941. [[CrossRef](#)]
65. Čuček, L.; Varbanov, P.S.; Klemeš, J.J.; Kravanja, Z. Total Footprints-Based Multi-Criteria Optimisation of Regional Biomass Energy Supply Chains. *Energy* **2012**, *44*, 135–145. [[CrossRef](#)]
66. Jonkman, J.; Kanellopoulos, A.; Bloemhof, J.M. Designing an Eco-Efficient Biomass-Based Supply Chain Using a Multi-Actor Optimisation Model. *J. Clean. Prod.* **2019**, *210*, 1065–1075. [[CrossRef](#)]
67. Lee, C.Y.; Sun, W.C.; Li, Y.H. Biodiesel Economic Evaluation and Biomass Planting Allocation Optimisation in Global Supply Chain. *IEEE Trans. Eng. Manag.* **2019**, 1–14. [[CrossRef](#)]
68. De Matta, R.; Miller, T. Formation of a Strategic Manufacturing and Distribution Network with Transfer Prices. *Eur. J. Oper. Res.* **2015**, *241*, 435–448. [[CrossRef](#)]
69. Gonela, V.; Zhang, J.; Osmani, A.; Onyeaghala, R. Stochastic Optimization of Sustainable Hybrid Generation Bioethanol Supply Chains. *Transp. Res. Part E Logist. Transp. Rev.* **2015**, *77*, 1–28. [[CrossRef](#)]
70. Razm, S.; Nickel, S.; Sahebi, H. A Multi-Objective Mathematical Model to Redesign of Global Sustainable Bioenergy Supply Network. *Comput. Chem. Eng.* **2019**, *128*, 1–20. [[CrossRef](#)]
71. Proskurina, S.; Junginger, M.; Heinimö, J.; Vakkilainen, E. Global Biomass Trade for Energy—Part 1: Statistical and Methodological Considerations. *Biofuels Bioprod. Biorefin.* **2019**, *13*, 358–370. [[CrossRef](#)]
72. Fingerman, K.R.; Nabuurs, G.J.; Iriarte, L.; Fritsche, U.R.; Staritsky, I.; Visser, L.; Mai-Moulin, T.; Junginger, M. Opportunities and Risks for Sustainable Biomass Export from the South-Eastern United States to Europe. *Biofuels Bioprod. Biorefin.* **2019**, *13*, 281–292. [[CrossRef](#)]
73. Pelkmans, L.; Van Dael, M.; Junginger, M.; Fritsche, U.R.; Diaz-Chavez, R.; Nabuurs, G.J.; Del Campo Colmenar, I.; Gonzalez, D.S.; Rutz, D.; Janssen, R. Long-Term Strategies for Sustainable Biomass Imports in European Bioenergy Markets. *Biofuels Bioprod. Biorefin.* **2019**, *13*, 388–404. [[CrossRef](#)]
74. IRENA (International Renewable Energy Agency); ACE (ASEAN Centre for Energy). *Renewable Energy Outlook for ASEAN*; IRENA: Abu Dhabi, UAE; ACE: Jakarta, Indonesia, 2016.
75. Masjuki, H.H.; Kalam, M.A.; Mofijur, M.; Shahabuddin, M. Biofuel: Policy, Standardization and Recommendation for Sustainable Future Energy Supply. *Energy Procedia* **2013**, *42*, 577–586. [[CrossRef](#)]
76. MIDA (Malaysian Investment Development Authority). Time to Implement Malaysia’s Biodiesel Mandate. Available online: www.mida.gov.my/home/6751/news/time-to-implement-malaysia-s-biodiesel-mandate/ (accessed on 27 December 2019).
77. Abdul-Manan, A.F.N.; Baharuddin, A.; Chang, L.W. A Detailed Survey of the Palm and Biodiesel Industry Landscape in Malaysia. *Energy* **2014**, *76*, 931–941. [[CrossRef](#)]
78. MPI (Ministry of Primary Industry). Malaysia Biofuel Programme. Available online: mpi.gov.my/index.php/en/media-2/mpic-in-the-news/255-mpic-di-dalam-akhbar-2019/berita-biobahan-api/575-program-biobahan-api-malaysia-bi (accessed on 27 December 2019).
79. Zainal, H. B7 Biodiesel to Be Launched to Replace B5 at Petrol Stations from Nov 1. Available online: www.thestar.com.my/news/nation/2014/10/29/b7-biodiesel-to-be-launched-lower-emission-fuel-to-replace-b5-at-petrol-stations-from-nov-1 (accessed on 27 December 2019).
80. Wahab, A.G. *Malaysia Biofuels Annual*; United States Department of Agriculture (USDA) Global Agricultural Information Network (GAIN): Washington, DC, USA, 2018.
81. MPOC (Malaysian Palm Oil Council). Palm Oil: B7 and B10 Biodiesel Will Use 450,000 Tonnes Additional CPO. Available online: mpi.gov.my/index.php/en/media-2/mpic-in-the-news/254-news-b10/2112-palm-oil-b7-and-b10-biodiesel-will-use-450-000-tonnes-additional-cpo (accessed on 27 December 2019).
82. Wahab, A.G. *Malaysia Biofuels Annual*; United States Department of Agriculture (USDA) Global Agricultural Information Network (GAIN): Washington, DC, USA, 2019.
83. Tye, Y.Y.; Lee, K.T.; Wan Abdullah, W.N.; Leh, C.P. Second-Generation Bioethanol as a Sustainable Energy Source in Malaysia Transportation Sector: Status, Potential and Future Prospects. *Renew. Sustain. Energy Rev.* **2011**, *15*, 4521–4536. [[CrossRef](#)]
84. Derman, E.; Abdulla, R.; Marbawi, H.; Sabullah, M.K. Oil Palm Empty Fruit Bunches as a Promising Feedstock for Bioethanol Production in Malaysia. *Renew. Energy* **2018**, *129*, 285–298. [[CrossRef](#)]
85. Abdulrazik, A.; Elsholkami, M.; Elkamel, A.; Simon, L. Multi-Products Productions from Malaysian Oil Palm Empty Fruit Bunch (EFB): Analyzing Economic Potentials from the Optimal Biomass Supply Chain. *J. Clean. Prod.* **2017**, *168*, 131–148. [[CrossRef](#)]

86. Rahmadi, A.; Aye, L.; Moore, G. The Feasibility and Implications for Conventional Liquid Fossil Fuel of the Indonesian Biofuel Target in 2025. *Energy Policy* **2013**, *61*, 12–21. [CrossRef]
87. Putrasari, Y.; Praptijanto, A.; Santoso, W.B.; Lim, O. Resources, Policy, and Research Activities of Biofuel in Indonesia: A Review. *Energy Rep.* **2016**, *2*, 237–245. [CrossRef]
88. Ministry of Energy and Mineral Resources Indonesia. Bioenergy in Indonesia: Rules and Implementations. Available online: www.ieabioenergy.com/wp-content/uploads/2018/09/1.5-Elis-Heviati.pdf (accessed on 27 December 2019).
89. REUTERS. Indonesia Launches B30 Biodiesel to Cut Costs, Boost Palm Oil. Available online: www.theedgemarkets.com/article/indonesia-launches-b30-biodiesel-cut-costs-boost-palm-oil (accessed on 27 December 2019).
90. Lecksiwilai, N.; Gheewala, S.H.; Silalertruksa, T.; Mungkalasiri, J. LCA of Biofuels in Thailand Using Thai Ecological Scarcity Method. *J. Clean. Prod.* **2017**, *142*, 1183–1191. [CrossRef]
91. Thailand Ministry of Energy. Thailand Power Development Plan. Available online: www.eppo.go.th/index.php/en/policy-and-plan/en-tieb/tieb-pdp (accessed on 27 December 2019).
92. Boyd, C. *Thailand Alternative Fuels Update 2017*; United State Department of Energy: Washington, WA, USA, 2017.
93. Hong, C.S. Thailand’s Renewable Energy Transitions: A Pathway to Realize Thailand 4.0. Available online: thediplomat.com/2019/03/thailands-renewable-energy-transitions-a-pathway-to-realize-thailand-4-0/ (accessed on 27 December 2019).
94. Oils & Fats International. B10 Biodiesel Introduced in Thailand. Available online: www.ofimagazine.com/news/b10-biodiesel-introduced-in-thailand (accessed on 27 December 2019).
95. Sapp, M. Thai B20 Mandate Set for End-April. Available online: www.biofuelsdigest.com/bdigest/2019/04/08/thai-b20-mandate-set-for-end-april/ (accessed on 27 December 2019).
96. Asia Biomass Office. Introduction Status for Biofuel in Thailand. Available online: www.asiabiomass.jp/english/topics/1505_01.html (accessed on 27 December 2019).
97. Permpool, N.; Bonnet, S.; Gheewala, S.H. Greenhouse Gas Emissions from Land Use Change Due to Oil Palm Expansion in Thailand for Biodiesel Production. *J. Clean. Prod.* **2016**, *134 Pt. B*, 532–538. [CrossRef]
98. Mukherjee, I.; Sovacool, B.K. Palm Oil-Based Biofuels and Sustainability in Southeast Asia: A Review of Indonesia, Malaysia, and Thailand. *Renew. Sustain. Energy Rev.* **2014**, *37*, 1–12. [CrossRef]
99. Abdul-Manan, A.F.N.; Baharuddin, A.; Chang, L.W. Application of Theory-Based Evaluation for the Critical Analysis of National Biofuel Policy: A Case Study in Malaysia. *Eval. Program Plan.* **2015**, *52*, 39–49. [CrossRef] [PubMed]
100. Čuček, L.; Klemeš, J.J.; Kravanja, Z. A Review of Footprint Analysis Tools for Monitoring Impacts on Sustainability. *J. Clean. Prod.* **2012**, *34*, 9–20. [CrossRef]
101. Tan, K.T.; Lee, K.T.; Mohamed, A.R.; Bhatia, S. Palm Oil: Addressing Issues and towards Sustainable Development. *Renew. Sustain. Energy Rev.* **2009**, *13*, 420–427. [CrossRef]
102. Chien Bong, C.P.; Ho, W.S.; Hashim, H.; Lim, J.S.; Ho, C.S.; Peng Tan, W.S.; Lee, C.T. Review on the Renewable Energy and Solid Waste Management Policies towards Biogas Development in Malaysia. *Renew. Sustain. Energy Rev.* **2017**, *70*, 988–998. [CrossRef]
103. Maulia, E.; Kumar, P.P. Palm Oil: Indonesia and Malaysia Push Back as EU Clamps Down. Available online: asia.nikkei.com/Spotlight/Asia-Insight/Palm-oil-Indonesia-and-Malaysia-push-back-as-EU-clamps-down (accessed on 27 December 2019).
104. Kraxner, F.; Nordström, E.M.; Havlík, P.; Gusti, M.; Mosnier, A.; Frank, S.; Valin, H.; Fritz, S.; Fuss, S.; Kindermann, G.; et al. Global Bioenergy Scenarios—Future Forest Development, Land-Use Implications, and Trade-Offs. *Biomass Bioenergy* **2013**, *57*, 86–96. [CrossRef]
105. Chanthawong, A.; Dhakal, S.; Jongwanich, J. Supply and Demand of Biofuels in the Fuel Market of Thailand: Two Stage Least Square and Three Least Square Approaches. *Energy* **2016**, *114*, 431–443. [CrossRef]
106. Mekhilef, S.; Siga, S.; Saidur, R. A Review on Palm Oil Biodiesel as a Source of Renewable Fuel. *Renew. Sustain. Energy Rev.* **2011**, *15*, 1937–1949. [CrossRef]
107. EPA (Environmental Protection Agency). Renewable Fuel Annual Standards. Available online: <https://www.epa.gov/renewable-fuel-standard-program/renewable-fuel-annual-standards> (accessed on 3 February 2020).

108. Shafie, S.M.; Mahlia, T.M.I.; Masjuki, H.H.; Andriyana, A. Current Energy Usage and Sustainable Energy in Malaysia: A Review. *Renew. Sustain. Energy Rev.* **2011**, *15*, 4370–4377. [[CrossRef](#)]
109. Hosseini, S.E.; Wahid, M.A. Necessity of Biodiesel Utilization as a Source of Renewable Energy in Malaysia. *Renew. Sustain. Energy Rev.* **2012**, *16*, 5732–5740. [[CrossRef](#)]



© 2020 by the authors. Licensee MDPI, Basel, Switzerland. This article is an open access article distributed under the terms and conditions of the Creative Commons Attribution (CC BY) license (<http://creativecommons.org/licenses/by/4.0/>).

Article

Optimal Design of Welded Plate Heat Exchanger for Ammonia Synthesis Column: An Experimental Study with Mathematical Optimisation

Leonid Tovazhnyansky¹, Jiří Jaromír Klemeš², Petro Kapustenko^{1,3,*}, Olga Arsenyeva⁴, Olexandr Perevertaylenko¹ and Pavlo Arsenyev^{3,*}

¹ Department of Integrated Technologies, Processes and Apparatuses, National Technical University “Kharkiv Polytechnic Institute”, Dep. ITPA, 2 Kyrpychova St., 61002 Kharkiv, Ukraine; radnyk@kpi.kharkov.ua (L.T.); pau@kpi.kharkov.ua (O.P.)

² Sustainable Process Integration Laboratory—SPIL, NETME Centre, Faculty of Mechanical Engineering, Brno University of Technology—VUT Brno, Technická 2896/2, 616 69 Brno, Czech Republic; jiri.klemes@vutbr.cz

³ AO Spivdruzhnist-T LLC, 2 Kaplunovskiy per., 19, 61002 Kharkiv, Ukraine

⁴ Department of Automatic Control and Computer Integrated Engineering, OM Beketov National University of Urban Economy in Kharkiv, 17 Marshal Bazhanov St., 61002 Kharkiv, Ukraine; o.p.arsenyeva@gmail.com

* Correspondence: sodrut@gmail.com (P.K.); spivdruzhnist.t@gmail.com (P.A.)

Received: 6 May 2020; Accepted: 26 May 2020; Published: 3 June 2020

Abstract: The production of ammonia, consuming up to 5% of natural gas global production, accounts for about 2% of world energy. Worldwide, the Haber–Bosch process is the mainly used method of ammonia catalytic synthesis, involving temperatures up to 600 °C and pressures up to 32 MPa. In this paper, the results of the development and study of the special welded construction of plate heat exchanger (WPHE) for a column of ammonia synthesis are presented. The heat transfer and hydraulic performance of developed WPHE are investigated on a one-pass model in laboratory conditions. An equation for the relation between heat transfer effectiveness and the number of heat transfer units is proposed. A mathematical model of multi-pass WPHE is developed using these results. The validity of this model is confirmed by results of industrial tests performed with the prototype WPHE installed in operating column of ammonia synthesis at temperatures about 500 °C and pressure about 32 MPa. The tests confirmed the reliability of WPHE and its efficiency compared to a tubular heat exchanger. A method of optimal design of WPHE that allows finding the optimal height of corrugations and the number of passes in WPHE for specified conditions of operation is developed.

Keywords: ammonia synthesis; plate heat exchanger; heat transfer; multi-pass arrangement; optimal design; energy efficiency

1. Introduction

The sustainable development of modern society requires the efficient energy usage to limit the depletion of fossil fuels resources and minimise the environmental hazard of their combustion, which is leading to the generation of harmful emissions and, especially, CO₂ and greenhouse gases. It is the most important for industries with high levels of energy involved in production processes. One of such processes is the synthesis of such valuable product as ammonia, which is widely used in different industrial applications, such as the production of fertilisers, fibres, polymers and plastics, papers, acids and explosive materials [1]. It is also can be used as a carbon emission-free carrier of hydrogen, offering a high energy density that could be used in a system for energy transport, storage and power generation [2].

Up to 72% of industrial ammonia production worldwide is based on the steam reforming of methane from natural gas [3]. It is mainly performed using the Haber–Bosch process, requiring gaseous nitrogen from air and hydrogen. Their mixture is forming syngas that is moving through the catalyst at temperatures up to 600 °C and pressures up to 32 MPa. The synthesis reaction is exothermic, with the generation of large amounts of heat energy that have to be removed with a good cooling system. This industrial process is responsible for consumption up to 5% of natural gas global production, accounting for nearly 2% of the world's energy generation and emitting about 1% of greenhouse gases [4].

The practical industrial realisation of this process is performed mostly with reactors of three different types: reactors with direct internal cooling, reactors of adiabatic quench cooling and indirect adiabatic cooling. [5] reports a comparison of these reactor cooling systems, showing the advantage in the efficiency of the internal direct cooling system. An exergy approach for modelling and optimisation of an industrial ammonia synthesis unit was presented in [6]. It was concluded that the biggest part of exergy destruction is happening in the ammonia reactor. The exergy study of two concepts in ammonia synthesis loop configurations is presented in [7]. It includes an adiabatic reactor with three stages including intermediate quench cooling and indirect-cooled reactor. It is concluded that the major equipment (reactor, heat exchangers) must be accounted for first for improvement of the overall design with consideration for the implementation of heat integration.

In recent years, to reduce fossil fuel usage and the impacts on the environment of conventional ammonia production, green processes of ammonia production with the use of green hydrogen have been investigated. The comparative study of such production schemes, presented in [8], has shown the importance of maximising the heat recovery of the overall system that requires efficient heat exchangers. The use of ammonia synthesis combined with nitrogen production and power generation is discussed in [9]. The uses of solar energy in ammonia production and optimisation for energy, cost and carbon emission are studied in [10]. The thermochemical storage systems of solar energy based on ammonia are investigated in [11]. The efficient and compact recuperative heat exchangers are needed to increase heat recuperation and save energy in all these processes involving ammonia synthesis. The principles of heat transfer intensification are the major tool in developing the construction of such heat exchangers [12].

Plate Heat Exchangers (PHEs) are one of the high-efficiency types of compact heat exchangers with intensified heat transfer. The main construction features and principles of operation and design for PHE have been well discussed in publications (see, e.g., [13]). The most known is plate-and-frame PHE, which was initially developed and used in food production and later confirmed its efficiency in many different applications. It is proved in many research results; for example, in [14] it was shown that, for water to water heat transfer, plate-and-frame PHE has about a 13% lower cost than a tubular heat exchanger at the same position. The high efficiency of PHE is confirmed at the chemical industry [15], in the process of the CO₂ capture [16], for waste heat utilisation from exhaust gas [17]. However, the range of operating conditions for plate-and-frame PHE is limited by pressure below 25 bar and a temperature not more than 180 °C, mostly by the presence of elastomeric gaskets. For severe working conditions with aggressive fluids, the cost of gaskets from sophisticated elastomers can substantially increase the cost of the whole PHE.

To increase the field of PHE applications in different industries by limiting the use of elastomeric gaskets, constructions of the brazed (BPHE) and welded (WPHE) types of PHE were developed. In WPHE, the sealing of passages between plates is made by welding, allowing an increase of the working temperatures and pressures significantly. Currently, different types of WPHE are developed and fabricated by PHE producers. The most frequently used are Plate-and-Block (Compabloc) PHE and Plate-and-Shell HE (PSHE), compared in [18]. Now, WPHEs finding their way in many applications, e.g., more than 750 Compabloc heat exchangers were installed at different positions in the oil refining industry [19]. The welded construction allows an increase in working temperatures below 400 °C and pressure up to 42 bar.

The main feature of Compabloc WPHE is the use of crossflow of streams in one pass and the overall counter-flow arrangement in a whole heat exchanger. Such a construction feature is also used in WPHE, specially developed for operation inside the shell of the column for ammonia synthesis at temperatures up to 525 °C and pressures about 320 bar [13] (pp. 79–80). It consists of round, corrugated plates, like the one shown in Figure 1. The plates are produced with different diameters to fit the columns, with inside diameters from 600 to 1200 mm. In the manufacturing process, plates are collected and welded together to form criss-cross flow channels with multiple contact points at the edges of corrugations. It makes a robust construction capable of withstanding high-pressure difference between heat-exchanging streams. The created round block of welded plates is equipped with welded collectors and baffles that are organising the multi-pass flow of heat exchanging streams through the channels systems. There is a crossflow of streams in an individual pass with globally countercurrent flow arrangement in WPHE as a whole. From the point of flow distribution in a channel and the pressure drop in it, such an arrangement has an advantage compared to plate-and-frame PHE where the flow is distributed from a relatively small port to the full width of the channel. It involves additional pressure loss in that distribution zone that can be avoided with crossflow of streams in one pass of considered WPHE. However, the crossflow can involve a considerable reduction in the effective mean temperature difference between streams, and the deterioration of heat transfer effectiveness, the overall countercurrent flow in multi-pass WPHE is organised to limit this effect. However, the influence of crossflow in individual passes has to be considered accurate enough for an engineering applications design of WPHE.



Figure 1. The plate of WPHE for an ammonia synthesis column.

The convenient way to account for crossflow in a heat exchanger is the use of the relationship between effectiveness, ϵ , of heat transfer and the number NTU of heat transfer units. Equations of such a relationship for idealised flow models of both fluids—mixed and unmixed—and one fluid mixed, and another unmixed, are presented in the book [20]. But in real heat exchangers, such a relationship can differ significantly, depending on the heat exchanger type and the level of flows mixing in its channels. This phenomenon was investigated by a number of researchers. The case of two unmixed fluids with the development of approximate equation for it was studied by Triboix [21]. For compact heat exchangers with different and complex finned surfaces, a hybrid method was proposed in [22]. The survey of recent developments on heat transfer in crossflow tubular and tubes-and-fins heat exchangers is presented in [23]. For crossflow tubular heat exchangers with different tube passes, closed-form relationships of temperature effectiveness are proposed by Magazoni et al. [24]. The results of the study of multi-row cross flow tubes-and-fins heat exchangers are reported in [25] and approach to calculate overall heat transfer coefficient for water–air tubes-and-fins heat exchanger in [26]. The results of the parametric study of cross flow heat exchangers with heat transfer enhancement by external and internal recycles were reported by Luo [27]. For compact diffusion-bonded crossflow heat exchangers, the results of theoretical and experimental study of heat transfer were reported in [28], with further

development in [29]. In their study of the cabinet cooling system, Borjigin et al. [30] have found that, at certain conditions with crossflow PHE, the system has lower thermal resistance and better cooling performance with counter-flow PHE.

Presently, there are very few published data accurate enough to perform design and optimisation of the considered WPHE type for the engineering applications. The correlations obtained for counter-flow PHEs need to be validated and adopted for the considered type of channels with the crossflow and variable angle of corrugations on the surface of forming round channel plates. There are no data allowing adequate estimations of the level of fluid mixing in PHE channels for the use of published relations for the crossflow correction factor, depending on the level of fluids mixing in channels.

The aim of the present paper is to develop a method of modelling and optimisation, which considers WPHE for an ammonia synthesis column with round plates that is accurate enough for engineering applications. It is based on mathematical modelling and experimental data on heat transfer and pressure drop in WPHE channels. Reported here are the results of an experimental study, in laboratory conditions, of the thermal and hydraulic performance of a one-pass crossflow model of WPHE for ammonia synthesis column. On that basis, the mathematical model of multi-pass WPHE is developed, and its validation in industry performed. After that, the use of the model for optimisation of WPHE for specific conditions of its operation is described.

2. Laboratory Experiment

For the accurate modelling and design of WPHE, the reliable correlations for a calculation of heat transfer and pressure drop in channels of specific geometry are required. Such correlations for the models of criss-cross flow channels of PHEs with countercurrent flow are presented in [31], and the approach for their application for commercial plates in [13] (pp. 228–231). To check the validity of these correlations and to adopt them for specific construction of developed WPHE with crossflow of streams, the experimental data are needed.

The experimental study of heat transfer and pressure losses is performed with the model of WPHE having 15 plates welded together for modelling one pass of WPHE. There are 14 channels formed between plates; seven channels are for the hot stream, and the other seven channels are for the cold stream. The geometries of the channels at the hot and cold sides are different. At the cold stream, the side channel is formed by two plates, assembled in WPHE, which have different corrugation angles to the main flow direction. On one plate, corrugations are mainly (at 2/3 of plates area) situated parallel to the main flow. The corrugations on the other plate are inclined with the angle of 60° to the direction of the main flow. The average corrugation angle in this part of the channel is 30° . In the other third of the channel area, the angle of corrugations on both plates forming the channel is 60° . The averaged channel area angle of corrugations is $\beta_2 = 40^\circ$. The averaged on another channel area angle of corrugations to the main flow direction in this channel is $\beta_1 = 50^\circ$. These forms of corrugations at channel walls are made for facilitating the removal of possible dust in a stream, leaving a catalyser that can start to appear with catalyser aging. The geometrical parameters of the WPHE model, its plates and channels, are given in Table 1.

The thermal and hydraulic parameters of the WPHE model are determined from measurements at the test rig with distilled water flowing as hot and cold fluids. The structure of the test rig is shown in Figure 2. It has a closed water circuit. The water is pumped from its reservoir to the shell-and-tube steam heater to maintain specified temperature t_{11} of the hot stream at the model inlet. Inside the WPHE model it is being cooled to a temperature t_{12} at the outlet, and afterwards, it is directed to the additional PHE for cooling to temperature t_{21} by cold water from the centralised circuit with the cooling tower. With this temperature cold stream entering the WPHE model, it is heated to the cold stream outlet temperature t_{22} and is coming back into the water reservoir. The circulating water flowrate is measured with orifice meter. The temperatures at the entrances and exits of heat exchanging streams in the WPHE model are measured with an accuracy of $\pm 0.05^\circ\text{C}$ by thermocouples copper–constantan. Two differential pressure gauges are used to measure pressure drops of hot- and cold-water streams.

The tests are performed in a stable regime. The water temperature after the steam heater was varied from 55 to 85 °C. The temperature of cold water in the reservoir was in the range of 30 to 45 °C. The flowrate of circulating water was in the range of 0.8 and 4.5 kg/s.

Table 1. The parameters of WPHE experimental model.

Parameter	Value
Model area of heat transfer, F_{am} , m ²	4.2
Number of plates, N_{pl}	15
One plate area of heat transfer, F_{pl} , m ²	0.32
The cross-section area of one channel, f_{ch} , m ²	0.0022
Plate outside diameter, D_o , m	0.626
The plate wall thickness, δ_w , m	0.001
Plate material	AISI304
Plate metal heat conductivity, λ_w , W/(m·K)	16
Corrugation depth, b , m	0.004
Corrugation pitch, S , m	0.018
The average channel width, W_{ch} , m	0.55
Channel equivalent diameter, d_e , m	0.008
The averaged angle of corrugations, degrees:	
hot side, β_1	50
cold side, β_2	40
Width of inlet/exit area of channel, W_{inx} , m	0.4

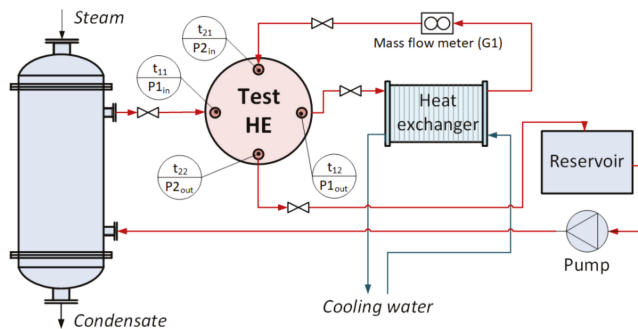


Figure 2. Structure of the test rig.

The heat load Q of the model is determined as an average of the calculated for cold stream Q_2 and for hot stream Q_1 , W:

$$Q_2 = G \cdot c_{p2} \cdot (t_{22} - t_{21}); \quad Q_1 = G \cdot c_{p1} \cdot (t_{11} - t_{12}); \quad Q = (Q_1 + Q_2)/2, \quad (1)$$

where G is mass flowrate of water, kg/s; c_{p1} is the specific heat capacity of a hot stream, J/(kg·K); c_{p2} is the specific heat capacity of a cold stream, J/(kg·K).

In a closed water circuit, the mass flowrates of hot and cold streams are the same, and the heat capacity difference is less 0.3%, so heat capacity flowrates are equal, and the mean temperature difference is

$$\Delta t_m = \frac{(t_{11} + t_{12}) - (t_{21} + t_{22})}{2} \quad (2)$$

The experimental value of overall heat transfer coefficient, W/(m²·K), is as follows:

$$U_{ex} = \frac{Q}{\Delta t_m \cdot F_{am}} \quad (3)$$

The experimental results are compared with calculated by Equation (4):

$$U_{cl} = \left(\frac{1}{h_1} + \frac{1}{h_2} + \frac{\delta_w}{\lambda_w} + R_f \right)^{-1} \tag{4}$$

where h_i are the film heat transfer coefficients for cold (index $i = 2$) and hot (index $i = 1$) sides, $W/(m^2 \cdot K)$; λ_w is a thermal conductivity of plate metal, $W/(m \cdot K)$; δ_w thickness of the plate metal, m ; R_f is the fouling thermal resistance in WPHE, $m^2 \cdot K/W$. In laboratory experiments, it is taken that $R_f = 0$.

The film heat transfer coefficients are calculated based on the modified analogy of heat and momentum transfer [31]:

$$Nu_i = 0.065 \cdot Re_i^{\frac{6}{7}} \cdot \left(\frac{\psi_i \cdot \zeta_i}{F_X} \right)^{\frac{3}{7}} \cdot Pr_i^c \cdot \left(\frac{\mu_i}{\mu_{wi}} \right)^{0.14} \tag{5}$$

where μ_i is fluid dynamic viscosity at the main flow temperature, Pa-s; μ_{wi} is fluid dynamic viscosity at the wall temperature, Pa-s; $Nu = h_i \cdot d_e / \lambda_i$ is Nusselt number; λ_i is fluid thermal conductivity, $W/(m \cdot K)$; Pr_i is Prandtl number; ζ_i is the friction factor; ψ_i is the ratio of friction pressure loss to a total loss of pressure; F_X is the factor of area enlargement because of corrugations.

The value of ψ_i is calculated by Equation proposed in [32]:

$$\psi_i = \left\{ \frac{Re_i}{380} \cdot [\tan(\beta_i)]^{1.75} \right\}^{-0.15 \cdot \sin(\beta_i)} \geq 1 \tag{6}$$

For calculation of friction factor, Equation (7) is used [31]:

$$\zeta_i = 8 \cdot \left[\left(\frac{12 + p_{2i}}{Re_i} \right)^{12} + \frac{1}{(A_i + B_i)^{\frac{3}{2}}} \right]^{\frac{1}{12}}, \tag{7}$$

$$A_i = \left[p_{4i} \cdot \ln \left(\frac{p_{5i}}{\left(\frac{7 \cdot p_{3i}}{Re_i} \right)^{0.9} + 0.27 \cdot 10^{-5}} \right) \right]^{16}, \quad B_i = \left(\frac{37530 \cdot p_{1i}}{Re_i} \right)^{16}$$

where $p_{1i}, p_{2i}, p_{3i}, p_{4i}, p_{5i}$ are the parameters depending on the corrugation geometry:

$$p_{1i} = e^{-0.15705 \cdot \beta_i}; p_{2i} = \frac{\pi \cdot \beta_i \cdot \gamma_i^2}{3}; p_{3i} = \exp\left(-\pi \cdot \frac{\beta_i}{180} \cdot \frac{1}{\gamma_i^2}\right)$$

$$p_{4i} = \left[0.061 + (0.69 + \tan \beta_i)^{-2.63} \right] \cdot \left[1 + (1 - \gamma_i) \cdot 0.9 \cdot \beta_i^{0.01} \right]; p_{5i} = 1 + \frac{\beta_i}{10};$$

$\gamma_i = 2 \cdot b/S$ is double height to pitch ratio of corrugation; β_i is the angle of corrugation to the main flow direction, degrees; $Re_i = w_i \cdot d_e \cdot \rho / \mu_i$ is Reynolds number; w_i is the flow velocity, m/s ; $d_e = 2 \cdot b$ is the channel equivalent diameter, m ; μ_i is fluid dynamic viscosity, Pa-s; ρ_i is the fluid density, kg/m^3 .

The experimental and calculated values of overall heat transfer coefficients at different cold-water velocities in channels are compared. The calculated results are higher than experimental ones, with deviations up to +8%. The explanation is in a reduction of real average temperature difference compared to that calculated by Equation (2) because of the crossflow. The heat transfer effectiveness of the WPHE model is as follows:

$$\varepsilon = \frac{t_{22} - t_{21}}{t_{11} - t_{21}} \tag{8}$$

Effectiveness dependence from the number of heat transfer units (NTU) is presented in Figure 3. NTU is determined using calculated value U_{cl} of overall heat transfer coefficient by Equation (9):

$$NTU = \frac{F_a \cdot U_{cl}}{G_2 \cdot c_{p2}} \tag{9}$$

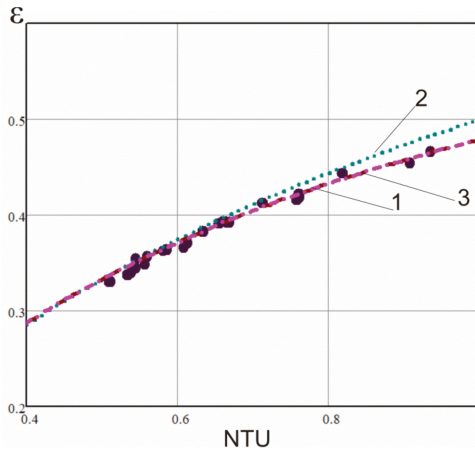


Figure 3. The relation ϵ -NTU for WPHE model: 1—experiment; 2—counter- current; 3—calculated by Equation (10) for crossflow in WPHE for the ammonia synthesis column.

The heat transfer effectiveness, ϵ , experimental values are smaller than calculated by Equation for countercurrent flow (curve 2 in Figure 3). It is better approximated by the Equation presented in [20] for cross flow and stream, with a higher corrugation angle $\beta_1 = 50^\circ$, mixed, and another with lower corrugation angle $\beta_1 = 40^\circ$, unmixed. For a better approximation, the corrected factor 0.97 is added:

$$\epsilon = 1 - e^{-\frac{1+e^{-R \cdot NTU}}{R \cdot 0.97}} \tag{10}$$

where R is the ratio of heat capacities flowrates:

$$R = \frac{G_1 \cdot c_{p1}}{G_2 \cdot c_{p2}} \tag{11}$$

Equation (10) is suitable for the calculation of one pass effectiveness when calculating multi-pass WPHE by the ϵ -NTU method described by Arsenyeva et al. [33].

Besides thermal efficiency, the hydraulic performance of the WPHE is of primary importance for its correct design. The experimental results on Euler number $Eu_i = \Delta P_i / (\rho_i \cdot w_i^2)$ for streams are presented in Figure 4.

For the channel with a bigger corrugation angle $\beta_1 = 50^\circ$, the pressure losses are higher than for another channel of $\beta_2 = 40^\circ$. Following the approach proposed in [34] for the estimation of pressure drop in plate-and-frame PHE at the main corrugation field and channel distribution zones at the entrance and exit separately, the total pressure drop at the stream in multi-pass WPHE can be summarised as follows:

$$\Delta P_i = \left(\zeta_i \cdot \frac{L_{pl}}{d_e} \cdot \frac{\rho_i \cdot w_i^2}{2} + \zeta_{Dzi} \cdot \frac{\rho_i \cdot w_{inx,i}^2}{2} \right) \cdot X_i \tag{12}$$

where $w_{inx,i}$ is the velocity at channel entrance/exit, m/s; ζ_{Dzi} is the coefficient of local hydraulic resistance in entrance/exit zones; X_i is a number of passes.

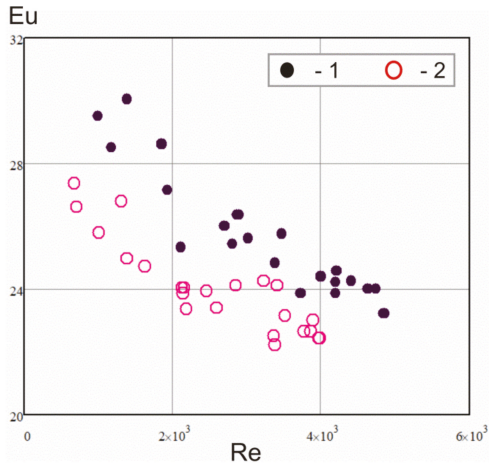


Figure 4. The experimental data for pressure losses: 1—hot stream; 2—cold stream.

By comparison of the calculation by Equation (12) with the ζ_i determined by Equation (7), the coefficients of local hydraulic resistance in the channels’ distribution zones were obtained: $\zeta_{DZ1} = 11$, $\zeta_{DZ2} = 17$. The error of estimation by Equation (12)—the experimentally measured pressure drop in channels—does not exceed $\pm 8\%$, as illustrated in Figure 5.

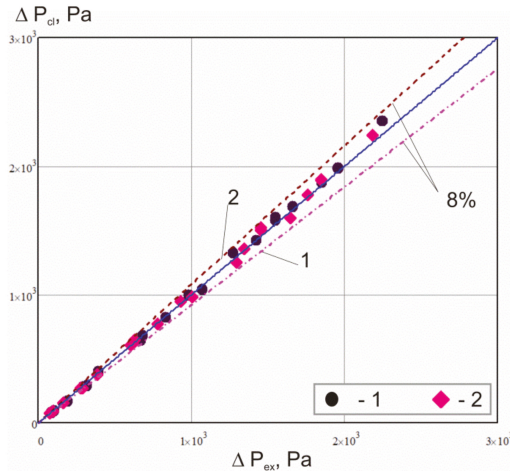


Figure 5. The comparison of experimental pressure drop calculated by Equation (12): 1—hot stream; 2—cold stream.

3. Mathematical Modelling

The reliable and accurate mathematical model of a heat exchanger is the base for the development of its design and optimisation of construction elements. The task of modelling WPHE thermal performance for its rating consists in finding its total effectiveness of heat transfer in WPHE ε_T for the specified NTU, a value which is determined by a given WPHE construction and stream flowrates by Equation (9) in the assumption that thermo-physical properties in the calculation of heat transfer coefficients are taken for streams’ average temperatures. For any pass’s arrangement, the general method in the matrix form proposed for Compabloc WPHE in [18] can be used. But for the construction

features of a considered WPHE for ammonia synthesis column, the number of pass combinations is limited. The bigger number of passes for one streamside has to be an integer multiple of the smaller passes number for another streamside or $X_1 = X_2 \times k$, where k is an integer. An example of flow arrangements for a smaller number of passes, $n = 4$, is presented in Figure 6a for passes 4×4 and 8×4 . For such conditions, a simplified mathematical model can be used based on Equation (13) proposed for total effectiveness ε_T at equal passes arrangement with an overall countercurrent flow [35]. It is made considering the stream, with smaller pass numbers, n blocks of plates, with a flow arrangement of $1 \times k$ and a heat transfer effectiveness, ε_x , of individual blocks for $R \neq 1$:

$$\varepsilon_T = \frac{\left(\frac{1-\varepsilon_x \cdot R}{1-\varepsilon_x}\right)^n - 1}{\left(\frac{1-\varepsilon_x \cdot R}{1-\varepsilon_x}\right)^n - R} \tag{13}$$

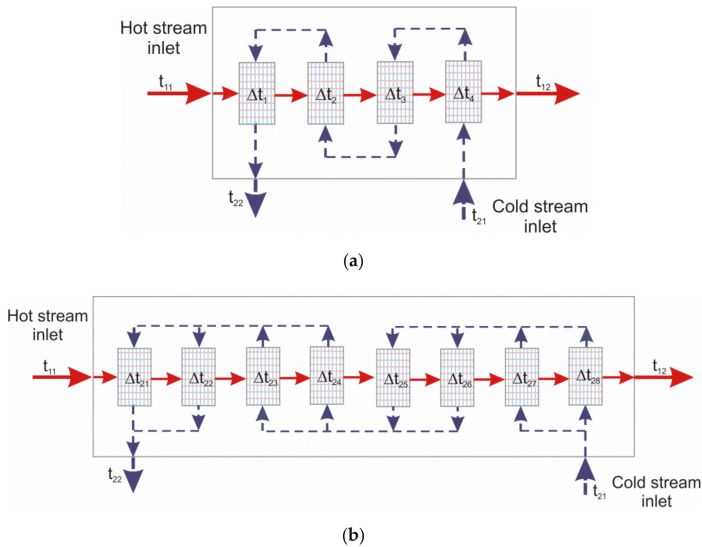


Figure 6. The schematic flow arrangements in 4×4 WPHE (a) and in 8×4 WPHE (b).

For the special case, when $R = 1$, to avoid uncertainty, it is calculated as:

$$\varepsilon_T = \frac{n \cdot \varepsilon_x}{1 + (n - 1) \cdot \varepsilon_x} \tag{14}$$

For the symmetric arrangement of passes, when the passes numbers are equal $X_1 = X_2 = n$ for both streams in WPHE, such a block of plates is a symmetric one-pass heat exchanger with heat transfer area F_a/n . Its heat transfer effectiveness, ε_x , is equal to the effectiveness of one-pass heat exchanger, ε_0 , calculated in the following Equation (10) as:

$$\varepsilon_x = \varepsilon_{0s} = 1 - e^{-\frac{1+e^{-RNTU_{0s}}}{R \cdot 0.97}} \tag{15}$$

where NTU_{0s} number in the symmetric block of plates is equal to NTU/n .

With unsymmetrical passes arrangements (see Figure 6b), one block consists of two sub-blocks of plates. For the cold side, there is one pass, and for the hot side, two sub-passes—as for $k = 2$ —is shown

in Figure 6b. For the last pass on the cold stream (first from the left in Figure 6b), the temperature drops of hot stream in the first sub-block is δt_{11} and, in the second, δt_{12} :

$$\delta t_{11} = \Delta \cdot \varepsilon_{02} \cdot R_{02} \quad (16)$$

$$\delta t_{12} = (\Delta - \delta t_{11}) \cdot \varepsilon_{02} \cdot R_{02} \quad (17)$$

where $\Delta = t_{11} - t_{24}$ is the difference of temperatures at streams incoming into considered sub-blocks; $R_{02} = R/2$ is the ratio of heat capacities flowrates in sub-blocks of plates; ε_{02} is heat transfer effectiveness of the sub-block of plates which consist from 1/8 of the plates total number. The individual effectiveness of all sub-blocks is assumed the same, as all have the same heat transfer area and streams flowrates. The effectiveness of one block of plates consisting of two sub-blocks:

$$\varepsilon_x = \frac{t_{25} - t_{24}}{\Delta} = \frac{\delta t_{11} + \delta t_{12}}{R \cdot \Delta} = \varepsilon_{02} - \varepsilon_{02}^2 \cdot \frac{R}{4} \quad (18)$$

The heat transfer effectiveness of one sub-block, ε_{02} , is determined by Equation (10) with NTU in one sub-block $NTU_{02} = NTU/8$, assuming its equal distribution in all WPHE and the ratio of heat capacities flowrates is R_{02} . By substitution of $X_1 = 2X_2$ received from Equation (18) into Equation (13), the total heat transfer effectiveness of WPHE is obtained for the case of unsymmetrical passes arrangement $X_1 = 2 \cdot X_2$. The other values of k in relation $X_1 = k \cdot X_2$ are not presenting practical interest and not considered in this paper. When the heat transfer effectiveness of WPHE ε_T is found, the outlet temperatures can be calculated, as well as heat load and all other parameters required for WPHE thermal modelling.

The calculation of pressure drop in the hydraulic design of WPHE is made by Equation (12) for each of the streams.

4. Industrial Tests

The validation of the developed mathematical model is checked using the results of industrial tests of prototype WPHE installed in high-pressure column operating at an ammonia production unit. The column structure is presented in Figure 7. The reactor catalyser box (3) with connected WPHE (1) is placed inside the shell (4) which diameter is 800 mm. The shell is designed for a temperature up to 525 °C to accommodate working pressure up to 32 MPa. The incoming syngas is fed from the top and flowing down inside the annular gap between the shell and equipment inside it reaching inlet of WPHE at temperature t_{21} . In WPHE syngas is heated to temperature t_{25} by the stream of gas after the reactor. Syngas leaving the WPHE is mixing with bypass gas that is supplied at the column bottom having temperature t_{b1} . It is going through special channels at the WPHE sides. It is coming next by the central pipe (5) to the top of the catalyser box (3) and then into internal (9) and external (7) field tubes. It is heated there and after coming directly to contact with catalyser (8). Leaving catalyser zone (6) through a header (2), a gas of temperature t_{11} is supplied to WPHE for cooling down to temperature t_{19} and going out from the bottom of the column.

The main parameters of tested WPHE are presented in Table 2. The flow of streams in it arranged, as shown in Figure 6b with eight passes on the hot side and four passes on the cold side. The measurements of temperatures of streams coming in and out of the WPHE were performed with chromel–alumel thermocouples. For the entering of thermocouples into a column, the special high-pressure nozzle was installed. The flowrates of supplied syngas and bypass were measured by orifice flow meters. High-pressure gauges are used for measurement of gas pressures at its entrance and exit from the column.

The data of the four tests are given in Table 3. There are also presented results of modelling of WPHE performance. The experimental values of heat transfer effectiveness are calculated by Equation (8). These values are in good agreement with calculated using Equations (13), (15) and (18) of the developed mathematical model. The accuracy of the developed mathematical model can be

considered as sufficient for practical applications. It can be used for the design of this type of WPHEs. The calculation of pressure drop in WPHE is performed using Equation (12), and results are also presented in Table 3. The total pressure drop on both streams is not exceeding 100 kPa, within the limits of technical requirements; however, to compare it with test data accurately is not possible, as measured results include all the ways in which gases pass through the column, including the catalyser zone that takes the biggest part of total pressure losses. The comparison with data obtained before with the tubular heat exchanger has not revealed any differences in pressure losses.

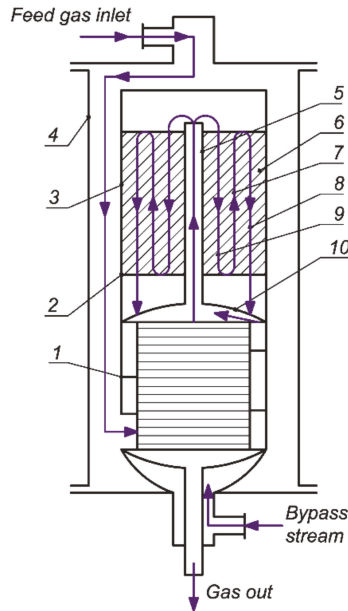


Figure 7. The schematic structure of the column for ammonia synthesis: 1—WPHE; 2—header; 3—catalyser box; 4—high pressure shell; 5—central pipe; 6—catalyser zone; 7—external field tubes; 8—catalyser; 9—internal field tubes; 10—upper cover.

Table 2. Parameters of tested WPHE.

Parameter	Value
Total heating area, F_a , m^2	114.2
Number of plates, N_p	359
One plate area, F_{pl} , m^2	0.320
The cross-section area of one channel, f_{ch} , m^2	0.00220
The outside diameter of the plate, D_o , m	0.6260
Height of WPHE, m	1.82
The thickness of the plate wall, δ_w , m	0.001
Plate material	AISI304
Corrugation depth, b , m	0.0040
Corrugation pitch, S , m	0.0180
The average width of the channel, W_{ch} , m	0.54
Channel equivalent diameter, d_e , m	0.0080
The averaged angle of corrugations:	
hot side, β_1 , degrees	40
cold side, β_2 , degrees	50
Width of inlet/exit area of channel, W_{inx} , m	0.40

Table 3. The results of WPHE tests in the industry.

Parameter	Test #1	Test #2	Test #3	Test #4
Hot gas flow rate, kg/s	8.44	8.36	5.55	5.54
Cold gas flow rate, kg/s	7.42	7.38	5.55	5.54
Temperature:				
hot gas inlet t_{11} , °C	506	505	496	495
hot gas outlet t_{19} , °C	177	180	190	198
cold gas inlet t_{21} , °C	30	40	78	75
cold gas outlet t_{25} , °C	390.7	395	373	380
Pressure:				
column entrance P_{in} , MPa	30.5	30.5	30	29
column exit P_{out} , MPa	29.0	29.0	28.5	27.5
The calculated pressure drop of cold gas, kPa	10.52	10.40	6.61	6.57
The calculated pressure drop of hot gas, kPa	80.25	78.74	38.79	38.77
Ammonia concentration in the cold feed gas, %mol	3.3	3.3	3.3	3.3
Ammonia concentration in hot gas, %mol	17.2	17.2	17.2	17.2
Calculated temperature of cold gas outlet t_{22calc} , °C	396.4	397.5	382.5	380.9
Overall heat transfer coefficient U (calculated), W/(m ² ·K)	1452	1445	1146	1145
NTU (calculated)	6.307	6.311	6.46	6.45
Heat transfer effectiveness ϵ_T (calculated)	0.77	0.769	0.729	0.728
Heat transfer effectiveness ϵ_{TE} (experiment)	0.758	0.763	0.706	0.726
Discrepancy, %	1.6	0.8	-3.2	0.32
Counter current flow heat transfer effectiveness ϵ_{Tcc}	0.894	0.893	0.853	0.853
The loss of effectiveness due to crossflow, %	15.2	14.6	17.2	14.9

Before the column renovation, a tubular heat exchanger with a length of 3 m, heat transfer area of 148 m² and weight of 2992 kg was installed. The weight of WPHE is 1694 kg, occupying a volume of 0.96 m³, that compared to tubular, is only 0.48 m³ smaller. In the remaining spare volume, an additional catalyser was added with proper modernisation of a catalyser box. It leads to a 15% increase in ammonia output.

The heat transfer effectiveness, ϵ_T , is reduced compared to its value for a pure countercurrent flow arrangement from 14.6% to 17.2%. This reduction in effectiveness is caused by the asymmetrical arrangement of passes. The conclusion is that, with the crossflow in individual passes, the symmetric arrangement of passes in WPHE is preferable. The detailed analysis of this problem is made with an optimisation approach to WPHE design presented in the next sections.

5. Optimal Design of WPHE for Ammonia Synthesis Column

The mathematical model presented Section 3, validated in industrial conditions, can be used for the calculation of the optimal parameters of WPHE construction, as well as for WPHE optimal design based on plates of specific geometry. Here, the problem of WPHE optimisation consisting of finding the best construction parameters satisfying specified process conditions on heat transfer and pressure drop performance is considered. An approach discussed in [36] is used. The objective function is the heat transfer surface area of WPHE. There are a number of constraints that must be satisfied:

- (i) The diameter of the plate must be equal to the value that allows installing WPHE inside a high-pressure shell of the column with specified internal diameter (equality constraint);
- (ii) The geometry of plate corrugations is chosen experimentally from the same type of investigation, with differences only in the corrugation's height;
- (iii) The heat transfer effectiveness ϵ_T is not lower than specified ϵ_{TS} ;
- (iv) The pressure drop is not higher than the allowable value;
- (v) The symmetric flow arrangements only are considered $X_1 = X_2 = n$. The optimising variables are the integer number of streams passes n and plates corrugations height b .

The estimation of the heat transfer performance of the WPHE is done through the determination of heat transfer effectiveness ε_T . The total effectiveness of the heat exchanger with symmetric passes and countercurrent flow is determined by Equation (13) with the ratio of heat capacities flowrates R calculated by Equation (11). The value of effectiveness in one-pass ε_x , required to satisfy the effectiveness of the whole WPHE, can be derived from Equation (13) as follows:

$$\varepsilon_x = \left[\left(\frac{1 - \varepsilon_T \cdot R}{1 - \varepsilon_T} \right)^{\frac{1}{n}} - 1 \right] \cdot \left[\left(\frac{1 - \varepsilon_T \cdot R}{1 - \varepsilon_T} \right)^{\frac{1}{n}} - R \right]^{-1} \quad (19)$$

The number of transfer units in one block of plates corresponding to one pass of crossflow WPHE from Equation (15):

$$NTU_x^0 = - \frac{\ln(1 + 0.97 \cdot R \cdot \ln(1 - \varepsilon_x))}{R} \quad (20)$$

It is required for fulfilment by WPHE of specified thermal process conditions. The number NTU_x that can be obtained in one block of WPHE plates corresponding to one pass is according to the heat transfer ability of the block:

$$NTU_x = \frac{F_{ax} \cdot U}{G_2 \cdot c_{p2}} \quad (21)$$

where F_{ax} is the heat transfer area of the block of plates, m^2 .

Expressing F_{ax} through the number of plates in one block and G_2 through the number of channels and flow velocity in channel w_2 and channel cross-section area it is obtained:

$$NTU_x = \frac{2 \cdot F_{pl} \cdot U}{c_{p2} \cdot w_2 \cdot \rho_2 \cdot f_{ch}} \quad (22)$$

where F_{pl} is the heat transfer area of one plate, m^2 ; ρ_2 is the density of the cold fluid, kg/m^3 ; $f_{ch} = W \cdot b$ is the channel cross-section area, m^2 ; W is the width of the channel, m .

The plate heat transfer surface area:

$$F_{pl} = L_{pl} \cdot W \cdot F_X \quad (23)$$

For the WPHE of ammonia synthesis column, the length of the plate L_{pl} is equal to its width W and, from Equation (22), when the thermal constraint (iii) is completely satisfied ($NTU_x = NTU_x^0$), Equation (24) follows:

$$\frac{L_{pl}}{b} = \frac{NTU_x^0 \cdot c_{p2} \cdot w_2 \cdot \rho_2}{2 \cdot U \cdot F_X} \quad (24)$$

Following the approach of [36], let us determine the plate length for the condition that pressure drop of the hot stream is strictly satisfied. From Equation (12), when the pressure drop ΔP_1 is equal to the allowable pressure drop ΔP_1^0 ,

$$\frac{L_{pl}}{b} = \frac{2}{\zeta_1(w_1)} \cdot \left(\frac{\Delta P_1^0 \cdot 2}{\rho_1 \cdot w_1^2 \cdot n} - \zeta_{DZ1} \cdot \left(\frac{W_{ch}}{W_{enx}} \right)^2 \right) \quad (25)$$

The flows velocities at the cold side (w_2) and hot side (w_1) are linked by Equation (26):

$$w_2 = w_1 \cdot \frac{G_2 \cdot \rho_1}{G_1 \cdot \rho_2} \quad (26)$$

When the hydraulic conditions by Equation (25) and thermal conditions by Equation (24) are satisfied simultaneously, the right sides of Equations (25) and (24) are equal. Accounting for Equation (26) for velocity in the hot channel, Equation (27) follows:

$$w_1 = \sqrt{\frac{\Delta P_1^0}{n \cdot \rho_1} \cdot \frac{1}{\frac{\zeta_{DZ1}}{2} \cdot \left(\frac{W_{ch}}{W_{enx}}\right)^2 + \zeta_1(w_1) \cdot \frac{NTU_x^0 \cdot c_{p2} \cdot w_1 \cdot G_2 \cdot \rho_1}{8 \cdot U(w_2, w_1) \cdot F_x \cdot G_1}}}} \quad (27)$$

The variables ζ and U at the right side of Equation (27) are the nonlinear functions of velocity w_1 expressed by Equations (4)–(7). The solution of Equation (27) gives the value of w_1 at which constraints (iii) and (iv) are satisfied as equalities and a corresponding value of overall heat transfer coefficient U is estimated. As a result, the value of WPHE heat transfer area for WPHE with n passes:

$$F_a = \frac{NTU_x^0 \cdot G_2 \cdot c_{p2}}{U} \cdot n \quad (28)$$

The relations determining this objective function include nonlinear Equations and integer variable number of passes n . Besides, the numbers of plates and channels are also integers. To find the optimum of such function is the problem of Mixed-Integer Nonlinear Programming (MINLP). The numbers of plates and channels have rather big values and, on the first stage of finding the solution, can be treated as continuous variables. The Equation (27) is a recurrent relation relative to velocity w_1 . Its solution by iterations gives the value of the velocity of a hot stream that, for a plate with specified geometrical parameters, strictly satisfies the thermal conditions and allowable pressure drop at the hot stream in a one-pass block of plates. When this velocity is obtained, the required plate length L_{pl} can be calculated by Equations (24) or (25). In case of a correct solution for w_1 , both are giving the same results. To satisfy the constraint (i), this plate length must be equal to the value specified for a given diameter of the column. The problem is solved by finding local optimums of plate spacing $b_{opt,i}$ at which constraint (i) for plate length is satisfied as equality. It is made for the series of increasing pass numbers n , starting from 2. The calculations are finished when $b_{opt,i}$ begin to increase. The value of $b_{opt,i}$ corresponding to a minimum of objective function F_a and corresponding it passes number n are regarded as an optimal solution. After that, the number of plates in one block is rounded up, and rating design of WPHE performed. The method is implemented as a software for PC. The time of calculations for different conditions have not exceeded 200 s. The process of finding a solution is illustrated in the following case study.

6. Case Study

The ammonia synthesis column with diameter 0.8 m is considered. The limiting WPHE plate diameter to fit in this column is 0.6 m, corresponding to an effective plate length of $L_{pl} = 0.54$ m. The operating conditions required by the process are given in Table 4. In the process of design, the height of corrugations b was changed from 0.3 to 0.5 mm and, correspondingly, the cross-section area of the channel, f_{ch} . It is done for consecutive numbers of passes n in the heat exchanger. The fixed design parameters are given in Table 5. The average angle of corrugation is $\beta_1 = 40^\circ$ for the hot side and $\beta_2 = 50^\circ$ for the cold side. The coefficients $\zeta_{DZ1} = 11$ for the hot side, and $\zeta_{DZ2} = 17$ for the cold side are taken according to laboratory tests. The design is made for bypass 20% on the cold stream to enable process control with the aging of the catalyser.

Attempts to calculate one-pass WPHE have shown that, at given temperatures, programming one-pass WPHE is not feasible at any increase of heat transfer area. The calculations with not fixed L_{pl} for different pass numbers show the existence of local optimums with certain minimal values of WPHE heat transfer in area F. That value is lower for a smaller number of passes. However, for its fulfilment, an unacceptable plate length can be required; e.g., for a two-pass WPHE with a corrugation height of 3 mm, the minimal heat transfer area is 95 m² and required plate length 0.9 m. In this case,

the loss of mean temperature difference due to crossflow is too big. The calculations for WPHE with a number of passes, $n = 3$ and higher, produce the heat transfer area from 64 to 90 m² with smaller required plate lengths. However, there is also an adverse influence of crossflow in one pass that is more emphasised at smaller passes numbers. In these cases, WPHE construction features and imposed constraints must be accounted for.

Table 4. The required operating conditions for case study.

Parameter	Value
Hot gas mass flowrate G_1 , kg/s	8.375
Cold gas mass flowrate G_2 , kg/s	6.7
Heat load Q^0 , kW	9320
Maximal pressure loss on the hot side ΔP , kPa	25
The temperature:	
hot gas inlet t_{11} , °C	505
hot gas outlet t_{12} , °C	180
cold gas inlet t_{21} , °C	40
cold gas outlet t_{22} , °C	431.5

Table 5. The fixed values in the WPHE optimal design.

Parameter	Value
Corrugations aspect ratio γ	0.444
Average channel width and length, m	0.54
Plate thickness, δ_w , m	0.001
Plate metal	AISI304
The area enlargement factor, F_x	1.1

As is discussed in [13] (pp. 54–65), for compact heat exchangers, the decrease of the equivalent diameter of channels leads to a smaller heat transfer area and improved compactness. However, then the problem of adjusting the plate length into its required limits arises. In the considered case, to fit into the high-pressure shell, the specified plate length is $L_{plS} = 0.54$ m. The locally optimal value for the given passes number can be selected only if they fit values of corrugation height b at which $L_{pl} = L_{plS}$. In the case under consideration, these values are $b = 3.3$ mm at $n = 3$ with $F = 68.3$ m² (that is considered as global optimum) and $b = 4.7$ mm at $n = 4$ with $F = 72.9$ m² that is shown in Figure 8. Line (1) in Figure 8 shows the minimal values of the heat transfer area that could be achieved without constraint for plate length. By line (2), there is also a designated heat transfer area that is needed to satisfy the required process conditions with inequality constraints for heat load Q^0 or pressure drop ΔP^0 at $L_{pl} = 0.54$ m. In that case, only one constraint is satisfied strictly, but another with some margin. At b , lower than the locally optimal value, the optimal plate length is smaller than L_{plS} . The number of plates in WPHE and its heat transfer area must be increased to fulfil pressure drop requirement $\Delta P = \Delta P^0$ and WPHE can transfer more heat $Q > Q^0$. At b , higher than the locally optimal value, the optimal plate length is bigger than L_{plS} . The number of plates in WPHE and its heat transfer area has to also be increased to make it shorter, but to satisfy constraint strictly on the heat load, $Q = Q^0$. With this, the pressure drop became smaller than required, $\Delta P < \Delta P^0$.

When a designer has already manufactured plate, as the example in Figure 1 investigated here, the required number of plates in WPHE and heat transfer area can be estimated by calculations for specified corrugations height $b = 4$ mm. The results of such calculations are shown at graphs in Figure 8 for the number of passes $n = 3$ and for $n = 4$. For $n = 3$, the heat load is strictly satisfied at $F = 132.94$ m² with pressure drop 4430 Pa, that on 82% lower than specified. For $n = 4$, strictly satisfied is a pressure drop at $F = 85.12$ m² while heat load has 3.1% of margin. This second option is preferable not only for a smaller heat transfer area but also for better utilisation of pressure drop which is leading to high velocities and wall shear stress in channels that can mitigate possible fouling with catalyst

dust. While this heat transfer area is on 24.6% bigger than an optimal global solution, it is 25.4% smaller than of prototype WPHE with unsymmetrical passes arrangement described above in Section 4. The heat transfer effectiveness with symmetrical passes arrangement $n = 4$ is 0.842 compared to 0.862 at pure countercurrent flow or the loss is only 2.3% compared to 14.6%–17.2% for the asymmetrical arrangement in Table 3.

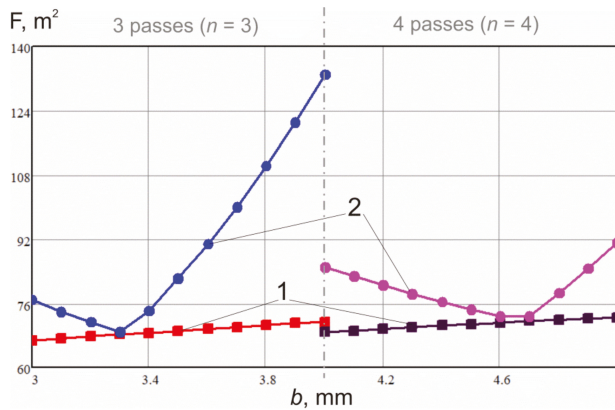


Figure 8. The calculated results for the set of corrugations height b and symmetrical flow arrangement: line 1—the WPHE area for L_{pl} not fixed; line 2—the WPHE area for $L_{pl} = 0.54$ m.

7. Conclusions

- (i) The experimental study of thermal and hydraulic performance in one pass of WPHE developed for operation at high temperature, and pressure in the ammonia synthesis column is conducted. It confirmed the accuracy of correlations for calculation of film heat transfer and pressure losses in channels between cross-corrugated plates with a different angle of corrugations in conditions of streams' crossflow. The relation between heat transfer effectiveness ϵ and number of transfer units NTU in such conditions are also established as coefficients of local hydraulic resistance at entrance and exit zones of investigated channels.
- (ii) The mathematical model of WPHE with multi-pass flow arrangement for the column of ammonia synthesis is developed based on the data of laboratory study. The model is validated on the results of tests in industrial conditions.
- (iii) The industrial tests of prototype WPHE installed in the operating ammonia synthesis column have confirmed its reliable operation and higher heat transfer efficiency compared to conventional at this application tubular heat exchanger. The WPHE has on 43% lower weight and occupies on 40% smaller volume that allowed increasing the production capacity of the column on 15%. Industrial tests confirmed results of mathematical modelling; however, the asymmetrical passes arrangement is leading to a substantial decrease of WPHE effectiveness due to crossflow in individual passes.
- (iv) The method of WPHE heat transfer area optimisation is presented, which uses plate corrugations' height and number of passes as optimisation variables. In case of plates with a specified corrugations height, it can be used for optimal selection of the passes number in WPHE design. Its application is illustrated by the case study.
- (v) The presented WPHE of construction with round plates specially developed for ammonia synthesis column has higher heat transfer efficiency than traditional tubular heat exchanger. Such WPHE can be used for an increase of the ammonia synthesis column production capacity by saving space for an additional catalyser. Another option is the increase in heat recuperation and energy efficiency at the same ammonia production capacity. The developed mathematical model

and methodology for optimal design can be used for optimal selection of WPHE plates and flow arrangement for specified process conditions in different ammonia synthesis columns, as well as for optimisation of the whole ammonia production unit. It opens the prospect for further research in applications of WPHE for ammonia condensing columns and processes like a synthesis of methanol and others operating in high-pressure and -temperature conditions.

Author Contributions: Conceptualisation, L.T., P.K. and J.J.K.; methodology, P.K., J.J.K. and O.A.; software, P.K. and O.A.; validation, O.P., P.A. and L.T.; formal analysis, O.A.; investigation, O.P. and P.A.; resources, L.T.; data curation, P.A.; writing—original draft preparation, P.K.; J.J.K. project administration, writing—review and editing, P.K. and J.J.K.; supervision, L.T.; project administration, L.T. All authors have read and agreed to the published version of the manuscript.

Funding: This research received no external funding.

Acknowledgments: This research has been supported by the EU project “Sustainable Process Integration Laboratory—SPIL”, project No. CZ.02.1.01/0.0/0.0/15_003/0000456 funded by EU “CZ Operational Programme Research, Development and Education”, Priority I: Strengthening capacity for quality research in a collaboration agreement with National Technical University “Kharkiv Polytechnic Institute”.

Conflicts of Interest: The authors declare no conflict of interest.

References

- Klemeš, J.J.; Wang, Q.-W.; Varbanov, P.S.; Zeng, M.; Chin, H.H.; Lal, N.S.; Li, N.-Q.; Wang, B.; Wang, X.-C.; Walmsley, T.G. Heat transfer enhancement, intensification and optimisation in heat exchanger network retrofit and operation. *Renew. Sustain. Energy Rev.* **2020**, *120*, 109644. [CrossRef]
- Valera-Medina, A.; Xiao, H.; Owen-Jones, M.; David, W.I.F.; Bowen, P. Ammonia for power. *Prog. Energy Combust. Sci.* **2018**, *69*, 63–102. [CrossRef]
- Dincer, I.; Bicer, Y. Ammonia production. In *Comprehensive Energy Systems*; Elsevier: Amsterdam, The Netherlands, 2018; Volume 3, pp. 41–94.
- Wang, Q.; Guo, J.; Chen, P. Recent progress towards mild-condition ammonia synthesis. *J. Energy Chem.* **2019**, *36*, 25–36. [CrossRef]
- Khademi, M.H.; Sabbaghi, R.S. Comparison between three types of ammonia synthesis reactor configurations in terms of cooling methods. *Chem. Eng. Res. Des.* **2017**, *128*, 306–317. [CrossRef]
- Flórez-Orrego, D.; de Oliveira Junior, S. Modeling and optimisation of an industrial ammonia synthesis unit: An exergy approach. *Energy* **2017**, *137*, 234–250. [CrossRef]
- Penkuhn, M.; Tsatsaronis, G. Comparison of different ammonia synthesis loop configurations with the aid of advanced exergy analysis. *Energy* **2017**, *137*, 854–864. [CrossRef]
- Zhang, H.; Wang, L.; Van Herle, J.; Maréchal, F.; Desideri, U. Techno-economic comparison of green ammonia production processes. *Appl. Energy* **2020**, *259*, 114135. [CrossRef]
- Aziz, M.; Oda, T.; Morihara, A.; Kashiwagi, T. Combined nitrogen production, ammonia synthesis, and power generation for efficient hydrogen storage. *Energy Procedia* **2017**, *143*, 674–679. [CrossRef]
- Ishaq, H.; Dincer, I. Analysis and optimization for energy, cost and carbon emission of a solar driven steam-autothermal hybrid methane reforming for hydrogen, ammonia and power production. *J. Clean. Prod.* **2019**, *234*, 242–257. [CrossRef]
- Chen, C.; Zhao, L.; LaVine, A.S. Feasibility of using ammonia-based thermochemical energy storage to produce high-temperature steam or sCO₂. *Sol. Energy* **2018**, *176*, 638–647. [CrossRef]
- Gough, M.; Farrokhpahan, S.; Bulatov, I. Retrofit process heat transfer enhancement to upgrade performance, throughput and reduced energy use. *Clean Technol. Environ. Policy* **2013**, *15*, 423–431. [CrossRef]
- Klemeš, J.J.; Arsenyeva, O.; Kapustenko, P.; Tovazhnyanskyy, L. *Compact Heat Exchangers for Energy Transfer Intensification: Low Grade Heat and Fouling Mitigation*; CRC Press: Boca Raton, FL, USA, 2015; Available online: <https://www.taylorfrancis.com/books/9780429161049> (accessed on 30 May 2020).
- Hajabdollahi, H.; Naderi, M.; Adimi, S. A comparative study on the shell and tube and gasket-plate heat exchangers: The economic viewpoint. *Appl. Therm. Eng.* **2016**, *92*, 271–282. [CrossRef]
- Kapustenko, P.; Boldryrev, S.; Arsenyeva, O.; Khavin, G. The use of plate heat exchangers to improve energy efficiency in phosphoric acid production. *J. Clean. Prod.* **2009**, *17*, 951–958. [CrossRef]

16. Perevertaylenko, O.Y.; Gariev, A.O.; Damartzis, T.; Tovazhnyanskyy, L.; Kapustenko, P.O.; Arsenyeva, O. Searches of cost effective ways for amine absorption unit design in CO₂ post-combustion capture process. *Energy* **2015**, *90*, 105–112. [[CrossRef](#)]
17. Arsenyeva, O.; Čuček, L.; Tovazhnyanskyy, L.; Kapustenko, P.O.; Savchenko, Y.A.; Kusakov, S.K.; Matsegora, O.I. Utilisation of waste heat from exhaust gases of drying process. *Front. Chem. Sci. Eng.* **2016**, *10*, 131–138. [[CrossRef](#)]
18. Arsenyeva, O.; Tovazhnyanskyy, L.; Kapustenko, P.O.; Khavin, G.; Yuzbashyan, A.P.; Arsenyev, P. Two types of welded plate heat exchangers for efficient heat recovery in industry. *Appl. Therm. Eng.* **2016**, *105*, 763–773. [[CrossRef](#)]
19. Andersson, E.; Quah, J.; Polley, G.T. 2009, Experience in Application of Compabloc Heat Exchangers in Refinery Pre-Heat Trains. In Proceedings of the International Conference on Heat Exchanger Fouling and Cleaning VIII-2009, Schlading, Austria, 14–19 June 2009; pp. 39–43.
20. Shah, R.K.; Sekuli, D.P. *Fundamentals of Heat Exchanger Design*; John Wiley & Sons: Hoboken, NJ, USA, 2003.
21. Triboix, A. Exact and approximate formulas for cross flow heat exchangers with unmixed fluids. *Int. Commun. Heat Mass Transf.* **2009**, *36*, 121–124. [[CrossRef](#)]
22. Starace, G.; Fiorentino, M.; Longo, M.; Carluccio, E. A hybrid method for the cross flow compact heat exchangers design. *Appl. Therm. Eng.* **2017**, *111*, 1129–1142. [[CrossRef](#)]
23. Mangrulkar, C.K.; Dhoble, A.; Chamoli, S.; Gupta, A.; Gawande, V.B. Recent advancement in heat transfer and fluid flow characteristics in cross flow heat exchangers. *Renew. Sustain. Energy Rev.* **2019**, *113*, 109220. [[CrossRef](#)]
24. Magazoni, F.C.; Cabezas-Gómez, L.; Alvaríño, P.F.; Sáiz-Jabardo, J.M. Closed form relationships of temperature effectiveness of cross-flow heat exchangers. *Therm. Sci. Eng. Prog.* **2019**, *9*, 110–120. [[CrossRef](#)]
25. An, C.S.; Kim, M.-H. Thermo-hydraulic analysis of multi-row cross-flow heat exchangers. *Int. J. Heat Mass Transf.* **2018**, *120*, 534–539. [[CrossRef](#)]
26. Khaled, M.; Ramadan, M.; El Hage, H. Innovative approach of determining the overall heat transfer coefficient of heat exchangers—Application to cross-flow water-air types. *Appl. Therm. Eng.* **2016**, *99*, 1086–1092. [[CrossRef](#)]
27. Luo, X. Parametric study of heat transfer enhancement on cross-flow heat exchangers. *Chem. Eng. Process. Process. Intensif.* **2017**, *121*, 81–89. [[CrossRef](#)]
28. Morteau, M.; Paiva, K.; Mantelli, M. Diffusion bonded cross-flow compact heat exchangers: Theoretical predictions and experiments. *Int. J. Therm. Sci.* **2016**, *110*, 285–298. [[CrossRef](#)]
29. Morteau, M.V.V.; Cisterna, L.; Paiva, K.; Mantelli, M. Thermal and hydrodynamic analysis of a cross-flow compact heat exchanger. *Appl. Therm. Eng.* **2019**, *150*, 750–761. [[CrossRef](#)]
30. Borjigin, S.; Zhang, S.; Ma, T.; Zeng, M.; Wang, Q. Performance Enhancement of Cabinet Cooling System by Utilising Crossflow Plate Heat Exchanger. *Energy Convers. Manag.* **2020**, *213*, 112854. [[CrossRef](#)]
31. Arsenyeva, O.; Tovazhnyanskyy, L.; Kapustenko, P.O.; Demirskiy, O.V. Generalised semi-empirical correlation for heat transfer in channels of plate heat exchanger. *Appl. Therm. Eng.* **2014**, *70*, 1208–1215. [[CrossRef](#)]
32. Kapustenko, P.O.; Arsenyeva, O.P.; Dolgonosova, O. The Heat and Momentum Transfers Relation in Channels of Plate Heat Exchangers. *Chem. Eng. Trans.* **2011**, *25*, 399–404.
33. Arsenyeva, O.P.; Tovazhnyanskyy, L.L.; Kapustenko, P.O.; Khavin, G.L. Mathematical Modelling and Optimal Design of Plate-and-Frame Heat Exchangers. *Chem. Eng. Trans.* **2009**, *18*, 791–796.
34. Arsenyeva, O.; Kapustenko, P.; Tovazhnyanskyy, L.; Khavin, G. The influence of plate corrugations geometry on plate heat exchanger performance in specified process conditions. *Energy* **2013**, *57*, 201–207. [[CrossRef](#)]
35. Kays, W.M.; London, A.L. *Compact Heat Exchangers*; McGraw-Hill: New York, NY, USA, 1984. Available online: <https://www.osti.gov/biblio/6132549> (accessed on 30 May 2020).
36. Arsenyev, P.Y.; Tovazhnyanskyy, L.; Klemeš, J.J.; Arsenyeva, O.P.; Perevertaylenko, O.Y.; Kapustenko, P.O. The Optimal Design of Welded Plate Heat Exchanger with Intensified Heat Transfer for Ammonia Synthesis Column. *Chem. Eng. Trans.* **2019**, *76*, 61–66.



Article

Carbon Emissions Constrained Energy Planning for Aluminum Products

Rok Gomilšek ^{1,2}, Lidija Čuček ^{2,*}, Marko Homšak ³, Raymond R. Tan ⁴ and Zdravko Kravanja ²

¹ Talum Inštitut d.o.o., Tovarniška cesta 10, SI-2325 Kidričevo, Slovenia; rok.gomilsek@talum.si

² Faculty of Chemistry and Chemical Engineering, University of Maribor, Smetanova ulica 17, SI-2000 Maribor, Slovenia; zdravko.kravanja@um.si

³ Talum d.d., Tovarniška cesta 10, SI-2325 Kidričevo, Slovenia; marko.homsak@talum.si

⁴ Chemical Engineering Department, De La Salle University, 2401 Taft Avenue, Manila 0922, Philippines; raymond.tan@dlsu.edu.ph

* Correspondence: lidija.cucek@um.si; Tel.: +38-622-294-454

Received: 26 April 2020; Accepted: 22 May 2020; Published: 1 June 2020

Abstract: The production of primary aluminum is an energy-intensive industry which produces large amounts of direct and indirect greenhouse gas emissions, especially from electricity consumption. Carbon Emissions Constrained Energy Planning proved to be an efficient tool for reducing energy-related greenhouse gas emissions. This study focuses on energy planning constrained by CO₂ emissions and determines the required amount of CO₂ emissions from electricity sources in order to meet specified CO₂ emission benchmark. The study is demonstrated on and applied to specific aluminum products, aluminum slugs and aluminum evaporator panels. Three different approaches of energy planning are considered: (i) an insight-based, graphical targeting approach, (ii) an algebraic targeting approach of cascade analysis, and (iii) an optimization-based approach, using a transportation model. The results of the three approaches show that approximately 2.15 MWh of fossil energy source should be replaced with a zero-carbon or 2.22 MWh with a low-carbon energy source to satisfy the benchmark of CO₂ emissions to produce 1 t of aluminum slug; however, this substitution results in higher costs. This study is the first of its kind demonstrated on and applied to specific aluminum products, and represents a step forward in the development of more sustainable practices in this field.

Keywords: CO₂ emissions; electricity planning; CO₂ Constrained Energy Planning (CCEP); approaches for CCEP; aluminum products

1. Introduction

The current increase in global greenhouse gas (GHG) emissions should be substantially reversed to mitigate climate change and prevent global temperatures from rising beyond the 2 °C target [1]. Currently, global GHG emissions are attributed mainly to energy (more than 70% of GHG emissions), while the remaining are due to agriculture, land-use change and forestry, and industrial processes and waste [2]. In the European Union (EU), a binding target has been set to reduce GHG emissions by at least 40% by 2030 compared to 1990 levels [3].

In the EU, energy-intensive industries including iron, steel, cement and aluminum either have to pay carbon taxes or, if they are included in the EU's Emissions Trading System (EU ETS), they need to have sufficient allowances to cover all emissions produced [4]. Under EU ETS, installations could receive free allocation allowances every year and/or buy (remaining) emission allowances on the market. Every year, aluminum producers in the EU receive some allowances allocated for free, owing to international competitiveness of carbon leakage [5]. The number of free allocations is being decreased

gradually each year, with the goal of reducing emissions and stimulating companies to invest in the transition to low-carbon technologies [4].

Aluminum (or aluminium in British spelling) is the second most used metal in the world after iron. The production of aluminum is a highly energy-intensive process, with electricity representing a large share of the energy consumed. The industry accounts for 3.5% of global electricity consumption [6]. Consequently, the aluminum industry produces a large amount of direct and especially indirect GHG emissions. During electrolysis, primary aluminum is produced via the reduction of alumina (Al_2O_3); this alumina is, in turn, refined from bauxite (aluminum ore). According to the data from the International Aluminum Institute [6], on average, 14.22 MWh of electricity was used to produce 1 t of primary aluminum in 2019.

Electricity can be generated from fossil, nuclear and/or renewable sources. Around half of the electricity in the EU is generated from fossil fuels, and the remaining half from nuclear power stations and renewable sources (both $\approx 25\%$) [7]. Wind turbines (11.4%) and hydropower plants (10.4%) account for most of the renewable energy sources [7]. Fossil fuels have been widely regarded as a prime cause of climate change because of the GHG emissions released by their burning [8]. Nuclear power plants pose serious potential risks to the environment and human health [9]. For most renewables, the main obstacles are their comparably lower energy output, intermittency and lower availability [10].

Carbon Emissions or CO_2 -Constrained Energy Planning is often labeled as Carbon Constrained Energy Planning (CCEP). It is a set of techniques that is suitable for power generation planning constrained by CO_2 emissions [11]. Several techniques have been developed, such as insight-based approaches under the framework of Carbon Emission Pinch Analysis (CEPA) [12], algebraic targeting approaches to CCEP [13] and optimization-based targeting techniques for single- and multi- period scenarios [14]. Various extensions of the methodology have been proposed, such as an algebraic targeting approach (cascade analysis technique) for land-constrained energy planning [13], a graphical Pinch approach for water footprint-constrained energy planning, applied to biofuel production [15], improved application of CEPA to large transport systems [16], a graphical approach of CEPA applied to economic systems [17], source-sink superstructure optimization of energy planning under multiple footprint constraints [18], and various other CCEP methodology extensions. Hybrid CEPA techniques have also been developed, for instance with P-graph for macro-level [19] and plant-level planning [20] problems.

CCEP belongs to a broader category of Process Integration (PI) [21], which includes Heat Integration [22], Total Site (TS) Integration [23], Heat and Power Integration [24], Mass Integration and Resource Conservation [25], Hydrogen Pinch Analysis (PA) [26], Oxygen PA [27], Targeting Supply Chains performance [28], Targeting Property-Based Material Reuse [29], Targeting Carbon Footprint Reduction [30] and others. PI is a widely researched area, and many advancements have been made over the years. On the Science Direct platform, there are 8959 entries containing “Process Integration” in their title from 2019–2020 (search made on 8 May 2020). Also, various PI works have been published in the *Energies* journal. Among recent works are a review on progress towards efficient and clean PI [31], an analysis of PI options for different types of heat pumps through Pinch Technology [32], a proposed novel PA methodology to target cooling, heating and power in TSs [33], the incorporation of location aspects in PI methodology [34] and others, while only one work is related to carbon emissions planning [35].

Most studies applying CCEP techniques have focused on power generation, while only a few have focused on industries or specific industrial products. Tjan et al. [30] developed a graphical variant and applied it to the analysis of bulk and specialty chemicals; this method was later extended to consider allocation issues in multiproduct biorefineries [36]. Quin et al. [37] investigated product-based CCEP focused on energy-emission planning for the methanol production industry in China. Sinha and Chaturvedi [38] focused on CCEP for steel manufacturing, while Abdul Aziz et al. [39] presented a newly developed framework for low- CO_2 -emission industrial site planning. Recently,

Sinha and Chaturvedi [40] reviewed carbon reduction technologies in industries with a focus on carbon emission limits planning.

Based on the literature review, it was found that none of the studies focused on CCEP applied to the aluminum industry and to specific aluminum products. It is also worth noting that most of the CCEP studies considered only one approach to energy planning for specific applications, while this study considers three different approaches: the first is the graphical approach of CEPA, the second is the algebraic approach implementing a cascade analysis technique, and the third is the optimization-based approach, applying a transportation model [13].

The aim of this study is the determination of the required amount of CO₂ emissions from electricity sources to meet specified CO₂ emission limits, considering the aforementioned approaches. All three approaches are systematic, which provides decision support in determining an appropriate energy mix to achieve a specific target, by considering the characteristics of energy sources and demands. CCEP techniques provide support in planning for more sustainable production of industrial products. They can also be used to optimize the energy supply mix based on carbon emission constraints subject to economic and other environmental constraints, except for carbon footprint and the like. This study focuses on the production of more sustainable aluminum products, and is the first CCEP work applied to the aluminum industry. CCEP approaches are applied to one aluminum product, i.e., aluminum slugs (graphical and numerical approaches), and two aluminum products, i.e., slugs and evaporator panels (all three approaches). All three approaches are finally compared and discussed.

2. Carbon Emission-Constrained Electricity Planning for Aluminum Products

Aluminum is widely available and is the second most widely used metal worldwide. Aluminum is used in several sectors, including transportation, packaging, building and construction, furniture, equipment and machinery. However, the aluminum industry is highly energy-consuming, especially in the production of primary aluminum. Aluminum production consumes about 3.5% of electricity globally [41], while in China [42] and the US [43], that figure is around 5% and in Montenegro it is more than 25% [44]. According to data from the Slovenian Ministry of Infrastructure [45] and the data collected by the authors, aluminum production in Slovenia consumed about 8.9% of the total electricity produced in 2017. Primary production of aluminum starts with bauxite mining and further refining of alumina from bauxite. Alumina is further processed into aluminum via electrolysis, known also as the Hall-Héroult process. Subsequently, aluminum is processed into a range of products by casting, rolling, extrusion and other operations [46]. The highest energy consumption and CO₂ emissions are due to electrolysis [47]. The production of secondary or recycled aluminum, on the other hand, requires less than 5% of the energy required to produce aluminum from ore [48].

The aim of this study is to minimize CO₂ emissions in order to meet specified CO₂ emission limits, which could be set at the national or regional level. The emission limit (target) for this study was set at 0.376 t CO₂/MWh [5]. This value was set by the European Commission in delegated regulation (EU) 2019/331, where transitional rules for the free allocation of emission allowances were set for the period 2021–2030. This emission factor is used for the determination of indirect emissions, where a given factor (0.376 t CO₂/MWh) is multiplied by the electricity consumption required to produce specific products.

In this study, two aluminum products are considered, aluminum slugs and evaporator panels. The production of aluminum slugs and evaporator panels is described in Figure 1. Both products are made from molten aluminum produced by the electrolysis process, while slugs are also made from recycled aluminum produced as process waste material from the further processing of slugs. This study performs CCEP of aluminum products for a Slovenian aluminum company. In the company, aluminum slugs are produced from around 0.67 t of electrolysis aluminum per t of slugs; the remaining material used for their production is secondary aluminum. Aluminum evaporator panels are produced only from electrolysis aluminum, where from 1 t of molten aluminum, about 1 t of evaporator panels are produced.

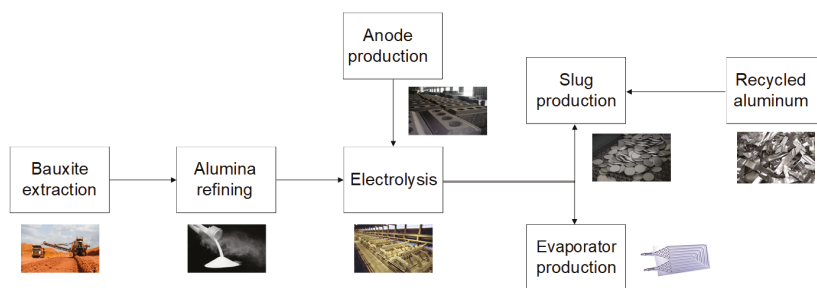


Figure 1. Production of aluminum slugs and evaporator panels (modified from [47]).

Aluminum slug production (see Figure 1) consists of casting, the production of the narrow strip, hot and cold rolling, stamping, annealing, surface treatment and packaging [47]. The production process of Roll-Bond evaporator panels also consists of several steps: casting of the wide strip, rolling it into the band for evaporator panels, roll-bonding, recrystallization annealing, inflation of imprinted channels, final dimension cut or stamping and packaging, and final assembly of the evaporator panels according to the needs of the customer. Both production processes follow the same value chain up to slug and evaporator panel production.

For the sake of simplification, the same amount of the primary aluminum used in the production of aluminum slugs and evaporator panels is assumed; 0.67 t of primary aluminum is required for the production of 1 t of aluminum slugs, and the same amount of primary aluminum is used for 0.67 t of aluminum evaporator panels. To produce 0.67 t of primary aluminum, 0.063 MWh of electricity are required for the anode production and 9.12 MWh for the electrolysis. This consumption is the same for both products, since they follow the same value chain up to the final steps. They have similar electricity consumption, although the production of evaporator panels requires slightly more electricity. For slug production, an additional 0.263 MWh of electricity is required for 1 t of the product, while for evaporator panels, an additional 1.016 MWh of electricity is required for 0.67 t of the product. Total electricity consumption for 1 t of slugs is 9.446 MWh, and for 0.67 t of evaporator panels is 10.199 MWh.

The electricity delivered to a company is generated from a mix of fossil, nuclear and renewable energy sources. Electricity sources of fossil origin are coal, lignite, natural gas and oil. Hydro, wind, photovoltaics, geothermal, biomass, biogas and biodiesel are considered types of renewable energy. For the sake of simplification, energy sources are grouped into three main categories. Fractions of energy sources in the electricity mix, and emission factors of the different sources are summarized in Table 1. Average values for prices and emission factors are used for each energy source. The prices for each energy source are regarded as confidential and thus they are not presented.

Table 1. Data used in the study.

Energy Source	Fraction	Emission Factor (t CO ₂ /MWh)	Product	Consumption (MWh/t)
Nuclear	0.2602	0.008	Slug	9.446
Renewable	0.1509	0.038	Evaporator panels	10.199
Fossil	0.5889	1.015		

Three different energy planning approaches (graphical, algebraic and optimization-based approaches) will be demonstrated in the following sections. The first two approaches are presented and illustrated on one aluminum product (aluminum slugs) and are shown for zero- and low-carbon energy sources (in the current work, the low-carbon energy source is renewable energy). The third approach deals with two aluminum products (aluminum slugs and evaporator panels) and considers

two cases: the case where electricity is pinched for each product, and the hypothetical case where only one Pinch exists for both products. In the case of optimization, the trade-off solution is obtained between emissions and the cost of energy sources to achieve a given benchmark.

Graphical and numerical approaches consist of several steps and follow similar algorithms whose detailed steps are described in related previous papers. First, energy supply and demand are defined; then, they are arranged into emission intervals (segments) by increasing the emission factors from the lowest to the highest. By the graphical approach, the energy source and demand curves are then plotted on the energy consumption–emissions diagram. The energy source curve is further shifted horizontally until it intersects with the energy demand curve (at the “Pinch Point”) [12]. By the numerical approach, the energy surplus/deficit is cascaded through the intervals, and the cumulative net energy consumption should be non-negative. The deficit should then be added to the zero- or low-carbon energy source [13]. The optimization approach, on the other hand, involves formulating a working model whose solution is determined numerically via established solution techniques (i.e., Simplex algorithm) that is embedded in standard optimization software. The data and variables should be defined, and together with the constraints, they form a feasible region. The optimal solution is then defined based on the given objective, which is minimized or maximized. The procedure for each approach is described in more detail, together with the case studies, in the following section.

3. Graphical Targeting Approach

The first technique for CCEP is the insight-based graphical targeting approach, called CEPA, originally developed in 2007 by Tan and Foo [12]. CEPA uses a graphical approach based on the principles of conventional PA [21]; it enables the identification of the minimum amount of low- or zero-carbon energy needed to satisfy demand-side emission constraints (target) [49]. Note that the term “zero-carbon” is usually applied to sources with very low CO₂ intensity compared to fossil fuels, even if the actual magnitude is nonzero. Various applications and extensions of the CEPA methodology have been developed recently, such as applications to energy sectors in different countries (Ireland [50], New Zealand [51], USA [52], China [53], Nigeria [54], the Baltic States [55], the EU [56] and others), alternative metrics and footprints (land [13], water [15]), and other sectors, such as transport systems [16], economic systems [17] and others. Conceptual or graphical techniques applied in PA are useful tools in the preliminary stages of energy planning, energy policy [57], in graphical representation, in step-by-step user control and in the verification of results. The graphical display also provides visualization that is useful for the analysis of a problem and subsequent communication of the results. On the other hand, graphical methods are limited to relatively simple problems [12]. Another limitation could be the accuracy of the results, which depends on the quality of the graphical display [12].

All the steps of the CEPA algorithm are presented in detail by Tan and Foo [12]. The first step in the CEPA procedure is the preparation of the energy source and demand data, which are shown in Table 2. Energy sources are sorted in order of increasing emission factors (see also Table 1). The consumption described in Table 2 (in MWh/t) was obtained by multiplying the fraction of the energy source by the total consumption of electricity for the production of aluminum slugs (9.446 MWh/t). As stated previously, only one product (aluminum slugs) was considered for the graphical and algebraic approaches. Emissions (in t CO₂/t) were obtained by multiplying the emission factor and total electricity consumption for 1 t of slugs. Energy demand represents the total consumption of electricity for 1 t of slugs with target emission constraints (benchmark of 0.376 t CO₂/MWh [5]). Emissions (3.552 t CO₂/t) were obtained by multiplying the benchmark emission factor and total electricity consumption.

The second step in the CEPA procedure is the generation of source and demand composite curves (CCs). Source curves for energy supply were obtained as CO₂ emissions vs. electricity supply plots, and demand curves as CO₂ emissions vs. electricity demand plots. The horizontal axis represents electricity supply or demand, while CO₂ emissions are plotted as the vertical axis. The slope of each electricity source is equal to its emission factor, while the slope of electricity demand is equal to

benchmark emission factor. Fossil energy has the highest emission factor (1.015 t CO₂/MWh; see also Table 1) of all electricity sources and a much steeper slope compared to renewable and nuclear energy.

Table 2. Data required for CEPA.

Source	Consumption (MWh/t)	Emissions (t CO ₂ /t)	Demand	Consumption (MWh/t)	Emissions (t CO ₂ /t)
Nuclear	2.458	0.020	Slugs	9.446	3.552
Renewable	1.425	0.054			
Fossil	5.563	5.646			
SUM	9.446	5.720			

The next step is to construct source and demand CCs (see Figures 2 and 3). The source curve consists of three segments, i.e., nuclear, renewable, and fossil segments, and is constructed by arranging the segments end-to-end in ascending order of emission factors. The resulting source CC curls upwards [12]. The demand curve consists of only one segment, i.e., target CO₂ emissions for 1 t of aluminum slugs. The demand curve is thus linear over the entire interval.

To supply suitable energy sources that meet the CO₂ emissions targets, the source CC is then shifted to the right. The Pinch Point is where the demand curve touches the shifted source curve. On the lower end of the shifted source CC (minimum distance between origin and shifted CC) is the minimum amount of zero-carbon energy sources needed to meet the CO₂ emission limit, while at the upper end (distance between the Pinch Point and the end of the shifted source CC) is excess energy from fossil sources. At the lower end, it is generally desirable to maximize the use of zero- or low-carbon sources [58], while at the upper end, it is desirable to minimize the use of the most carbon-intensive energy source. Figure 2 shows a Pinch diagram for 1 t of aluminum slug production while minimizing the zero-carbon energy source.

The minimum amount of zero-carbon energy (Figure 2) in this study is the same as the excess of the fossil source because of the same amount of electricity supply and demand. The graphical approach shows that for 1 t of aluminum slugs, about 2.14 MWh of the fossil source should be replaced with zero-carbon energy to achieve an emission limit of 3.552 t CO₂. As is shown in the left-upper window of Figure 2, the zero-carbon source has a zero slope, and nuclear energy, which is the lowest carbon emission source, is shifted for the minimum zero-carbon energy source to the right.

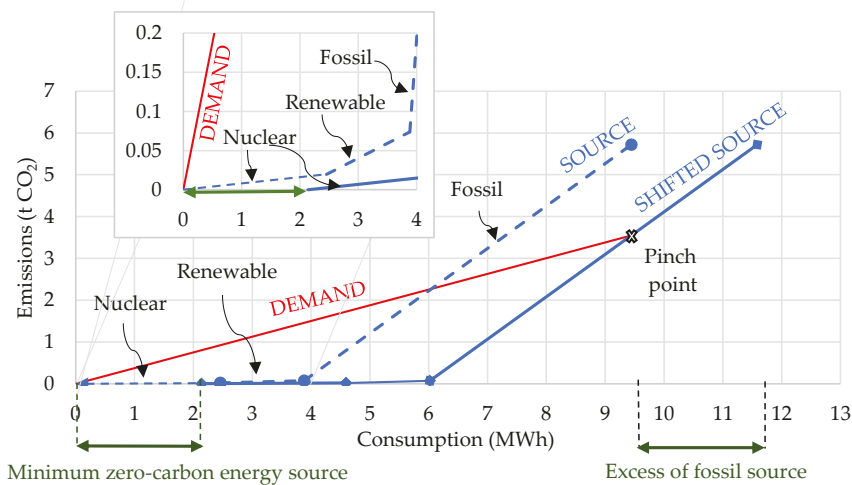


Figure 2. Pinch diagram for 1 t of aluminum slugs with a minimum zero-carbon source.

either a zero-carbon or a low-carbon source. In the next column, the CO₂ emission load at interval *k* (*E_k*) is calculated as:

$$E_k = F_k \cdot \Delta c_k \tag{1}$$

Next, the cumulative CO₂ load (ΔE_k) between successive rows of *E_k* is calculated. If ΔE_k has a negative value, the CO₂ limit has been exceeded, and the cascade is infeasible. In the last column, clean source demand at interval *k* (*F_{CS,k}*) is shown, which is calculated as:

$$F_{CS,k} = \frac{\Delta E_k}{c_k - c_{CS}} \tag{2}$$

where *c_{CS}* represents an emission factor or the clean (zero- or low-carbon) energy source.

In the following section, both cases will be shown, i.e., the minimum demand for the zero- and low-carbon energy sources. The cascade analysis approach was implemented in Excel by using the actual (not rounded) numbers for calculations.

4.1. Minimum Demand for the Zero-Carbon Source

First, the demand for the zero-carbon source was determined to achieve the specified emission limits. The data used in the study are as shown in Table 1. Cascade analysis was applied to one aluminum product, i.e., aluminum slugs, and is shown in Table 3.

The analysis in Table 3 shows an infeasible cascade for a minimum zero-carbon energy source. A feasible cascade should have a non-negative value for the cumulative CO₂ load in the last interval. A feasible cascade is shown in Table 4, where almost all the steps remain the same as before. The exception is that the largest negative value of *F_{CS,k}* is considered as the quantity of the zero-carbon energy source, and is taken as an absolute positive value.

Table 3. Cascade analysis for zero-carbon energy source where not all CO₂ loads are non-negative.

<i>c_k</i> (t CO ₂ /MWh)	Δc_k (t CO ₂ /MWh)	<i>D_j</i> (MWh)	<i>S_i</i> (MWh)	<i>S_i</i> – <i>D_j</i> (MWh)	<i>F_k</i> (MWh)	<i>E_k</i> (t CO ₂)	ΔE_k (t CO ₂)	<i>F_{CS,k}</i> (MWh)
0								
0.008	0.008		2.458	2.458	0	0	0	0
0.038	0.030		1.425	1.425	2.458	0.074	0	
0.376	0.338	9.446			3.883	1.312	0.074	1.941
1.015	0.639		5.563	5.563	–9.446	–3.555	1.386	3.687
					–5.563		–2.169	–2.137
					0			

Table 4. Minimum zero-carbon energy solution applying cascade analysis.

<i>c_k</i> (t CO ₂ /MWh)	Δc_k (t CO ₂ /MWh)	<i>D_j</i> (MWh)	<i>S_i</i> (MWh)	<i>S_i</i> – <i>D_j</i> (MWh)	<i>F_k</i> (MWh)	<i>E_k</i> (t CO ₂)	ΔE_k (t CO ₂)	<i>F_{CS,k}</i> (MWh)
0			2.137	2.137				
0.008	0.008		2.458	2.458	2.137	0.017		
0.038	0.030		1.425	1.425	4.595	0.138	0.017	2.137
0.376	0.338	9.446			6.020	2.035	0.155	4.077
1.015	0.639		5.563	5.563	–9.446	–2.190	2.190	5.823
					–3.426		0*	0
					2.137			

* Pinch Point.

The negative value of $F_{CS,k}$ in the last interval from Table 3 (−2.137 MWh) is the amount of required zero-carbon energy source S_i in the first interval in Table 4 (where emission factor c_k is zero). In this way, the cascade is adjusted to become feasible. From Table 4, it can also be seen that the excess energy from the fossil source is the same as the minimum amount of zero-carbon energy (2.137 MWh; last interval of F_k). The Pinch Point is obtained at interval k , where ΔE_k is equal to zero, which is at 1.015 t CO₂/MWh.

4.2. Minimum Demand for the Low-Carbon Source

The algebraic targeting approach is further extended to determine the amount of the low-carbon energy source to achieve the specified emission limits. All steps in the cascade analysis remain the same as for the zero-carbon example, except that S_i for the renewable energy source is now the sum of the previous amount of renewable energy source (1.425 MWh) plus the minimum amount of zero-carbon energy obtained above (2.137 MWh, see Table 4). $F_{CS,k}$ was obtained by considering a c_{CS} of 0.038 (see also Table 1). The cascade analysis determining the minimum amount of the low-carbon energy source is shown in Table 5.

Table 5. Cascade analysis for the low-carbon energy source where not all CO₂ loads are non-negative.

c_k (t CO ₂ /MWh)	Δc_k (t CO ₂ /MWh)	D_j (MWh)	S_i (MWh)	$S_i - D_j$ (MWh)	F_k (MWh)	E_k (t CO ₂)	ΔE_k (t CO ₂)	$F_{CS,k}$ (MWh)
0								
0.008	0.008		2.458	2.458	0	0	0	0
0.038	0.030		3.562	3.562	2.458	0.074	0	0
0.376	0.338	9.446			6.020	2.035	0.074	Undef *
1.015	0.639		5.563	−9.446	−3.426	−2.189	2.109	6.238
				5.563	2.137		−0.081	−0.083

* undef—result is undefined because of division by zero.

Table 6. Minimum low-carbon energy solution applying cascade analysis.

c_k (t CO ₂ /MWh)	Δc_k (t CO ₂ /MWh)	D_j (MWh)	S_i (MWh)	$S_i - D_j$ (MWh)	F_k (MWh)	E_k (t CO ₂)	ΔE_k (t CO ₂)	$F_{CS,k}$ (MWh)
0								
0.008	0.008		2.458	2.458	0	0	0	0
0.038	0.030		3.645	3.645	2.458	0.074	0	0
0.376	0.338	9.446			6.103	2.063	0.074	undef
1.015	0.639		5.563	−9.446	−3.343	−2.136	2.136	6.321
				5.563	2.220		0 *	0

* Pinch Point.

The cascade analysis in Table 5 gives an infeasible solution for the low-carbon source owing to the negative value of ΔE_k in the last interval. A feasible solution to the cascade analysis is shown in Table 6, where again, the most negative value of $F_{CS,k}$ (−0.083 MWh) is added to the low-energy source (S_i for renewable energy source with c_k of 0.038). This is the amount (in absolute numbers) of the required addition to the low-carbon supply shown in Table 5 (3.562 MWh, increased to 3.645).

As obtained also by the graphical approach, the amount of excess energy from fossil sources is increased to 2.22 MWh. The Pinch Point is again obtained at 1.015 t CO₂/MWh.

In the following section, the optimization-based approach is used to minimize the cost of electricity sources while achieving CO₂ emission targets. Two products are considered for optimization, i.e., aluminum slugs and aluminum evaporator panels.

5. Optimization-Based Approach

Mathematical Programming (MP) is another broad category of PI methodologies [60]. MP enables the search to be automated, while finding the optimal solution among many design alternatives [61]. The simplest representation of the MP model is defined as a deterministic model (the model where all the parameters are constant and not uncertain or random), and is written in the form of a Linear Program (LP). One advantage over the previous two approaches is the flexibility to change the objective function to suit the context of the problem. For PI problems, one of the first problem formulations of MP was the transportation model [62].

The transportation model (its variants are also known as the source-sink model or resource-allocation problem) is based on the principle that a product is transported from a number of sources to a number of sinks (destinations) based on a given objective (minimum cost, maximum profit, etc.). Dealing with both mass and energy for CCEP problems as extensive properties, in contrast to temperature in Heat Integration, which is an intensive property, the transportation model is a suitable approach for solving CCEP problems. The transportation model, which is written in a generic way and could be applied to any transportation or planning problem, is shown in Equations (3)–(7). The sets, data and variables applied in the transportation model are described on the left.

$$\sum_j x_{ij} \leq a_i, \forall i \in I \quad (3)$$

$$\sum_i x_{ij} = b_j, \forall j \in J \quad (4)$$

$$\sum_i x_{ij} F_i = E_j, \forall j \in J \quad (5)$$

$$w_{ij} = \frac{x_{ij}}{b_j}, \forall i \in I, j \in J \quad (6)$$

$$\min z = \sum_{ij} x_{ij} P_i \quad (7)$$

Sets

I source (fossil, nuclear, renewable) with elements $i \in I$

J demand (slug, evaporator panels) with elements $j \in J$

Parameters

a_i supply or availability of energy source i (MWh/y)

b_j demand for electricity to produce product j (MWh)

F_i emission factor for electricity source i (t CO₂/MWh)

P_i price of electricity source i (EUR/MWh)

Positive variable

x_{ij} amount of electricity from source i to demand j (MWh/y)

w_{ij} fraction of electricity source i to produce product j (-)

E_j CO₂ emissions for each product j (t CO₂/t products)

Equation (3) is calculated for each source i , and implies that the sum of specific electricity source i consumed for all j products (x_{ij}) should be greater than or equal to the availability of that electricity source i (a_i). Equation (4) is calculated for each demand for energy j and requires that the amount of electricity from all the sources satisfy the demand for electricity to produce each product j (b_j). CO₂ emissions originating from electricity consumption for the production of each product j (E_j) are

calculated with Equation (5), where the amounts of electricity consumed x_{ij} are multiplied by the emission factors for energy source i (F_i). Equation (6) calculates the fraction of electricity source i (w_{ij}) used to produce each product j . Finally, Equation (7) represents the objective, which is to minimize the cost of the electricity supply mix, which is calculated by multiplying the amount of electricity consumed (x_{ij}) by the price of each electricity source i (P_i).

Three different cases are studied:

- *Current case:* The electricity mix for producing aluminum slugs and evaporator panels is fixed to the current shares of each energy source in the mix. To simulate the current case, CO₂ emissions are also fixed to their current emission values. To calculate the cost for the supply of electricity mix, Equations (3)–(7) are applied.
- *Case 1:* It is assumed that the electricity mix delivered to the company allows optimal fractions of the main energy sources to be in the electricity supply mix. Also, emission levels for each aluminum product should be achieved for every product. The upper emission limit is set to 3.55 t CO₂/t slugs and to 3.835 t CO₂ per 0.67 t of evaporator panels. As explained previously, the emission limit is set to 0.376 t CO₂/MWh of electricity, while 9.446 MWh are required for 1 t of slugs and 10.199 MWh for 0.67 t of evaporator panels. To calculate the cost for this case, Equations (3)–(7) are applied. where Equation (5) is reformulated so that emissions from electricity consumed do not exceed the upper emission limits for each product j (3.55 t and 3.835 t CO₂):

$$\sum_i x_{ij}F_i \leq E_j, \forall j \in J \quad (8)$$

- *Case 2:* This case is similar to Case 1, but here, it is assumed that the total emission level should be achieved for both aluminum products together. The upper emission limits are the same as those for the first case. Equation (5) is again reformulated to consider the upper limit on emissions for both products combined:

$$\sum_{i,j} x_{ij}F_i \leq \sum_j E_j \quad (9)$$

The models for the three cases determine the minimum cost of the electricity supply mix considering emission limits. The main results of the transportation model for the three cases are summarized in Table 7, where the fractions of the electricity sources used to produce each product and the total cost of electricity supply are shown. It should be noted that, for reasons of confidentiality, the values of cost are normalized, where a value of 1 represents the cost for current electricity mix.

Table 7 shows that the cost of the current electricity supply mix is lower by 26% compared to cases considering emission limits (Case 1 and 2). Currently, there is a relatively high share of fossil sources in the electricity mix, which is cheaper compared to nuclear and renewable sources. With the current electricity mix, however, emission levels cannot be achieved because of the higher emission factor of fossil energy (see also Table 1). For both the current case and Case 1, the fractions of electricity sources in the mix are the same for both products. Case 2 is a hypothetical case, where the fractions of sources in the electricity mix for slugs and evaporator panels are different. Renewable energy is not selected in either Case 1 and 2, owing to the higher emission factor and lower cost compared to nuclear energy.

The Pinch diagrams in the next sections show where an electricity consumption Pinch occurs for each product (Case 1), and when only one Pinch for all the products combined should be achieved (Case 2).

Table 7. Main results from optimization.

Product/Scenario	Slugs			Evaporator Panels			Cost
	w_{fossil}	w_{nuclear}	$w_{\text{renewable}}$	w_{fossil}	w_{nuclear}	$w_{\text{renewable}}$	
Current	0.590	0.260	0.150	0.590	0.260	0.150	1
Case 1	0.365	0.635	0	0.365	0.635	0	1.26
Case 2	0	1	0	0.704	0.296	0	1.26

5.1. Electricity Consumption Pinch for Each Product

Case 1 presents the case whereby for each product, the emission limit should not be exceeded. Electricity consumption is pinched for each product, as shown in Figure 4. The source CC represents the current case, where emissions and the composition of the electricity mix for both products are fixed. The demand curve consists of two segments, one for each product. However, both segments have the same slope, since the CO₂ emission benchmark is the same for both products (0.376 t CO₂/MWh [5], as stated previously). For Case 1, it can be seen that both products use nuclear and fossil energy to reach the target, as presented in Table 7. Renewable energy is not selected, as it has a higher emission factor and is more expensive than nuclear.

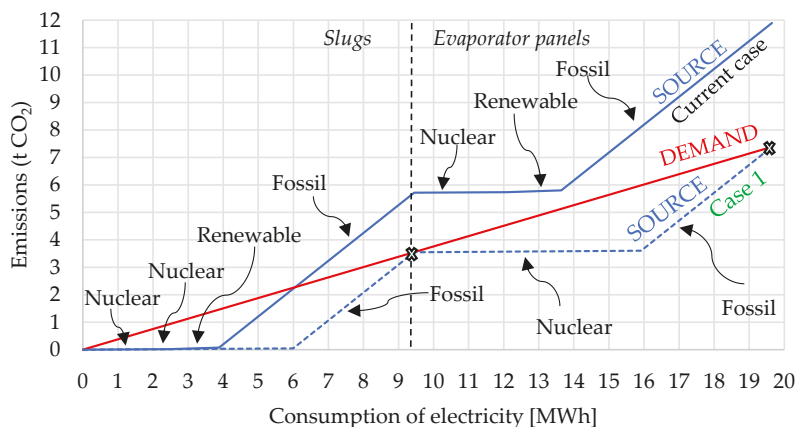


Figure 4. Pinch diagram for Case 1 when electricity consumption is pinched for each product.

A sensitivity analysis was further performed by fixing the fraction of renewable energy in the electricity supply mix. It is expected that the share from renewable sources will rise in future, while the expansion of nuclear in the future is less certain. The fraction of renewable energy is increased from 0% to 100%. The results of the sensitivity analysis are shown in Figure 5 for fractions of fossil and nuclear sources (left) and cost (right).

It can be seen that the fraction of nuclear energy in the electricity mix decreases almost linearly with the increase in the renewable energy share in the electricity mix up to $w_{\text{renewable}}$ reaching about 0.7. Subsequently, nuclear energy is no longer selected because of cheaper fossil electricity, while the emission limit is satisfied. Fossil source, on the other hand, remains almost constant, between $w_{\text{renewable}}$ 0 and about 0.7. At higher values of $w_{\text{renewable}}$, the fraction of w_{fossil} starts decreasing almost linearly with the increase in $w_{\text{renewable}}$. It should be noted that $w_{\text{renewable}} + w_{\text{fossil}} + w_{\text{nuclear}}$ should always be equal to 1.

The cost of the electricity supply mix is shown in Figure 5 on the right. For reasons of confidentiality, the values of cost, on the vertical axis, are hidden. The lowest cost was obtained with no renewable energy in the supply mix (as shown in Table 7). It should be noted that renewable energy is the most expensive of all the sources (see Table 1), and the cost of electricity is constantly increasing with

increasing the share of $w_{\text{renewable}}$. The cost increases slightly for $w_{\text{renewable}} < 0.6$, where renewable energy replaces nuclear. It begins to increase more significantly for $w_{\text{renewable}} > 0.6$, when renewable replaces fossil energy, owing to the significant differences in price.

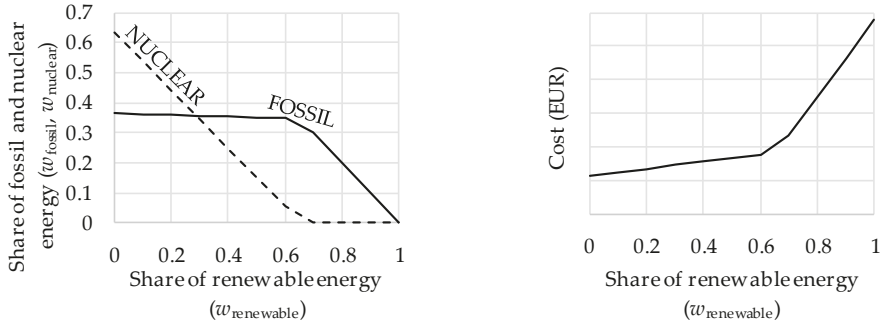


Figure 5. Composition of energy mix (left) and cost (right) while increasing the fraction of renewable energy in the electricity mix.

5.2. Electricity Consumption Pinch for All the Products Considered

Case 2 presents a hypothetical case where for all products, the overall emission limit should not be exceeded. Only one electricity Pinch is obtained for the total electricity demand, as shown in Figure 6. The demand curve is the same as in Case 1, while the source curves for the Current case and Case 2 are now different. Both source curves are arranged in ascending order of emission factors for all the products combined. It can be seen that for slugs, only nuclear energy is used, while for evaporator panels, first nuclear energy is used, and later, also fossil energy to satisfy benchmark CO₂ emissions. It should be noted that even here, fossil energy is the preferred source because it has the lowest cost; thus Cases 1 and 2 both exhibit the same cost, as shown in Table 7.

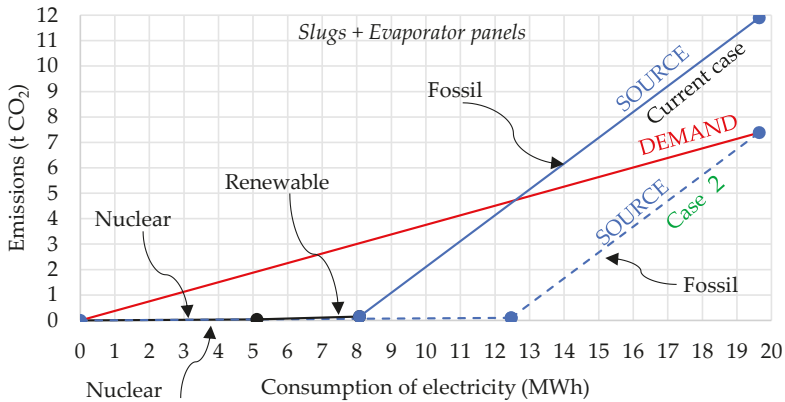


Figure 6. Pinch diagram for Case 2 when electricity consumption is pinched for all the products combined.

6. Conclusions

In this work, an extension of CEPA was developed and applied to the energy- and carbon-intensive aluminum industry. Graphical, algebraic and optimization-based approaches for CCEP were applied for the production of specific aluminum products, i.e., aluminum slugs and evaporator panels. Graphical and algebraic approaches determined the minimum amount of zero- and low-carbon energy sources required to achieve the specified emission limit. The transportation model was further applied

to energy planning for two specific products to calculate the optimal electricity mix to reach the specified emission limit with minimum cost.

All the approaches yielded similar results; the first two showed that about 2.14 MWh of zero-carbon or 2.22 MWh of low-carbon, and the same amounts of excess energy (2.14 MWh or 2.22 MWh), are obtained for 1 t of aluminum slugs. The third approach was based on cost optimization and showed that 26% higher electricity cost would be required to achieve the specified CO₂ emission target compared to the current case. In principle, this incremental cost can potentially be covered by economic incentives such as an emissions tax. CCEP can thus be used in the future to estimate the amount of such incentives needed to drive industrial fossil-based GHG emissions abatement.

Each approach showed its strengths and weaknesses, as summarized in Table 8. The graphical and algebraic approaches proved to be powerful tools for energy planning of industrial products, since they are intuitive and provide better insights into the problem for both analysis and communication. Optimization-based results are less intuitive; however, optimization automates the procedure and could include more details, including cost optimization. Hybrid approaches are suggested which combine different methods to yield the synergistic advantages of each separate method [63].

Table 8. Comparison of the approaches.

Approach	Strengths	Weaknesses
Graphical	<ul style="list-style-type: none"> - useful approach for preliminary planning - enables graphical (visual) presentation - useful for communication of results <ul style="list-style-type: none"> - enables user control - enables verification of results 	<ul style="list-style-type: none"> - limited to simple problems - limited accuracy of results - size and unit dependence <ul style="list-style-type: none"> - not flexible - procedure is not automated - cannot include details and objectives, such as cost optimization
Algebraic	<ul style="list-style-type: none"> - application to both simple and complex problems - precision of results - more systematic approach - provides insight into the problem - useful for communication of results 	<ul style="list-style-type: none"> - size and unit dependence <ul style="list-style-type: none"> - not flexible - procedure is not automated - cannot include details and objectives, such as cost optimization
Optimization	<ul style="list-style-type: none"> - application to both simple and complex problems - precision of results <ul style="list-style-type: none"> - flexible - automated procedure - equations can be modified - could include more details and various objectives - relatively simple input/code determination 	<ul style="list-style-type: none"> - requires background of mathematical modeling - more difficult communication of results <ul style="list-style-type: none"> - verification of results is less straightforward

This work demonstrated the usefulness of CCEP approaches in the move towards a more sustainable aluminum industry. Since aluminum is widely used in various applications and is highly energy intensive, optimizing the electricity supply mix used in its production could significantly contribute to conserving resources and decreasing the global carbon footprint. However, regarding the optimization of the electricity mix, more detailed exploration regarding the electricity sector should be performed in terms of the cost, emissions, sustainability and availability of low-, zero- and negative-carbon emission sources.

In the future, CCEP analyses will be extended for targeting GHG (CO₂ Equation emissions) and other footprints. Various options for carbon capture could be incorporated, including technologies to achieve GHG emissions reductions. Additionally, CO₂ emissions reductions could be analyzed by including mass integration to minimize emissions and the use of materials. Analyses could also be expanded to more aluminum products and to include more details regarding types of energy sources

(renewable energy could be separated to hydro, photovoltaics, geothermal, wind, biomass, etc.), and their availability and pricing (e.g., hourly based), including future prices. Multiscale application of PI techniques could be used to improve material and energy efficiency to reduce energy consumption and emissions at the process, TS and supply chain network levels [33]. The methodology will be extended to account for variations in the ratio of primary and secondary aluminum within a circular economy framework and to account for negative emission technologies, and will include the combined use of all three proposed approaches.

Author Contributions: R.G., L.Č. and Z.K.: conceptualization and methodology; R.G.: data curation, formal analysis, and original draft preparation; L.Č.: resources and supervision; L.Č., M.H., R.R.T. and Z.K.: writing-review and editing. All authors have read and agreed to the published version of the manuscript.

Funding: The authors are grateful for funding support from the companies Talum d.d. and Talum Inštitut d.o.o. and from the Slovenian Research Agency (research core funding No. P2-0412 and P2-0032 and projects N2-0138 and J7-1816).

Conflicts of Interest: The authors declare no conflict of interest.

Abbreviations

CCEP	Carbon-constrained energy planning
CEPA	Carbon Emission Pinch Analysis
ETS	Emissions Trading System
EU	European Union
GHG	Greenhouse gas
LP	Linear Program
MP	Mathematical Programming
OBJ	objective function
PA	Pinch Analysis
PI	Process Integration
TS	Total Site

References

1. Fan, Y.V.; Tan, R.R.; Klemeš, J.J. A system analysis tool for sustainable biomass utilisation considering the Emissions-Cost Nexus. *Energy Convers. Manag.* **2020**, *210*, 112701. [CrossRef]
2. Climate Watch. Global Historical GHG Emissions (Data Source: CAIT). Available online: [Climatewatchdata.org/ghg-emissions?breakBy=sector&chartType=percentage&source=71](https://climatewatchdata.org/ghg-emissions?breakBy=sector&chartType=percentage&source=71) (accessed on 4 April 2020).
3. European Commission. 2030 Climate & Energy Framework. Available online: [Ec.europa.eu/clima/policies/strategies/2030_en#tab-0-0](https://ec.europa.eu/clima/policies/strategies/2030_en#tab-0-0) (accessed on 4 April 2020).
4. European Commission. EU Emissions Trading System (EU ETS). Available online: [Ec.europa.eu/clima/policies/ets_en](https://ec.europa.eu/clima/policies/ets_en) (accessed on 8 February 2020).
5. European Commission. Commission delegated regulation (EU) 2019/331 of 19 December 2018 determining transitional Union-wide rules for harmonised free allocation of emission allowances pursuant to Article 10a of Directive 2003/87/EC of the European Parliament and of the Council. *Off. J. Eur. Union Bruss.* **2019**, *59*, 25.
6. Primary Aluminium Smelting Energy Intensity. Available online: [World-aluminium.org/statistics/primary-aluminium-smelting-energy-intensity](https://world-aluminium.org/statistics/primary-aluminium-smelting-energy-intensity) (accessed on 23 January 2020).
7. European Commission. Electricity Production, Consumption and Market Overview. Available online: [Ec.europa.eu/eurostat/statistics-explained/index.php/Electricity_production_consumption_and_market_overview#Electricity_generation](https://ec.europa.eu/eurostat/statistics-explained/index.php/Electricity_production_consumption_and_market_overview#Electricity_generation) (accessed on 8 February 2020).
8. Lee, J.-Y.; Lin, H.-F. Multi-Footprint Constrained Energy Sector Planning. *Energies* **2019**, *12*, 2329. [CrossRef]
9. Akyüz, E. Advantages and disadvantages of nuclear energy in Turkey: Public perception. *Eurasian J. Environ. Res.* **2017**, *1*, 1–11.
10. Petrescu, F.I.; Apicella, A.; Petrescu, R.V.; Kozaitis, S.; Bucinell, R.; Aversa, R.; Abu-Lebdeh, T. Environmental protection through nuclear energy. *Am. J. Appl. Sci.* **2016**, *13*, 941–946. [CrossRef]

11. Tan, R.R.; Sum Ng, D.K.; Yee Foo, D.C. Pinch analysis approach to carbon-constrained planning for sustainable power generation. *J. Clean. Prod.* **2009**, *17*, 940–944. [[CrossRef](#)]
12. Tan, R.R.; Foo, D.C. Pinch analysis approach to carbon-constrained energy sector planning. *Energy* **2007**, *32*, 1422–1429. [[CrossRef](#)]
13. Foo, D.C.; Tan, R.R.; Ng, D.K. Carbon and footprint-constrained energy planning using cascade analysis technique. *Energy* **2008**, *33*, 1480–1488. [[CrossRef](#)]
14. Ooi, R.E.H.; Foo, D.C.Y.; Tan, R.R. Targeting for carbon sequestration retrofit planning in the power generation sector for multi-period problems. *Appl. Energy* **2014**, *113*, 477–487. [[CrossRef](#)]
15. Tan, R.R.; Foo, D.C.Y.; Aviso, K.B.; Ng, D.K.S. The use of graphical pinch analysis for visualizing water footprint constraints in biofuel production. *Appl. Energy* **2009**, *86*, 605–609. [[CrossRef](#)]
16. Walmsley, M.R.W.; Walmsley, T.G.; Atkins, M.J.; Kamp, P.J.J.; Neale, J.R.; Chand, A. Carbon Emissions Pinch Analysis for emissions reductions in the New Zealand transport sector through to 2050. *Energy* **2015**, *92*, 569–576. [[CrossRef](#)]
17. Tan, R.R.; Aviso, K.B.; Foo, D.C.Y. Carbon emissions pinch analysis of economic systems. *J. Clean. Prod.* **2018**, *182*, 863–871. [[CrossRef](#)]
18. Pékala, L.M.; Tan, R.R.; Foo, D.C.Y.; Jeżowski, J.M. Optimal energy planning models with carbon footprint constraints. *Appl. Energy* **2010**, *87*, 1903–1910. [[CrossRef](#)]
19. Tan, R.R.; Aviso, K.B.; Foo, D.C. P-graph and Monte Carlo simulation approach to planning carbon management networks. *Comput. Chem. Eng.* **2017**, *106*, 872–882. [[CrossRef](#)]
20. Mu, P.; Yang, Y.; Han, Y.; Gu, X.; Zhu, Q. Raw material management networks based on an improved P-graph integrated carbon emission pinch analysis (CEPA-P-graph) method. *Can. J. Chem. Eng.* **2020**, *98*, 676–689. [[CrossRef](#)]
21. Klemeš, J.J. *Handbook of Process Integration (PI): Minimisation of Energy and Water Use, Waste and Emissions*; Woodhead Publishing Limited: Cambridge, UK, 2013.
22. Linnhoff, B.; Flower, J.R. Synthesis of heat exchanger networks: I. Systematic generation of energy optimal networks. *AIChE J.* **1978**, *24*, 633–642. [[CrossRef](#)]
23. Dhole, V.R.; Linnhoff, B. Total site targets for fuel, co-generation, emissions, and cooling. *Comput. Chem. Eng.* **1993**, *17*, S101–S109. [[CrossRef](#)]
24. Colmenares, T.R.; Seider, W.D. Heat and power integration of chemical processes. *AIChE J.* **1987**, *33*, 898–915. [[CrossRef](#)]
25. El-Halwagi, M.M.; Manousiouthakis, V. Synthesis of mass exchange networks. *AIChE J.* **1989**, *35*, 1233–1244. [[CrossRef](#)]
26. Alves, J.J.; Towler, G.P. Analysis of Refinery Hydrogen Distribution Systems. *Ind. Eng. Chem. Res.* **2002**, *41*, 5759–5769. [[CrossRef](#)]
27. Zhelev, T.; Ntlhakana, J. Energy-environment closed-loop through oxygen pinch. *Comput. Chem. Eng.* **1999**, *23*, S79–S83. [[CrossRef](#)]
28. Singhvi, A.; Shenoy, U. Aggregate planning in supply chains by pinch analysis. *Chem. Eng. Res. Des.* **2002**, *80*, 597–605. [[CrossRef](#)]
29. Foo, D.C.Y.; Kazantzi, V.; El-Halwagi, M.M.; Manan, Z.A. Surplus diagram and cascade analysis technique for targeting property-based material reuse network. *Chem. Eng. Sci.* **2006**, *61*, 2626–2642. [[CrossRef](#)]
30. Tjan, W.; Tan, R.R.; Foo, D.C. A graphical representation of carbon footprint reduction for chemical processes. *J. Clean. Prod.* **2010**, *18*, 848–856. [[CrossRef](#)]
31. Klemeš, J.J.; Varbanov, P.S.; Ochoa, P.; Chin, H.H. Towards Efficient and Clean Process Integration: Utilisation of Renewable Resources and Energy-Saving Technologies. *Energies* **2019**, *12*, 4092. [[CrossRef](#)]
32. Gai, L.; Varbanov, P.S.; Walmsley, T.G.; Klemeš, J.J. Critical Analysis of Process Integration Options for Joule-Cycle and Conventional Heat Pumps. *Energies* **2020**, *13*, 635. [[CrossRef](#)]
33. Jamaluddin, K.; Wan Alwi, S.R.; Abdul Manan, Z.; Hamzah, K.; Klemeš, J.J. A Process Integration Method for Total Site Cooling, Heating and Power Optimisation with Trigeneration Systems. *Energies* **2019**, *12*, 1030. [[CrossRef](#)]
34. Büttin, H.; Kantor, I.; Maréchal, F. Incorporating Location Aspects in Process Integration Methodology. *Energies* **2019**, *12*, 3338. [[CrossRef](#)]
35. Chen, Y.; Zhu, J. A Graph Theory-Based Method for Regional Integrated Energy Network Planning: A Case Study of a China–US Low-Carbon Demonstration City. *Energies* **2019**, *12*, 4491. [[CrossRef](#)]

36. Yap, J.Y.; Tan, J.; Foo, D.C.; Tan, R.R.; Papadokonstantakis, S.; Badr, S. A graphical method for carbon dioxide emissions reduction in multi-product plants. *Process Saf. Environ. Prot.* **2020**, *133*, 51–63. [[CrossRef](#)]
37. Qin, Z.; Tang, K.; Wu, X.; Yu, Y.; Zhang, Z. Product-based Carbon Constraint Energy Planning with pinch analysis for sustainable methanol industry in China. *Chem. Eng. Trans.* **2017**, *61*, 103–108.
38. Sinha, R.K.; Chaturvedi, N.D. A graphical dual objective approach for minimizing energy consumption and carbon emission in production planning. *J. Clean. Prod.* **2018**, *171*, 312–321. [[CrossRef](#)]
39. Abdul Aziz, E.; Wan Alwi, S.R.; Lim, J.S.; Abdul Manan, Z.; Klemeš, J.J. An integrated Pinch Analysis framework for low CO₂ emissions industrial site planning. *J. Clean. Prod.* **2017**, *146*, 125–138. [[CrossRef](#)]
40. Sinha, R.K.; Chaturvedi, N.D. A review on carbon emission reduction in industries and planning emission limits. *Renew. Sustain. Energy Rev.* **2019**, *114*, 109304. [[CrossRef](#)]
41. Edenhofer, O.; Pichs-Madruga, R.; Sokona, Y.; Minx, J.C.; Farahani, E.; Kadner, S.; Seyboth, K.; Adler, A.; Baum, I.; Brunner, S.; et al. *Climate Change 2014: Mitigation of Climate Change*; Cambridge University Press: New York, NY, USA, 2015; Volume 3.
42. Zhang, Y.; Sun, M.; Hong, J.; Han, X.; He, J.; Shi, W.; Li, X. Environmental footprint of aluminum production in China. *J. Clean. Prod.* **2016**, *133*, 1242–1251. [[CrossRef](#)]
43. Emsley, J. *Nature's Building Blocks: An A-Z Guide to the Elements*; Aluminium or Aluminum (USA); Oxford University Press: New York, NY, USA, 2011.
44. Durković, V.; Đurišić, Ž. Analysis of the potential for use of floating PV power plant on the Skadar Lake for electricity supply of aluminium plant in Montenegro. *Energies* **2017**, *10*, 1505. [[CrossRef](#)]
45. Ministry of Infrastructure of the Republic of Slovenia. Energy Balance for the Republic of Slovenia for 2017. Available online: Energetika-portal.si/fileadmin/dokumenti/publikacije/energetska_bilanca/ebrs_2017.pdf (accessed on 22 April 2020). (In Slovenian)
46. Salonitis, K.; Jolly, M.; Pagone, E.; Papanikolaou, M. Life-Cycle and Energy Assessment of Automotive Component Manufacturing: The Dilemma between Aluminum and Cast Iron. *Energies* **2019**, *12*, 2557. [[CrossRef](#)]
47. Gomilšek, R.; Čuček, L.; Homšak, M.; Kravanja, Z. Towards GHG Emissions Neutrality of Aluminium Slug Production: An Industrial Study. *Chem. Eng. Trans.* **2019**, *76*, 217–222.
48. Haraldsson, J.; Johansson, M.T. Energy efficiency in the supply chains of the aluminium industry: The cases of five products made in Sweden. *Energies* **2019**, *12*, 245. [[CrossRef](#)]
49. Tan, R.R.; Aviso, K.B.; Foo, D.C. P-Graph Approach to Carbon-Constrained Energy Planning Problems. In *Computer Aided Chemical Engineering*; Elsevier: Amsterdam, The Netherlands, 2016; Volume 38, pp. 2385–2390.
50. Crilly, D.; Zhelev, T. Emissions targeting and planning: An application of CO₂ emissions pinch analysis (CEPA) to the Irish electricity generation sector. *Energy* **2008**, *33*, 1498–1507. [[CrossRef](#)]
51. Atkins, M.J.; Morrison, A.S.; Walmsley, M.R. Carbon emissions pinch analysis (CEPA) for emissions reduction in the New Zealand electricity sector. *Appl. Energy* **2010**, *87*, 982–987. [[CrossRef](#)]
52. Walmsley, M.R.; Walmsley, T.G.; Atkins, M.J. Achieving 33% renewable electricity generation by 2020 in California. *Energy* **2015**, *92*, 260–269. [[CrossRef](#)]
53. Jia, X.; Li, Z.; Wang, F.; Foo, D.C.; Tan, R.R. Multi-dimensional pinch analysis for sustainable power generation sector planning in China. *J. Clean. Prod.* **2016**, *112*, 2756–2771. [[CrossRef](#)]
54. Salman, B.; Nomanbhay, S.; Foo, D.C. Carbon emissions pinch analysis (CEPA) for energy sector planning in Nigeria. *Clean Technol. Environ. Policy* **2019**, *21*, 93–108. [[CrossRef](#)]
55. Baležentis, T.; Štreimikienė, D.; Melnikienė, R.; Zeng, S. Prospects of green growth in the electricity sector in Baltic States: Pinch analysis based on ecological footprint. *Resour. Conserv. Recycl.* **2019**, *142*, 37–48. [[CrossRef](#)]
56. Su, W.; Ye, Y.; Zhang, C.; Baležentis, T.; Štreimikienė, D. Sustainable energy development in the major power-generating countries of the European Union: The Pinch Analysis. *J. Clean. Prod.* **2020**, *256*, 120696. [[CrossRef](#)]
57. Andiappan, V.; Foo, D.C.; Tan, R.R. Process-to-Policy (P2Pol): Using carbon emission pinch analysis (CEPA) tools for policy-making in the energy sector. *Clean Technol. Environ. Policy* **2019**, *21*, 1383–1388. [[CrossRef](#)]
58. Lee, S.C.; Sum Ng, D.K.; Yee Foo, D.C.; Tan, R.R. Extended pinch targeting techniques for carbon-constrained energy sector planning. *Appl. Energy* **2009**, *86*, 60–67. [[CrossRef](#)]
59. Manan, Z.A.; Tan, Y.L.; Foo, D.C.Y. Targeting the minimum water flow rate using water cascade analysis technique. *AIChE J.* **2004**, *50*, 3169–3183. [[CrossRef](#)]

60. Klemeš, J.J.; Kravanja, Z. Forty years of heat integration: Pinch analysis (PA) and mathematical programming (MP). *Curr. Opin. Chem. Eng.* **2013**, *2*, 461–474. [[CrossRef](#)]
61. Čuček, L.; Boldyryev, S.; Klemeš, J.J.; Kravanja, Z.; Krajačić, G.; Varbanov, P.S.; Duić, N. Approaches for retrofitting heat exchanger networks within processes and Total Sites. *J. Clean. Prod.* **2019**, *211*, 884–894. [[CrossRef](#)]
62. Cerda, J.; Westerberg, A.W.; Mason, D.; Linnhoff, B. Minimum utility usage in heat exchanger network synthesis A transportation problem. *Chem. Eng. Sci.* **1983**, *38*, 373–387. [[CrossRef](#)]
63. Fraser, D.M. Retrofit Mass Integration of Acid Gas Removal Systems in Petrochemical Plants. In *Handbook of Process Integration (PI)*; Klemeš, J.J., Ed.; Woodhead Publishing Limited: Cambridge, UK, 2013; pp. 725–751.



© 2020 by the authors. Licensee MDPI, Basel, Switzerland. This article is an open access article distributed under the terms and conditions of the Creative Commons Attribution (CC BY) license (<http://creativecommons.org/licenses/by/4.0/>).

An Extended Grid Diagram for Heat Exchanger Network Retrofit Considering Heat Exchanger Types

Bohong Wang ^{1,*}, Jiří Jaromír Klemeš ¹, Petar Sabev Varbanov ¹ and Min Zeng ²

¹ Sustainable Process Integration Laboratory–SPIL, NETME Centre, Faculty of Mechanical Engineering, Brno University of Technology–VUT Brno, Technická 2896/2, 616 69 Brno, Czech Republic; jiri.klemes@vutbr.cz (J.J.K.); varbanov@fme.vutbr.cz (P.S.V.)

² Key Laboratory of Thermo-Fluid Science and Engineering, Ministry of Education, Xi'an Jiaotong University, Xi'an 710049, Shangxi, China; zengmin@mail.xjtu.edu.cn

* Correspondence: wang.b@fme.vutbr.cz

Received: 26 April 2020; Accepted: 22 May 2020; Published: 24 May 2020

Abstract: Heat exchanger network (HEN) retrofit is a vital task in the process design to improve energy savings. Various types of heat exchangers such as shell and tube, double-pipe, compact plate, and spiral tube have their working temperature ranges and costs. Selecting suitable types of heat exchangers according to their temperature ranges and costs is a crucial aspect of industrial implementation. However, considering the type of heat exchangers in the HEN retrofit process is rarely seen in previous publications. This issue can be solved by the proposed Shifted Retrofit Thermodynamic Grid Diagram with the Shifted Temperature Range of Heat Exchangers (SRTGD-STR). The temperature ranges of six widely used heat exchanger types are coupled in the grid diagram. This diagram enables the visualisation of identifying the potential retrofit plan of HEN with heat-exchanger type selection. The retrofit design aims to minimise utility cost and capital cost. An illustrative example and a case study are presented to show the effectiveness of the method.

Keywords: heat exchanger network (HEN); retrofit; Shifted Retrofit Thermodynamic Grid Diagram (SRTGD); Pinch Analysis; type selection

1. Introduction

Heat recovery has been regarded as a major measure to increase energy efficiency in process systems engineering. It can also help to reduce the environmental burden by reducing waste heat emission. Heat exchanger network (HEN) retrofit is an effective way to utilise heat from process streams and to minimise the energy consumption [1]. In the industrial application of HEN retrofit, different types of heat exchangers have their working temperature ranges and costs. The type of heat exchanger should be wisely selected for different usages and applications to ensure the heat exchangers can work under certain conditions with a relatively economic investment cost.

In the HEN retrofit problem, there are generally three approaches, i.e., Pinch Analysis (PA), mathematical programming, and a combined method [2]. The first work of PA was developed by Linnhoff and Flower [3]. Following their innovation, many PA-based graphical methods were proposed for HEN retrofits such as the Retrofit Thermodynamic Diagram (RTD) [4], Stream Temperature vs. Enthalpy Plot (STEP) [5], Temperature Driving Force (TDF) [6], and Energy Transfer Diagram (ETD) [7], which are widely used in the retrofit applications. Some extended methods and applications based on the above studies were reported. Lai et al. [8] proposed a combined STEP and heat exchanger area versus enthalpy (A vs. H) plot to customise a retrofit design toward a desired investment payback period. Kamel et al. [9] applied TDF on an existing HEN in an Egyptian refinery to improve energy saving with minor structural modifications. Lal et al. [10] modified the ETD and proposed a heat surplus-deficit table for the HEN retrofit to achieve energy saving.

RTD has been a particularly useful graphical visual tool. It can display the driving force around the heat exchanger and heat capacity flow rate graphically. Yong et al. [11] modified the RTD and proposed a Shifted Retrofit Thermodynamic Diagram (SRTD). In SRTD, the hot streams are shifted by subtracting the minimum allowed temperature difference (ΔT_{\min}), and then the feasibility of implementing a heat exchanger can be visually seen by connecting both lower and higher temperature sides of hot and cold streams. If the slope of the connecting lines is negative, then it illustrates that the heat exchanger implementing plan violates the Pinch Rule. SRTD was later extended to the Shifted Retrofit Thermodynamic Grid Diagram (SRTGD) by Yong et al. [12]. It uses a dashed line to indicate the location of the Process Pinch. By applying this diagram, pinches can be detected, and the retrofit plan can be determined easier.

Apart from these graphical methods for HEN retrofit, mathematical programming has also been used in the retrofit design. Pan et al. [13] developed mixed-integer linear programming (MILP)-based iterative method for HEN retrofit. Their method fixed the logarithmic mean temperature difference (LMTD) in the original problem and executed two iteration loops to achieve certain energy-saving or net present value. Zhang and Rangaiah [14] applied integrated differential evolution to solve the HEN retrofit problem in one step. Onishi et al. [15] proposed a mathematical programming model for HEN retrofit, considering the pressure recovery of process streams to enhance heat integration. Pavão et al. [16] proposed an extended superstructure model and a corresponding meta-heuristic solution approach for the HEN retrofit problem. Wang et al. [17] developed a mathematical model based on the structure of the SRTGD and a two-stage method. In the first stage, the mathematical model was solved to obtain the topology of the HEN, with the aim of minimising utility and investment costs. While in the second stage, a particle swarm optimisation (PSO) algorithm was applied to adjust the inlet and outlet temperatures of each heat exchanger to achieve the goal of minimising the payback period based on the obtained topology from the first stage. This method considers the cost of utility and investment. It makes the retrofit design based on SRTGD more effective.

In the HEN retrofit process, achieving energy saving is one important task; another issue is to ensure the selected heat exchanger type can satisfy the heat transfer requirement between streams and has a relatively lower cost. Different types of heat exchangers such as shell and tube, double-pipe, compact plate, and spiral tube have their working temperature ranges and capital costs. These issues should be considered in the retrofit design process to determine an economic plan. Soršak and Kravanja [18] proposed a mixed-integer nonlinear programming (MINLP) model for HEN synthesis and modelled the selection of heat exchanger types. Fieg et al. [19] developed a hybrid genetic algorithm for HEN design. The investment and utility costs were calculated separately in a user subroutine to consider the specificity of heat exchangers. Sun et al. [20] presented the Stream Temperature vs. Enthalpy Plot Supertargeting (STEPS) method to optimise the cost of HEN. In their proposed step-by-step method, the heat exchanger types are considered and the capital cost is calculated. These previous papers considered the selection of heat exchanger types for the synthesis problem, the HEN retrofit with the consideration of heat exchanger types requires study. A method should be developed to consider both insights of thermodynamic and suitable heat exchanger type selection for HEN retrofit for potential industrial implementation.

The capital cost is the main criterion used to determine the selected heat exchanger type. Rathjens and Fieg [21] proposed a MINLP model and a genetic algorithm coupled with a deterministic local optimisation approach for HEN synthesis. In their model, the cost functions for each connection of heat source and sink are considered to make solutions more efficient. Aguitoni et al. [22] proposed a combined simulated annealing and differential evolution algorithm to minimise the sum of heat exchanger investment and energy cost. Kang and Liu [23] proposed three strategies to minimise the investment cost for the multi-period HEN retrofit. Ayotte-Sauvé et al. [24] proposed a stepwise approach for HEN retrofit to minimise the investment costs for new and retrofit heat exchangers as well as utility costs. Nemet et al. [25] proposed an MINLP model for the optimal design of HEN, considering the lifetime cost.

There are several advantages of using SRTGD as a visualisation tool in the HEN retrofit applications. It can identify the Process Pinch through the diagram. It is easy to check whether the retrofit plan violates the Pinch Rule [26], and to find if there is still potential for more heat recovery. It also shows the temperature range of each heat exchanger for hot and cold streams, which is a benefit that can be used in the heat exchanger type selection. However, there is still a need to develop a tool that can be used to help designers to select suitable types of heat exchangers visually. This tool should be easy to master and can show insights into network design.

To solve the above-mentioned issue, an SRTGD with the shifted temperature ranges of heat exchangers (SRTGD-STR) is developed as an effective tool for determining the retrofit plan of HENs and selecting feasible and cost-minimised heat exchanger types. The structure of the paper is organised as follows: Section 2 presents the detailed method of utilising this proposed visualisation tool to increase heat recovery and debottleneck an existing process. An illustrative example of how to implement this method is studied. Section 3 demonstrates a case study of the SRTGD-STR to show its effectiveness, and Section 4 presents the conclusion.

2. Methodology

There are several different variants of heat exchangers, with the common types employed in the industry [27] including:

- Shell and tube heat exchangers;
- Double-pipe heat exchangers;
- Compact plate heat exchangers;
- Spiral plate heat exchangers;
- Spiral tube heat exchangers;
- Scraped-wall heat exchangers.

Illustrations of these heat exchangers and a detailed list of heat exchanger types can be found in Ref. [27].

This paper develops SRTGD-STR. This diagram considers these previously mentioned heat exchanger types in the retrofit design process. The detailed method of implementing the SRTGD-STR is introduced in this section using Example 1 data (Table 1).

Table 1. Stream data for Example 1.

Stream	T_S (°C)	T_T (°C)	CP (kW/°C)	h (kW/m ² ·°C)	Pressure (MPa)
1	520	420	4	0.85	2.9
2	420	230	4	0.85	1.3
3	280	470	5	0.80	2.9

Note: T_S is the supply temperature, (°C); T_T is the target temperature, (°C); CP is the heat capacity flow rate, (kW/°C), and h is the heat transfer coefficient, (kW/m²·°C).

The notation of the heat transfer used in this work for all topology diagrams is the following:

H(number): Utility heater;

C(number): Utility cooler;

E(number): Recovery heat exchanger.

2.1. Process Visualised Using SRTGD

The first step is to identify the hot and cold process streams that have the potential for heat exchange. The flow rates, supply and target temperatures, and heat capacities of streams should be used to determine the utility targets. The stream conditions such as medium, pressure, viscosity, individual heat transfer coefficient, and material corrosiveness should also be extracted. Table 1 is

an example to show the data extracted from a process. There are three streams, and an existing heat exchanger is connecting stream 1 and 3 for heat recovery. In this example, ΔT_{\min} is set at 20 °C.

The developed SRTGD-STR is the extension of SRTGD proposed by Yong et al. [12]. SRTGD is used to identify the potential retrofit plan regarding heat recovery. The streams extracted are presented on the SRTGD according to their temperature ranges and heat capacity flow rates (CPs). For better visualisation, the cold streams are usually presented on the downside of the graph and hot streams are on the upside of the graph. If the slope of the link between heat exchangers is negative, this indicates an infeasible implementation of heat exchangers. Stream names are shown on the right side of each stream. The heat capacity flow rate of each stream can be observed on the y-axis. Supply and target temperatures of streams and heat exchangers can be observed on the x-axis. Pinch points are identified when the link between one cold and one hot stream is vertical.

SRTGD is capable of providing visual information in choosing heat paths. The temperatures of hot streams are shifted in the SRTGD. It can also help the designers to find the Network Pinch and identify the retrofit plan for maximum heat recovery. The detailed method for drawing an SRTGD and using SRTGD for HEN retrofit can be found in Ref. [12]. Figure 1 shows the SRTGD of illustrative Example 1.

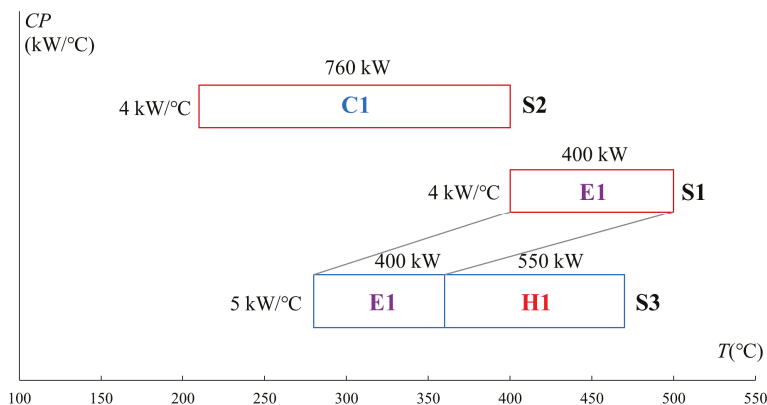


Figure 1. Shifted Retrofit Thermodynamic Grid Diagram (SRTGD) of the existing HEN for Example 1.

2.2. Potential Heat Exchanger Type Selection Using SRTGD-STR

When the heat paths are identified by SRTGD, the next step is to select the feasible and economical heat exchangers used for heat recovery. In the proposed SRTGD-STR, the allowable temperature ranges of different heat exchanger types are coupled in the diagram. The area of hot and cold streams connected by one heat exchanger should be in its temperature range. When determining a retrofit plan, this diagram can help easily identify the boundary of the heat exchangers.

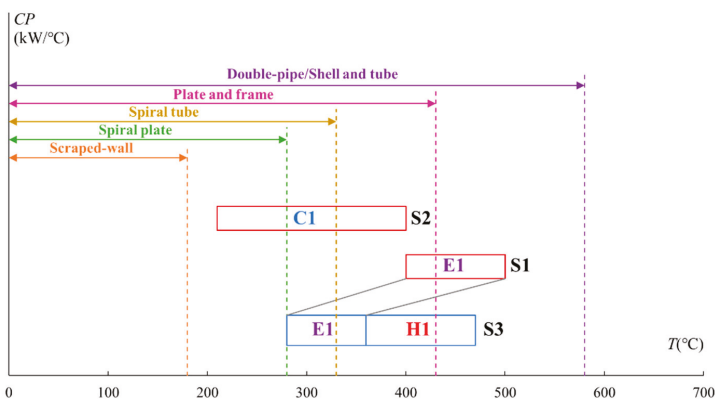
The shifted temperature ranges of heat exchangers are added in the SRTGD-STR to help select the heat exchanger types according to the data given in Table 2. As the temperatures of hot streams are shifted temperature in the SRTGD scale, the upper boundary of temperature ranges of heat exchangers in the diagram should also be shifted by minus ΔT_{\min} of the studied case. The suitability of each heat exchanger type for transferring heat between streams depends on the specifications and requirements of the application. Table 2 lists several commonly used heat exchanger types, their temperature ranges, and normal area ranges. In the retrofit design process, these factors should be considered together with the aim of utility saving.

Table 2. Heat exchanger types and their temperature and area ranges.

Heat Exchanger Type	Maximum Pressure (MPa)	Temperature Approximate Range (°C)	Normal Area Approximate Range (m ²)
Double-pipe (liquid and gas) [20]	30	−100 to 600	0.25 to 20
Shell and tube (liquid and gas) [20]	30	−200 to 600	3 to 1,000
Scraped-wall (liquid) [20]	~0.01	Up to 200	2 to 20
Spiral plate (liquid and gas) [20]	2	Up to 300	10 to 200
Spiral tube (liquid and gas) [20]	50	Up to 350	1 to 50
Plate and frame [28]	4	Up to 450	14 to 1,394

If the temperature of some potential heat recovery range passes through the temperature range boundary of some types of heat exchangers or temperature ranges of some heat exchangers are in the range of more than one heat exchanger type, then focus should be given to this heat path. If the heat recovery range passes through the temperature range boundaries, then whether to implement more than two heat exchangers on one heat path should also be considered to achieve the minimum retrofit cost.

By implementing the data from Table 2 to illustrative Example 1, the corresponding SRTGD-STR is shown in Figure 2. The working temperature range of these heat exchanger types is shifted by minus ΔT_{\min} , which is 20 °C in this example. As seen in Figure 2, stream S2 is within the shifted temperature range of plate and frame, double-pipe, and shell-and-tube heat exchangers, which means these three types of heat exchangers can be applied without the consideration of supply and target temperatures. S2 also comes across the upper-temperature boundaries of the spiral tube and spiral plate heat exchangers. It indicates the possibility of using different types of heat exchangers on a single stream, and these two types of heat exchangers should be examined based on the Pinch Rules.

**Figure 2.** SRTGD-STR of the existing HEN for Example 1.

To fully utilise the heat from the hot stream, four retrofit plans are proposed based on SRTGD-STR. The first retrofit plan is shown in Figure 3 and uses one new heat exchanger between streams 2 and 3.

As can be observed from Figure 3, some parts of the shifted temperature range of the new heat exchanger are higher than 330 °C, which is higher than the upper bound of the spiral tube heat exchanger. Double-pipe, plate and frame, or shell and tube heat exchangers can be used. The method to determine which type of heat exchanger should be used is explained in Section 2.3. In this plan, 480 kW of heat is exchanged between the streams S2 and S3. To not violate the Pinch Rule, stream 2 uses E2 and C1 to reach the target temperature. The vertical line indicates the Process Pinch.

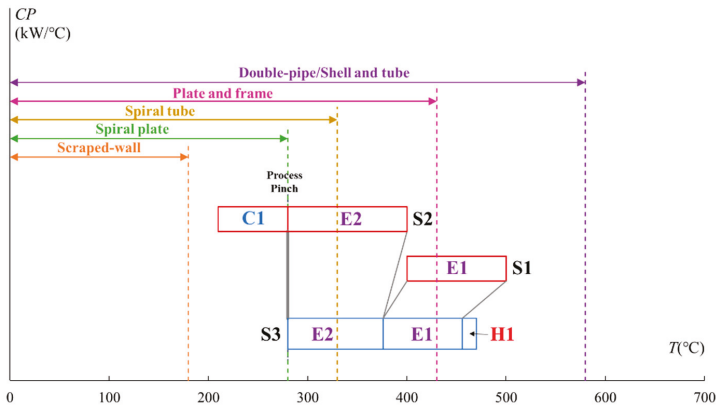


Figure 3. SRTGD-STR of the first retrofit plan for Example 1.

The second retrofit plan (Figure 4) considers implementing a spiral tube heat exchanger for this HEN. It is easy to identify the retrofit plan based on the SRTGD-STR. To implement a spiral tube heat exchanger to this HEN, the highest shifted temperature on both hot and cold streams could not be higher than 330 °C, which is also marked on the diagram. For heat exchanger E3 (spiral tube), considering the hot stream S2 has a relatively lower heat capacity flow rate than the cold stream, the shifted inlet temperature in the hot stream should not be higher than the shifted upper bound of implementing a spiral tube heat exchanger. The inlet and outlet temperatures of heat exchanger E2 as well as E1 can also be determined.

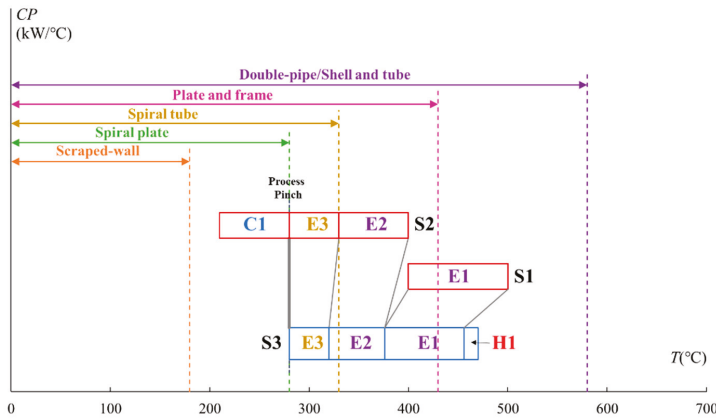


Figure 4. SRTGD-STR of the second retrofit plan for Example 1.

Using a spiral plate for heat recovery is considered. However, the upper-temperature boundary of the spiral plate heat exchanger minus the ΔT_{\min} equals the inlet temperature of stream S3. It is not feasible to use a spiral plate heat exchanger.

There is another potential option for implementing two double-pipe heat exchangers. The heat transfer area of the double-pipe heat exchanger has a 20 m² upper limit. For this case, if only one double-pipe heat exchanger is implemented, then the required heat transfer area is higher than the upper limit for the unit. Considering the relatively low capital cost of double-pipe heat exchangers, it is possible to add two double-pipe heat exchanger units to satisfy both the heat recovery requirement

and the heat-transfer area limitation. The Pinch Point for this option is still 280 °C. The range of the normal area of the double-pipe is 0.25–20 m². By adjusting the inlet and outlet temperatures of heat exchangers E3 and E2 (both are double-pipe heat exchangers), the retrofit plan of implementing two double-pipe heat exchangers is shown in Figure 5.

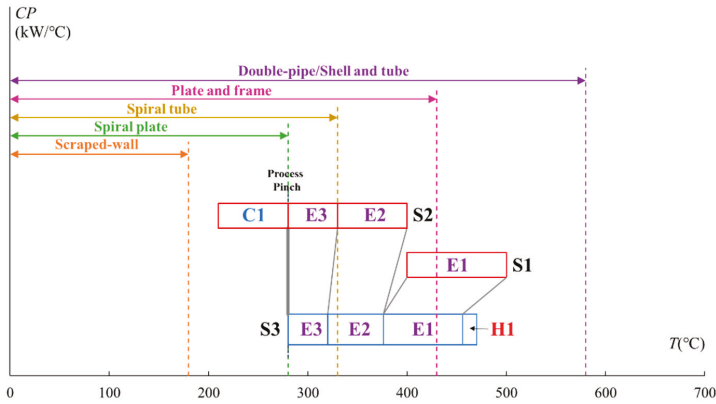


Figure 5. SRTGD-STR of the third retrofit plan for Example 1.

The potential retrofit plan using a plate and frame heat exchanger is considered. As seen in Figure 2, stream S1 passes through the upper-temperature boundary of the plate and frame heat exchanger, which makes implementing this type of heat exchanger possible. In the retrofit plan illustrated in Figure 6, the heat of stream S1 is recovered by two heat exchangers. The one in the higher temperature range is a double-pipe heat exchanger, and the other one is a frame and plate heat exchanger.

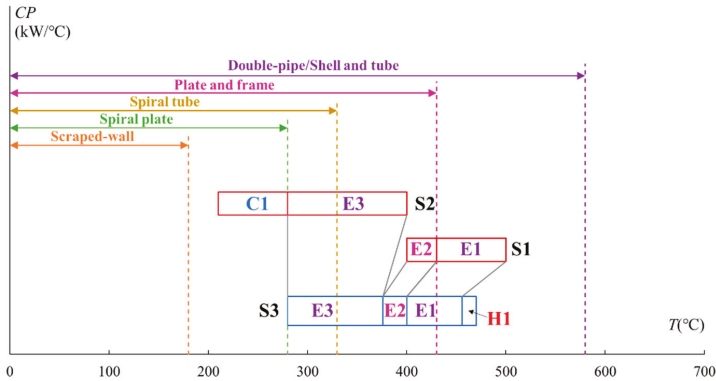


Figure 6. SRTGD-STR of the fourth retrofit plan for Example 1.

This step identifies the potential retrofit plans considering the temperature range. When the plans are obtained, then further actions are required to examine other factors, including pressure, area, and corrosiveness. After excluding these inappropriate plans, the next step is calculating the utility and capital cost.

2.3. Utility Cost and Capital Cost Calculation

Besides the temperature and area ranges, the capital cost is another factor that is considered in designing and choosing a heat exchanger. The capital costs of heat exchangers are listed in Table 3.

Table 3. The capital cost of heat exchanger types [29] Reproduced from [29], John Wiley & Sons: 2010.

Heat Exchanger Type	Capital Cost (\$)
Shell and tube	$C^{st} = [0.9803 + 0.018(\frac{P \times 145}{100}) + 0.0017(\frac{P \times 145}{100})^2] \times [a + (\frac{10.76 \times A}{100})^b] \times e^{11.667 - 0.8709 \ln(10.76 \times A) + 0.09005[\ln(10.76 \times A)]^2}$ (1)
Double-pipe	$C^{dt} = 2 \times [0.8510 + 0.1292(\frac{P \times 145}{100}) + 0.0198(\frac{P \times 145}{100})^2] \times e^{7.1460 + 0.16 \ln(10.76 \times A)}$ (2)
Spiral plate	$C^{sp} = 6,200 \times (10.76 \times A)^{0.42}$ (3)
Spiral tube	$C^{st} = e^{8.0757 + 0.4343 \ln(10.76 \times A) + 0.03812[\ln(10.76 \times A)]^2}$ (4)
Plate and frame	$C^{pf} = 8,880 \times (10.76 \times A)^{0.42}$ (5)

C^{st} , C^{dt} , C^{sp} , C^{st} , C^{pf} are the capital costs of shell and tube, double-pipe, spiral plate, spiral tube, and plate and frame heat exchangers; A is the heat transfer area in m^2 ; P is the shell-side pressure in MPa, and parameters a and b are materials of construction factors when the shell is made of carbon steel and the tube is made of Cr–Mo steel, the values of a and b are 1.55 and 0.05. For the shell and tube heat exchanger with floating head, carbon steel for shell, and Cr–Mo steel for tube, the capital cost calculation can be formulated as Equation (1). For the double-pipe heat exchanger, the capital cost equation for an outer pipe of carbon steel and an inner pipe of stainless steel is formulated as Equation (2). The capital cost of the spiral plate can be calculated by Equation (3). The capital cost of the spiral tube heat exchanger can be calculated by Equation (4). Finally, the plate and frame heat exchanger capital cost can be calculated by Equation (5).

Other fundamental equations used to determine the heat load, the overall heat transfer coefficient, $LMTD$, and the heat transfer area are listed as follows.

$$Q = A \times U \times LMTD \tag{6}$$

where Q is the heat load, kW; A represents the heat transfer area, m^2 ; U is the overall heat transfer coefficient, $kW/(m^2 \cdot ^\circ C)$; $LMTD$ represents the logarithmic mean temperature difference, $^\circ C$. The overall heat transfer coefficient can be calculated by Equation (7) if the inner and outer surfaces of the tube are almost identical. When the wall thickness of the tube is small and the thermal conductivity of the tube material is high, the overall heat transfer coefficient simplifies to Equation (8).

$$\frac{1}{U} = \frac{1}{h_h} + \frac{dx_w}{k} + \frac{1}{h_c} \tag{7}$$

$$\frac{1}{U} = \frac{1}{h_h} + \frac{1}{h_c} \tag{8}$$

where h_h and h_c are the individual heat transfer coefficients of the connected hot and cold process streams, $kW/(m^2 \cdot ^\circ C)$; dx_w represents the wall thickness, m; k represents the thermal conductivity of the material, $kW/(m \cdot ^\circ C)$.

The equations for calculating $LMTD$ and the heat transfer area (A) are listed in Equations (9) and (10).

$$LMTD = \frac{(T_{in}^H - T_{out}^C) - (T_{out}^H - T_{in}^C)}{\ln \frac{(T_{in}^H - T_{out}^C)}{(T_{out}^H - T_{in}^C)}} \tag{9}$$

$$A = \frac{Q}{U \times LMTD} \tag{10}$$

where T_{in}^H and T_{out}^H are the inlet and outlet temperatures of hot streams, °C; T_{in}^C and T_{out}^C are the inlet and outlet temperatures of cold streams, °C.

For this illustrative example, as can be observed from Figure 3 to Figure 6, the utility cost of all four of these retrofit plans is the same. They can recover an additional 480 kW of heat compared to the existing HEN. The difference among these plans is the selection of heat exchanger types and their capital costs. The comparison of the capital cost for all retrofit plans is shown in Table 4. For plan 1, three types of heat exchangers (i.e., double-pipe, plate and frame, and shell and tube) are pre-selected in Section 2.2. The double-pipe can be excluded as the heat transfer area (38.3 m²) is higher than the upper limit of the area ranges of the double-pipe heat exchanger. The shell and tube heat exchanger is selected for plan 1 because the cost for the plate and frame exchanger is higher than the shell and tube heat exchanger. The total capital cost for the third retrofit plan is the cheapest. Two new double-pipe heat exchangers are selected. Another feasible plan is plan 1. One shell and tube heat exchanger should be implemented. For plan 2, the capital cost for the spiral tube heat exchanger is too high. Although it has a higher maximum bearing pressure, in this example, there is no need to use this type of heat exchanger. The plate and frame heat exchanger used in plan 4 has a relatively high cost for a small heat transfer area, and it is not recommended in this retrofit application.

Table 4. Comparison of the results for Example 1.

Plans		Plan 1		Plan 2			Plan 3			Plan 4		
Items	Type	Area (m ²)	Cost (k\$)	Type	Area (m ²)	Cost (k\$)	Type	Area (m ²)	Cost (k\$)	Type	Area (m ²)	Cost (k\$)
HE1	D-P	18.2	10.4	D-P	18.2	10.4	D-P	18.2	10.4	D-P	12.0	9.7
HE2	S&T	38.3	46.0	D-P	12.5	9.8	D-P	18.6	10.4	P-F	6.2	51.8
HE3	-	-	-	S-T	25.8	123.5	D-P	19.7	10.5	S&T	38.3	46.0
Sum	-	-	56.4	-	-	143.7	-	-	31.3	-	-	107.5

Note: S&T refers to the shell and tube heat exchanger, D-P refers to the double-pipe heat exchanger, S-T refers to the spiral tube heat exchanger, and P-F refers to the plate and frame heat exchanger.

3. Case Study

A case study is used to illustrate the proposed method for HEN retrofit, considering heat exchanger types. The data is obtained from Ref. [11], and the target temperature of heat exchanger E3 is modified from 370 °C to 410 °C for a better illustration of the method. The case has one cold stream and six hot streams. The cold stream is heated by six heat exchangers connecting other streams. The ΔT_{min} of this HEN is designed as 10 °C. The stream data for the case study are listed in Table 5.

Table 5. Data pertaining to the existing HEN in the case study.

Stream	T_S (°C)	T_T (°C)	CP (kW/°C)	h (kW/m ² ·°C)
1	30	600	5	0.85
2	185	20	4	0.85
3	250	170	5	0.72
4	570	320	3	0.8
5	410	340	2	0.72
6	468	368	3	0.85
7	560	525	10	0.7

Note: T_S is the supply temperature, (°C); T_T is the target temperature, (°C); CP is the heat capacity flow rate, (kW/°C); and h is the heat transfer coefficient, (kW/m²·°C).

Figure 7 shows the SRTGD-STR of the existing HEN. The temperatures of hot streams are shifted. According to this figure, two potential cold utilities can be removed or their power reduced. For cold utility C1, a vertical dotted line on the left side of stream 1 denotes the lowest cold stream temperature at 30 °C. Any hot stream segments spanning to the left of this vertical line can only be cooled by using

a cold utility. Cold utility C2 has the potential to be removed as cold stream S1 can still receive the heat from stream 4.



Figure 7. SRTGD-STR of the existing HEN for the case study.

If the heat of stream 4 is fully used for heat recovery and the sequence of the heat exchangers in the existing HEN is not changed, then this retrofit plan would be infeasible, as shown in the red circle marked in Figure 8. The slopes of links between these two heat exchangers are negative. Re-piping and re-sequencing are needed to utilise the heat. By re-piping heat exchangers E4 and E5 between E2 and E3, the retrofit plan is feasible. The results are shown in Figure 9.

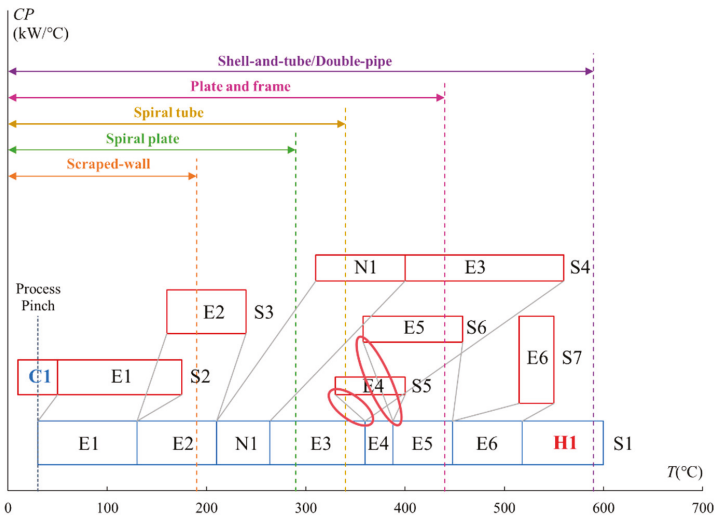


Figure 8. SRTGD-STR if the sequences of heat exchangers are not changed for the case study.

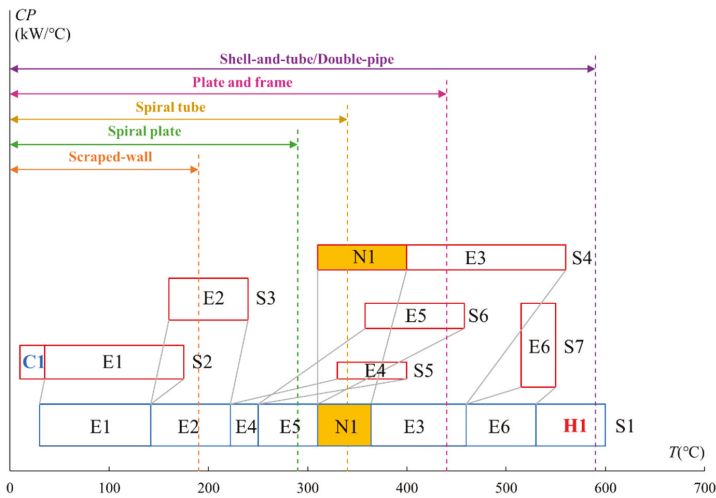


Figure 9. SRTGD-STR if one heat exchanger is added for the case study.

In this retrofit plan, the cold utility C2 is replaced by a heat exchanger to transfer heat from hot stream S4 to cold stream S1. The sequences of heat exchanger E3, E4, and E5 are changed to not violate the Pinch Rule. This reduces the 270 kW of utility used in this HEN.

In this retrofit process, the heat exchanger types are not considered. However, the capital cost of heat exchangers could also influence the retrofit plan optimisation. For the temperature range of this new heat exchanger N1, there are several choices, i.e., using shell and tube, double-pipe, or plate and frame heat exchangers. The selection of heat exchanger types should also be based on the normal area range of heat exchangers. The feasible and cheapest types should be selected.

As can be observed from Figure 7, the temperature range of cold utility C2 crosses over the temperature boundary of the spiral tube, which indicates another option, implementing two new heat exchangers for heat recovery. Another retrofit plan is illustrated in Figure 10 based on SRTGD-STR considering this possibility. In this plan, heat exchangers E4 and E5 on the cold stream S1 are still moved to the left side of E3, and two new heat, N1 and N2, are implemented between E5 and E3 on S1.

Under these circumstances, there are several choices about the heat exchanger types. The following four combinations can be selected, both shell and tube heat exchangers, both double-pipe heat exchangers, both plate and frame heat exchangers, or one double-pipe and one spiral tube. All these retrofit plans are listed in Table 6, and their capital costs are calculated according to equations provided in Section 2.3.

The results (Table 6) show that the feasible and cheapest retrofit plan is using two double-pipe heat exchangers for heat recovery. Its capital cost is 19.9 k\$. The utility cost saving of all these seven solutions is the same. An additional 270 kW of heat can be recovered by the new heat exchangers, which saves 10.7% of the maximum potential for heat recovery (2,520 kW) of this HEN. Although solution 2 has the minimum capital cost, its heat transfer area is 27.9 m². It is higher than the normal area range of the double-pipe heat exchanger, which makes this plan infeasible. The plan implementing two plate and frame heat exchangers has the highest cost. For a relatively small heat transfer area, the double-pipe heat exchanger is the most recommended as it has an advantage in the cost. For a larger heat transfer area, the most economical option could be the shell-and-tube heat exchanger.

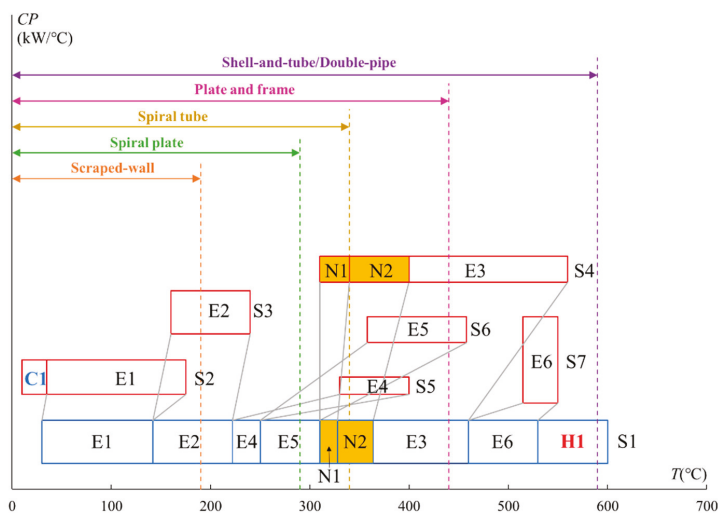


Figure 10. SRTGD-STR if two heat exchangers are added for this case study.

Table 6. Comparison of the results for the case study.

Number	N1			N2			Sum Cost (k\$)	
	Items	Type	Area (m ²)	Cost (k\$)	Type	Area (m ²)		Cost (k\$)
Solution 1	S&T		27.9	43.1			43.1	
Solution 2	D-P		27.9	11.1			11.1	
Solution 3	P&F		27.9	97.5			97.5	
Solution 4	S&T		14.4	39.9	S&T	13.4	39.7	79.6
Solution 5	D-P		14.4	10.0	D-P	13.4	9.9	19.9
Solution 6	P&F		14.4	73.7	P&F	13.4	71.7	145.4
Solution 7	S-T		14.4	75.6	D-P	13.4	9.9	85.5

Note: S&T refers to the shell and tube heat exchanger, D-P refers to the double-pipe heat exchanger, S-T refers to the spiral tube heat exchanger, P&F refers to the plate and frame heat exchanger.

4. Conclusions

This paper develops an Extended Grid Diagram named SRTGD-STR by considering the shifted temperature range of heat exchangers for HEN retrofit design. It inherits the advantage of SRTGD for HEN information (topology and stream data) illustration and easy retrofit options identification. The extended method also considers the types and capital costs of heat exchangers, which makes the retrofit application more practical. Six types of widely used heat exchangers are considered, and their shifted working temperature ranges are coupled in the diagram.

By using the novel SRTGD-STR, the retrofit plan can be easily determined. It can provide insight into the identification of the Process Pinch and Network Pinch. The combination of the shifted temperature ranges of different types of heat exchangers and the grid diagram can help engineers to identify potential HEN retrofit plans with the consideration of heat exchanger types and illustrate these plans visually. The illustrative example and case study show the advantages of using this tool in the retrofit process. The case study shows that an extra 10.7% of heat can be recovered by adding additional heat exchangers for the studied HEN. In addition, seven solutions can be identified by the proposed SRTGD-STR. The easy identification of these solutions could help the designers compare the retrofit plans and make a wiser decision. The correct selection of heat exchanger types can help to achieve a relatively lower capital cost.

Future research should further consider other issues such as phase change, freezing risk, and material cost in the retrofit design to extend the application field of this tool. Moreover, this approach can be further developed by considering the uncertainty temperature variation margins to make the retrofit plan adapt to a wider range of working conditions. Although the SRTGD-STR could identify retrofit plans according to the insight of thermodynamics, there still exists some potential to minimise the sum of the energy cost and investment cost by a trade-off of these two costs.

Author Contributions: Conceptualization, B.W. and J.J.K.; Methodology, B.W., J.J.K. and P.S.V.; Software, B.W.; Investigation, B.W.; Writing-Original Draft Preparation, B.W.; Writing-Review & Editing, J.J.K., P.S.V. and M.Z.; Visualization, B.W.; Supervision, J.J.K.; Project Administration, J.J.K. and M.Z.; Funding Acquisition, J.J.K. and M.Z. All authors have read and agreed to the published version of the manuscript.

Funding: This research was funded by [Czech Ministry of Education, Youth and Sports] grant number [LTACH19033], [National Key Research and Development Program of China] grant number [2018YFE0108900], and [Czech Republic Operational Programme Research and Development, Education] grant number [No. CZ.02.1.01/0.0/0.0/15_003/0000456]” under collaboration agreement with Xi’an Jiaotong University, China and by the project LTACH19033 “Transmission Enhancement and Energy Optimised Integration of Heat Exchangers in Petrochemical Industry Waste Heat Utilisation”, under the bilateral collaboration of the Czech Republic and the People’s Republic of China.

Acknowledgments: The project LTACH19033 “Transmission Enhancement and Energy Optimised Integration of Heat Exchangers in Petrochemical Industry Waste Heat Utilisation”, under the bilateral collaboration of the Czech Republic and the People’s Republic of China (partners Xi’an Jiaotong University and Sinopec Research Institute Shanghai; SPIL VUT, Brno University of Technology and EVECOSRO, Brno), programme INTER-EXCELLENCE, INTER-ACTION of the Czech Ministry of Education, Youth and Sports; and by the National Key Research and Development Program of China (2018YFE0108900) and the EU-supported project Sustainable Process Integration Laboratory (SPIL), funded as project No. CZ.02.1.01/0.0/0.0/15_003/0000456, by Czech Republic Operational Programme Research and Development, Education, Priority 1: Strengthening the capacity for quality research in the collaboration agreement with Xi’an Jiaotong University, China, based on the SPIL project, are gratefully acknowledged.

Conflicts of Interest: The authors declare no conflict of interest.

References

1. Klemeš, J.J.; Wang, Q.-W.; Varbanov, P.S.; Zeng, M.; Chin, H.H.; Lal, N.S.; Li, N.-Q.; Wang, B.; Wang, X.-C.; Walmsley, T.G. Heat transfer enhancement, intensification and optimisation in heat exchanger network retrofit and operation. *Renew. Sustain. Energy Rev.* **2020**, *120*, 109644. [\[CrossRef\]](#)
2. Klemeš, J.J.; Kravanja, Z. Forty years of Heat Integration: Pinch Analysis (PA) and Mathematical Programming (MP). *Curr. Opin. Chem. Eng.* **2013**, *2*, 461–474. [\[CrossRef\]](#)
3. Linnhoff, B.; Flower, J.R. Synthesis of heat exchanger networks: I. Systematic generation of energy optimal networks. *AIChE J.* **1978**, *24*, 633–642. [\[CrossRef\]](#)
4. Lakshmanan, R.; Bañares-Alcántara, R. A Novel Visualization Tool for Heat Exchanger Network Retrofit. *Ind. Eng. Chem. Res.* **1996**, *35*, 4507–4522. [\[CrossRef\]](#)
5. Wan Alwi, S.R.; Manan, Z.A. STEP—A new graphical tool for simultaneous targeting and design of a heat exchanger network. *Chem. Eng. J.* **2010**, *162*, 106–121. [\[CrossRef\]](#)
6. Gadalla, M.A. A new graphical method for Pinch Analysis applications: Heat exchanger network retrofit and energy integration. *Energy* **2015**, *81*, 159–174. [\[CrossRef\]](#)
7. Bonhivers, J.-C.; Moussavi, A.; Alva-Argaez, A.; Stuart, P.R. Linking pinch analysis and bridge analysis to save energy by heat-exchanger network retrofit. *Appl. Therm. Eng.* **2016**, *106*, 443–472. [\[CrossRef\]](#)
8. Lai, Y.Q.; Wan Alwi, S.R.; Manan, Z.A. Customised retrofit of heat exchanger network combining area distribution and targeted investment. *Energy* **2019**, *179*, 1054–1066. [\[CrossRef\]](#)
9. Kamel, D.A.; Gadalla, M.A.; Abdelaziz, O.Y.; Labib, M.A.; Ashour, F.H. Temperature driving force (TDF) curves for heat exchanger network retrofit—A case study and implications. *Energy* **2017**, *123*, 283–295. [\[CrossRef\]](#)
10. Lal, N.S.; Walmsley, T.G.; Walmsley, M.R.W.; Atkins, M.J.; Neale, J.R. A novel Heat Exchanger Network Bridge Retrofit method using the Modified Energy Transfer Diagram. *Energy* **2018**, *155*, 190–204. [\[CrossRef\]](#)
11. Yong, J.Y.; Varbanov, P.S.; Klemeš, J.J. Shifted retrofit thermodynamic diagram: A modified tool for retrofitting heat exchanger networks. *Chem. Eng. Trans.* **2014**, *39*, 97–102. [\[CrossRef\]](#)

12. Yong, J.Y.; Varbanov, P.S.; Klemeš, J.J. Heat exchanger network retrofit supported by extended Grid Diagram and heat path development. *Appl. Therm. Eng.* **2015**, *89*, 1033–1045. [[CrossRef](#)]
13. Pan, M.; Bulatov, I.; Smith, R.; Kim, J.-K. Novel MILP-based iterative method for the retrofit of heat exchanger networks with intensified heat transfer. *Comput. Chem. Eng.* **2012**, *42*, 263–276. [[CrossRef](#)]
14. Zhang, H.; Rangaiah, G.P. One-step approach for heat exchanger network retrofitting using integrated differential evolution. *Comput. Chem. Eng.* **2013**, *50*, 92–104. [[CrossRef](#)]
15. Onishi, V.C.; Ravagnani, M.A.S.S.; Caballero, J.A. Retrofit of heat exchanger networks with pressure recovery of process streams at sub-ambient conditions. *Energy Convers. Manag.* **2015**, *94*, 377–393. [[CrossRef](#)]
16. Pavão, L.V.; Costa, C.B.B.; Ravagnani, M.A.S.S. Heat exchanger networks retrofit with an extended superstructure model and a meta-heuristic solution approach. *Comput. Chem. Eng.* **2019**, *125*, 380–399. [[CrossRef](#)]
17. Wang, B.; Klemeš, J.J.; Varbanov, P.S.; Chin, H.H.; Wang, Q.-W.; Zeng, M. Heat exchanger network retrofit by a shifted retrofit thermodynamic grid diagram-based model and a two-stage approach. *Energy* **2020**, *198*, 117338. [[CrossRef](#)]
18. Soršak, A.; Kravanja, Z. Simultaneous MINLP synthesis of heat exchanger networks comprising different exchanger types. *Comput. Chem. Eng.* **2002**, *26*, 599–615. [[CrossRef](#)]
19. Fieg, G.; Hou, X.-R.; Luo, X.; Ma, H.-G. The optimal design of heat exchanger networks considering heat exchanger types. In *Computer Aided Chemical Engineering*; Jeżowski, J., Thullie, J., Eds.; Elsevier: Amsterdam, The Netherlands, 2009; Volume 26, pp. 659–664, ISBN 1570-7946.
20. Sun, K.N.; Wan Alwi, S.R.; Manan, Z.A. Heat exchanger network cost optimisation considering multiple utilities and different types of heat exchangers. *Comput. Chem. Eng.* **2013**, *49*, 194–204. [[CrossRef](#)]
21. Rathjens, M.; Fieg, G. Cost-Optimal Heat Exchanger Network Synthesis Based on a Flexible Cost Functions Framework. *Energies* **2019**, *12*, 784. [[CrossRef](#)]
22. Aguitoni, M.C.; Pavão, L.V.; Antonio da Silva Sá Ravagnani, M. Heat exchanger network synthesis combining Simulated Annealing and Differential Evolution. *Energy* **2019**, *181*, 654–664. [[CrossRef](#)]
23. Kang, L.; Liu, Y. Minimising investment cost for multi-period heat exchanger network retrofit by matching heat transfer areas with different strategies. *Chin. J. Chem. Eng.* **2015**, *23*, 1153–1160. [[CrossRef](#)]
24. Ayotte-Sauvé, E.; Ashrafi, O.; Bédard, S.; Rohani, N. Optimal retrofit of heat exchanger networks: A stepwise approach. *Comput. Chem. Eng.* **2017**, *106*, 243–268. [[CrossRef](#)]
25. Nemet, A.; Klemeš, J.J.; Kravanja, Z. Minimisation of a heat exchanger networks' cost over its lifetime. *Energy* **2012**, *45*, 264–276. [[CrossRef](#)]
26. Klemeš, J.J. *Handbook of Process Integration (PI): Minimisation of Energy and Water Use, Waste and Emissions*; Woodhead/Elsevier: Amsterdam, The Netherlands, 2013; ISBN 0-85709-725-3.
27. Klemeš, J.J.; Arsenyeva, O.; Kapustenko, P.; Tovazhnyanskyy, L. *Compact Heat Exchangers for Energy Transfer Intensification: Low Grade Heat and Fouling Mitigation*; CRC Press: Boca Raton, FL, USA, 2015; ISBN 1-4822-3260-X.
28. Gunnarsson, J.; Sinclair, I.J.C.; Alanis, F. Compact Heat Exchangers: Improving Heat Recovery. *Chem. Eng.* **2009**, *116*, 44.
29. Seider, W.D.; Seader, J.D.; Lewin, D.R.; Widagdo, S. *Product and Process Design Principles: Synthesis, Analysis and Evaluation*, 3rd ed.; John Wiley & Sons: Hoboken, NJ, USA, 2010.



© 2020 by the authors. Licensee MDPI, Basel, Switzerland. This article is an open access article distributed under the terms and conditions of the Creative Commons Attribution (CC BY) license (<http://creativecommons.org/licenses/by/4.0/>).

Article

Renewable Energy Integration for Steam Supply of Industrial Processes—A Food Processing Case Study

Ron-Hendrik Hechelmann ^{1,*}, Jan-Peter Seevers ¹, Alexander Otte ¹ and Jan Sponer ¹ and Matthias Stark ²

¹ Department for Sustainable Products and Processes (upp), University Kassel, Kurt-Wolters-Straße 3, 34125 Kassel, Germany; seevers@upp-kassel.de (J.-P.S.); alexander_otte@gmx.net (A.O.); jsponer@outlook.de (J.S.)

² Technische Hochschule Ingolstadt, Institute of new Energy Systems, Esplanade 10, 85049 Ingolstadt, Germany; Matthias.Stark@thi.de

* Correspondence: hechelmann@upp-kassel.de; Tel.: +49-561-3444

Received: 20 March 2020; Accepted: 14 May 2020; Published: 16 May 2020

Abstract: This study highlights the $CO_{2,e}$ -emission reduction potentials and related economic consequences for changing steam generation from fossil to renewable. Seven different utility concepts are developed, including a steam accumulator for load management. Peculiarities for the integration of biogas boilers, biomass-fuelled boilers, electrode steam boilers, biomethane-fuelled solid oxide fuel cells, micro gas turbine, solar energy systems, heat pumps and steam accumulators into a steam system with fluctuating steam demand are explained and the energy balance based models for the simulation study are described. The characteristics of batch processes, start up times and part load efficiency are considered via an annual dynamic simulation. Based on a detailed process analysis and dimensioning of the utilities and the accumulator a comprehensive simulation study is conducted for a pet food processing company having an average steam demand of 18,000 MWh at around 9 bar and 3 t/h. The results show that the highest $CO_{2,e}$ -emissions reduction of up to 63% is achieved by the transition to a solid biomass-fuelled boiler system. This leads to an increase of the operating costs by 27.8%.

Keywords: biomass boilers; fuel cell; solar thermal; electrode boiler; steam systems; food processing industry; decarbonisation; energy costs

1. Introduction

As part of the global energy transition and to avoid climate change, the Paris Agreement envisages a reduction of greenhouse gas emissions to 40% by 2040, starting from the base year 1990 [1]. There is a growing interest in companies to solve the question of their own climate neutrality in a transparent and sustainable way. In addition to their own motivation, customer demands for climate neutrality are becoming increasingly important from an economic point of view. Industry has a sector goal of reducing emissions by 49% to 51% (compared to 1990) by 2030 in Germany. To reach these goals industrial processing companies need to perform three steps. The first step is minimizing the energy demand by energy efficiency measures and secondly substituting fossil fuels by changing processes or implementing renewable energies. Compensating unavoidable emissions should only be the last step.

Process steam is widely used in the industry and is one of the main consumers of thermal energy. It is currently still often produced with fossil-fired steam boilers for economic reasons. In 2016, around 21.4% of Germany's total energy consumption was needed for processing heat. The share of renewable energies in this consumption was only 5.2% [2]. By 2050, the share of renewable energies in industry must rise to over 63% [3].

Bühler et al. [4] showed that an industrial integration of renewable energy based generation technologies is a complex problem due to many assumptions which have to be made as well as numerous statistical uncertainties. Therefore, different case studies from different industrial sectors and production system types are crucial to elucidate challenges and propose solutions for the energy transition. The paper does not consider solar thermal or biomass energy sources. Besides, it is focused on costs not emissions. For choosing the best energy supply for industrial sites top-down models often struggle to include technological explicitness [5]. This is especially important for batch processes with a fluctuating steam demand. For industrial sites, the most attractive renewable energy sources are biomass, solar radiation (thermal or photovoltaics), ground heat and wind [6]. This indicates an electrification of the steam supply via heat pumps (HP) and electric boilers (EB) or a substitution of fossil fuels with renewable energy sources.

To reach a 100% renewable energy supply in New Zealand and California for milk production plants, Walmsley et al. [7] analysed geothermal steam and renewable electricity for the mechanical vapor recompression, a biomass boiler with a two-stage ammonia heat pump using the boiler flue gases and solar thermal energy. Also, the integration of solar thermal energy for a Danish milk powder factory was analysed [8]. For the state of California, 48 TWh per year for industrial heating demands below 260 °C can be covered by solar power technologies [9]. Solar thermal energy offers a good solution especially in sunny states like Spain, like Silva et al. [10] showed for saturated steam at 7 bar. Stark et al. [11] investigated a pharmaceutical production facility with several overlapping steam batch processes. The majority of the steam demand is supplied from a biomass CHP plant. By utilising a steam accumulator, the share of bio-steam can be increased and the supply stability is improved. Further, the design parameters and the influence on the turbine system of the plant were investigated by Stark et al. [12]. To process stability as well as the share of bio-steam which is used in the supply system can be improved. Pérez-Uresti et al. [13] presented a method for calculating levelised steam costs based on solar thermal energy, biomass or biogas. For medium pressure (MP) steam and a plant capacity of 30 kg/s the presented steam costs for biomass are 19.36 €/t, for solar thermal 30.65 €/t and biogas 25.73 €/t.

Peesel et al. [14] showed that the $CO_{2,e}$ -emissions can be reduced by up to 42% by the transition to a solid biomass-fuelled boiler system and up to 27% using a biomethane fuelled solid oxide fuel cell but the operating costs increase significantly. A bottom up methodology for assessing electrification options for industrial process was presented by Wiertzema et al. [15]. The authors highlighted that the energy and carbon footprint consequences of electrification are hard to predict and therefore detailed simulation studies are required. For the year 2050, Johansson et al. [16] estimated the $CO_{2,e}$ -emissions reduction potential for the European petroleum refining industry including energy efficiency measures, fuel switching and carbon capture and storage. For a complex oil refinery four pathways for $CO_{2,e}$ -emissions reduction were analysed [17]. Energy efficiency measures followed by biomass gasification with carbon capture and storage is the most cost-effect pathway. Besides, industrial sites with an almost constant energy demand, part load characteristic may change the energy efficiency and cost calculation for steam systems. The part load performance of boilers and steam turbines is considered by Sun et al. [18] for analysing the steam costs by using a cumulative cost profile based on the marginal cost of steam.

However, a variety of technologies has to be investigated and different pathways should be investigated and implemented [6]. This is especially important as new developments can trigger significant cost reductions in certain technologies, like for example, optimized control [19] or load management. A system approach should be not restricted to certain technologies. Hybrid approaches are an option, for example, direct steam generation with solar collectors combined with biomass boilers [20].

In the food processing industry, the sterilisation process is the main energy consumer. For providing the steam often natural gas boilers are implemented. The short reaction times of the boilers help to manage the fluctuating steam demand due to batch sterilisation processes. A literature review and analysis of the present process revealed that sterilisation processes have been optimized in terms of temperature, time, material properties, heating medium and heat transfer coefficient [21]. To reduce high peak demands thermal process scheduling is possible [22]. Furthermore, a detailed analysis of the starting temperature and heat recovery potential has been carried out [23]. For batch processes, the time aspect and accumulators have to be considered as well. Especially for fluctuating renewable energy sources and fluctuating production energy demands [24]. For the technical requirements for the different steam utility systems the start up times are highly relevant especially for batch steam processes [25].

Although, alternative process steam generation technologies with renewable energies have already been investigated, there is a lack for the special requirements of batch processes. In addition, the volatile energy supply and energy demand require a dynamic simulation to represent the interaction of main supply technologies, steam accumulators and peak load boilers with sufficient accuracy. Furthermore, the cost and energy efficiency are highly depending on the steam's temperature, pressure and quality. This paper analyses the ratio of emissions savings and costs via a dynamic simulation for a total of seven technologies including specific investment and energy costs for a food processing plant with MP steam in Spain.

The purpose of this study is to highlight the $CO_{2,e}$ -emission reduction potentials and related economic consequences for changing the steam supply system to renewable energies. The seven different concepts include biomethane-fuelled solid oxide fuel cells (FC), biomass-fuelled boilers (BMB), biogas (BGB) or biomethane-fuelled boilers, micro gas turbines (MGT), EB, solar energy systems (SES) and HP are evaluated for their different implementation options in combination with load management measures, including a steam accumulator. In addition, the concepts are optimized in terms of the costs per saved $CO_{2,e}$ emissions per annum.

2. Description of Technologies

In this section the technical functionality of seven different technologies for substituting the fossil fuel fired steam boilers are briefly described and an overview of the technical and economical data is given. Peculiarities for the integration into a steam system with fluctuating steam demand are explained and the models for the simulation study are described.

2.1. Biogas and Biomethane Boiler

Steam is often used in industry as a heat transfer medium. In order to be able to provide steam safely and continuously, a complex plant structure consisting of burner, boiler, water treatment, condensate treatment and pumps is required, mostly economisers and, if necessary, other thermal apparatuses with the respective control technology are necessary [26]. The efficiency of a steam system depends on numerous factors due to its complexity. The main factors contributing to the reduction in efficiency are flue gas losses through the chimney, desalination and blow down losses during regeneration of the boiler water, radiation losses over the boiler surface and ventilation losses when starting the burner [27]. The part load efficiency of natural gas and Biogas and Biomethane Boiler (BGB) varies between 94% and 95% with an economiser. For substituting natural gas, biomethane or biogas can be used for firing the boilers. In case of biogas a specific burner is necessary. Biogas must be used at the place of production or in the immediate vicinity. Biomethane, on the other hand, is fed into the public gas grid. Biomethane is produced by upgrading biogas. In a number of process steps all components other than methane are separated from the gas mixture. Before being fed into the gas grid, further steps can be taken to achieve local feed-in requirements [28]. If biogas is not available, the switch to biomethane offers a convenient option for users of natural gas to reduce $CO_{2,e}$ emissions

regardless of the place of production of the biomethane. For this purpose the quantity of gas or energy withdrawn must be measured and balanced by the feed-in of biomethane into the grid.

2.2. Electrode Boiler

Electrode Boiler (EB) convert electrical energy into thermal energy through electrical resistance heating. In conventional EB metallic heating elements are heated, in the EB water is electrified to heat or vaporize it [29]. The electrodes are immersed in a triangular arrangement in weakly conductive water. The immersion depth of the electrodes into the water and thus the power of the boiler is regulated by a pump. EB can react very quickly and precisely to load changes. Starting from the “keep-warm” operation the maximum power is reached within seconds. The power range is variable and there is no minimum load. EB convert electrical energy into thermal energy with an efficiency of over 99%. Exhaust and ventilation losses omitted, there are only radiation losses [30].

According to Gruber et al. (2015), the substitution of conventional, fuel-based heat supply by electric boilers up to temperatures of 240 °C is relatively easy to implement [31]. That indicates a large technical potential for electricity generation and flexibility of heat in the industrial sector.

2.3. Solid Biomass-Fuelled Boiler

For providing steam by solid biomass, it is burned in a modern BMB. The heat, generated in the combustion chamber, is transferred to water via a heat exchanger and evaporated accordingly. The amount of steam to be produced is regulated by the amount of fuel supplied. If the amount is reduced or increased, there is a delay in the supply of steam. Although a reduction in the steam demand results in a lower fuel supply, the remaining fuel in the combustion chamber is still used and provides steam to the system. With an increase of the steam, more biomass is fed into the combustion chamber, which ignites with a delay due to the increased quantity [32]. With these plants a wide range of performance can be covered, whereby strict regulations exist in Germany and plants larger than 1000 kW are subject to legal approval [33]. These legal requirements are caused by the emission of nitrogen oxides and ashes, among other things, whereby large plants must be equipped with special exhaust gas purification filters. Besides, the amount of occurring pollutants depends on the choice of biomass and the moisture content of the fuel [34].

It exists a variety of biomass energy sources, from which wood pellets and chips are most widely used. These are characterised by their good storage properties and their relatively high energy content (5.21 kWh/m³). Irrespective of the energy source, a continuously operated system requires both a corresponding storage area and a supply chain for the fuel. Due to the low energy content of the biomass fuels, a large amount of fuel is required, depending on the plant design. The fuel demand of the BMB E_{BM} depends on the steam demand $E_{steam,demand}$ for the boiler and the part load efficiency η of the operating state of the boiler. This is presented by Equation (1).

$$E_{BM} = E_{steam,demand} \cdot \eta \left(\frac{P_{BM,partload}}{P_{BM,max}} \right). \quad (1)$$

2.4. Fuel Cell

The number of newly installed Fuel Cells (FCs) has been rising steadily for several years. Although the number of FC in use is still relatively low compared to conventional energy generators, the constant research and development of the cells, for example in the automotive industry, contributes to the constant growth. Since the use of FC does not lead to combustion or gasification, the emissions are limited to a minimum. In addition, FC are usually operated as a combined heat and power (CHP) plant [32]. They provide both waste heat and electricity. Disadvantages are the very high investment costs and the short service life [35]. Depending on the electrolyte used, five different FC types can be distinguished: Alkaline Fuel Cell (AFC), Polymer Electrolyte Fuel Cell (PEFC), Phosphoric Acid Fuel Cell (PAFC), Molten Carbonate Fuel Cell (MCFC) and Solid Oxide Fuel Cell (SOFC). The electrolyte

has an influence on the operating temperatures, efficiencies and the costs of the fuel cell. For example, the operating temperature of a PEFC is approx. 65–85 °C, while an SOFC is operated at approx. 700–1000 °C and MCFC at approx. 600–700 °C. Accordingly, only the MCFC and SOFC are suitable for the steam supply. In this paper a SOFC is used. It has good prerequisites for steam production due to its high temperatures and efficiencies. The amount of heat generated depends on the area of use and density of the cell, which varies depending on the operating point of the cell. Simplified, this represents the so-called heat-to-power ratio (HTPR), which describes the ratio of the electrical energy produced to the thermal energy [36]. In the SOFC in particular, biomethane/- gas is usable. Biomethane/-gas contains small amounts of hydrogen, hydrogen sulphide and other trace gases. These pollutants contained in the gas can damage both the components of the FC and normal engines and turbines. Therefore, it is necessary to pretreat the gas. For high-temperature FC, the removal of the sulphur compounds is sufficient. Typical processes for desulphurisation include fermenters, bioscrubbers and activated carbon filters. In addition to desulphurisation and processing, it is necessary for most FC types to reform the gas before use. This means that the methane is converted into hydrogen. For a SOFC, this process is not necessary because the reforming can take place within the cell. The fuel demand of the FC E_{FC} depends on the steam demand $E_{steam,demand}$ for FC and the part load efficiency η (Equation (2)). The electricity provided by the FC $P_{el,FC}$ is defined by HTPR and the thermal power of the FC $P_{steam,FC}$ (Equation (3)).

$$E_{FC} = E_{steam,demand} \cdot \eta \left(\frac{P_{FC,partload}}{P_{FC,max}} \right), \quad (2)$$

$$P_{el,FC} = \dot{Q}_{steam,FC} \cdot HTPR. \quad (3)$$

The simulation model is based on measurement data retrieved from an energy monitoring system. In addition, the simulation scenarios are designed for a constant load and the FC system is not exposed to fluctuations and behavioural changes. The created FC model is limited to the output data of a FC, which are defined and influenced by the heat-to-power ratio, the electrical and thermal efficiency as well as the reaction, heat and start up times.

2.5. Micro Gas Turbine

Micro Gas Turbines (MGTs) are compact power-heat-coupling systems with a small power range. MGT as a CHP technology are expressly suitable for the use of alternative fuels, such as low calorific gases like biogas [37]. A comprehensive description of the technology with a focus on the possible applications in small and medium-sized companies is found in Lucas et al. (2004) emphasizing the suitability for providing steam, heating thermal oil and drying [38].

MGTs are highly suitable for joint use with steam boilers since the heat contained in the turbine exhaust gas can be used directly in the boiler's burner due to the high oxygen content. This enables very high waste heat utilisation rates of up to 97%. To increase the overall power capacity and flexibility, several MGTs can be combined.

As cogeneration plants, MGTs provide the two co-products electrical energy and heat. If the fuel input is to be assigned to the individual products, for example to split costs and $CO_{2,e}$, different allocation methods are available. This paper uses the Finnish method. The reference efficiency for separate generation of heat using gaseous fuels (biogas or biomethane) for steam production is $\eta_{th,ref} = 0.87$, for electrical energy $\eta_{el,ref} = 0.53$ [39].

The fuel demand of the MGT E_{MGT} depends on the steam demand $E_{steam,demand}$ for MGT and the part load efficiency η (Equation (4)). The electricity provided by the MGT $P_{el,MGT}$ is defined by HTPR and the thermal power of the MGT $\dot{Q}_{steam,MGT}$ (Equation (5)).

$$E_{MGT} = E_{steam,demand} \cdot \eta \left(\frac{P_{MGT,partload}}{P_{MGT,max}} \right), \quad (4)$$

$$P_{el,FC} = \dot{Q}_{steam,MGT} \cdot HTPR. \quad (5)$$

2.6. Solar Thermal Systems

The Linear Fresnel Reflector (LFR) technology is based on an array of linear mirror strips that concentrate the solar rays coming from the sun onto a linear fixed receiver. The advantage of this technology is the construction of large absorber tubes. Secondary reflectors are mounted above the receiver to reflect the solar irradiation that does not impact directly on it from the primary reflectors. This fact can considerably increase the optical efficiency of the system.

The concentrated radiation reaching the receiver tube heats the liquid circulating through it and converts the solar radiation into useful heat. Water or thermal oil is used as the working fluid. Furthermore, a selective coating layer is applied to the absorber tube to improve solar absorption. LFRs can effectively generate heat at temperatures between 50–400 °C. [40].

Collectors are manufactured by bending a reflective sheet material into a parabolic shape. In operation, the receiver tube moves at the same time as the parabolic collector due to a solar-tracking system. Besides, its surface is covered with a selective coating with high absorbance for solar radiation but low emittance for thermal radiation losses.

Parabolic Trough Collectors (PTC) are widely used in process heat application in the industry and it is also the most mature technology for Heliostat Field Collectors to generate heat for processes or solar thermal electricity generation. The PTCs reach high temperatures up to 400 °C with better efficiency than LFRs [40]. To improve efficiency of the process, a thermal oil with good properties is used instead of water as the working medium. A glass cover tube around the receiver tube reduces the convective heat loss from the receiver. Besides, the space between the glass cover and the receiver tube can be evacuated to achieve lower convective heat losses. However, small transmittance losses occur when the reflected light pass through the glass to reach the absorber.

The operating costs are determined as follows, depending on size and investment [41]:

- LFR small-sized (100 m²) = 5% of capital investment
- LFR large-sized (15,000 m²) = 4% of capital investment
- PTC small-sized (100 m²) = 5% of capital investment
- PTC large-sized (15,000 m²) = 4% of capital investment

Both solar thermal systems require a steam accumulator and provide steam for the baseload.

2.7. Heat Pump

The operating principle of HP is based on the supply of high temperature heat to a heat sink thanks to the heat supplied by a low temperature source combined with mechanical work performed by a compressor. The sum of the heat supplied by the source plus the mechanical work of the compressor is the useful thermal heat obtained.

Currently commercial high temperature heat pumps can reach sink temperatures of at least 90 °C up to 165 °C with heating capacities ranging between 20 kW and 20 MW. The heat source temperatures range between 20–65 °C from brine, water or waste heat [42].

Because of the limited maximum temperature of 165 °C a closed cycle for a heat pump system is technically not possible for the sterilisation process of pet food which is analysed in the following case study. In food processing plants, there is an opportunity to take advantage of a large amount of water with still a high energy potential from waste heat that is available after cooling the processes. This water is stored in a reservoir at about 70–80 °C. To take advantage of this potential, a steam recovery system with a multi-stage of 8 blowers for the open cycle simulation has been designed. Commercial industrial heat pumps can achieve coefficients of performance (COP) ranging between 2 and 6.

2.8. Steam Accumulator

It is fundamental to consider the implementation of a steam accumulator for BMB, biomethane—fuelled FC, SES and HP due to the difference between the steam demand of the process and the steam supply. When the production is higher than the demand, the steam accumulator is charged, increasing the pressure inside while at the same time part of the steam condenses. When the steam accumulator is discharged due to a deficit of steam production, the pressure inside decreases and part of the water evaporates. Hence, the pressure level of the steam accumulator defines the load-level of the storage. To estimate the behaviour of the steam accumulator, the equilibrium model of Stevanovic et al. [43] is chosen (Equation (6)). Even, a more complex and detailed non equilibrium model is available, Biglia et al. [44] proposed the utilisation of the equilibrium model. Depending on the mass and energy balance of the steam accumulator, the pressure change and the pressure p inside of the vessel with a constant Volume V can be calculated. The mass balance $\dot{m}_{nB} = \dot{m}_{n,in} - \dot{m}_{n,out}$ and the energy balance $(\dot{m} \cdot h)_{nB} = (\dot{m} \cdot h)_{n,in} - (\dot{m} \cdot h)_{n,out}$ for liquid and vapourous considers the system boundaries as evaporation enthalpy $r = h'' - h'$ is also considered to depicture the evaporation and condensation inside of the accumulator. With the specific volume the saturated liquid v' and vapourous v'' state, the total mass M is calculated.

$$\frac{dp}{dt} = \frac{(\dot{m} \cdot h)_{1B} + (\dot{m} \cdot h)_{2B} + (\frac{rV}{v''-v'} - h)(\dot{m}_{1B} + \dot{m}_{1B})}{M(\frac{dh'}{dp} + \frac{V}{v''-v'} \cdot \frac{dr}{dp} - \frac{r}{v''-v'} \cdot \frac{dv'}{dp} - r \cdot \frac{V}{(v''-v')^2} \cdot \frac{d(v''-v')}{dp}) - V} \tag{6}$$

The steam accumulator is operated within a maximum pressure of 13 bar and a minimum pressure of 9 bar. A pressure difference of 4 bar is utilized. This pressure difference has a significant influence on the storage capacity of the steam accumulator. For the simulation runs, different storage vessel volumes should therefore be considered.

2.9. Summary of Technical and Economical Data

The following two Tables 1 and 2 give an overview of the technical and economical data of the different technologies. The described parameters are the basis for the technical and economical analyses of substituting a steam system with natural gas fired boilers. The two tables include more technologies than analysed in the upcoming case study. For this reason the compared technologies are marked bold in the tables.

Table 1. Technical data.

Technology	Maximum Temperature	Range of Power	Efficiency of Conversion	Availability	Start-up-Time
	in °C	in MW	in %	in %	in min
Electric resistance heater	800	5	>99 [30]	99	none
Electrode heater	240	60	>99 [30]	99	none
Biomass boiler	226	13	92	70–90	4–25 [45]
Biogas boiler	235	24.5	>95.5	depending on country ¹	none
CHP—Combustion Turbine	500 [46]	50 [47]	η_{el} : 24–36 [47] η_{heat} : 33–42 [47]	90–98 [46]	10–60 [48]
CHP—Micro Gas Turbine	350 [48]	1 [46]	η_{el} : 20–30 [48] η_{heat} : 50–60 [48]	90–99 [48]	1 [48]
CHP—Combustion Engine	650 [46]	80 [47]	η_{el} : 35–50 [46] η_{heat} : 35–53 [46]	90–98 [48]	0.16 [48]
Fuel Cell	650 [32]	5 [32]	30–60 [32]	95–99 [48]	180 min–3d [48]
Parabolic Trough Collectors	400 [40]	1 kW/m ² [49]	depending on country ¹	60–several hours	
Heat Pump	165 [42]	3 [42]		91 [42]	

¹ = Maximum service period depending on country.

Table 2. Economic data and others for steam systems with 9 bar and 175 °C.

Technology	Cost of Invest	Energy Costs	GHG Emission Factor
	in €/kW	in €/kWh	kg/MWh
Electric resistance heater	100–350 [50]	0.1268 [51]	23–1000 [52]
Electrode heater	50–600 [53]	0.1268 [51]	23–1000 [52]
Biomass boiler	160–200	0.02829 [54]	25–29 [55]
Biogas boiler	43–50 [56]	BG: 0.064 [51] BMe: 0.095 [55]	71–146 [52]
CHP—Combustion Turbine	1010–2190 _{el} [46]	NG: 0.0261 [51]	163–303 [52]
	1100–2650 _{th} [46]	BMe: 0.095 [55]	
CHP—Micro Gas Turbine	2190 _{el}	NG: 0.0261 [51] BMe: 0.095 [55]	114–212 [52]
CHP—Combustion Engine	1150–1450 _{el} [46]	NG: 0.0261 [51]	129–240 [52]
	1370–1550 _{th} [46]	BMe: 0.095 [55]	
Fuel Cell	2500–5500 [35]	NG: 0.0261 [51] BMe: 0.095 [55]	137–254 [52]
Parabolic Trough Collectors	Small ¹ : 425 [41] Large ¹ : 260 [41]	-	None
Heat Pump	1000–2000	0.1268 [51]	23–1000 [52]

¹ = Small-sized: 100 m², Large-sized: 15,000 m²; NG = Natural gas, BG = biogas BMe = Biomethane, Biomass = wood pellets or wood chips.

3. Methods

This section presents the methods and concepts for analysing the steam production costs and CO_{2,e}-emission reduction potentials via a dynamic simulation for one year. First, the different integration concepts for the technologies are described, followed by a description of dynamic simulation. The last section describes the basics of the economic analyses.

3.1. Steam Utility Concepts

Since the seven different technologies have different technical restrictions in terms of availability of steam supply and start up time, different concepts of implementation have been analysed. Except the BGB and the EB, all technologies only provide base load steam which therefore requires an additional peak load boiler for the fluctuating steam demand. In addition, the MGT and FC provide electrical energy as a byproduct. This electrical energy is first used to meet the plant's electrical energy demand and only excess energy is sold at the stock market.

Figure 1 gives an overview of the set up of the reference case and first four concepts and subconcepts which are compared to the CO_{2,e}-emission reduction potentials and related economic consequences for changing the steam generation from fossil to renewable energy.

The first concept is split into two subconcepts. Subconcept 1.1 replaces the two natural gas boilers with two BGB by changing the burner of the existing boilers. Subconcept 1.2 uses biomethane instead of natural gas. In the second concept one EB replaces both natural gas boilers due to the quick reaction times of the EB a back up is not necessary. Both, subconcepts 3.1 and 3.2, integrate a BMB into an existing utility system. In subconcept 3.1 a natural gas boiler is used as a backup boiler and in 3.2 a BGB is used accordingly. The fourth concept uses a biomethane-fuelled FC for the baseload and a natural gas boiler as a backup boiler. Figure 2 shows the concepts 5, 6 and 7 in order to substitute the two natural gas boilers.

In fifth concept, the MGT is used to pre-heat the combustion air of a BGB and the produced electricity is sold to the market. The PTC and HP are integrated as baseload technologies which charge the steam accumulator. Both, PTC and HP, use a natural gas boiler for backup and peak loads.

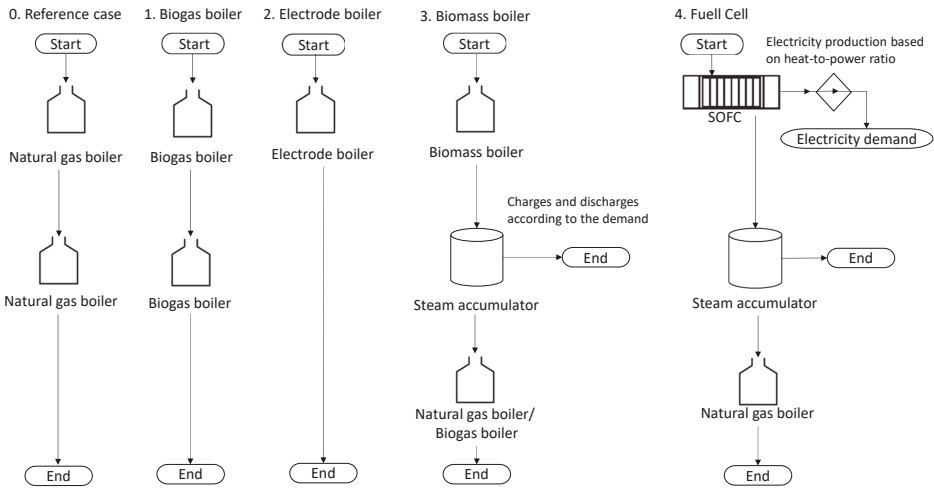


Figure 1. Overview of reference case and steam utility concepts 1–4.

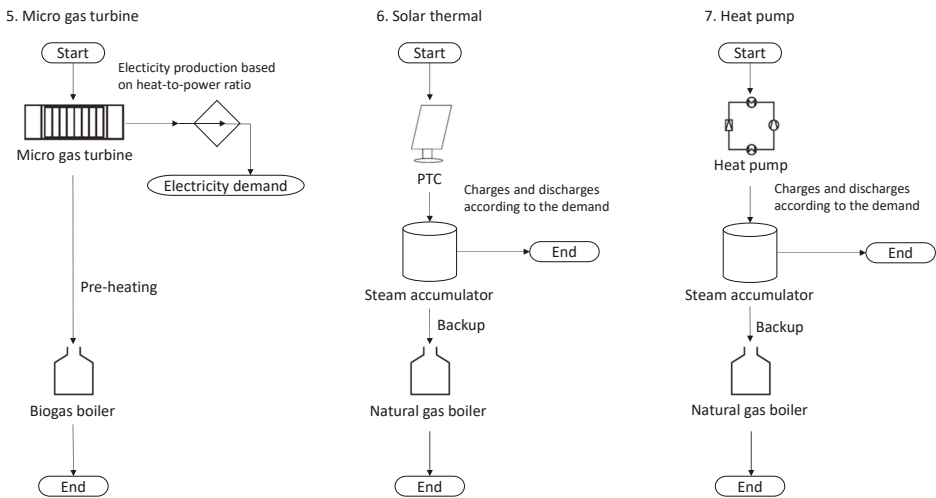


Figure 2. Overview of steam utility concepts 5–7.

3.2. Simulation

A dynamic annual simulation in Matlab/Simulink [57] is used to determine the effects of the volatile steam demand profile on energy demand and costs. The modelling is based on the energy balance of the system, whereby for the technologies the part load efficiency in each operating state and the thermal inertia must be determined. The technical characteristics of the models are described in Section 2. The Runge-Kutta method with a variable step size is used to solve the energy balance. In the energy model, the main utility and the backup boiler are connected in series, each with an internal storage component. The stored energy is calculated from the masses of water and steam and the respective enthalpies at the given pressure. To determine energy demand, costs and $CO_{2,e}$, the operating point of the utility is determined at the current output. On the basis of the operating point, the efficiency is determined, which leads to the energy demand for the thermal output. The absolute costs and $CO_{2,e}$ -emissions are calculated using the current values of the energy carrier demand and

the related costs and $CO_{2,e}$ -emissions. Energy losses and restrictions in the start up time or part-load performance of the different utility systems are considered in the modelling.

Due to the strongly fluctuating demand profile of the considered application, the steam storage size is optimised. The accumulator is dimensioned based on the average maximum overload and the maximum overload. These measures aim at offsetting all surplus and overload intervals by analysing all recorded intervals for one year. For all concepts including a steam accumulator, it is charged if there is a surplus of produced steam and the pressure in the storage is below 13 bar. It is discharged, if the produced steam of steam supply utility is less than the demand and the pressure in the storage is higher than 9 bar. In case the total produced steam by both one steam utility and the accumulator is less than the demand, the backup boiler supports.

For the electricity provided by the FC or MGT, both a cost-oriented and an emission-oriented variant are investigated. For this purpose, the costs and emissions of the generated electricity are allocated via the Finish Method. These values are compared to the current market values. Whether the electrical energy generated is used for own consumption or sold and fed into the grid depends on the aforementioned trade-off between minimising emissions or costs. The corresponding process type of electricity generation results in accounting effects for the recorded $CO_{2,e}$ -emissions as well as economic effects for sale and purchase of electricity.

3.3. Economical Analyses

Due to varying investment costs depending on supplier and client, several offers for the described technologies were obtained to determine the costs for the case study and the mean value was chosen for further consideration. The investment costs include all associated costs as well as set-up and commissioning cost. For the annual costs of the investment the straight-line depreciation for a period of 15 years for the boiler and 10 for all other technologies and the steam accumulator is applied. The annual costs for the technologies $C_{technology}$ are the sum of depreciation costs C_{depr} , the fuel costs for biomass p_{BM} , natural gas p_{NG} , biogas p_{BG} , biomethane $p_{biomethane}$ and electricity p_{el} . Equation (7) shows an example for calculating the costs for the concept with the biomass boiler. All technologies without electricity generation are calculated accordingly.

$$C_{BM} = C_{depr} + E_{steam,BM} \cdot p_{BM} + E_{steam,B} \cdot p_{NG}. \quad (7)$$

The electricity generation costs for the FC $C_{el,FC}$ and the MGT $C_{el,MGT}$ are added to the annual costs and the earnings from the usage of the generated electricity or selling S_{el} it to the grid are subtracted from the annual costs (Equation (8)).

$$C_{FC} = C_{depr} + E_{steam,FC} \cdot p_{biomethane} + E_{steam,B} \cdot p_{NG} + C_{el,FC} - S_{el}. \quad (8)$$

4. Use Case Wet Pet Food

In this section the production process of wet pet food is introduced and the basic condition for the case study are presented. Figure 3 shows the process flow diagram for wet pet food.

The frozen meat is first crushed and then processed in the grinder to a homogeneous mass. In the mixer, fresh meat and water are added. The mixing process requires thermal energy at a temperature level between 65 and 80 °C. The water-meat mixture is then emulsified and cooked in the steam tunnel and then cooled. Together with the gravy water, the mixture is filled into pouches and then sterilized in the retorts. The process concludes with the packaging of the pouches in boxes and cartons. Over 60% of the steam is used for the sterilisation process, while 6–8% are needed for the steam tunnels at 3 bar. Around 18% are required for the mixing, cleaning, hot water and other processes. The rest are losses and demands for pre-heating the fresh boiler water. Depending on the level of heat recovery and the set up of the production plant these values may differ.

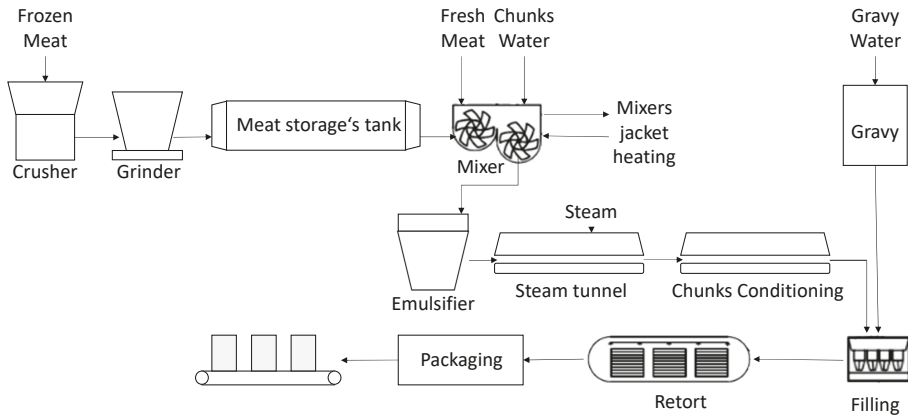


Figure 3. Process flow diagram for wet pet food.

In the following, the process data of a wet pet food processing plant located in Spain is used within a simulation study to analyse different integration concepts for the presented technologies. Approximately 27,440 t of steam and 7800 MWh of electricity are required annually at this location. The steam is supplied at 9 bar and approximately 175 °C. The average steam demand is 3.1 t/h. However, the demand fluctuates between 1 t/h and 7 t/h. Higher peak demands up to 10 t/h occur rarely during the year. Figure 4 shows an example of the steam demand for four hours. Both, the minimum of 0 t/h and the maximum mass flow of 10 t/h as well as the strong fluctuations caused by the batch operation of the sterilization process are clearly visible. The irregularity in the steam demand places high requirements on the flexibility of steam production, which not every technological alternative can meet without restrictions.

In the reference case, the steam is produced by two conventional natural gas boilers. One acts as the leading boiler and the other one is a backup boiler. When the steam demand cannot be entirely satisfied by the leading boiler and its storage, the backup boiler supplies the rest. For the comparison of the different technologies the dimensions of power and steam accumulator has been optimised in a previous step.

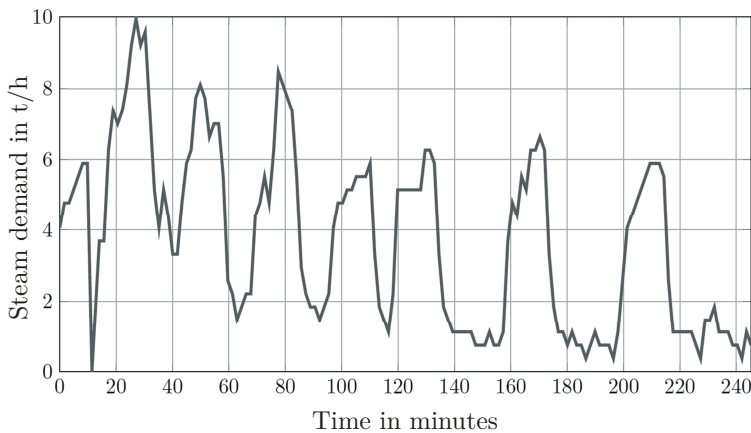


Figure 4. Steam demand profile over four hours.

Table 3 shows the thermal and electrical energy demands, the corresponding energy costs and the $CO_{2,e}$ emission for the described reference case.

Table 3. Reference case.

Parameter	Value
Steam demand	27,440 t
Thermal energy demand	21,589 MWh
Natural gas demand	1,856,321 m ³
Thermal energy costs	554,038 €
Thermal emissions	5203 t $CO_{2,e}$
Electrical energy demand	7582 MWh
Electrical energy costs	663,557 €
Electrical emissions	2038 t $CO_{2,e}$

For the calculation of the operating costs, the natural gas price varies between 0.027 €/kWh and 0.031 €/kWh. These natural gas prices were retrieved from the annual bill of the industrial site. For the case study, the prices are assumed to be fixed—biomass 0.028 €/kWh [54], biogas 0.0644 €/kWh and biomethane 0.095 €/kWh. For self-used electricity and sold electricity the Spanish stock market price [58] of 2017 in each time step is considered. The chosen values for emissions of natural gas are 241 g/kWh, of biomass 27 g/kWh [55], biogas 135 g/kWh [59], biomethane 146 g/kWh [59] and the emission for electricity are based on the grid electricity mix in each time step. This value varies between 90.13 g/kWh and 486.49 g/kWh [60]. For year 2017, the Spanish electricity mix is divided as follows—hydro 6.89%, wind 17.88%, solar photovoltaic 3.14%, other renewables 3.68%, nuclear 20.73%, combined cycle 13.84%, coal 16.81%, cogeneration 10.53%, others 3.08% and cross-border exchange 3.42% [61].

Table 4 summarises the investigated scenarios for the steam accumulator volumes, the size of the new technologies and the size of the backup boiler fired by natural gas or biogas.

Table 4. Overview concept analyses.

Concept	Steam Accumulator	New Technology	Backup Natural Gas	Backup Biogas
	in m ³	in kW	in kW	in kW
0.0 Reference case	-	-	2 · 5432	-
1.1 Biogas boiler	-	2 · 5432	-	-
1.2 Biomethane boiler	-	2 · 5432	-	-
2.0 Electrode boiler	-	7000	-	-
3.1 Biomass boiler—conventional backup	130	2055	5432	-
3.2 Biomass boiler—biogas backup	130	2055	-	5432
4.0 Fuel cell	130	2055	5432	-
5.0 Micro gas turbine	-	395	-	5432
6.0 Solar thermal	70	1800	5432	-
7.0 Heat pump	75	8 · 66	5432	-

5. Results

For the dynamic simulations of one year, the results show that maximal reduction of $CO_{2,e}$ emissions is limited to 63.75%. This maximal reduction is reached by using a BMB for base load and a BGB for peak load. Figure 5 shows the increase of the total energy costs for the steam supply and electricity supply in comparison to the reference case for one year. In addition, the $CO_{2,e}$ emission reduction is visualised. The installation of PTC results in the lowest cost increase by 6.6%. Since only the depreciation and maintenance costs are determining the energy costs, the increase is very small compared to other technologies.

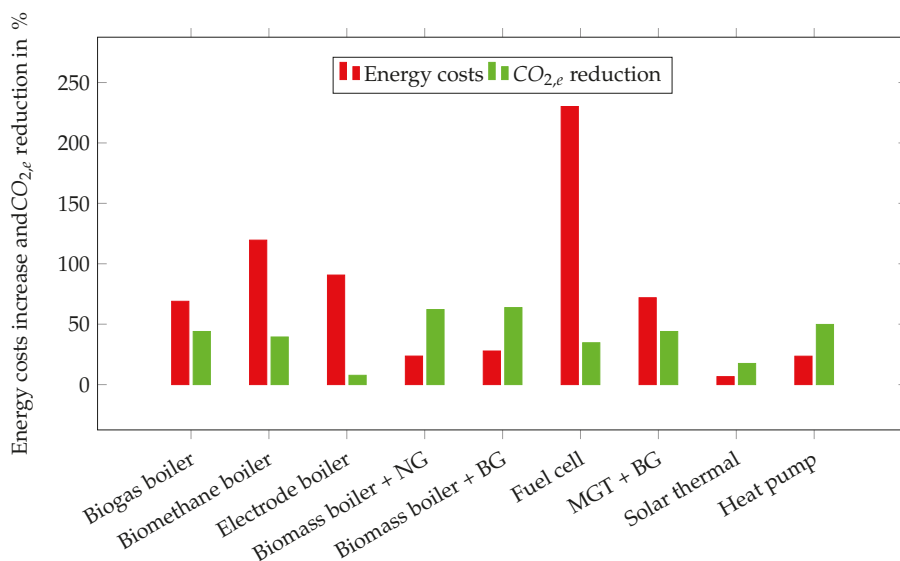


Figure 5. Comparison of energy costs increase and CO_{2,e} emission reduction.

However, the limited availability during a day and a year leads to high running hours of the conventional backup boiler. This is the reason why the CO_{2,e} emission reduction is only 17.51%.

Both, BMB with a natural gas fired or biogas fired backup boiler take advantage of the low fixed price for biomass of 0.028 €/kWh. This results in an energy costs increase of 23.61% for the combination biomass system/conventional boiler and 27.81% for the combination with a BGB backup. Also, the emission reductions of 62.12% and 63.75% are the highest of all concepts. The low carbon footprint of biomass and the high steam supply share of the BMB explain the high CO_{2,e} emission reduction.

The use of an HP results in a similar cost increase of 23.53%. The share of the conventional backup boiler of more than 25% leads to emissions of 2612 t CO_{2,e} which results in a reduction of 49.80%.

Because of the fuel price ratio between natural gas and biogas, the retrofit to a biogas burner increases the energy costs by 68.96%. The CO_{2,e} emissions are reduced by 43.97%.

The MGT needs to be fired with biogas to reduce CO_{2,e} emissions. A reduction of 43.97% is possible with an energy cost increase of 71.9%. When operated with natural gas, the simulation shows an annual savings potential of about 33,000 €. These savings can be explained by the cheaper supply of electrical energy. However, CO_{2,e} emissions increase due to production of electricity and the low average electricity grid emissions of 267 g/kWh in Spain.

The EB has 7.71% lower CO_{2,e} emissions than the natural gas-fired boilers of the existing system, although the assumed average emissions of electrical energy per kilowatt hour are greater than those of natural gas. The savings can be explained by the higher efficiency, the elimination of switching losses and heat losses of the second boiler. These low emission savings are offset by significantly higher costs of 90.66%.

In the simulation study, the implementation of a FC has the highest increase in costs and only a emission reduction by 34.65%. High investment costs of over 6.8 million € and low thermal efficiency compared to other technologies result in very high steam production costs. Because of the limited flexibility, a secondary peak load boiler needs to provide a significant share of the overall steam demand. Therefore, the emissions reduction is limited.

The results for the forms of energy conversion show that higher energy costs do not automatically lead to the highest CO_{2,e} emission savings. To evaluate the best technology for the presented case study the ratio of additional costs to emission savings is essential. In Figure 6, the costs are offset against the corresponding CO_{2,e} emission reduction to obtain the costs per tons of CO_{2,e} saved for one year.

The costs per saved ton of CO_{2,e} per year are between 89 € and 2753 €. According to this, the use of a BMB and PTC are the most efficient ways of providing steam in terms of economic efficiency and CO_{2,e}-emissions avoided. The installation of a EB results in the highest costs per ton CO_{2,e}-emissions avoided under the assumed circumstances of relative high electricity costs and CO_{2,e}-emissions of the electricity mix.

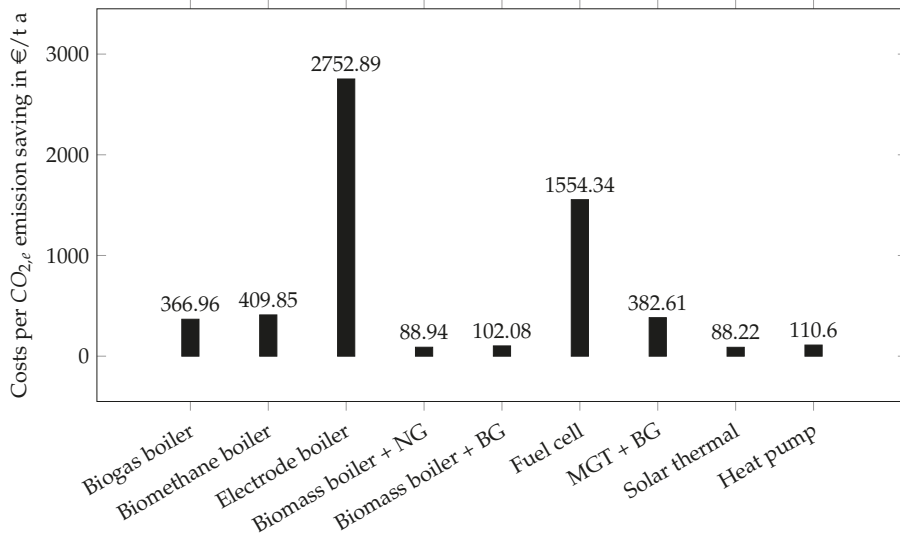


Figure 6. Ratio of CO_{2,e} emission saving and energy costs per year.

Table 5 summarises the costs and CO_{2,e} emissions for all technologies and the corresponding used types of fuel.

Table 5. Results of dynamic simulation.

Concept	Investment Costs	Steam Production Costs	Electricity Costs without Steam	CO _{2,e} Emissions Steam
	in €	in €	in €	in t CO _{2,e}
0.0 Reference case	0	554,038	663,556	5203
1.1 Biogas boiler	50,000	1,393,635	663,556	2915
1.2 Biomethane boiler	0	2,009,937	663,556	3152
2.0 Electrode boiler	1,000,000	1,644,968	676,533	4802
3.1 Biomass boiler—conventional backup	915,129	836,206	668,853	1971
3.2 Biomass boiler—biogas backup	965,129	887,331	668,853	1886
4.0 Fuel cell	6,839,200	2,749,271	1,270,795	3400
5.0 Micro gas turbine	650,000	1,401,852	691,164	2915
6.0 Solar thermal	1,805,027	634,407	663,556	4292
7.0 Heat pump	2,096,878	840,590	663,556	2612

6. Discussion

The results indicate that the BMB with natural gas or BGB have the highest emission reduction and the lowest increase in cost. Although the steam production costs of around 30 €/t are higher than those presented by Pérez-Uresti et al. [13], the statement that biomass is the most economical alternative in 2019 is consistent. The comparison between the steam production costs of the BGB and the BMB shows that the investment costs with an assumed depreciation between 10 to 15 years have a very small impact on the steam production costs. For production plants with a high thermal energy demand the fuel prices is determining the overall steam production costs. The depreciation period should be reduced for production plants with frequently changing products and changes in thermal processes. Thus the influence of investment costs increases linearly with the reduction. However, a complete substitution of all thermal steam processes with BMB may exceed the sustainable supply. This can lead to an increase in the cost of biomass, which is not yet included in the model. For example, Börjesson et al. [62] showed that an increasing forest fuel demand by 30–40 TWh for Sweden for the upcoming decades exceeds the potential increase in sustainable supply of logging residues.

The implementation of SES and HP results in a relatively low increase in the overall energy costs. The limited flexibility impede a complete reduction of emissions. Therefore, these technologies can only be auxiliary technologies for reducing the $CO_{2,e}$ emissions of a steam supply system. For the SES, the high space demand for the installation of the solar field reduces the potential for a decentralised solution. For a closed cycle HP, the fluctuating steam demand and steam temperature exceed current available options in the market for industrial and high temperature HP. Furthermore, in accordance with Bühler et al. [4] and Apargaus et al. [42], the potential of HP for energy-efficient electrification for steam supply is estimated to be high once temperatures above 165 °C are reached. In addition, for the food processing industry the steam temperature level is not given by the process (e.g., sterilisation), which usually need temperatures below 150 °C. The temperature restrictions are set by the required quick reaction time of the control system. A process adaption focusing on lower $CO_{2,e}$ emissions and resulting in lower steam supply temperatures may increase the implementation potential for HP and SES.

Regarding the still relatively high emissions of EB, an increase of renewable energies in the electricity mix leads to a further reduction of $CO_{2,e}$ emissions as well as probably electrical energy costs reductions. There is already the option of providing and purchasing electrical energy without emissions, at least on the balance sheet, thus the compensation of the total $CO_{2,e}$ emissions is possible. However, to achieve the planned reduction of $CO_{2,e}$ emissions through electrification in the food processing industry, a significant increase in the installed capacity of renewable energies is required. As Philipp et al. [63] showed, the timing and the share of renewable electricity in the respective country is decisive for a positive $CO_{2,e}$ emission reduction effect. Besides BMB, EB have the potential to reduce the emissions significantly if the electricity mix is dominated by wind power. Short start up times and a very flexible load control offer a solution in the future if electrical energy costs and electrical grid emissions are reduced.

The fuel switch to biogas or biomethane results in the lowest investment costs and implementation effort. Therefore, both concepts are very sensitive to a change in the fuel prices. For biomethane the fuel price varies between 60–95 €/MWh depending on costs for conditioning and grid. For a low fuel price level, a steam production cost reduction of 35% is possible and a boiler fired with biomethane is an easy and cost attractive option to reduce $CO_{2,e}$ emissions. Biogas is produced from various

substrates, mainly renewable raw materials, excrements, municipal biowaste and residual materials from industry, trade and agriculture. The substrates differ in price, methane yield and the resulting related state subsidies. For this reason, producer prices and emissions of biogas can also vary strongly from plant to plant [55]. In order to assess the economic and ecological effects, special attention must be paid to local conditions. For locally produced biogas, it is possible to achieve favourable prices and low $CO_{2,e}$ emissions.

For the MGT, a fuel price reduction is also necessary to be competitive with the BMB. However, CHP technologies increase the overall fuel demand significantly. The amount of available biomethane or biogas might limit integration potential of MGT and FC.

7. Conclusions

The investigations in this paper show the significant potential of reducing $CO_{2,e}$ emissions in industrial facilities. Especially, the combination of biomass boilers and steam accumulator leads to an adequate ratio of $CO_{2,e}$ emissions reduction and steam production costs. Due to an expected future increase in the volatility of the power supply system, the characteristics of batch processes, start-up times and partial load are of crucial importance when planning a steam supply system. In contrast to previous research work, an annual dynamic simulation model was developed which takes these characteristics as well as a variety of new technologies into account. It was applied to a practical case study which demonstrates the complex relationships of steam supply systems in batch processes.

The steam supply in industrial plant systems is defined by their steam demand load profile. The results from this work cannot be transferred directly to any other case. So, a detailed investigation of various steam demand situations should be considered to transfer this results into other concepts. Similar results are expected for other industries, that is, dairy and galvanic, with a discontinuous steam demand and steam temperatures below 175 °C. Before changing the steam supply, a substitution of the steam demand by hot water processes should be analysed. This increases the integration potential of renewable energies and leads to higher $CO_{2,e}$ emission reductions.

Since energy cost increase and the $CO_{2,e}$ emission reduction are strongly dependent on the demand profile, the optimum design size for each individual utility must be determined. For the detailed evaluation and analysis of the transmission of energy supply sector in accordance with load management of steam processes, it is necessary to investigate technology combinations such as electrode boilers and micro gas turbines in future research. These could bring further advantages, especially regarding load management and grid stabilisation. Due to the inertia of the biomass boiler, fuel cell, solar thermal system and heat pump, these technologies do not show any potential for grid stabilisation. Soon, concepts of the fuel cell will become more attractive. Due to the strong development and research in this area, significantly decreasing investment costs and increasing efficiencies are predicted until 2030.

Author Contributions: Conceptualization, R.-H.H.; methodology, R.-H.H.; software, J.S.; validation, J.S., A.O.; formal analysis, J.-P.S. and M.S.; writing—original draft preparation, R.-H.H.; writing—review and editing, J.-P.S.; visualization, R.-H.H. All authors have read and agreed to the published version of the manuscript.

Funding: This research received no external funding.

Conflicts of Interest: The authors declare no conflict of interest.

Abbreviations

The following abbreviations are used in this manuscript:

AFC	Alkaline fuel cell
BGB	Biogas boiler
BMB	Solid biomass-fuelled boiler
BMe	Biomethane
CHP	Combined heat and power
COP	Coefficients of performance
EB	Electrode boiler
FC	Fuel cell
GHG	Greenhouse gas
HP	Heat pump
HTPR	Heat-to-power-ratio
NG	Natural gas
MCFC	Molten carbonate fuel cell
MGT	Micro gas turbine
MP	Medium pressure steam
LFR	Linear fresnel reflector
PAFC	Phosphoric acid fuel cell
PEFC/PEFMFC	Polymer electrolyde fuel cell
PTC	Parabolic trough collectors
SOFC	Solid oxide fuel cell

References

1. European Commission. *A Roadmap for Moving to a Competitive Low Carbon Economy in 2050*; European Commission: Brussels, Belgium, 2011.
2. Bundesministerium für Wirtschaft und Energie. *Facts and figures Energy Data: National and International Development [In German: Zahlen und Fakten Energiedaten: Nationale und Internationale Entwicklung]*; Bundesministerium für Wirtschaft und Energie: Berlin, Germany, 2018.
3. IRENA; C2E2. *Synergies between Renewable Energy and Energy Efficiency: A Working Paper Based on Remap 2030*; IRENA: Abu Dhabi, UAE; C2E2: Copenhagen, Denmark, 2015.
4. Bühler, F.; Zühlsdorf, B.; Nguyen, T.V.; Elmegaard, B. A comparative assessment of electrification strategies for industrial sites: Case of milk powder production. *Appl. Energy* **2019**, *250*, 1383–1401. [[CrossRef](#)]
5. Rehfeldt, M.; Fleiter, T.; Worrell, E. Inter-fuel substitution in European industry: A random utility approach on industrial heat demand. *J. Clean. Prod.* **2018**, *187*, 98–110. [[CrossRef](#)]
6. Butturi, M.A.; Lolli, F.; Sellitto, M.A.; Balugani, E.; Gamberini, R.; Rimini, B. Renewable energy in eco-industrial parks and urban-industrial symbiosis: A literature review and a conceptual synthesis. *Appl. Energy* **2019**, *255*, 113825. [[CrossRef](#)]
7. Walmsley, M.R.; Walmsley, T.G.; Atkins, M.J.; Neale, J.R. Sustainable Milk Powder Production using Enhanced Process Integration and 100% Renewable Energy. *Chem. Eng. Trans.* **2016**, *2016*, 559–564.
8. Bühler, F.; Nguyen, T.V.; Elmegaard, B.; Modi, A. Process and Economic Optimisation of a Milk Processing Plant with Solar Thermal Energy. In *26th European Symposium on Computer Aided Process Engineering; Computer Aided Chemical Engineering*; Elsevier: Amsterdam, The Netherlands, 2016; Volume 38, pp. 1347–1352.
9. Kurup, P.; Turchi, C. Potential for solar industrial process heat in the United States: A look at California. In *SolarPACES 2015*; Rajpaul, V., Richter, C., Eds.; Conference collection; AIP Publishing: Melville, LA, USA; New York, NY, USA, 2016; p. 110001.
10. Silva, R.; Cabrera, F.J.; Pérez-García, M. Process Heat Generation with Parabolic Trough Collectors for a Vegetables Preservation Industry in Southern Spain. *Energy Procedia* **2014**, *48*, 1210–1216. [[CrossRef](#)]
11. Stark, M.; Philipp, M.; Saidi, A.; Trinkl, C.; Zörner, W.; Greenough, R. Steam Accumulator Integration for Increasing Energy Utilisation of Solid Biomass-Fuelled CHP Plants in Industrial Applications. *Chem. Eng. Trans.* **2018**, *70*, 2137–2142.

12. Stark, M.; Philipp, M.; Saidi, A.; Trinkl, C.; Zörner, W.; Greenough, R. Design Parameters of Steam Accumulators for the Utilization in Industrial Solid Biomass-Fuelled CHP Plants. *Chem. Eng. Trans.* **2019**, *76*, 817–822.
13. Pérez-Uresti, S.I.; Martín, M.; Jiménez-Gutiérrez, A. Estimation of renewable-based steam costs. *Appl. Energy* **2019**, *250*, 1120–1131. [[CrossRef](#)]
14. Peesel, R.H.; Otte, A.; Stark, M. Transition of Steam Utility Systems to Solid Biomass-Fuelled Boilers and Biomethane-Fuelled Fuel Cells in the Wet Pet Food Processing Industry. *Chem. Eng. Trans.* **2019**, *76*, 931–936.
15. Wiertzema, H.; Åhman, M.; Harvey, S. Bottom-up methodology for assessing electrification options for deep decarbonisation of industrial processes. In *Eceee Industrial Summer Study Proceedings*; European Council for an Energy Efficient Economy (ECEEE): Copenhagen, Denmark, 2018; Volume 2018, pp. 389–397.
16. Johansson, D.; Rootzén, J.; Berntsson, T.; Johnsson, F. Assessment of strategies for CO₂ abatement in the European petroleum refining industry. *Energy* **2012**, *42*, 375–386. [[CrossRef](#)]
17. Berghout, N.; Meerman, H.; van den Broek, M.; Faaij, A. Assessing deployment pathways for greenhouse gas emissions reductions in an industrial plant—A case study for a complex oil refinery. *Appl. Energy* **2019**, *236*, 354–378. [[CrossRef](#)]
18. Sun, L.; Doyle, S.; Smith, R. Understanding steam costs for energy conservation projects. *Appl. Energy* **2016**, *161*, 647–655. [[CrossRef](#)]
19. Arousseau, A.; Vuillerme, V.; Bezan, J.J. Control systems for direct steam generation in linear concentrating solar power plants—A review. *Renew. Sustain. Energy Rev.* **2016**, *56*, 611–630. [[CrossRef](#)]
20. Giglio, A.; Lanzini, A.; Leone, P.; Rodríguez García, M.M.; Zarza Moya, E. Direct steam generation in parabolic-trough collectors: A review about the technology and a thermo-economic analysis of a hybrid system. *Renew. Sustain. Energy Rev.* **2017**, *74*, 453–473. [[CrossRef](#)]
21. Simpson, R.; Cortés, C.; Teixeira, A. Energy consumption in batch thermal processing: model development and validation. *J. Food Eng.* **2006**, *73*, 217–224. [[CrossRef](#)]
22. Simpson, R.; Abakarov, A. Optimal scheduling of canned food plants including simultaneous sterilization. *J. Food Eng.* **2009**, *90*, 53–59. [[CrossRef](#)]
23. Peesel, R.H.; Philipp, M.; Schumm, G.; Hesselbach, J.; Walmsley, T.G. Energy Efficiency Measures for Batch Retort Sterilization in the Food Processing Industry. *Chem. Eng. Trans.* **2016**, *2016*, 163–168.
24. Liew, P.Y.; Theo, W.L.; Alwi, S.R.W.; Lim, J.S.; Manan, Z.A.; Klemeš, J.; Varbanov, P.S. Total Site Heat Integration planning and design for industrial, urban and renewable systems. *Renew. Sustain. Energy Rev.* **2017**, *68*, 964–985. [[CrossRef](#)]
25. Merritt, C. *Process Steam Systems: A Practical Guide for Operators, Maintainers, and Designers*; John Wiley & Sons Inc.: Hoboken, NJ, USA, 2015.
26. Sattler, G.; Schibel, T. *Design Manual Steam [In German: Planungshandbuch Dampf]*; Viessmann Werke: Allendorf, Germany, 2011.
27. Kulterer, K.; Rieder, H. *Steam Guidelines [In German: Dampfleitfaden]*; Austrian Energy Agency: Wien, Austria, 2011.
28. Adler, P.; Billig, E.; Brosowski, A.; Daniel-Gromke, J.; Falke, I.; Fischer, E. *Guide to Biogas Upgrading and Feed-In. [In German: Leitfaden Biogasaufbereitung und -einspeisung]*, 5., vollständig überarbeitete auflage ed.; Fachagentur für Nachwachsende Rohstoffe e. V. (FNR): Gülzow-Prüzen, Germany, 2014.
29. Biedermann, F.; Kolb, M. *Power to Heat*; Arbeitsgemeinschaft der Hessischen Industrie- und Handelskammern: Wetzlar, Germany, 2014.
30. Pieper, C.; Sykora, N.; Beckmann, M.; Böhning, D.; Hack, N.; Bachmann, T. The economic use of power-to-heat systems in the balancing energy market [In German: Die wirtschaftliche Nutzung von Power-to-Heat-Anlagen im Regelenergiemarkt]. *Chemie Ingenieur Technik* **2015**, *87*, 390–402. [[CrossRef](#)]
31. Gruber, A.; Biedermann, F.; von Roon, S. *Industrial Power-to-Heat Potential [In German: Industrielles Power-to-Heat Potenzial]*; FfE Forschungsgesellschaft für Energiewirtschaft mbH: München, Germany, 2015.
32. Zahoransky, R.; Allelein, H.J.; Bollin, E. *Power Engineering: Systems for Energy Conversion. Compact Knowledge for Studies and Work [In German: Energietechnik: Systeme zur Energieumwandlung. Kompaktwissen für Studium und Beruf]*, 6., überarb. u. erw. aufl. 2013 ed.; Springer Fachmedien Wiesbaden: Wiesbaden, Germany, 2013.
33. Schabbach, T.; Wesselak, V. *Energy: The Future Becomes Renewable [In German: Energie: Die Zukunft wird erneuerbar]*; SpringerLink Bücher, Springer Vieweg: Berlin/Heidelberg, Germany, 2012.

34. Kaltschmitt, M.; Hartmann, H.; Hofbauer, H., Eds. *Energy from Biomass: Principles, Techniques and Processes [In German: Energie aus Biomasse: Grundlagen, Techniken und Verfahren]*, 3., aktualisierte und erweiterte auflage ed.; Springer Vieweg: Berlin/Heidelberg, Germany, 2016.
35. Niakolas, D.K.; Daletou, M.; Neophytides, S.G.; Vayenas, C.G. Fuel cells are a commercially viable alternative for the production of “clean” energy. *Ambio* **2016**, *45* (Suppl. 1), S32–S37. [[CrossRef](#)]
36. Liso, V.; Zhao, Y.; Brandon, N.; Nielsen, M.P.; Kær, S.K. Analysis of the impact of heat-to-power ratio for a SOFC-based mCHP system for residential application under different climate regions in Europe. *Int. J. Hydrog. Energy* **2011**, *36*, 13715–13726. [[CrossRef](#)]
37. Rahms, H.; Giese, A.; Schmitz, I.; Scherer, V. *Development of Flexible Firing Systems for the Combustion of Lean Gases in Microturbine Combustion Chambers [In German: Entwicklung flexibler Feuerungssysteme zur Verbrennung von Schwachgasen in Mikrogasturbinen-Brennkammern]*; Gaswärme-Institut e. V.: Essen, Germany, 2008.
38. Lucas, K.; Kuperjans, I.; Bouvy, C. *Final Report of the AIF-Funded Project Decision and Planning Aid for the Use of Micro Gas Turbines in kmU [In German: Abschlussbericht des AIF-geförderten Projektes “Entscheidungs- und Planungshilfe für den Einsatz von Mikro-Gasturbinen in kmU”]*; Institut für Energie- und Umwelttechnik e. V.: Duisburg, Germany, 2004.
39. European Commission. *Commission Delegated Regulation (EU) 2015/2402 12 October 2015 Reviewing Harmonised Efficiency Reference Values for Separate Production of Electricity and Heat in Application of Directive 2012/27/EU of the European Parliament and of the Council and repealing Commission Implementing Decision 2011/877/EU*; European Commission: Brussels, Belgium, 2015.
40. Kalogirou, S. *Solar Energy Engineering: Processes and Systems*, 2nd ed.; Academic Press: Waltham, MA, USA, 2014.
41. Advanced Technology Centre for Renewable Energies. *Market Potential in Spain and Applications in Medium Temperature Solar Concentration Technologies [In Spanish Mercado Potencial en España y Aplicaciones en Tecnologías Solares de Concentración de Media Temperatura]*; Ministerio de Economía y Competitividad: Madrid, Spain, 2015.
42. Arpagaus, C.; Bless, F.; Uhlmann, M.; Schiffmann, J.; Bertsch, S.S. High temperature heat pumps: Market overview, state of the art, research status, refrigerants, and application potentials. *Energy* **2018**, *152*, 985–1010. [[CrossRef](#)]
43. Stevanovic, V.D.; Petrovic, M.M.; Milivojevic, S.; Maslovaric, B. Prediction and Control of Steam Accumulation. *Heat Transf. Eng.* **2015**, *36*, 498–510. [[CrossRef](#)]
44. Biglia, A.; Comba, L.; Fabrizio, E.; Gay, P.; Ricauda Aimonino, D. Steam batch thermal processes in unsteady state conditions: Modelling and application to a case study in the food industry. *Appl. Therm. Eng.* **2017**, *118*, 638–651. [[CrossRef](#)]
45. Win, K.M.; Persson, T.; Paavilainen, J. Emissions Characteristics of residential pellet boilers during start-up and stop periods. In Proceedings of the International Scientific Conference on Energy Systems with IT, Stockholm, Sweden, 16–17 March 2010; pp. 120–130.
46. Darrow, K.; Tidball, R.; Wang, J.; Hampson, A. *Catalog of CHP Technologies*; United States Environmental Protection Agency: Washington, DC, USA, 2017.
47. Duffy, A.; Rogers, M.; Ayompe, L. *Renewable Energy and Energy Efficiency: Assessment of Projects and Policies*, 1. publ ed.; Wiley-Blackwell: Chichester, UK, 2015.
48. ONSITE SYCOM Energy Corporation. *The Market and Technical Potential for Combined Heat and Power in the Commercial/Institutional Sector*; ONSITE SYCOM Energy Corporation: Washington, DC, USA, 2000.
49. Kutscher, C.; Burkholder, F.; Kathleen Stynes, J. Generation of a Parabolic Trough Collector Efficiency Curve From Separate Measurements of Outdoor Optical Efficiency and Indoor Receiver Heat Loss. *J. Sol. Energy Eng.* **2012**, *134*, 011012. [[CrossRef](#)]
50. Fürstenwerth, D.; Richts, C.; Hochloff, P. *Power-to-Heat to Integrate Otherwise Regulated Electricity from Renewable Energies [In German: Power-to-Heat zur Integration von ansonsten abgeregeltem Strom aus erneuerbaren Energien: Handlungsvorschläge basierend auf einer Analyse von Potenzialen und energiewirtschaftlichen Effekten]*; Agora Energiewende: Berlin, Germany, 2014.
51. Statistisches Bundesamt. *Prices—Data on Energy Price Trends: Long-Time Series from January 2000 to February 2018*; Statistisches Bundesamt: Wiesbaden, Germany, 2018.

52. Umweltbundesamt. *Development of the Specific Carbon Dioxide Emissions of the German Electricity Mix in the Years 1990–2016* [In German: *Entwicklung der Spezifischen Kohlendioxid-Emissionen des Deutschen Strommix in den Jahren 1990–2016*]; Umweltbundesamt: Dessau-Rosslau, Germany, 2017.
53. Eller, D. *Integration of Renewable Energies with Power-to-Heat in Germany* [In German: *Integration erneuerbarer Energien mit Power-to-Heat in Deutschland*]; Springer Fachmedien Wiesbaden: Wiesbaden, Germany, 2015.
54. Agrar-Rohstoff Marketing- und Energie-Netzwerk e.V. *Price Development for Forest Chips—The Energy Wood Index* [In German: *Preisentwicklung bei Waldhackschnitzeln—Der Energieholz-Index*]; Agrar-Rohstoff Marketing- und Energie-Netzwerk e.V.: Straubing, Germany, 2018.
55. Fachagentur Nachwachsende Rohstoffe e.V. *Thumb Numbers* [In German: *Faustzahlen*]; Fachagentur Nachwachsende Rohstoffe e.V.: Gülzow-Prüzen, Germany, 2018.
56. Lukas, K. *Derivation of Cost Functions for Components of Rational Energy Use* [In German: *Ableitung von Kostenfunktionen für Komponenten der rationellen Energienutzung*]; Institut für Energie- und Umwelttechnik e.V.: Duisburg-Rheinhausen, Germany, 2002.
57. MATLAB. 9.7.1190202 (R2019b); The MathWorks Inc.: Natick, MA, USA, 2018.
58. OMI, Polo Español S.A. (OMIE). *Daily Market Hourly Prices*; OMI, Polo Español S.A. (OMIE): Madrid, Spain, 2017.
59. Memmler, M.; Lauf, T.; Wolf, K.; Schneider, S. *Emission Balance of Renewable Energy Sources: Determination of Avoided Emissions in 2016* [In German: *Emissionsbilanz erneuerbarer Energieträger: Bestimmung der vermiedenen Emissionen im Jahr 2016*]; Umweltbundesamt: Dessau-Rosslau, Germany, 2017.
60. Lajoie, B.; Corradi, O. *Electricity Map Average Carbon Intensity—Spain—2017*; Tomorrow: Copenhagen, Denmark, 2017.
61. Red Eléctrica de España. *The Spanish Electricity System 2017*; Red Eléctrica de España: Madrid, Spain, 2018.
62. Börjesson, P.; Hansson, J.; Berndes, G. Future demand for forest-based biomass for energy purposes in Sweden. *For. Ecol. Manag.* **2017**, *383*, 17–26. [[CrossRef](#)]
63. Philipp, M.; Schumm, G.; Peesel, R.H.; Walmsley, T.G.; Atkins, M.J.; Schlosser, F.; Hesselbach, J. Optimal energy supply structures for industrial food processing sites in different countries considering energy transitions. *Energy* **2018**, *146*, 112–123. [[CrossRef](#)]



© 2020 by the authors. Licensee MDPI, Basel, Switzerland. This article is an open access article distributed under the terms and conditions of the Creative Commons Attribution (CC BY) license (<http://creativecommons.org/licenses/by/4.0/>).

Article

Determination of Various Parameters during Thermal and Biological Pretreatment of Waste Materials

Robert Hren, Aleksandra Petrovič, Lidija Čuček * and Marjana Simonič

Faculty of Chemistry and Chemical Engineering, University of Maribor, Smetanova ulica 17, SI-2000 Maribor, Slovenia; robert.hren1@student.um.si (R.H.); aleksandra.petrovic@um.si (A.P.); marjana.simonc@um.si (M.S.)

* Correspondence: lidija.cucek@um.si; Tel.: +386-2-229-44-54

Received: 3 April 2020; Accepted: 1 May 2020; Published: 4 May 2020

Abstract: Pretreatment of waste materials could help in more efficient waste management. Various pretreatment methods exist, each one having its own advantages and disadvantages. Moreover, a certain pretreatment technique might be efficient and economical for one feedstock while not for another. Thus, it is important to analyze how parameters change during pretreatment. In this study, two different pretreatment techniques were applied: thermal at lower and higher temperatures (38.6 °C and 80 °C) and biological, using cattle rumen fluid at ruminal temperature (\approx 38.6 °C). Two different feedstock materials were chosen: sewage sludge and riverbank grass (*Typha latifolia*), and their combinations (in a ratio of 1:1) were also analyzed. Various parameters were analyzed in the liquid phase before and after pretreatment, and in the gas phase after pretreatment. In the liquid phase, some of the parameters that are relevant to water quality were measured, while in the gas phase composition of biogas was measured. The results showed that most of the parameters significantly changed during pretreatments and that lower temperature thermal and/or biological treatment of grass and sludge is suggested for further applications.

Keywords: waste materials; sewage sludge; riverbank grass; rumen fluid; pretreatment of waste; determination of parameters

1. Introduction

Depletion of the world's natural resources and an increase in the environmental footprint [1] has stimulated the increased utilization of renewable energy sources, resource efficiency, better waste management, circular economy and sustainability. Among the solutions is greater utilization of waste materials, which could partially address the challenges of resource depletion and ecosystem health. Waste materials are widely available and often mismanaged [2]. Developed and developing countries produce large amounts of waste per capita, with a significant increase in recent decades, owing to a higher level of consumption [3]. Waste management continues to improve in several countries; however, significant amounts of potential secondary raw materials are lost, such as metals, wood, paper and other waste streams [4]. Waste could also be a potential source of several value-added products, such as enzymes, fuels, fertilizers, pesticides, polymers, and plastics [5].

The use of several waste types is limited, despite their vast availability. Waste materials such as sewage sludge and organic waste contain significant amounts of elements such as carbon, nitrogen, phosphorus that could be efficiently used by thermal or biological processes [6]. The EU's Landfill Directive [7] requires that waste should be pretreated by physical, thermal, chemical or biological processes to reduce its negative impact on the environment and to help increase the scope of waste recycling and recovery. However, there are several limitations to their use, such as their complex structure, the non-homogeneity of waste and the presence of hazardous waste. On the other hand,

advances in microbiology, biotechnology and genetic engineering are leading to new concepts for converting these materials into valuable products [8].

Several solid waste products and waste from municipal sources have higher shares of lignocelluloses [9]. Such examples are agricultural residues, forest woody residues, industrial waste, microalgae and municipal solid waste [10]. Lignocellulosic materials are also widely abundant renewable materials, and are composed mainly of cellulose, hemicellulose, and lignin [11]. Pretreatment of waste materials facilitates further hydrolysis and fermentation [11] for the production of fuels, chemicals and other materials [12]. Pretreatment can partially remove lignin and hemicellulose, and often also cellulose (such as by cellulose-degrading enzymes [13], rumen fluid [14], white rot fungi [15], etc.). Ideally, pretreatment should be simple, with a low environmental footprint [16] and should be economically efficient [17], while it should produce pretreated substrate that is easily hydrolyzed/fermented, and should avoid the loss of the desirable fraction of the material and the formation of inhibitory compounds [18].

Pretreatment of waste materials could help in reducing the amount of waste, in stabilizing waste, overcoming the recalcitrance of lignocellulosic waste, and in more efficient utilization of waste materials as fuels and/or chemicals. Various pretreatment methods exist, which can be classified into chemical, physical, physico-chemical, biological and combined or multiple pretreatment methods. However, each pretreatment method acts differently on lignocellulosic structures [12]. Each method has only limited applications, as no pretreatment technique suits all types of waste material. Commonly used pretreatment techniques still do not meet sustainable industrial production requirements despite being studied for a number of years [17]. A combination of more than one pretreatment technique and/or novel techniques has the potential to significantly improve the efficiency of the process [17]. In order to better understand and improve specific pretreatment process(es), it is important to analyze the changes in the properties of waste materials during pretreatment [19].

The literature review has shown that there has been limited research on analyzing changes in the various parameters during pretreatment that are typical in related fields, such as wastewater characterization, anaerobic digestion and composting. Further, to the best of the authors knowledge, no studies have been performed on pretreatment of sewage sludge, grass and rumen fluid. The aim of this work was to examine the change of parameters during thermal pretreatment of sewage sludge and grass *Typha latifolia* and to investigate the impact of cattle rumen fluid (microbial consortium) presence on pretreatment.

In this work, various parameters have been measured during thermal and biological pretreatment of two waste materials, sewage sludge and riverbank grass (*Typha latifolia*), and their combination (1:1 ratio on a dry basis). Thermal pretreatment was studied at both an elevated temperature of 80 °C, which lasted for 5 days, and at milder conditions of 38.6 °C, which lasted for 8 days. Biological pretreatment was also studied at 38.6 °C by adding an enzyme mixture (cattle rumen fluid) to the waste materials. An analysis of various parameters in the liquid phase was conducted before and after pretreatment and in the gas phase after pretreatment. In the liquid phase, the following parameters were measured: nitrogen, phosphorus and potassium (NPK) content, total organic carbon (TOC), chemical oxygen demand (COD), pH and conductivity, and in the gas phase concentrations of CH₄, CO₂ and H₂S were measured.

2. Materials and Methods

In this section, applied materials and methods are described. First, collection of samples, their preparation for analysis and characterization are described, and then the experimental setup is presented, where two experiments were conducted under various conditions. The chemical analyses performed to determine various parameters during pretreatment are then described.

2.1. Feedstock Preparation and Characterization

The following feedstock materials were used in the experiments: riverbank grass *Typha latifolia* (G), sewage sludge (S) and rumen fluid (R). Sewage sludge was taken from a local municipal wastewater treatment plant (latitude and longitude coordinates of 46°24'29.3" N and 15°52'51.0" E) employing a tertiary biological treatment of wastewater in sequential basins with the capacity of 68,000 population equivalents (PE) and a maximal inflow of 350 L/s wastewater. The *Typha latifolia* grass (cattail) was gathered near the Dravinja riverbank near city Ptuj, Slovenia (coordinates of 46°21'01.5" N and 15°49'48.8" E). The *Typha latifolia* grass was chopped into pieces smaller than 1 × 0.5 cm before being used in experiments. Rumen fluid was acquired from a nearby slaughterhouse. Before it was used in experiments, it was filtered through fabric in order to remove larger particles. All feedstock materials were gathered in the middle of May 2019.

For the characterization of feedstock materials, the following analytical methods were used: SIST EN 16168:2013 for determining total nitrogen content using dry combustion [20], SIST EN ISO 11885:2009 by the inductively coupled plasma optical emission spectrometry (ICP-OES) analyzer for the total phosphorus content [21], SIST EN 13137:2002 for total organic carbon content based on catalytic oxidation combustion technique [22] and SIST EN 14346:2007 for the dry matter content [23]. The content of heavy metals was determined by the ICP-OES analyzer according to the EN 16170:2016 method [24]. For the determination of total dry solids content (TS), substrates were dried in a laboratory drying chamber (ED 115, producer Binder) at 105 °C until constant weight.

2.2. Experimental Setup

Two pretreatment methods were tested on selected waste: biological pretreatment with the addition of an enzyme mixture (i.e., cattle rumen fluid) and lower and higher temperature thermal pretreatment (at 38.6 and 80 °C). For biological pretreatment, the temperature was set at a ruminal temperature of about 38.6 °C [25]. The temperature of 38.6 °C was chosen, since it is within the mesophilic temperature range that is optimal for microorganisms' growth and metabolism, and it is an optimal temperature for microorganisms present in the rumen fluid.

For lower temperature thermal pretreatment (mesophilic temperature range, 38.6 °C) and biological pretreatment with rumen fluid, batch assays were maintained by using a Thermo Scientific™ SC100 immersion circulator in a heated bath filled with deionized water. Samples placed in 1 L glass containers were exposed to pretreatment conditions for 8 days. Assays in containers were hand-mixed two to three times during pretreatments. If necessary, to reduce the pressure in containers, the gases were released to the atmosphere and containers were closed shortly afterwards. Figure 1 shows schematic representation of the experimental set-up for lower temperature thermal and biological pretreatment.

Higher temperature thermal pretreatment at 80 °C was performed in a laboratory drying chamber (ED 115, Binder), where the pretreatment time was 5 days.

All samples were prepared in triplicate, containing 6 wt.% of solids based on average dry matter (DM) content. The samples were prepared on a 500 g wet basis (30 g dry basis) and are shown in Table 1. Reaction mixture G contains only grass substrate, while reaction mixture S contains only sludge (both were diluted by distilled water to 6 wt.%). Other samples represent mixtures of the chosen substrates. For example, sample G + S was a mixture of grass and sewage sludge in a ratio of 1:1. For biological pretreatment, in addition to 500 g of material (G, S and G+S) 50 mL of rumen fluid was added. The addition of rumen fluid in reaction mixtures is denoted as R.

2.3. Chemical Analyses

Before and after pretreatment studies, various parameters were measured in the liquid phase of the samples. Chemical oxygen demand (COD), total organic carbon (TOC), and the amounts of nitrogen, phosphorus and potassium (NPK) content were analyzed by cuvette tests. The following NANOCOLOR®(Macherey-Nagel) cuvette tests were used: CSB 160 and 1500,

TOC 300, TNb220, ortho-Phosphate 15 and Potassium 50. Digestion of samples was performed with a NANOCOLOR®VARIO C2 (Macherey-Nagel) heating block. Analyses of COD, TOC and NPK in filtered samples were determined photometrically using a compact photometer PF-12^{Plus} (Macherey-Nagel). The conductivity and pH were measured by using wireless pH and conductivity sensors (Pasco), which were connected through a tablet computer and recorded via the SPARKvue app.

Untreated samples were analyzed on the first day of the experiments (day zero) and are denoted in the next section as “untreated”. Samples from lower temperature thermal pretreatment at 38.6 °C and biological pretreatment (at the same temperature) were analyzed on the 8th day of the experiments, while samples from higher temperature thermal pretreatment at 80 °C were analyzed on the 5th day. The concentration of gases (CH₄, CO₂ and H₂S) formed during pretreatment in the gas phase was monitored by an Optima 7 Biogas analyzer. Measurements in the gas phase were performed on the last day of each experiment (on the 5th or 8th day of the experiments).

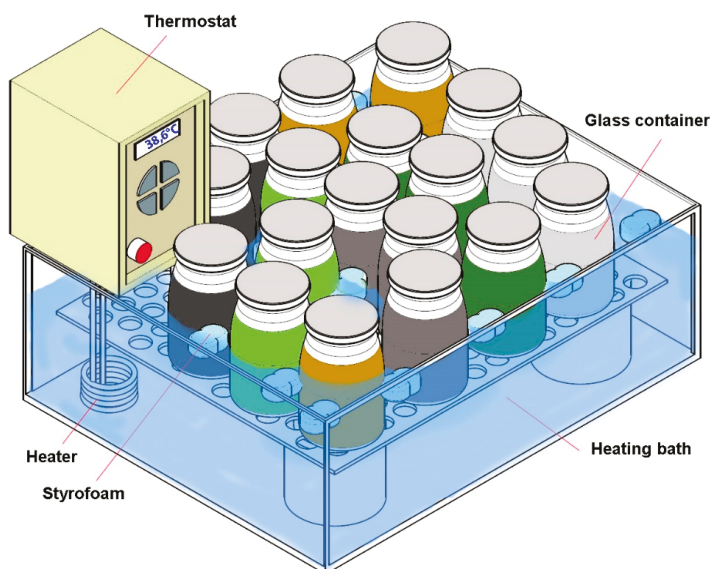


Figure 1. Schematic representation of set-up for thermal and biological pretreatment (illustration made by authors).

Table 1. Composition of samples used in pretreatment tests.

Reaction Mixture	Rumen Fluid (mL)	<i>Typha latifolia</i> Grass (g)	Sewage Sludge (g)	Water (g)
G (grass)	/	405.40	/	94.60
S (sludge)	/	/	161.27	338.73
G + S	/	202.70	80.65	216.65
G + R	50	405.40	/	94.60
S + R	50	/	161.27	338.70
G + S + R	50	202.70	80.65	216.65

The results of chemical analyses for treated and untreated samples were statistically tested (in Excel) for significant differences using the *t*-test (90% confidence level, two tailed, homoscedastic type). The deviations of the results between parallel samples were expressed with standard deviation and error bars (error bar represents one standard deviation).

3. Results and Discussion

In this section, results and discussion regarding the characterization of feedstock materials and pretreatment analysis are presented. First, results for the liquid phase are shown in Sections 3.2.1–3.2.4 (NPK, TOC, C/N ratio, COD, pH and conductivity) and results for the gas phase are presented in Section 3.2.5 (concentrations of CH₄, CO₂ and H₂S).

3.1. Feedstock Characterization Results

The basic characteristics of sewage sludge, *Typha latifolia* grass and cattle rumen fluid, such as total dry solids content (TS), water content, total nitrogen (TN) content, total phosphorus (TP) content and total carbon (TC) content are gathered in Table 2. Sewage sludge contained 18.6% of dry solids, grass 7.4% and rumen fluid 2.3%. The content of heavy metals and the content of TN were higher in sewage sludge samples than in the grass samples. As expected, grass contained high amounts of potassium (K), but did not contain much phosphorus (TP). Among heavy metals, the concentration of Zn ions stands out from the results for sewage sludge. Other values were in the range typical of sewage sludge [26] and grass samples [27].

3.2. Results of the Pretreatment Tests

In this section the results for the liquid phase are first given (they are shown before and after pretreatment), and subsequently the results for the gas phase are presented (shown after pretreatment).

3.2.1. Results of N, P and K Analysis

Concentrations of nitrogen, potassium and phosphorus (NPK) in the samples are expressed in the form of N, P₂O₅ and K₂O, since NPK values in the organic substrates are often expressed in that way [28]. Table 3 shows the results for P₂O₅ and K₂O content, and Figure 2 shows the content of TN.

Table 2. Basic characteristics of the materials in use.

Parameter	Sewage Sludge (S)	<i>Typha latifolia</i> Grass (G)	Rumen Fluid (R)
Total dry solids (TS, %)	18.60	7.40	2.34
Water content (%)	81.40	92.60	97.66
TN (% TS)	7.85	3.46	3.70
TP (% TS)	0.92	0.32	0.07
TC (% TS)	45.61	46.62	31.22
Cd (mg/kg DM)	1.01	1.03	/
Cu (mg/kg DM)	172.82	6.42	/
Cr (mg/kg DM)	46.36	1.39	/
Zn (mg/kg DM)	739.99	27.03	/
Ni (mg/kg DM)	24.55	1.72	/
Pb (mg/kg DM)	27.06	1.91	/
K (mg/kg DM)	8,211.80	34,398.43	/

Results in Table 3 show that the lowest concentrations of K₂O and P₂O₅ values were generally obtained in untreated samples (samples G or S). After lower temperature thermal pretreatment at 38.6 °C, concentrations of K₂O and P₂O₅ in all samples increased as compared to untreated samples (Table 3). The highest values of K₂O were obtained in the mixture of grass and sludge (sample G + S), while the highest P₂O₅ value occurred in the sludge sample (S). It is also interesting to note that in the case of biologically-pretreated samples with the addition of rumen fluid (samples G + R and G + S + R), the K₂O and P₂O₅ content decreased, compared to the same samples without rumen fluid. Based on these results, it can be concluded that enzymes and bacteria in rumen fluid break down the cell membranes and degrade these nutrients [29]. In addition, if anaerobic fermentation occurs because of the presence of enzymes in the sewage sludge, any released polyphosphate can be completely degraded to PO₄³⁻-P [30].

In the case of higher temperature thermal pretreatment (80 °C), concentrations of K₂O decreased, while the concentration of P₂O₅ increased slightly in comparison with the lower temperature pretreatment. Among all samples, the concentration of P₂O₅ was highest in the samples treated at 80 °C, especially for the S and G + S samples; this shows that thermal pretreatment deformed the chemical bonds in the sludge and grass, and thus P is released from the raw substrates. According to Zou and Li [30], the cell membranes of sludge could be disrupted via thermal pretreatment, so that P (mainly in the form of polyphosphate) could easily diffuse out of the cytoplasm. Kuroda et al. [31], on the other hand, discovered that nearly all the polyphosphate could be released from activated sludge simply by heating it at 70 °C for only a few hours.

Table 3. Concentration of potassium in the form of K₂O and phosphorus expressed as P₂O₅ in the samples.

Sample	K ₂ O (mg/L)	P ₂ O ₅ (mg/L)
G, untreated	1486 ± 89	476 ± 8
S, untreated	1120 ± 43	3554 ± 95
R, untreated	731 ± 19	1078 ± 21
G, 38.6 °C	5823 ± 47	679 ± 10
G + R, 38.6 °C	3092 ± 151	541 ± 26
S, 38.6 °C	2015 ± 113	4725 ± 77
S + R, 38.6 °C	3193 ± 95	3974 ± 49
G + S, 38.6 °C	11,747 ± 124	4146 ± 128
G + S + R, 38.6 °C	9940 ± 168	3991 ± 85
G, 80 °C	3855 ± 59	497 ± 37
S, 80 °C	1807 ± 62	5786 ± 152
G + S, 80 °C	6024 ± 87	4874 ± 74

For the purpose of the further use of these substrates for biofuels and biochemicals (e.g., for production of biogas and biofertilizer), a combination of grass and sludge is suggested rather than using mono substrates, owing to the high NPK content, which is efficient for biofertilizer production. However, it should be noted that such pretreated materials that contain sewage sludge have restricted further applications [32]. Figure 2 shows the results for total nitrogen concentrations (TN). The highest amount of TN was observed in the sewage sludge sample and its mixtures, which is in accordance with the fact that the raw sewage sludge contained more TN than grass or rumen fluid (as shown in Table 2).

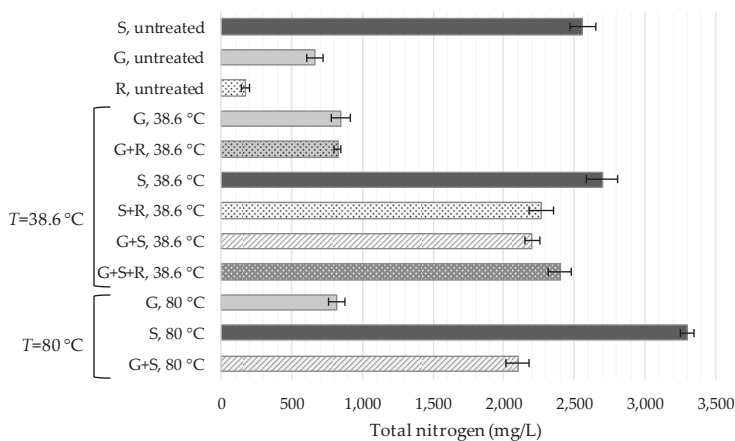


Figure 2. Concentrations of total nitrogen (mg/L).

With thermal pretreatment of samples at 38.6 °C, the amount of TN increased. The increase can be explained by the decomposition of proteins under the effect of heat and the action of microorganisms [33]. In the case of sewage sludge, the higher the temperature, the higher the TN concentration. The presence of anammox and denitrifying bacteria in the sludge (and also rumen fluid [34]) contribute importantly to the conversion of ammonium and nitrite into N₂ [35].

For mixtures of sludge and rumen fluid (S + R), concentration of TN decreased, compared to the sample containing only sludge (S) under the same conditions (38.6 °C). On the other hand, in the case of mixtures of grass, sludge and rumen fluid (G + S + R), the concentration of TN after pretreatment was higher than in the same mixture without rumen fluid (G + S). This indicates that rumen fluid actively participated in the degradation of grass, although the degradation mechanisms are still quite unclear, since the composition of rumen fluid is complex [36]. The main microbial population of rumen fluid includes bacteria, fungi, archaea, and protozoa, of which bacteria and fungi are mainly involved in lignocellulose degradation, while archaea are related to CH₄ formation [37]. The degradation process occurs via lignocellulolytic enzymes that are capable of digesting lignocellulosic materials (mainly consisting of cellulose, hemicellulose and lignin) into proteins, volatile fatty acids (VFAs) and gases [38].

At the highest pretreatment temperature (80 °C), TN concentrations were similar to those at the lower temperature (38.6 °C), while in the sample of sewage sludge (S) the concentrations were even higher. Similar results regarding TN release during thermal pretreatment have been reported previously [39].

Statistical *t*-tests performed for TN concentration show significant differences in the values between treated and untreated samples (at 90% confidence interval). The tests also showed significant differences among the different feedstock materials (sludge, grass, and rumen fluid). On the other hand, less significant differences were found in the case of biologically treated samples when compared to the same biologically untreated samples. The *t*-tests comparing results of the higher and lower temperature thermal pretreatment provided similar results, since in many cases the differences were insignificant.

3.2.2. TOC Values and C/N Ratio

An optimal C/N ratio in the feedstocks is important for the optimal growth of microorganisms [40], for the reduction of VFA accumulation [41], to prevent inhibition [39], to mitigate C and N emissions [42], to analyze organic matter in aquatic ecosystems [43], and for the production of lipids in yeasts [44], among other effects. For example, the optimal C/N ratio for anaerobic digestion [45] and composting [46] is between 20 and 30.

Sewage sludge is known for its lower C/N ratios due to high losses through ammonia emissions [47]. Similarly, low C/N ratios occur in slurries [41], manures [48] and slaughterhouse waste [49]. On the other hand, grass has a higher C/N ratio, between 10 and 25 [50]. For some biomass and waste sources, significantly higher values of C/N ratios have also been reported, up to more than 500 for wood shavings [50]. The C/N ratio is defined as the ratio between organic carbon (TOC) and total nitrogen (TN). Figure 3 shows the results for TOC values and the C/N ratio.

From Figure 3, it can be seen that the C/N ratios for untreated samples are within ranges as reported previously. As expected, the highest values were found in untreated grass samples (C/N ratio of 13.5). After thermal or biological pretreatment of the grass (G) samples, the C/N ratio decreased. There are various reasons for this decrease, one being that the C/N ratio decreased as a result of increased TN. Another reason for C/N decrease after biological pretreatment is that micro-organisms consume more carbon than nitrogen. The decrease in the C/N ratio could also be the result of a loss of carbon as CO₂ by mineralization during the process [33].

The C/N ratio for all pretreated samples at both temperatures was between 4 and 7. For the mixtures with sludge (S + R, G + S, G + S + R) after thermal treatment, the C/N ratios were still higher compared to those from the sludge samples (S), indicating that the presence of grass and rumen fluid did positively affect the C/N ratio. However, C/N ratios in all samples after pretreatment were significantly

lower than is suitable for anaerobic digestion and composting processes. Thus, the problem could be solved by mixing different organic substrates, such as grass and other organic waste.

TOC values in all samples containing sewage sludge (S) increased after thermal or biological pretreatment, and the highest value was detected in the sample thermally treated at 80 °C. These results confirmed that thermal pretreatment accelerates the biodegradation of materials such as sewage sludge and grass, and thus increases the TOC content in the liquid samples [39]. At a lower temperature (38.6 °C), the highest amount of organic carbon was released in the cases when rumen fluid was added to the reaction mixtures (S + R and G + S + R). This is in accordance with previous studies, where it has been reported that microbial cultures from rumen fluid have a great capacity to increase the hydrolysis of lignocellulosic substrates [51] such as grass [52]. Therefore, it can be concluded that rumen fluid significantly affects the biodegradation of organic materials. Thus, a combination of lower temperature thermal treatment and biological treatment could be interesting for such a purpose. Similar conclusions could be adopted for both the *t*-tests performed with the results of TOC measurements and those performed for TN concentration.

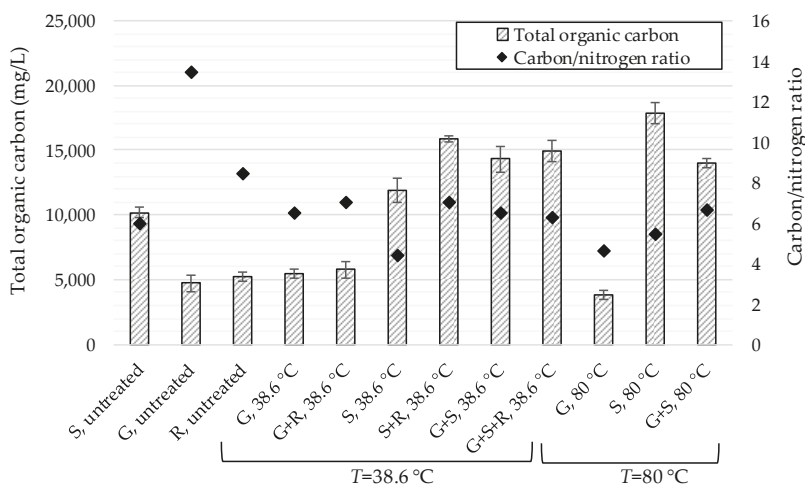


Figure 3. Total organic carbon (TOC) results (mg/L) and the carbon to nitrogen ratio (C/N).

3.2.3. Chemical Oxygen Demand (Soluble COD) Measurements

The COD represents the amount of oxygen required to oxidize organic material into water and CO₂ and is therefore a measure of the quantity of organic material present in the material. Values of soluble COD measurements before and after pretreatment are shown in Figure 4. In general, as shown, the highest COD values were measured in all the samples exposed to thermal pretreatment at 38.6 °C, while at 80 °C the values were lower (except for sewage sludge).

The COD values for the grass samples significantly increased after thermal pretreatment at 38.6 °C as compared to the untreated sample and decreased after thermal pretreatment at 80 °C as compared to the value at 38.6 °C. However, both values were higher than in the untreated sample.

This increase is in agreement with the findings of previous studies, which state that thermal pretreatment breaks down the cell walls, which enables the transfer of organic material to the liquid phase and consequently increases the COD [39]. A study by Ariunbaatar et al. [53] also confirmed that thermal pretreatment increased solubilization of organic solids and/or increased hydrolysis, making the substrates more available for anaerobic microorganisms; thus, in the subsequent anaerobic digestion process, biomethane production was enhanced.

As in the grass samples, the sewage sludge samples also yielded increased COD values after thermal pretreatment. After pretreatment at 38.6 °C, the highest COD was detected in the mixture of grass and sewage sludge (G + S). On the other hand, the presence of rumen fluid in the samples with grass (biological pretreatment at 38.6 °C) caused a slight drop in COD values. This can be explained by the fact that the microorganisms from the rumen fluid hydrolyze the macromolecules (lignocellulose and proteins) in the grass, thus reducing the amount of organic material [54]. Again, statistical hypothesis testing showed similar conclusions for TN and TOC measurements.

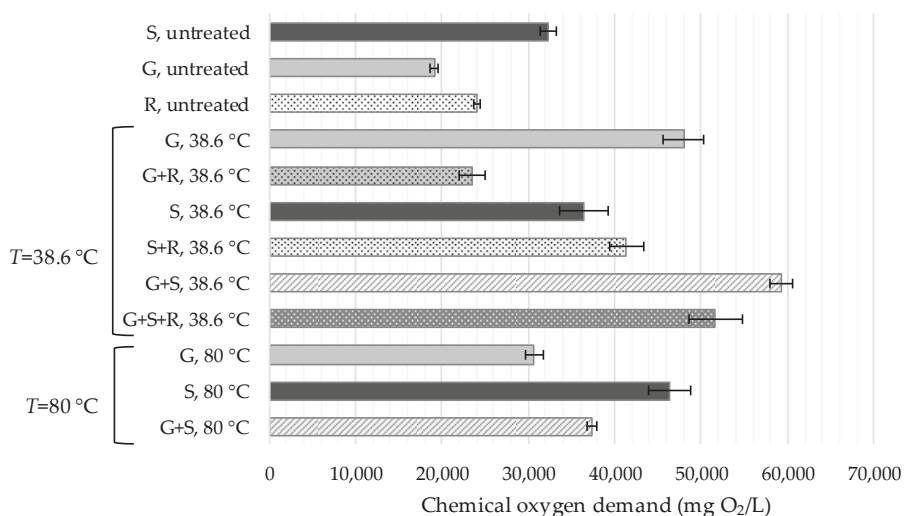


Figure 4. The soluble chemical oxygen demand (COD) results (mg O₂/L).

3.2.4. pH and Conductivity

Monitoring pH value is an indicator of the degree of biological and biochemical decomposition [33]. Electrical conductivity is a commonly used parameter for monitoring the amounts of nutrients, salts and impurities in the solution [55]. Since the composition of substrates could significantly change during pretreatment, pH and conductivity values could also significantly fluctuate. pH and conductivity measurements in the analyzed samples are shown in Figure 5.

pH values were generally higher in the untreated samples, and decreased during pretreatment, especially for the grass samples. This can be explained by the fact that, because of the degradation of organic compounds during thermal pretreatment, amino acids, ammonia and fatty acids are formed, which cause a drop in pH [29]. At higher temperatures, amino acids could also be degraded, and the pH increases again [56]. This can be clearly noticed in the sample with the combination of sewage sludge and grass (G + S), where an increase in pH is noticed at 80 °C, as compared with the pH value at 36.8 °C. Another interesting observation is that, in the case of samples containing only sewage sludge (S), the pH value after thermal pretreatment at 38.6 °C increased slightly and decreased after pretreatment at a higher temperature (80 °C). This could be related to the release of NH₄⁺, which could increase the pH of the solution when present in higher concentrations.

When biological pretreatment was performed, pH increased slightly with the addition of rumen fluid, most likely because of the slightly alkaline environment of rumen fluid (the pH of untreated sample was 7.5). For high degradation efficiency, maintaining a pH value in the optimal range is important, and the natural buffering ability of rumen fluid plays a major role in that process [57]. However, the optimal pH for most lignocellulose-degrading enzymes should be between 4.5 and 6.0 [58], and for methanogenic bacteria, the optimal range is between 6.6 and 7.6 [59], although a wider

range (between 6.5 and 8.2) has also been reported [60]. Hu et al. [52] reported that acidogenesis of cattail by rumen cultures is possible at higher pH (pH of 6.9). Similar values for treated samples were found in the present study (pH values between 5.1 and 7.2).

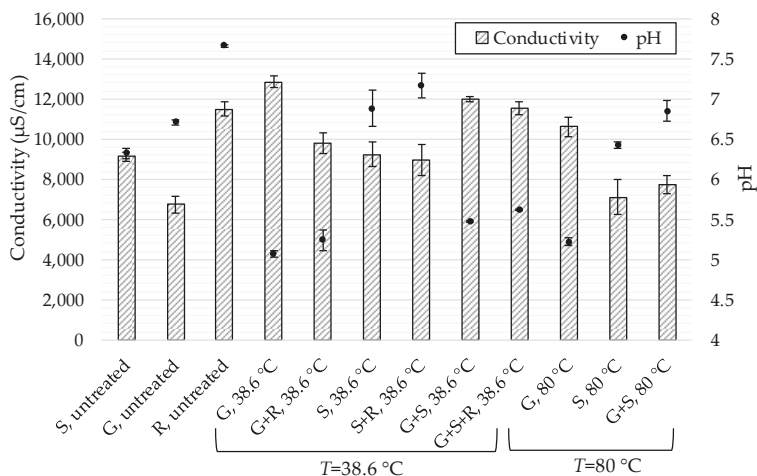


Figure 5. pH and conductivity ($\mu\text{S}/\text{cm}$) measurements.

Conductivity of the samples increased with pretreatment at lower temperatures ($38.6\text{ }^{\circ}\text{C}$) and decreased with pretreatment at higher temperatures ($80\text{ }^{\circ}\text{C}$). This can be confirmed by the findings of some authors who stated that electrical conductivity increases at temperatures up to $50\text{ }^{\circ}\text{C}$ and becomes linear over time with any further increase in temperature [61].

The highest conductivity was measured in the grass sample (G) after pretreatment at $38.6\text{ }^{\circ}\text{C}$, because ions were dissolved from the grass, which thus increased conductivity. In one of the previous studies [61], it was likewise found that with the temperature increase, the conductivity in vegetable materials increases up to four times. Since the composition of these materials is comparable to grass, similar findings could be expected.

High conductivity values were also noted in the case of a mixture of grass and sludge (G + S), and a combination of grass, sludge and rumen fluid (G + S + R). This is due to the presence of grass, since sludge exhibits smaller conductivity values. In all the samples with rumen fluid (G + R, S + R and G + S + R), conductivity decreases as compared to the samples without rumen fluid (G, S and G + S). On the other hand, the conductivity of untreated rumen fluid is relatively high, owing to dissolved ions. The decrease in conductivity in mixtures with rumen fluid could be connected to the buffering capacity of rumen fluid [62].

3.2.5. Gas Phase Composition

The composition of the gas phase in the samples is shown in Table 4. In the samples containing sewage sludge and/or rumen fluid pretreated at $38.6\text{ }^{\circ}\text{C}$, significant concentrations of CH_4 were observed in the gas phase. The addition of rumen fluid increases cell wall degradation and thus allows microorganisms easier access to nutrients; therefore, more CH_4 is formed [56].

Besides CH_4 , other gases such as CO_2 and H_2S were also analyzed and detected in the gas phase of the samples. The mixture of grass and rumen fluid (G + R) contains the highest amount of CO_2 . Rumen fluid degrades the lignocellulosic fibers in the grass and consumes oxygen, which leads to CO_2 increase [63]. Accordingly, CO_2 production could be used as an indicator of the degradation efficiency of lignocellulosic biomass during rumen fermentation [30].

The concentrations of H₂S were more significant in the samples containing rumen fluid (G + R and G + S + R). Slightly higher concentrations of this gas were found in mixtures containing grass. The production of H₂S comes mostly from microbial degradation of organic matter [64].

Table 4. Gas phase composition.

Sample	H ₂ S (ppm)	CH ₄ (%)	CO ₂ (%)
G, 38.6 °C	397 ± 49	0.13 ± 0.03	15.43 ± 3.60
G + R, 38.6 °C	1744 ± 293	6.26 ± 0.65	26.16 ± 4.24
S, 38.6 °C	237 ± 24	7.30 ± 0.46	14.23 ± 1.15
S + R, 38.6 °C	181 ± 48	13.88 ± 2.09	12.78 ± 1.88
G + S, 38.6 °C	881 ± 182	4.25 ± 0.40	12.25 ± 2.87
G + S + R, 38.6 °C	1003 ± 140	5.15 ± 0.08	13.42 ± 3.06
G, 80 °C	22 ± 1	0.07 ± 0.02	2.06 ± 0.16
S, 80 °C	24 ± 7	0.08 ± 0.03	2.45 ± 0.58
G+S, 80 °C	18 ± 4	0.06 ± 0.02	1.43 ± 0.40

On the other hand, when pretreatment was performed at 80 °C, production of the gases under analysis was negligible. The reason for such results is that bacteria in materials are highly active only in mesophilic ranges (between 25 and 42 °C) [65] and thermophilic ranges (between 50 and 65 °C) [66]. At temperatures below 15 °C and above 70 °C, methanogenic bacteria are limited in activity [67].

4. Conclusions and Future Research

In this study, thermal and biological pretreatment techniques were applied to two waste materials: sewage sludge and riverbank grass (*Typha latifolia*) and their combination (in the ratio 1:1). Lower and higher temperature thermal pretreatments (at 38.6 and 80 °C) and biological pretreatments (at a ruminal temperature of 38.6 °C) were studied. Various parameters were measured in the liquid and gas phases.

NPK, TOC and COD values, and the C/N ratio showed that low temperature thermal treatment is preferred, because of its better biodegradation characteristics of waste materials. pH values were mainly in the optimal range, while pretreated grass samples exhibited pH values below the optimal, which could be improved by biological pretreatment and mixing with other waste materials. Additionally, the results of the gas phase showed that the most suitable pretreatment technique(s) for further applications are low temperature thermal and/or biological treatment. The best result in the gas phase was obtained for biologically pretreated sludge, as it yielded the highest concentration of CH₄ and the lowest concentration of H₂S. Based on the results, it was found that pretreatment technique(s) should be carefully chosen, owing to some inhibitory effects at elevated temperatures, which could exert a negative impact on the further treatment of waste materials.

However, an important consideration for future studies is the further use of pretreated materials which contain sewage sludge, as it may contain heavy metals, pathogens and persistent organic pollutants (POPs). Thus, further handling of these materials is suggested, such as removal of heavy metals, extraction of POPs from sludge, reduction of pathogens and so on. Future studies could be aimed at further hydrolysis and fermentation of pretreated materials, and at identifying and reducing contaminants from treated sewage sludge.

Author Contributions: Conceptualization, L.Č. and M.S.; methodology, L.Č. and A.P.; investigation, R.H. and A.P.; writing—original draft preparation, R.H. and A.P.; writing—review and editing, L.Č. and M.S.; visualization, R.H. and A.P.; supervision, L.Č.; project administration, A.P. and L.Č.; funding acquisition, L.Č. and A.P. All authors have read and agreed to the published version of the manuscript.

Funding: The authors acknowledge financial support from the Slovenian Research Agency (research core funding No. P2-0412 and P2-0032 and project No. J7-1816) and the Slovenian Ministry of Education, Science and Sport (project No. C3330-19-952041). The authors also acknowledge support in chemical analytics and consultancy in the field of sewage sludge management from the IKEMA d.o.o. company.

Conflicts of Interest: The authors declare no conflict of interest.

Nomenclature

COD	Chemical oxygen demand
C/N	Carbon/Nitrogen ratio
DM	Dry matter
G	Grass <i>Typha latifolia</i>
ICP-OES	Inductively coupled plasma optical emission spectrometry
NPK	Nitrogen (N), phosphorus (P ₂ O ₅) and potassium (K ₂ O)
PE	Population Equivalent
POP	Persistent organic pollutants
R	Rumen fluid
S	Sewage sludge
TC	Total carbon
TN	Total nitrogen
TOC	Total organic carbon
TP	Total phosphorus
TS	Total solids
VFA	Volatile fatty acid

References

1. Čuček, L.; Klemeš, J.J.; Varbanov, P.S.; Kravanja, Z. Significance of environmental footprints for evaluating sustainability and security of development. *Clean Technol. Environ. Policy* **2015**, *17*, 2125–2141. [CrossRef]
2. Bezama, A.; Agamuthu, P. *Addressing the Big Issues in Waste Management*; SAGE: London, UK, 2019.
3. Ferronato, N.; Torretta, V. Waste Mismanagement in Developing Countries: A Review of Global Issues. *Int. J. Environ. Res. Public Health* **2019**, *16*, 1060. [CrossRef] [PubMed]
4. European Commission. Waste. Available online: ec.europa.eu/environment/waste/index.htm (accessed on 28 March 2020).
5. Balasubramanian, S.; Tyagi, R.D. 2—Value-Added Bio-products From Sewage Sludge. In *Current Developments in Biotechnology and Bioengineering*; Wong, J.W.C., Tyagi, R.D., Pandey, A., Eds.; Elsevier: Amsterdam, The Netherlands, 2017; pp. 27–42.
6. Alibardi, L.; Cossu, R. Composition variability of the organic fraction of municipal solid waste and effects on hydrogen and methane production potentials. *Waste Manag.* **2015**, *36*, 147–155. [CrossRef] [PubMed]
7. European Parliament and the Council of the European Union. Directive (EU) 2018/850 of the European Parliament and of the Council of 30 May 2018 Amending Directive 1999/31/EC on the Landfill of Waste. Available online: <https://eur-lex.europa.eu/legal-content/EN/TXT/PDF/?uri=CELEX:32018L0850&from=EN> (accessed on 3 May 2020).
8. Behera, S.; Arora, R.; Nandhagopal, N.; Kumar, S. Importance of chemical pretreatment for bioconversion of lignocellulosic biomass. *Renew. Sustain. Energy Rev.* **2014**, *36*, 91–106. [CrossRef]
9. Anawar, H.M.; Strezov, V. Technical and Economic Assessment of Biogas and Liquid Energy Systems from Sewage Sludge and Industrial Waste: Lifecycle Assessment and Sustainability. In *Renewable Energy Systems from Biomass*; CRC Press: Boca Raton, FL, USA, 2018; pp. 57–73.
10. Fatma, S.; Hameed, A.; Noman, M.; Ahmed, T.; Shahid, M.; Tariq, M.; Sohail, I.; Tabassum, R. Lignocellulosic biomass: A sustainable bioenergy source for the future. *Protein Pept. Lett.* **2018**, *25*, 148–163. [CrossRef]
11. Kumar, A.K.; Sharma, S. Recent updates on different methods of pretreatment of lignocellulosic feedstocks: A review. *Bioresour. Bioprocess.* **2017**, *4*, 7. [CrossRef]
12. Seidl, P.R.; Goulart, A.K. Pretreatment processes for lignocellulosic biomass conversion to biofuels and bioproducts. *Curr. Opin. Green Sustain. Chem.* **2016**, *2*, 48–53. [CrossRef]
13. Kumar, A.K.; Parikh, B.S. Cellulose-degrading enzymes from *Aspergillus terreus* D34 and enzymatic saccharification of mild-alkali and dilute-acid pretreated lignocellulosic biomass residues. *Bioresour. Bioprocess.* **2015**, *2*, 7. [CrossRef]
14. Zhang, H.; Zhang, P.; Ye, J.; Wu, Y.; Fang, W.; Gou, X.; Zeng, G. Improvement of methane production from rice straw with rumen fluid pretreatment: A feasibility study. *Int. Biodeterior. Biodegrad.* **2016**, *113*, 9–16. [CrossRef]

15. Rouches, E.; Herpoël-Gimbert, I.; Steyer, J.P.; Carrere, H. Improvement of an anaerobic degradation by white-rot fungi pretreatment of lignocellulosic biomass: A review. *Renew. Sustain. Energy Rev.* **2016**, *59*, 179–198. [[CrossRef](#)]
16. Mahmud, N.; Rosentrater, K.A. Life-Cycle Assessment (LCA) of Different Pretreatment and Product Separation Technologies for Butanol Bioprocessing from Oil Palm Frond. *Energies* **2020**, *13*, 155. [[CrossRef](#)]
17. Hassan, S.S.; Williams, G.A.; Jaiswal, A.K. Emerging technologies for the pretreatment of lignocellulosic biomass. *Bioresour. Technol.* **2018**, *262*, 310–318. [[CrossRef](#)] [[PubMed](#)]
18. Agbor, V.B.; Cicek, N.; Sparling, R.; Berlin, A.; Levin, D.B. Biomass pretreatment: Fundamentals toward application. *Biotechnol. Adv.* **2011**, *29*, 675–685. [[CrossRef](#)] [[PubMed](#)]
19. Karimi, K.; Taherzadeh, M.J. A critical review on analysis in pretreatment of lignocelluloses: Degree of polymerization, adsorption/desorption, and accessibility. *Bioresour. Technol.* **2016**, *203*, 348–356. [[CrossRef](#)] [[PubMed](#)]
20. SIST EN 16168:2013. *Sludge, Treated Biowaste and Soil—Determination of Total Nitrogen Using Dry Combustion Method*; Slovenian Institute for Standardization (SIST): Ljubljana, Slovenia, 2013.
21. SIST EN ISO 11885:2009. *Water Quality—Determination of Selected Elements by Inductively Coupled Plasma Optical Emission Spectrometry (ICP-OES) (ISO 11885:2007)*; Slovenian Institute for Standardization (SIST): Ljubljana, Slovenia, 2009.
22. SIST EN 13137:2002. *Characterization of Waste—Determination of Total Organic Carbon (TOC) in Waste, Sludges and Sediments*; Slovenian Institute for Standardization (SIST): Ljubljana, Slovenia, 2002.
23. SIST EN 14346:2007. *Characterization of Waste—Alculation of Dry Matter by Determination of Dry Residue or Water Content*; Slovenian Institute for Standardization (SIST): Ljubljana, Slovenia, 2007.
24. EN 16170:2016. *Sludge, Treated Biowaste and Soil—Determination of Elements Using Inductively Coupled Plasma Optical Emission Spectrometry (ICP-OES)*; European Committee for Standardization: Brussels, Belgium, 2016.
25. Turbill, C.; Ruf, T.; Mang, T.; Arnold, W. Regulation of heart rate and rumen temperature in red deer: Effects of season and food intake. *J. Exp. Biol.* **2011**, *214*, 963–970. [[CrossRef](#)] [[PubMed](#)]
26. Fijalkowski, K.; Rorat, A.; Grobelak, A.; Kacprzak, M.J. The presence of contaminations in sewage sludge—The current situation. *J. Environ. Manag.* **2017**, *203*, 1126–1136. [[CrossRef](#)] [[PubMed](#)]
27. Bedoić, R.; Čuček, L.; Čosić, B.; Krajnc, D.; Smoljanić, G.; Kravanja, Z.; Ljubas, D.; Pukšec, T.; Duić, N. Green biomass to biogas—A study on anaerobic digestion of residue grass. *J. Clean. Prod.* **2019**, *213*, 700–709. [[CrossRef](#)]
28. Marliah, A.; Anhar, A.; Hayati, E. Combine organic and inorganic fertilizer increases yield of cucumber (*Cucumis sativus* L.). *IOP Conf. Ser. Earth Environ. Sci.* **2020**, *425*, 012075. [[CrossRef](#)]
29. Nguyen, L.N.; Nguyen, A.Q.; Jahir, M.A.H.; Guo, W.; Ngo, H.H.; Chaves, A.V.; Nghiem, L.D. Application of rumen and anaerobic sludge microbes for bio harvesting from lignocellulosic biomass. *Chemosphere* **2019**, *228*, 702–708. [[CrossRef](#)]
30. Zou, J.; Li, Y. Anaerobic fermentation combined with low-temperature thermal pretreatment for phosphorus-accumulating granular sludge: Release of carbon source and phosphorus as well as hydrogen production potential. *Bioresour. Technol.* **2016**, *218*, 18–26. [[CrossRef](#)]
31. Kuroda, A.; Takiguchi, N.; Gotanda, T.; Nomura, K.; Kato, J.; Ikeda, T.; Ohtake, H. A simple method to release polyphosphate from activated sludge for phosphorus reuse and recycling. *Biotechnol. Bioeng.* **2002**, *78*, 333–338. [[CrossRef](#)] [[PubMed](#)]
32. Hudcová, H.; Vymazal, J.; Rozkošný, M. Present restrictions of sewage sludge application in agriculture within the European Union. *Soil Water Res.* **2019**, *14*, 104–120. [[CrossRef](#)]
33. Boutchich, G.E.K.; Tahiri, S.; Mahi, M.; Gallart-Mateu, D.; de la Guardia, M.; Aarfane, A.; Lhadi, E.; El Krati, M. Characterization of activated sludge from domestic sewage treatment plants and their management using composting and co-composting in aerobic silos. *J. Mater. Env. Sci.* **2015**, *6*, 2206–2220.
34. Liu, L.; Xu, X.; Cao, Y.; Cai, C.; Cui, H.; Yao, J. Nitrate decreases methane production also by increasing methane oxidation through stimulating NC10 population in ruminal culture. *AMB Express* **2017**, *7*, 76. [[CrossRef](#)]
35. Wang, X.; Yang, R.; Guo, Y.; Zhang, Z.; Kao, C.M.; Chen, S. Investigation of COD and COD/N ratio for the dominance of anammox pathway for nitrogen removal via isotope labelling technique and the relevant bacteria. *J. Hazard. Mater.* **2019**, *366*, 606–614. [[CrossRef](#)]

36. Henderson, G.; Cox, F.; Ganesh, S.; Jonker, A.; Young, W.; Abecia, L.; Angarita, E.; Aravena, P.; Nora Arenas, G.; Ariza, C.; et al. Rumen microbial community composition varies with diet and host, but a core microbiome is found across a wide geographical range. *Sci. Rep.* **2015**, *5*, 14567. [[CrossRef](#)]
37. Campanaro, S.; Treu, L.; Cattani, M.; Kougiass, P.G.; Vendramin, V.; Schiavon, S.; Tagliapietra, F.; Giacomini, A.; Corich, V. In vitro fermentation of key dietary compounds with rumen fluid: A genome-centric perspective. *Sci. Total Environ.* **2017**, *584–585*, 683–691. [[CrossRef](#)]
38. Xing, B.-S.; Han, Y.; Wang, X.C.; Ma, J.; Cao, S.; Li, Q.; Wen, J.; Yuan, H. Cow manure as additive to a DMBR for stable and high-rate digestion of food waste: Performance and microbial community. *Water Res.* **2020**, *168*, 115099. [[CrossRef](#)]
39. Risberg, K.; Sun, L.; Levén, L.; Horn, S.J.; Schnürer, A. Biogas production from wheat straw and manure—impact of pretreatment and process operating parameters. *Bioresour. Technol.* **2013**, *149*, 232–237. [[CrossRef](#)]
40. Baba, Y.; Tada, C.; Fukuda, Y.; Nakai, Y. Improvement of methane production from waste paper by pretreatment with rumen fluid. *Bioresour. Technol.* **2013**, *128*, 94–99. [[CrossRef](#)]
41. Karthikeyan, O.P.; Visvanathan, C. Bio-energy recovery from high-solid organic substrates by dry anaerobic bio-conversion processes: A review. *Rev. Environ. Sci. Bio/Technol.* **2013**, *12*, 257–284. [[CrossRef](#)]
42. Brassard, P.; Godbout, S.; Raghavan, V.; Palacios, J.H.; Grenier, M.; Zegan, D. The Production of Engineered Biochars in a Vertical Auger Pyrolysis Reactor for Carbon Sequestration. *Energies* **2017**, *10*, 288. [[CrossRef](#)]
43. Venkatesh, M. Appraisal of the carbon to nitrogen (C/N) ratio in the bed sediment of the Betwa River, Peninsular India. *Int. J. Sediment Res.* **2020**, *35*, 69–78. [[CrossRef](#)]
44. Yang, S.; Wang, W.; Wei, H.; Van Wychen, S.; Pienkos, P.T.; Zhang, M.; Himmel, M.E. Comparison of Nitrogen Depletion and Repletion on Lipid Production in Yeast and Fungal Species. *Energies* **2016**, *9*, 685. [[CrossRef](#)]
45. Zheng, Z.; Liu, J.; Yuan, X.; Wang, X.; Zhu, W.; Yang, F.; Cui, Z. Effect of dairy manure to switchgrass co-digestion ratio on methane production and the bacterial community in batch anaerobic digestion. *Appl. Energy* **2015**, *151*, 249–257. [[CrossRef](#)]
46. Zhu, N. Effect of low initial C/N ratio on aerobic composting of swine manure with rice straw. *Bioresour. Technol.* **2007**, *98*, 9–13. [[CrossRef](#)]
47. Żukowska, G.; Mazurkiewicz, J.; Myszcza, M.; Czekala, W. Heat Energy and Gas Emissions during Composting of Sewage Sludge. *Energies* **2019**, *12*, 4782. [[CrossRef](#)]
48. Neshat, S.A.; Mohammadi, M.; Najafpour, G.D.; Lahijani, P. Anaerobic co-digestion of animal manures and lignocellulosic residues as a potent approach for sustainable biogas production. *Renew. Sustain. Energy Rev.* **2017**, *79*, 308–322. [[CrossRef](#)]
49. Zver, A.; Bernik, R.; Mihelič, R. Effect of Pressure on the Removal of NH₃ from Hydrolyzed and Pre-Fermented Slaughterhouse Waste for Better Biomethanization. *Energies* **2019**, *12*, 1868. [[CrossRef](#)]
50. Steffen, R.; Szolar, O.; Braun, R. *Feedstocks for Anaerobic Digestion*; Institute of Agrobiotechnology Tulin, University of Agricultural Sciences: Vienna, Austria, 1998.
51. Čater, M.; Zorec, M.; Logar, R.M. Methods for improving anaerobic lignocellulosic substrates degradation for enhanced biogas production. *Springer Sci. Rev.* **2014**, *2*, 51–61. [[CrossRef](#)]
52. Hu, Z.-H.; Yu, H.-Q. Anaerobic digestion of cattail by rumen cultures. *Waste Manag.* **2006**, *26*, 1222–1228. [[CrossRef](#)] [[PubMed](#)]
53. Ariunbaatar, J.; Panico, A.; Yeh, D.H.; Pirozzi, F.; Lens, P.N.L.; Esposito, G. Enhanced mesophilic anaerobic digestion of food waste by thermal pretreatment: Substrate versus digestate heating. *Waste Manag.* **2015**, *46*, 176–181. [[CrossRef](#)] [[PubMed](#)]
54. Dölle, K.; Wagnmüller, F. Determination of the Chemical Oxygen Demand (COD) of Hydrothermal Pretreated Hay Samples. *Curr. J. Appl. Sci. Technol.* **2015**, *8*, 356–360. [[CrossRef](#)]
55. Zhang, J.; Li, D.; Wang, C.; Ding, Q. An Intelligent Four-Electrode Conductivity Sensor for Aquaculture. In Proceedings of the Computer and Computing Technologies in Agriculture VI, Zhangjiajie, China, 19–21 October 2012; pp. 398–407.
56. Budiyo, B.; Widiyasa, I.N.; Johari, S.; Sunarso, S. Increasing biogas production rate from cattle manure using rumen fluid as inoculums. *Int. J. Sci. Eng.* **2014**, *6*, 31–38. [[CrossRef](#)]
57. Xing, B.-S.; Han, Y.; Wang, X.C.; Wen, J.; Cao, S.; Zhang, K.; Li, Q.; Yuan, H. Persistent action of cow rumen microorganisms in enhancing biodegradation of wheat straw by rumen fermentation. *Sci. Total Environ.* **2020**, *715*, 136529. [[CrossRef](#)] [[PubMed](#)]

58. Lange, L.; Pilgaard, B.; Herbst, F.-A.; Busk, P.K.; Gleason, F.; Pedersen, A.G. Origin of fungal biomass degrading enzymes: Evolution, diversity and function of enzymes of early lineage fungi. *Fungal Biol. Rev.* **2019**, *33*, 82–97. [[CrossRef](#)]
59. Bermúdez-Penabad, N.; Kennes, C.; Veiga, M.C. Anaerobic digestion of tuna waste for the production of volatile fatty acids. *Waste Manag.* **2017**, *68*, 96–102. [[CrossRef](#)] [[PubMed](#)]
60. Carotenuto, C.; Guarino, G.; Morrone, B.; Minale, M. Temperature and pH effect on methane production from buffalo manure anaerobic digestion. *Int. J. Heat Technol.* **2016**, *34*, S425–S429. [[CrossRef](#)]
61. Wang, W.C.; Sastry, S.K. Changes in electrical conductivity of selected vegetables during multiple thermal treatments. *J. Food Process Eng.* **1997**, *20*, 499–516. [[CrossRef](#)]
62. Le Ruyet, P.; Tucker, W. Ruminant buffers: Temporal effects on buffering capacity and pH of ruminal fluid from cows fed a high concentrate diet. *J. Dairy Sci.* **1992**, *75*, 1069–1077. [[CrossRef](#)]
63. Qiao, W.; Yan, X.; Ye, J.; Sun, Y.; Wang, W.; Zhang, Z. Evaluation of biogas production from different biomass wastes with/without hydrothermal pretreatment. *Renew. Energy* **2011**, *36*, 3313–3318. [[CrossRef](#)]
64. Long, Y.; Fang, Y.; Shen, D.; Feng, H.; Chen, T. Hydrogen sulfide (H₂S) emission control by aerobic sulfate reduction in landfill. *Sci. Rep.* **2016**, *6*, 38103. [[CrossRef](#)] [[PubMed](#)]
65. Thomas, C.; Idler, C.; Ammon, C.; Herrmann, C.; Amon, T. Inactivation of ESBL-/AmpC-producing *Escherichia coli* during mesophilic and thermophilic anaerobic digestion of chicken manure. *Waste Manag.* **2019**, *84*, 74–82. [[CrossRef](#)] [[PubMed](#)]
66. Sánchez-Ramírez, J.E.; Pastor, L.; Martí, N.; Claros, J.; Doñate, S.; Bouzas, A. Analysis of uncontrolled phosphorus precipitation in anaerobic digesters under thermophilic and mesophilic conditions. *Environ. Technol.* **2019**, 1–10. [[CrossRef](#)]
67. De Vrieze, J.; Hennebel, T.; Boon, N.; Verstraete, W. Methanosarcina: The rediscovered methanogen for heavy duty biomethanation. *Bioresour. Technol.* **2012**, *112*, 1–9. [[CrossRef](#)]



© 2020 by the authors. Licensee MDPI, Basel, Switzerland. This article is an open access article distributed under the terms and conditions of the Creative Commons Attribution (CC BY) license (<http://creativecommons.org/licenses/by/4.0/>).

Article

A Comparative Techno-Economic Analysis of Different Desalination Technologies in Off-Grid Islands [†]

Michael Castro, Myron Alcanzare, Eugene Esparcia, Jr. * and Joey Ocon *

Laboratory of Electrochemical Engineering (LEE), Department of Chemical Engineering, University of the Philippines Diliman, Diliman 1101, Philippines; mtcastro1@up.edu.ph (M.C.); mtalcanzare1@up.edu.ph (M.A.)

* Correspondence: eaesparcia@upd.edu.ph (E.E.J.); jdocon@up.edu.ph (J.O.)

[†] This paper is an extended version of our paper published in: Castro, M.T.; Esparcia, E.A.; Odulio, C.M.F.; Ocon, J.D. Technoeconomics of reverse osmosis as demand-side management for Philippine off-grid islands. *Chem. Eng. Trans.* **2019**, *76*, 1129–1134., also presented at 22nd Conference on Process Integration for Energy Saving and Pollution Reduction (PRES'19), Crete, Greece, 20–23 October 2019.

Received: 15 January 2020; Accepted: 23 April 2020; Published: 4 May 2020

Abstract: Freshwater in off-grid islands is sourced from rain, groundwater, or mainland imports, which are unreliable, limited, and expensive, respectively. Sustainable freshwater generation from desalination of abundant seawater is another alternative worth exploring. Model-based techno-economic simulations have focused on reverse osmosis desalination due to its low energy consumption and decreasing costs. However, reverse osmosis requires frequent and costly membrane replacement. Other desalination technologies have advantages such as less stringent feedwater requirements, but detailed studies are yet to be done. In this work, a techno-economic comparison of multi-effect distillation, multi-stage flash, mechanical vapor compression, and reverse osmosis coupled with solar photovoltaic-lithium ion-diesel hybrid system was performed by comparing power flows to study the interaction between energy and desalination components. Optimization with projected costs were then performed to investigate future trends. Lastly, we used stochastic generation and demand profiles to infer uncertainties in energy and desalination unit sizing. Reverse osmosis is favorable due to low energy and water costs, as well as possible compatibility with renewable energy systems. Multi-effect distillation and multi-stage flash may also be advantageous for low-risk applications due to system robustness.

Keywords: desalination; multi-effect distillation; multi-stage flash; mechanical vapor compression; reverse osmosis; renewable energy

1. Introduction

Small off-grid islands have costly, limited, and intermittent supply of electricity and water due to dependence on importation. In the case of the Philippines, they are often electrified by diesel generators that are supplied with diesel imported from the mainland, resulting in high electricity prices (i.e., six times that of the mainland) because of high transportation costs [1]. In addition, freshwater for general purposes on these islands is sourced from an unreliable rainwater supply or a limited and vulnerable groundwater source [2]. Drinking water may be imported from the mainland at a cost of around 1 USD/L [3]. Economic activity on these islands are adversely affected as a result of the high costs of electricity and water. In particular, the International Labor Organization identified that freshwater scarcity hinders economic growth, as businesses would compete with residents for the resource [4]. The scarcity of clean freshwater can be solved through seawater desalination, but it is

energy intensive [5]. Putting additional conventional power generation capacity must be considered alongside desalination capacity, but this may be an unsustainable and more costly option [1]. In contrast, putting up renewable energy (RE) generation capacity to augment desalination may be more feasible because of the decreasing costs of solar photovoltaic (PV) [6] and battery energy storage systems (BESS) [7]. Hybrid energy systems consisting of solar PV, diesel generators, and energy storage were shown to reduce electricity costs in off-grid areas [8]. In the Philippines, Ocon and Bertheau estimated a 20% energy generation cost reduction for Philippine off-grid islands upon transition from a diesel-only system to a solar PV-based hybrid system [1], while Bertheau and Blechinger considered a 10-year load growth in their analysis and found the same trend [9]. Note that the works mentioned were focused on finding the lowest leveled cost of electricity only.

Table 1 summarizes the literatures that conducted feasibility studies for both energy and desalination systems. Some works have focus on the optimal combination of components. For example, Fernández-Gil and Petrakopoulou showed that implementing RE-desalination systems on Skyros Island, Greece yields freshwater at a cost of 2.75 USD/m³, which is 52% lower than imported freshwater [10]. Tafech et al. show that reverse osmosis (RO) powered by a PV-wind system can yield freshwater at a cost of 1.87 USD/m³ on King Island, Australia [11]. For comparison, the freshwater cost in those literatures reviewed are more expensive than that of mainland Philippine water cost which amounts to 0.70 USD/m³ [12]. Other works focused on dispatch algorithms. For instance, Gökçek simulated solar PV, wind, and diesel-based energy systems coupled with RO as an additional electrical load [13]. Corsini and Tortora demonstrated the load leveling capabilities of RO by absorbing excess RE generation in a PV-diesel hybrid system [14]. Lastly, Bognar et al. compared different RO dispatch strategies which shows both energy and water generation costs may be minimized by treating RO as a deferrable load [15]. Note that excessive desalination turndown could arise, which will damage the desalination plant [16].

Table 1. Summary of energy-desalination feasibility studies. RO: reverse osmosis; PV: photovoltaic.

Ref.	Energy				Desalination		Remarks
	PV	Wind	Diesel	Batt	RO	Other	
[17]	✓	✓	✓		✓		<ul style="list-style-type: none"> Case study in off-grid areas in Iraq Solar-wind-diesel-RO system has lowest water generation costs
[11]	✓	✓	✓	✓	✓		<ul style="list-style-type: none"> Case study based on King Island, Australia Solar PV-RO has the lowest water generation cost Water storage important for dealing with uncertainties
[18]	✓	✓			✓		<ul style="list-style-type: none"> Case study in Algarve, Portugal Decentralized system yields lowest generation cost
[19]					✓	✓	<ul style="list-style-type: none"> Economic feasibility of supplying water demand of US coastline via RO US electricity consumption will increase by only 0.5%
[10]					✓	✓	<ul style="list-style-type: none"> Case study in Skyros, Greece Freshwater generated from desalination is cheaper than imported freshwater
[20]					✓		<ul style="list-style-type: none"> Compared different brackish water RO methods Batch and closed-circuit desalination designs are energy efficient
[21]		✓			✓		<ul style="list-style-type: none"> Analyzed the use of desalinated water for agriculture Case study in Canary Islands, Spain

Table 2 compares different desalination technologies from different works in the literature, which generally shows insufficient technical detail. In contrast, research listed in Table 1 involve rigorous

model-based simulations, but are mostly limited to RO. This is not surprising considering that the technology has a low energy consumption [19] and decreasing investment costs [22], making it practical for installation. The technology constitutes the largest share of installed global desalination capacity with 69% of the global desalinated water production [23].

Table 2. Review of comparative desalination studies. MED: multi-effect distillation; MSF: multi-stage flash; MVC: mechanical vapor compression.

Ref.	Desalination				Remarks
	MED	MSF	MVC	RO	
[24]	✓	✓	✓	✓	<ul style="list-style-type: none"> • Discusses merits of other technologies • MED needs less pretreatment than RO • MVC has more compact installations
[25]	✓	✓	✓	✓	<ul style="list-style-type: none"> • Review of costing methodologies • Correlate desalination cost with installed capacity or growth rate
[26]	✓	✓		✓	<ul style="list-style-type: none"> • Parameters for logistic growth curves of cumulative installed capacity
[27]					<ul style="list-style-type: none"> • Estimated 29% learning rate¹ between desalination cost and cumulative installed capacity • Not specific to any desalination method
[22]				✓	<ul style="list-style-type: none"> • Estimated 15% learning rate¹ for RO
[28]	✓			✓	<ul style="list-style-type: none"> • Compared MED, RO, and novel capillary-driven desalination (CDD) • CDD has good balance between energy consumption and water production

¹ Learning rate in these studies refers to the percentage by which the cost of desalination decreases when the cumulative installed capacity doubles. Other definitions, such as those based on the doubling of cumulative generation, also exist [29].

RO is a membrane-based desalination technology in which saltwater passes through a semipermeable membrane that blocks ions and other contaminants. Freshwater is collected at the other end of the membrane [5]. In a continuous process, the feedwater channel, membrane, and freshwater permeate collectors are pressed and wound in a cylindrical package (Figure 1). At the center of the cylinder is the permeate tube with freshwater [30]. Despite its advantages, the technology is still hindered by frequent membrane degradation [31]. Many works have tackled the technical issue by using different membrane types [32] and managing membrane fouling [33]. This has led some studies to consider other desalination methods. Other membrane-based technologies include electrodialysis (ED), wherein saltwater is passed between alternating layers of anodic and cathodic exchange membranes. These membranes allow only anions and cations to pass, respectively. Ions are separated and trapped between every other layer when an electric field is applied, forming alternating layers of freshwater and brine [34].

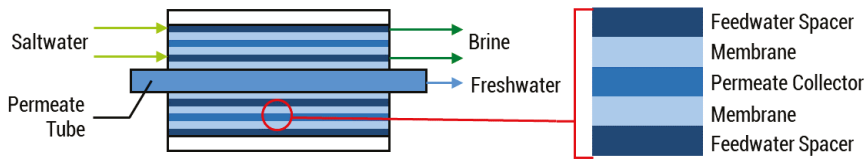


Figure 1. Reverse Osmosis (RO).

Thermal desalination systems generally produce freshwater from the vapors of heated saltwater [24]. An example is multi-effect distillation (MED, Figure 2). Saltwater is placed in a series of heat exchange vessels. The first stage receives external heating and some steam is produced. This steam serves as the heat source of the next stage and is collected as freshwater upon condensing. This is repeated across several stages. At the final stage, the steam preheats the feed saltwater before condensing [35]. Another thermal desalination system is multi-stage flash (MSF, Figure 3) [36]. The saltwater is heated using recovered heat and external heating sources. It is then flashed at the first stage to produce steam and concentrated saltwater. The steam condenses after heating the feed saltwater. The condensate is collected as freshwater. The concentrated saltwater is flashed at a lower pressure in the next stage. In mechanical vapor compression (MVC, Figure 4) [37], saltwater partially vaporizes in a closed vessel. The vapors are passed into a compressor, which raises the temperature of the vapor stream. Heat is then exchanged with the saltwater in the feed and the vessel to produce more vapor. Although this technology is classified as a thermal process, it does not use external heating sources [38]. MSF and MED constitute 18% and 7% of the global desalinated water generation, respectively [23].

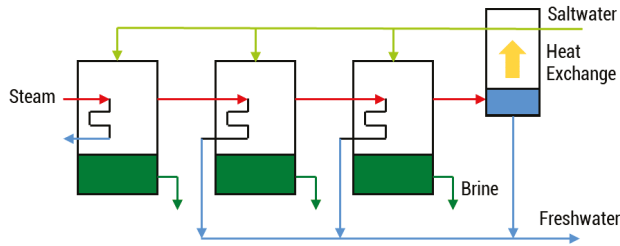


Figure 2. Multi-effect distillation (MED).

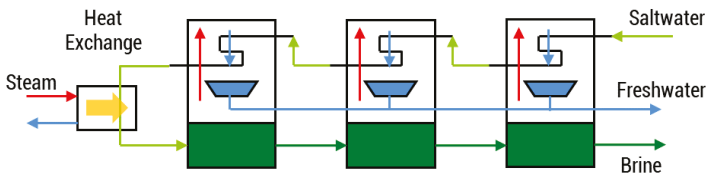


Figure 3. Multi-stage flash (MSF).

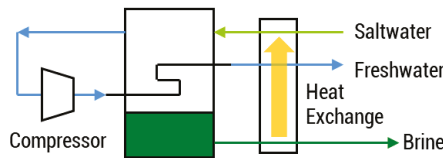


Figure 4. Mechanical vapor compression (MVC).

Performing techno-economic studies to integrate water desalination to the off-grid energy systems requires accurate models [39], while different economic dispatch algorithms must be tested as they generate varying results. In addition, results that use deterministic generation and demand profiles such as the literatures reviewed may not be accurate due to uncertainties in demand and/or RE generation [40]. Lastly, results that use constant cost over time may also not be accurate as it is expected that desalination costs will decrease as the technology matures [26]. For the Philippine context, Castro et al. have reviewed different RO dispatch algorithms. The results suggest that treating RO as a sink while demanding additional generation when water storage is low can minimize water generation costs [41]. However, testing the techno-economic feasibility of different desalination technologies under different economic dispatch algorithms while accounting stochastic behavior of generation and demand profiles and projected decreasing technology has not been done yet.

In this work, a techno-economic comparison of MED, MSF, MVC, and RO desalination coupled to a solar PV-diesel hybrid system with lithium ion (Li-ion) BESS is performed. The desalination technologies were selected based on their commercial maturity. The analysis of the desalination technologies was divided into four parts. First, the optimum sizes of energy and desalination components and their uncertainties were determined using stochastic generation and demand profiles. Second, power flows were generated to investigate the interaction between energy and desalination components. Third, energy and water generation costs were calculated at different starting periods to analyze the risks and tradeoffs of delaying plant construction. Lastly, a sensitivity analysis of optimum sizes to the overnight diesel and coal cost was conducted to account for uncertainties in diesel prices.

2. Materials and Methods

2.1. System Architecture

The coupling of the energy and water system is shown in Figure 5. The energy system supplies both the electrical demand of the island and the desalination unit. The electrical demand of the desalination system depends on the water storage level and is discussed further in Section 2.3. If excess RE generation is present, it is dispatched to the desalination system to generate more water. The generated water is sent to the water storage, from where the water demand is drawn. Details on the operation of the energy system is shown in Appendix A.

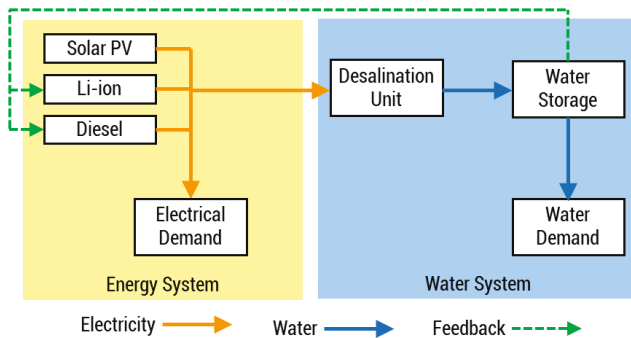


Figure 5. Architecture of the coupled energy and water system.

2.2. Modelling Approach

The calculations were performed using Island System LCOE_{min} Algorithm (ISLA), an in-house microgrid optimization software written in Python 3. The solar PV, diesel, Li-ion BESS, and desalination modules in ISLA were used. Microgrid energy system optimizations were validated with HOMER Pro® (HOMER Energy LLC: Golden, CO, USA). The software simulates the interaction of energy

and water components for one representative year in hourly resolution and calculates the levelized cost of electricity (LCOE), levelized cost of water (LCOW), and net present costs (NPC) as shown in Equations (1)–(3), respectively [42]:

$$LCOE = \frac{CRF \cdot \sum_{el} C_i}{\sum_{t=0}^{8759} P_{ld}(t)\Delta t}, \tag{1}$$

$$LCOW = \frac{CRF \cdot \sum_{wt} C_i + LCOE \cdot \sum_{t=0}^{8759} P_{de}(t)\Delta t}{\sum_{t=0}^{8759} \dot{V}_{ld}(t)\Delta t}, \tag{2}$$

$$NPC = \sum C_i, \tag{3}$$

In the equations above, $P_{ld}(t)$ is the electrical load, $\dot{V}_{ld}(t)$ is the water demand, $P_{de}(t)$ is the power entering the desalination unit, $\sum_{el} C_i$ is the total annualized cost of electrical components, $\sum_{wt} C_i$ is the total annualized cost of water components, and $\sum C_i$ is the total annualized cost of all components. The capital recovery factor (CRF) is defined in Equation (4), wherein i is the discount rate and t_s is the project lifetime [y] [42]:

$$CRF = \frac{i(1+i)^{t_s}}{(1+i)^{t_s} - 1}, \tag{4}$$

ISLA finds the component sizes S_i that minimize the NPC as shown in Equation (5). The optimization is constrained such that both electricity and water demand are always satisfied during the representative year. These are formalized in Equations (6) and (7). In these equations, $P_{PV}(t)$, $P_{Li}(t)$, and $P_{ds}(t)$ are the power outputs of solar PV, Li-ion BESS, and diesel genset, respectively. $V_{tank}(t)$ is the volume of water in storage. These variables are subject to additional constraints based on the component models and sizes S_i . The models for energy and water components are discussed in Appendix A and Section 2.3, respectively.

$$\min NPC(S_i), \tag{5}$$

$$P_{PV}(t) + P_{Li}(t) + P_{ds}(t) \geq P_{ld}(t) + P_{de}(t) \quad \forall t \in [0, 8759], t \in \mathbb{N}, \tag{6}$$

$$V_{tank}(t) \geq \dot{V}_{ld}(t)\Delta t \quad \forall t \in [0, 8759], t \in \mathbb{N}, \tag{7}$$

The optimization process is performed using an iterative search space algorithm as demonstrated in Figure 6. Sets of component sizes are generated, and the NPC of each combination is calculated. The combination with the lowest NPC is selected, and a finer search space is generated from this combination. The generation of the initial search space is crucial to obtain a proper optimum value, which is discussed further in Appendix B.

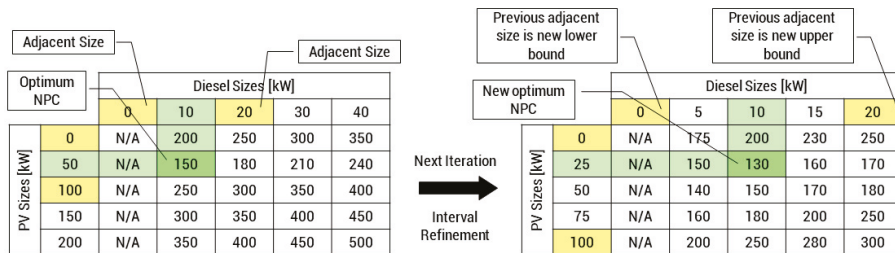


Figure 6. Iterative search space algorithm used by Island System LCOE_{min} Algorithm (ISLA) on a hypothetical PV-Diesel system. N/A values in the figure indicate a technically infeasible system and are ignored. LCOE: levelized cost of electricity.

2.3. Desalination Model

The energy required for a desalination plant to generate one volumetric unit of freshwater is defined as the energy intensity (EI). It is divided into electrical energy intensity (EI_{el}) for mechanical processes and a thermal energy intensity (EI_{th}) for heating processes [19]. MVC and RO, which do not have external heating, have zero EI_{th} [19]. Equation (8) relates the EI_{el} to the water generated $\dot{V}_{de}(t)$ and the electrical power entering the desalination plant $P_{de}(t)$ at time t . For desalination technologies that require external heating, the mass of coal used $\dot{m}_{cl}(t)$ [kg/h] is given by Equation (9), wherein ΔH is the lower heating value of coal (17.89 MJ/kg) [43]:

$$\dot{V}_{de}(t) = \frac{P_{de}(t)}{EI_{el}}, \tag{8}$$

$$\dot{m}_{cl}(t) = \frac{P_{de}(t)}{\Delta H} \times \frac{EI_{th}}{EI_{el}}, \tag{9}$$

The generated water is then sent to a storage tank, where the water demanded is simultaneously drawn. This is summarized by Equation (10), wherein $V(t)$ is the volume of water in the tank, $\dot{V}_{ld}(t)$ is the water demand, and Δt is the simulation time step (1 h):

$$V(t + \Delta t) = V(t) + [\dot{V}_{de}(t) - \dot{V}_{ld}(t)]\Delta t, \tag{10}$$

The power that enters the desalination plant depends on the water level. If the water level is above 20%, then the minimum power requirement $P_{de}^{min}(t)$ depends on the turndown ratio (TDR). The TDR is the ratio between minimum and rated production, and operation below this point will damage the desalination plant. If the water level is below 20%, the minimum power requirement will be set to restore the water level to at least 20%. This is summarized by Equation (11), wherein V_{tank} is the volume of the storage tank:

$$P_{de}^{min}(t) = \begin{cases} \text{TDR} \cdot S_{de} & V(t) \geq 0.2V_{tank} \\ \frac{EI_{el}}{\Delta t} \left(0.2 - \frac{V(t)}{V_{tank}} \right) & V(t) < 0.2V_{tank} \end{cases}, \tag{11}$$

The EI and TDR of the considered desalination technologies are shown in Table 3.

Table 3. Energy intensity (EI) and turndown ratio (TDR) of desalination technologies.

Desalination	EI_{el} [kWh/m ³]	Ref.	EI_{th} [kWh/m ³]	Ref.	TDR	Ref.
MED	2.50	[44–46]	53.20	[44,45]	0.50	[47]
MSF	4.17	[44–46]	64.79	[44,45]	0.70	[48]
MVC	12.41	[19,45]	-	[19,44]	0.50	[49]
RO	4.35	[19,44,45]	-	[19,44]	0.33	[50]

2.4. Techno-Economic Assumptions

The techno-economic parameters as of 2015 of each desalination technology are shown in Table 4. The operating costs were adjusted so that electrical and thermal requirements were excluded, as these were modeled explicitly. The techno-economic parameters of the energy components are shown in Appendix C.

Table 4. Techno-economic parameters of desalination technologies.

Component	Parameter	Unit	Value	Ref.
MED	CapEx	USD/(m ³ /d)	1150	[25,46]
	OpEx	USD/m ³	0.232	[25]
	Lifetime	y	6	[31]
MSF	CapEx	USD/(m ³ /d)	1425	[25,46]
	OpEx	USD/m ³	0.232	[25]
	Lifetime	y	10	[51]
MVC	CapEx	USD/(m ³ /d)	1000	[52]
	OpEx	USD/m ³	0.232	[25]
	Lifetime	y	10	[51]
RO	CapEx	USD/(m ³ /d)	1250	[25,46]
	OpEx	USD/m ³	0.232	[25]
	Lifetime	y	10	[51]
Water Storage	CapEx	USD/m ³	1000	[13]
	OpEx	USD/m ³ /y	10	
	Lifetime	y	20	
Coal	Unit Cost	USD/kg	0.09	[53,54]
	Inflation Rate	%	3	

2.5. Future Costs

The capital cost of a desalination technology $C_{cap}(t)$ at year t is given by Equation (12). The capital cost decreases with the cumulative installed capacity $X(t)$ given by Equation (13). In these equations, a is a normalization constant, b is an empirical parameter based on learning rates, K is the saturation capacity, r is the growth rate, and t_m is the year when half of the saturation capacity is installed [26]. The parameter values for each desalination technology are given in Table 5, while the future cost parameters for energy components are shown in Appendix D.

$$\frac{C_{cap}(t)}{C_{cap}(2015)} = a[X(t)]^{-b}, \quad (12)$$

$$X(t) = \frac{K}{1 + \exp[-r(t - t_m)]}, \quad (13)$$

Table 5. Future cost parameters of desalination technologies.

Component	K [GW(h)]	r [y ⁻¹]	t_m [y]	Ref.	b	Ref.
MED	10.30	0.1126	2011	[26]	0.3771	[55]
MSF	21.10	0.0935	1999	[26]	0.5146	[55]
MVC	0.24	0.1888	1966	[56]	0.4941	[27]
RO	147.20	0.1256	2019	[22]	0.2345	[22]

2.6. Case Study

In this work, Camasusu Island, Masbate (12.2 °N; 123.2 °E) and Lubang Island, Occidental Mindoro (13.8 °N; 120.1 °E) in the Philippines are selected as case studies to represent small and big islands, respectively. The daily water demand profiles were estimated from the work of the California Public Utilities Commission [57], with monthly variations based on Griffin and Chang [58]. The resulting water demand profiles were scaled to meet the 20-L water requirement per day per capita estimate by the World Health Organization [56]. Camasusu and Lubang Island have a population of 532 and 18,556, respectively, which yields an annual water demand of 3.88×10^3 m³/y and 1.35×10^5 m³/y. This

estimate includes water for drinking and activities such as bathing and laundry [56]. The normalized water demand profile is shown in Figure 7. The details regarding demand and generation profiles of the energy components are given in Appendix E.

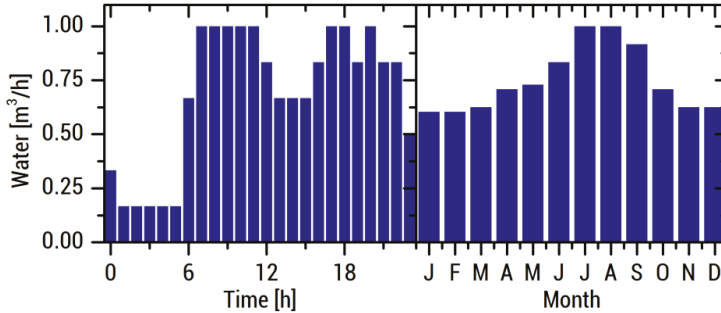


Figure 7. Normalized water demand profile. This is scaled up to match the annual demand. The left panel shows the daily average demand in hourly resolution, while the right panel shows the monthly variation over a year.

2.7. Stochastic Profile Generation

Stochastic energy and water demand profiles were generated using Equations (14) and (15). In these equations, $P_{ld}(t)$ and $\dot{V}_{ld}(t)$ are the deterministic energy and water profiles, $\delta_{hr}(t)$ is a random number that varies every hour, and $\delta_{dy}(t)$ varies every day. Both random numbers are drawn from a normal distribution centered at 0 with 5% variance. Generation of the stochastic hourly solar insolation profiles are discussed by Bendt et al. in [59] and Graham et al. in [60,61].

$$P_{ld}^{stoc}(t) = P_{ld}(t)[1 + \delta_{hr}(t) + \delta_{dy}(t)], \quad (14)$$

$$\dot{V}_{ld}^{stoc}(t) = \dot{V}_{ld}(t)[1 + \delta_{hr}(t) + \delta_{dy}(t)], \quad (15)$$

After each set of generation and demand profiles are formed, a Monte-Carlo approach calculated the corresponding optimum sizes and metrics 100 times to determine their distribution. The number of simulation points were chosen to balance computation time and accuracy.

3. Results

3.1. Optimum Sizes

Figures 8–10 present the results of the Monte-Carlo simulation. Figure 8 shows that diesel-favored systems need less energy storage capacity, while solar PV-favored systems will need larger Li-ion BESS capacities. For these hybrid systems, larger Li-ion BESS sizes indicate higher RE shares. Bimodal distributions indicate the possibility of either RE-favored generation or diesel-favored generation. Figure 8 also presents that low energy and water demand on an island such as in Camasusu would result in diesel-favored generation systems, as the installation costs for diesel-favored generations are lower than that of RE. At low energy demands, the large installation cost required makes RE less economical than diesel-generation. In contrast, larger islands with more energy and water demands such as in Lubang prefer RE-favored systems. On these islands, the large installation cost of RE is offset by the decreased fuel consumption.

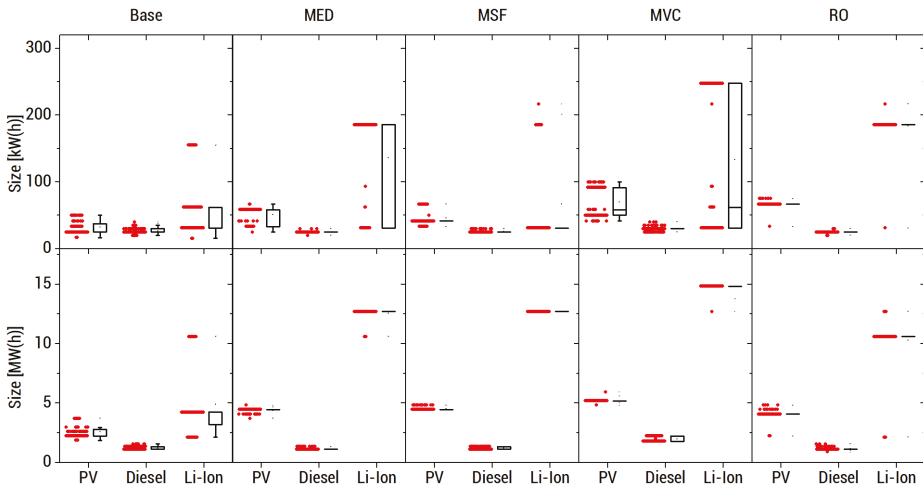


Figure 8. Distribution of optimum sizes of energy components on Camasusu Island (**top**) and Lubang Island (**bottom**). Systems in Camasusu have small Li-ion BESS installation sizes, except for RO, where the Li-ion BESS installation is large. Systems in Lubang have large Li-ion BESS installations.

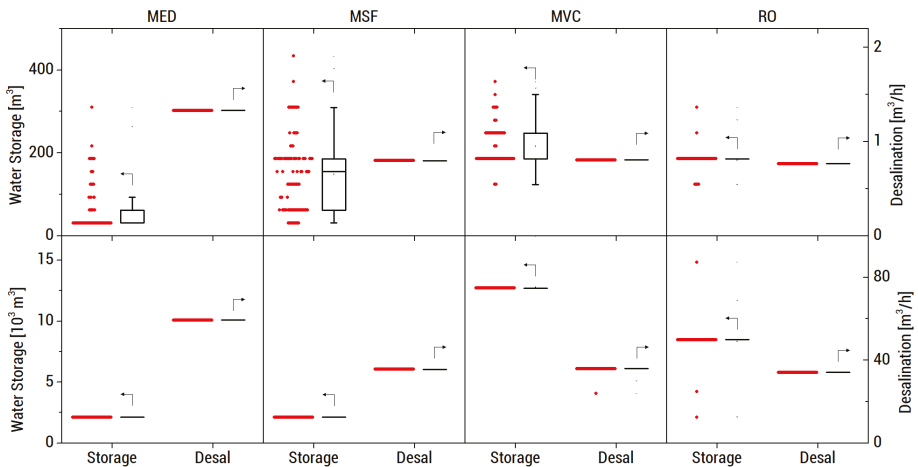


Figure 9. Distribution of optimum sizes of water storage (**left axis**) and desalination unit (**right axis**) on Camasusu Island (**top**) and Lubang Island (**bottom**). There is high uncertainty in the optimum water storage sizes in Camasusu, except for RO.

Figure 9 shows how diesel-dominated systems compensate for the lack of Li-ion BESS capacity. As these systems do not have energy storage, they use the desalination plant as an energy sink to produce and store water that will be utilized daily. The same figure presents that if the desalination plant is used as an energy sink, the resulting storage sizes for water have large uncertainty or spread. The RO system in Camasusu is an exception to the trends observed earlier. RO has a high turndown capability that allows RE intermittence as seen in the spread between solar PV and Li-ion BESS installation in Figure 8. In cases where RE is heavily preferred over diesel-generators, RO systems are suggested for small islands.

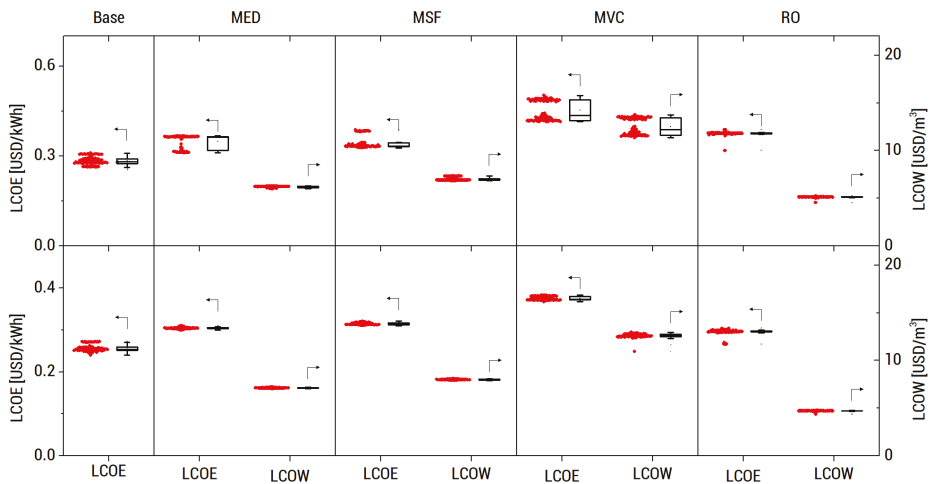


Figure 10. Distribution of optimum LCOE (left axis) and levelized cost of water (LCOW) (right axis) on Camasusu Island (top) and Lubang Island (bottom). The metrics of the MED and MVC systems in Camasusu exhibit a bimodal distribution.

As for the optimum metrics shown in Figure 10, RO desalination provides the lowest water generation costs from its low energy intensity and fuel independence. Electricity generation costs are comparable for MED, MSF, and RO because the corresponding desalination unit has low electricity consumption, although MED may achieve a lower cost. The larger Lubang Island has lower generation costs than Camasusu Island, further demonstrating the effectiveness of RE systems on larger islands. Figure 10 also reflects the importance of desalination turndown on the stability of generation costs. RO systems have a more distinct generation cost distribution because shortage in generation due to intermittencies is allowed by larger turndown; thus, additional generation capacity and the associated costs are unnecessary. In other systems, however, turndown is limited and therefore, intermittency is met with additional generation capacity. The amount of additional generation is unpredictable, and this reflects as uncertainties in generation costs.

3.2. Hourly Power and Water Flows

Figure 11 shows the power flows of a representative day associated with each desalination technology coupled with hybrid energy systems on both islands. The power flows confirm that systems on Camasusu Island are diesel-favored, while those on Lubang Island are RE-favored. An exception is the RO system on Camasusu Island, which uses an RE-favored system because of its high turndown capability. The diesel-favored systems have batteries that drain to 20% outside of sun-hours, which result in diesel generation to meet the baseload. In contrast, the RE-favored systems only utilize diesel generation during days with low solar irradiation.

Figure 12 compares the power consumed by the different desalination units and demonstrates how water is stored. In MED and MSF, water output is continuous because of the low turndown, increasing water level over time. In RO systems, however, water storage is drained until it reaches the minimum water level. After this, the RO plant will start producing water to meet the demand, explaining the uneven energy demand profile. Because of this, the RO system behaves as an additional load during the day. This is evidenced by the monthly average water level shown in Figure 13 wherein MED and MSF water storage tanks are full, while RO water storage is minimum.

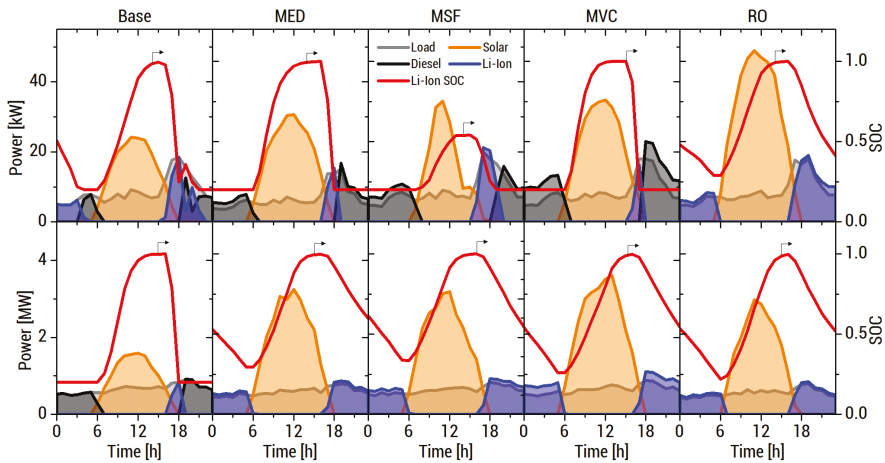


Figure 11. Hourly power output of electrical components and Li-ion BESS state of charge (SOC) on Camasusu Island (**top**) and Lubang Island (**bottom**). Li-ion BESS usage is high on Lubang Island.

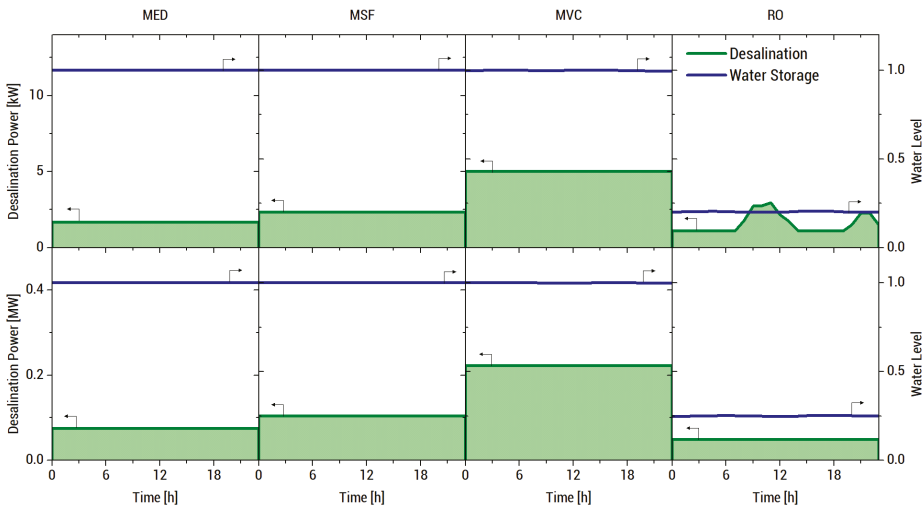


Figure 12. Hourly desalination energy consumption and water storage fraction on Camasusu Island (**top**) and Lubang Island (**bottom**). Power consumption is uneven in the RO system on Camasusu Island.

3.3. Future LCOE and LCOW

Figure 14 shows the projected LCOE and LCOW of one representative case for both islands from 2015 to 2050. Note that the LCOE and LCOW of a particular year does not account construction time. The results suggest that RO will provide the lowest water generation costs, followed by MED and MSF. MED, MSF, and RO have comparable electricity generation costs, which is also suggested by Figure 10. The systems in Camasusu and the MVC system in Lubang have a small price spike. This suggests a transition to RE-favored generation in the future.

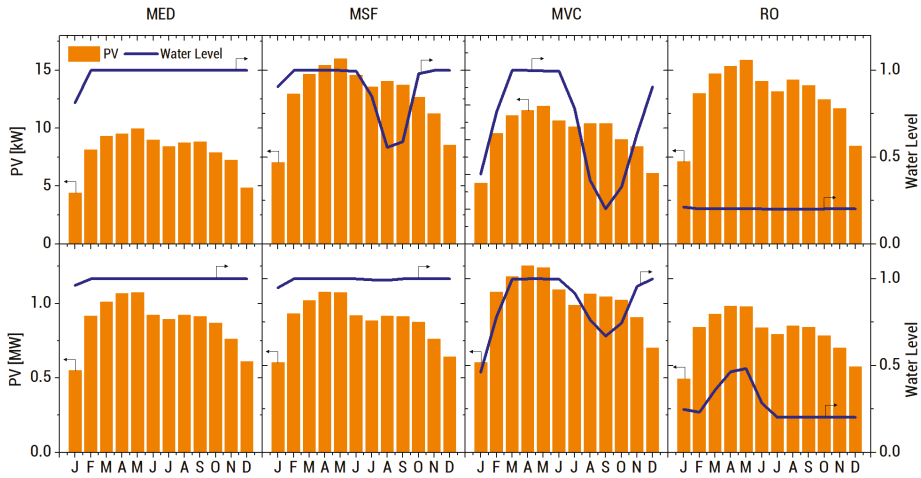


Figure 13. Monthly average PV power and water level on Camasusu Island (top) and Lubang Island (bottom). Note that stability of the system is ensured due to an imposed minimum water level of 20%.

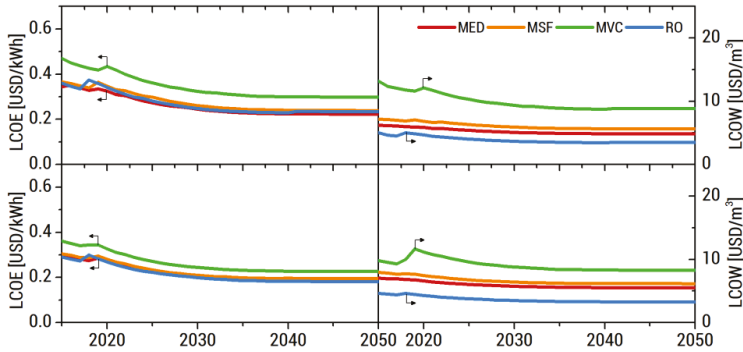


Figure 14. Projected LCOE and LCOW on Camasusu Island (top) and Lubang Island (bottom). The bumps near 2020 indicates a shift to a more RE-favored optimum configuration.

3.4. Sensitivity Analysis

3.4.1. -25% Overnight Fuel Cost

At a 25% decrease of the overnight diesel and coal price, the Li-ion BESS installation sizes sharply decreased, as shown by Figure 15. The bimodal distribution that was once present in MED and MVC systems in Camasusu have become a tight distribution, suggesting that RE-favored generation is no longer feasible. Systems on Lubang Island also favored diesel. Figure 16 also shows that all systems exhibit uncertainty in optimum storage sizes. Generation costs have decreased (Figure 17), especially for MVC, which consumes large quantities of diesel due to its high electrical energy intensity. Bimodal spreads of LCOE and LCOW have disappeared due to systems heavily favoring diesel over RE.

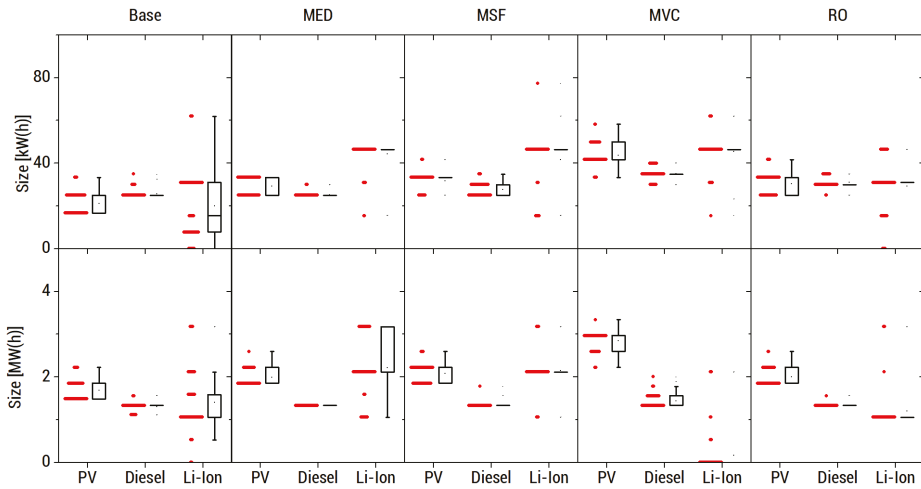


Figure 15. Distribution of optimum sizes of energy components on Camasusu Island (top) and Lubang Island (bottom) at -25% overnight fuel price.

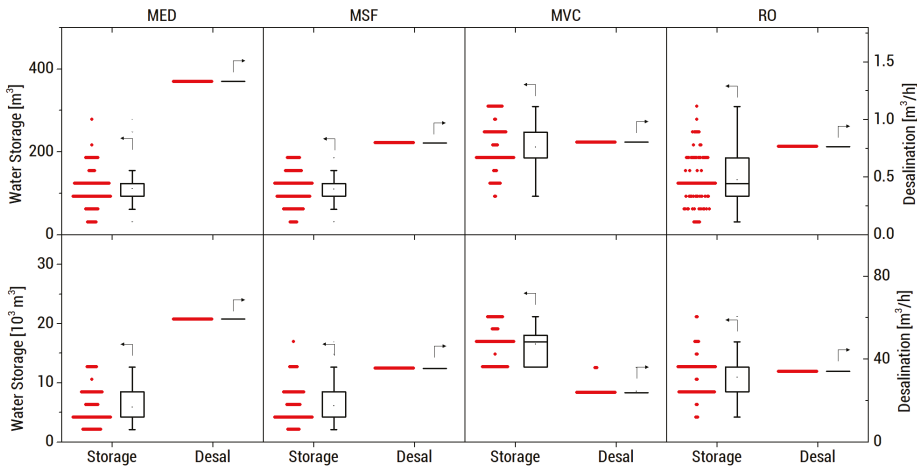


Figure 16. Distribution of optimum sizes of water storage and desalination unit on Camasusu Island (top) and Lubang Island (bottom) at -25% overnight fuel price. There is high uncertainty in the optimum water storage sizes in all systems on both islands.

3.4.2. +25% Overnight Fuel Cost

At a 25% increase in overnight diesel and coal cost, all systems have large Li-ion BESS installation sizes (Figure 18) preferring RE-favored generation due to prohibitive diesel costs. Figure 19 also shows minimal uncertainty in optimum storage sizes, confirming that RE-favored generation is favored. Generation costs have increased (Figure 20) especially in MVC systems, wherein diesel is used for energy generation, which in turn powers the MVC plant. This is less efficient than MED and MSF, which use the fuel directly.

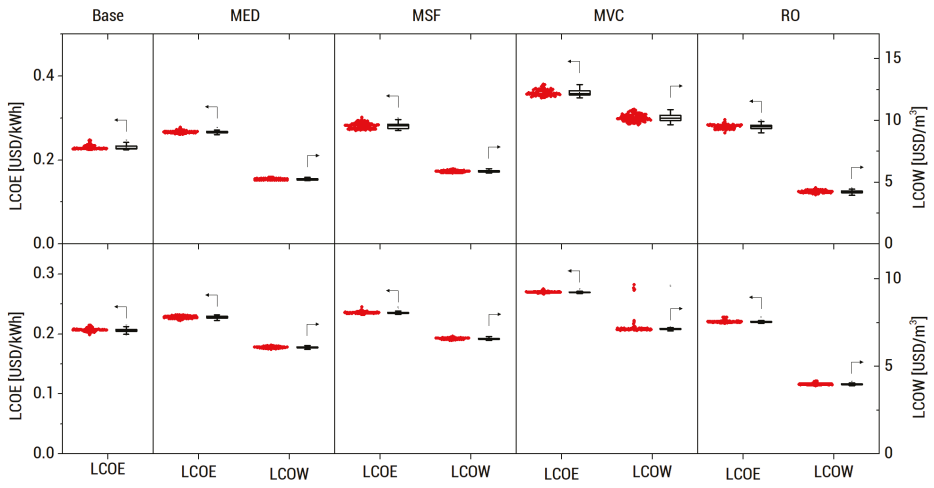


Figure 17. Distribution of optimum LCOE and LCOW on Camasusu Island (**top**) and Lubang Island (**bottom**) at -25% overnight fuel price. There is minimal uncertainty for these metrics.

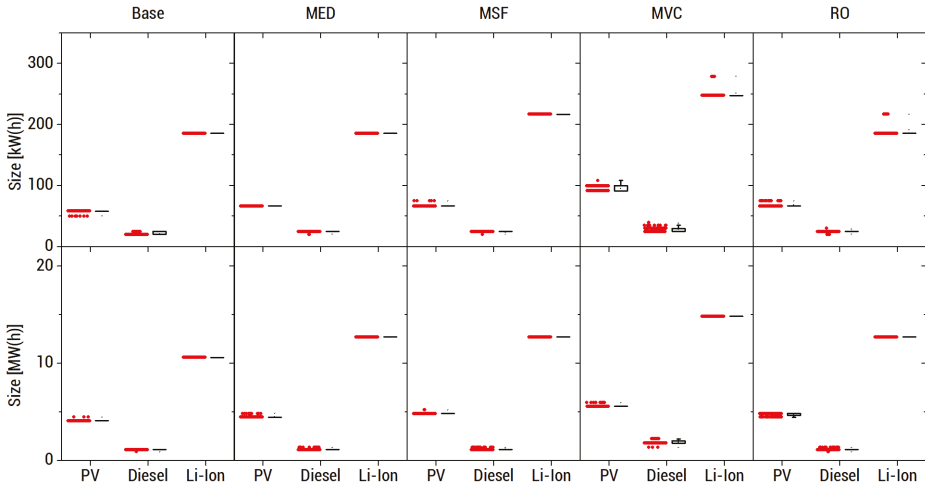


Figure 18. Distribution of optimum sizes of energy components on Camasusu Island (**top**) and Lubang Island (**bottom**) at $+25\%$ overnight fuel price.

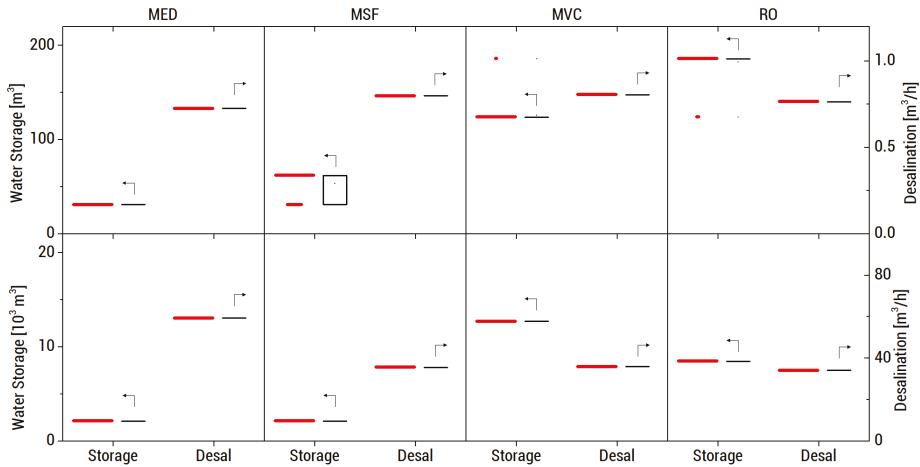


Figure 19. Distribution of optimum sizes of water storage and desalination unit on Camasusu Island (top) and Lubang Island (bottom) at +25% overnight fuel price. There is minimal uncertainty in optimum sizes in all systems on both islands.

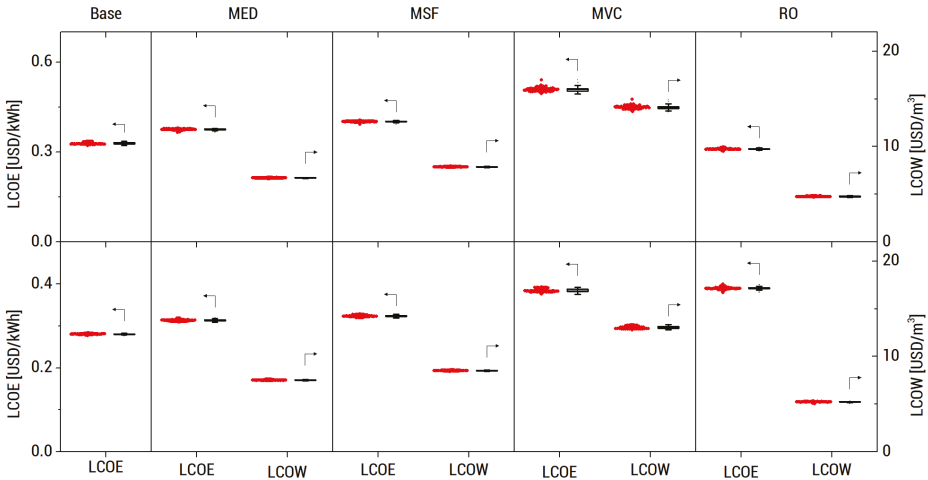


Figure 20. Distribution of optimum LCOE and LCOW for Camasusu Island (top) and Lubang Island (bottom) at +25% overnight fuel price. There is minimal uncertainty for these metrics.

4. Discussion

Upon analysis of the optimum size and metric distributions, RO systems have the lowest water generation cost. The low energy use and high turndown of RO allows for possible coupling with RE-favored generation. The average LCOW of RO systems is 5.11 USD/m³ and 4.70 USD/m³ for Camasusu and Lubang, respectively. Compared to the mainland price of 0.70 USD/m³, however, water generation costs are still higher by 630% and 572% for Camasusu and Lubang, respectively. As for electricity generation costs, MED systems have the lowest average LCOE of 0.348 USD/kWh in Camasusu, while RO systems have the lowest average LCOE of 0.296 USD/kWh in Lubang. These are 74% and 47% more expensive for Camasusu and Lubang, respectively, compared to the mainland price of 0.2 USD/kWh [62]. Overall, RO systems provide cost-effective water and electricity, especially for larger islands, where RE-favored generation is preferred.

For project developers, MED and MSF could be more attractive because these systems are less RE-dependent than RO due to the limited turndown. This allows easier entry into off-grid islands currently powered by diesel generators. There is also less uncertainty in optimum sizes, especially for MSF, implying that there is less risk of installing an undersized system. Seasonal weather patterns also do not strongly affect the stored water level. Lastly, these technologies have smaller water storage sizes that are more appropriate for off-grid islands. However, due to the large typical sizes of MED and MSF plants, these technologies are favorable for larger islands only [44].

Energy-desalination systems on small islands prefer diesel-favored generation, while larger islands prefer RE-favored generation, as shown by the power flows. Cost projection analysis, however, suggests that RE-favored generation will be more favorable in the future even for small islands. RO desalination is therefore a favorable investment as its high turndown allows it to accept RE intermittency, in addition to its low generation costs. Given that most of the off-grid islands are currently powered by diesel generators [1] and that PV-based installations are gradually being deployed [63], energy-RO systems for energy and water cogeneration may be feasible in the near future.

The sensitivity analysis shows that energy-desalination system configurations heavily depend on diesel and coal prices. If fuel prices are low, the fuel share in thermal desalination systems increases and uncertainty in water storage installation size increases. Energy and water generation costs are reduced especially for MED, MSF, and MVC, as they rely on fuel. If fuel prices are high, RE-favored generation becomes favorable. There is less uncertainty in the optimum sizes of both energy and water components because Li-ion BESS energy storage minimizes intermittencies. However, large Li-ion BESS installations for RE-dominated generation result in high costs of energy and water.

In addition to the fuel dependence of the optimum configuration, the sensitivity analysis also has implications on system resiliency on fuel price shocks. If fuel prices were to surge upwards, the generation costs of RO systems will be affected the least due to its low dependence on fuel. MVC systems will have the largest increase in generation costs due to its inefficient fuel usage. Small islands are more susceptible to fuel price surges, as these tend to have diesel-favored energy systems. In contrast, large islands are more likely to have RE-favored generation, which is optimal at higher fuel prices. This incentivizes the implementation of RE-RO systems, as they are favorable for small islands and are resistant to fuel price shocks.

5. Conclusions

The RO desalination systems have favorable properties due to high turndown capabilities and low energy use. Coupled energy-RO systems provide a low energy generation cost and the lowest water generation cost due to the efficient energy use of RO. Its high turndown allows for compatibility with RE-favored generation and makes it a future-proof investment as RE installations increase in the future. RO-RE systems have greater resistance to fuel price surges, providing resiliency against the decreasing fuel supply and current political climate.

MED and MSF are easier to implement given the present configuration on off-grid islands in the Philippines. These desalination technologies are more compatible with diesel-favored generation, which is the status-quo on Philippine off-grid islands. The MED and MSF systems are robust against weather patterns, making them a viable investment in the Philippines. These technologies may also have niche applications where diesel prices are low or if small water storage units are preferable.

Author Contributions: Conceptualization, methodology, validation, and formal analysis was done by M.C. and J.O. Writing—original draft preparation was done by M.C. and M.A. Writing—review and editing and supervision was done by M.A., E.E.J., and J.O. Funding acquisition was done by J.O. All authors have read and agreed to the published version of the manuscript.

Funding: This research is part of the Energy Research Fund (ERF) project entitled “ElectriPHI—Electrification Planning in Small Off-grid Islands in the Philippines” funded through the University of the Philippines Office of the Vice-President for Academic Affairs (UP OVPA) and the Senate Committee on Energy led by Sen. Sherwin T. Gatchalian.

Acknowledgments: J.O. would like to acknowledge the Federico Puno Professorial Chair Award and the US-ASEAN Science & Technology Fellowship. M.C. would like to acknowledge the Department of Science and Technology Science Education Institute (DOST-SEI) Merit Scholarship Program.

Conflicts of Interest: The authors declare no conflict of interest.

Appendix A

A.1. Energy System Models

A.1.1. Solar PV

The power output of the solar system is given by Equation (A1). It is proportional to the incident radiation on the tilted surface $G(t)$ and is partly influenced by the cell temperature $T_C(t)$. Details regarding the calculation of these parameters can be found in [64]. In Equation (A1), S_{PV} is the rated size of the solar PV installation, η_{PV} is the derating factor (0.8), G_{STC} is the irradiance at standard test conditions (STC, 1 kW/m²), α_P is the temperature coefficient of power (-0.005 K^{-1}), and T_{STC} is the temperature at STC.

$$P_{PV}(t) = S_{PV}\eta_{PV}\frac{G(t)}{G_{STC}}[1 + \alpha_P(T_C(t) - T_{STC})], \quad (\text{A1})$$

A.1.2. Diesel

Diesel generators can output any power below its rated size S_{ds} . A minimum power ratio r (0.1) is implemented and the minimum power output of a diesel generator is given by Equation (A2):

$$P_{ds}^{min}(t) = rS_{ds}, \quad (\text{A2})$$

The amount of fuel consumed by the plant is directly proportional to the rated size and the power output $P_{ds}(t)$ as given by Equation (A3). Both C_0 and C_1 are arbitrary constants [65].

$$\dot{V}_{fl}(t) = C_0S_{ds} + C_1P_{ds}(t), \quad (\text{A3})$$

The fuel efficiency is given by Equation (A4), wherein ρ is the density of diesel (820 kg/m³) and ΔH_{LHV} is the lower heating value of diesel (43.2 MJ/kg). The efficiency is specified as 0.3 and 0.4 at the minimum and maximum loading, respectively. This allows the coefficients in Equation (A3) to be determined.

$$\eta_{ds}(t) = \frac{P_{ds}(t)}{\rho\dot{V}_{ds}(t)\Delta H_{LHV}}, \quad (\text{A4})$$

A.1.3. Li-Ion BESS

The charging and discharging rate of the Li-ion BESS is limited by either the C-rate or the state of charge (SOC) as shown by Equations (A5) and (A6). In these equations, S_{Li} is the rated size of the Li-ion BESS installation, C is the C-rate, and the $\min\{x, y\}$ function returns whichever is smaller among x or y . The negative sign indicates charging, as this will be relevant in the later equations. In Equation (A6), a maximum depth of discharge (DOD_{\max}) of 0.8 is implemented as too much discharge that will damage the BESS:

$$P_c^{max}(t) = -\min\{ S_{Li}C, S_{Li}(1 - \text{SOC}(t)) \}, \quad (\text{A5})$$

$$P_{dc}^{max}(t) = \min\{ S_{Li}C, S_{Li}(\text{SOC} - (1 - \text{DOD}_{\max})) \}, \quad (\text{A6})$$

Next, the power entering one battery module $P(t)$ is determined as shown in Equations (A7) and (A8) for charging and discharging, respectively. A charge ϵ_c and discharge ϵ_{dc} efficiency of 0.95 is

applied, which results in a roundtrip efficiency of 0.90 when combined. S_{nom} is the nominal size of one battery module (4.8 kWh).

$$P(t) = \frac{P_c(t)\epsilon_c}{S_{st}/S_{nom}}, \tag{A7}$$

$$P(t) = \frac{P_{dc}(t)/\epsilon_{dc}}{S_{st}/S_{nom}}, \tag{A8}$$

The Li-ion battery chemistry is modeled using the Thevenin equivalent circuit as shown in Figure A1. $P(t)$ represents the power at the terminals. R_1 (1.4 Ω) is the resistance due to the electrolyte, while R_2 (0.5 Ω) and C (52 F) are resistances at the electrode interface [66].

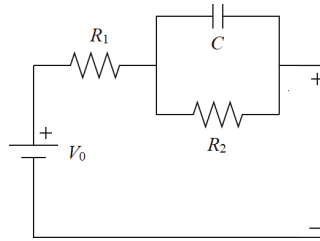


Figure A1. Thevenin equivalent circuit for modelling Li-ion battery chemistry.

The current through the EMF element is determined and the SOC for the next timestep is given by Equation (A9). $V_0(t)$ is the open circuit voltage (OCV) of the battery module.

$$\text{SOC}(t+1) = \text{SOC}(t) - \frac{I(t)V_0(t)}{S_{nom}}, \tag{A9}$$

The module OCV is given as a function of SOC by Figure A2.

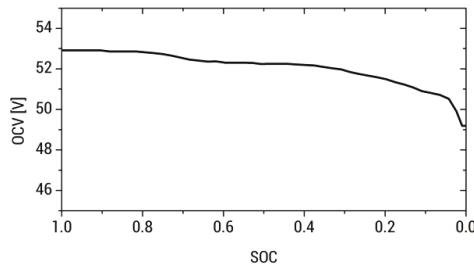


Figure A2. Open circuit voltage (OCV) as a function of SOC for a 48 V Li-ion battery module.

A.2. Dispatch Algorithm

The dispatch algorithm decides how energy is distributed throughout the system. ISLA uses a load-following dispatch algorithm that has been modified to accommodate desalination as shown in Figure A3. First, the algorithm checks if solar PV power at that timestep can supply both the electrical demand and desalination power. If so, the BESS is charged, and any more excess power is absorbed by the desalination plant. Otherwise, power is drawn from the Li-ion BESS. If the Li-ion BESS does not suffice, additional diesel generation is called. If this still does not suffice, then a power outage is declared, and the system is infeasible.

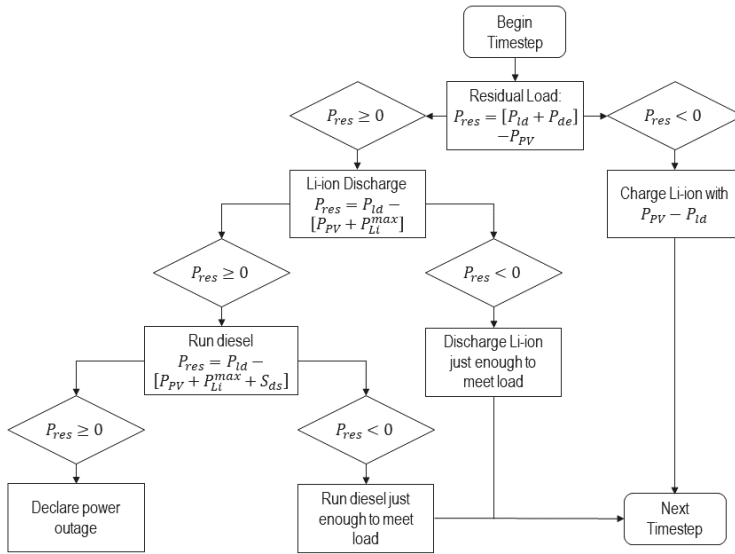


Figure A3. Load-following dispatch algorithm used by ISLA. To reduce carbon emissions, the system prioritizes the usage of stored Li-ion BESS energy over diesel power if solar PV power is insufficient.

Appendix B

To ensure that a physically sensible optimum is obtained, the initial search space must be generated properly. The procedure below shows how ISLA generates the initial search space, but this does not guarantee a global optimum value as with nonlinear optimization problems. Nonetheless, the results generated by ISLA for energy-only microgrid systems were consistent with those from HOMER Pro®.

The sizes of solar PV, diesel, and the desalination unit are rated based on their maximum power [kW] or flowrate [m³/h] generation, thus, the optimum value must be based on the peak demand. A crude approximation of the peak electrical demand P_{pk} is calculated as shown in Equation (A10). The constant 10 kW/(m³/h) was arbitrarily chosen such that it is near the electrical energy intensities EI_{el} of the desalination units in this study.

$$P_{pk} = \max \left\{ P_{ld}(t) + \frac{10 \text{ kW}}{\text{m}^3/\text{h}} \dot{V}_{ld}(t) \right\}, \tag{A10}$$

The initial search spaces of solar PV $\{S_{PV}\}_0$, diesel $\{S_{ds}\}_0$, and the desalination unit $\{S_{de}\}_0$ are shown in Equations (A11)–(A13). Constants are multiplied to P_{pk} due to the possibility of the optimum size deviating from the crudely approximated peak demand. The diesel generator has a small associated constant because its optimum size must be near the peak demand. Smaller sizes may be technically infeasible, while larger sizes will incur high capital cost. Solar PV has a larger associated constant because it has power peaks during the day that are much larger than the peak demand.

$$\{S_{PV}\}_0 = \left[0, 5P_{pk} \right], \tag{A11}$$

$$\{S_{ds}\}_0 = \left[0, 3P_{pk} \right], \tag{A12}$$

$$\{S_{de}\}_0 = \left[0, \frac{2P_{pk}}{EI_{el}} \right], \tag{A13}$$

The Li-ion BESS and water storage undergo daily cycles of influx and efflux; thus, it is unlikely to have a Li-ion BESS or water storage that drains in less than a day. Their search spaces are therefore

based on daily consumption. A crude approximation of the daily power consumption E_{dy} is given by Equation (A14). Compared to Equation (A10), a smaller constant of 5 kW/(m³/h) was chosen because the average daily power consumption is less sensitive to sharp peaks in the actual demand profile.

$$E_{dy} = \frac{1}{365} \left[\sum_{i=0}^{8759} P_{ld}(t) \Delta t + \frac{5 \text{ kW}}{\text{m}^3/\text{h}} \cdot \sum_{i=0}^{8759} \dot{V}_{ld}(t) \Delta t \right], \quad (\text{A14})$$

The initial search spaces of Li-ion BESS $\{S_{Li}\}_0$ and water storage $\{S_{tank}\}_0$ are shown in Equations (A15) and (A16). Constants are multiplied to E_{dy} due to the possibility of the optimum size deviating from the crudely approximated daily energy consumption. These constants are smaller, however, because caution against sharp peaks in the actual demand profile is unnecessary.

$$\{S_{Li}\}_0 = \left[0, 2E_{dy} \right], \quad (\text{A15})$$

$$\{S_{tank}\}_0 = \left[0, \frac{2E_{dy}}{\text{El}_{el}} \right], \quad (\text{A16})$$

Appendix C

The techno-economic parameters of the energy generation components are shown in Table A1. These parameters are valid for the year 2015.

Table A1. Techno-economic parameters of energy components.

Component	Parameter	Unit	Value	Ref.
PV	CapEx	USD/kW	1200	[67]
	OpEx	USD/kW/y	25	
	Lifetime	y	20	[68]
Li-ion BESS	CapEx	USD/kWh	300	[69]
	OpEx	USD/kWh/y	3	
	Lifetime	y	10	
	RT Efficiency	%	90	
Diesel Generator	CapEx	USD/kW	500	
	OpEx	USD/kWh	0.03	
	Lifetime	h	15,000	
Diesel	Cost	USD/L	0.9	
	Inflation Rate	%	3	
Project	CapEx	USD	0	
	OpEx	USD/y	0	
	Discount Rate	%	10	
	Lifetime	y	20	

Appendix D

The future cost parameters of energy components are summarized in Table A2.

Table A2. Future cost parameters of energy components.

Component	K [GW(h)]	r [y^{-1}]	t_m [y]	Ref.	b	Ref.
PV	200	1.7362	2004	[6]	0.376	[6]
Li-ion BESS	2600	2.7363	2011	[6]	0.251	[6]

Appendix E

The global horizontal irradiance (GHI), energy demand, and water demand of Camasusu Island and Lubang Island are shown in Figures A4 and A5, respectively. The GHI profiles were obtained from PHIL-LIDAR 2 dataset, while the electrical demand load profiles were obtained from the work of Navarro [70].

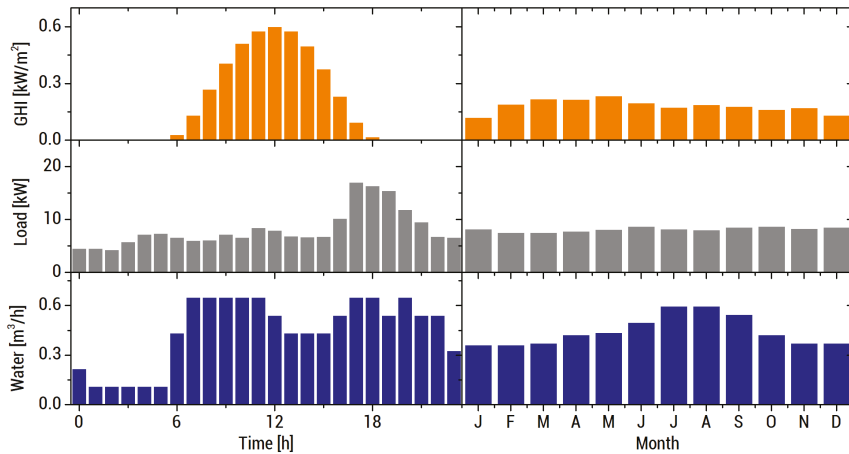


Figure A4. Daily and monthly average electric, water, and GHI profiles on Camasusu Island.

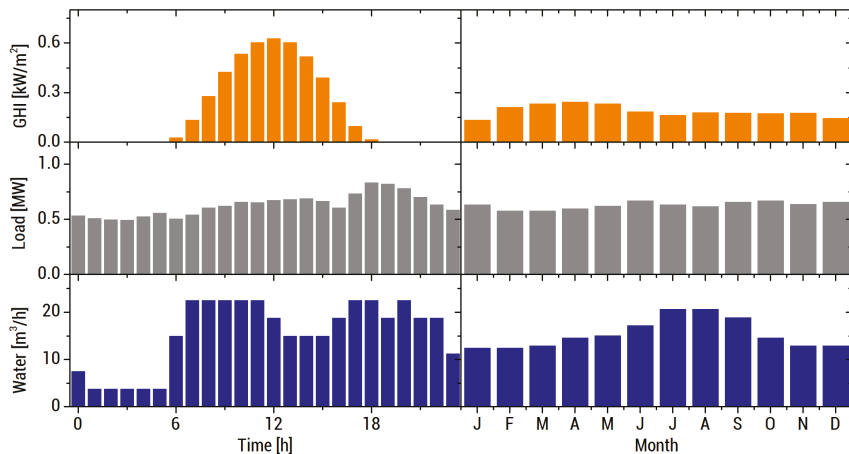


Figure A5. Daily and monthly average electric, water, and GHI profiles on Lubang Island.

References

- Ocon, J.D.; Bertheau, P. Energy Transition from Diesel-based to Solar Photovoltaics-Battery-Diesel Hybrid System-based Island Grids in the Philippines—Techno-Economic Potential and Policy Implication on Missionary Electrification. *J. Sustain. Dev. Energy Water Environ. Syst.* **2019**, *7*, 139–154. [CrossRef]
- Holding, S.; Allen, D.M.; Foster, S.; Hsieh, A.; Larocque, I.; Klassen, J.; Van Pelt, S.C. Groundwater vulnerability on small islands. *Nat. Clim. Chang.* **2016**, *6*, 1100–1103. [CrossRef]
- NEA to Give Romblons Cobrador Island Potable Water Thru Hydropanels. Available online: <https://www.ikot.ph/nea-to-give-romblons-cobrador-island-potable-water-thru-hydropanels> (accessed on 24 April 2020).

4. International Labor Organization. *Report V: Sustainable Development, Decent Work and Green Jobs*; International Labor Organization: Geneva, Switzerland, 2013.
5. Lilane, A.; Saifaoui, D.; Hariss, S.; Jenkal, H.; Chouiekh, M. Modeling and simulation of the performances of the reverse osmosis membrane. *Mater. Today Proc.* **2019**, *24*, 114–118. [[CrossRef](#)]
6. Schmidt, O.; Hawkes, A.; Gambhir, A.; Staffell, I. The future cost of electrical energy storage based on experience rates. *Nat. Energy* **2017**, *2*, 1–8. [[CrossRef](#)]
7. Schmidt, O.; Melchior, S.; Hawkes, A.; Staffell, I. Projecting the Future Levelized Cost of Electricity Storage Technologies. *Joule* **2019**, *3*, 81–100. [[CrossRef](#)]
8. Bajpai, P.; Dash, V. Hybrid renewable energy systems for power generation in stand-alone applications: A review. *Renew. Sustain. Energy Rev.* **2012**, *16*, 2926–2939. [[CrossRef](#)]
9. Bertheau, P.; Blechinger, P. Resilient solar energy island supply to support SDG7 on the Philippines: Techno-economic optimized electrification strategy for small islands. *Util. Policy* **2018**, *54*, 55–77. [[CrossRef](#)]
10. Fernández-Gil, G.; Petrakopoulou, F. Sustainable water generation on a mediterranean island in Greece. *Energies* **2019**, *12*, 4247. [[CrossRef](#)]
11. Tafech, A.; Milani, D.; Abbas, A. Water storage instead of energy storage for desalination powered by renewable energy—King Island case study. *Energies* **2016**, *9*, 839. [[CrossRef](#)]
12. Philstar Global Water Rates up in July 2018. Available online: <https://www.philstar.com/headlines/2018/06/15/1824833/water-rates-july-2018> (accessed on 24 April 2020).
13. Gökçek, M. Integration of hybrid power (wind-photovoltaic-diesel-battery) and seawater reverse osmosis systems for small-scale desalination applications. *Desalination* **2018**, *435*, 210–220. [[CrossRef](#)]
14. Corsini, A.; Tortora, E. Sea-Water Desalination for Load Levelling of Gen-Sets in Small Off-Grid Islands. *Energies* **2018**, *11*, 2068. [[CrossRef](#)]
15. Bognar, K.; Pohl, R.; Behrendt, F. Seawater reverse osmosis (SWRO) as deferrable load in micro grids. *Desalin. Water Treat.* **2013**, *51*, 1190–1199. [[CrossRef](#)]
16. International Atomic Energy Agency. *Use of Nuclear Reactors for Seawater Desalination*; International Atomic Energy Agency: Vienna, Austria, 1990.
17. Khalifa, A.J.N. Evaluation of different hybrid power scenarios to Reverse Osmosis (RO) desalination units in isolated areas in Iraq. *Energy Sustain. Dev.* **2011**, *15*, 49–54. [[CrossRef](#)]
18. Azinheira, G.; Segurado, R.; Costa, M. Is renewable energy-powered desalination a viable solution for water stressed regions? A case study in Algarve, Portugal. *Energies* **2019**, *12*, 4651. [[CrossRef](#)]
19. Rao, P.; Morrow, W.R.; Aghajanzadeh, A.; Sheaffer, P.; Dollinger, C.; Brueske, S.; Cresko, J. Energy considerations associated with increased adoption of seawater desalination in the United States. *Desalination* **2018**, *445*, 213–224. [[CrossRef](#)]
20. Qiu, T.; Davies, P.A. Comparison of configurations for high-recovery inland desalination systems. *Water* **2012**, *4*, 690–706. [[CrossRef](#)]
21. Monterrey-Viña, A.; Musicki-Savic, A.; Díaz-Peña, F.J.; Peñate-Suárez, B. Technical and agronomical assessment of the use of desalinated seawater for coastal irrigation in an insular context. *Water* **2020**, *12*, 272. [[CrossRef](#)]
22. Caldera, U.; Breyer, C. Learning Curve for Seawater Reverse Osmosis Desalination Plants: Capital Cost Trend of the Past, Present, and Future. *Water Resour. Res.* **2017**, *53*, 10523–10538. [[CrossRef](#)]
23. Jones, E.; Qadir, M.; van Vliet, M.T.H.; Smakhtin, V.; Kang, S. mu The state of desalination and brine production: A global outlook. *Sci. Total Environ.* **2019**, *657*, 1343–1356. [[CrossRef](#)]
24. Ullah, I.; Rasul, M.G. Recent developments in solar thermal desalination technologies: A review. *Energies* **2019**, *12*, 119. [[CrossRef](#)]
25. Reddy, K.V.; Ghaffour, N. Overview of the cost of desalinated water and costing methodologies. *Desalination* **2007**, *205*, 340–353. [[CrossRef](#)]
26. Mayor, B. Growth patterns in mature desalination technologies and analogies with the energy field. *Desalination* **2019**, *457*, 75–84. [[CrossRef](#)]
27. Sood, A.; Smakhtin, V. Can desalination and clean energy combined help to alleviate global water scarcity? *J. Am. Water Resour. Assoc.* **2014**, *50*, 1111–1123. [[CrossRef](#)]
28. Ahmadvand, S.; Abbasi, B.; Azarfar, B.; Elhashimi, M.; Zhang, X.; Abbasi, B. Looking beyond energy efficiency: An applied review of water desalination technologies and an introduction to capillary-driven desalination. *Water* **2019**, *11*, 696. [[CrossRef](#)]

29. Williams, E.; Hittinger, E.; Carvalho, R.; Williams, R. Wind power costs expected to decrease due to technological progress. *Energy Policy* **2017**, *106*, 427–435. [[CrossRef](#)]
30. Maqbool, N.; Saleem, Z.; Jamal, Y. Open Access Journal of Waste Management & Xenobiotics A Short Review on A Short Review on Reverse Osmosis Membranes: Fouling and Control. *A Short Rev. Reverse Osmosis Membr. Fouling Control* **2019**, *2*. [[CrossRef](#)]
31. Coutinho de Paula, E.; Amaral, M.C.S. Extending the life-cycle of reverse osmosis membranes: A review. *Waste Manag. Res.* **2017**, *35*, 456–470. [[CrossRef](#)]
32. Yang, Z.; Zhou, Y.; Feng, Z.; Rui, X.; Zhang, T.; Zhang, Z. A review on reverse osmosis and nanofiltration membranes for water purification. *Polymers* **2019**, *11*, 1252. [[CrossRef](#)]
33. Ruiz-García, A.; Melián-Martel, N.; Nuez, I. Short review on predicting fouling in RO desalination. *Membranes* **2017**, *7*, 62. [[CrossRef](#)]
34. Al-Amshawee, S.; Yunus, M.Y.B.M.; Azoddein, A.A.M.; Hassell, D.G.; Dakhil, I.H.; Hasan, H.A. Electrodialysis desalination for water and wastewater: A review. *Chem. Eng. J.* **2020**, *380*, 122231. [[CrossRef](#)]
35. Carballo, J.A.; Bonilla, J.; Roca, L.; De la Calle, A.; Palenzuela, P.; Alarcón-Padilla, D.C. Optimal operating conditions analysis for a multi-effect distillation plant according to energetic and exergetic criteria. *Desalination* **2018**, *435*, 70–76. [[CrossRef](#)]
36. Nannarone, A.; Toro, C.; Sciubba, E. Multi-stage flash desalination process: Modeling and simulation. In Proceedings of the 30th International Conference on Efficiency, Cost, Optimization, Simulation and Environmental Impact of Energy Systems-ECOS 2017, San Diego, CA, USA, 2–6 July 2017.
37. El-Feky, A.K. Mechanical Vapor Compression (MVC) Desalination System Optimal Design. *Arab J. Nucl. Sci. Appl.* **2016**, *94*, 1–13.
38. Jamil, M.A.; Zubair, S.M. On thermoeconomic analysis of a single-effect mechanical vapor compression desalination system. *Desalination* **2017**, *420*, 292–307. [[CrossRef](#)]
39. Namany, S.; Al-Ansari, T.; Govindan, R. Optimisation of the energy, water, and food nexus for food security scenarios. *Comput. Chem. Eng.* **2019**, *129*, 106513. [[CrossRef](#)]
40. Mandelli, S.; Brivio, C.; Colombo, E.; Merlo, M. Effect of load profile uncertainty on the optimum sizing of off-grid PV systems for rural electrification. *Sustain. Energy Technol. Assess.* **2016**, *18*, 34–47. [[CrossRef](#)]
41. Castro, M.T.; Esparcia, E.A.; Odulio, C.M.F.; Ocon, J.D. Technoeconomics of reverse osmosis as demand-side management for Philippine off-grid islands. *Chem. Eng. Trans.* **2019**, *76*, 1129–1134.
42. Gökçek, M.; Gökçek, Ö.B. Technical and economic evaluation of freshwater production from a wind-powered small-scale seawater reverse osmosis system (WP-SWRO). *Desalination* **2016**, *381*, 47–57. [[CrossRef](#)]
43. Ozonoh, M.; Aniketete, T.C.; Oboirien, B.O.; Daramola, M.O. Techno-economic analysis of electricity and heat production by co-gasification of coal, biomass and waste tyre in South Africa. *J. Clean. Prod.* **2018**, *201*, 192–206. [[CrossRef](#)]
44. Abdelkareem, M.A.; El Haj Assad, M.; Sayed, E.T.; Soudan, B. Recent progress in the use of renewable energy sources to power water desalination plants. *Desalination* **2018**, *435*, 97–113. [[CrossRef](#)]
45. Ghalavand, Y.; Hatamipour, M.S.; Rahimi, A. A review on energy consumption of desalination processes. *Desalin. Water Treat.* **2015**, *54*, 1526–1541. [[CrossRef](#)]
46. Ghaffour, N.; Missimer, T.M.; Amy, G.L. Technical review and evaluation of the economics of water desalination: Current and future challenges for better water supply sustainability. *Desalination* **2013**, *309*, 197–207. [[CrossRef](#)]
47. Aquatech International Corporation. *Case Study: Seawater Desalination at Rabigh Refinery*; Aquatech International Corporation: Canonsburg, PA, USA, 2020.
48. Rahimi, B.; Chua, H. *Low Grade Heat Driven Multi-effect Distillation and Desalination*, 1st ed.; Elsevier: Amsterdam, The Netherlands, 2017.
49. Elsayed, M.L.; Mesalhy, O.; Mohammed, R.H.; Chow, L.C. Transient and thermo-economic analysis of MED-MVC desalination system. *Energy* **2019**, *167*, 283–296. [[CrossRef](#)]
50. Kim, J.S.; Garcia, H.E. *Hybrid Energy: Combining Nuclear and Other Energy Sources*; Idaho National Lab. (INL): Idaho Falls, ID, USA, 2015.
51. Papapetrou, M.; Cipollina, A.; La Commare, U.; Micale, G.; Zaragoza, G.; Kosmadakis, G. Assessment of methodologies and data used to calculate desalination costs. *Desalination* **2017**, *419*, 8–19. [[CrossRef](#)]
52. Lara, J.; Osunsan, O.; Holtzapfel, M. Advanced mechanical vapor-compression desalination system. In *Desalination, Trends and Technologies*; Schorr, M., Ed.; IntechOpen: London, UK, 2012.

53. De Andrade Cruz, M.; Araújo, O.d.Q.F.; de Medeiros, J.L.; de Castro, R.d.P.V.; Ribeiro, G.T.; de Oliveira, V.R. Impact of solid waste treatment from spray dryer absorber on the leveled cost of energy of a coal-fired power plant. *J. Clean. Prod.* **2017**, *164*, 1623–1634. [[CrossRef](#)]
54. Wang, F.; Deng, S.; Zhao, J.; Zhao, J.; Yang, G.; Yan, J. Integrating geothermal into coal-fired power plant with carbon capture: A comparative study with solar energy. *Energy Convers. Manag.* **2017**, *148*, 569–582. [[CrossRef](#)]
55. Mayor, B. Unraveling the Historical Economies of Scale and Learning Effects for Desalination Technologies. *Water Resour. Res.* **2020**, *56*, 1–10. [[CrossRef](#)]
56. Cipollina, A.; Micale, G.; Rizzuti, L. *Seawater Desalination: Conventional and Renewable Energy Processes*; Springer: Berlin, Germany, 2012; ISBN 9781608054220.
57. California Public Utilities Commission. *Embedded Energy in Water Studies Study 3: End Use Water Demand Profiles*; California Public Utilities Commission: San Francisco, CA, USA, 2011.
58. Griffin, R.C.; Chang, C. Seasonality in Community Water Demand. *West. J. Agric. Econ.* **1991**, *16*, 207–217.
59. Bendt, P.; Collares-Pereira, M.; Rabl, A. The frequency distribution of daily insolation values. *Sol. Energy* **1981**, *27*, 1–5. [[CrossRef](#)]
60. Graham, V.A.; Hollands, K.G.T.; Unny, T.E. A time series model for Kt with application to global synthetic weather generation. *Sol. Energy* **1988**, *40*, 83–92. [[CrossRef](#)]
61. Graham, V.A.; Hollands, K.G.T. A method to generate synthetic hourly solar radiation globally. *Sol. Energy* **1990**, *44*, 333–341. [[CrossRef](#)]
62. MERALCO Local DU Rate. Available online: www.meralco.com.ph (accessed on 24 April 2020).
63. National Power Corporation NPC Holds Groundbreaking of Solar Power Plant in Limasawa Island. Available online: <https://www.napocor.gov.ph/index.php/news/archived-news/189-npc-holds-groundbreaking-of-solar-power-plant-in-limasawa-island> (accessed on 24 April 2020).
64. Duffie, J.; Beckman, W. *Solar Engineering of Thermal Processes*; Wiley: New York, NY, USA, 2013; ISBN 9780470873663.
65. McGowan, J.G.; Manwell, J.F.; Connors, S.R. Wind/diesel energy systems: Review of design options and recent developments. *Sol. Energy* **1988**, *41*, 561–575. [[CrossRef](#)]
66. He, H.; Xiong, R.; Fan, J. Evaluation of lithium-ion battery equivalent circuit models for state of charge estimation by an experimental approach. *Energies* **2011**, *4*, 582–598. [[CrossRef](#)]
67. Fu, R.; Feldman, D.; Margolis, R. *US Solar Photovoltaic System Cost Benchmark: Q1 2018*; NREL/TP-6A20-72399; National Renewable Energy Laboratory: Golden, CO, USA, 2018.
68. Blechinger, P. *Barriers and Solutions to Implementing Renewable Energies on Caribbean Islands in Respect of Technical, Economic, Political, and Social Conditions, Schriftenreihe der Reiner Lemoine-Stiftung*; Shaker Verlag: Herzogenrath, Germany, 2015.
69. Diorio, N.; Dobos, A.; Janzou, S.; Nelson, A.; Lundstrom, B. *Technoeconomic Modeling of Battery Energy Storage in SAM*; NREL Technical Report; National Renewable Energy Laboratory: Golden, CO, USA, 2015.
70. Navarro, S. Hybrid opportunities in SPUG areas using HOMER. In Proceedings of the Asian Clean Energy Forum, Manila, Philippines, 6–10 June 2016.



© 2020 by the authors. Licensee MDPI, Basel, Switzerland. This article is an open access article distributed under the terms and conditions of the Creative Commons Attribution (CC BY) license (<http://creativecommons.org/licenses/by/4.0/>).

Article

Thermodynamics-Based Process Sustainability Evaluation

Petar Sabev Varbanov ^{1,*}, Hon Huin Chin ¹, Alexandra Elena Plesu Popescu ²
and Stanislav Boldyryev ³

¹ Sustainable Process Integration Laboratory-SPIL, NETME Centre, Faculty of Mechanical Engineering, Brno University of Technology-VUT Brno, 61669 Brno, Czech Republic; chin@fme.vutbr.cz

² Department of Chemical Engineering and Analytical Chemistry, Faculty of Chemistry, University of Barcelona, 08028 Barcelona, Spain; a_plesu@ub.edu

³ Research School of Chemistry & Applied Biomedical Sciences, Tomsk Polytechnic University, 634050 Tomsk, Russia; sboldyryev@tpu.ru

* Correspondence: varbanov@fme.vutbr.cz; Tel.: +420-778-723-400

Received: 6 January 2020; Accepted: 21 April 2020; Published: 28 April 2020

Abstract: This article considers the problem of the evaluation of the sustainability of heterogeneous process systems, which can have different areas of focus: from single process operations to complete supply chains. The proposed method defines exergy-based concepts to evaluate the assets, liabilities, and the exergy footprint of the analysed process systems, ensuring that they are suitable for Life Cycle Assessment. The proposed concepts, evaluation framework and cumulative Exergy Composite Curves allow the quantitative assessment of process systems, including alternative solutions. The provided case studies clearly illustrate the applicability of the method and the close quantitative relationship between the exergy profit and the potential sustainability contribution of the proposed solutions. The first case study demonstrates how the method is applied to the separation and reuse of an acetic-acid-containing waste stream. It is shown that the current process is not sustainable and needs substantial external exergy input and deeper analysis. The second case study concerns Municipal Solid Waste treatment and shows the potential value and sustainability benefit that can be achieved by the extraction of useful chemicals and waste-to-energy conversion. The proposed exergy footprint accounting framework clearly demonstrates the potential to be applied to sustainability assessment and process improvement while simultaneously tracking different kinds of resources and impacts.

Keywords: exergy footprint; sustainability; process systems engineering; exergy accounting

1. Introduction

The efficient use of energy is of utmost importance for process sustainability and emission reduction [1]. This is an area of increasing research and practical interest that has persisted to this day [2]. All major economic sectors are under investigation, including industry [3], transportation [4] and agriculture [5].

The use of all types of resources and the impacts of processes on the surroundings can be related to the use of the energy necessary to complete the tasks. The evaluation of industrial systems is most frequently performed by using mathematical models for the consistent estimation of their thermodynamic properties and related energy use. Commercial simulators provide this functionality [6].

When comparing alternative processes, the energy demand is not always a suitable metric because it may not take into account the quality of the energy used. In this context, exergy is the property that can be used as a combined indicator of energy quality and quantity [7]. This property of exergy allows the optimisation of the process design and operation based on realistic estimates of how much energy can be sourced, converted, supplied or reused. Extended Exergy Analysis also takes into account the

economic aspects of a resource; e.g., a wind turbine in a more windy place has a higher exergy efficiency because it produces more energy with similar investment and operation costs [8]. This concept can be applied to an isolated unit (e.g., a wind turbine), to an industrial process (e.g., concrete industry [9]) or a farming system (e.g., canola [10]).

Process systems can no longer be considered in isolation [11], dealing only with the maximisation of their standalone efficiency. While process efficiency is important for obtaining profit, its environmental impact spans beyond the boundaries of the current system. This conflict between the usefulness of the streams and resources of a process and their effect on natural storage is solved by the concept of circularity [12], in which the overall life cycle is considered.

The exergy concept has been shown to be key to addressing sustainability issues [13]. The use of renewable resources is beneficial, as this takes advantage of natural energy flows across the Earth, without depleting accumulated terrestrial energy reserves, such as fossil fuels [14]. Therefore, the share of renewable resources used in the economy should be increased, although the exergy obtained in some of the harvesting paths may be small. Another confirmation of the usefulness of exergy for sustainability modelling comes from the domain of water management and water treatment plants [15]. However, despite being proven to be potentially useful, the use of the exergy concept is frequently limited only to the estimation of the exergy efficiency of various process contexts [16], such as the exergy efficiency of a process or the share of exergy from the renewables provided to a process.

There are examples of exergy assessment in the literature. Changes in the concentration of a solvent give rise to a massive exergy loss, indicating the importance of solvent selection [17]. An exergy analysis to evaluate the performance of a continuous Directional Solvent Extraction (DSE) desalination process using octanoic acid was presented in [18]. Extractive solvent regeneration is a potential method to substitute stripping and reduce the exergy demands of CO₂ capture systems [19].

To compare process alternatives using exergy, the selection of system boundaries and reference points (e.g., ambient conditions) must provide comparable output streams. The same issue is also typical for the implementations of the Life Cycle Assessment (LCA) framework [20], where the choice of the system boundary and selection of life cycle stages is crucial to obtaining credible results. This similarity is useful for the potential integration of exergy-based criteria within the framework.

There have been many attempts to define a universal reference state [21]. The restricted dead state is defined as the physical thermodynamic equilibrium with the reference state. However, a dead state which takes the chemical equilibrium into account is required for environmental assessments. A widely used variant is based on an Earth similarity condition [22], where a reference substance is chosen for every element [23]. Substance exergies are determined to start from those of the reference substances, considering balanced chemical reactions. Regrettably, some chemical exergies are negative, and the reference is not entirely consistent [24].

The initial reference state has been updated according to new and more accurate geochemical and geological information. Thanatia [25] is a thermodynamically dead planet in which all materials have reacted, dispersed and mixed; i.e., it represents a complete dispersed state of minerals and the complete combustion of fossil fuels. Thanatia is not a reference state but a baseline used to calculate concentration exergies, therefore providing the exergy replacement costs. To assess the exergy degradation of the natural capital, the reference environment has evolved to a Thermo-Ecological Cost (TEC) methodology which in combination with the concept of Exergy Replacement Costs (ERC) results in the TERC (Thermal-Exergy Replacement Cost) methodology, which is used to assess the degradation of fossil and mineral capital [25].

The choice of the reference conditions can also have a significant effect on the evaluation of the chemical exergy of particular substances such as fuels [26]. This is even more important for the evaluation of the exergy efficiency of large-scale systems, such as the Turkish industrial sector. A study of the trends in this area [27] revealed an increase from 25% to 29% when the ambient reference temperature decreased from 298 to 273 K.

From the perspectives of ecological modelling and the life cycle, it is possible to use the concept of embodied exergy: the cumulative amount of exergy inputs necessary to deliver a product or a service [28]. The cited work has applied the concept to exergy costing and accounting for energy sector applications, linking exergy spending to monetary costs.

Although exergy is very useful for assessing the loss of resource quality, its use has not been widespread in environmental impact evaluation. LCA is one of the well-established techniques with which exergy has been combined to conduct the exergy analysis of a complete product life cycle [29].

One method to quantify the environmental impact of a process based on exergy is the use of the environmental compatibility indicator, which takes into account the input exergy to the process and the exergy requirements for the abatement of process emissions and waste [30]. In an ideal case (no impact considered), the discussed process emits only heat.

Furthermore, the highest exergy efficiency does not correspond to minimum costs [31] or minimum environmental impact [32]. Exergy efficiency, in that sense, is a local evaluation criterion and is only appropriate to specific energy conversion or use schemes.

Circular economic flow is based on the separation of technology and the economy as the main condition [33]. This concept considers the inputs and outputs of operations during industrial production and focuses on cause-effect relationships. The author considers the circularity concept in terms of temporally repeating cycles of economic activity and presents the realisation that the economy cannot be considered separately from the environment.

Different industrial approaches to the improvement of the sustainability of human society and the environment have been attempted. The simple approaches to the substitution of materials and the end-of-pipe reduction of harmful emissions have been superseded by LCA-based methods for ecological design and economics [34]. The understanding of the interconnections, inputs and outputs for the entire supply leads to the goals of the circular economy [35]. In this context, close attention has to be paid to the full life cycle, including the facility construction and decommissioning, as has been shown in an analysis of the reuse of materials from wind turbines after their end of service [36].

The utilisation and reuse of different types of waste may be analysed by systematic approaches: e.g., P-Graph offers a solution for closed-loop processing and the analysis of its impact [37]. Process Integration also has great potential for analysing circular flows, especially in improving the sustainability of energy systems [38].

For the effective application of targeting and optimisation models in the design, operation and retrofitting of industrial processes for the circular economy, it is necessary to have flexible and scalable modelling concepts and tools. Conventional logic treats process streams as either inputs or outputs, where the outputs are either products or waste streams [39]. The waste streams were traditionally thought of as needing to be treated and disposed of. The circular economy paradigm for process design [40] requires non-product outlet streams to be treated as sources of potential resources as well.

Besides research, regulatory action has also been taken; for example, the EU action plan for the circular economy [41]. Some ideas related to circularity have been developed previous to the popularisation of the circularity concept; e.g., reuse, remanufacturing or recycling [42]. Sustainable Consumption and Production (SCP) tools have been identified as a booster of circularity [43]. The implementation of circularity has resulted in innovation opportunities [44]. This is the case with the redesign of pharmaceutical supply chains to prevent the waste of medical supplies [45].

A clear example of circularity is the mass flow in nature [46]: a mixture of dead biomass is decomposed by microorganisms and fungi to simple molecules that are captured by plant roots to generate complex molecules again using solar energy. This nutrient flow takes place in natural environments but not in agriculture, where the products are transported away to consumers without returning back to fields [46], breaking the natural cycle.

There is intensive research available in the literature about circularity in the industry, such as in metals processing [47], including copper [48] and steel [49]. Other fields have also been researched, such as construction [50] or forest wood harvesting and utilisation [51]. However, the global economy

is not circular because large amounts of materials are used only once to provide energy or commercial value and are thus not available for recycling [52].

Examples of circularity in the chemical industry are related to plastics recycling as a consequence of the strategy of the European Commission [53]. The practices include plastic sorting [54], product design [55], or the design of chemical bonds suitable for biodegradation [56].

Many authors have defined circularity and its advantages and provided tools to quantify it. Examples include Corona et al. in 2019 [57], who focused on the circularity metrics, and Sassanelli et al. [58], who dealt with the assessment methods and the identification of the systematic taxonomy of the indicators used for circular economy evaluation by Saidani et al. [59].

The provided state-of-the-art review has shown that various tools and practices are available for process network optimisation, allowing the identification of the potential reuse paths for material components. However, accounting for the reuse of multiple resources within complex networks, containing multiple loops, creates a multi-dimensional optimisation problem if only approached directly. This observation reveals the need for an accounting framework and concepts that would measure the degree of sustainability and favorability of process networks adequately, taking into consideration the heterogeneous nature of the networks both in terms of their activities and the multitude of resources tracked.

The current work presents a system of analytical concepts, a framework and tools for evaluating the impacts of process systems based on thermodynamics. The framework is based on the concept of exergy as the unifying performance metric. It defines the tools of exergy assets and liabilities that enable the assessment of the sustainability of the considered systems. The trade-offs between the different feedstock and product flows and environmental impacts are modelled using the exergy assets and liabilities, leading to the calculation of the exergy footprint. The remaining content of the article presents the model and framework (Section 2), followed by illustrative case studies (Section 3) and a concluding discussion in Section 4.

2. Model and Framework

Process systems and supply chains consist of various process units and sub-systems, each of them having input and output interfaces and internal relationships. The heterogeneity of processes and their characteristics are complemented by the system scalability: the ability of various process units and systems to be integrated as parts of larger systems, forming nested hierarchies. This section starts with the development of the modelling concepts and framework, including the material flow cycles and the energy cascading principle; that is followed by the formulation of the accounting framework and the modelling equations.

2.1. General Trends and Issues

To derive a unifying criterion for the assessment of heterogeneous process systems of varying sizes, it is necessary to formulate a suitable framework. This should be based on a common process representation and allow the scalability of the evaluation scope. An essential property of the desired framework is that it be based on indicators that quantify the resource supply, demand, availability and deficit in a seamless way. The quantitative criteria also have to reflect the need to attain a sustainable development path of the considered system. These requirements form the basis for selecting reference conditions for the desired system designs.

At the process level, there can be multiple inputs and outputs. An example can be taken from the domain of agriculture [60]. As illustrated in Figure 1, there are various input streams as well as output streams, which are of different natures and have different environmental impacts and economic significance. While input-output analysis is helpful in quantifying the net resource and footprint impacts, it is difficult to use in revealing possible reuse and recycling patterns because of the different natures and compositions of the inlet and outlet streams.

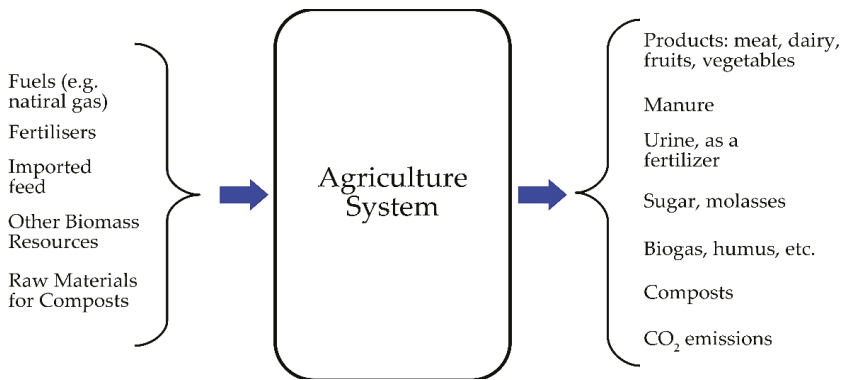


Figure 1. A multi-input–output process for an example of an agriculture system.

They are good examples of recycling from chemical processes involving reactors at the process level, where the unreacted feed is separated from the reaction products and recycled. Such an arrangement can be found in the ethanol production process by the hydration of ethylene [57]. The usual pattern is a reactor (or a reactor network) followed by separators. Figure 2 shows a summary of the process arrangement of the example given in [61]. The key reactants are ethylene and water. First, the ethylene is separated by flashing and washing, and then the resulting water–ethanol mixture is separated in a series of distillation columns. The system features two loops: one for the ethylene recycling and another for the water recycling.

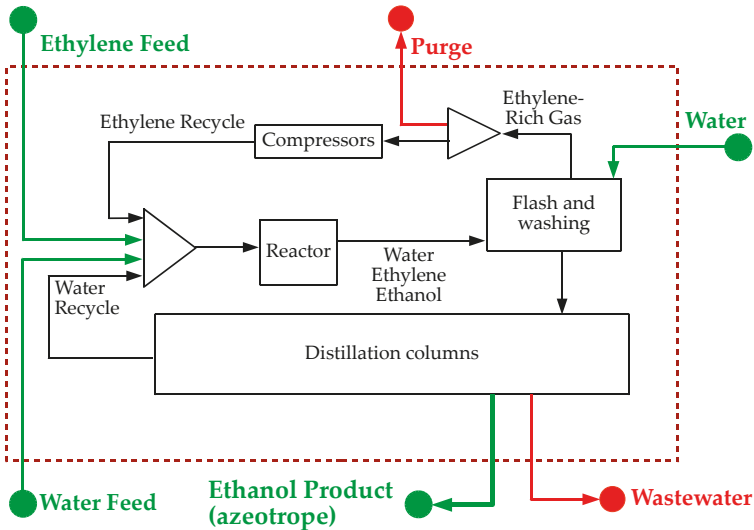


Figure 2. Ethanol production from ethylene summarised from the example in [61].

Several types of nexuses have been discussed in the research literature. Of these, the best-known is the energy–water nexus [62], but the correlations among other resources and product flows have also been investigated; for example the energy–water–food nexus [63], the joint consideration of water, land and food [64], and even the consideration of terrain–emission interactions [65]. All these nexuses

can be represented as having two major parts: material and energy flows. An analysis of these two parts is presented below.

2.1.1. Material Flows and Their Cycles

At the regional level, placing industrial sites within the environmental context reveals that the significant material flows feature two types of cycles (Figure 3), which can be extrapolated to a global (planetary) level. One type of material cycle is the traditional one: extracting resources (primary raw materials) from environmental storage sites, processing them into intermediate materials and further to products, the delivery and use of those products, the generation of waste streams and the disposal of the waste into the environment. The second cycle travels a shorter path, consisting of diverting part of the material flow of waste to the generation of secondary raw materials, which are used to substitute primary raw materials. Of these cycle types, the traditional route is more straightforward and is perceived as economically more favourable. While this may have been the case at the beginning of the industrial age, the increasing waste generation makes the recycling–reuse pattern desirable and viable for key materials such as paper [66], metals [67], and even electronic waste [68].

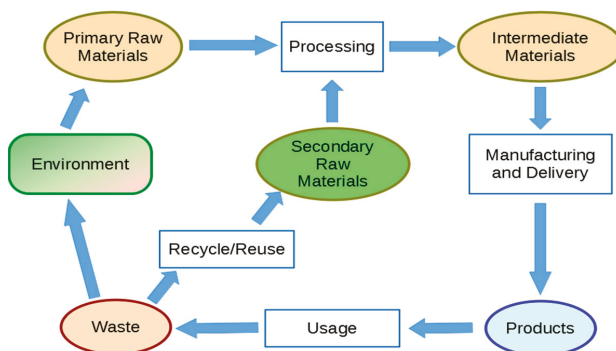


Figure 3. Global material cycles.

One obvious essential feature is that both material flow patterns form closed cycles. In this sense, the major degree of freedom within the material flows network is the split between the recycled and non-recycled fractions of the generated waste.

2.1.2. Energy Flows—Cascading

Energy can be sourced either from renewable sources (mainly of solar origin) or from terrestrial deposits (Figure 4). Energy flows follow the Laws of Thermodynamics, cascading from higher to lower quality [69]. Harvested energy flows can be used to power various processes, resulting in the movement of the material flows within a system; i.e., an enterprise, a municipality, or a region. At the system level, at various scales, energy can be sourced, converted and used and ultimately is left to dissipate in the environment. The share of the losses to dissipation reaches two-thirds [70]. This pattern reveals that there are two types of global system interface flows: energy inlets (renewable) and energy outlets (dissipation). Any non-renewable energy sources are internal to the system. This allows the classification of renewable energy sources as long-term degrees of freedom and the non-renewable as short term ones.

Energy cascading is thus used to power the closed material cycles for industrial and other activities in the global economy. Establishing this principle allows us to set up a framework for system state accounting which can be used to evaluate and optimise the system design and operation for various objective functions linked to the energy supply.

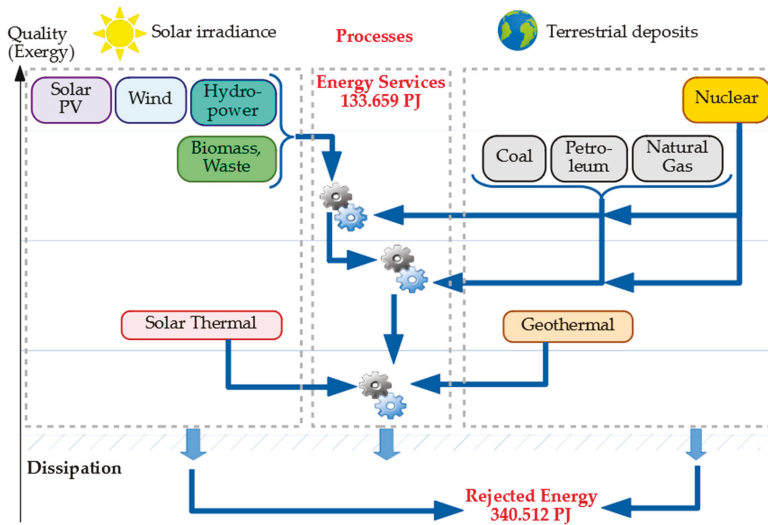


Figure 4. Energy cascading; data extracted from [70]. PV: photovoltaics.

The analysis in this section clearly points to energy harvesting and use as the dominating factor, representing a key degree of freedom in driving the economy and societal activities. Moreover, energy is stored in various forms for conversion, transport and use. This view of energy transformations allows the consideration of industrial and business processes as networks of states and transitions, where the states are related to the energy content of materials and process streams, while the transitions are either intentional process operations or spontaneous transitions, transforming process streams from one state to another at the expense of exergy conversion and destruction.

There have been many proposed circular economy indicators; e.g., a recent review [59] analysed 55 sets of circularity indicators. The choice and most beneficial use of indicators depends on the considered context. Within the context of a given supply chain or an industrial process, the degree of recycling of key materials is the most widely used indicator; in this context, the Circular Material Use rate (CMU) has been adopted by Eurostat [71] to determine the degree of circularity of systems at various scales. In the case of Eurostat, this is applied to measure the circularity of the economies of EU member states. CMU is defined, within the context of a specific material, as the fraction of the recycled material (U) within the overall material intake by the system (M):

$$CMU = \frac{U}{M} \tag{1}$$

While CMU is a crucial indicator, it alone is not sufficient to characterise the sustainability of the considered systems. Additional indicators are therefore needed to provide sufficient characterisation. The model proposed here uses energy as the main indicator, in the form of exergy, with all remaining system properties used as specifications to ensure the sustainable conditions of all parts of the environment–economy–society macro-system.

2.1.3. Exergy as the Unifying Performance Metric

The identified need for an energy-based indicator needs to be put in the correct context. The process systems are evaluated based on certain requirements, which are intended to minimise or eliminate any adverse environmental impacts of the system.

Referring to Figures 3 and 4, the material outputs of each process system cannot simply be released to the ambient environment. Before release, they have to be brought to a certain desired state at the

point of release to the environment characterised by composition (or an equivalent specification) and temperature. Naturally, suitable pressure also has to be selected and specified.

Such a state is usually defined by the environmental regulations concerning the corresponding natural storages. For instance, for wastewater discharge to environmental basins in the European Union, it is required that they contain a maximum of 25 mg/L BOD5 (Biological Oxygen Demand) at 20 °C [72], which can be used to estimate the content of the main contaminants.

Similarly, there are regulatory limits on effluent discharge temperature. For instance, King County, Seattle, US [73], allows a maximum of 40 °C at the entry of wastewater treatment plants. The Environmental Protection Agency of Taiwan [74] imposes limits from 35 to 42 °C for the points of discharge at sea, with the addition of a requirement that the water stream does not deviate from the surrounding surface water by more than 4 °C. The significance of this stipulation is that it relates the target stream temperature to that of the ambient conditions.

From the above reasoning, it becomes clear that all energy flows and storage contents that relate to the considered process systems are limited only to the energy that can be extracted as a difference from the conditions of the surrounding environment. This is equivalent to the definition of exergy, also known as availability [69].

In this case, the referenced environmental conditions are not necessarily the currently existing conditions but those mandated in the environmental regulations and standards. This provides a reference point for estimating the exergy balance (deficit or excess) to achieve zero deviation from the desired environmental conditions and minimise the potential environmental impacts.

The observations below aid in establishing the basis of the evaluation model:

- (1) For any process system, only the interface streams—inputs and outputs—can be considered as producing environmental impacts. Internal streams have no direct impact on the environment.
- (2) The inputs represent the demands of the system which are passed to upstream providers of resources, products and services. Similarly, the outputs represent the interface with their downstream counterparts: users/consumers, utilities, artificial (landfills, tailing ponds) and natural storage systems (the atmosphere, rivers, lakes, oceans, the ground).

The next section defines the necessary elements for using exergy as the metric to determine the quality of a process stream by defining exergy components associated with the stream, divided into assets and liabilities. The follow-up sections build on this by formulating the overall framework for exergy accounting and computing the exergy profit or loss associated with a process system.

2.2. Exergy Accounting Framework

For the evaluation of a process system's performance regarding its environmental impacts and its sustainability, it is necessary to capture the interfaces—i.e., the inlet and outlet streams (Figure 2)—as only they have the potential for impact. The internal constraints and internal flows are resolved by the system calculation model; i.e., simulation or optimisation. EXA and EXL denote the exergy assets and the exergy liabilities of a stream, respectively.

Consider again Figure 2, in which the input and output streams are highlighted. The process inputs are the streams labelled as ethylene feed, water feed, and water (wash water). The outputs are the streams labelled as "purge", wastewater, and ethanol product.

Inputs and outputs can be distinguished from the interface streams. An output stream is either a product or waste. In the case of product output, liabilities are not assigned because a product stream only carries useful value but does not involve the exergy penalty. Exergy assets can be assigned to a product stream only if the stream content implies or has the goal of retrieving exergy capable of driving economic activities such as chemical processes or transport operations.

For waste streams, the determination of exergy assets or liabilities employs a notional (potential) workflow (Figure 5). The workflow involves attempted operations for exergy extraction/recovery first, followed by the end of pipe treatment of the residual stream and finally discharge. Any potential for

exergy extraction and utilisation is defined as an asset, and the need to add exergy to the remaining potential workflow is added to the liabilities.

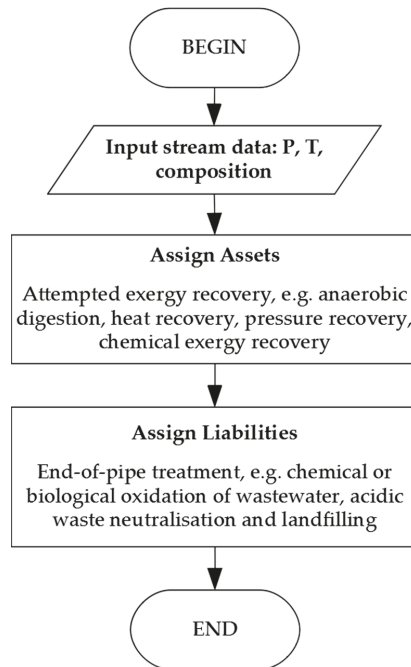


Figure 5. Procedure for assigning exergy assets and liabilities.

The input streams to the processing system have to be considered. For this, it is necessary to realise that the input to any human-operated process system is a product output of an upstream system. This includes, besides intermediate products, the resource streams extracted from nature (since the extraction itself is already an operation). Following the principles defined for products, the direct exergy liabilities are not assigned to the input streams, while exergy assets are assigned only in the case of an energy conversion system as the main object of evaluation.

The above discussion only reflects the perspective of the local to downstream impacts of a process system. To enable accounting for complete supply chains as well as the overall LCA [75], it is important also to include the upstream environmental impacts, leading to the need to account for the embodied exergy [28]. In this case, instead of the potential downstream exergy flows, the account includes the upstream exergy inputs (liabilities/credit) and the exergy content of the evaluated streams, assigned as assets.

Having estimated the exergy assets and liabilities for each of the interface streams for a process system, they are summed up, producing the total exergy assets (Equation (2)) and the total exergy liabilities (Equation (3)) of the system.

$$EX_{\text{asset}} = \sum_{\text{input},i} EX_{\text{asset},i} + \sum_{\text{output},j} EX_{\text{asset},j} \quad (2)$$

$$EX_{\text{liability}} = \sum_{\text{input},i} EX_{\text{liability},i} + \sum_{\text{output},j} EX_{\text{liability},j} \quad (3)$$

Equations (2) and (3) can be applied to various contours, including specific process systems, supply chains or complete life cycles. They can be used to evaluate downstream and/or upstream impacts.

2.3. Exergy Content of a Single Process Stream

Referring to the observations formulated at the end of Section 2.1.3, the values of EXA and EXL can be estimated for any stream in the considered system. Each process stream is modelled as having two exergy sets: EXA is assigned positive values, and EXL is assigned negative values. Summing the assets and the liabilities for the stream produces the net balance, resulting in the potential exergy profit (positive balance) or loss (negative balance).

The model development starts with the identification of the potential components of the exergy content in a stream. According to the theory presented in [7], the following components can be distinguished in the exergy content of a thermodynamic system, including a process stream [7]:

- (1) Thermo-mechanical/physical exergy: This is based on the thermal and pressure conditions of the system and can be expressed as in Equation (4) when no pressurised gas is present:

$$Ex_{phy} = (H - H_0) - T_0 \times (S - S_0) \quad (4)$$

where Ex_{phy} (MW) is the thermo-mechanical exergy flow rate, H and H_0 are the enthalpy flow rates of the stream (MW) at the current conditions and at the reference conditions, respectively, T_0 ($^{\circ}\text{C}$) is the temperature at the reference conditions, and S and S_0 are the entropy flow rates ($\text{kW}/^{\circ}\text{C}$). The typical reference conditions are 25°C and 1 atm. It has to be noted that the temperature-related quantities are given in $^{\circ}\text{C}$. While the definitions of the thermodynamic properties are based on the Kelvin scale, the usual temperature specifications are in $^{\circ}\text{C}$, which is the much more commonly used scale in engineering calculations.

- (2) Chemical exergy: This is the retrievable exergy from the system by applying potential chemical and physical conversions or the exergy input required for cleaning/separation. This component can be expressed in different ways, depending on the particular processes (chemical and/or biochemical). For chemical reactions, the chemical exergy can be evaluated as

$$Ex_{chem} = \sum_i (\mu_i - \mu_{i,0}) \times N_i \quad (5)$$

where Ex_{chem} (kW) is the chemical exergy flow rate, μ_i and $\mu_{i,0}$ (kJ/kmol) are the chemical potentials at current, and reference conditions, respectively, and N_i (kmol/s) is the molar flow rate of the flow. In this work, the reference state of the materials is evaluated based on the Szargut method [76]. The detailed calculation steps of the chemical exergy are shown in [6]. For simplicity, an open-source online tool [77] is used to estimate the chemical exergy of materials in this paper.

- (3) Gravitational exergy: This expresses the potential energy (directly convertible to exergy; see [7]) resulting from the elevation of the system above a certain base point:

$$Ex_G = m \times g \times \Delta h \quad (6)$$

where Ex_G (kW) is the gravitational (potential) exergy, m (kg/s) is the mass flow rate, g (m/s^2) is the acceleration due to gravity, and Δh (m) is the elevation difference between the current location of the stream and the location of the environmental reservoir selected for the reference point.

- (4) Kinetic exergy: This expresses the kinetic energy (directly convertible to exergy).

$$Ex_K = \frac{1}{2} \times m \times v^2 \quad (7)$$

where EX_k (kW) is the kinetic exergy, m (kg/s) is the mass flow rate, and v (m/s) is the velocity of the stream.

- (5) Electromagnetic exergy: The component (EX_{EM}) can also be defined for electrochemical systems and problems, expressing the potential of the system within an electromagnetic field. This can be calculated as equivalent to the energy delivered by the electric current [7].

For each modelling context, the significance and the relevance of each of the components have to be evaluated, and only the significant ones should be retained in the model. In the current work, only the thermo-mechanical and the chemical exergy components are evaluated. The other components are relevant to specific applications: the gravitational component is applicable to accounting for process layout, and the electromagnetic component is relevant to the electrochemistry and electromagnetism domains.

2.4. Exergy Profit and Exergy Footprint

The exergy assets and liabilities for a stream are both calculated using the equations in Section 2.3. They assign exergy extraction and utilisation potentials to the assets, and the exergy demands to the liabilities. Establishing the balance of the total exergy assets (EX_{asset}) (Equation (2)) and the total exergy liabilities ($EX_{liability}$) (Equation (3)) produces the exergy profit (EX_{profit}) of the process system:

$$EX_{profit} = EX_{asset} - EX_{liability} \quad (8)$$

The opposite difference (the negation) of the exergy profit is termed the exergy footprint ($EX_{footprint}$):

$$EX_{footprint} = -EX_{profit} = EX_{liability} - EX_{asset} \quad (9)$$

In this way, a positive value for the footprint means an adverse impact on the environment by imposing the equivalent demand to be supplied from outside sources. With this criterion, the sustainability contribution of the evaluated process system can be clearly measured. A higher exergy profit, meaning a lower exergy footprint, also translates to a better sustainability contribution of the system.

All exergy components can be used in the general case. However, in the current study, only the thermo-mechanical and the chemical components are evaluated, since they are the most typical for chemical and waste processing.

3. Case Studies

In this work, two case studies are used to demonstrate the exergy footprint evaluation of process systems. The scalability of the concepts and their applicability to problems from different domains are tested using two case studies.

The first case study deals with a single process of recovery of a chemical component. It involves the evaluation of the exergy profit of acetic acid from waste streams. Two processes involving acetic acid (AA) as the input and output—i.e., methanol carbonylation and vinyl acetate monomer (VAM) production—are chosen. The exergy profit is determined by taking the exergy needed for the processes and the exergy contents of the outlet streams into account.

The second case study considers a larger-scale, distributed system involving the potential treatment processes of Municipal Solid Waste (MSW), which is the output from private households. The exergy profit of the MSW stream is evaluated, considering the exergy requirement for the treatment processes, such as landfill and recycling, as well as the useful exergy content of the secondary products. For the exergy calculations, the specification of the reference point is 25 °C and 1 atm = 101.325 kPa.

3.1. Case Study 1: Material Streams Recovery—Acetic Acid

The global consumption of acetic acid (AA) as a chemical product in 2018 was estimated at over 16×10^6 t. BP Chemicals is the largest supplier of acetic acid. The overall acetic acid output

is shared between the manufacturing of vinyl acetate monomer (VAM) at 33%, acetic anhydride at 18%, monochloroacetic acid (MCA) at 17%, acetate esters at 17%, and terephthalic acid at 17% [78]. The manufacturing of acetic acid by the carbonylation of methanol represents the largest part of the market, at about 75%. This share shows continuous growth. Besides methanol, the synthesis may start from dimethyl ether (DME) and later from materials leading to syngas, such as biogas and biomass. For this reason, acetic acid may be a 100% green product [79]. For example, if both acetic acid and ethylene are manufactured using methanol obtained from syngas, then the vinyl acetate is a bio-product, as well as the valuable acrylic paints produced from it. In this way, a variety of products issued from a syngas bio-refinery can replace traditional petrochemicals.

Diluted solutions of acetic acid in water are typical for side streams in several production processes including terephthalic acid synthesis, acetyl cellulose manufacture and biochemical processes. Since the concentration of AA in those streams is typically in the range of 10% to 40% (mass), it may be profitable to recover and recycle it as a solvent [80]. However, the separation processes are often expensive and energy-intensive; these processes include reactive distillation, extractive distillation, and membrane separation. Thus, the side streams are commonly diluted and eliminated in a wastewater treatment plant. This makes acetic acid one of the major water pollutants treated in the chemical industry, especially in petrochemical or fine chemical industries [81].

In Section 3.1.1, the exergy footprint of the AA waste stream is evaluated. The AA waste stream comes from a methanol carbonylation process, while VAM production is considered as a potential downstream process that may utilise AA. Section 3.1.2 evaluates the exergy profit of using the acetic acid waste stream as input for VAM production.

3.1.1. Exergy Profit of Waste Acetic Acid Streams.

To define the exergy footprint/profit of the waste acetic acid stream, the potential downstream process and the boundary need to be defined. In this paper, the methanol carbonylation process is chosen as the process that produces the pure acetic acid and the waste stream containing the acetic acid. The potential downstream process—namely vinyl acetate production—utilises the waste acetic acid as a secondary input. Figure 6 shows the identified processing options.

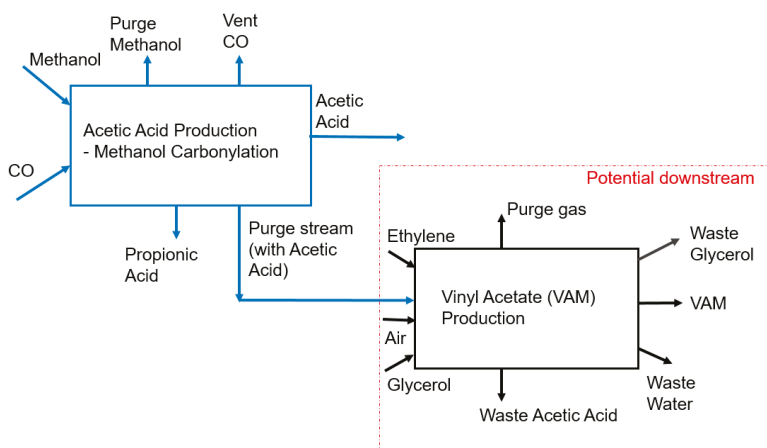


Figure 6. Exergy profit evaluation of waste acetic acid stream.

The purge stream containing acetic acid is the waste stream under evaluation. The methanol carbonylation process mainly synthesises acetic acid as the main product. The waste stream (purge stream) contains a significant concentration of acetic acid (see Table 1). The mass and energy balance data

are retrieved from [79]. The waste stream is not likely to be marketable but can be used to retrieve a secondary raw material for the vinyl acetate (VAM) production process. Figure 7 shows the Aspen HYSYS [82] simulation of the VAM process. The parameters for equipment sizing can be retrieved from [83]. Tables 1 and 2 show the mass balance data of the two processes. The exergy to be added to the process includes the exergy inputs of the energy streams and the workstreams. In this work, the reference state of the materials is evaluated based on the Szargut method [76]. The detailed calculation steps of the chemical exergy are shown in [6]. For simplicity, an open-source online tool [77] is used to estimate the chemical exergy of materials in this paper.

Table 1. Data of acetic acid production, derived from [79].

Exergy to be Added to the Process, EX _{add} (MW/t/h of AA Produced)	0.532							
	Mass Balances	Input			Output			
		Methanol	CO	Purge Methanol	Propionic Acid	Vent CO	Acetic Acid	Purge Stream
Pressure (bara)	40	2	1.1	1.5	35	1.1	1.3	
Temperature (°C)	20	25	36	125	5	33	125	
Mass flow (kg/kg of AA)	0.838	0.491	0.265	0.00583	0.0136	1	0.0167	
Enthalpy, H (kJ/kg)	-7491	-3948	-7752	-6467	-7392	-7666	-7344	
Entropy, S (kJ/kg/°C)	2.282	6.849	1.045	2.048	2.361	1.273	1.419	
H ₀ (kJ/kg)	-7473	-3948	-7682	-6665	-7295	-7678	-7519	
S ₀ (kJ/kg/°C)	1.457	7.051	1.557	1.025	2.195	1.184	0.592	
Mass chemical exergy (kJ/kg)	0.705	0.351	0.633	0.288	0.723	0.251	0.258	
Total mass exergy (physical + chemical) (kJ/kg)	-263.145	60.547	83.209	-106.566	-145.745	-14.271	-71.247	
Vapour fraction	0	1	0	0	1	0	0	
Mass Compositions								
Methanol	1	0	0.894	0.000	0.918	0.000	0.000	
CO	0	1	0.002	0.000	0.029	0.000	0.000	
CO ₂	0	0	0.003	0.000	0.024	0.000	0.000	
CH ₄	0	0	0.000	0.000	0.029	0.000	0.000	
Methyl acetate	0	0	0.062	0.000	0.000	0.000	0.000	
Acetic acid	0	0	0.000	0.000	0.000	0.997	0.400	
H ₂ O	0	0	0.002	0.000	0.000	0.001	0.300	
CH ₃ I	0	0	0.037	0.000	0.000	0.000	0.000	
Propionic acid	0	0	0.000	1.000	0.000	0.002	0.300	

The basic data for exergy calculations of various streams have been found in [6]. The feed used in the VAM production process is a pure acetic acid. As an input stream type, no EX_{Asset} or EX_{Liability} values are assigned to it.

The exergy liabilities and assets have to be determined first to compute the exergy profit of the waste acetic acid stream. The exergy profit is, therefore, the difference between the assets and the liabilities. The exergy asset and liability can be calculated based on Equations (2), (3) and (8):

$$EX_{\text{asset, AA Waste}} = \sum_j EX_{\text{output},j} \quad (10)$$

$$EX_{\text{liability, AA Waste}} = \sum_i EX_{\text{input},i} + EX_{\text{add}} \quad (11)$$

$$EX_{\text{profit, AA Waste}} = EX_{\text{asset, AA Waste}} - EX_{\text{liability, AA Waste}} \quad (12)$$

where EX_{add} represents the exergy to be added to the downstream process, *i* represents the set of input material *i* in the downstream process, and *j* represents the set of output material *j* in the downstream process. Note that the exergy mentioned here is the total exergy (chemical + physical).

Table 2. Simulation results of vinyl acetate production.

Exergy to be Added to the Process, EX _{add} (MW per 1 t/h of AA Feed)	Input						Output					
	Air	Ethylene	Acetic Acid	Glycerol	Waste Acetic Acid	Vinyl Acetate	Waste-Water	Waste Glycerol	Purge Gas			
0.458	1.013	1.013	1.013	2	9	2	112.3	4	9			
Pressure (bara)	25	25	25	100	200.2	100	5	208.7	214.5			
Temperature (°C)	0.382	0.394	1	0.0556	0.0679	0.0556	0.0131	0.0607	1.64			
Mass flow (kg/kg of AA)	-0.282	1864	-7669	-7160	-7369	-7160	-13820	-7503	-3301			
Enthalpy, H (kJ/kg)	5.258	6.28	0.548	0.2259	1.535	0.2259	3.578	1.826	4.166			
Entropy, S (kJ/kg K)	-0.282	1864	-7669	-7358	-7670	-7358	-14630	-8034	-3785			
H ₀ (kJ/kg)	5.258	6.28	0.548	-0.9517	0.5497	-0.9517	1.558	-0.6789	3.063			
S ₀ (kJ/kg K)	0.00169	1.74	0.250	0.205	0.250	0.205	0.194	0.251	0.482			
Mass chemical exergy (kJ/kg)	0.00169	1.74	0.250	-152.92	7.38	-152.92	208.0	-215.46	155.3			
Total mass exergy (physical + chemical) (kJ/kg)	1	1	0	0	0	0	0	0	1			
Vapour fraction												
Mass Compositions												
Acetic acid	0	0	1	0	0.894	0	0	0.0037	0.0014			
CO ₂	0	0	0	0	0.002	0	0	0	0			
Ethylene	0	1	0	0	0.003	0	0.0008	0	0			
Glycerol	0	0	0	1	0.000	0	0.0001	0	0.9187			
H ₂ O	0	0	0	0	0.062	0	0	0.8573	0.0799			
Nitrogen	0.7671	0	0	0	0.000	0	0	0	0			
Oxygen	0.2329	0	0	0	0.002	0	0	0	0			
Vinyl acetate	0	0	0	0	0.037	0	0.9991	0.139	0			

Table 3 shows the calculation results, assuming a value of 100 kg/h of the purge stream. The detailed calculation steps are given in the Supplementary Materials (Part 1). It can be observed from the table that the exergy profit of the stream is -0.0497 MW. The original exergy content of the purge stream is -0.000198 MW. This shows that the exergy profit is lower than the exergy content of the stream without undergoing the downstream VAM process. The negative sign of the exergy indicates that extra work needs to be inputted to bring the materials to the reference conditions since it is not a spontaneous process. According to the results, it can be deduced that higher exergy needs to be invested in reusing the purge stream for the VAM production process, translating to an exergy footprint of 0.0497 MW.

Table 3. Calculation results of the waste acetic acid stream, on the basis of a value of 100 kg/h of the purge stream.

Exergy of Purge Stream (MW)	-0.000198
Exergy liability (MW)	0.0530
Exergy asset (MW)	0.0033
Exergy profit (MW)	-0.0497

3.1.2. Exergy Profit of Input Acetic Acid Streams

Next, we consider the acetic acid inlet to the VAM production process (see Figure 8, derived from Figure 6). The potential upstream process and the boundary need to be defined to evaluate the exergy footprint/profit of the input acetic acid stream. A similar case study is used to demonstrate the exergy accounting for the input stream. The specific process example evaluated is the VAM production process. The acetic acid feed stream is chosen for evaluation.

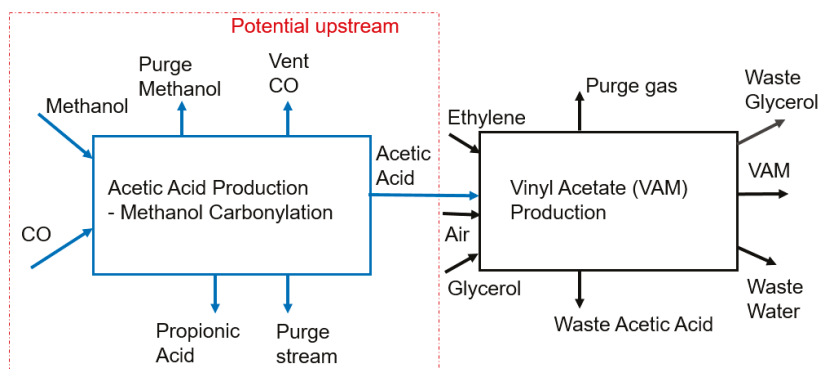


Figure 8. Exergy profit evaluation of inlet acetic acid stream.

Equations (2), (3) and (8) are applied to the evaluation, taking the following form:

$$EX_{\text{liability,AA feed}} = \sum_i EX_{\text{input},i} + EX_{\text{add}} \quad (13)$$

$$EX_{\text{asset,AA feed}} = \sum_j EX_{\text{output},j} \quad (14)$$

$$EX_{\text{profit, AA feed}} = EX_{\text{asset, AA feed}} - EX_{\text{liability,AA feed}} \quad (15)$$

where EX_{add} represents the exergy to be added to the upstream process, i represents the set of input material i in the upstream process, and j represents the set of output material j in the upstream process.

Table 4 shows the calculation results, assuming a value of 100 kg/h of the acetic acid stream is fed to the VAM production process. The detailed calculation steps are provided in Part 2 of the

Supplementary Materials. The exergy liability is much higher than the exergy of the acetic acid stream. The original exergy content of the acetic acid stream is -0.000069 MW. The results show that the actual exergy required to produce 100 kg/h of acetic acid from the chosen upstream process is higher than the exergy of the stream itself. The exergy profit shows how much exergy input is needed to produce the acetic acid input stream.

Table 4. Calculation results of input acetic acid stream, on the basis of a value of 100 kg/h of the acetic acid input stream.

Exergy of the Acetic Acid Stream (MW)	-0.000069 *
Exergy liability (MW)	0.0492
Exergy asset (MW)	0.0023
Exergy profit (MW)	-0.0468

* The exergy content of the acetic acid stream is supposed to be 0.000069 MW. However, since this is an input stream, this means that work is needed to produce this stream (a liability) from the reference conditions. A negative sign is thus shown for the exergy value.

3.2. Case Study 2: Waste-to-Energy Process—Municipal Solid Waste

The second case study evaluates a waste-to-energy process to demonstrate the methodology for a different process system type. MSW contains a significant portion of the paper, wood, garden, food and other organic waste materials comprising lignocellulosic and biodegradable organic fractions. The lignocelluloses consist of cellulose (38–50%), hemicellulose (23–32%), lignin (15–25%), and inorganic ashes and can be extracted from municipal solid waste (MSW) or urban or household waste [84].

The lignocellulose compounds contained in the MSW can be degraded thermochemically [85] or biochemically [86]. The common waste treatment involves thermochemical processing, such as incineration [87], resulting in an energy product stream, as well as gasification [88] and pyrolysis [89] producing chemical and energy products; e.g., syngas, bio-oil, and residual waste heat.

In the case of biomass hydrolysis—e.g., enzymatic hydrolysis [90]—the liberated glucose can be used to synthesise high-value chemical products; e.g., 5-hydroxymethylfurfural (HMF) and levulinic acid (LA) [91]. These building-block chemicals are sometimes labelled as “sleeping giants” due to their vast potentials in the emerging bio-based economy and their key positions in the production of biomass-derived intermediates. This aids in the transition from a fossil-based to a bio-based economy, which promotes the concept of the circular economy.

In spite of the intensive investigations into extracting these two target chemicals from MSW, there is currently no research on how the thermochemical processes can be completely integrated within biorefineries utilising MSW. The available resources that can be extracted from the MSW are metals, refuse-derived fuel (RDF), chemicals (e.g., LA), fertilisers, and energy [92].

3.2.1. Municipal Solid Waste Exergy Profit Evaluation

To investigate the potential of resource recovery from MSW via integrated mechanical biological chemical treatment (MBCT), the case study in [84] is used. The exergy profit of the MSW is determined based on the selected downstream processes: material recovery, pulping, recovery of chemicals, and anaerobic digestion for biogas generation. In Figure 9, the selected potential process for MBCT for MSW, adapted from [84], is shown. The mass balances between the input and output are presented in Figure 9.

For this case study, the Municipal Solid Waste (MSW) is chosen as the output stream from a private household. The equation to calculate the specific exergy of MSW (adapted from [93]), which is a function of its heating value, is presented below:

$$EX_{MSW} = 376.461 \times C + 791.018 \times H - 57.819 \times O + 45.473 \times N - 1536.24 \times S + 100.981 \times Cl \quad (16)$$

In Equation (16), EX_{MSW} is the specific exergy of MSW (kJ/kg), C is the carbon content in %, H is the hydrogen content in %, O is the oxygen content in %, N is the nitrogen content in %, S is the sulfur content in %, and Cl is the chlorine content in %. All of the element percentages should be determined on a dry ash-free basis. The composition data of MSW are presented in Table 5, retrieved from [84].

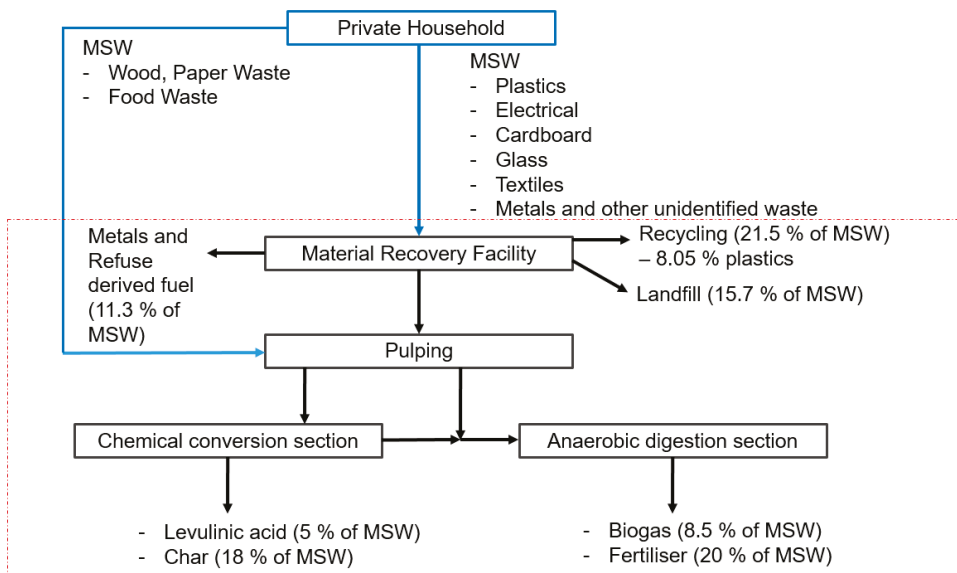


Figure 9. Mechanical biological chemical treatment (MBCT) of Municipal Solid Waste (MSW), with mass balances between input and output, adapted from [84].

Table 5. Data of Municipal Waste, from [84].

Elements	Amount (wt%)	
Plastic	10.4	
Cardboard	5.2	
Glass	6.8	
Electrical waste	2.3	
Textiles	2.9	
Metals and unidentified waste	18.6	
Paper	14	
Wood, garden and food waste	37.3	
Other organic	2.5	
Composition of Fuels	Amount (wt% wet Basis)	Amount (wt% Dry Ash-Free Basis)
Carbon	26.7	57
Hydrogen	3.37	7.19
Oxygen	16.14	34.46
Nitrogen	0.52	1.11
Sulfur	0.11	0.235
Ashes	11.87	-
Water	41.3	-
Volatile material	41.86	41.86

To evaluate the exergy profit of the MSW stream, it is imperative to evaluate the exergy performances of the treatment processes. Based on the diagram above, the treatment processes

are recycling, landfill, chemical conversion and anaerobic digestion (AD). The exergy profit of the MSW is calculated based on the implementation of Equations (2), (3) and (8) for the MSW case:

$$EX_{\text{liability, MSW}} = \sum_i EX_{\text{input},i} \quad (17)$$

$$EX_{\text{asset, MSW}} = \sum_j EX_{\text{output},j} \quad (18)$$

$$EX_{\text{profit, MSW}} = EX_{\text{asset, MSW}} - EX_{\text{liability, MSW}} \quad (19)$$

Table 6 shows the exergy data needed for various waste treatment processes. The superscripts in the table reflect the data sources and the contexts.

Table 6. Exergy calculation data for the MSW case study.

Process	Cumulative Exergy to be Added (MJ/kg of Waste Feed)	Cumulative Useful Exergy of the Secondary Product (MJ/kg of Waste Feed)
Incineration ^a	1.2	16.586
Landfill ^a	0.336	0.242
Recycling ^a	10.442 ^e	33.086 ^e
Anaerobic digestion (AD) ^{b,c}	1.09	1.41
Chemical conversion ^{c,d}	3.01	9.83

- The average exergy values are retrieved from [94]. Due to the lack of data availability, the data for plastic wastes are used.
- Products = 150 m³ of biogas/t of waste; electricity = 1.81 kWh/m³ of biogas; heat (at 55 °C) = 2.27 kWh/m³ of biogas; density of biogas = 1.15 kg/m³ [95]. The exergies of fertilisers are assumed to be zero since the nutrients are returned to the environment [96]
- The cumulative exergy added is estimated based on the exergy requirement from the process heat and work streams. The exergy of the secondary product is estimated based on the exergy contents of the products: biogas for the anaerobic digestion (AD), char and levulinic acid for chemical conversion process [84]. The biogas and char are assumed to be secondary fuels, and their exergies can be assumed to be equal to their higher heating value [97].
- The data for energy and work streams can be retrieved from [84].
- The exergy values are for plastic recyclables only.

The exergy asset of the MSW stream is evaluated as the cumulative useful exergy of the secondary products after the waste treatment processes; i.e., the products after the incineration, landfill, recycling, AD and chemical conversion. The exergy liability is calculated by summing the cumulative exergy to be input to the waste treatment processes (see Table 6). The detailed calculation steps are presented in Part 3 of the Supplementary Materials.

Table 7 shows the calculation results, assuming a basis of 1 t/h of MSW produced. The original exergy of the MSW stream is calculated using Equation (16), which is a function of its heating value. The net exergy profit represents the exergy of the MSW stream after it passes through the potential downstream treatment via the MBCT system.

Table 7. Calculation results for MSW stream, on the basis of 1 t/h of MSW produced.

Exergy of MSW Stream (MW)	6.90
Exergy liability (MW)	0.484
Exergy asset (MW)	1.39
Net exergy profit (MW)	0.906

According to the calculation results, the exergy of the MSW stream is 6.90 MW, showing that it has high potential as a fuel. The above MBCT system shows that there is an exergy profit for the MSW stream (0.906 MW), due to the potential useful products. This is a significant chemical conversion section, as the exergy assets of the secondary products are high. The levulinic acid has a high exergy value, and the char also has potential as a fuel. Despite the recycling process requiring high exergy, it is only applied to the plastic recovery for the recyclables. The small amount of plastic in the recyclables (8.05%) reduces the useful exergy as well as its exergy liability.

3.2.2. Cumulative Exergy Composite Curves

To compare different scenarios with the MSW treatment system, the current waste practices in the Czech Republic [95] are used for comparison with the MBCT system in this study. The data used in this study are based on Table 6, assuming both scenarios use waste treatment technologies with similar efficiencies. Figure 10 illustrates the scenarios, showing the distribution of the MSW.

Scenario analysis

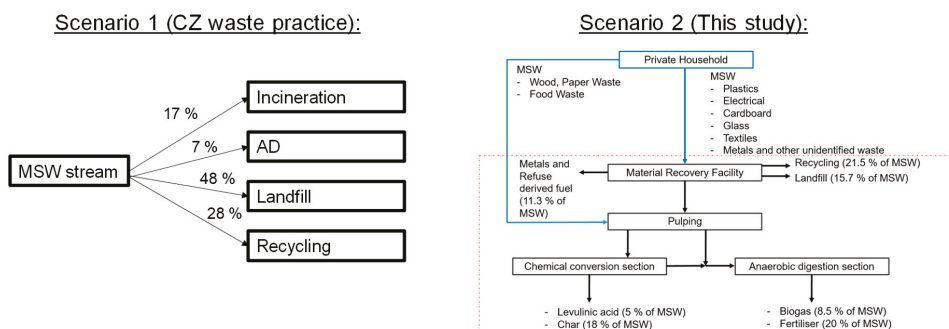


Figure 10. Workflows for MSW treatment under comparison.

The exergy liabilities and the exergy profit for the individual waste treatment processes are plotted in composite curves, as shown in Figures 11 and 12. The steps taken to draw the composite curves are explained below:

- (1) The waste practices are arranged in ascending order of exergy value (expenditure or profit) per kg of the waste amount.
- (2) The cumulative waste amount and the cumulative exergy (liability and net profit) are determined based on the order from Step (1).
- (3) The Composite Curves are plotted with a cumulative waste amount on the x -axis and cumulative exergy (liability or profit) on the y -axis.

Based on Figures 11 and 12, the cumulative exergy liability for Scenario 2 is much higher than that of Scenario 1. However, the exergy profit for Scenario 2 (0.91 MW) is slightly higher than that in Scenario 1 (0.89 MW). This is specifically thanks to the chemical conversion process. This shows that the practices in Scenario 2 yield a somewhat higher exergy profit, but they also require a great deal more exergy.

According to Table 6, although incineration has a higher exergy profit per unit waste, a greater amount of waste is sent to the chemical conversion in Scenario 2, making its exergy profit surpass that of Scenario 1. It can be shown that the chemical conversion process has the highest specific exergy liability due to the requirement of steam for pulping and the other conversion processes. Nevertheless, the exergy profit for the chemical conversion is still highest due to the high exergy asset

level of the levulinic acid and that of the char as a secondary fuel. It is worthy of note that the specific exergy profit of landfill is lower, although its specific exergy liability is the lowest because the useful exergy asset level of the process is very low (see Table 6).

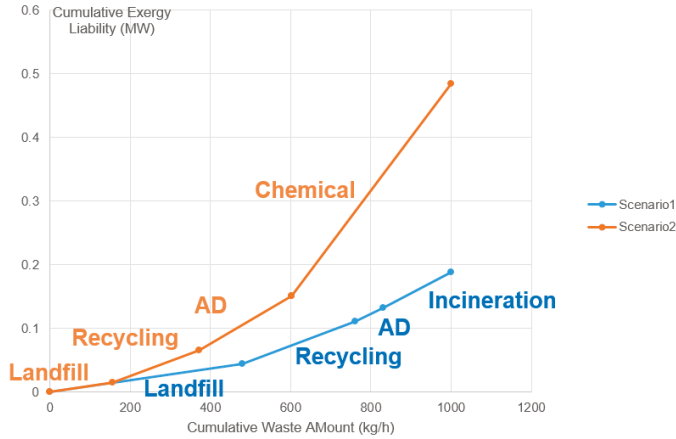


Figure 11. Composite Curves for the exergy liabilities of the MSW treatment under comparison.

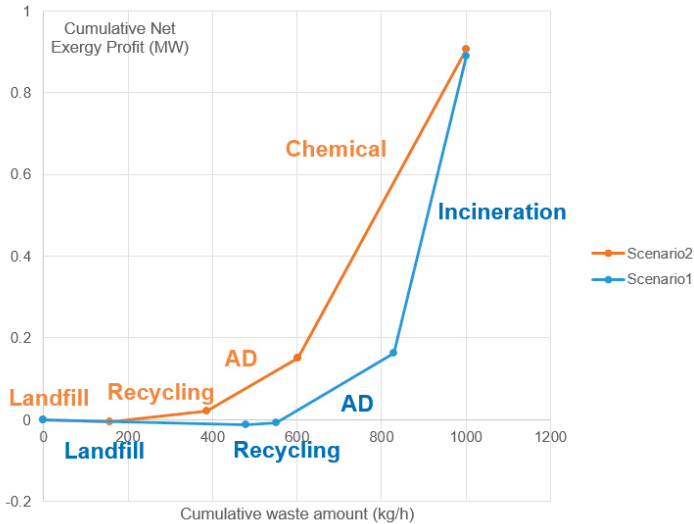


Figure 12. Composite Curves for the exergy profit of the MSW treatment under comparison.

It can also be seen that incineration has the highest specific exergy liability for Scenario 1, but it also has the highest specific exergy profit, as the products have a high amount of useful exergy content. The composite curves are useful to compare process systems and pinpoint the processes with a high exergy liability or exergy profit, allowing mitigation actions to be targeted to improve the waste treatment practices.

4. Conclusions

This article reveals that the fundamental trade-offs between the various resource flows and environmental impacts—such as water–energy and water–energy–food nexuses—converge to the issues of material flow circularity and energy flow cascading. Based on this understanding, the concepts of exergy assets, exergy liabilities, and exergy profit/footprint are formulated, supplemented with a comprehensive evaluation framework.

Two case studies from completely different industrial domains are provided which illustrate the applicability of the framework for the seamless assessment of the energy/exergy needs of the process systems. These include the processes of acetic acid production and MSW treatment areas.

The results from the first case study show that the separation and reuse of the acetic-acid-containing purge stream are exergy-prohibitive and that it is not probable that such a solution would be sustainable. The follow-up analysis of the acetic acid production shows that the process requires a substantial external exergy input. Determining the degree of sustainability of such a process needs further analysis of the possible sources of providing such exergy.

The second case study clearly shows the sustainability potential of the MSW treatment for obtaining either useful energy directly or first extracting useful chemicals before the waste-to-energy process. The developed cumulative Exergy Composite Curves show a marginal advantage (less than 10%) of the chemical extraction route over the direct waste-to-energy route. The developed curves demonstrate that the proposed framework represents a useful toolset for evaluating process systems and alternative solutions.

The proposed concept can be further developed to create a complete framework which is capable of accounting for the thermodynamic irreversibility of processes. This will help us to reach a deeper understanding of the exergy flows, storages and losses and their relation to process sustainability.

Building on this, future work should incorporate economic metrics into the evaluation, leading to a complete toolset accounting for both the technical and economic performance of the considered process systems. This will make the tools suitable for decision-making in real engineering projects and for use by process managers and potential investors.

The correct selection of the system boundaries for the analysis of exergy footprints is key to the practical applicability of the concept. Full Life Cycle Assessment requires the collection of a large amount of information, which sometimes depends on subjective considerations. In many cases, not all stages of the life cycle are really significant with respect to the chosen criteria. In this context, further work should also be directed towards embedding this accounting framework within the Life Cycle Assessment framework, allowing for the scalability of the concepts and their adaptation to the modelling contexts.

Supplementary Materials: The following are available online at <http://www.mdpi.com/1996-1073/13/9/2132/s1>.

Author Contributions: P.S.V.; conceptualisation and methodology formulation; H.H.C.; development of the case studies, formulation of the cumulative Exergy Composite Curves; A.-E.P.P.; state-of-the-art analysis, verification of the exergy models and calculations; S.B.: Introduction section development, feedback on the development of the concept in Section 2.3. proofreading. All authors have read and agree to the published version of the manuscript.

Funding: The EU-supported project Sustainable Process Integration Laboratory—SPIL funded as project No. CZ.02.1.01/0.0/0.0/15_003/0000456, by Czech Republic Operational Programme Research and Development, Education, Priority 1: Strengthening capacity for quality research, based on the SPIL project, is gratefully acknowledged. The research was also supported by the Tomsk Polytechnic University (VIU-RSCABS-142/2019).

Acknowledgments: Alexandra Elena Plesu Popescu is a Serra Hunter fellow.

Conflicts of Interest: The authors declare no conflict of interest.

Nomenclature

P	Pressure (MPa)
T	Temperature (°C)
V	Volume (m ³)
S	Entropy (kJ/kg/°C)
GHG	Greenhouse gas
HEN	Heat exchange network
MUD	Material-utilisation diagram
DSE	Directional solvent extraction
TBS	Thermomorphic biphasic solvent
LLPS	Liquid–liquid phase separation
LCA	Life Cycle Assessment (Analysis)
SCP	Sustainable consumption and production
PV	Photovoltaic (panels)
CMU	Circular material use (rate)
BOD5	Five-day biochemical oxygen demand (mg/L)
EX _{asset}	Exergy assets (MW)
EX _{liability}	Exergy liabilities (MW)
EX _{profit}	Exergy profit of a stream (MW)
EX _{footprint}	Exergy footprint of a stream (MW)
EX _{phys}	Thermo-mechanical/physical exergy flow rate (MW)
EX _{chem}	Chemical exergy flow rate (MW)
H (H ₀)	Enthalpy flow rates of the stream (MW) at the current conditions, and at the reference conditions
T ₀	Temperature at the reference conditions (°C)
S (S ₀)	Entropy flow rates (kW/°C) at current and at reference conditions
μ _i (μ _{i,0})	Chemical potentials at current and reference conditions (kJ/kmol)
N _i	Molar flow rate (kmol/s)
ExG	Gravitational (potential) exergy (kW) or (MW)
m	Mass flow rate (kg/s)
g	Acceleration due to gravity (m/s ²)
Δh	Elevation difference between the current and the reference location
EX _{EM}	Electromagnetic exergy (MW)
AA	Acetic acid
VAM	Vinyl acetate monomer
MSW	Municipal Solid Waste
MCA	Monochloroacetic Acid
DME	Di-Methyl Ether
HMF	5-hydroxymethylfurfural
LA	Levulinic acid
RDF	Refuse-derived fuel
MBCT	Mechanical biological chemical treatment
AD	Anaerobic digestion
TEC	Thermo-Ecological Cost methodology
ERC	Exergy Replacement Costs concept
TERC	Thermal-Exergy Replacement Cost

References

1. Klemeš, J.; Huisingh, D. Economic use of renewable resources, LCA, cleaner batch processes and minimising emissions and wastewater. *J. Clean. Prod.* **2008**, *16*, 159–163. [[CrossRef](#)]
2. Klemeš, J.J.; Varbanov, P.S.; Ocloň, P.; Chin, H.H. Towards Efficient and Clean Process Integration: Utilisation of Renewable Resources and Energy-Saving Technologies. *Energies* **2019**, *12*, 4092. [[CrossRef](#)]
3. Gerbens-Leenes, P.W.; Hoekstra, A.Y.; Bosman, R. The blue and grey water footprint of construction materials: Steel, cement and glass. *Water Resour. Ind.* **2018**, *19*, 1–12. [[CrossRef](#)]

4. Fan, Y.V.; Perry, S.; Klemeš, J.J.; Lee, C.T. A review on air emissions assessment: Transportation. *J. Clean. Prod.* **2018**, *194*, 673–684. [[CrossRef](#)]
5. Bong, C.P.C.; Lim, L.Y.; Ho, W.S.; Lim, J.S.; Klemeš, J.J.; Towprayoon, S.; Ho, C.S.; Lee, C.T. A review on the global warming potential of cleaner composting and mitigation strategies. *J. Clean. Prod.* **2017**, *146*, 149–157. [[CrossRef](#)]
6. Ghannadzadeh, A.; Thery-Hetreux, R.; Baudouin, O.; Baudet, P.; Floquet, P.; Joulia, X. General methodology for exergy balance in ProSimPlus® process simulator. *Energy* **2012**, *44*, 38–59. [[CrossRef](#)]
7. Dinçer, İ.; Rosen, M. *Exergy: Energy, Environment, and Sustainable Development*; Elsevier: Amsterdam, The Netherlands, 2007; ISBN 978-0-08-044529-8.
8. Ehyaei, M.A.; Ahmadi, A.; Rosen, M.A. Exergy, economic and advanced and extended exergy analyses of a wind turbine. *Energy Convers. Manag.* **2019**, *183*, 369–381. [[CrossRef](#)]
9. Song, D.; Lin, L.; Wu, Y. Extended exergy accounting for a typical cement industry in China. *Energy* **2019**, *174*, 678–686. [[CrossRef](#)]
10. Amiri, Z.; Asgharipour, M.R.; Campbell, D.E.; Armin, M. Extended exergy analysis (EAA) of two canola farming systems in Khorramabad, Iran. *Agric. Syst.* **2020**, *180*, 102789. [[CrossRef](#)]
11. Wan Alwi, S.R.; Manan, Z.A.; Klemeš, J.J.; Huisingsh, D. Sustainability engineering for the future. *J. Clean. Prod.* **2014**, *71*, 1–10. [[CrossRef](#)]
12. Avraamidou, S.; Baratsas, S.G.; Tian, Y.; Pistikopoulos, E.N. Circular Economy-A challenge and an opportunity for Process Systems Engineering. *J. Clean. Prod.* **2020**, *133*, 106629. [[CrossRef](#)]
13. Dincer, I.; Rosen, M.A.; Al-Zareer, M. 5.5 Exergy Management. In *Comprehensive Energy Systems*; Dincer, I., Ed.; Elsevier: Amsterdam, The Netherlands, 2018; pp. 166–201. ISBN 978-0-12-814925-6.
14. Makarieva, A.M.; Gorshkov, V.G.; Li, B.-L. Energy budget of the biosphere and civilization: Rethinking environmental security of global renewable and non-renewable resources. *Ecol. Complex.* **2008**, *5*, 281–288. [[CrossRef](#)]
15. Gallegos-Muñoz, A.; Zaleta-Aguilar, A.; González-Rolón, B.; Rangel-Hernandez, V.H. On an Exergy Efficiency Definition of a Wastewater Treatment Plant. *Int. J. Thermodyn.* **2003**, *6*, 169–176.
16. Magnanelli, E.; Berglihn, O.T.; Kjelstrup, S. Exergy-based performance indicators for industrial practice. *Int. J. Energy Res.* **2018**, *42*, 3989–4007. [[CrossRef](#)]
17. Yamamoto, M.; Ishida, M. New Graphical Method for Representing Characteristic Features of Extraction. *Ind. Eng. Chem. Res.* **2002**, *41*, 277–284. [[CrossRef](#)]
18. Alotaibi, S.; Ibrahim, O.M.; Wang, Y.; Luo, T. Exergy Analysis of Directional Solvent Extraction Desalination Process. *Entropy* **2019**, *21*, 321. [[CrossRef](#)]
19. Zhang, J.; Qiao, Y.; Agar, D.W. Intensification of low temperature thermomorphic biphasic amine solvent regeneration for CO₂ capture. *Chem. Eng. Res. Des.* **2012**, *90*, 743–749. [[CrossRef](#)]
20. Suh, S.; Lenzen, M.; Treloar, G.J.; Hondo, H.; Horvath, A.; Huppes, G.; Jolliet, O.; Klann, U.; Krewitt, W.; Moriguchi, Y.; et al. System Boundary Selection in Life-Cycle Inventories Using Hybrid Approaches. *Environ. Sci. Technol.* **2004**, *38*, 657–664. [[CrossRef](#)]
21. Szargut, J.; Valero, A.; Stanek, W.; Valero, A. Towards an International Reference Environment of Chemical Exergy. In Proceedings of the Conference ECOS 2005, Trondheim, Norway, 6 June 2005; pp. 409–420.
22. Szargut, J. International progress in second law analysis. *Energy* **1980**, *5*, 709–718. [[CrossRef](#)]
23. Szargut, J. Chemical exergies of the elements. *Appl. Energy* **1989**, *32*, 269–286. [[CrossRef](#)]
24. Gaudreau, K.; Fraser, R.A.; Murphy, S. The Characteristics of the Exergy Reference Environment and Its Implications for Sustainability-Based Decision-Making. *Energies* **2012**, *5*, 2197–2213. [[CrossRef](#)]
25. Valero, A.; Valero, A.; Stanek, W. Assessing the exergy degradation of the natural capital: From Szargut’s updated reference environment to the new thermoecological-cost methodology. *Energy* **2018**, *163*, 1140–1149. [[CrossRef](#)]
26. Ertesvåg, I.S. Sensitivity of chemical exergy for atmospheric gases and gaseous fuels to variations in ambient conditions. *Energy Convers. Manag.* **2007**, *48*, 1983–1995. [[CrossRef](#)]
27. Utlu, Z.; Hepbasli, A. Energetic and exergetic assessment of the industrial sector at varying dead (reference) state temperatures: A review with an illustrative example. *Renew. Sustain. Energy Rev.* **2008**, *12*, 1277–1301. [[CrossRef](#)]

28. Colombo, E.; Rocco, M.V.; Toro, C.; Sciubba, E. An exergy-based approach to the joint economic and environmental impact assessment of possible photovoltaic scenarios: A case study at a regional level in Italy. *Ecol. Model.* **2015**, *318*, 64–74. [CrossRef]
29. Cornelissen, R.L.; Hirs, G.G. The value of the exergetic life cycle assessment besides the LCA. *Energy Convers. Manag.* **2002**, *43*, 1417–1424. [CrossRef]
30. Dewulf, J.; Langenhove, H.V.; Mulder, J.; van den Berg, M.M.D.; van der Kooi, H.J.; de Arons, J.S. Illustrations towards quantifying the sustainability of technology. *Green Chem.* **2000**, *2*, 108–114. [CrossRef]
31. Michailos, S.; Parker, D.; Webb, C. Design, Sustainability Analysis and Multiobjective Optimisation of Ethanol Production via Syngas Fermentation. *Waste Biomass Valor* **2019**, *10*, 865–876. [CrossRef]
32. Quiroz-Ramirez, J.J.; Sánchez-Ramírez, E.; Segovia-Hernández, J.G. Energy, exergy and techno-economic analysis for biobutanol production: A multi-objective optimization approach based on economic and environmental criteria. *Clean Techn. Environ Policy* **2018**, *20*, 1663–1684. [CrossRef]
33. Leontief, W. The economy as a circular flow. *Struct. Chang. Econ. Dyn.* **1991**, *2*, 181–212. [CrossRef]
34. Nakajima, N. A Vision of Industrial Ecology: State-of-the-Art Practices for a Circular and Service-Based. *Bull. Sci. Technol. Soc.* **2000**, *30*, 54–69. [CrossRef]
35. Del Borghi, A.; Moreschi, L.; Gallo, M. Circular economy approach to reduce water–energy–food nexus. *Curr. Opin. Environ.* **2020**, *13*, 23–28. [CrossRef]
36. Hao, S.; Kuah, A.T.H.; Rudd, C.D.; Wong, K.H.; Lai, N.Y.G.; Mao, J.; Liu, X. A circular economy approach to green energy: Wind turbine, waste, and material recovery. *Sci. Total Environ.* **2020**, *702*, 135054. [CrossRef] [PubMed]
37. Fan, Y.V.; Klemeš, J.J.; Walmsley, T.G.; Bertók, B. Implementing Circular Economy in municipal solid waste treatment system using P-graph. *Sci. Total Environ.* **2020**, *701*, 134652. [CrossRef] [PubMed]
38. Manan, Z.A.; Nawi, W.N.R.M.; Alwi, S.R.W.; Klemeš, J.J. Advances in Process Integration research for CO₂ emission reduction-A review. *J. Clean. Prod.* **2017**, *167*, 1–13. [CrossRef]
39. Smith, R. *Chemical Process Design and Integration*, 2nd ed.; Wiley: Hoboken, NJ, USA, 2016; ISBN 978-1-119-99014-7.
40. Korhonen, J.; Honkasalo, A.; Seppälä, J. Circular Economy: The Concept and its Limitations. *Ecol. Econ.* **2018**, *143*, 37–46. [CrossRef]
41. European Commission. Communication from the Commission to the European Parliament, The Council, The European Economic and Social Committee and the Committee of the Regions. Closing the Loop—An EU Action Plan for the Circular Economy COM/2015/0614 Final. Available online: https://eur-lex.europa.eu/resource.html?uri=cellar:8a8ef5e8-99a0-11e5-b3b7-01aa75ed71a1.0012.02/DOC_1&format=PDF (accessed on 5 January 2020).
42. Lieder, M.; Rashid, A. Towards circular economy implementation: A comprehensive review in context of manufacturing industry. *J. Clean. Prod.* **2016**, *115*, 36–51. [CrossRef]
43. Marrucci, L.; Daddi, T.; Iraldo, F. The integration of circular economy with sustainable consumption and production tools: Systematic review and future research agenda. *J. Clean. Prod.* **2019**, *240*, 118268. [CrossRef]
44. Pieroni, M.P.P.; McAloone, T.C.; Pigosso, D.C.A. Business model innovation for circular economy and sustainability: A review of approaches. *J. Clean. Prod.* **2019**, *215*, 198–216. [CrossRef]
45. Viegas, C.V.; Bond, A.; Vaz, C.R.; Bertolo, R.J. Reverse flows within the pharmaceutical supply chain: A classificatory review from the perspective of end-of-use and end-of-life medicines. *J. Clean. Prod.* **2019**, *238*, 117719. [CrossRef]
46. van der Wiel, B.Z.; Weijma, J.; van Middelaar, C.E.; Kleinke, M.; Buisman, C.J.N.; Wichern, F. Restoring nutrient circularity: A review of nutrient stock and flow analyses of local agro-food-waste systems. *Resour. Conserv. Recycl. X* **2019**, *3*, 100014. [CrossRef]
47. Gorman, M.R.; Dzombak, D.A. A review of sustainable mining and resource management: Transitioning from the life cycle of the mine to the life cycle of the mineral. *Resour. Conserv. Recycl.* **2018**, *137*, 281–291. [CrossRef]
48. Abadías Llamas, A.; Valero Delgado, A.; Valero Capilla, A.; Torres Cuadra, C.; Hultgren, M.; Peltomäki, M.; Roine, A.; Stelter, M.; Reuter, M.A. Simulation-based exergy, thermo-economic and environmental footprint analysis of primary copper production. *Miner. Eng.* **2019**, *131*, 51–65. [CrossRef]
49. Pinto, J.T.M.; Diemer, A. Supply chain integration strategies and circularity in the European steel industry. *Resour. Conserv. Recycl.* **2020**, *153*, 104517. [CrossRef]

50. Anastasiades, K.; Blom, J.; Buyle, M.; Audenaert, A. Translating the circular economy to bridge construction: Lessons learnt from a critical literature review. *Renew. Sustain. Energy Rev.* **2020**, *117*, 109522. [CrossRef]
51. Jarre, M.; Petit-Boix, A.; Priefer, C.; Meyer, R.; Leipold, S. Transforming the bio-based sector towards a circular economy-What can we learn from wood cascading? *For. Policy Econ.* **2020**, *110*, 101872. [CrossRef]
52. Haas, W.; Krausmann, F.; Wiedenhofer, D.; Heinz, M. How Circular is the Global Economy?: An Assessment of Material Flows, Waste Production, and Recycling in the European Union and the World in 2005. *J. Ind. Ecol.* **2015**, *19*, 765–777. [CrossRef]
53. European Commission. A European Strategy for Plastics in a Circular Economy. Available online: <https://ec.europa.eu/environment/circular-economy/pdf/plastics-strategy-brochure.pdf> (accessed on 5 January 2020).
54. Hahladakis, J.N.; Iacovidou, E. An overview of the challenges and trade-offs in closing the loop of post-consumer plastic waste (PCPW): Focus on recycling. *J. Hazard. Mater.* **2019**, *380*, 120887. [CrossRef]
55. Mesa, J.A.; Esparragoza, I.; Maury, H. Trends and Perspectives of Sustainable Product Design for Open Architecture Products: Facing the Circular Economy Model. *Int. J. Precis. Eng. Manuf. Technol.* **2019**, *6*, 377–391. [CrossRef]
56. Post, W.; Susa, A.; Blaauw, R.; Molenveld, K.; Knoop, R.J.I. A Review on the Potential and Limitations of Recyclable Thermosets for Structural Applications. *Polym. Rev.* **2019**, 1–30. [CrossRef]
57. Corona, B.; Shen, L.; Reike, D.; Rosales Carreón, J.; Worrell, E. Towards sustainable development through the circular economy—A review and critical assessment on current circularity metrics. *Resour. Conserv. Recycl.* **2019**, *151*, 104498. [CrossRef]
58. 58 Sassanelli, C.; Rosa, P.; Rocca, R.; Terzi, S. Circular economy performance assessment methods: A systematic literature review. *J. Clean. Prod.* **2019**, *229*, 440–453. [CrossRef]
59. Saidani, M.; Yannou, B.; Leroy, Y.; Cluzel, F.; Kendall, A. A taxonomy of circular economy indicators. *J. Clean. Prod.* **2019**, *207*, 542–559. [CrossRef]
60. Tamura, S.; Fujie, K. Material Cycle of Agriculture on Miyakojima Island: Material Flow Analysis for Sugar Cane, Pasturage and Beef Cattle. *Sustainability* **2014**, *6*, 812–835. [CrossRef]
61. Pejpichestakul, W.; Siemanond, K. Process heat integration between distillation columns for ethylene hydration process. *Chem. Eng. Trans.* **2013**, *35*, 181–186.
62. Tsolas, S.D.; Karim, M.N.; Hasan, M.M.F. Optimization of water-energy nexus: A network representation-based graphical approach. *Appl. Energy* **2018**, *224*, 230–250. [CrossRef]
63. Tian, H.; Lu, C.; Pan, S.; Yang, J.; Miao, R.; Ren, W.; Yu, Q.; Fu, B.; Jin, F.-F.; Lu, Y.; et al. Optimizing resource use efficiencies in the food–energy–water nexus for sustainable agriculture: From conceptual model to decision support system. *Curr. Opin. Environ. Sustain.* **2018**, *33*, 104–113. [CrossRef]
64. Rulli, M.C.; Bellomi, D.; Cazzoli, A.; Carolis, G.D.; D’Odorico, P. The water-land-food nexus of first-generation biofuels. *Sci. Rep.* **2016**, *6*, 22521. [CrossRef]
65. Wang, X.-C.; Klemeš, J.J.; Dong, X.; Fan, W.; Xu, Z.; Wang, Y.; Varbanov, P.S. Air pollution terrain nexus: A review considering energy generation and consumption. *Renew. Sustain. Energy Rev.* **2019**, *105*, 71–85. [CrossRef]
66. Ewijk, S.V.; Stegemann, J.A.; Ekins, P. Global Life Cycle Paper Flows, Recycling Metrics, and Material Efficiency. *J. Ind. Ecol.* **2018**, *22*, 686–693. [CrossRef]
67. Awasthi, A.K.; Li, J. An overview of the potential of eco-friendly hybrid strategy for metal recycling from WEEE. *Resour. Conserv. Recycl.* **2017**, *126*, 228–239. [CrossRef]
68. Xue, M.; Kendall, A.; Xu, Z.; Schoenung, J.M. Waste Management of Printed Wiring Boards: A Life Cycle Assessment of the Metals Recycling Chain from Liberation through Refining. *Environ. Sci. Technol.* **2015**, *49*, 940–947. [CrossRef] [PubMed]
69. Balmer, R.T. *Modern Engineering Thermodynamics*; Academic Press: Cambridge, MA, USA, 2011; ISBN 978-0-12-374996-3.
70. Forman, C.; Muritala, I.K.; Pardemann, R.; Meyer, B. Estimating the global waste heat potential. *Renew. Sustain. Energy Rev.* **2016**, *57*, 1568–1579. [CrossRef]
71. European Commission. *Statistical Office of the European Union Circular Material Use Rate: Calculation Method: 2018 Edition*; Eurostat, European Commission: Brussels, Belgium, 2018; ISBN 978-92-79-96698-9.
72. Directive, E.U.W. EC Council Directive of 21 May 1991 concerning urban waste-water treatment. *Off. J. Eur. Communities* **1991**, *34*, 40–52.

73. High Temperature-King County. Available online: <https://www.kingcounty.gov/services/environment/wastewater/industrial-waste/limits-regulations/limits-prohibited/high-temperature.aspx> (accessed on 14 December 2019).
74. Turner, T. Effluent Standards; UN FAO, 2019; p. 16. Available online: <https://oaout.epa.gov.tw/law/Download.ashx?FileID=851> (accessed on 14 December 2019).
75. Klemeš, J.J. (Ed.) *Assessing and Measuring Environmental Impact and Sustainability*; Butterworth-Heinemann/Elsevier: Oxford, UK, 2015; ISBN 978-0-12-799968-5.
76. Szargut, J.; Morris, D.R.; Steward, F.R. *Exergy Analysis of Thermal, Chemical, and Metallurgical Processes*; Hemisphere: New York, NY, USA, 1988.
77. Chemical Exergy Calculator—The Exergoecology Portal. Available online: www.exergoecology.com/excalc (accessed on 28 December 2019).
78. Berre, C.L.; Serp, P.; Kalck, P.; Torrence, G.P. Acetic Acid. In *Ullmann's Encyclopedia of Industrial Chemistry*; American Cancer Society: Atlanta, GA, USA, 2014; pp. 1–34. ISBN 978-3-527-30673-2.
79. Dimian, A.C.; Bildea, C.S.; Kiss, A.A. Acetic Acid. In *Applications in Design and Simulation of Sustainable Chemical Processes*; Elsevier: Amsterdam, The Netherlands, 2019; pp. 483–519. ISBN 978-0-444-63876-2.
80. Galli, F.; Previtali, D.; Casagrande, S.; Pirolo, C.; Manenti, F.; Boffito, D.C. Simulation of the Water-Acetic Acid Separation via Distillation Using Different Entrainers: An Economic Comparison. *Chem. Eng. Trans.* **2017**, *57*, 1159–1164.
81. Langell, M.A.; Berrie, C.L.; Nassir, M.H.; Wulser, K.W. Adsorption of acetic acid on hydroxylated NiO(111) thin films. *Surf. Sci.* **1994**, *320*, 25–38. [[CrossRef](#)]
82. Aspen HYSYS. Available online: <https://www.aspentech.com/en/products/engineering/aspen-hysys> (accessed on 21 November 2019).
83. Contreras, J.P.; Naranjo, J.C.G.; Ramírez, S.G.; Martínez, D.M. Vinyl Acetate from ethylene, acetic acid and oxygen Industrial Plant Simulation. In Proceedings of the Computing and Systems Technology Division, American Institute of Chemical Engineers (AIChE) Annual Meeting, Nashville, TN, USA, 10–15 November 2009; pp. 249–259.
84. Sadhukhan, J.; Ng, K.S.; Martínez-Hernandez, E. Novel integrated mechanical biological chemical treatment (MBCT) systems for the production of levulinic acid from fraction of municipal solid waste: A comprehensive techno-economic analysis. *Bioresour. Technol.* **2016**, *215*, 131–143. [[CrossRef](#)]
85. Bhaskar, T.; Steele, P.H. Thermo-chemical Conversion of Biomass. *Bioresour. Technol.* **2015**, *178*, 1. [[CrossRef](#)]
86. Batalha, L.A.R.; Han, Q.; Jameel, H.; Chang, H.; Colodette, J.L.; Borges Gomes, F.J. Production of fermentable sugars from sugarcane bagasse by enzymatic hydrolysis after autohydrolysis and mechanical refining. *Bioresour. Technol.* **2015**, *180*, 97–105. [[CrossRef](#)]
87. Ferdan, T.; Pavlas, M.; Šomplák, R.; Nevrlý, V.; Klemeš, J.J.; Pitschke, T. Allocation analysis of waste treatment nodes for economic optimisation considering reduced greenhouse gas emissions. *Chem. Eng. Trans.* **2017**, *61*, 967–972.
88. Pan, Z.; Chan, W.P.; Veksha, A.; Giannis, A.; Dou, X.; Wang, H.; Lisak, G.; Lim, T.-T. Thermodynamic analyses of synthetic natural gas production via municipal solid waste gasification, high-temperature water electrolysis and methanation. *Energy Convers. Manag.* **2019**, *202*, 112160. [[CrossRef](#)]
89. Yang, Y.; Heaven, S.; Venetsaneas, N.; Banks, C.J.; Bridgwater, A.V. Slow pyrolysis of organic fraction of municipal solid waste (OFMSW): Characterisation of products and screening of the aqueous liquid product for anaerobic digestion. *Appl. Energy* **2018**, *213*, 158–168. [[CrossRef](#)]
90. Licari, A.; Monlau, F.; Solhy, A.; Buche, P.; Barakat, A. Comparison of various milling modes combined to the enzymatic hydrolysis of lignocellulosic biomass for bioenergy production: Glucose yield and energy efficiency. *Energy* **2016**, *102*, 335–342. [[CrossRef](#)]
91. Mukherjee, A.; Dumont, M.-J.; Raghavan, V. Review: Sustainable production of hydroxymethylfurfural and levulinic acid: Challenges and opportunities. *Biomass Bioenergy* **2015**, *72*, 143–183. [[CrossRef](#)]
92. Fodor, Z.; Klemeš, J.J. Waste as alternative fuel—Minimising emissions and effluents by advanced design. *Process Saf. Environ. Prot.* **2012**, *90*, 263–284. [[CrossRef](#)]
93. Eboh, F.C.; Ahlström, P.; Richards, T. Estimating the specific chemical exergy of municipal solid waste. *Energy Sci. Eng.* **2016**, *4*, 217–231. [[CrossRef](#)]
94. Dewulf, J.; Langenhove, H.V. Thermodynamic optimization of the life cycle of plastics by exergy analysis. *Int. J. Energy Res.* **2004**, *28*, 969–976. [[CrossRef](#)]

95. Fan, Y.V.; Klemeš, J.J.; Chin, H.H. Extended Waste Management Pinch Analysis (E-WAMPA) Minimising Emission of Waste Management: EU 28. *Chem. Eng. Trans.* **2019**, *74*, 283–288.
96. Wu, Y.; Yang, W.; Blasiak, W. Energy and Exergy Analysis of High Temperature Agent Gasification of Biomass. *Energies* **2014**, *7*, 2107–2122. [[CrossRef](#)]
97. Dincer, I.; Rosen, M.A. Chapter 21-Exergy Analysis of Countries, Regions, and Economic Sectors. In *Exergy*, 2nd ed.; Dincer, I., Rosen, M.A., Eds.; Elsevier: Amsterdam, The Netherlands, 2013; pp. 425–450. ISBN 978-0-08-097089-9.



© 2020 by the authors. Licensee MDPI, Basel, Switzerland. This article is an open access article distributed under the terms and conditions of the Creative Commons Attribution (CC BY) license (<http://creativecommons.org/licenses/by/4.0/>).

Article

A Method for Analyzing Energy-Related Carbon Emissions and the Structural Changes: A Case Study of China from 2005 to 2015

Honghua Yang ^{1,2}, Linwei Ma ^{1,2,*} and Zheng Li ¹

¹ State Key Laboratory of Power Systems, Department of Energy and Power Engineering, Tsinghua-BP Clean Energy Research and Education Centre, Tsinghua University, Beijing 100084, China; yhh18@mails.tsinghua.edu.cn (H.Y.); lz-dte@tsinghua.edu.cn (Z.L.)

² Tsinghua-Rio Tinto Joint Research Centre for Resources, Energy and Sustainable Development, Tsinghua University, Beijing 100084, China

* Correspondence: malinwei@tsinghua.edu.cn

Received: 28 February 2020; Accepted: 19 April 2020; Published: 21 April 2020

Abstract: To systematically analyze energy-related carbon emissions from the perspective of comprehensive energy flow and allocate emissions responsibility, we introduce energy allocation analysis to carbon flow process based on Sankey diagrams. Then, to quantitatively compare different diagrams and evaluate the structural changes of carbon flow, we define changes from three dimensions including total amount change, relative growth rate and occupation ratio change (TRO), propose TRO index. The method is applied to China's case study from 2005 to 2015. We map China's energy-related carbon flow Sankey diagrams with high technical resolution from energy sources, intermediate conversion, end-use devices, passive systems to final services, and conduct TRO index decomposition by stages. The results indicate that in energy sources, the emission share of coal has declined due to energy transition although coal is still the largest contributor to China's energy-related carbon emissions. In passive systems, the factory passive systems are the largest contributors, among them, emission reduction should focus on the steel, non-ferrous and chemical industries; the building passive systems should pay attention to household appliances; the vehicle passive systems should focus on cars. In final services, the demand for structural materials is the strongest driving force for carbon emissions growth.

Keywords: energy-related carbon emissions; carbon flow; Sankey diagrams; structural changes; TRO index; energy allocation analysis; energy system

1. Introduction

Controlling energy-related carbon emissions and realizing a low-carbon transition in the energy system are important ways to globally address climate change and achieve sustainable development [1]. Considering that energy-related carbon emissions are closely related to complex energy flows in the energy system, it is necessary for policymakers to understand carbon emissions from the perspective of overall energy systems so as to formulate more targeted emission reduction policies [2]. As climate change becomes more severe, recent researches are stimulated to analyze energy-related carbon emissions and emission responsibility underlying the entire process of energy flow, and to discern the changing trend.

In the area of energy system analysis, Sankey diagrams are popular and useful tools for visualizing processes [3], which use arrows to show the flow of a certain object (e.g., energy, exergy, resources, etc.) with width representing the quantity and the colors indicating the types. Some recent examples of Sankey diagrams applied to energy system analysis are shown in Table 1. The literature shows

that the Sankey diagrams have been widely used to analyze energy flow or greenhouse gas (CO₂) flow processes.

Table 1. Studies applying Sankey diagrams to energy system analysis.

Source	Region, Metric and Date	Stages of Energy Flow
Cullen and Allwood 2010 [4]	Global Energy flow (EJ) 2005	Energy sources, end-use conversion devices, passive systems, final services.
UK DOECC 2010 [5]	UK Energy flow (Mtoe) 2010	Primary supply, oil refineries and power stations, end use sectors
Ma et al. 2012 [6]	China Energy flow (EJ) 2005	Energy sources, end-use conversion devices, passive systems, final services, demand drivers
Chong et al. 2015 [7]	Malaysia Energy flow (Mtoe) 2011	Primary supply, secondary supply, end use
Li et al. 2018 [8]	Beijing, Tianjin, Hebei province Energy flow (EJ) 2013	Energy supply, transformation, end use
Davis et al. 2018 [9]	Territories of Canada Energy flow (PJ) 2012	Primary supply, electricity generation and oil products, end use
Mu et al. 2013 [10]	China CO ₂ flow (Mt) 2008	Energy sources, transformation, end use sectors
Li et al. 2017 [11]	China CO ₂ flow (Mt) 2013	Energy sources, end use sectors
Ma et al. 2018 [12]	China CO ₂ flow (100 Mt) 2004, 2014	Energy supply, transformation, end use

Abbreviations: GHG: Greenhouse gas; Mtoe: Million tons of oil equivalent; EJ: 10¹⁸ Joules; PJ: 10¹⁵ Joules; CHP: Combined heat and power; Mtce: Million tons of coal equivalent; Mt: Million tons.

In this field, Cullen and Allwood [4] were early scholars who proposed a systematic energy allocation analysis method based on Sankey diagrams. The method suggested that energy losses in energy conversion sectors should be calculated into and compensated for in the end-use energy consumption but not be presented separately, so as to evaluate the primary energy consumption responsibility of end use sectors and final energy services. This method was then followed by many other scholars, for example, Ma et al. [6] applied the method to national level mapping China's energy flow diagram, Chong et al. [7] introduced it to Malaysia showing the allocation of primary energy consumption responsibility in the energy system. Furthermore, the method was applied to regional energy flow such as China's provinces [8] and Canada's territories [9]. Recent researches also used the method to map CO₂ flow diagrams [12], however, through our literature review, we found some limitations in three main aspects:

- Although the application of Sankey diagrams in the analysis of complex energy flow process was popular including comprehensive stages, the application in the analysis of energy-related carbon emissions flow was relatively limited. In the published work about carbon flow diagrams, the division of energy stages was somewhat simple with only supply and end use sides [11]. The resolution of the carbon flow diagram needs to be increased.
- Research gap also existed in some other diagrams [10] in which a large amount of carbon emissions caused by energy loss in the conversion sector were calculated as a loss, which made it difficult to observe the carbon emission responsibility allocation of the end-use sectors well. It is needed to

apply the idea of energy allocation analysis to carbon allocation analysis to show the emission responsibility comprehensively.

- Most of existing work using Sankey diagrams focused on the situation of a certain year. Although some research presented carbon flow diagrams in different years [12], it still lacked systematical comparison of diagrams in different years. While comparing these diagrams might reveal in-depth structural changes and trends of energy transition. Considering this, a new method for comparing Sankey diagrams and evaluating structural changes is needed.

Recognizing the above limitations, this paper aims to develop a method for analyzing energy-related carbon flow from the perspective of comprehensive energy flow, quantitatively comparing different Sankey diagrams and evaluating the structural changes and trends with energy transition. Firstly, we introduced energy allocation analysis to carbon flow analysis, fully considering the carbon emission responsibility allocation in the whole energy flow process from energy sources, intermediate conversion, end-use conversion devices, passive systems to final services. Secondly, we mapped the energy flow and the energy-related carbon flow Sankey diagrams. Thirdly, we defined the structural changes of Sankey diagrams from three dimensions, proposed index including total amount change (T), relative growth rate (R) and occupation ratio change (O), i.e., TRO index, compared different Sankey diagrams and discussed the political and practical reasons behind these changes.

To apply the method to actual objects, we chose China as a case for its tremendous and dynamic energy consumption and energy-related carbon emissions (see Appendix A, Figure A1). China accounted for 23.6% of global energy consumption and 27.8% of global energy-related CO₂ emissions as the largest energy consumer and CO₂ emission source in 2018 [13]. We chose the decade of 2005–2015 as the research period, because in this decade China's energy development experienced a tough transition. In this period, to achieve energy transition, China issued a package of energy plans ([14–19] as listed in Appendix B, Table A1). These policies resulted in great influences on the energy system and energy-related carbon emissions. Choosing this period can help us understand the notable changes of carbon emissions brought by the transition of the energy system and compare the results with relevant policies to verify this method.

The contribution of this work is to provide a method for analyzing national energy-related carbon emissions and evaluating structural changes based on Sankey diagrams and apply this method to China's case study from 2005 to 2015. Although some parts of methodology referred closely to previous work of energy allocation analysis of China [6], we further introduced the method to carbon allocation analysis of China, mapped its energy-related carbon flow Sankey diagrams in 2005 and 2015 (as well as a newly updated energy flow Sankey diagram in 2015). Additionally, the TRO index was proposed to compare the Sankey diagrams. This method can help us comprehensively understand national energy-related carbon emissions and the structural changes behind energy transition.

The rest of this paper is organized as follows: Section 2 introduces the method for depicting carbon flow process, evaluating structural changes, and data input; Section 3 discusses the carbon flow Sankey diagram results, TRO index decomposition, and the uncertainty; finally, Section 4 presents the conclusions.

2. Methodology and Data Input

The procedure of the methodology applied in this study is divided into three steps: In the first step, we conducted energy allocation analysis to fully understand the features of China's energy system and mapped China's energy flow Sankey diagram in 2015. In the second step, based on the energy flow Sankey diagram in 2015 and a previous one in 2005 [6], we calculated carbon emissions of each section in the energy system by introducing relevant emission factors. Then we plotted China's energy-related carbon flow diagrams in 2005 and 2015 showing carbon emissions underlying the whole process of energy flow. In the last step, in order to analyze the main trend of carbon flow and determine the key structural changes quantitatively, we applied TRO index decomposition method on these two carbon flow diagrams and analyzed the results of several main sectors.

2.1. The Framework for Energy Allocation Analysis Based on Sankey Diagrams

This study divided the energy flow process into five sub-sections: energy sources, intermediate conversion, end-use conversion devices, passive system and final services. In order to keep in line with previous work for later comparison, the concept and scope of each section refer to Ma et al. [6], which is detailed described in Appendix C, Table A2.

We used the Sankey diagram tool to present the energy flow process. The diagrams were plotted on the software called “e!Sankey” [20]. The framework of the energy flow Sankey diagram is shown as Figure 1. In the diagram, the energy flows from left to right with the allocation in different departments. The vertical lines show different stages of energy flow. In the specific Sankey diagrams, the width of the arrow shows the values of energy and the colors show different energy types or uses.

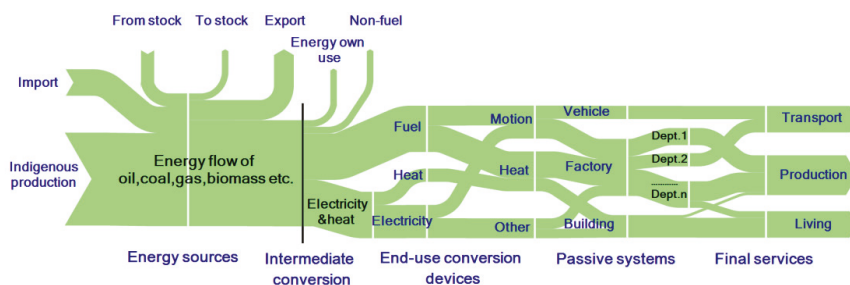


Figure 1. The framework of the energy flow Sankey diagram.

The core of energy allocation analysis is to allocate the energy loss in intermediate conversion stage into the energy consumption responsibility of the end-use stages. Therefore, the energy loss is not shown in energy flow process, and there are only energy allocation among different uses in the whole process from supply to service. How should we look at the energy allocation diagram? Except the clear demonstration of the energy flow process distinguished in different categories, different departments and different links, one of the advantages of the map is an effective combination of three levels of supply-conversion-demand: looking from the left side, it's the distribution of supplies (such as energy sources), from the right side, it's the allocation of demands (such as final services), while in the middle is the condition of specific technical departments (such as end-use conversion devices and passive systems). These will also be the key links to be discussed in the following text.

2.2. Carbon Allocation Analysis Based on Energy Allocation Analysis

2.2.1. The Carbon Flow Sankey Diagram

As carbon allocation analysis is based on energy allocation analysis, the structure of carbon flow Sankey diagram is similar to that of energy flow Sankey diagram (see Figure 1). However, it should be noted that the real carbon emissions occur in the intermediate conversion stage where the energy is burned as direct fuel, electricity generation, heating and energy system own-use. At this stage, the carbon which cannot be oxidized in the fuel will be left, thus leading to a 'non-oxidation' flow in the diagram. In the previous stage of conversion, emissions have not occurred, so the flow shows the total carbon embodied in relevant energy. While in the subsequent stage of conversion, emissions have occurred, this part of diagram shows the carbon emission responsibility of each department because we allocate the energy loss into the end-use energy consumption responsibility, the carbon emission loss is the same.

2.2.2. Carbon Emissions Calculation

Because this study only focuses on energy-related carbon emissions, the calculation of emissions is based on the fossil fuel consumption. There are mainly three broad categories and 18 types of fossil fuel (see Table 2) considered in this paper. Equation (1) is used to calculate fuel-related carbon emissions:

$$C_i = \sum_j E_{ij} \times NCV_j \times CCV_j \times O_j \quad (1)$$

In this equation, the subscripts i and j denote the i -th sector and the j -th fuel, respectively, C_i is the total carbon emissions of different sectors, E_{ij} represents the different energy consumption in different sectors, NCV_j refers to the net calorific value of different energy types, CCV_j is the carbon content per calorific value of different fuels, O_j is the carbon oxidation rate of the fuel. Due to the possible error between the actual carbon emission factors of China's coal and that recommended by Intergovernmental Panel on Climate Change (IPCC) [21], the data of NCV_j , CCV_j and O_j used in this paper are mainly taken from China's official statistics including General Principles for Calculation of the Comprehensive Energy Consumption [22] and Guidelines for GHG Inventories [23], a few of the data not published are from the default value recommended by IPCC [24], all of them are shown in Table 2.

Table 2. Parameters for Calculating Carbon Emissions.

Category	Fuel	NCV	CCV ³	O
Coal	Raw coal	20,908 kJ/kg	26.37 t C/TJ	0.94
	Cleaned coal	26,344 kJ/kg	25.41 t C/TJ	0.98
	Briquettes	17,562 kJ/kg	33.60 t C/TJ	0.90
	Other washed coal	8363 kJ/kg	25.41 t C/TJ	0.98
	Coke	28,435 kJ/kg	29.50 t C/TJ	0.93
	Other coking products ¹	38,052 kJ/kg	29.50 t C/TJ	0.93
Gas	Coke oven gas	17,353 kJ/m ³	13.58 t C/TJ	0.99
	Blast furnace gas	3763 kJ/m ³	13.00 t C/TJ	0.99
	Other Gas	5227 kJ/m ³	13.00 t C/TJ	0.99
	Natural Gas	38,931 kJ/m ³	15.30 t C/TJ	0.99
	Refinery gas	46,055 kJ/m ³	18.20 t C/TJ	0.98
Oil	Crude oil	41,816 kJ/kg	20.10 t C/TJ	0.98
	Gasoline	43,070 kJ/kg	18.90 t C/TJ	0.98
	Kerosene	43,070 kJ/kg	19.50 t C/TJ	0.98
	Diesel oil	42,652 kJ/kg	20.20 t C/TJ	0.98
	Fuel oil	41,816 kJ/kg	21.10 t C/TJ	0.98
	LPG	50,179 kJ/kg	17.20 t C/TJ	0.98
	Other petroleum products ²	35,125 kJ/kg	20.00 t C/TJ	0.98

^{1,2} Data of other coking products and other petroleum products are from the IPCC [24], while other values are from China's official statistics [22,23]. ³ TJ is 10¹² Joules.

2.3. The Method for Evaluating Structural Changes of Sankey Diagrams—TRO index

Through our literature review, we found that the method for evaluating structural changes of the Sankey diagram itself was still limited. It is difficult to systematically and quantitatively compare two Sankey diagrams and to discern the structural changes, because there are too many complex departments with detailed data in the diagram and the changes are reflected in many aspects. In order

to solve this problem, we proposed TRO index to evaluate the structural changes, defining the structural change from three dimensions: total amount change, relative growth rate and occupation ratio change. In this study, specifically, the method was applied to compare carbon flow Sankey diagrams.

The meaning of TRO index is to help us quickly identify structural changes in complex carbon flow Sankey diagrams, including both obvious total amount changes and relative growth rate that is not easy to visualize. TRO is not only a mathematical indicator, but also has actual physical meaning, e.g., the total amount change reveals change in the industrial production capacity, the relative growth rate reveals potential development trends, and the occupation ratio change reflects the results of structural transition. These three indicators are complementary to each other for comprehensively revealing the structural changes. The meaning and calculation method of each index is explained in detail in the following text.

2.3.1. Total Amount Change (T)

Total amount change T refers to the change of the total carbon emissions in a relevant section in the Sankey diagrams between different years. To a certain degree, total amount change reflects the change in the size of the industry's production capacity. The sectors with larger total amount change should be paid more attention for emission reduction, because improving the same energy efficiency or reducing the same carbon intensity in these sectors may lead to more emission reduction. The formula of the total amount change of sector i is as Equation (2):

$$T_i = C_{Ti} - C_{ti} \quad (2)$$

where C_{ti} is the total carbon emissions of sector i in the base year t , C_{Ti} is the total carbon emissions of sector i in the observed year T .

2.3.2. Relative Growth Rate (R)

Relative growth rate R refers to the ratio of the carbon emission change of a relevant section in the Sankey diagrams during the observed period to the carbon emission in base year. It can make up for the shortcomings when T index is used for the industry that used to be small and unconcerned but has rapid development in recent years thus leading to high emission growth rate. R index also reflects the orientation of relevant policies and changes of market demand to some extent. These parts are also the ones that should be paid special attention to, because they are likely to become the main driving force for the growth of carbon emissions in the future. Identifying this indicator can help policy makers adjust the energy structure of relevant industries at an early stage, so as to control carbon emissions more effectively. The formula for calculating the relative growth rate of carbon emissions of sector i is as shown in Equation (3):

$$R_i = \frac{C_{Ti} - C_{ti}}{C_{ti}} \quad (3)$$

2.3.3. Occupation Ratio Change (O)

Occupation ratio change O refers to the change of the proportion of a relevant sector in the corresponding stage of the Sankey diagrams during observed period. It reflects the actual changes of carbon flow structure that influenced by energy structure transition. The formula for calculating the occupation ratio change of sector i is seen in Equation (4):

$$O_i = P_{Ti} - P_{ti} \quad (4)$$

In this equation, P_{ti} is the ratio of carbon emissions of sector i to the total emissions in the corresponding link in the base year t , P_{Ti} is that in the observed year T .

2.4. Data Input

China's energy data for 2015 are obtained and calculated from China's official statistics sources such as China Energy Statistical Yearbook 2016 [25], The 11th Five-Year Plan for Energy Development [14], The 12th Five-Year Plan for Energy Development [18], and a series of reports such as Energy Data of China 2016 [26], and Survey Analysis of Lighting Power Consumption in China [27]. The China's energy data in 2005 are from Ma et al. [6]. The carbon emission factors are calculated from General Principles for Calculation of the Comprehensive Energy Consumption [22], China Guidelines [23] and IPCC Guidelines [24]. Some other data are from authors' calculation. Detailed data sources and processing are shown in Appendix D, and some key data in the processing are listed in Tables A3–A9.

3. Results and Discussion

3.1. China's Energy Flow and Energy-Related Carbon Flow Sankey Diagrams

Based on energy allocation analysis method, we first plotted a Sankey diagram of China's energy flow in 2015, as shown in Figure 2, which is a latest Sankey diagram that reflects energy flow process in China's energy system. In the diagram, the energy flow is traced from left to right, and allocated to five stages: energy sources, intermediate conversion, end-use conversion devices, passive systems and final services. The detailed description of each stage can be seen in Table A2. The colors of the various arrows indicate different energy types and different departments, as shown in the legend on the right of the diagram. The thickness of each arrow represents the scale of energy flow, with numbers on it giving the values. The whole energy flow obeys the energy conservation law. Energy losses are not shown in the map but remain included in the energy flow to illustrate the energy allocation through all stages. The energy values are shown in EJ (10^{18} J).

Based on the Figure 2 and a previous energy flow diagram of China in 2005 [6], by introducing carbon emission factors, we further mapped China's energy-related carbon flow Sankey diagrams in 2005 and 2015, as shown in Figures 3 and 4.

The framework of carbon flow Sankey diagrams is consistent with that of the energy flow Sankey diagrams. The only difference is that the energy-related carbon flow diagram shows the flow of carbon but not energy. In this work, we assumed that energy-related carbon emissions only come from three broad categories and eighteen types as listed in Table 2. Therefore, in the stage of energy sources and intermediate conversion, there are only oil, coal and gas in the diagram. The colors of the various arrows indicate carbon emissions coming from different energy types and consumed by different departments, as shown in the legend on the right of the diagram. The thickness of each arrow represents the scale of carbon flow, with numbers giving the values. The whole carbon flow obeys the law of carbon conservation. The carbon values are reported in 10 Million tons (10^7 tons).

The main advantage of the carbon flow Sankey diagram is that it shows the carbon emission responsibility of each sector in each stage of the energy system because energy losses are allocated into consumption sectors but not presented separately. The arrows in energy sources stage show the total amount of carbon entering the system. The arrows in energy conversion stage show actual carbon emissions. In the conversion stage, the carbon in fuels is oxidized and released, while the non-oxidized parts flow to 'non-oxidation'. The arrows in passive systems and final services reflect the carbon emissions embodied in users' consumption and demand. According to Figures 2–4, the general situation of China's energy system and energy-related carbon emissions can be seen as follows:

- (1) Coal dominated in China's energy supply and consumption, accounting for 64.0% of primary energy supply in 2005 and 57.6% in 2015, and its contribution to energy-related carbon emissions was as high as 79.4% and 78.1%, respectively.
- (2) At the intermediate conversion stage, more than half of the primary energy was directly used as fuel (54.0% in 2005, 50.7% in 2015), contributing 49.0% and 48.0% of energy-related carbon emissions, followed by electricity generation (accounting for 37.0% in 2005, 39.1% in 2015), and its contribution to energy-related carbon emissions increased from 34.5% to 36.3%.

- (3) In passive systems, the factory passive system was the largest energy consumer, in which the carbon emissions increased by 83.1% from 3182 Mt CO₂ to 5826 Mt CO₂, followed by building passive system, but its contribution to carbon emissions decreased from 23.0% to 20.1%. In the factory passive system, the steel and chemical industries took the main carbon emission responsibility, accounting for 32.0% and 22.2% of factory emissions in 2015. In the building passive system, heated/cooled space was the main energy consumption and carbon emission source with 14.9 EJ energy consumption and 821 Mt CO₂ emissions in 2015. In the vehicle passive system, the largest contributor changed from trucks (accounting for 39.4% carbon emissions of vehicle in 2005) to cars (accounting for 39.8% carbon emissions of vehicle in 2015).
- (4) As for final services, the structural material is the most important demand. In 2015, it accounted for 52.6% of energy consumption and contributed 54.7% of carbon emission responsibility as 4638 Mt CO₂. Demand for thermal comfort, sustenance, freight transportation, passenger transportation, illumination, communication, and hygiene accounted for 11.6%, 8.7%, 6.9%, 6.4%, 4.8%, 3.7%, and 3.2%, respectively.

3.2. The Structural Changes of Carbon Flow Sankey Diagrams

After getting the full picture of carbon emissions allocation, to evaluate the structural changes more comprehensively, we conducted TRO index decomposition of each section in the diagram to compare the situation of energy-related carbon emissions. The results of the TRO index decomposition of several important sections including energy sources, three passive systems (vehicle, building and factory), and final services are shown as Table 3 and Figure 5. In the following text, the results of each section are discussed one by one and are compared with relative policies, other statistics, and other studies to verify the method.

Table 3. The TRO index decomposition of relevant sections.

Item	Section ¹	T ² /Mt	R/%	O/%	Section ¹	T ² /Mt	R/%	O/%
Energy sources	Coal	3076	71	-1.2	Oil	532	58	-1.6
	Gas	414	205	2.8				
Vehicle	Car	231	158	9.5	Truck	106	56	-8.1
	Agro-V	26	140	0.8	Plane	48	163	2.0
	Ship	11	18	-5.2	Train	44	120	0.9
Building	Hot water	143	76	2.2	H/CS	242	42	-4.7
	Appliance	110	158	4.1	ILLS	117	45	-1.6
Factory	Steel	851	84	0.2	Non-Ferrous	326	171	2.9
	Mineral	308	60	-2.0	Food	66	60	-0.5
	Textile	70	48	-0.9	Paper	22	23	-1.0
	Chemical	649	101	2.0	Machinery	172	89	0.2
	Agriculture	33	24	-1.4	Construction	88	126	0.5
Final services	Other	59	84	0.0				
	Passenger	341	166	2.1	Freight	213	57	-0.9
	Structure	2218	92	3.9	Sustenance	224	43	-2.2
	TC	323	49	-2.3	COMM	136	76	-0.1
	Hygiene	139	109	0.5	ILL	128	45	-1.1

¹ Abbreviations: Agro-V: Agro-vehicle; H/CS: Heated/cooled space; ILLS: Illumination space; TC: Thermal comfort; COMM: Communication; ILL: Illumination. ² The total amount change of carbon emissions here is calculated as carbon dioxide while the data in Sankey diagrams are calculated as carbon element.

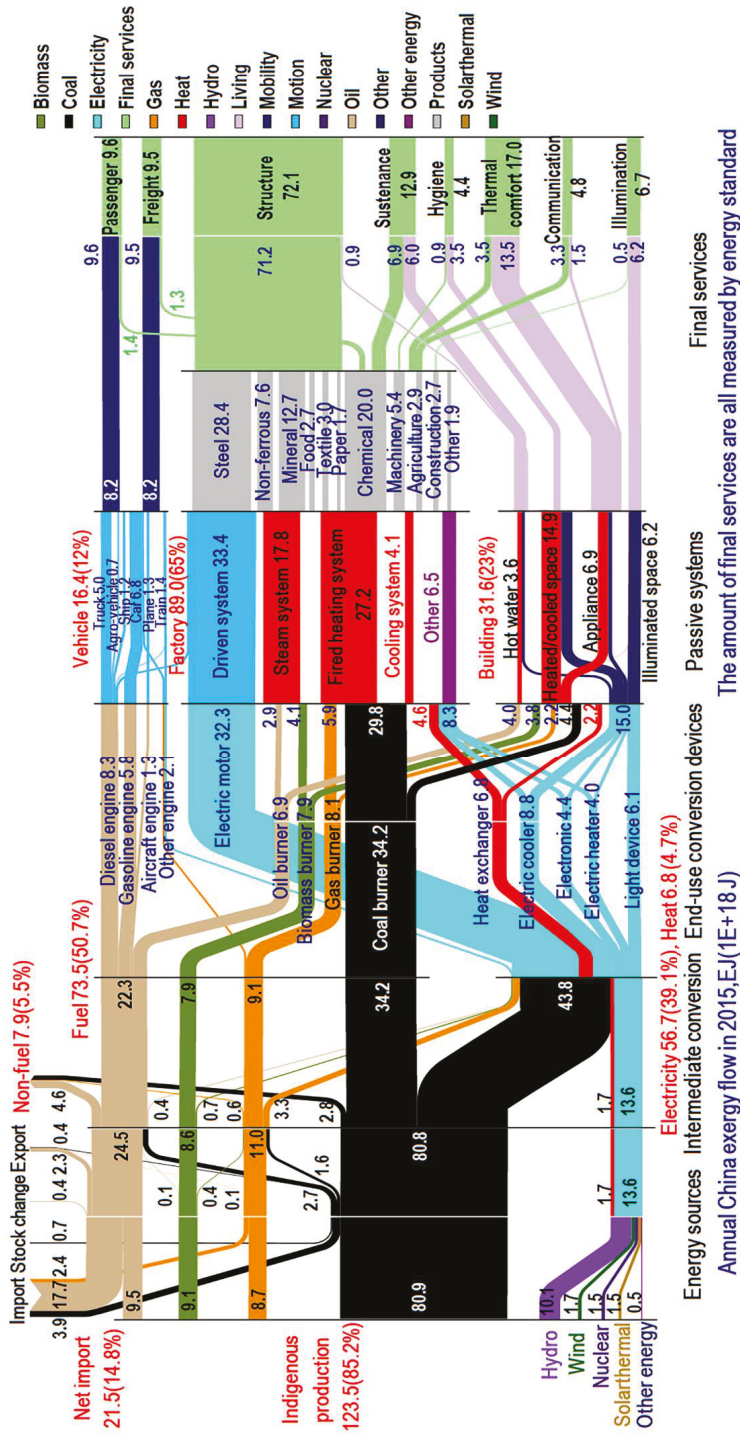
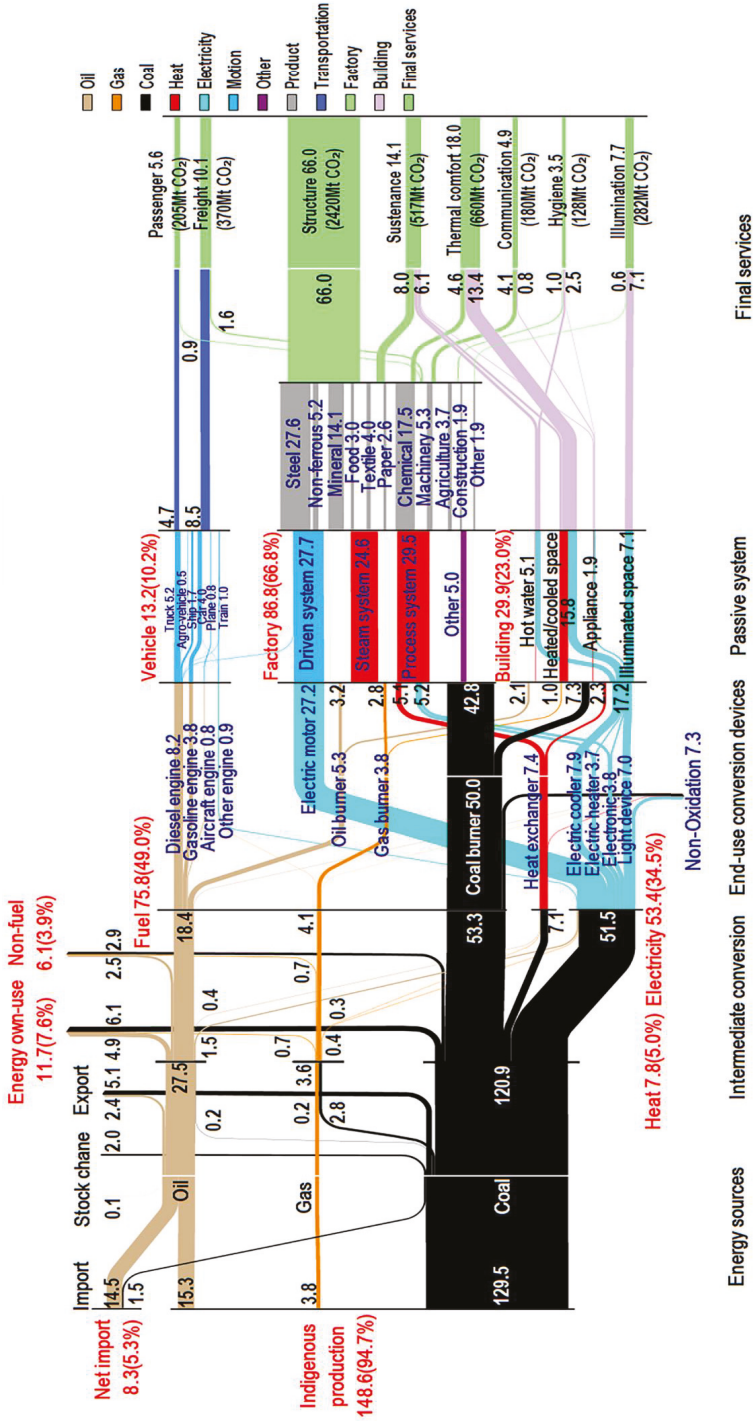


Figure 2. China's energy flow diagram in 2015, unit in EJ (10¹⁸ J).

The amount of final services are all measured by energy standard



Annual China carbon flow in 2005, 10 Million tons (1E+7 tons)

Figure 3. China's energy-related carbon flow diagram in 2005, unit in 10 Mt C (10⁷ tons C).

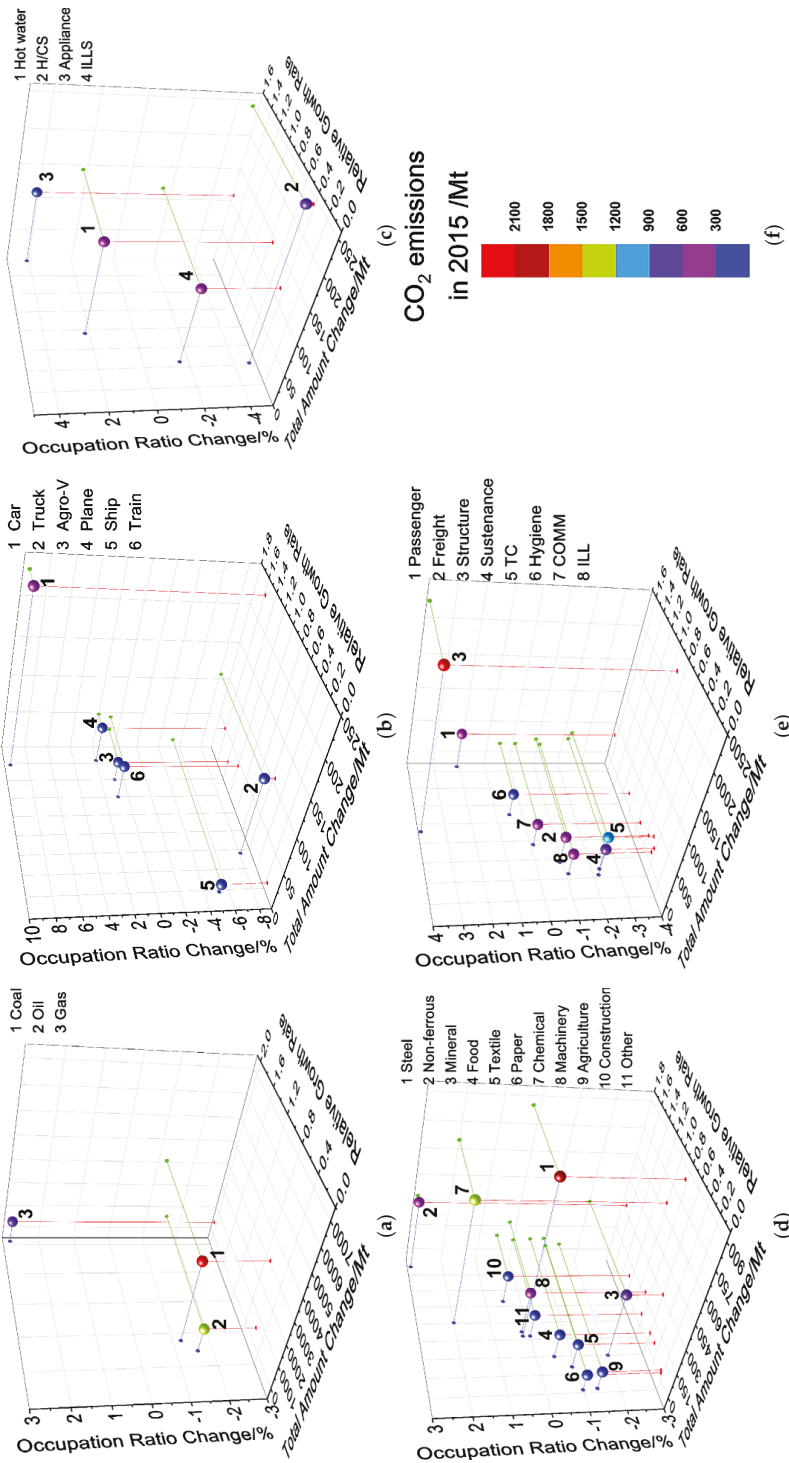


Figure 5. The TRO index decomposition of energy-related CO₂ emissions in 5 sections including: (a) Energy sources; (b) Vehicle; (c) Building; (d) Factory; (e) Final services. (f) The color of the dots in the diagram represents the total CO₂ emissions of relevant sectors in 2015.

3.2.1. The Energy Sources Level

In energy sources (Figure 5a), results show that the most significant structural changes were from coal. During 2005–2015, although the coal was still the largest contributor to energy-related carbon emissions with largest increment (total amount increased by 3076Mt), its proportion conversely decreased a lot (occupation ratio decreased by 1.2%). Compared with China's policy objectives [18], it can be seen that the effect of coal reduction work in China during this period was quite successful. The proportion of coal in China's energy structure decreased by 6.4% in this period. For one reason, it was related to the national efforts to increase the proportion of natural gas and non-fossil energy consumption [15]. For another reason, it was also closely related to the industrial upgrading and technological progress of the coal industry itself [28].

In contrast, natural gas has become an important energy source for replacing coal in the transition of China's energy structure leading to a rapid growth rate of carbon emissions by 205%, which was closely related to China's strong investment in natural gas infrastructure construction and deep international cooperation. Facts show that in 2009, China cooperated with Russia and Central Asian countries to build the first natural gas pipeline for the introduction of long-distance natural gas delivery from Central Asia; in 2013, China-Myanmar natural gas pipeline was established in cooperation with Myanmar, which became the second onshore natural gas pipeline; in the meantime, the liquefied natural gas (LNG) business was also booming, and the countries China imported LNG from had expanded from Australia, Indonesia and Malaysia to Qatar and Brunei [29]. Renewable energy represented by wind and solar power also developed rapidly in China during this period. For example, the wind power became the energy source with fastest relative growth rate (by 55.7 times) in the decade and contributed a lot of increase of the proportion in energy structure (increased by 1.1 %). The rise of natural gas and renewable energy had slowed the growth of energy-related carbon emissions to some degree.

3.2.2. The Vehicle Passive System Level

In the vehicle passive system (Figure 5b), results show that the largest driving force was the passenger car, which not only had the largest increase in total amount change (231Mt CO₂) but also remained a high relative growth rate (158%), making its occupation ratio increased by 9.5% in vehicle passive system and exceed trucks as the largest emission source. While trucks and ships represented a significant decline in the occupation ratio of the emissions structure (trucks reduced by 8.1%, ships reduced by 5.2%). Compared with other statistics, the results kept in line with the fact that China's highway infrastructure had been gradually improved in the past decade (in 2015, the total length of China's highways reached 4.57 Million km, the total length of freeways reached 123,500 km, the proportion of towns with roads reached 99.99% [30]), and the number of civilian vehicles increased rapidly (reached 163 million in 2015, which was ten times more than that in 2005 [26]). In this period, new energy vehicles such as electric vehicles had not been promoted, so the increment of private cars were mainly gasoline-powered cars, which significantly increased the carbon emissions of passenger cars. The transition of the economic structure was another proof. In 2015, the proportion of increased GDP in the tertiary industry exceeded 50% for the first time [31]. As in this period, the tertiary industry had less demand for physical goods compared with the primary and secondary industry, the overall freight demand and the growth rate of the road freight industry slowed down in 2015. Thus the energy consumption growth of trucks and ships slowed down, and carbon emissions did not increase significantly.

3.2.3. The Building Passive System Level

In the building passive system (Figure 5c), in terms of the energy consumption, the most significant increase came from hot water systems (relative energy consumption growth rate by 157%, energy consumption proportion increased by 4.9%), but as for carbon emissions, household appliance was

noteworthy. Although appliances energy consumption growth rate was only 19%, the relative growth rate of carbon emissions was as high as 158%, and its occupation ratio in the emissions structure increased the most by 4.1%. This result shows the role of R index to reveal potential trends. To explain this, we further calculated the carbon emissions per unit energy consumption (CPE) of these two sectors and found the difference. In this period, the CPE of the hot water system decreased by 31.4%, but that of the household appliance increased by 116.8%. This finding was consistent with another statistics [26], which shows that in the process of replacing traditional home appliances, a large part of the original biofuel appliances were replaced (such as electric cookers, gas stoves replaced firewood stoves, biofuel direct use decreased by 29.7% from 2010 to 2015 [26]), which made carbon emissions of appliances increase significantly although the total energy consumption did not change so much, for biomass was assumed to be carbon neutral. As a policy implication, it could be solved by adjusting the power source structure and introducing more non-fossil energy or biomass power.

The heated/cooled space system contributed the largest increase in total amount change (242 Mt CO₂), but considering its large emission base, the relative growth rate is just 42%, which is the smallest in the building system, its occupation ratio also decreased by 4.7%. This was mainly due to the gradual improvement of the infrastructure of municipal heat pipe networks. Centralized heat-supply and gas heat-supply replaced traditional heating methods and improved heating efficiency. The changes were also related to the improvement of energy efficiency of household devices such as heaters. Wang et al. [32] also agreed that China's domestic heating reformation could play a crucial role in achieving energy saving and emission reduction goals. At the spiritual level, this trend reflected a significant improvement of the residents' living standards, the constantly increasing demand for life quality.

3.2.4. The Factory Passive System Level

In the factory passive system (Figure 5d), the steel mining industry was still the sector with the largest carbon emissions and increment (CO₂ emissions increased by 851 Mt). This was related to the over-capacity inertia of the steel industry in China, and it was difficult to achieve de-capacity in short term which was also pointed out by Zhou and Yang [33]. Results also show that the non-ferrous metal mining industry and chemical industry had become new driving forces of carbon emission growth (the relative growth rate of non-ferrous metal industry reached 171%, accounting for an increase of 2.9% in the emission structure, and the chemical industry's emission growth rate reached 1.01, accounting for an increase of 2.0% in the emission structure). The improvement of macroeconomics, industrialization and urbanization had brought huge demand for non-ferrous metal materials and chemical raw materials, and also provided a good economic environment for relevant manufacturing. The significant profit growth of chemical industry (in 2015, its profit increased by 7.7%, which is the largest increase in all industrial sectors of China [34]) brought great opportunities for the development of chemical-related enterprises.

Compared with previous work in this field, Li et al. [11] conclude that in 2013 the 'electricity and heating' emitted the most in the secondary industry (factory), following by 'metals' (including ferrous and non-ferrous), while chemical industry just accounted for nearly 3.1%. This differs from our results, as the division of stages of carbon flow diagram in their work only included energy sources and end use sectors, and the 'electricity and heating' was regarded in a parallel relation with other industrial sectors. But in fact, most of electricity and heating served as secondary energy supply and were consumed by steel, non-ferrous metal and chemical industries. When we discuss carbon emissions responsibility, it is inappropriate to allocate all of these emissions to the electricity generation sector. Concerning this, in another work, Li et al. [35] allocated the emission responsibility of electricity generation to end use sectors and kept in line with our result that the ferrous (steel) industry took the largest CO₂ emissions responsibility, but the main difference was that the non-ferrous metal industry only accounted for 3% of end use sectors responsibility in their study. This was because in their carbon flow Sankey diagram, a large amount of emissions caused by energy loss in the conversion stage such as electricity and heat generation were regarded as conversion loss and not allocated to end use responsibility. However, the

fact is that the non-ferrous industry consumed a lot more electricity and heat but less direct fuels than other industries [25]. Since the emissions responsibility of electricity generation had been allocated to end use sectors, the loss of this stage should also be considered. This just illustrates the importance of energy allocation analysis method in carbon emissions analysis.

We also found that the industry whose growth of carbon emissions slowed significantly was the non-metallic mineral mining manufacturing industry. Although it had large emissions (517 Mt CO₂ in 2005), the relative growth rate was only 60%, and the occupation ratio of emissions shrunk by 2.0%. This partly differs from previous work [11] concluding that the non-metallic mineral would continue to increase rapidly. Actually, during the “12th Five-Year Plan” period when China had strengthened the management and rectification of non-metallic mineral mines, standardized the mining order, and shut down nearly 10,000 nonstandard enterprises [36]. The result illustrates the effectiveness of comprehensively considering TRO index to analyze the changing trend.

3.2.5. The Final Services Level

In final services (which is also the demand side, as shown in Figure 5e), results show the strongest driving force of carbon emissions was the demand for structural materials (CO₂ emissions increased by 2218Mt, the occupation ratio of emissions increased by 3.9%) and passenger service (the relative growth rate was as high as 166%, the occupation ratio increased by 2.1%). The increase of demand for structural materials was closely related to the rapid urbanization process and the rapid development of the infrastructure construction industry in China in the past decade. Compared with national economic statistics [37], during 2006–2011, the total output value of the construction industry maintained a super-high-speed growth of more than 20% for six consecutive years as the pillar industry of economic growth, which caused large demand for structural materials.

In contrast, the occupation ratio of thermal comfort and sustenance demands in emission responsibility significantly reduced (thermal comfort reduced by 2.3% and sustenance reduced by 2.2%). The slowdown in emissions growth of thermal comfort was mainly related to the improvement of energy efficiency of heated/cooled system in building passive systems, which had been explained in Section 3.2.3. The slowdown in emissions growth of sustenance was related to the reduction of proportion of the primary industry such as agriculture [26]. This also reflected the rising of people's life pursuit from sustenance to high-quality life.

3.2.6. Overall Trends

After comprehensively considering above analysis of each section, if we review the carbon flow Sankey diagrams combing demand side and supply side, we can discern the overall trends and interpret the inherent dilemma and of China's energy low-carbon transition during 2005–2015. In this period, China was still in the stage of rapid industrialization and urbanization investing huge amounts of infrastructure construction and fixed assets (China invested CNY 4 trillion in infrastructure construction during 2008–2010 [38]), which kept the demand for structural materials huge and growing. This made the industry represented by steel, chemical and non-ferrous metal maintain booming, some even over-capacity. These energy-intensive industries relied on coal and electricity, which brought difficulty for the energy system to cut coal consumption and to decarbonize. Meanwhile, the structure of energy final services did have changed. An obvious trend was that people's demand for high-quality life kept increasing, for example, the demand for passenger transportation, hygiene and communication services grew rapidly. Accordingly, the energy consumption and carbon emissions underlying the cars, planes, hot water supply and modern appliances increased rapidly, which could be new driving forces for energy-related carbon emissions. Discerning the trends may help policy makers to formulate more effective emission reduction strategies.

3.3. Uncertainties

Although authors have tried to make the method and data more accurate, uncertainties still exist in two aspects. One is the uncertainty of energy consumption data. When mapping the energy flow Sankey diagram, due to the lack of local data, the proportion of energy consumption in some sectors of factory passive systems and building passive systems referred to the average level of global-level research (see Appendix D.3.). Due to the outdated statistical data of the electric motors and light devices, we extrapolated relevant historical energy consumption data. Non-commercial energy consumption (although mainly are biomass including straw and wood which adopt carbon neutrality assumptions) related to CO₂ emissions was not audited in this study due to a lack of official statistical data.

The other one is the uncertainty of carbon emission data. Although most of the emission factors used in this paper were from China's local official statistics, there were still some data not provided referring the default values recommended by the IPCC [24], which lacked aboriginality to some extent. Carbon capture and storage technology were not discussed in this study as well.

4. Conclusions

This study proposed a method for systematically analyzing energy-related carbon emissions and quantitatively evaluating internal structural changes from the perspective of energy system. The method includes visualizing carbon flow process and emission responsibility allocation based on Sankey diagrams and energy allocation analysis and analyzing structural changes of carbon emissions based on TRO index decomposition which was put forward for the first time in our work. Then, this method was applied to China's case. We mapped China's energy-related carbon flow Sankey diagrams in 2005 and 2015 from energy sources, end-use conversion devices, passive systems to final services, then used TRO index decomposition to compare these two diagrams and reveal internal structural changes of carbon emissions caused by energy transition, finally discussed the trend and relevant reasons.

The results indicate that China's huge investment on infrastructure construction during 2005–2015 expanded the demand for structural materials on the consumption side, which made some high energy-intensive industries such as steel, chemical and non-ferrous metal maintain their booming status or even led to over-capacity, thus making it difficult for the energy system to cut coal consumption and decarbonize, while a new trend was that people's demand for high-quality of life kept increasing, and the demand for passenger transportation, hygiene and communication services grew rapidly. Accordingly, the energy consumption and carbon emissions underlying the cars, planes, hot water supply and modern appliances increased rapidly, which needed attention as new driving forces for energy-related carbon emissions. The results also provide a new perspective to analyze structural changes of energy-related carbon emissions from the terminal demand side. Compared with other statistics and studies, the method proved to be effective for analyzing energy-related carbon flow and evaluating structural changes.

However, there is still some uncertainty in processing of the energy data and emission factors. The limitation also lies in that the carbon emissions of energy loss in conversion stage were not considered separately in the analysis. In future work, the accuracy of the relevant data will be further improved, the impact of energy efficiency will be shown separately in carbon flow diagrams, and this method will be applied to more regions.

Author Contributions: H.Y. coordinated the main theme of this paper and wrote this manuscript. L.M. provided methodological guidance. L.M. and Z.L. discussed the research results and reviewed the manuscript. All authors have read and agreed to the published version of the manuscript.

Funding: This research received no external funding.

Acknowledgments: This work was supported by Tsinghua-BP Clean Energy Research and Education Centre. The authors also gratefully acknowledge support from Institute of Climate Change and Sustainable Development as well as Tsinghua-Rio Tinto Joint Research Centre for Resources, Energy and Sustainable Development. Finally, Honghua Yang wants to thank, in particular, the invaluable support from Yiwei Dai over the years.

Conflicts of Interest: The authors declare no conflict of interest.

Appendix A

Historical data of China’s primary energy consumption and energy-related CO₂ emissions in 1965–2018 from British Petroleum (BP) statistics [13].

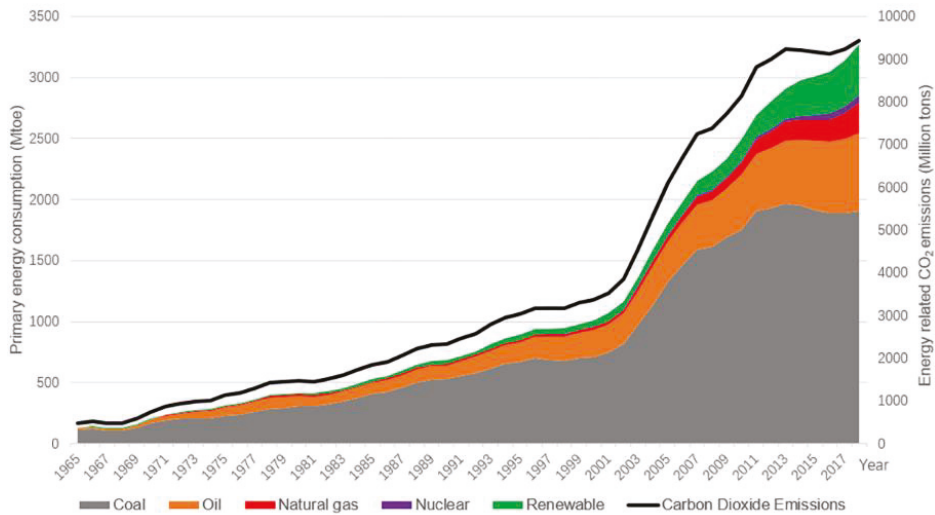


Figure A1. China’s primary energy consumption and energy-related CO₂ emissions in 1965–2018, data from BP statistics [13] (the renewable energy includes hydroelectricity).

Appendix B

Table A1. China’s important energy policies during 2005–2015.

Policy	Issue Date
The 11th Five-Year Plan for Energy Development [14]	2007
The Mid-Long Term Plan for Renewable Energy Development [15]	2007
The 11th Five-Year Plan for Renewable Energy Development [16]	2011
Renewable Energy Law of the People’s Republic of China [17]	2012
The 12th Five-Year Plan for Energy Development [18]	2013
Enhanced Actions on Climate Change: China’s Intended Nationally Determined Contributions [19]	2015

Appendix C

In the energy Sankey diagram of this study, the energy sources reflect the sources (including indigenous production, import, export, and stock change) of various primary energy (including oil, coal, gas, biomass, and other) that input into the energy system. The intermediate conversion reflects different forms of utilization of primary energy, e.g., directly used as fuels for engines and burners, used for power generation and heat generation, used by energy industrials themselves, and transformed to other industrial materials. The end-use conversion devices are devices where the primary energy is converted into useful energy such as motion, heat, cooling etc. The passive systems are places where useful energy output by end-use conversion devices is lost as low-grade heat in exchange for final services, such as vehicle, factory and building. The final services are the goods and services provided by useful energy in passive systems, such as transport services, production services and living services. The detailed classification and description of each part in the Sankey diagram is listed in Table A2.

Table A2. Classification and description of each part in the Sankey diagram ¹.

Stages	Items	Sub-Items	Description
Energy sources	Source supply	Indigenous production Import Export Stock	Primary energy produced in China Primary energy imported to China, including the fuel consumption of China's aircraft and ships in foreign countries Primary energy exported from China, including the fuel consumption of foreign aircraft and ships in China Primary energy from stock and to stock
	Primary energy	Oil Coal Gas Biomass Other	Crude oil, petroleum products, and liquids produced from other primary sources such as coal and biomass Hard coal, lignite, coke, and coking products such as coke tar Natural gas, coal bed methane, coke oven gas, gas works, and bio-gas Combustible plant/animal products, and municipal/industrial wastes Electricity from nuclear power and hydro, electricity/heat from geothermal, solar, wind, tide, and wave energy; and electricity imported and exported
	Intermediate conversion	Fuel Electricity Heat	Oil, biomass, gas, and coal directly used as fuel for engines and burners Electricity from power generation plant (including electricity for CHP plant) and other sources such as nuclear and renewable Heat from utility plants, CHP plants (heat proportion), and renewable sources such as solar thermal water heater and geothermal
End-use conversion devices	Energy own use	Non-fuel	Energy consumed by energy industries themselves The non-fuel use of energy sources for example in industrial materials
	Motion	Diesel engine Gasoline engine Aircraft engine Other engine Electric motor	Compression ignition diesel (or fuel oil) engine: truck, bus, ship, train; agricultural machinery Spark ignition Otto engine: car only; and LPG engine Kerosene engine: turboprop and turboprop engine Natural gas (CNG) vehicles and electricity vehicles/train AC/DC induction motor (excl. refrigeration)
	Heat	Oil burner Biomass burner Gas burner Electric heater Heat exchanger	Oil combustion device: boiler, petrochemical cracker, and chemical reactor Wood/biomass combustion device: open fire, stove, and boiler Gas combustion device: open fire, stove, boiler etc. Electric resistance heater, and electric arc furnace Direct heat application: district heat, heat from CHP, geothermal, and solar thermal
Other	Cooler Light device Electronic	Refrigeration, air conditioning: industry, commercial, and residential Lighting: tungsten, fluorescent, halogen etc. Computers, televisions, handheld and portable devices	
Vehicle	Car Truck Plane Ship Train Agro-vehicle	Light-duty vehicle: car, mini-van, SUV, and pick-up Heavy duty vehicle: urban delivery, long-haul, and bus Aircraft: jet and propeller engines Ocean, lake and river craft: ship, barge, and ferry Rail vehicle: diesel, diesel-electric, electric, and steam Agriculture vehicles such as tractors	

Table A2. Cont.

Stages	Items	Sub-Items	Description
Passive systems	Factory	Steel	Mining and processing of ferrous metal ores, smelting and pressing of ferrous metals and manufacture of metal products
		Non-ferrous Mineral	Mining and processing of non-ferrous metal ores, smelting and pressing of non-ferrous metals
		Food	Mining and processing of nonmetal ores; manufacture of non-metallic mineral products
		Textile	Processing of food from agricultural products; manufacture of foods, beverages and tobacco
	Chemical Machinery	Paper	Manufacture of textiles, apparel, footwear, and headgear
			Manufacture of paper and paper products, articles for culture, education and sport activity; printing, reproduction of recording media
	Agriculture Construction Other		Manufacture of raw chemical materials and chemical products, medicines, chemical fibers, rubber, and plastics
			Manufacture of general-purpose machinery, special purpose machinery, transport equipment, electrical machinery, communication equipment, computers and other electronic equipment, measuring instruments and machinery for cultural activity and office work
			Farming, forestry, animal husbandry, fishery & water conservancy
			Construction
Final services	Building	Hot water system	Mining of other ores, manufacture of artwork and other manufacturing, recycling and disposal of waste, production and distribution of water, processing of timber, manufacture of wood, bamboo, rattan, palm, straw products, leather, fur, feather, furniture and related products
		Heated/cooled space	Hot tap water, e.g., shower water heaters and hot water for washing and drinking
		Appliance	Residential/commercial indoor space Refrigerators, cookers, washers, dryers, dishwashers, and electronic devices
	Transport	Passenger	Residential/commercial indoor space, and outdoor space
		Freight	Transported by car, train, ship, and plane
	Production	Structure	Transported by truck, agro-vehicle, train, ship, and plane
		Sustenance	Materials used to provide structural support
		Hygiene	Preparation, storage, and cooking of food
	Living	Communication	Clothes washing/drying, hot water use, and other household appliances
		Thermal comfort	Digital and written communication
Illumination		Heating and cooling of air in buildings, clothes, and other textile products Provision of light	

¹ Reproduced with permission from [6], Elsevier, 2012.

Appendix D

Appendix D.1 Data for Energy Sources and Intermediate Conversion

The data for energy sources and intermediate conversion are mainly obtained from the 2015 Energy Balance Sheet (Standard Quantity) in the China Energy Statistical Yearbook 2016 [25], including data of energy sources, conversion, and end use. The data of some renewable energy that are not contained in the yearbook (e.g., photovoltaics, solar heating and geothermal energy) are from China's Utilization of Renewable Energy Sheet in the Energy Data of China 2016 [26].

Appendix D.2 Data for End-use Conversion Devices

The data for energy consumed for motion supply are calculated from oil and gas consumption by final sectors, which are referring to the 2015 Energy Balance Sheet [25]. The allocation of electricity among end-use conversion devices are assessed based on China's official statistics of end-use power consumption [26,27]. The energy flows from conversion devices to passive systems are allocated as classification in Table A2.

Appendix D.3 Data for Passive Systems

In passive systems, the energy flows from engines (including diesel engines, gasoline engines, aircraft engines, and other engines) are input into the vehicle passive system. All of electric motors, and most of electric heater and electronic devices are input into the factory passive system. The rest of electric devices are allocated to the building passive system.

The flows of different vehicles are based on previous flows of engines and the proportion are estimated based on the energy consumption data of transportation [26], as shown in Table A3 (e.g., the diesel engines are used not only by trucks, but also by trains, ships, agro-vehicles and motors in factories).

Table A3. The shares of engines energy flows to different vehicles of China in 2015.

Engines \ Vehicles	Car	Truck	Train	Plane	Ship	Agro-Vehicle	To Factory
Diesel	-	59%	4%	-	15%	9%	13%
Gasoline	100%	-	-	-	-	-	-
Aircraft	-	-	-	100%	-	-	-
Other	48%	-	52%	-	-	-	-

The proportion of heat flows into the factory and the building [25] is shown in Table A4.

Table A4. The shares of heat flows into the factory and the building of China in 2015.

Heat Device \ Passive System	Oil Burner	Biomass Burner	Gas Burner	Coal Burner	Heat Exchanger
Factory	42%	52%	73%	87%	67%
Building	58%	48%	27%	13%	33%

Due to lack of indigenous data, after getting the total input data, the fuel directly used in the factory is estimated based on the proportion of fuel used in U.S. industry [39] as shown in Table A5.

Table A5. The shares of fuel directly used in the factory.

	Fired Heating	Cooling	Steam	Other
Fuel use	47%	2%	42%	9%

And the energy allocation of fuel and heat used in the building is estimated by the shares of household energy use on global average [40] as shown in Table A6.

Table A6. The shares of flows from fuel and heat to building systems on global average.

Building System	Energy Type				
	Coal	Biomass	Oil	Gas	Heat
Hot water	13.4%	10%	10.3%	13.4%	-
Space heating	59.1%	44.1%	51.6%	61.8%	82.2%
Space cooling	-	-	0.1%	1.2%	17.8%
Appliance	27.5%	45.9%	36.1%	23.0%	-
Illuminated space	-	-	1.9%	0.6%	-

Appendix D.4 Data for Final Services

The energy flows from vehicles to transportation services are estimated from transportation statistics [26]. In this study, road transportation has been allocated (cars for passenger, trucks for freight), but shares of passenger and freight transport in other transportation (e.g., train, ship, plane) are estimated according to their utilization as shown in Table A7.

Table A7. The shares of flows from vehicles to transport services in China in 2015.

Transport	Vehicle				
	Car	Truck	Train	Ship	Plane
Passenger	100%	-	33%	-	71%
Freight	-	100%	67%	100%	29%

The energy flows from buildings to final services is estimated based on the global average data of household fuel use [40] and the data of electricity consumption by home appliances in China [26], as shown in Table A8.

Table A8. The shares of final services from building systems in China in 2015.

Final Services	Building Systems			
	Hot Water	Heated/Cooled Space	Appliance	Illuminated Space
Structure	-	-	12%	-
Sustenance	2%	11%	16%	-
Thermal comfort	-	89%	1%	-
communication	-	-	63%	-
Hygiene	98%	-	7%	-
Illumination	-	-	1%	100%

It is difficult to allocate energy flows from the factory passive system into various final services, because there are too many sub-sectors in the system serving for different final services. To simply the calculation, firstly, we divided the industrial sectors in the sheet of 2015 Final Energy Consumption by Industrial Sector (Standard Quantity) [25] into 11 groups as shown in Table A2 (factory). Then, the allocation of energy flows into relevant final services is estimated based on these subdivided departments. For instance, the steel, mineral, non-ferrous metals and construction are allocated into structure. The energy used for producing transport equipment is reckoned to be divided equally between the passenger and the freight. Some items in the machinery and other industrials whose usage can not be easily sorted (e.g., manufacture of general equipment, recycling of the waste) are assumed to be equally allocated among the various final services. Food and agriculture are allocated to sustenance. Textile flows to thermal comfort. Paper is allocated to communication.

Appendix D.5 Data for Energy-Related Carbon Emissions

In this study, we assumed that biomass is carbon neutral, other renewable energy (hydroelectricity, wind power, solar power and geothermal) and nuclear have no carbon emissions. Therefore, only the fuels listed in Table 2 are considered. The allocation of carbon emission responsibility in different sectors is calculated according to various types of fuel the sector uses. Since the use of different fuel types in the secondary energy (electricity and heat) is difficult to be distinguished in the consumption stage, we calculated the comprehensive emission factors of electricity and heat according to the supply structure in the 2015 Energy Balance Sheet [25], as shown in Table A9.

Table A9. The carbon emission factors of electricity and heat in 2015.

	Electricity	Heat
Emission factor	16.42 t C/TJ	19.35 t C/TJ

References

1. IPCC. AR5 Synthesis Report: Climate Change 2014. Available online: https://www.ipcc.ch/site/assets/uploads/2018/02/SYR_AR5_FINAL_full.pdf (accessed on 10 February 2020).
2. Manepalli, J. Ways of “greening the economy”. In *Green Energy Technology, Economics and Policy*; CRC Press Inc.: Vienna, Austria, 2010.
3. Soundararajan, K.; Ho, H.K.; Su, B. Sankey diagram framework for energy and exergy flows. *Appl. Energy* **2014**, *136*, 1035–1042. [[CrossRef](#)]
4. Cullen, J.M.; Allwood, J.M. The efficient use of energy: Tracing the global flow of energy from fuel to service. *Energy Policy* **2010**, *38*, 75–81. [[CrossRef](#)]
5. UK Department of Energy and Climate Change. Energy Flow Chart 2010. Available online: <https://webarchive.nationalarchives.gov.uk/20130106133854/http://www.decc.gov.uk/assets/decc/11/stats/publications/flow-chart/2276-energy-flow-chart-2010.pdf> (accessed on 10 February 2020).
6. Ma, L.; Allwood, J.M.; Cullen, J.M.; Li, Z. The use of energy in China: Tracing the flow of energy from primary source to demand drivers. *Energy* **2012**, *40*, 174–188. [[CrossRef](#)]
7. Chong, C.; Ni, W.; Ma, L.; Liu, P.; Li, Z. The Use of Energy in Malaysia: Tracing Energy Flows from Primary Source to End Use. *Energies* **2015**, *8*, 2828–2866. [[CrossRef](#)]
8. Li, X.; Chong, C.; Ma, L.; Liu, P.; Shen, X.; Jia, Z.; Wang, C.; Li, Z.; Ni, W. Coordinating the Dynamic Development of Energy and Industry in Composite Regions: An I-SDOP Analysis of the BTH Region. *Sustainability* **2018**, *10*, 2093. [[CrossRef](#)]
9. Davis, M.; Ahiduzzaman, M.; Kumar, A. Mapping Canadian energy flow from primary fuel to end use. *Energy Convers. Manag.* **2018**, *156*, 178–191. [[CrossRef](#)]
10. Mu, H.; Li, H.; Zhang, M.; Li, M. Analysis of China’s carbon dioxide flow for 2008. *Energy Policy* **2013**, *54*, 320–326. [[CrossRef](#)]
11. Li, X.; Cui, X.; Wang, M. Analysis of China’s carbon emissions base on carbon flow in four main sectors: 2000–2013. *Sustainability* **2017**, *9*, 634. [[CrossRef](#)]
12. Ma, L.; Chong, C.; Zhang, X.; Liu, P.; Li, W.; Li, Z.; Ni, W. LMDI Decomposition of Energy-Related CO₂ Emissions Based on Energy and CO₂ Allocation Sankey Diagrams: The Method and an Application to China. *Sustainability* **2018**, *10*, 344. [[CrossRef](#)]
13. BP. Statistical Review of World Energy—All data, 1965–2018. Available online: <https://www.bp.com/en/global/corporate/energy-economics/statistical-review-of-world-energy.html> (accessed on 10 February 2020).
14. The 11th Five-Year Plan for Energy Development. Available online: <https://www.ndrc.gov.cn/fggz/fzlggh/gjjzxgh/200709/P020191104623138936402.pdf> (accessed on 10 February 2020).
15. The Mid-Long Term Plan for Renewable Energy Development. Available online: <https://www.ndrc.gov.cn/xxgk/zcfb/ghwb/200709/W020190905497518622709.pdf> (accessed on 10 February 2020).
16. The 11th Five-Year Plan for Renewable Energy Development. Available online: http://www.nea.gov.cn/2011-08/22/c_131065984.htm (accessed on 10 February 2020).

17. Renewable Energy Law of the People's Republic of China. Available online: http://www.nea.gov.cn/2012-01/04/c_131260380.htm (accessed on 10 February 2020).
18. The 12th Five-Year Plan for Energy Development. Available online: http://www.gov.cn/zwggk/2013-01/23/content_2318554.htm (accessed on 10 February 2020).
19. Enhanced Actions on Climate Change: China's Intended Nationally Determined Contributions. Available online: http://www.gov.cn/xinwen/2015-06/30/content_2887330.htm (accessed on 10 February 2020).
20. IFU Hamburg. e!Sankey Software (2020). Available online: <https://www.ifu.com/en/e-sankey/> (accessed on 10 February 2020).
21. Liu, Z.; Guan, D.; Wei, W.; Davis, S.J.; Ciaisi, P.; Bai, J.; Peng, S.; Zhang, Q.; Hubacek, K.; Marland, G.; et al. Reduced carbon emission estimates from fossil fuel combustion and cement production in China. *Nature* **2015**, *524*, 335–338. [[CrossRef](#)] [[PubMed](#)]
22. General Principles for Calculation of the Comprehensive Energy Consumption of the People's Republic of China. Available online: <http://c.gb688.cn/bzgk/gb/showGb?type=online&hcno=F2113A2857611297ECF9A1683BE77F15> (accessed on 10 February 2020).
23. China Guidelines for Provincial Greenhouse Gas Inventories. Available online: <http://www.cbcsd.org.cn/sjk/nengyuan/standard/home/20140113/download/shengjiwenshiqiti.pdf> (accessed on 10 February 2020).
24. IPCC. *2006 IPCC Guidelines for National Greenhouse Gas Inventories*; United Kingdom Meteorological Office: Backnell, UK, 2006.
25. China's National Bureau of Statistics. *China Energy Statistical Yearbook 2016*; China Statistics Press: Beijing, China, 2016.
26. Wang, Q. *Energy Data of China 2016*; China Energy Group: Beijing, China, 2016.
27. Zheng, B.; Gao, F.; Guo, X. Survey Analysis of Lighting Power Consumption in China. *China Light Lighting* **2016**, *10*, 18–22.
28. The 12th Five-Year Plan for Coal Industry Development. Available online: <http://zfxgk.nea.gov.cn/auto85/201203/W020120322368710161760.pdf> (accessed on 10 February 2020).
29. Zhang, G. The Way of Natural Gas Development in China: Concentrate on Making Great Achievements and Promote Development Through all Ownership Systems. International Gas Cooperation & Development Forum, Wuhan, China, 13 September 2017. Available online: <http://www.ceweekly.cn/2017/09/13/205096.shtml> (accessed on 10 February 2020).
30. The 13th Five-Year Plan for Modern Comprehensive Transportation System Development. Available online: http://www.mot.gov.cn/zhuanti/shisanwujtysfzgh/guihuawenjian/201703/t20170301_2170528.html (accessed on 10 February 2020).
31. National Economic and Social Development Statistics Bulletin 2015. Available online: http://www.stats.gov.cn/tjsj/zxfb/201602/t20160229_1323991.html (accessed on 10 February 2020).
32. Wang, J.; Zhou, Z.; Zhao, J.; Zheng, J.; Guan, Z. Towards a cleaner domestic heating sector in China: Current situations, implementation strategies, and supporting measures. *Appl. Therm. Eng.* **2019**, *152*, 515–531. [[CrossRef](#)]
33. Zhou, K.; Yang, S. Emission reduction of China's steel industry: Progress and challenges. *Renew. Sustain. Energy Rev.* **2016**, *61*, 319–327. [[CrossRef](#)]
34. Profit Data of China's Industrial Enterprises above Designated Size in 2015. Available online: http://www.stats.gov.cn/tjsj/zxfb/201601/t20160127_1310925.html (accessed on 10 February 2020).
35. Li, H.; Wei, Y.; Mi, Z. China's carbon flow: 2008–2012. *Energy Policy* **2015**, *80*, 45–53. [[CrossRef](#)]
36. The Status of the Development of China's Non-Metallic Mineral Industry and the Prospect of the 13th Five Year. Available online: http://www.cgs.gov.cn/ddzt/kydh/2016kydh/mitbb/201609/t20160922_405026.html (accessed on 10 February 2020).
37. The 13th Five-Year Plan for Construction Industry Development. Available online: <http://www.mohurd.gov.cn/wjfb/201705/W020170504041246.pdf> (accessed on 10 February 2020).
38. China's State Council Executive Meeting Deploys Measures to Expand Domestic Demand and Promote Economic Growth. Available online: http://www.gov.cn/ldhd/2008-11/09/content_1143689.htm (accessed on 10 February 2020).

39. Energy Use, Loss and Opportunities Analysis: U.S. Manufacturing & Mining. Available online: https://www.energy.gov/sites/prod/files/2013/11/f4/energy_use_loss_opportunities_analysis.pdf (accessed on 10 February 2020).
40. Nakicenovic, N.; Gilli, P.V.; Kurz, R. Regional and global exergy and energy efficiencies. *Energy* **1996**, *21*, 223–237. [[CrossRef](#)]



© 2020 by the authors. Licensee MDPI, Basel, Switzerland. This article is an open access article distributed under the terms and conditions of the Creative Commons Attribution (CC BY) license (<http://creativecommons.org/licenses/by/4.0/>).

Article

Biowaste Treatment and Waste-To-Energy—Environmental Benefits

Martin Pavlas ^{1,*}, Jan Dvořáček ², Thorsten Pitschke ³ and René Peche ³

¹ Sustainable Process Integration Laboratory—SPIL, NETME Centre, Faculty of Mechanical Engineering, Brno University of Technology—VUT Brno, 616 69 Brno, Czech Republic

² Institute of Process Engineering, Faculty of Mechanical Engineering, Brno University of Technology—VUT Brno, 616 69 Brno, Czech Republic; 161220@vutbr.cz

³ Bifa Umweltinstitut GmbH, 86167 Augsburg, Germany; TPitschke@bifa.de (T.P.); RPeche@bifa.de (R.P.)

* Correspondence: martin.pavlas@vutbr.cz

Received: 22 March 2020; Accepted: 14 April 2020; Published: 17 April 2020

Abstract: Biowaste represents a significant fraction of municipal solid waste (MSW). Its separate collection is considered as a useful measure to enhance waste management systems in both the developed and developing world. This paper aims to compare the environmental performance of three market-ready technologies currently used to treat biowaste—biowaste composting, fermentation, and biowaste incineration in waste-to-energy (WtE) plants as a component of residual municipal solid waste (RES). Global warming potential (GWP) was applied as an indicator and burdens related to the operation of facilities and credits obtained through the products were identified. The environmental performance of a WtE plant was investigated in detail using a model, implementing an approach similar to marginal-cost and revenues, which is a concept widely applied in economics. The results show that all of the treatment options offer an environmentally friendly treatment (their net GWP is negative). The environmental performance of a WtE plant is profoundly affected by its mode of its operation, i.e., type of energy exported. The concept producing environmental credits at the highest rate is co-incineration of biowaste in a strictly heat-oriented WtE plant. Anaerobic digestion plants treating biowaste by fermentation produce fewer credits, but approximately twice as more credits as WtE plants with power delivery only.

Keywords: biowaste; waste-to-energy; composting; fermentation; greenhouse gases; global warming potential

1. Introduction

Biowaste represents a significant component of MSW. In general, biowaste can be considered as a mixture of similar proportions of kitchen and garden waste from households. According to the definition in the EU's Waste Framework Directive (2008) [1], biowaste means “biodegradable garden and park waste, food and kitchen waste from households, restaurants, caterers and retail premises and comparable waste from food processing plants”. Thanks to its properties, it is considered to be a renewable and sustainable source for energy production, and therefore its potential should be examined thoroughly.

There are two principal ways of biowaste collection, which also determines biowaste treatment systems. These collection systems are often running in parallel (see Figure 1). First, a dedicated infrastructure for biowaste collection and biowaste treatment is established. Biowaste is source-separated by citizens and handled as a specific stream (See Figure 1 left). Generally, the collection system is diverse, covering a range of options as traditional door-to-door or more sophisticated pneumatic underground system as reported in [2]. This stream ends in composting plants or digesters and is denoted as SEP-BIO later in the text. However, biowaste is also present in

residual municipal waste (RES), and we name this stream RES-BIO. Landfilling is the standard disposal method for RES in developing countries. In contrast, incineration with heat recovery (WtE) is preferred in countries with developed waste management systems. The benefits of WtE were evaluated in [3].

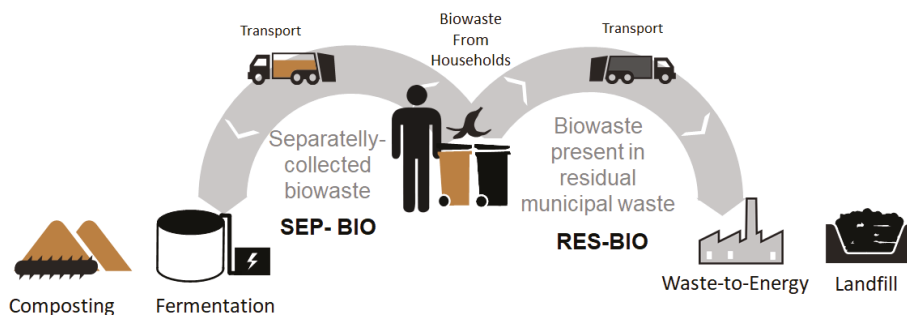


Figure 1. Two sources of biowaste and technologies considered in the analysis.

Depending on the segregation efficiency, the amount of biowaste treated as SEP-BIO or as RES-BIO varies.

The motivation for the investigations presented in this paper is to compare the environmental performance of different routes of waste streams commonly present in RES and treated by WtE. As follows from Figure 1, the main focus is on biowaste. However, the same approach can be applied to other components of RES (discussion on plastics separation and limited recycling options is a hot topic today).

Several studies with comparison of different biowaste treatment methods and biowaste management strategies have been published recently. Papers concerned with biowaste only are shortly reviewed first. Kong et al. [4] performed a comprehensive LCA confirming that the efforts to divert biowaste from landfilling to other ways of treatment (composting and fermentation) bring environmental benefits and reduce (GHG). Ardolino et al. [5] executed an LCA comparing the environmental impacts of different ways of utilisation of biogas produced in an anaerobic digestion plant. The biowaste-to-biomethane scenario, where biogas is upgraded to biomethane and used for transportation, provided higher benefits than traditional biogas treatment by burning in combined heat and power (CHP) unit and subsequent energy production.

LCA studies on residual waste (RES) are widespread. Laurent et al. [6] presented a comprehensive review of LCA studies in the waste management field. Nearly 100 papers dealing with mixed waste were identified. The majority of them is dedicated to RES from households. For example, Arena et al. [7] compared two options of thermal treatment of RES. Dong et al. [8] analysed the environmental performance of gasification and incineration technologies treating RES. The study was based on operational data from existing plants.

However, there are papers also dedicated to biowaste treatment, where biowaste is subject to thermal treatment with air excess. In this case, technologies processing SEP-BIO and RES are analysed together, and biowaste is only a part of the input to the WtE plant. Guereca et al. [9] performed an LCA analysis of biowaste management system for the city of Barcelona. Waste-to-energy was included in the current and proposed scenario. Pubule et al. [10] analysed an optimum solution for biowaste treatment in the Baltic States area. Incineration with and without energy delivery has been included as well. Thomsen et al. [11] carried out a comparative life cycle assessment (LCA) of diverting of the organic fraction of the household waste away from waste-to-energy (WtE) plant to manure-based and sludge-based biogas plants.

The results of the diversion showed a net increase in electricity production but a decrease in heat production. Greenhouse gases emissions (GHG) expressed as global warming potential (GWP) were

reduced by 10%. Di Maria et al. [12] conducted a study on the sustainability of biowaste treatment in WtE facilities using a life cycle approach and the cumulative energy demand index. The case study indicated that the treatment of biowaste in WtE plants operated in CHP was more efficient in exploiting the energy content of waste for replacing primary energies than biowaste treatment in anaerobic digestion plants. In addition, the significance of CHP proved to be a critical factor for efficient and effective waste utilization in WtE. In general, the life cycle approach is currently a widely used and favourite tool for research in waste management. Zhou et al. [13] carried out a comprehensive review of LCA tools available for WtE and provided several recommendations for their applications. Mehta et al. [14] successfully applied this principle combined with economic analysis for the assessment of multiple waste management options in Mumbai, India.

Economic performance of a WtE plant treating RES as a mixture of several components was investigated in detail in [15]. In comparison to [16], where the economic model of WtE plant addressed one ton of RES, outcomes of [15] figured out contributions of individual components like paper, plastics, biowaste. A method of the marginal cost was applied. For example, biowaste marginal cost was 160 EUR/t, whereas average of all components, which is also the cost of RES treatment, was 100 EUR/t. For comparison, the cost of plastics was 290 EUR/t. Following the same logic, Ferdan et al. [17] presented an environmental impact of a WtE plant processing RES. The contribution of individual components to the overall performance of WtE was missing. While some LCA studies above focused on biowaste treated in WtE plants, the mechanism of contribution of biowaste treated in a mixture with other components in one processing facility was not sufficiently explained.

In this paper, three ways of ecologically suitable biowaste treatment are discussed—composting, fermentation, and incineration with energy recovery in a WtE plant. The article is concerned with the environmental performance, production of GHG, with a focus on biowaste. This paper aims to compare the environmental impact of the methods mentioned above using the GWP indicator. While GHG production of aerobic and anaerobic treatment of separately collected biowaste are reviewed for comparison reasons, the contribution of biowaste component during thermal treatment of RES in WtE is investigated in detail to cope with uncertainty as mentioned above. An approach inspired by marginal cost [15] is developed, explained, and tested through a case study. Once the contribution of biowaste is known, the influence of the energy-effectiveness of the WtE plant on GHG burdens and credits related to biowaste only is also analysed. Burdens related to the performance of WtE are mainly subject to biowaste content in the input waste [17]. For example, the study [18] analysed fossil-based CO₂ emissions from 10 WtE plants in Austria. Credits are bound with form and amount of energy produced in WtE. Both credits and burdens are profoundly affected by WtE location:

- The amount of utilised heat is firmly bound with the possibility to absorb heat in district heating systems (DHS) or for industrial heating.
- If such a heat sink is not available, less efficient power production is enforced.
- The share of biowaste in RES, technological advancement, and facilities availability will differ; for instance, in developed and developing countries.

Based on the information above, it is suggested that these parameters also influence the feasibility of diverting of biowaste component of RES from WtE treatment to other treatment methods. This paper further explores how the WtE plant operation mode (heat-oriented, power-oriented) influences the environmental performance of the plant. Using the results, the importance of this parameter for the trade-off of the environmental performance of several biowaste treatment methods is evaluated. The published papers concerned with a similar problem (e.g., [11]) did not consider such an aspect in their studies, although the necessity of such evaluation was indicated.

In addition, the detached effect of any component on the environmental performance of WtE plant, if known and described, would be beneficial for sophisticated modelling and simulation of waste management. Bing et al. [19] highlighted the need for holistic network flow models in waste management. An example of such a model is paper [20], where flows of several municipal fractions

are optimised in one complex multiobjective problem. The task demands input data and hardware since it cannot be separated due to WtE processing of all the components of RES.

Section 2 describes the treatment methods—composting, fermentation, and thermal treatment in WtE—considered in this paper, together with the specifications of the chosen treatment plants. It also explains the proposed modelling approach based on marginal change. Section 3 presents the results obtained for each treatment method and a comparison of their environmental performance.

2. Methodology

A generally accepted and suitable indicator to describe the environmental impact of solid waste management systems is the GWP [21]. Even though there are many other assessment categories (respiratory inorganics, terrestrial ecotoxicity, carcinogens), the impact on global warming is the most relevant for assessment is this area [7]. GWP represents the amount of GHG produced or saved in $\text{kg}(\text{CO}_2)_{\text{eq}}$, and the calculated environmental impact can be both positive or negative. In this paper, an inventory related to subsequent GWP evaluation is performed during the calculations of the WtE case. In the case of other treatment methods—composting and fermentation—an LCA inventory was used for evaluation and follow-up trade-off.

2.1. Goal and Scope

The goal of this paper is to compare the environmental impact of biowaste treatment in a composting plant, an anaerobic digestion plant, and a WtE plant using the GWP indicator. Biowaste treatment in WtE is investigated in detail using a small case study. Correctly, an energy production-related analysis is used to examine the influence of the WtE plant mode of operation on environmental performance. The following text describes the investigated treatment methods and lists the specifications of the chosen treatment facilities.

2.2. Fermentation and Composting Processes

2.2.1. Description

Composting is a naturally occurring process of aerobic breakdown of natural matter by microorganisms. Reyes-Torres et al. [22] carried out a systematic review of green waste composting. The raw input material for composting is biowaste, as defined earlier. The process itself is relatively simple. However, the composting plant has to be controlled and operated well. In another case, there is an increased risk of excess odour, and greenhouse emissions production, low quality of the output products, and the process itself can be considerably slower [22]. Details of the composting process and technology used can be found in [23] and are not described in this paper in detail.

Fermentation, when compared with composting, occurs without access to oxygen—it is an anaerobic process. It is also often described as the anaerobic digestion process. The input material for this treatment process is any biologically degradable compound called the substrate. The output products are two—digestate, which is usually present in liquid form; and biogas with its two main components, methane and carbon dioxide. The process of anaerobic digestion is a complex of chemical reactions and its description and other details on fermentation processes are given in, for instance, in [12]. Fan et al. [24] analysed the carbon emission footprint in pre-and post-treating MSW in fermentation processes.

An LCA analysis is used to determine GHG production from these two processes. As the reference unit, the disposal of one ton of separately collected biowaste (SEP-BIO) is set.

The following processes are to be considered within the system boundaries (Figure 2): the specific waste treatment process (fermentation, composting) itself, including the further treatment of intermediates from the disposal process and all linked material and energy, flows related to the need for materials and supplies. In addition, the emissions from the collection and transport of the inputs (SEP-BIO) are considered. Additional benefits such as energy and secondary materials

(e.g., fertilisers, organic matter) result from the disposal processes. Corresponding amounts of energy or products/articles do not need to be produced conventionally from primary processes. The environmental impacts that would be associated with the conventional manufacturing/production of each of the substituted primary raw material are thus “saved” or “avoided”. The provision and maintenance of infrastructure (construction, service and repair of buildings, machine, industrial facilities) are not considered, as they are not expected to have a decisive influence.

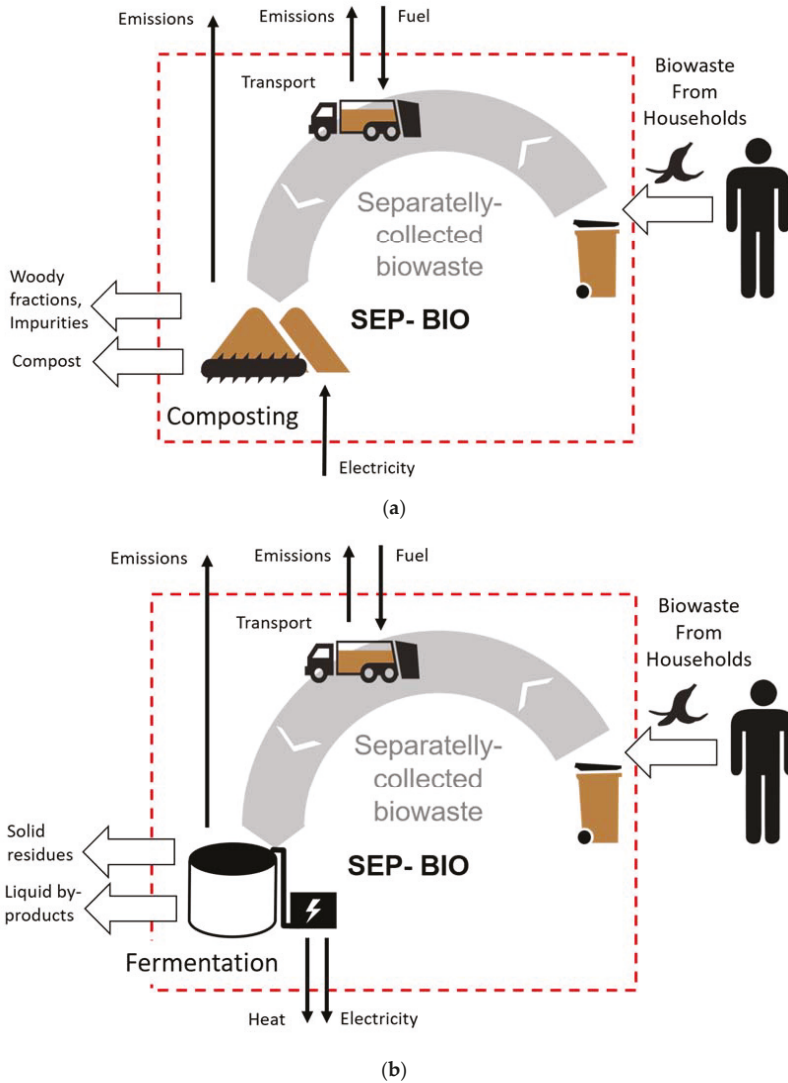


Figure 2. System boundaries for separately collected biowaste (SEP-BIO) treatment routes: (a) composting; (b) fermentation.

2.2.2. Specifications

The collection of biowaste for both treatment methods is realised by door-to-door collection. The GWP value of $1.25 \text{ kg}(\text{CO}_2)_{\text{eq}} \cdot \text{t}_{\text{waste}}^{-1} \cdot \text{km}^{-1}$ was considered for a collection vehicle [25] and value

of $0.088 \text{ kg}(\text{CO}_2)_{\text{eq}} \cdot \text{t}_{\text{waste}}^{-1} \cdot \text{km}^{-1}$ for a EURO5 truck [26] used in transport. The distance driven by the collection vehicle was estimated as 10 km, and the transport distance to a treatment facility was set to 50 km for both cases.

In the case of the composting plant, it is assumed that 10% of composting plants are open and 90% of the plants are closed. Any impurities are separated, and the plants produce ready-made compost only. The amount of compost yield is 440 kg/t of biowaste. As for the anaerobic digestion plant, a continuous dry fermentation with composting of solid fermentation residues was supposed. The biogas yield is assumed with $100 \text{ m}_N^3/\text{t}$ of biowaste.

2.3. WtE Process

Waste can also be effectively treated in WtE facilities. Typically, large WtE plants thermally treat RES by incineration and the released heat is recovered using CHP production. According to [27], approximately 27% of all MSW generated in EU28 in 2014 was processed by incineration with energy recovery. In case of WtE, which is of the most importance in this paper, positive values of GWP are so-called GWP burdens, and they are the result of production of GHG and release of their emissions into the air.

On the other hand, negative values are GWP credits, and they characterise decrease in global production of GHG, thanks to the replacement of fossil fuels and primary raw materials. GWP calculation method for WtE plant is based on the work [15], where the author introduced inventory analysis. Here, GHG production is calculated similarly following the same assumptions and data.

To operate the WtE facility effectively and sustainably, it is essential to pay attention to a range of conditions—one of them is also the input waste composition. Table A1 in Appendix A lists the RES composition used in the calculations in this paper. Biowaste share for particular RES composition is relatively high (28.9%) when compared to other components. Waste composition significance and its effect on the efficiency and operating conditions of the plant was described in [15]. Biowaste is characterised by zero content of fossil-based carbon. Therefore, its incineration is free of GWP burdens and generates GWP credits as replacement of traditional fossil-based resources. On the other side, its calorific value is only $4.6 \text{ GJ} \cdot \text{t}^{-1}$, which is quite low when compared, e.g., with plastics.

Modelling Approach

In the following text, the calculation of GWP of the WtE plant is described in detail. All the calculations were done using a computational model designed in Microsoft Excel. The calculation procedure itself consisted of several steps. To be able to assess GWP credits, the amount of energy recovered from the treatment process had to be determined. In this case, a techno-economic model of a WtE (TE model) thoroughly described in [17] was used and is briefly discussed further in the text. The values of GWP burdens were determined from the basic combustion equations and the amount of the products (CO_2). Both of this information is highly influenced by the waste composition and its properties such as the content of fossil-based carbon and calorific value of the waste. A specialised tool called JUSTINE, available at the workplace of the authors, was used to satisfy the requirement for high-quality data estimation. This tool is further described in [28]. After gathering both GWP credits and GWP burdens, a simple balance was performed and the net GWP obtained by the approach is summarised in [17]. Using this method, the resulting GWP of thermal treatment of RES without distinguishing its components can be readily determined. However, the paper aims to determine the GWP of biowaste component of RES.

To obtain such information, a concept of marginal change was proposed in this contribution. This concept is widely applied in economics. We then speak about marginal cost. The marginal cost concept has been employed in the field of waste management in a complex [15], where the impact of RES components on WTE plant economy has been investigated. However, the authors are not aware of any application of this concept for GWP analysis.

Figure 3 shows the steps required to apply such an approach in this case:

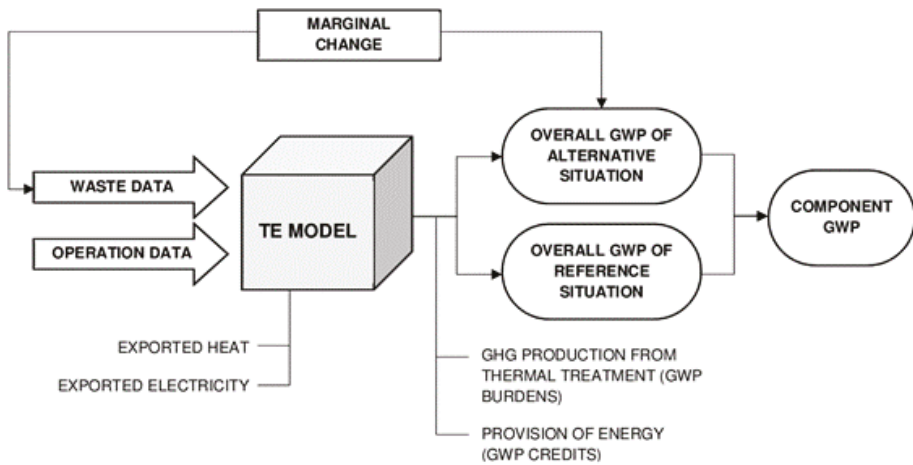


Figure 3. Calculation concept using the marginal change approach to evaluate GWP related to processing components of residual waste (RES) in waste-to-energy (WtE).

- i Firstly, the overall GWP for the whole amount of RES processed in WtE per year is calculated according to the procedure described in the previous paragraph, and according to [17], the resulting GWP is denoted as reference one and corresponds to the current composition of RES, $GWP_{REFERENCE}$.
- ii Secondly, the marginal change of the input RES is defined, and its effects on results are assessed. The marginal change is the diversion of a specific amount of one of the waste components from the original composition of RES—in this case, biowaste. This change is denoted as $m_{MARGINAL}$, and it expresses the biowaste removed from the input RES, i.e., the amount of input RES processed in WtE per year is decreased. The calculation procedure in the step (i) is then repeated. The overall balance of the WtE plant is slightly modified, and the calculations lead to a new GWP value, which is called $GWP_{ALTERNATIVE}$. This value, therefore, represents the overall GWP for the whole amount of RES processed in WtE per year decreased by $m_{MARGINAL}$.
- iii Finally, based on the assumption that the marginal change is exclusively related to one of the RES components, the GWP corresponding to the specific component—biowaste, in this case—can be computed. Such value is denoted as GWP_{COMP} or GWP_{BIO} , and results from a simple equation:

$$GWP_{COMP} = GWP_{BIO} = \frac{GWP_{REFERENCE} - GWP_{ALTERNATIVE}}{m_{MARGINAL}} \quad (1)$$

Such a component-specific GWP calculation is a base for WtE process evaluation, according to system boundaries displayed in Figure 4.

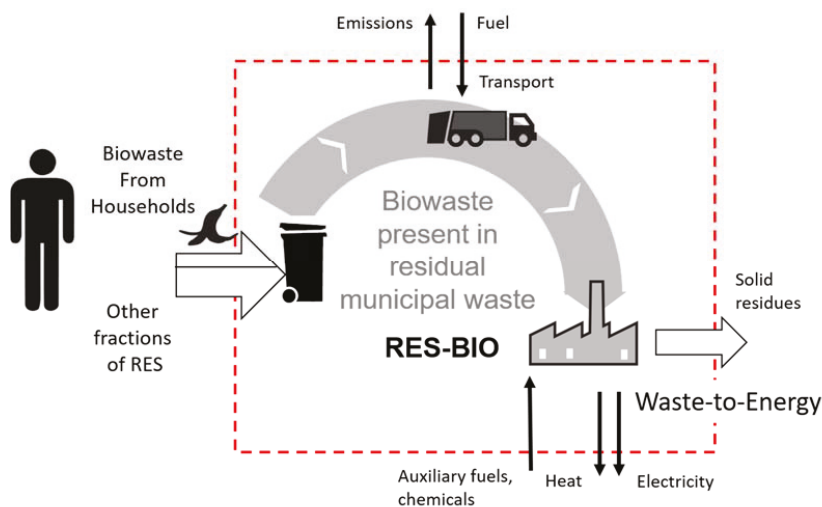


Figure 4. System boundaries for biowaste treated with other components of residual waste (RES-BIO) in WtE plants.

The case study considered in this paper is adjusted to suit current European conditions and is mainly focused on the Czech Republic. The input waste data, technological advancement, infrastructure availability (e.g., heat distribution network), and WtE plant specifications were chosen accordingly:

- RES composition is listed in Table A1 in Appendix A and was estimated specifically for The Czech Republic using tool JUSTINE [28].
- The fuel mix for power and heat industry in the Czech Republic used for GWP calculations is given in Table A2 in Appendix A.
- The WtE plant capacity was selected as 100 kt of RES per year. Technological specifications are according to [17]. The released heat is utilised in a heat recovery steam generator (HRSG) to generate superheated steam at 4 MPa and 400 °C. This steam is further used in cogeneration by the employment of extraction condensing steam turbine. In such type of turbine, the ratio between heat and power can be freely adjusted. Heat is exported in the form of hot water and supplied into the district heating system. The exported electricity is sold to the national electricity grid. The operational hours of the plant are stated as 8000 h/y.
- The amount of biowaste diversion is 5%, which at plant capacity yields approximately 1.45 kt of biowaste per year.
- The processes considered within the system boundaries are of the same nature as given for composting and fermentation.

3. Results

The results obtained by both LCA inventory and GWP inventory are presented below.

3.1. Composting

The environmental impact of biowaste treatment by composting is summarised in Figure 5. The overall value of GWP burdens of biowaste composting is $94.9 \text{ kg}(\text{CO}_2)_{\text{eq}} \cdot \text{t}_{\text{waste}}^{-1}$ consisting from environmental burdens from collection and transport ($16.9 \text{ kg}(\text{CO}_2)_{\text{eq}} \cdot \text{t}_{\text{waste}}^{-1}$) and from the treatment itself ($78 \text{ kg}(\text{CO}_2)_{\text{eq}} \cdot \text{t}_{\text{waste}}^{-1}$). On the other side, a positive effect—GWP credits with a value of $-152 \text{ kg}(\text{CO}_2)_{\text{eq}} \cdot \text{t}_{\text{waste}}^{-1}$ —result mainly from the substitution of primary resources such as fertilisers

or substrates. The net GWP value of biowaste treatment, including transport and collection, is equal to $-57.1 \text{ kg}(\text{CO}_2)_{\text{eq}} \cdot \text{t}_{\text{waste}}^{-1}$.

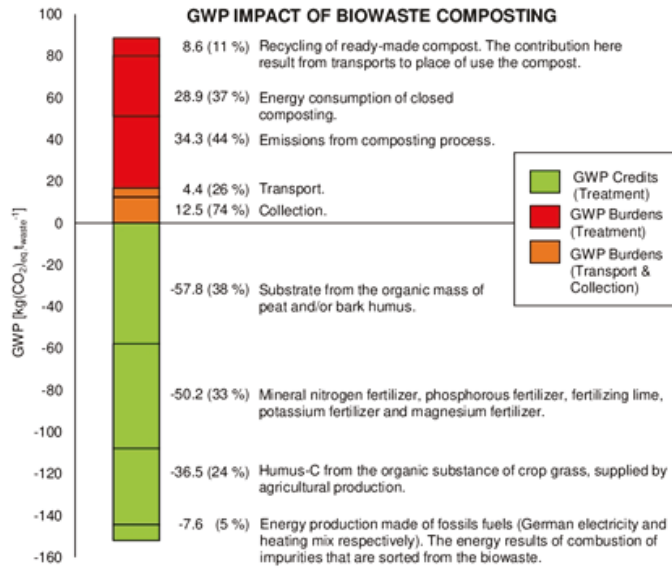


Figure 5. The overview of the environmental impact of biowaste composting expressed using GWP via SEP-BIO.

3.2. Fermentation

Figure 6 shows the environmental impacts of a biowaste recycling process via fermentation. In this case, the net GWP result of this process, including biowaste transport and collection, is reduced by $206.1 \text{ kg}(\text{CO}_2)_{\text{eq}} \cdot \text{t}_{\text{waste}}^{-1}$. GWP credits are mainly obtained by the substitution of primary resources as well as from the saved energy and yield $-315 \text{ kg}(\text{CO}_2)_{\text{eq}} \cdot \text{t}_{\text{waste}}^{-1}$. On the contrary, burdens from the fermentation process only are nearly similar to that of composting with a value of $92 \text{ kg}(\text{CO}_2)_{\text{eq}} \cdot \text{t}_{\text{waste}}^{-1}$. Burdens from collection and transport are the same as in the previous case, thus $16.9 \text{ kg}(\text{CO}_2)_{\text{eq}} \cdot \text{t}_{\text{waste}}^{-1}$.

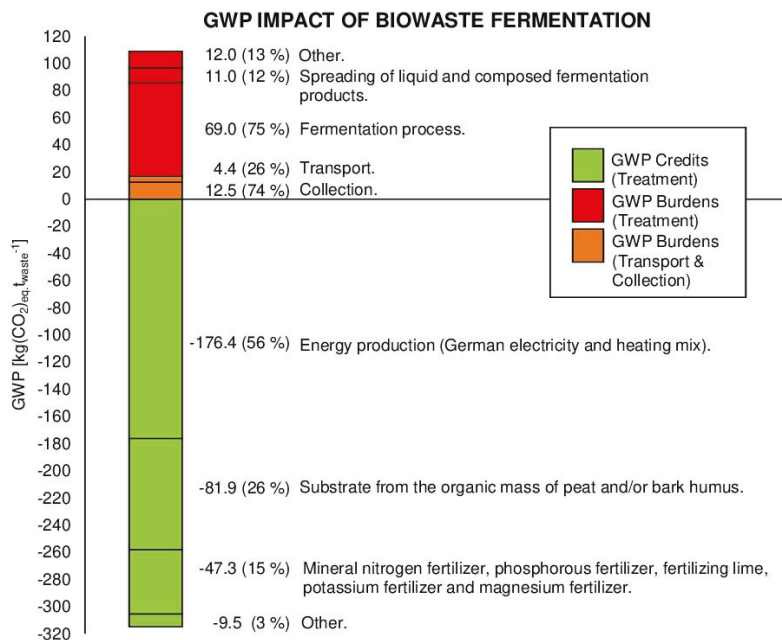


Figure 6. An overview of the environmental impact of biowaste fermentation expressed using GWP, via SEP-BIO.

3.3. Incineration with Energy Recovery

While composting and fermentation processes use SEP-BIO (separation is done by producers/citizens), WtE handles biowaste present in residual waste (RES-BIO).

Figure 7 shows the resulting GWP of biowaste treatment in the WtE plant as a function of percentage utilisation of heat production. The horizontal axis displays the ratio between heat and power production during cogeneration. If the value is equal to 100%, the plant is heat-oriented, and it maximises the export of thermal energy into the network still working as a combined heat and power plant. Maximum steam goes through the extraction valve of the turbine. On the other hand, 0% indicates a strictly power-oriented plant, where no heat for export is produced, and electricity generation is maximised. All the steam flows through the condensing stage of the turbine.

It can be observed that the overall environmental effect of biowaste utilisation is in this case, always positive. This can be explained as follows: The values of GWP burdens are of the same value for both cases—before and after biowaste diversion. That is because biowaste component of RES does not contain any fossil-based carbon and therefore does not participate in GHG production during oxidation of waste. On the other hand, GWP credits are related to BIO share. When an amount of biowaste with a heating value of approximately 4.6 GJ.t⁻¹ is removed, both exported heat and electricity decrease and therefore fewer credits from fossil fuels substitution are obtained. The highest overall GWP value of -272 kg(CO₂)_{eq}.t_{waste}⁻¹ is achieved when all the available energy is exported as heat. If all the energy is exported as electricity, the GWP credits are more than twice lower at -115 kg(CO₂)_{eq}.t_{waste}⁻¹. Please note that although the result of the calculation of Equation (1) is positive, a positive environmental impact of biowaste treatment in WTE is desired, and therefore, the value is considered to be negative. The values of both GWP burdens and credits produced per year are summarised in Table 1 for strictly heat-oriented and power-oriented plants.

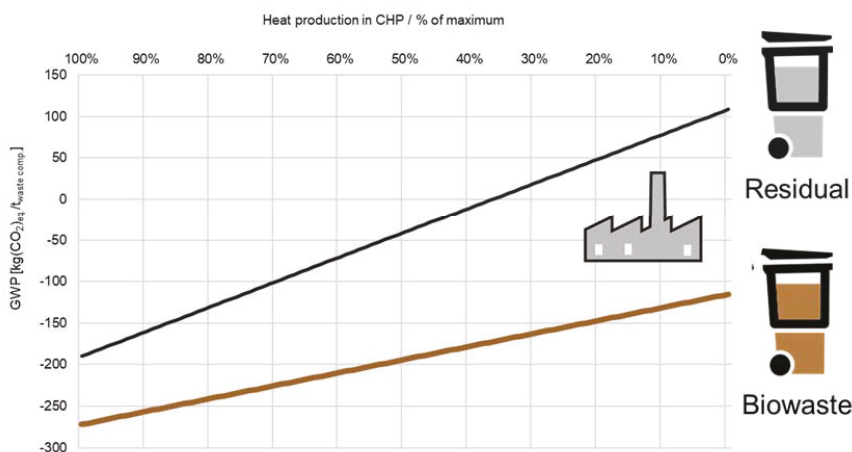


Figure 7. GWP as a function of percentage utilization of heat produced in WtE—the total balance for RES and contribution of its component biowaste (RES-BIO).

Table 1. Global warming potential (GWP) of residual waste (RES) in waste-to-energy (WtE) before and after biowaste component diversion.

Source	GWP Impact	100% Heat Prod. in CHP GWP [kt(CO ₂) _{eq} .y ⁻¹]		0% Heat Prod. in CHP GWP [kt(CO ₂) _{eq} .y ⁻¹]	
		Before	After	Before	After
GHG from waste incineration	burden	37.140	37.140	37.140	37.140
Heat export	Credit	−49.570	−49.192	0.000	0.000
Electricity export	Credit	−6.671	−6.656	−26.584	−26.418
Net result	overall	−19.101	−18.708	10.556	10.723

GWP is sensitive to waste composition, WtE plant efficiency, and fuel mix for power. The result for electricity-oriented operations is similar to other works published. For example, total emissions of CO₂, eq. with a positive sign (burdens prevail over credits) for WtE operated as a power plant have been reported in [7]. On the other hand, previous investigations into WtE plants with a high share of heat delivery are missing, since only a few countries and regions have district heating systems with sufficient demand on heat, compared to required WtE capacity. The future potential for centralised systems of heat delivery in Europe has been analysed by the Heat Roadmap Europe initiative (see [29]).

The result of GWP of biowaste can also be compared with GWP of RES, considering it as a mixture of various components. GWP of RES treatment in the WtE plant as a function of percentage utilisation of heat production is also shown in Figure 2. Although the lower heating value of biowaste is low, biowaste is a component of RES, which offers significant credits for WtE operation and RES incineration.

The standard operating mode for a typical WtE plant in the Czech Republic, considering the seasonal fluctuations of heat demand, would be approximately 75% heat production in CHP. The structure of GWP burdens and credits of biowaste processing in a WtE plant operating in this mode is shown in Figure 8.

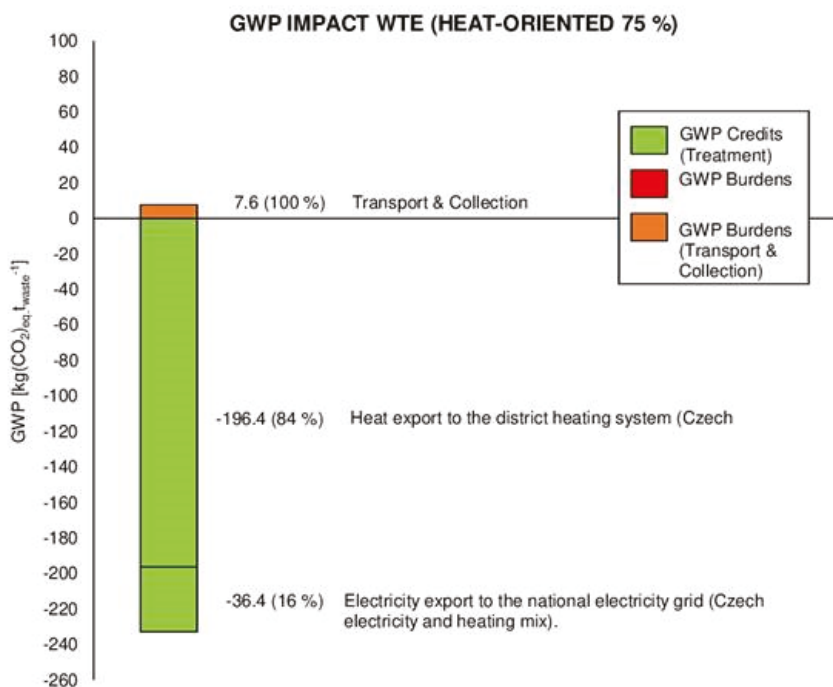


Figure 8. GWP impact of biowaste (SEP-BIO) incineration in WtE with heat production with CHP 75% of the maximum.

The values in this figure were obtained by applying Equation (1); therefore, they express the difference between the reference and alternative situation. In this case, the net value of GWP is equal to $-225.2 \text{ kg}(\text{CO}_2)_{\text{eq}}.\text{t}_{\text{waste}}^{-1}$. The GWP burdens are close to zero because biowaste component of RES does not contain any fossil-based carbon and therefore no additional GHG is produced. The GWP credits resulting from heat production are equal to $-196.4 \text{ kg}(\text{CO}_2)_{\text{eq}}.\text{t}_{\text{waste}}^{-1}$ and from power production $-36.4 \text{ kg}(\text{CO}_2)_{\text{eq}}.\text{t}_{\text{waste}}^{-1}$. The GWP burdens resulting from transport are estimated at $7.6 \text{ kg}(\text{CO}_2)_{\text{eq}}.\text{t}_{\text{waste}}^{-1}$.

3.4. Biowaste Treatment Methods Comparison and Discussion

Based on the data above, the environmental performance of the three previously discussed ways of biowaste treatment can be compared in Figure 9.

Each of the net results of individual treatment method is negative, which means all of the abovementioned methods are beneficial from an environmental point of view, thus saving GHG.

The least credits are obtained by biowaste composting, which is also considered as a less investment-demanding method. The values of GWP for treatment in anaerobic digestion plants and WtE plants are comparable—depending on the operational mode of WtE. If the WtE plant is mostly heat-oriented, its environmental performance is more favourable than treatment by fermentation. However, if the WtE plant is strictly power-oriented, it generates fewer GWP credits than an anaerobic digestion plant.

There is a worldwide trend towards environmentally friendly waste management, with an effort to reduce the consumption of primary raw materials. This trend is known as the circular economy, and the EU, in particular, is very active in supporting circularity principles in waste management.

One of the significant achievements of EU legislation is the gradual implementation of the circular economy package. Since an increase in the share of municipal waste recovered materially to 65% by 2035 is obligatory for EU member states, WtE appears as a less important part of the system. Instead, separate collection of various fractions of MSW is stipulated. Reduction of RES is anticipated at the same time. In this respect, the separation of biowaste is becoming more and more popular and common. The two basic treatment methods of separated biowaste are composting and fermentation. The easiest and at the moment, the most widespread method, is composting. When compared with fermentation, it has fewer requirements for technical equipment and is less demanding on both capital and operational costs. From an environmental point of view, based on the obtained data, composting is a less-favourable method of biowaste treatment than fermentation, as worse GWP results suggest. The separation of biowaste as a single component is connected with the requirement for additional infrastructure such as specialised biowaste containers and collection, which increases the price. A collection of biowaste as a component of RES and its subsequent incineration with energy recovery in WtE plant can help avoid the extra expense. The simple GWP evaluation and related energy production-related analysis showed that the environmental impact of this method heavily depends on the operational mode of the plant. Based on the calculations performed, strictly power-operated WtE plants using normal steam parameters perform environmentally worse than anaerobic digestion plants. However, environmental performance improves with increased heat production in CHP. The more waste heat is used to export heat, the better results are obtained. The operational mode, CHP, proved to be the decisive parameter for the environmental performance of the WtE plant.

Considering these results, biowaste treatment as a component of RES incinerated in WtE showed the most significant environmental potential and should not be excluded from the range of choices of biowaste treatment methods during waste management planning. The results of this small case study correspond with the results in [12] with WtE proving to be more environmentally-friendly under certain conditions and at the current state of technological development. While composting and fermentation methods are currently more favoured (recycling) than waste incineration with energy recovery for biowaste streams, the contribution of WtE is also significant when heat is positively utilised.

The presented result is subject to boundary conditions. The figures presented are based on data for the Czech Republic. The most important aspect is the composition of RES and energy mix, which could be country-specific (see Appendix A). The extent of variation is in accordance with previous studies, where comprehensive sensitivity analysis was done (e.g., in [8]).

The need for sustainable energy production through MSW treatment is also highlighted in the study [30]. However, it should be pointed out that material products from composting and fermentation have the potential to provide nutrients (especially phosphorus) and organic matter to supply the soil. This additional environmental benefit with a view to the conservation of resources cannot be provided by WtE use of biowaste. A more detailed study further exploring both environmental and economic aspects of biowaste treatment in chosen plants should be conducted and then reviewed. The research presented in this paper confirmed that the potential of biowaste treatment can be environmentally beneficial and must be further explored.

The results of the calculations and, especially the methodology of marginal change, can also be further used in more detailed stages of waste management planning, e.g., when solving so-called reverse logistic problems, which are tools used for the detailed description of waste streams and complex waste management systems planning [19]. The methodology could be applied to other components of RES, which can provide input data for the reverse model, where components of RES are considered in detached problems. For example, plastics treatment chains are hot candidates for further investigation and optimisation due to recent unfavourable changes in the secondary material market.

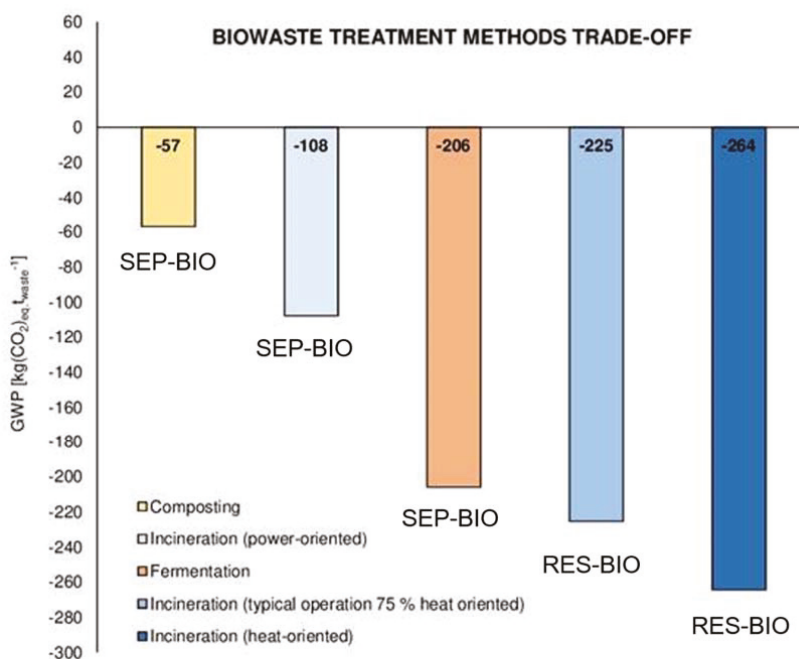


Figure 9. Biowaste treatment methods' comparison, SEP-BIO and RES-BIO alternatives.

4. Conclusions

Biowaste separate collection and its subsequent treatment by composting or fermentation are considered a sustainable way of handling this waste stream. First, an inventory of GHG for a composting process and fermentation process was carried out. The modelled cases suited current European conditions and are mainly focused on the Czech Republic's conditions. The net GWP value of biowaste treatment by composting, including transport and collection, was equal to $-57.1 \text{ kg}(\text{CO}_2)_{\text{eq}} \cdot \text{t}_{\text{waste}}^{-1}$. Positive effect resulting in GWP credits, which result mainly from the substitution of primary resources such as fertilisers or substrates, are burdens from the collection, transport, and treatment itself. Much positive effect can be achieved through fermentation, where net GWP of $-206.1 \text{ kg}(\text{CO}_2)_{\text{eq}} \cdot \text{t}_{\text{waste}}^{-1}$ can be achieved. In comparison with composting and fermentation, WtE processes biowaste present in residual waste. Therefore, the effect of biowaste incineration as a component of residual MSW was investigated next. A simulation model based on a marginal change concept was proposed for this purpose. Since net GHG emissions (burdens plus credits) are, in the case of WtE, dependent on heat utilisation rate (district heating systems), the primary goal of the case study was to carry out an energy production-related analysis. In the case of high heat delivery (75% of the thermal output of the boiler), the effect is comparable with the impact of fermentation/composting. In the case of missing heat demand (electricity generation), separate collection and fermentation is preferred.

Author Contributions: Conceptualization, M.P.; Investigation, J.D., T.P. and R.P.; Methodology, M.P., J.D. and T.P.; Software: J.D.; Supervision: M.P.; Visualization, M.P. and J.D.; Writing—original draft preparation, J.D. and M.P.; Writing—review and editing, T.P. All authors have read and agreed to the published version of the manuscript.

Funding: The authors gratefully acknowledge the financial support provided by the project Sustainable Process Integration Laboratory—SPIL, funded as Project No. CZ.02.1.01/0.0/0.0/15_003/0000456, by Czech Republic Operational Programme Research and Development, Education, Priority 1: Strengthening capacity for quality research.

Conflicts of Interest: The authors declare no conflict of interest.

Appendix A

The share of biowaste on the total composition of RES can vary greatly depending on different factors such as economic and social development of the country, legislation, or geographical location. It has to be highlighted that accurate and reliable data on waste composition is a critical input for environmental assessment calculations [31]. Consequently, a great deal of attention has to be paid when assessing these data. In this paper, the composition of RES for the Czech Republic obtained using tool JUSTINE was used. Such values would also be typical for other similarly developed countries in Europe.

Table A1. RES composition for the Czech Republic obtained using tool JUSTINE [28] for 2016.

Component	RES Composition [%]	Fossil-Derived Carbon [kg t^{-1}]	Calorific Value [GJ t^{-1}]
Metals	2.68	0.0	0.0
Glass	5.12	0.0	0.0
Paper	7.78	0.0	13.0
Composite packaging	2.99	219.0	18.0
Plastic	9.32	0.0	34.0
Biowaste	28.92	0.0	4.6
Textile	5.72	172.0	15.0
Mineral waste	3.32	19.0	0.0
Hazardous waste	0.62	416.0	17.0
Electronic waste	0.42	441.0	22.9
Other combustibles	14.38	45.0	4.4
Fine fraction (under 40 mm)	21.73	46.0	5.1
Total	100	101.3	8.46

Table A2. The fuel mix for the power and heat industry in the Czech Republic (Slivka, 2011) [32].

Reference	Power		Reference	Heat	
	Share [%]	CO ₂ Production [kg(CO ₂)/GJ ⁻¹ of Produced Power]		Share [%]	CO ₂ Production [kg(CO ₂)/GJ ⁻¹ of Produced Heat]
Coal	51	337	Coal	59	112
Natural gas	8	187	Natural gas	24	62
Nuclear	30	0	Other gases	4	73
Water	1	0	Renewables	9	0
Solar	3	0	Heating oil	4	85
Wind	1	0			
Biomass	6	0			
Total	100	187	Total		88

References

1. Directive 2008/98/EC of the European Parliament and of the Council of 19 November 2008 on Waste and Repealing Certain Directives. Available online: <https://eur-lex.europa.eu/legal-content/EN/TXT/PDF/?uri=CELEX:32008L0098&from=EN> (accessed on 6 February 2019).
2. Laso, J.; García-Herrero, I.; Margallo, M.; Bala, A.; Fullana-i-Palmer, P.; Irabien, A.; Aldaco, R. LCA-Based Comparison of Two Organic Fraction Municipal Solid Waste Collection Systems in Historical Centres in Spain. *Energies* **2019**, *12*, 1407. [CrossRef]
3. Vakalis, S.; Moustakas, K. Applications of the 3T Method and the R1 Formula as Efficiency Assessment Tools for Comparing Waste-to-Energy and Landfilling. *Energies* **2019**, *12*, 1066. [CrossRef]
4. Kong, D.; Shan, J.; Iacoboni, M.; Maguin, S.R. Evaluating greenhouse gas impacts of organic waste management options using life cycle assessment. *Waste Manag. Res.* **2012**, *30*, 800–812. [CrossRef] [PubMed]

5. Ardolino, F.; Parrillo, F.; Arena, U. Biowaste-to-biomethane or biowaste-to-energy? An LCA study on anaerobic digestion of organic waste. *J. Clean. Prod.* **2018**, *174*, 462–476. [[CrossRef](#)]
6. Laurent, A.; Bakas, I.; Clavreul, J.; Bernstad, A.; Niero, M.; Gentil, E.; Hauschild, M.Z.; Christensen, T.H. Review of LCA studies of solid waste management systems—part I: Lessons learned and perspectives. *Waste Manag.* **2014**, *34*, 573–588. [[CrossRef](#)]
7. Arena, U.; Ardolino, F.; Di Gregorio, F. A life cycle assessment of environmental performances of two combustion- and gasification-based waste-to-energy technologies. *Waste Manag.* **2015**, *41*, 60–74. [[CrossRef](#)]
8. Dong, J.; Tang, Y.; Nzihou, A.; Chi, Y.; Weiss-Hortala, E.; Ni, M.; Zhou, Z. Comparison of waste-to-energy technologies of gasification and incineration using life cycle assessment: Case studies in Finland, France and China. *J. Clean. Prod.* **2018**, *203*, 287–300. [[CrossRef](#)]
9. Güereca, L.P.; Gassó, S.; Baldasano, J.M.; Jiménez-Guerrero, P. Life cycle assessment of two biowaste management systems for Barcelona, Spain. *Resour. Conserv. Recycl.* **2006**, *49*, 32–48. [[CrossRef](#)]
10. Pubule, J.; Blumberga, A.; Romagnoli, A.; Blumberga, D. Finding an optimal solution for biowaste management in the Baltic States. *J. Clean. Prod.* **2015**, *88*, 214–223. [[CrossRef](#)]
11. Thomsen, M.; Seghetta, M.; Mikkelsen, M.H.; Gyldenkærne, S.; Becker, T.; Caro, D.; Frederiksen, P. Comparative life cycle assessment of biowaste to resource management systems—A Danish case study. *J. Clean. Prod.* **2017**, *142*, 4050–4058. [[CrossRef](#)]
12. Di Maria, F.; Sisani, F.; Contini, S. Are EU waste-to-energy technologies effective for exploiting the energy in bio-waste? *Appl. Energ.* **2018**, *230*, 1557–1572. [[CrossRef](#)]
13. Zhou, Z.; Tang, Y.; Chi, Y.; Ni, M.; Buekens, A. Waste-to-energy: A review of life cycle assessment and its extension methods. *Waste Manag. Res.* **2018**, *36*, 3–16. [[CrossRef](#)]
14. Mehta, Y.D.; Shastri, Y.; Joseph, B. Economic analysis and life cycle impact assessment of municipal solid waste (MSW) disposal: A case study of Mumbai, India. *Waste Manag. Res.* **2018**, *36*, 1177–1189. [[CrossRef](#)] [[PubMed](#)]
15. Martínez-Sánchez, V.; Hulgaard, T.; Hindsgaul, C.; Riber, C.; Kamuk, B.; Astrup, T.F. Estimation of marginal costs at existing waste treatment facilities. *Waste Manag.* **2016**, *50*, 364–375. [[CrossRef](#)]
16. Xin-gang, Z.; Gui-wu, J.; Ang, L.; Yun, L. Technology, cost, a performance of waste-to-energy incineration industry in China. *Renew. Sust. Energ. Rev.* **2016**, *55*, 115–130. [[CrossRef](#)]
17. Ferdan, T.; Pavlas, M.; Nevrlý, V.; Šomplák, R. Greenhouse Gas Emissions from Thermal Treatment of Non-Recyclable Municipal Waste. *Front. Chem. Sci. Eng.* **2018**, *12*, 815–831. [[CrossRef](#)]
18. Schwarzböck, T.; Rechberger, H.; Cencic, O.; Fellner, J. Determining national greenhouse gas emissions from waste-to-energy using the Balance Method. *Waste Manag.* **2016**, *49*, 263–271. [[CrossRef](#)]
19. Bing, X.; Bloemhof, J.M.; Ramos, T.R.P.; Barbosa-Povoa, A.P.; Wong, C.Y.; Van Der Vorst, J.G.A.J. Research challenges in municipal solid waste logistics management. *Waste Manag.* **2016**, *48*, 584–592. [[CrossRef](#)]
20. Šomplák, R.; Smejkalová, V.; Nevrlý, V.; Pluskal, J.; Pavlas, M. Implementation of Circular Economy through the Mathematical Programming for the Complex System Evaluation. *Chem. Eng. Trans.* **2019**, *76*, 523–528. [[CrossRef](#)]
21. Jensen, M.B.; Møller, J.; Scheutz, C. Comparison of the organic waste management systems in the Danish-German border region using life cycle assessment (LCA). *Waste Manag.* **2016**, *49*, 491–504. [[CrossRef](#)] [[PubMed](#)]
22. Reyes-Torres, M.; Oviedo-Ocaña, E.R.; Dominguez, I.; Komilis, D.; Sánchez, A. A systematic review on the composting of green waste: Feedstock quality and optimization strategies. *Waste Manag.* **2018**, *77*, 486–499. [[CrossRef](#)] [[PubMed](#)]
23. Epstein, E. *Industrial Composting: Environmental Engineering and Facilities Management*; CRC Press, Taylor & Francis Group: Abingdon, UK, 2011.
24. Fan, Y.V.; Klemeš, J.J.; Lee, C.T.; Perry, S. Anaerobic digestion of municipal solid waste: Energy and carbon emission footprint. *J. Environ. Manage.* **2018**, *223*, 888–897. [[CrossRef](#)] [[PubMed](#)]
25. Ecoinvent. Dataset: Municipal Waste Collection Service by 21 Metric Ton Lorry (CH). Information/Dataset from Ecoinvent Database v3.4. 2017. Available online: <https://www.ecoinvent.org> (accessed on 23 November 2017).
26. Ecoinvent. Dataset: Transport, Freight, Lorry >32 Metric Ton, EURO5 (RER). Information/Dataset from Ecoinvent Database v3.4. 2017. Available online: <https://www.ecoinvent.org> (accessed on 23 November 2017).

27. *Report on the Production and Management of Municipal Solid Waste. Edizione 2016; Rapporti 251/2016; ISPRA: Ispra, Italy, 2016; ISBN 978-88-448-0791-7.*
28. Pavlas, M.; Šomplák, R.; Smejkalová, V.; Stehlík, P. Municipal solid waste fractions and their source separation—Forecasting for large geographical area and its subregions. *Waste Biomass Valor.* **2020**, *11*, 725–742. [[CrossRef](#)]
29. Möller, B.; Wiechers, E.; Persson, U.; Grundahl, L.; Connolly, D. Heat Roadmap Europe: Identifying local heat demand and supply areas with a European thermal atlas. *Energy* **2018**, *158*, 281–292. [[CrossRef](#)]
30. Halkos, G.; Petrou, K.N. Analysing the Energy Efficiency of EU Member States: The Potential of Energy Recovery from Waste in the Circular Economy. *Energies* **2019**, *12*, 3718. [[CrossRef](#)]
31. Bisinella, V.; Götze, R.; Conradsen, K.; Damgaard, A.; Christensen, T.H.; Astrup, T.F. Importance of waste composition for Life Cycle Assessment of waste management solutions. *J. Clean. Prod.* **2017**, *164*, 1180–1191. [[CrossRef](#)]
32. Slivka, V. *Study on the State of the Heating Industry; VŠB-Technical University of Ostrava: Ostrava, Czech Republic, 2011.*



© 2020 by the authors. Licensee MDPI, Basel, Switzerland. This article is an open access article distributed under the terms and conditions of the Creative Commons Attribution (CC BY) license (<http://creativecommons.org/licenses/by/4.0/>).

Reducing Energy Requirements in the Production of Acrylic Acid: Simulation and Design of a Multitubular Reactor Train

Kiara Capreece Premllal and David Lokhat *

School of Engineering, University of KwaZulu-Natal, Durban 4051, South Africa; lovekiara@hotmail.co.za

* Correspondence: lokhat@ukzn.ac.za; Tel.: +27-031-2601-897

Received: 26 February 2020; Accepted: 27 March 2020; Published: 16 April 2020

Abstract: Acrylic acid, a versatile chemical intermediate, is typically manufactured via a two-step process involving the selective oxidation of propylene and acrolein. This work presents an optimized simulation on Aspen Plus[®] (AspenTech, Bedford, MA, USA) of the production of acrylic acid, with focus on the optimum design and operation of the reactor train, and modification for reduction in energy usage. In the propylene oxidation reactor, an inert pre-heating zone was designed to make use of the excess energy present in the exothermic process fluid and carried within the molten salt cooling fluid circuit. In the acrolein oxidation reactor, injection of cold air was used as a means to absorb the reaction heat. The optimization methodology employed aimed to minimize the total capital expenditure (i.e., equipment sizing) and operating costs (heat exchange network) for the required acrylic acid production and design constraints. The design constraints were based on the selected reaction kinetics and design heuristics for an optimum reactor design in this service from literature. Sensitivity analyses conducted on Aspen Plus[®] (AspenTech, Bedford, MA, USA) were used to determine both the interactions between and grouping of the critical parameters for the optimization. Elimination of the conventional fired preheater from the propylene oxidation reactor resulted in energy savings of almost 7 MW, with the reduction in cooling fluid pumping power for the acrolein oxidation reactor amounting to 5 kW.

Keywords: acrylic acid; propylene oxidation; multitubular reactor; optimization

1. Introduction

Acrylic acid is a widely used chemical intermediate in the polymer and textile industry. There are numerous technologies available for the production of both ester and glacial acrylic acid, however the most popular route is via the partial oxidation of propylene. Propylene is contacted with steam and air in a two-step reactor train, which uses different catalysts. In the first reactor, propylene is oxidized to acrolein followed by acrolein oxidation to acrylic acid in the second reactor [1]. The main partial oxidation reactions occurring in each reactor are indicated by Equations (1) and (2). Several side reactions can also occur, with the main byproducts being acetic acid and carbon dioxide [2].





Presently, acrylic acid production occurs in multitubular reactors consisting of up to 30,000 tubes with small diameters to ensure that thermal radial gradients are reduced whilst increasing the available heat exchange area for optimal and rapid heat removal by a circulating heat transfer fluid on the shell side [3]. Propylene and acrolein partial oxidation reactions are highly exothermic and therefore susceptible to thermal runaway, catalyst degradation and the promotion of unwanted side reactions. As such, effective heat removal is essential to maintain the required production rates and avoid irregular hotspots within the reactor. Figure 1 illustrates the typical reactor train and heat transfer fluid heat exchange network.

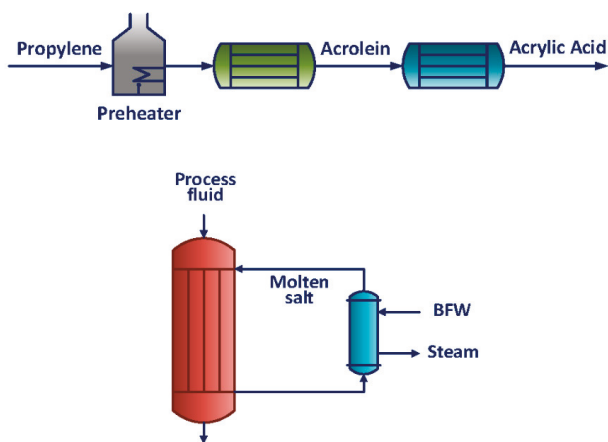


Figure 1. Typical reactor train and thermal fluid heat exchange network for acrylic acid production (BFW refers to boiler feed water).

The design, optimization and analysis of such a unit is a complicated task, since there are a large number of optimization variables to be considered. Proper representation of the reactor train in a process simulator is the first step towards heat integration, development of energy management strategies and overall understanding that could lead to intensification of the process [4]. Process simulation studies carried out on this process and reported in the literature have considered either adiabatic or fluidized bed reactor types with no in depth analysis of the more popular multitubular reactor configuration [2].

In this work, the rigorous design of a two-stage acrylic acid reactor train was undertaken and critical parameters identified for accurate representation of the unit in a process simulation platform. The study offers insight into the sensitivity of major performance criteria to the various operating parameters, many of which are unique to the multitubular reactor configuration.

2. Method Development

The reactor feed materials simulated in this work consists of a mixture of propylene with a purity of 94 mol % (containing equimolar impurities of propane and ethane), low-pressure steam (432 K, 5 bar) and compressed air (10 bar). The feed streams are fed into two multitubular fixed bed reactors in series, R-101 and R-102. The two-step oxidation process presented in this work contains a coordination of catalysts, with differing microstructures and operating conditions for each reactor. The partial oxidation of propylene, Equation (1), occurs exothermally within R-101. The tubes are packed with a bismuth molybdate catalyst. The reactor feed composition is comprised of a ratio of 5:30:65 of propylene, steam and air. Low-pressure steam is added to the reactor feed to act as thermal ballast [5].

R-102 operates within a lower temperature range and a vanadium molybdate catalyst. Molten salt was selected to be used as a coolant on the shell side to facilitate temperature control. The effluent from R-102 containing acrylic acid, unreacted propylene and associated byproducts, is then further processed and refined to the required grade of acrylic acid.

The multitubular fixed-bed reactor train was simulated on Aspen Plus® (AspenTech, Bedford, MA, USA) using the RPLUG (plug-flow reactor) model and the NRTL thermodynamic property method. The NRTL (non-random-two-liquid) thermodynamic property method was selected to simulate the physical properties of the reactant system, due to its ability to accurately predict highly nonideal chemical, polar or non-polar systems. The RPLUG model on Aspen Plus® (AspenTech, Bedford, MA, USA) employs ideal plug flow characteristics to the reacting systems. Therefore, radial velocity gradients were considered negligible. Interphase heat and mass transfer resistances and dispersion were also neglected. The RPLUG model required the following input parameters and reactor configuration choices for the rigorous design methodologies employed such as:

- Reaction kinetics
- Co-current or counter-current flow configurations
- Overall heat transfer coefficient
- Number of tubes, tube dimensions, reactor orientation
- Valid shell and tube side phases
- Catalyst bed voidage, particle density, particle diameter, particle shape factor

Reaction kinetics for the partial oxidation of propylene were extracted from Redlingshofer et al. [6], whilst Estenfelder and Lintz [7] reaction kinetics were used for the partial oxidation of acrolein to acrylic acid. The reaction kinetics used in this work were validated on Aspen Plus® (AspenTech, Bedford, MA, USA). A co-current flow configuration was selected. The overall heat transfer coefficient (per unit wall area) was interactively calculated using a macro-enabled excel spreadsheet which was coupled to the Aspen Plus® (AspenTech, Bedford, MA, USA) simulation platform for easy iteration during the development of the optimization methodology. Fouling factor resistances were extracted from literature. The overall heat transfer coefficient is given by Equation (7):

$$\frac{1}{U_i} = \frac{1}{h_i} + \frac{1}{h_{id}} + \frac{d_i \ln\left(\frac{d_o}{d_i}\right)}{2k_w} + \frac{d_i}{d_o} \frac{1}{h_{od}} + \frac{d_i}{d_o} \frac{1}{h_{od}} + R \quad (7)$$

where U_i is the overall heat transfer coefficient based on the inside area of the tube, h_i is the tube-side heat transfer coefficient, h_{id} is the tube-side dirt coefficient (fouling factor), d_o is the tube outside diameter, d_i is the tube inside diameter, k_w is the thermal conductivity of the tube wall material, h_{od} is the shell-side dirt coefficient and R is a heat transfer resistance parameter. The tube-side and shell-side heat transfer coefficients are functions of the tube bundle geometry, and fluid hydrodynamics on the tube-side and shell-side, respectively.

The wall heat transfer coefficient on the tube side was determined from a packed bed correlation to take into account the presence of the catalyst and is illustrated by Equations (8) to (11) [8]. Kern's shell side heat transfer coefficient correlation was used to approximate the heat transfer coefficient on the shell side [9].

$$\frac{h_w d_p}{k_g} = 0.16 \text{Re}'^{0.93} \quad (8)$$

$$20 < \text{Re}' < 800 \quad (9)$$

$$0.03 < d_p/d_t < 0.2 \quad (10)$$

$$d_p = 6V_p/S_p \quad (11)$$

In Equations (8) to (12), h_w is the wall heat transfer coefficient, d_p is the diameter of the catalyst particles, k_g and k_f are the thermal conductivities of the process gas and thermal fluid, respectively, d_e

is the equivalent diameter of the of the flow area on the shell-side, Re and Pr are the fluid Reynolds and Prandtl numbers, and μ and μ_w are the fluid viscosities in the bulk and at the wall, respectively.

The reactor train and heat exchange network optimizations considered the following variables, design constraints and possible optimizations:

Variables

- Reactor length
- Number of tubes
- Heat transfer fluid flow rate
- Heat transfer fluid heat exchange circuit
- Catalyst physical properties

Design Constraints/Possible Optimizations

- Conversion of propylene above 95%
- Complete conversion of acrolein
- Tube side pressure drop below 10%
- Shell side pressure drop
- Temperature of propylene oxidation reactor between 633 and 703 K as per the selected reaction kinetics
- Temperature of acrolein oxidation reactor between 533 and 573 K as per the selected reaction kinetics
- Removal of hotspots and subsequent limitation of susceptibility to thermal runaway
- Minimization of heat transfer fluid usage
- Heat integration

Similar optimization methodologies were developed for reactors R-101 and R-102, with differences occurring due to the varying extents of the respective exothermic reactions. The Wegstein method is usually the most reliable method for tear stream convergence, such as with the RPLUG model in Aspen Plus® (AspenTech, Bedford, MA, USA). Interactions between variables are ignored therefore the Wegstein method results in oscillating solutions whenever variables are strongly coupled. Owing to the heavily coupled nature between the parameters, the sensitivity of each variable to the next was difficult to determine even when using combinations of optimizations, sensitivities and design spec/vary models in Aspen Plus® (AspenTech, Bedford, MA, USA). Consequently, algorithms were derived iteratively using the RPLUG model on Aspen Plus® (AspenTech, Bedford, MA, USA) in addition to manual (offline) iterations to ensure that the most optimum design choices for the reactors were made. The optimization methodology used aimed at minimizing the total capital expenditure and operating costs, i.e., minimizing reactor sizing and heat input, for the required design constraints.

The optimization procedure, illustrated by Figure 2, entailed iteratively adjusting the tube length to determine the most efficient length for the reactor. The reactor tube length affects the tube and shell side pressure drops since pressure drop correlations are directly proportional to tube length. In addition, the tube length determines the overall dimensions of the reactor since the tube length is inversely proportional to the number of tubes. The tube length was therefore iteratively varied whilst Aspen Plus® (AspenTech, Bedford, MA, USA) models were used to determine the minimum number of tubes required for the respective tube length, the thermal fluid inlet temperature and thermal fluid flow rate required. The minimum number of tubes was governed by the propylene and acrolein conversions specified, which was ultimately dependent on the reaction kinetics and heat transfer within the reactor. Both the reaction kinetics and heat transfer were constrained by the allowable temperature ranges per reactor. The allowable temperature ranges per reactor were controlled by varying the thermal fluid inlet temperature and flow rate. Preliminary base case reactor optimizations illustrated large tube side pressure drops that were not conforming to the allowable 10% design constraint for economical and practical industrial reactors. Hollow cylinder catalyst particles were selected for the simulation

to improve the tube side pressure drop to within the design constraint. Following the optimization of the tube side pressure drop, preliminary analysis was conducted on the shell-side pressure drop. The shell-side pressure drop was increased to promote more efficient heat transfer on the shell side. The same methodology was applied to reactor R-102.

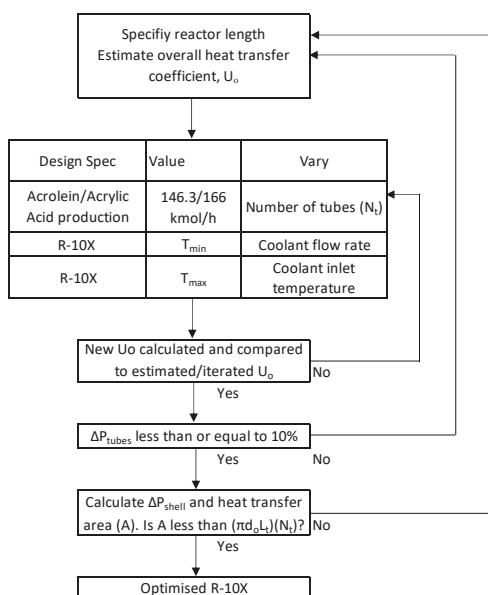


Figure 2. R-10X (X = 1 or 2) optimization algorithm.

The following subsections aim to discuss the differences in the optimization methodologies for R-101 and R-102.

Redlingshofer et al. [6] presented reaction kinetics that were valid in the temperature range from 633–703 K for the partial oxidation of propylene. Typically, a preheater would be used to ensure that the reactor feed temperature is within the required range for the reaction kinetics. The duty of heat exchange equipment required to increase the R-101 feed from a mixture temperature of 363 K to 633 K was calculated on Aspen Plus® (AspenTech, Bedford, MA, USA) as 6.19 MW. In typical Lurgi GmbH and Nippon Kayaku processes of acrylic acid, recovered heat from the exothermic reactions is used to generate steam. Instead of generating steam, in this work, an inert preheating zone was used in R-101, as illustrated by Figure 3, to use the heat absorbed by the molten salt circulating in R-101. This concept was derived from the production of phthalic anhydride.

Estenfelder and Lintz [7] presented reaction kinetics that were valid in the temperature range from 533–573 K for the partial oxidation of acrolein. When employing the method developed to optimize R-102 as per the design constraints, the reactor temperature could not be maintained within the required temperature range due to the formation of a hotspot near the entrance of the reactor. Dilution of catalysts with inert material is a widely practiced means of mitigating hotspots in wall-cooled reactors, therefore alternate mass % inert material were used to mitigate the hotspot, which is illustrated in Figure 3. As an initial estimate, 25 mass % inert material was simulated in R-102 to determine the extent to which the reactor temperature would be controlled within the reactor. Increasing the mass % of inert material however does increase the reactor dimensions as well as capital and operating costs.

An alternate method to remove the hotspot is therefore proposed in this work. With reference to the process of ethylene dehydrogenation, an air injection was used to lower the temperature of

R-101 effluent and introduce sufficient inert (nitrogen) into the process fluid to successfully remove the hotspot [10].

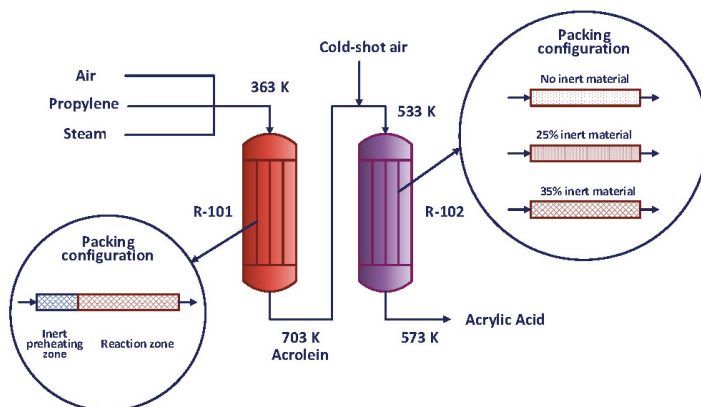


Figure 3. Studied process and catalyst packing configurations of multitubular fixed bed reactors R-101 and R-102.

3. Results and Discussion

3.1. Reaction Method Selection

Alternate paths are available for acrylic acid production. However, this work only explores the simulation and optimization of the partial oxidation of propylene to acrolein.

3.2. Reactor Configuration

Multitubular fixed bed reactors are commonly used for highly exothermic reactions to facilitate optimal heat removal. Tubular fixed bed reactors have an advantage that undesired consecutive reactions are suppressed to some extent.

The co-current flow arrangement was selected since parametric sensitivity behavior indicated that it would be the most attractive alternative from a steady state standpoint [11]. In the author's previous work on the partial oxidation of propylene to acrolein, the co-current configuration was selected as a method to effectively control the hotspot in comparison to a counter-current cooling circuit [3].

3.3. Heat Transfer Fluid Selection

The heat transfer fluid used on the shell side should be able to rapidly remove energy from the process without the requirement of impractically high flowrates. Molten salt heat transfer fluids were chosen due to their practicality for high temperature applications. Apart from being cost effective and nontoxic, molten salt has superior heat transport properties such as high heat capacities and high heat transfer coefficients such that the equipment size and surface areas for heat transfer can be held to a minimum. In addition, maintenance and power costs for circulating the molten salt are correspondingly low. Commercial HTS₁ (40% KNO₃ and 60% NaNO₃) and HTS₂ (53% KNO₃, 40% NaNO₂ and 7% NaNO₃) molten heat transfer salts were selected for their suitable operating temperature ranges, i.e., 422–853 K and 563–823 K, respectively [12]. Molten salt physical properties, if modeled as a concentration of nitrate and nitrite salts in water, are grossly underestimated on Aspen Plus® (AspenTech, Bedford, MA, USA) and therefore do not accurately represent the heat transfer capability of molten salt. Therefore, a molten salt component was built into Aspen Plus® (AspenTech, Bedford, MA, USA) with the respective physical properties manually input. The physical properties were estimated as per correlations in literature [13].

3.4. Catalyst Selection

Catalyst selection incorporated several fundamentals presented by Grasselli [14] such as the need for lattice oxygen, metal oxygen bonds and using the appropriate host structure. Lattice oxygen is a versatile and more selective oxidizing agent than gaseous dioxygen. The basic idea is to use the metal oxygen as a reactant such that only desired products are favored during the oxidation of hydrocarbons. Following the need for lattice oxygen, the metal oxygen bond type needed was explored. If the bond is too strong, no reaction will occur. Conversely, undesired overoxidation may occur prevalently. The host structure should be pliable, able to contain lattice oxygen and be reduced without structural collapse. Taking these properties into consideration, bismuth molybdate, $\text{Bi}(\text{MoO}_4)_3$, and vanadium molybdate, $\text{VMo}_3\text{O}_{11}$, catalysts were selected for R-101 and R-102. These catalysts reported high selectivities towards acrolein and acrylic acid [15].

3.5. Propylene Partial Oxidation Reaction Kinetics Validation

Reaction kinetics for the partial oxidation of propylene over a bismuth molybdate catalyst were extracted from Redlingshofer et al. [6]. Acrolein oxidation to formaldehyde was considered negligible due to the low range of selectivities i.e. 0.73–0.78% [16]. The redox reaction mechanism for acrolein formation proceeds via two steps: reduction and oxidation reactions. Models such as the Mars–van-Krevelen and Langmuir–Hinshelwood rate expressions account for the crossover from oxidation to reduction reactions in a single expression. However, the power law reduction reaction was favored since the α -bismuth molybdate catalyst selected, which has a high selectivity to acrolein of 88%–95%, operates optimally in a temperature range of 623–723 K [6]. The kinetics were determined by statistical parameter estimation using experimental data from isothermal investigations and were valid over a temperature range of 633–703 K. The kinetic parameters proved to be statistically significant as represented by their standard deviations, thereby validating the reaction kinetics presented. Further kinetic validations were conducted on Aspen Plus[®] (AspenTech, Bedford, MA, USA) to determine the feasibility of scaling up the lab-scale kinetics. The yield, conversion and selectivity profiles extracted from Redlingshofer et al. [16] correlated with the Aspen Plus[®] (AspenTech, Bedford, MA, USA) simulation results illustrated in Table 1, thereby validating the use of these kinetics in the design of an industrial-sized reactor as well as reinforcing the ease of scale-up with multitubular reactors.

Table 1. Validation of reactor kinetics for the partial oxidation of propylene by Redlingshofer et al. [16].

Value	Conversion of Propylene (%)	Selectivity to Acrolein (%)
Maximum	61.4	89.7
Minimum	59.6	89.1
Mean value	60.3	89.5

3.6. Acrolein Partial Oxidation Reaction Kinetics Validation

Estenfelder and Lintz [7] presented reaction kinetics for the partial oxidation of acrolein over vanadium molybdate oxide catalysts with varying compositions. The reactor network was treated as an isothermal plug flow reactor and kinetics were presented for 533 K and 573 K. In order to approximate the kinetics for the temperature range from 533 K to 573 K, linearization of the experimentally determined reaction rate constants was used. Kinetic validations were conducted on Aspen Plus[®] (AspenTech, Bedford, MA, USA) to determine the feasibility of scaling up the lab-scale kinetics. The yield and selectivities reported by Estenfelder and Lintz [7] correlated with the Aspen Plus[®] (AspenTech, Bedford, MA, USA) simulation results in Table 2, thereby validating the use of these kinetics in the design of an industrial-sized reactor as well as reinforcing the ease of scale-up with multitubular reactors.

Table 2. Validation of reactor kinetics for the partial oxidation of acrolein, based on kinetic parameters extracted from Estenfelder and Lintz [7].

Number of Tubes	¹ Selectivity of Acrylic Acid (%)	¹ Yield of Acrylic Acid (%)
500	96	97.92
5000	96	97.96
10,000	96	98.03
15,000	96	97.98
20,000	96	97.91

¹ Estenfelder and Lintz [7] reported a selectivity to acrylic acid of 98% and a yield of 95%.

3.7. Assumptions and Simulation

Rigorous design of multitubular reactors can be effectively carried out in the Aspen Plus[®] (AspenTech, Bedford, MA, USA) simulation platform, provided that mass transfer resistances are either designed-out or accounted for in the reaction rate [17]. Design heuristics, in Table 3, from the indicated literature sources were used to develop the optimized reactor configuration in this work. Heat and mass transfer approximations and calculations were critically evaluated in the reactor.

Table 3. General multitubular reactor design heuristics.

Recommended Ranges/Estimates	Reference
Shell side velocity ranges:	
0.3–1 m/s	[9]
0.9–1.5 m/s	[18]
0.25–0.65 m/s	
Catalyst particle diameter should be 10% of tube diameter to prevent channeling.	[19]
Liquids with viscosities more than 1 mPa·s are restricted to a maximum shell-side pressure drop within the range 50–70 kPa.	[9]
Ratio of the tube length to catalyst particle diameter should exceed 50 for negligible axial dispersion.	[19]
Reactor tube-side pressure drop that is less than 10%.	[19]
Ratio of the tube diameter to the catalyst particle diameter less than 30 for a flat velocity profile.	[19]

The RPLUG model on Aspen Plus[®] (AspenTech, Bedford, MA, USA) assumes ideal plug flow. Axial and radial dispersion was neglected since the tube length to particle diameter was large. Since both heat and mass transfer coefficients increase with increasing mass velocities, in most industrial reactors with large throughputs at high pressures, it is practical to avoid significant interphase gradients.

Convergence on the optimization model could not be achieved by varying all critical parameters together due to their heavily coupled nature therefore, the iterative methods in the algorithms illustrated by Figure 2 was used to best approximate a convergence sequence.

Sensitivities were conducted on the thermal fluid flow rate and inlet temperature using a base case reactor to determine which variable controlled the maximum and minimum temperatures within the reactor. For R-101, the heat transfer fluid flow rate affected the minimum temperature the most whilst the maximum temperature was affected by the heat transfer fluid inlet temperature the most, as illustrated by Table 4. The same methodology was applied to reactor R-102.

Table 4. R-101 sensitivity results to determine relationship between parameters.

Acrolein Production (kmol/h)	¹ Temperature Range (K)	Temperature of Heat Transfer Fluid (K)	Flow Rate of Heat Transfer Fluid (kmol/s)
172	613–693	578	3
169	623–703	588	3
162	624–731	588	2.5
158	631–747	598	2.5
155	632–767	598	2.25
162	633–724	600.5	3
166	633–705	600.5	3.5
169	633–697	600.5	3.75

¹ Required temperature range for R-101 was 633 to 703 K.

The overall heat transfer coefficient in exothermic reactions can independently determine the size of a reactor unit and is therefore of pivotal importance. All heat transfer resistances were taken into consideration when determining the overall heat transfer coefficient and then iterated in the optimization methodologies used.

The feasibility of the packed bed design is substantially dependent on the catalyst structure and packing matrix employed. The catalyst is also required to be resistant to crushing and abrasion. Spherical catalyst particles are commonly used for propylene partial oxidation in industry. However, owing to the large tube-side pressure drop, which exponentially surpassed the general design heuristic of 10%, the catalyst geometry was revisited and hollow cylinder catalyst pellets were selected [19]. The use of hollow cylinder catalyst pellets enhances conversion levels in reactors due to the better utilization of the catalytic material, with the most notable feature being the absence of the pellet core, which lowers internal transport resistances and the reactor pressure drop [20]. Greater catalyst surface areas result in smaller reactor volumes, which is arguably the ultimate design feasibility decision. Therefore, hollow cylinder catalysts were selected and ensured that the tube side pressure drop was within 10% [21]. Following the control of the tube side pressure drop, analysis was conducted on the shell-side pressure drop. Low shell-side pressure drops are indicative of low turbulence in the shell. Heat transfer coefficients are directly proportional to Reynolds number, which is an indication of the degree of turbulence. A high heat transfer coefficient would require a smaller heat transfer surface area, thereby reducing the size of the reactor, by increasing the overall heat transfer coefficient. As a result, higher turbulence on the shell side was required. The shell-side pressure drop was therefore increased by varying the reactor tube length until the tube-side pressure drop constraint was met. These results are illustrated in Table 5 for R-101. A similar optimization procedure was conducted for R-102.

Heat integration was employed within R-101 to negate the additional capital and operating costs associated with a waste heat exchanger network. Reactor R-101 is essentially modeled and simulated as two series reactors with an inert preheating zone and a reacting zone, as illustrated by Figure 3. The preheating zone was used as part of energy optimization since the temperature of molten salt needed to heat the feed to 633 K was close to the exiting molten salt temperature. The resultant temperature and composition profiles in R-101 are illustrated by Figure 4.

Table 5. R-101 optimization results.

Length (m)	Parameters	Value
1.5	Number of tubes:	11,717
	Overall heat transfer coefficient (W/m ² K)	409
	Coolant mole flow rate (kmol/s):	3.75
	Coolant inlet temperature (K):	652
	Tube-side pressure drop (Pa):	20,161
	Shell-side pressure drop (Pa):	9938
	Heat transfer surface area (m ²)	1844
1.75	Number of tubes:	9952
	Overall heat transfer coefficient (W/m ² K)	449
	Coolant mole flow rate (kmol/s):	3.75
	Coolant inlet temperature (K):	624
	Tube-side pressure drop (Pa):	32,908
	Shell-side pressure drop (Pa):	14,803
	Heat transfer surface area (m ²)	1827
2	Number of tubes:	9028
	Overall heat transfer coefficient (W/m ² K)	471
	Coolant mole flow rate (kmol/s):	3.75
	Coolant inlet temperature (K):	623
	Tube-side pressure drop (Pa):	45,185
	Shell-side pressure drop (Pa):	19,439
	Heat transfer surface area (m ²)	1805

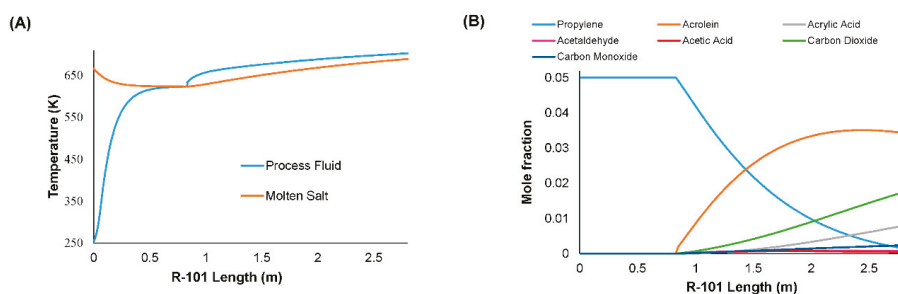


Figure 4. R-101 temperature and molar composition profiles: (a) process fluid and molten salt temperature profiles in R-101 for inert preheating and reacting zones; (b) molar composition profile in R-101 of major components.

The optimization algorithms for R-101 and R-102 are similar, with differences occurring due to the varying extents of the respective exothermic reactions. Temperature ranges and hotspot formation were more difficult to control in R-102 as compared to R-101 hence rigorous design changes to R-102 were made. As an initial estimate, 25 mass % inert material was assumed to be used in R-102 to determine the extent to which the reactor temperature would be controlled. In addition, the hotspot was required to be mitigated since the reaction is prone to rapid runaway with minor coolant variations. Figure 5 illustrates the results of sensitivities conducted on varying quantities of inert material (0 to 45 mass %) in an attempt to control the reaction temperature range as well as prevent the formation of the hotspot. The temperature profile along the reactor is typical of that for a highly exothermic and rapid reaction. When the temperature of the reaction mixture reaches a satisfactory value with fresh catalyst, the reaction takes off and a hotspot begins to develop. The reaction temperature rapidly exceeds the salt temperature. The reaction rate increases exponentially and the heat removal rate increases only linearly as the reaction mixture temperature exceeds the temperature of the molten salt. The temperature begins to decline as the reaction rate declines with increasing conversion.

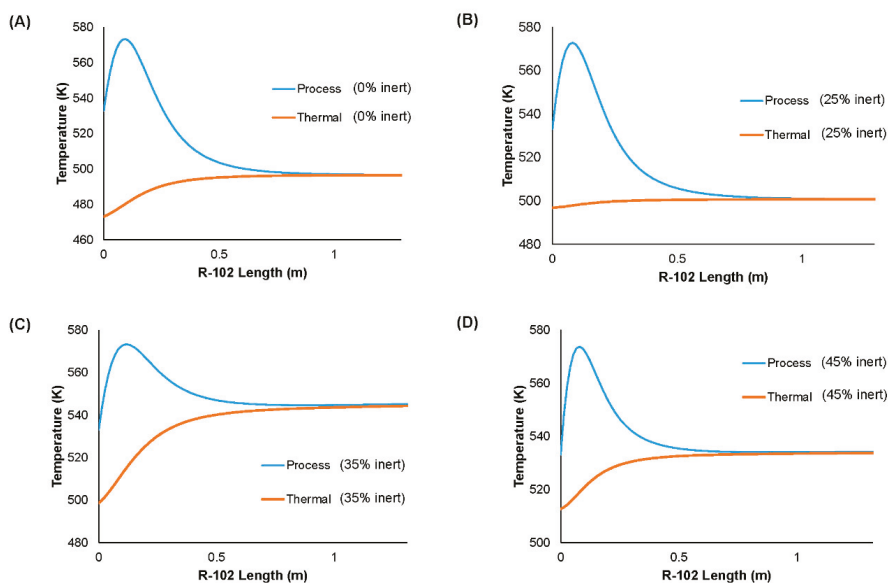


Figure 5. R-102 temperature profiles for varying inert compositions (— Process fluid temperature; — Molten salt temperature): (a) R-102 temperature profile for 0 mass % inert material; (b) R-102 temperature profile for 25 mass % inert material; (c) R-102 temperature profile for 35 mass % inert material; (d) R-102 temperature profile for 45 mass % inert material.

By incorporating inert material into the catalyst bed, the reaction and heat generation rate per unit volume is decreased, and it was postulated that this may be able to eliminate the hotspot. The actual shape and limits of the temperature profiles are dependent on the feed temperatures for the process fluid and thermal fluid, the driving force for heat transfer and the net generation of heat within the reaction zone [22]. As can be seen in Figure 5, all inert packing configurations exhibited hotspot behavior, thus the incorporation of inert material into the bed, even up to 45%, did not have the necessary effect on the temperature moderation and hence selectivity. In the case of 35% inert, the system exhibited a high final temperature, with a flatter and more sustained overtemperature in the response. Since the simulations were carried out with constraints on the overall conversion, the reduced rate at the start of the bed required a higher temperature towards the end of the bed to meet the necessary conversion value. Such behavior was not observed for the 45% inert system. Here the driving force for heat transfer was low and once the reaction was initiated, a rapid increase in temperature and conversion was observed, as in the case of 0% and 25% inert material.

As illustrated, since the reaction could still not be optimally controlled, literature was consulted to determine other methods of optimal temperature control in similar exothermic, runaway reactions. A multitubular reactor process for the oxidative dehydrogenation of ethylene was studied due to the similarities between the processes [10]. The reactor had a runaway temperature problem which was overcome by the use of distributed air injection schemes. The injection of cold feed is often used for the control of the reaction exotherm [23]. The ratio of oxygen to nitrogen in air essentially controls the reaction rate due to the inert nitrogen, hence allowing a wider range of operation. A similar methodology was applied to R-102. A cold injection of air was used to collectively cool R-101 effluent to the required temperature of 533 K whilst ensuring that the feed stream contained sufficient inert gases to control the reaction rate in R-102 and hence remove the formation of the hotspot. These results are illustrated by Figure 6.

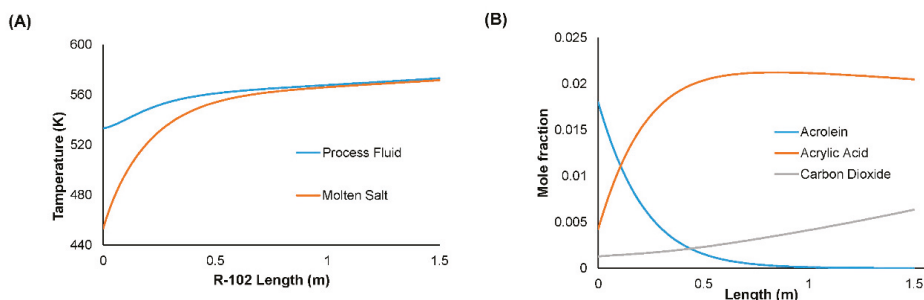


Figure 6. R-102 temperature and molar composition profiles: (a) process fluid and molten salt temperature profile in R-102; (b) molar composition profile in R-102 of major components.

4. Energy Analysis

In an attempt to quantify the energy savings from each of the design modifications proposed, we undertook calculations of the heat loads and associated pumping requirements for the molten salt heat transfer fluid systems for each reactor. For reactor R-101 (propylene oxidation reactor), the main design modification is the use of an inert preheating zone for preheating the feed. This is in lieu of a traditional fired preheater. The energy for preheating is obtained from the circulating thermal fluid and hence a higher flowrate of thermal fluid would be required when compared to the base case (traditional preheater and thermal fluid required only for cooling of the exothermic process fluid). The total heat duty required for pre-heating the propylene, air and steam mixture is 6190 kW, which translates into an increase of 1.64 kmol/s in the molten salt flowrate. Under the specified operating conditions of the unit, this equates to an additional 283 m³/h of molten salt. With a standard molten salt pump operating at 75% efficiency, this requires 3.5 kW additional pumping power. Because the inlet and outlet temperatures of the thermal fluid are approximately the same, there would be practically no need for a large heat rejection system, e.g. using a waste heat boiler, and hence a saving on capital and maintenance cost. The overall energy saving for R-101 would then be associated with the energy requirements for preheating the feed. At 90% efficiency for a traditional fired heater, this equates to 6878 kW, which is far greater than the associated increase in pumping power for the molten salt circuit.

In R-102 (the acrolein oxidation reactor), the main design modification is the cold injection of air (which is implemented without the introduction of inert solid material into the catalyst bed). We have compared the energy requirements of this process configuration to that of the base case (no injection of cold air nor the use of inert material), in terms of the total flowrate of molten salt and pumping requirements for the molten salt circuit. With reference to Figure 5a (base case) and Figure 6a (cold air injection), the base case is characterized by a rapid increase in process temperature due to the exothermic reaction, with practically all conversion occurring within the first quarter of the reactor. The total molten salt flowrate required for the base case is 10.13 kmol/s, or 1658 m³/h, which equates to a pumping power of 23 kW. The total molten salt flowrate required for the modified configuration (cold air injection) is 7.8 kmol/s, or 1278 m³/h, equating to a pumping power of 17.6 kW. The saving in terms of pumping power is therefore 5.4 kW, with the additional benefit of increased selectivity and overall yield of acrylic acid.

5. Future Work

Future work to be investigated includes:

- Rigorous thermodynamic model selection for the reactant and product components via experimental data regression.
- The Aspen Plus® (AspenTech, Bedford, MA, USA) simulation model operation in this work is at steady state. A dynamic simulation can be developed to understand the impact of common

operational changes, upsets and abnormal conditions; and thereafter develop a control procedure for the intensified process presented.

- The extent of the transferability of the optimized gas phase oxidation process in this work, to other highly exothermic, gas phase reactions.
- The optimized process in this work assumed negligible interphase heat and mass transfer resistances, axial dispersion and radial gradients. Future work can delve into the impacts of these non-idealities on the optimized process.
- Future work can explore the impact of catalyst deactivation on the optimized process, and the available levers to enable the optimized process until the catalyst end of run conditions.

6. Conclusions

The design of a multitubular fixed bed reactor train for the production of acrylic acid involves simultaneous consideration of various influencing parameters, including shell side heat transfer, shell side pressure drop, tube-side hotspot formation, tube side pressure drop, catalyst interfacial gradients and selection of inlet conditions. For both the propylene oxidation reactor (R-101) and acrolein oxidation reactor (R-102), the heat transfer fluid flow rate affected the minimum temperature the most whilst the maximum temperature was affected by the heat transfer fluid inlet temperature the most. Some of the energy carried in the molten salt recycle was utilized to preheat the feed to reactor R-101 by including an inert packed zone of approximately 0.8 m at the front of the reactor. This eliminated the need for a separate preheating exchanger before the reactor. Allowing for some reduction of the molten salt temperature at the front end of reactor R-101 also limited the overall temperature rise in this unit for both the process and thermal fluid. Dilution of catalyst was investigated as a means of regulating the bed temperature in the acrolein oxidation reactor R-102. However, employing solid inert material up to 45% did not significantly reduce the temperature rise or peak temperature in the reactor. An alternative strategy of cold air injection at the inlet of the reactor was successful in mitigating hotspot formation and allowing for a gradual increase in process side temperature, albeit with a higher final temperature than in the case of catalyst bed dilution. The accurate representation of the process performance on the Aspen Plus[®] (AspenTech, Bedford, MA, USA) platform allowed for probing of alternative energy utilization strategies. Owing to the elimination of the fired preheater from the front end of the process, the reduction in energy was almost 7 MW. The use of the cold air injection in the second reactor reduced thermal fluid pumping power requirements by over 5 kW.

Author Contributions: Conceptualization, D.L.; methodology, K.C.P.; software, K.C.P.; validation, K.C.P. and D.L.; formal analysis, K.C.P.; investigation, K.C.P.; resources, K.C.P.; data curation, K.C.P.; writing—original draft preparation, K.C.P. and D.L.; writing—review and editing, D.L.; visualization, K.C.P.; supervision, D.L.; project administration, D.L.; funding acquisition, D.L. All authors have read and agreed to the published version of the manuscript.

Funding: This work is based on research supported by the National Research Foundation of South Africa, unique grant number 120019. The authors also acknowledge financial support from ESKOM.

Conflicts of Interest: The authors declare no conflict of interest. The funders had no role in the design of the study; in the collection, analyses, or interpretation of data; in the writing of the manuscript, or in the decision to publish the results.

References

1. Turton, R.; Bailie, R.C.; Whiting, W.B.; Shaelwitz, J.A. *Analysis, Synthesis and Design of Chemical Processes*, 3rd ed.; Prentice Hall: Upper Saddle River, NJ, USA, 2009; p. B.9.
2. Sou, M.; Zhang, H.; Ye, Q.; Dai, X.; Yu, H.; Li, R. Design and control of an improved acrylic acid process. *Chem. Eng. Res. Des.* **2015**, *104*, 346–356.
3. Jiang, B.; Hao, L.; Zhang, L.; Sun, Y.; Xiao, X. Numerical investigation of flow and heat transfer in a novel configuration multi-tubular fixed bed reactor for propylene to acrolein process. *Heat Mass Trans.* **2015**, *51*, 67–84. [[CrossRef](#)]

4. Tripodi, A.; Compagnoni, M.; Martinazzo, R.; Ramis, G.; Rossetti, I. Process simulation for the design and scale up of heterogeneous catalytic process: Kinetic modelling issues. *Catalysts* **2017**, *7*, 159. [CrossRef]
5. Luyben, W. Economic Trade-offs in acrylic acid production. *Comp. Chem. Eng.* **2017**, *93*, 118–127. [CrossRef]
6. Redlingshofer, H.; Fischer, A.; Weckbecker, K.H.; Emig, G. Kinetic modelling of the heterogeneously catalyzed oxidation of propene to acrolein in a catalytic wall reactor. *Ind. Eng. Chem. Res.* **2003**, *42*, 5482–5488. [CrossRef]
7. Estenfelder, M.; Lintz, H.G. Simultaneous determination of reaction kinetics and oxygen activity in single-phase oxidic catalysts and their mixture during partial oxidations. *J Catal.* **2002**, *209*, 177–185. [CrossRef]
8. Stankiewicz, A. Advances in modelling and design of multitubular fixed-bed reactors. *Chem. Eng. Tech.* **1989**, *12*, 113–130. [CrossRef]
9. Sinnott, R.K. *Chemical Engineering Design*; Butterworth-Heinemann: Oxford, UK, 2005.
10. Fattahi, M.; Kazemini, M.; Khorasheh, F.; Darvishi, A.; Rashidi, A.M. Fixed-bed multi-tubular reactors for oxidative dehydrogenation in ethylene process. *Chem. Eng. Tech.* **2013**, *36*, 1691–1700. [CrossRef]
11. Borio, D.O.; Gatica, J.E.; Porras, J.A. Wall cooled fixed bed reactors: Parametric sensitivity as a design criterion. *AIChE J.* **1989**, *35*, 287–292. [CrossRef]
12. Kawakami, M.; Suzuki, K.; Yokoyama, S.; Takenaka, T. Heat Capacity Measurement of Molten NaNO₃-NaNO₂-KNO₃ by Drop Calorimetry. In Proceedings of the VII International Conference on Molten Slags Fluxes and Salts, Cape Town, South Africa, 25–28 January 2004; The South African Institute of Mining and Metallurgy: Johannesburg, South Africa, 2004; pp. 201–208.
13. Serrano-Lopez, R.; Fradera, J.; Cuesta-Lopez, S. Molten salts database for energy applications. *Chem. Eng. Process.* **2013**, *73*, 87–102. [CrossRef]
14. Grasselli, R.K. Fundamental principles of selective heterogeneous oxidation catalysis. *Top. Catal.* **2002**, *2*, 1–3. [CrossRef]
15. Snyder, T.P.; Hill, C.G. The mechanism for the partial oxidation of propylene over bismuth molybdate catalysts. *Catal. Rev.* **1989**, *31*, 43–95. [CrossRef]
16. Redlingshofer, H.; Krocher, O.; Bock, W.; Huthmacher, K.; Emig, G. Catalytic wall reactor as a tool for isothermal investigations in the heterogeneously catalyzed oxidation of propene to acrolein. *Ind. Eng. Chem. Res.* **2002**, *41*, 1445–1453. [CrossRef]
17. Zhu, J.; Araya, S.S.; Cui, X.; Sahlin, S.L.; Kaer, S.K. Modeling and design of a multi-tubular packed-bed reactor for methanol steam reforming over Cu/ZnO/Al₂O₃ catalyst. *Energies* **2020**, *13*, 610. [CrossRef]
18. Shah, R.K.; Sekulic, D.P. *Fundamentals of Heat Exchanger Design*; John Wiley and Sons: New York, NY, USA, 2003.
19. Rase, H.F. *Fixed Bed Reactor Design and Diagnostics: Gas-Phase Reactions*; Butterworths: Boston, MA, USA, 1990.
20. Asif, M. Conversion enhancement of fixed-bed reactors using two-dimensional hollow cylindrical catalyst pellet. *Int. J. Chem. React. Eng.* **2013**, *11*, 159–168. [CrossRef]
21. Afandizadeh, S.; Foumeny, E.A. Design of packed bed reactors: Guides to catalyst shape, size and loading selection. *Appl. Thermal Eng.* **2001**, *21*, 669–682. [CrossRef]
22. Schüler, C.; Wolf, M.; Hinrichsen, O. Contactless temperature measurements under static and dynamic reaction conditions in a single-pass fixed bed reactor for CO₂ methanation. *J. CO₂ Util.* **2018**, *25*, 158–169. [CrossRef]
23. Marlin, D.S.; Sarron, E.; Sigurbjörnsson, Ó. Process Advantages of Direct CO₂ to Methanol Synthesis. *Front. Chem.* **2018**, *6*, 446. [CrossRef] [PubMed]



© 2020 by the authors. Licensee MDPI, Basel, Switzerland. This article is an open access article distributed under the terms and conditions of the Creative Commons Attribution (CC BY) license (<http://creativecommons.org/licenses/by/4.0/>).

Numerical Study of Heat Transfer in Gravity-Driven Particle Flow around Tubes with Different Shapes [†]

Xing Tian ¹, Jian Yang ^{1,2,*}, Zhigang Guo ¹, Qiuwang Wang ^{1,*} and Bengt Sundén ²

¹ Key Laboratory of Thermo-Fluid Science and Engineering, Ministry of Education, Xi'an Jiaotong University, Xi'an 710049, China; tianxing12@stu.xjtu.edu.cn (X.T.); gzgc060811348@stu.xjtu.edu.cn (Z.G.)

² Department of Energy Sciences, Lund University, 22100 Lund, Sweden; Bengt.Sunden@energy.lth.se

* Correspondence: yangjian81@mail.xjtu.edu.cn (J.Y.); wangqw@mail.xjtu.edu.cn (Q.W.);
Tel.: +86-29-8266-3502 (J.Y.); +86-29-8266-5539 (Q.W.)

[†] This paper is an extended version of our paper published in the 22nd International Conference on Process Integration, Modelling, Optimization for Energy Saving and Pollution Reduction (PRES' 19), Aghios Nikolaos, Crete, Greece, 20–23 October 2019; pp. 235–240.

Received: 27 February 2020; Accepted: 14 April 2020; Published: 16 April 2020

Abstract: In the present paper, the heat transfer of gravity-driven dense particle flow around five different shapes of tubes is numerically studied using discrete element method (DEM). The velocity vector, particle contact number, particle contact time and heat transfer coefficient of particle flow at different particle zones around the tube are carefully analyzed. The results show that the effect of tube shape on the particle flow at both upstream and downstream regions of different tubes are remarkable. A particle stagnation zone and particle cavity zone are formed at the upstream and downstream regions of all the tubes. Both the stagnation and cavity zones for the circular tube are the largest, and they are the smallest for the elliptical tube. As the particle outlet velocity (v_{out}) changes from 0.5 mm/s to 8 mm/s at $d_p = 1.72$ mm/s, when compared with the circular tube, the heat transfer coefficient of particle flow for the elliptical tube and flat elliptical tube can increase by 20.3% and 15.0% on average, respectively. The proper design of the downstream shape of the tube can improve the overall heat transfer performance more efficiently. The heat transfer coefficient will increase as particle diameter decreases.

Keywords: gravity-driven particle flow; discrete element method; heat transfer enhancement

1. Introduction

In the recent years, the world's energy and environmental problems have become more and more prominent, which makes it urgent to improve energy efficiency and develop sustainable energy techniques. Moving bed heat exchanger (MBHE), with the advantages of low cost, clean energy and wide particle size adaptation, is gradually applied in many high temperature waste heat recovery industries [1], such as slag [2], cement [3], coke [4] and concentrated solar power (CSP) [5]. For the MBHE, the granular flow inside is driven by the gravity, and the heat transfer is relatively lower [6] as compared with packed bed [7] or fluidized bed [8]. Therefore, it is important to improve the heat transfer of particle flow in the MBHE.

The type of heat transfer element in the MBHE may include horizontal tubes, vertical tubes and parallel plates. For the MBHE with vertical tubes [9] or parallel plates inside [10], the solid particles move vertically along the tubes or plates without fully mixing, which would limit the heat transfer of particle flow along the tubes or plates in the MBHE. However, the particle flow around a horizontal tube should be disordered and fully mixed [11], and the heat transfer around the horizontal tube should be better. Many researchers have studied the effects of particle material, particle size, particle velocity, finned tube and layout of horizontal tubes in the MBHE. Qoaidar et al. [12] found that the

heat transfer performance of MBHE with mixed particles of 50% sand and 50% basalt particles were 30% better than that of MBHE with 100% sand particles by experiment. Increasing particle velocity can significantly improve the heat transfer coefficient, Al-Ansary et al. [13] found that the heat transfer coefficient would increase from 80 W/(m²·K) to 160 W/(m²·K) as the sand velocity increased from 1 mm/s to 3 mm/s. Nguyen et al. [14] found that, when the particle velocity changes from 3 mm/s to 10 mm/s, finned tubes can enhance heat transfer as compared with the smooth tubes. Liu et al. [1] analyzed the effects of particle diameter, particle velocity and tube arrangement on the performances of heat exchanger by experiment. They found that the heat transfer performance is better in staggered heat exchanger and the heat transfer coefficient increased as the particle size decreased or as the particle velocity increased. However, when the particles flowed around the horizontal tube, a stagnation zone would form at the upstream region of the tube and a cavity zone would form at the downstream region of the tube [15], which would seriously affect the flow and heat transfer of particles [16]. The particles in the stagnation zone move slowly or even remain stationary, while the particles in the cavity zone are almost untouched with the tube wall. Bartsch and Zunft studied the dense granular flow around horizontal tubes by CFD model [17], discrete element method (DEM) model and experiment [18]. The simulation results could well capture both the stagnation zone and cavity zone at the upstream and downstream of the tube, which was consistent with the experimental results. The heat transfer coefficient in these two zones was the lowest, and the heat transfer mainly occurred on the side region of the tube wall [19]. Therefore, it is an effective way to improve heat transfer performance of particle flow in the MBHE by reducing both the stagnation zone and cavity zone around the tube, such as using vibration or profiled tubes. Guo et al. [20] found that vibration could accelerate the renewal of particles at the upstream region of the tube, strengthen particle contact at the downstream region of the tube and increase the heat transfer coefficient of particle flow around the tube. However, the vibration may also significantly increase the wear rate of the tube. As for profiled tubes, Morris et al. [21] developed a continuum model for flowing particles heat transfer and studied the particle flow in the hexagonal tube array in the solar receiver [22], where the particle inlet velocity was up to 1 m/s and the thermal performance was obviously affected by the particle size. They found that the overall heat transfer increased as particle mass flow rate increased. Furthermore, Takeuchi [11] experimentally studied the heat transfer of particle flow around a circular tube, an elliptical tube and a lenticular tube. The study showed that the effect of tube shape on the heat transfer performance of particle flow around the tube was remarkable, and the performance of lenticular tube was the best.

According to the above studies, it should be noted that the effect of tube shape on the heat transfer of particle flow around tube is remarkable. In order to further understand the mechanism of this effect and improve the heat transfer performance of particle flow in the MBHE, the heat transfer of gravity-driven dense particle flow around different tubes was numerically investigated in the present study, including circular tube, elliptical tube, flat elliptical tube and the combination of elliptical tube and flat elliptical tube. A variety of factors, such as velocity vector, particle contact number, particle contact time and heat transfer coefficient of particle flow at different particle zones around the tube are carefully analyzed. Meanwhile, the effect of particle diameter on heat transfer is discussed. The results of the present study would be important and beneficial for the optimal design of MBHEs.

2. Physical Model and Computational Method

2.1. Physical Model

The physical model for particle flow around a single tube is presented in Figure 1. As shown in Figure 1a, the spherical particles flow around a single tube from the top to bottom in the particle flow channel and exchange heat with the tube wall. The dimensions of the particle flow channel are L (length) \times W (width) \times H (height), and the particle diameter (d_p) is mainly fixed at 1.72 mm. The tube is located in the channel center. All the vertical channel walls are adiabatic, and the temperature of tube wall is kept at $T_{\text{tube}} = 287$ K. Particles are generated at the entrance of the flow channel, and the

particle inlet temperature is kept at $T_{in} = 773$ K. All particles are driven by the gravity and have a dense filling in the flow channel. The particle velocity in the channel is controlled at the outlet [5], and the particle outlet velocity is kept constant along the vertical direction (z). As shown in Figure 1b, five different tubes are adopted for the study, including circular tube, elliptical tube, flat elliptical tube, elliptical-flat elliptical tube and flat elliptical-elliptical tube, where the perimeters of different tube cross sections are kept the same. Typical geometric parameters of the particle flow channel and tubes are presented in Table 1. In the present study, the particle flow around tube wall is divided into three zones, including the upstream region of the tube (Zone 1), the side region of the tube (Zone 2), and the downstream region of the tube (Zone 3). The geometric divisions of different particle zones are also presented in Figure 1b.

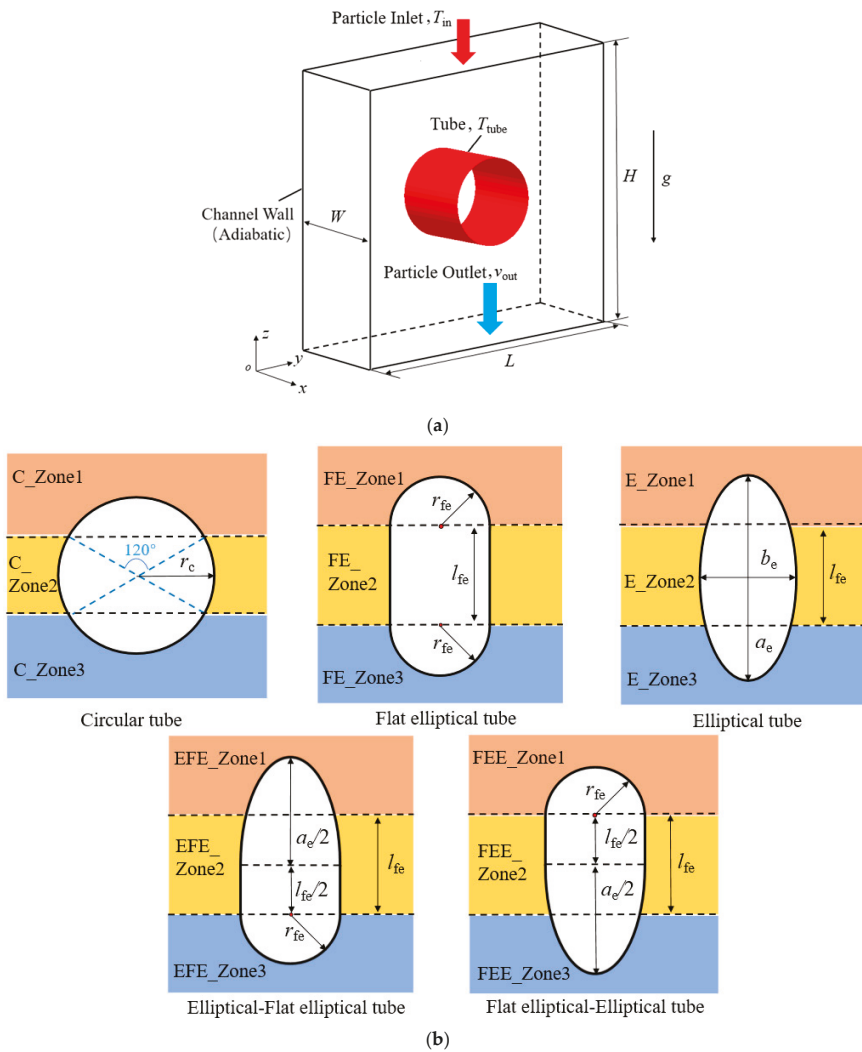


Figure 1. Physical model and cross section zones for particle flow around different tubes: (a) Physical model; (b) Cross section zones for different tubes.

Table 1. Typical geometric parameters of particle flow channel and tubes.

L (mm)	W (mm)	H (mm)	r _c (mm)	r _{fe} (mm)	l _{fe} (mm)	a _e (mm)	b _e (mm)
39	18	45	7.5	4.87	8.29	19.48	9.74

2.2. DEM Method and Heat Transfer Model

In the present study, the flow and heat transfer of particles are simulated with discrete element method (DEM). For DEM simulations, the Newton’s second law [23] is used to calculate the forces on each particle and track the particle motions. For gravity-driven dense particle flow, since the particle filling rate is high and particles move very slowly, the effect of the gas flow between particles is insignificant [24]. Therefore, the gas flow is not considered for the simulations, and the Hertz-Mindlin soft sphere model [25,26] is adopted to simulate the dense particle flow process, where the normal force and tangential force between particles are treated with equivalent spring, damper and slider to simplify the contact between particles. The contact force is calculated according to the normal overlap and tangential displacement of particles. The equations used to calculate the contact force of particle-particle or particle-wall are as follows:

$$F_n = \frac{4}{3}E_{eq} \sqrt{r_{eq}} \delta_n^{3/2} + 2 \sqrt{\frac{5}{6}} \frac{\ln e}{\sqrt{\ln^2 e + \pi^2}} \sqrt{2E_{eq} m_{eq}} \sqrt{r_{eq} \delta_n} V_n^{rel} \tag{1}$$

$$F_t = \begin{cases} 8G_{eq} \delta_t \sqrt{r_{eq} \delta_n} + 2 \sqrt{\frac{5}{6}} \frac{\ln e}{\sqrt{\ln^2 e + \pi^2}} \sqrt{8G_{eq} m_{eq}} \sqrt{r_{eq} \delta_n} V_t^{rel} & |F_t| < \mu_s |F_n| \\ \mu_s F_n \text{sign}(\delta_t) & |F_t| \geq \mu_s |F_n| \end{cases} \tag{2}$$

where F_n and F_t are the normal and tangential components of the contact force. E_{eq} , R_{eq} , and m_{eq} are the equivalent Young’s modulus, radius, and mass. δ_n and δ_t are normal and tangential displacements. V_n^{rel} and V_t^{rel} are the relative normal and tangential translational velocities. e and μ_s are the restitution coefficient and the translational friction coefficient.

As for heat transfer of particle flow, the heat transfer from particle to particle (p-p) or from particle to the tube wall (p-w) includes heat conduction, thermal convection and thermal radiation, where the heat conduction consists of heat conduction inside particles, physical contact heat conduction and heat conduction through gas film surround particles. In the present study, since particles move quite slowly, the gas convection heat transfer is very small [27]. The thermal convection of gas flow between particles is not considered in the simulations. The heat transfer model adopted in the present paper is based on the following assumptions, (1) the diameter of all particles is the same; (2) the gas heat capacity is ignored [28]; (3) particles are wrapped with gas film and its thickness is $0.1 d_p$ [29]; (4) the heat transfer between particles is along the radial direction of particles; (5) the thermal properties of gas and particles are kept constant, as listed in Table 2. The correlation of the heat transfer (Q) with temperature difference (ΔT), total thermal resistance (R_{total}) and time (t) is presented in Equation (3), and the total thermal resistance (R_{total}) is calculated based on the thermal resistance network, as shown in Figure 2.

$$Q = \Delta t \Delta T / R_{total} \tag{3}$$

Table 2. Typical physical properties of gas and particles (Liu et al. [1]).

Parameter	ρ_s (kg/m ³)	k_s (W/(m·K))	$c_{p,s}$ (J/(kg·K))	k_g (W/(m·K))
Value	2848	0.55	1210	0.0257

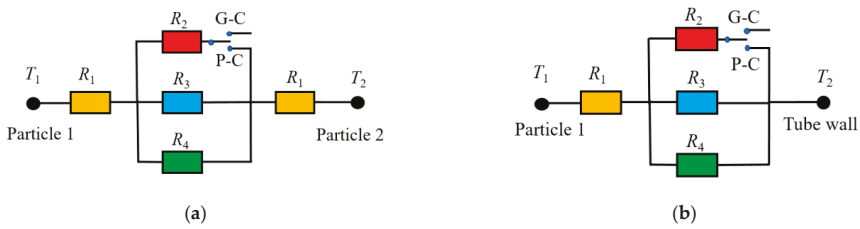


Figure 2. Schematic of thermal resistance network: (a) the case for particle–particle; (b) the case for particle–wall (R_1 : thermal conduction resistance inside particles; R_2 : physical contact thermal conduction resistance; R_3 : thermal conduction resistance through gas film; R_4 : thermal radiation resistance; “G-C” means contact only with gas film; “P-C” means physical contact).

The thermal conduction resistance includes thermal conduction resistance inside particles (R_1), physical contact thermal conduction resistance (R_2) and thermal conduction resistance through gas film (R_3). According to Fourier’s law [30], the thermal resistance R_1 and the thermal resistance R_3 are formulated as follows:

$$R_1 = \frac{\sqrt[3]{2} - 1}{2\pi k_s r (1 - \cos \alpha)} \tag{4}$$

$$R_3 = \left[\int_{\beta}^{\alpha} \frac{2\pi k_g r^2 \sin \theta \cos \theta}{l_{ij} - r \sin \theta - \sqrt{r^2 - (r \sin \theta)^2}} d\theta \right]^{-1} \tag{5}$$

where α is an angle related to the intersection of gas film and β is a starting point angle for the calculation of thermal conduction resistance through gas film, which are both presented in Figure 3 and Equations (6) and (7); l_{ij} is the distance for the case of particle-particle or particle-wall, as shown in Figure 3; r is the particle radius and r_g is the particle radius plus gas film ($r_g = 0.6 d_p$).

$$\alpha = \begin{cases} \arcsin\left(\sqrt{r_g^2 - \left(\frac{l_{ij}}{2}\right)^2} / r\right) & \text{(p-p)} \\ \arcsin\left(\sqrt{r_g^2 - l_{ij}^2} / r\right) & \text{(p-w)} \end{cases} \tag{6}$$

$$\beta = \arccos\left(\frac{l_{ij} - 6.8 \times 10^{-8}}{2r}\right) \tag{7}$$

when the contact is only with gas film and the gas film overlap is larger than gas free path, the value of β is equal to 0.

The physical contact thermal conduction resistance R_2 [31] is formulated as follows:

$$R_2 = \left[2k_s \left(\frac{3F_n r}{4E_{eq}} \right)^{1/3} \right]^{-1} \tag{8}$$

where F_n is normal direction force and E_{eq} is Young’s modulus.

According to the Stefan–Boltzmann law, the thermal radiation resistance (R_4) is presented in Equation (9). X_{ij} is the view factor, as presented in Equation (10). σ is the Stefan–Boltzmann constant and ε is the surface emissivity. When the particle contacts with the tube wall, X_{ij} is equal to 0.315 [32].

$$R_4 = \left[\frac{\sigma(T_i^2 + T_j^2)(T_i + T_j)}{\left(\frac{1-\varepsilon}{\varepsilon A}\right)_i + \frac{1}{A_i X_{ij}} + \left(\frac{1-\varepsilon}{\varepsilon A}\right)_j} \right]^{-1} \tag{9}$$

$$X_{ij} = \begin{cases} \left[1 - \sqrt{1 - \left(\frac{r_i}{l_{ij}}\right)^2} \right] \left[1 - \sqrt{1 - \left(\frac{r_j}{l_{ij}}\right)^2} \right] \left(\frac{l_{ij}}{r_i}\right)^2 & \text{(p-p)} \\ 0.315 & \text{(p-w)} \end{cases} \quad (10)$$

At the beginning of DEM simulations, randomly packed high-temperature particles were generated in the particle flow channel. Then, particles start to flow in the channel under gravity. High temperature particles are cooled when they flow around the tube. Meanwhile, new particles were generated and continuously enter into the channel at the inlet. During the whole simulation process, the total particle number inside the channel is kept constant. Typical mechanical parameters for the DEM simulations are listed in Table 3, and the heat transfer coefficient (h) of particle flow around the tube is defined as follows:

$$h = \frac{q}{A_{\text{tube}}(T_{\text{in}} - T_{\text{tube}})} \quad (11)$$

where q is the heat flux on the tube wall; A_{tube} is the heat transfer area of tube wall; T_{in} is the particle inlet temperature; T_{tube} is the tube wall temperature.

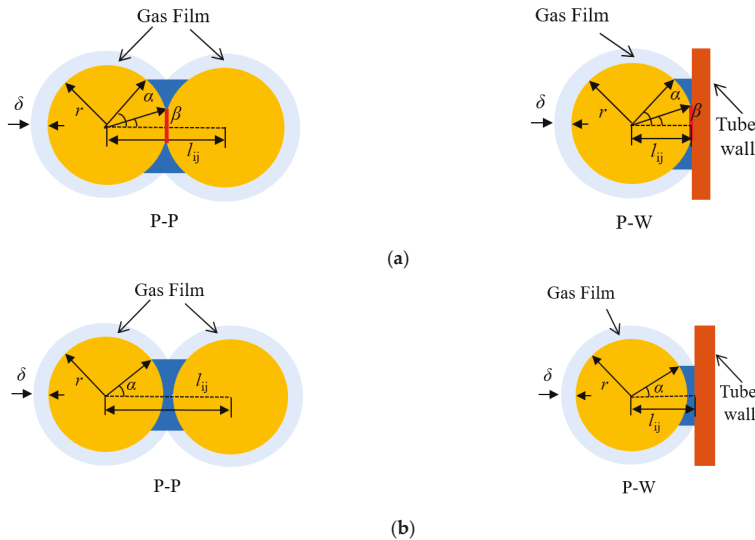


Figure 3. Schematic diagram of thermal conduction resistance calculation parameters: (a) physical contact for the case of particle-particle and particle-wall; (b) contact only with gas film for the case of particle-particle and particle-wall.

Table 3. Typical mechanical parameters for discrete element method (DEM) simulations.

Mechanical Parameters	Value	Mechanical Parameters	Value
E (particle, GPa)	0.55	Static friction coefficient (p-p)	0.154
E (wall, GPa)	182	Rolling friction coefficient (p-w)	0.1
Poisson's ratio (particle)	0.25	Rolling friction coefficient (p-p)	0.1
Poisson's ratio (wall)	0.30	Restitution coefficient (p-w)	0.5
Static friction coefficient (p-w)	0.154	Restitution coefficient (p-p)	0.3

The variations of heat flux (q) on the tube wall with time for the particle flow around a circular tube at $v_{\text{out}} = 0.5 \text{ mm/s}$ are presented in Figure 4. It shows that, when dq/dt is quite small ($dq/dt < 0.05\%$), the particle flow and heat transfer around the tube should be quasi-steady. In the present study, the simulation results within the 30 s after the quasi-steady state are extracted for the analysis.

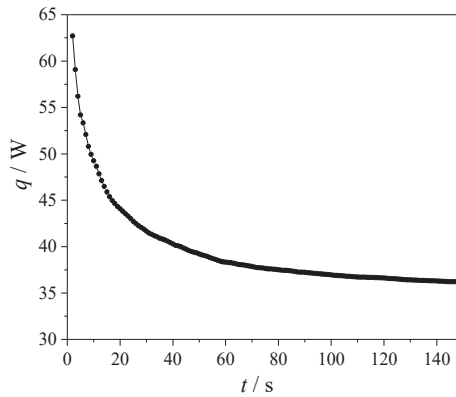


Figure 4. Variations of heat flux with time for the particle flow around a circular tube ($v_{out} = 0.5$ mm/s, $d_p = 1.72$ mm).

2.3. Model Validations

In order to validate the reliability and accuracy of present computational model and methods, the heat transfer coefficients obtained with DEM simulations are compared with the experimental results of Liu et al. [1]. The variations of heat transfer coefficient (h) for the particle flow through a tube row are presented in Figure 5. It is found that the variation trend of the heat transfer coefficients obtained by the DEM simulation is similar to the experimental results. The maximum deviation between the simulation and experimental results is 16.3%, and the average deviation is 11.8%. In the present simulation, the particle is simplified as sphere and the particle outlet velocity is kept constant for each certain case, while the particles used in the experiments [1] were irregular and the distribution of particle outlet velocity were not uniform. Therefore, the deviations exist between present simulation results and experimental results [1].

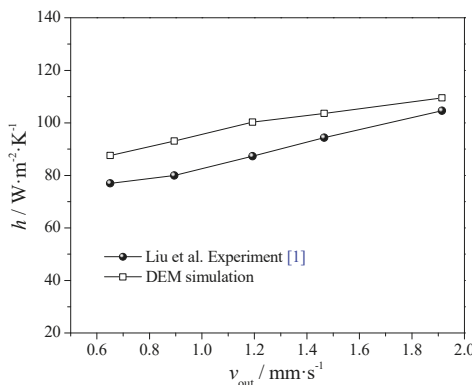


Figure 5. Comparison of heat transfer coefficients of simulation results and experimental measurement.

3. Results and Discussion

The velocity vector distributions of particle flowing around different tubes at a certain time are presented in Figure 6. This shows that the effect of tube shape on the particle flow at both upstream (Zone 1) and downstream (Zone 3) regions of different tubes is remarkable. It is noted that the particle velocity at the upstream region (Zone 1) of different tubes is very small and a particle stagnation zone is formed. Meanwhile, it is noted that, at the downstream region (Zone 3) of different tubes,

a particle cavity zone is formed, where particles are almost untouched on the tube wall. For particle flow around different tubes, it is found that both the stagnation and cavity zones for the circular tube are the largest, and they are the smallest for the elliptical tube. This may indicate that, for the elliptical tube, particles can renew faster at the upstream region (Zone 1) of the tube and the tube wall can be touched with more particles at the downstream region (Zone 3) of the tube. Therefore, the heat transfer of particle flow around an elliptical tube would be better. For the elliptical-flat elliptical tube and flat elliptical-elliptical tube, the characteristics of the stagnation zone and cavity zone are consistent with the tube with the same shapes at upstream region and downstream region.

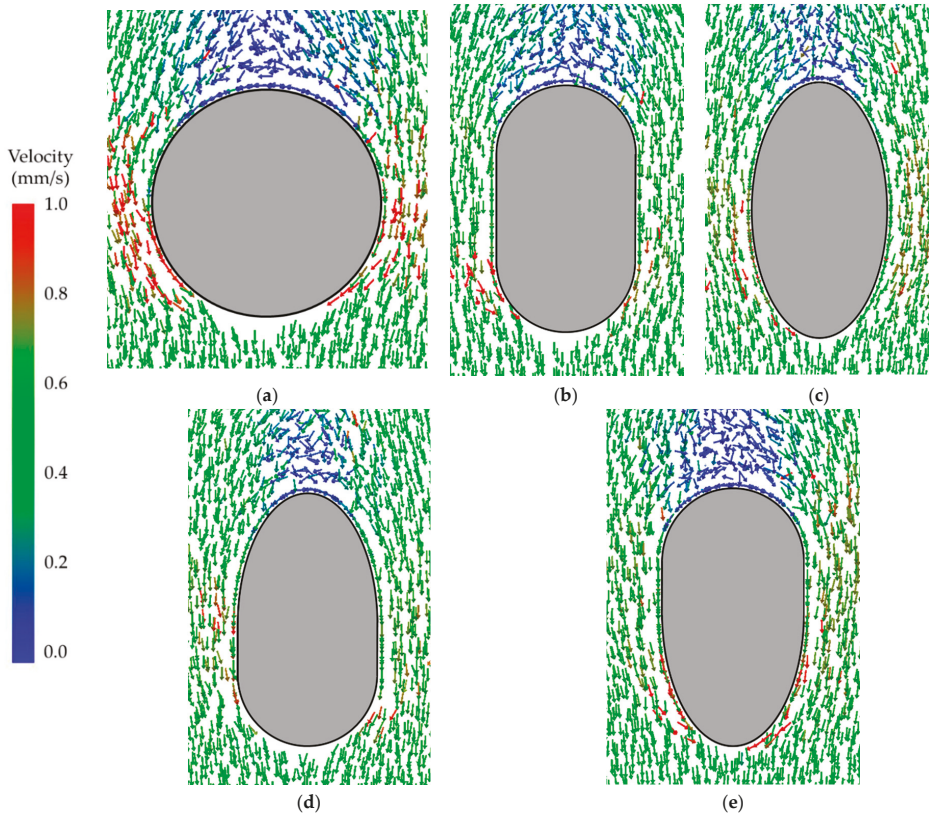


Figure 6. Velocity vector distributions of particle flow around different tubes ($v_{out} = 0.5$ mm/s, $d_p = 1.72$ mm): (a) Circular tube; (b) Flat elliptical tube; (c) Elliptical tube; (d) Elliptical-Flat elliptical tube; (e) Flat elliptical-Elliptical tube.

The variations of time-averaged particle contact number with v_{out} for different tubes are presented in Figure 7. The contacting situation between particles and tube wall is well reflected by using time-averaged particle contacting number on the unit area of tube surface. In the present study, the tube wall is considered to be touched by particles as the gas film surrounding the particle surface ($\delta = 0.1 d_p$) touches the tube wall. As shown in Figure 7, when the particle outlet velocity (v_{out}) varies from 0.5 mm/s to 8 mm/s, the particle contact numbers at different zones of all the tubes change very little with v_{out} . The particle contact numbers at Zone 1 of all the tubes are the highest and they are the lowest at Zone 3. At Zone 1 and Zone 2, the particle contact numbers of elliptical tube, flat elliptical tube, elliptical-flat elliptical tube and flat elliptical-elliptical tube are close to each other. At Zone 1, the

particle contact number of circular tube is a little higher than that of the elliptical tube, flat elliptical tube, elliptical-flat elliptical tube and flat elliptical-elliptical tube, while at Zone 2, the particle contact number of circular tube is a little lower. As for Zone 3, big differences of particle contact number existed for different tubes. As compared with the circular tube, the particle contact number at Zone 3 of the elliptical tube and flat elliptical tube can increase by 112.3% and 53.5%. Due to the same tube shape at the downstream region, the particle contact numbers at Zone 3 of the elliptical-flat elliptical tube and the flat elliptical-elliptical tube are quite close to those of the flat elliptical tube and elliptical tube.

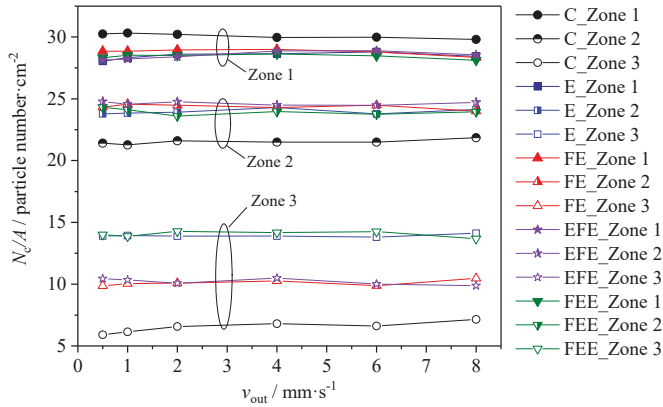


Figure 7. Variations of time-averaged particle contact number with v_{out} for different tubes ($d_p = 1.72$ mm).

In order to compare the particle renewal situations at the stagnation zone (Zone 1) of particle flow around different tubes, the variations of particle contact time with v_{out} at Zone 1 of different tubes are analyzed, as presented in Figure 8. The contacting time of particles with tube wall for unit length of tube is a cumulative variable. The contacting time of particles is accumulated when the tube wall is touched by the gas film surrounding the particle, which is the average result for particles contacting the tube at each time step. As shown in Figure 8, it is found that, as particle outlet velocity (v_{out}) increases from 0.5 mm/s to 8 mm/s, the particle contact time with the tube wall at Zone 1 of different tubes decreases rapidly, and the particle flow at the stagnation zone of all the tubes is accelerated. Furthermore, it is found that under the same particle outlet velocity (v_{out}), the particle contact time at Zone 1 of the circular tube is highest and it is the lowest for the elliptical tube, which means the particle flow renewal situation at the stagnation zone (Zone 1) of elliptical tube is the best. Due to the same tube shape at Zone 1, the particle contact times at Zone 1 of the elliptical-flat elliptical tube and the flat elliptical-elliptical tube are almost the same to those of the elliptical tube and flat elliptical tube. As compared with the circular tube, when $v_{out} = 0.5$ mm/s, the particle contact time at Zone 1 of the elliptical tube and flat elliptical tube can decrease by 39% and 21%.

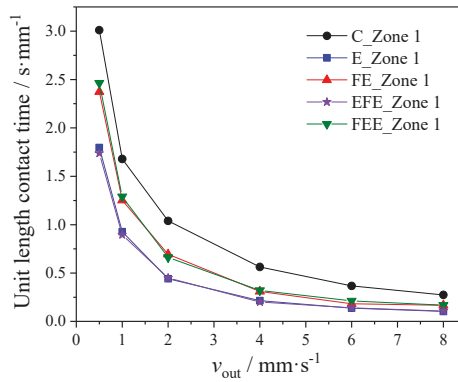


Figure 8. Variations of particle contact time with v_{out} at Zone 1 of different tubes ($d_p = 1.72 \text{ mm}$).

The variations of local heat transfer coefficients of particle flow with v_{out} for different tubes are presented in Figure 9. The local heat transfer coefficient of particle flow at Zone 1 of elliptical tube is a little higher than that of the flat elliptical tube, while the local heat transfer coefficient of circular tube is the lowest, as shown in Figure 9a. At Zone 1, the difference of particle contact number between different tubes is small (see Figure 7), while the particle contact time of the circular tube is obviously higher (see Figure 8); therefore, the local heat transfer of particle flow at Zone 1 on the circular tube is lower. When the particle outlet velocity (v_{out}) changes from 0.5 mm/s to 8 mm/s, as compared with the circular tube, the local heat transfer coefficient of particle flow at Zone 1 on the elliptical tube and flat elliptical tube can increase by 19.7% and 16.9% on average, respectively. As Zone 2 is concerned, it shows that the local heat transfer coefficients of particle flow on different tubes are quite similar, which may indicate that the particle contact situation at the side region of particle flow on different tubes should be similar, as shown in Figure 9b. For the circular tube, although the particle contact number at Zone 2 is the lowest when compared with other tubes, there are more new particles contacting with the tube wall at Zone 2 due to the highest contact time at Zone 1, which would lead to similar heat transfer coefficients to those of other tubes. At Zone 3, it shows that the difference of local heat transfer coefficients of particle flow for different tubes is relatively large, as shown in Figure 9b. The local heat transfer coefficient of particle flow at Zone 3 for the elliptical tube is the highest and it is the lowest for the circular tube. The cavity zone formed at downstream region of the elliptical tube is the smallest (see Figure 6) and particle contact number at Zone 3 for the elliptical tube is the highest (see Figure 7); therefore, the local heat transfer of particle flow at Zone 3 for the elliptical tube is the highest. When the particle outlet velocity (v_{out}) changes from 0.5 mm/s to 8 mm/s, as compared with the circular tube, the local heat transfer coefficient of particle flow at Zone 3 for the elliptical tube and flat elliptical tube can increase by 210.0% and 130.4% on average, respectively. Finally, it is found that the local heat transfer coefficients of the elliptical-flat elliptical tube and the flat elliptical-elliptical tube at Zone 1 and Zone 3 are almost the same to those of the tubes with the same shape at these zones.

The variations of heat transfer coefficients of particles flow with v_{out} for different tubes are presented in Figure 10. It shows that as the particle outlet velocity (v_{out}) increases, the heat transfer coefficient of particle for all the tubes increases gradually. The heat transfer coefficient of particle flow around elliptical tube is the highest and it is the lowest for the circular tube. As the particle outlet velocity (v_{out}) changes from 0.5 mm/s to 8 mm/s, when compared with the circular tube, the heat transfer coefficient of particle flow for the elliptical tube and flat elliptical tube can increase by 20.3% and 15.0% on average. As compared with the flat elliptical tube, the elliptical-flat elliptical tube would enhance the heat transfer at the upstream region of the tube, and the flat elliptical-elliptical tube would improve the heat transfer at the downstream region of the tube, as shown in Figure 9. The heat transfer coefficient of the flat elliptical-elliptical tube is higher than that of the elliptical-flat

elliptical tube, which shows that the optimization of particle flow and heat transfer at the downstream region of the tube can improve the overall heat transfer performance more efficiently. The heat transfer coefficients of these two shapes of tubes are higher than that of the flat elliptical tube but lower than that of the elliptical tube.

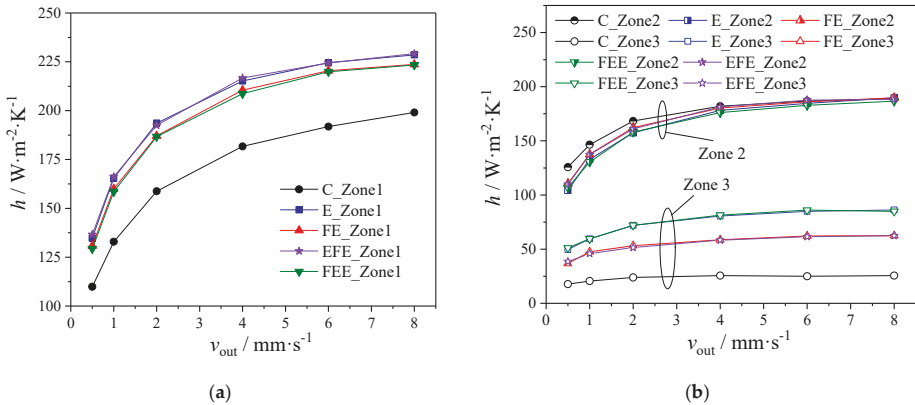


Figure 9. Variations of local heat transfer coefficients of particle flow with v_{out} for different tubes ($d_p = 1.72$ mm): (a) Zone 1; (b) Zone 2 and Zone 3.

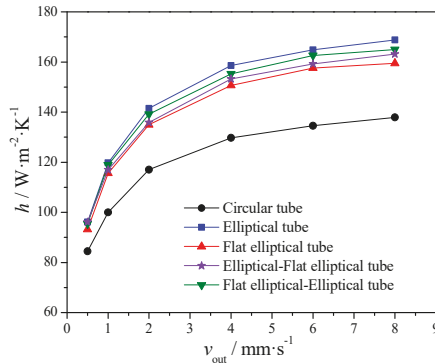


Figure 10. Variations of heat transfer coefficients of particle flow with v_{out} for different tubes ($d_p = 1.72$ mm).

Finally, the variations of heat transfer coefficients for the particle flow around an elliptical tube with different particle diameter (d_p) are presented in Figure 11. It shows that, as the particle diameter decreases from 2.5 mm to 1 mm, the heat transfer coefficients of particle flow around the elliptical tube increase, which is consistent with the experimental results of Liu et al. [1]. When $v_{out} = 2$ mm/s, as the particle diameter decreases from 2.5 mm to 1 mm, the local heat transfer coefficients of particle flow at the upstream region (E_Zone 1), side region (E_Zone 2) and downstream region (E_Zone 3) of an elliptical tube can increase by 61.1%, 59.4% and 102.6%, and the heat transfer coefficient around the elliptical tube can increase by 63.6% on average.

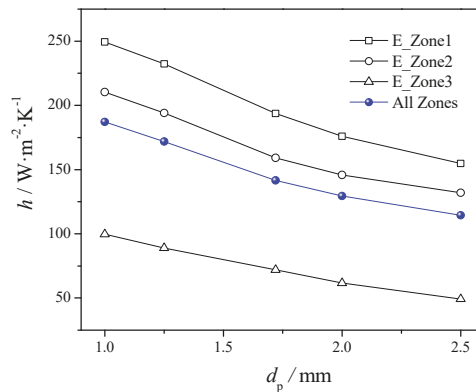


Figure 11. Variations of heat transfer coefficients of particle flow around an elliptical tube with different diameters ($v_{\text{out}} = 2 \text{ mm/s}$).

4. Conclusions

In the present study, the heat transfer of gravity-driven dense particle flow around different tubes was numerically investigated with discrete element method (DEM), including circular tube, elliptical tube, flat elliptical tube and the combination of elliptical tube and flat elliptical tube. A variety of factors, such as velocity vector, particle contact number, particle contact time and heat transfer coefficient of particle flow at different particle zones around the tube are carefully analyzed. Meanwhile, the effect of particle diameter on heat transfer is discussed. The main findings are as follows:

(1) The effect of tube shape on the particle flow at both upstream (Zone 1) and downstream (Zone 3) regions of different tubes is remarkable. A particle stagnation zone and particle cavity zone are formed at the upstream and downstream regions of all the tubes. Both the stagnation and cavity zones for the circular tube are the largest, and they are the smallest for the elliptical tube. Furthermore, the effect of tube shape on the particle contact number and particle contact time at different zones of particle flow for different tubes is quite different. As for the particle contact number, big differences existed at Zone 3 for different tubes. As compared with the circular tube, when $d_p = 1.72 \text{ mm}$, the particle contact number at Zone 3 of the elliptical tube and flat elliptical tube can increase by 112.3% and 53.5%, respectively. When $v_{\text{out}} = 0.5 \text{ mm/s}$ and $d_p = 1.72 \text{ mm}$, the particle contact time at Zone 1 of the elliptical tube and flat elliptical tube can decrease by 39% and 21% as compared with the circular tube.

(2) The heat transfer performances of particle flow around different tubes are different. It is found that, at Zone 3, the difference of local heat transfer coefficients of particle flow for different tubes is quite large. When the particle outlet velocity (v_{out}) changes from 0.5 mm/s to 8 mm/s at $d_p = 1.72 \text{ mm}$, as compared with the circular tube, the local heat transfer coefficient of particle flow at Zone 3 for the elliptical tube and flat elliptical tube can increase by 210.0% and 130.4% on average, respectively. Furthermore, as the particle outlet velocity (v_{out}) changes from 0.5 mm/s to 8 mm/s at $d_p = 1.72 \text{ mm}$, when compared with the circular tube, the heat transfer coefficient of particle flow for the elliptical tube and flat elliptical tube can increase by 20.3% and 15.0% on average, respectively. With proper design of the downstream shape of the tube, the overall heat transfer performance can be improved more efficiently. As the particle diameter (d_p) decreases from 2.5 mm to 1 mm at $v_{\text{out}} = 2 \text{ mm/s}$, the heat transfer coefficient of particle flow around an elliptical tube can increase by 63.6% on average.

The present results show that the heat transfer performance of particle flow around the elliptical tube is better than that of the circular tube and flat elliptical tube. Therefore, the elliptical tube would have a better application prospect in the MBHE. Furthermore, the heat transfer performance inside the tube and the economic analysis for the elliptical tube should be performed in the future.

Author Contributions: X.T. performed the calculations and wrote the paper; J.Y. and Q.W. supervised the work and revised the paper; Z.G. and B.S. contributed to revising the paper. All authors contributed to this work. All authors have read and agreed to the published version of the manuscript.

Funding: The financial support was provided by National Basic Research Program of China (No. 2017YFB0603500) and China Scholarship Council Fellowship (No. 201806285048).

Acknowledgments: We would like to acknowledge financial supports for this work provided by National Basic Research Program of China (No. 2017YFB0603500) and China Scholarship Council Fellowship (No. 201806285048).

Conflicts of Interest: The authors declare no conflict of interest.

Nomenclature

A	area (m^2)
a_e	major axis length of elliptical tube cross section (m)
b_e	minor axis length of elliptical tube cross section (m)
c_p	specific heat ($J/(kg \cdot K)$)
d_p	particle diameter (m)
D	distance from tube wall (m)
e	restitution coefficient
E	Young modulus (GPa)
F_n	normal component of the contact force (N)
F_t	tangential component of the contact force (N)
g	gravitational acceleration (m/s^2)
H	channel height (m)
h	heat transfer coefficient ($W/(m^2 \cdot K)$)
k	thermal conductivity ($W/(m \cdot K)$)
L	channel length (m)
l	distance of particle-particle or particle-wall (m)
l_{fe}	side length of flat elliptical tube (m)
m	mass (kg)
N	particle number
N_c	particle contact number
Q	heat (J)
q	heat flux (W)
R	thermal resistance (K/W)
r	particle radius (m)
r_c	circular tube radius (m)
r_{fe}	flat elliptical tube radius (m)
T	temperature (K)
t	time (s)
v	velocity (m/s)
V_n^{rel}	relative normal translational velocity (m/s)
V_t^{rel}	relative tangential translational velocity (m/s)
W	channel width (m)

Greek Letters

α, β, Θ	angles (rad)
δ	gas film thickness (m)
δ_n	normal displacement (m)
δ_t	tangential displacement (m)
ε	surface emissivity
μ_s	translational friction coefficient
ρ	density (kg/m^3)
σ	Stefan–Boltzmann constant ($W/(m^2 \cdot K^4)$)
φ	porosity

Subscripts

eq	equivalent parameters
g	gas
i, j	index
in	inlet
n	normal direction
out	outlet
s	solid

Abbreviations

DEM	discrete element method
G-C	only contact with gas film
MBHE	moving bed heat exchanger
P-C	physical contact
p-p	particle-particle
p-w	particle-wall

References

1. Liu, J.; Yu, Q.; Peng, J.; Hu, X.; Duan, W. Thermal energy recovery from high-temperature blast furnace slag particles. *Int. Commun. Heat Mass Transf.* **2015**, *69*, 23–28. [[CrossRef](#)]
2. Zheng, Y.; Cai, J.J.; Dong, H.; Feng, J.S.; Liu, J.Y. Experimental investigation of volumetric exergy transfer coefficient in vertical moving bed for sinter waste heat recovery. *Energy* **2019**, *167*, 428–439. [[CrossRef](#)]
3. Rahman, A.; Rasul, M.; Khan, M.M.K.; Sharma, S. Assessment of energy performance and emission control using alternative fuels in cement industry through a process model. *Energies* **2017**, *10*, 1996. [[CrossRef](#)]
4. Lee, W.J.; Kim, D.Y.; Choi, J.H.; Lee, J.W.; Kim, J.S.; Son, K.; Ha, M.J.; Kang, J. Utilization of petroleum coke soot as energy storage material. *Energies* **2019**, *12*, 3195. [[CrossRef](#)]
5. Baumann, T.; Zunft, S. Development and performance assessment of a moving bed heat exchanger for solar central receiver power plants. *Energy Procedia* **2015**, *69*, 748–757. [[CrossRef](#)]
6. Cheng, Z.; Guo, Z.; Tan, Z.; Yang, J.; Wang, Q. Waste heat recovery from high-temperature solid granular materials: Energy challenges and opportunities. *Renew. Sustain. Energy Rev.* **2019**, *116*, 109428. [[CrossRef](#)]
7. Wang, S.; Xu, C.; Liu, W.; Liu, Z. Numerical study on heat transfer performance in packed bed. *Energies* **2019**, *12*, 414. [[CrossRef](#)]
8. Vogtenhuber, H.; Pernsteiner, D.; Hofmann, R. Experimental and numerical investigations on heat transfer of bare tubes in a bubbling fluidized bed with respect to better heat integration in temperature swing adsorption systems. *Energies* **2019**, *12*, 2646. [[CrossRef](#)]
9. Zheng, B.; Sun, P.; Liu, Y.; Zhao, Q. Heat transfer of calcined petroleum coke and heat exchange tube for calcined petroleum coke waste heat recovery. *Energy* **2018**, *155*, 56–65. [[CrossRef](#)]
10. Natarajan, V.V.R.; Hunt, M.L. Heat transfer in vertical granular flows. *Exp. Heat Transf.* **2007**, *10*, 89–107. [[CrossRef](#)]
11. Takeuchi, H. Particles flow pattern and local heat transfer around tube in moving bed. *Part. Technol. Fluid.* **1996**, *42*, 1621–1626. [[CrossRef](#)]
12. Qoaidar, L.; Thabit, Q.; Kiwan, S. Innovative sensible heat transfer medium for a moving bed heat exchanger in solar central receiver power plants. *Appl. Sol. Energy* **2017**, *53*, 161–166. [[CrossRef](#)]
13. Al-Ansary, H.; El-Leathy, A.; Al-Suhaibani, Z.; Jeter, S.; Sadowski, D.; Alrished, A.; Golob, M. Experimental study of a sand–air heat exchanger for use with a high-temperature solar gas turbine system. *J. Sol. Energy Eng.* **2012**, *134*, 041017. [[CrossRef](#)]
14. Nguyen, C.; Sadowski, D.; Alrished, A.; Al-Ansary, H.; Jeter, S.; Abdel-Khalik, S. Study on solid particles as a thermal medium. *Energy Procedia* **2014**, *49*, 637–646. [[CrossRef](#)]
15. Chehata, D.; Zenit, R.; Wassgren, C.R. Dense granular flow around an immersed cylinder. *Phys. Fluids* **2003**, *15*, 1622. [[CrossRef](#)]
16. Tian, X.; Yang, J.; Guo, Z.G.; Wang, Q.W.; Sunden, B. Numerical study of flow and heat transfer in gravity-driven particle flow around a circular or elliptical tube. *Chem. Eng. Trans.* **2019**, *76*, 235–240.
17. Bartsch, P.; Zunft, S. Numerical investigation of dense granular flow around horizontal tubes: Qualification of CFD model with validated DEM model. *Sol. Energy* **2019**, *182*, 298–303. [[CrossRef](#)]

18. Bartsch, P.; Zunft, S. Granular flow around the horizontal tubes of a particle heat exchanger: DEM-simulation and experimental validation. *Sol. Energy* **2019**, *182*, 48–56. [[CrossRef](#)]
19. Niegsch, J.; Köneke, D.; Weinspach, P.M. Heat transfer and flow of bulk solids in a moving bed. *Chem. Eng. Process.* **1994**, *33*, 73–89. [[CrossRef](#)]
20. Guo, Z.G.; Tian, X.; Tan, Z.T.; Yang, J.; Wang, Q.W. Optimization of gravity-driven granular flow around the tube for heat transfer enhancement. *Chem. Eng. Trans.* **2019**, *76*, 247–252.
21. Morris, A.B.; Pannala, S.; Ma, Z.; Hrenya, C.M. A conductive heat transfer model for particle flows over immersed surfaces. *Int. J. Heat Mass Transf.* **2015**, *89*, 1277–1289. [[CrossRef](#)]
22. Morris, A.B.; Ma, Z.; Pannala, S.; Hrenya, C.M. Simulations of heat transfer to solid particles flowing through an array of heated tubes. *Sol. Energy* **2016**, *130*, 101–115. [[CrossRef](#)]
23. Zhang, H.; Zhou, Z.; Yu, A.B.; Kim, S.Y.; Jung, S.K. Discrete particle simulation of solid flow in a melter-gasifier in smelting reduction process. *Powder Technol.* **2017**, *314*, 641–648. [[CrossRef](#)]
24. Hilton, J.E.; Tordesillas, A. Drag force on a spherical intruder in a granular bed at low Froude number. *Phys. Rev. E. Stat. Nonlinear Soft Matter Phys.* **2013**, *88*, 062203. [[CrossRef](#)] [[PubMed](#)]
25. Johnson, K.L. *Contact Mechanics*; Cambridge University Press: Cambridge, UK, 1987.
26. Mindlin, R.D.; Deresiewicz, H. Elastic spheres in contact under varying oblique forces. *J. Appl. Mech.* **1953**, *20*, 327–344.
27. Zhang, R.; Yang, H.; Lu, J.; Wu, Y. Theoretical and experimental analysis of bed-to-wall heat transfer in heat recovery processing. *Powder Technol.* **2013**, *249*, 186–195. [[CrossRef](#)]
28. Molerus, O. Heat transfer in moving beds with a stagnant interstitial gas. *Int. J. Heat Mass Transf.* **1997**, *40*, 4151–4159. [[CrossRef](#)]
29. Chen, R.; Guo, K.; Zhang, Y.; Tian, W.; Qiu, S.; Su, G.H. Numerical analysis of the granular flow and heat transfer in the ADS granular spallation target. *Nucl. Eng. Des.* **2018**, *330*, 59–71. [[CrossRef](#)]
30. Bu, C.S.; Liu, D.Y.; Chen, X.P.; Liang, C.; Duan, Y.F.; Duan, L.B. Modeling and coupling particle scale heat transfer with DEM through heat transfer mechanisms. *Numer. Heat Transf. Part A Appl.* **2013**, *64*, 56–71. [[CrossRef](#)]
31. Vargas, W.L.; McCarthy, J.J. Stress effects on the conductivity of particulate beds. *Chem. Eng. Sci.* **2002**, *57*, 3119–3131. [[CrossRef](#)]
32. Antwerpen, W.V.; Rousseau, P.G.; Toit, C.G.D. Multi-sphere unit cell model to calculate the effective thermal conductivity in packed pebble beds of mono-sized spheres. *Nucl. Eng. Des.* **2012**, *247*, 183–201. [[CrossRef](#)]



© 2020 by the authors. Licensee MDPI, Basel, Switzerland. This article is an open access article distributed under the terms and conditions of the Creative Commons Attribution (CC BY) license (<http://creativecommons.org/licenses/by/4.0/>).

Article

Thermal Effects of Natural Gas and Syngas Co-Firing System on Heat Treatment Process in the Preheating Furnace

Piotr Józwiak ^{1,2,*}, Jarosław Hercog ¹, Aleksandra Kiedrzyńska ¹, Krzysztof Badyda ² and Daniela Olevano ³

¹ Thermal Processes Department, Institute of Power Engineering, 01-330 Warsaw, Poland; jaroslaw.hercog@ien.com.pl (J.H.); aleksandra.kiedrzyńska@ien.com.pl (A.K.)

² Institute of Heat Engineering, Warsaw University of Technology, 00-665 Warsaw, Poland; badyda@itc.pw.edu.pl

³ Centro Sviluppo Materiali S.p.A., 00128 Rome, Italy; daniela.olevano@rina.org

* Correspondence: piotr.jozwiak@ien.com.pl; Tel.: +48-22-3451-407

Received: 29 February 2020; Accepted: 1 April 2020; Published: 3 April 2020

Abstract: Preheating furnaces, which are commonly used in many production sectors (e.g., iron and steel), are simultaneously one of the most energy-intensive devices used in the industry. Partial replacement of natural gas with biomass-derived synthesis gas as a fuel used for heating would be an important step towards limiting industrial CO₂ emissions. The time dependent computational fluid dynamics (CFD) model of an exemplary furnace was created to evaluate whether it is possible to obtain 40% of energy from syngas combustion without deterioration of thermal parameters of the treated load. As an outcome, a promising method to organize co-firing in the furnace was indicated. The obtained results show that the co-firing method (up to 40% thermal natural gas replacement with syngas), assuming low air-to-fuel equivalence ratio ($\lambda_{NG} = 2.0$) and even distribution of power among the furnace corners, lead to satisfactory efficiency of the heat treatment process—the heat transferred to the load exceeds 95% of the heat delivered to the load in the reference case), while carbon dioxide emission is reduced from 285.5 to 171.3 kg CO₂/h. This study showed that it is feasible (from the heat transfer point of view) to decrease the environmental impact of the process industries by the use of renewable fuels.

Keywords: CFD modelling; heat treatment process; industrial furnaces; natural gas substitution; syngas co-firing

1. Introduction

Preheating furnaces use substantial amounts of energy in industrialized countries. A great number of furnaces and substantial energy consumption accompanying the heat treatment processes lead to the significant carbon footprint in Europe and beyond. In Germany, industrial processes are responsible for nearly 40% of natural gas consumption [1]. In Poland, over 45% of natural gas is used by industry and construction sectors [2]. High energy consumption of furnaces results from the need of heating the processed load to a specific temperature over a certain period of time. On an industrial scale, where the volume of the treated material is large, it means high demand for thermal power, associated with proportional operating cost and environmental impact.

On the other hand, it is deemed necessary to reduce the anthropogenic pressure on climate change [3] and the diversity of the biosphere, correlated with the CO₂ emissions from combusting fossil fuels. This is followed by concrete actions at the level of the European Union: 2020 climate and energy package, 2030 climate and energy framework, 2050 long-term strategy, and the resulting

initiatives for public-private partnerships like Sustainable Process Industry through Resource and Energy Efficiency aiming to make the European process industry more efficient and sustainable, and less resource consuming [4].

Natural gas is a commonly used energy source in the industry due to its wide applicability and availability at a low price. Although its CO₂ emission factor is the lowest of all hydrocarbons and it is considered as a much cleaner alternative to oil or coal, combustion of natural gas is still associated with polluting the atmosphere with greenhouse gases and the climatic consequences of that. Thus, measures limiting both fossil fuel consumption and gaseous emissions from the industry are sought. In the steel industry, the process by-products such as coke oven gas (COG), blast furnace gas (BFG) [5], and basic oxygen furnace gas (BOFG) can be used as a feedstock for reheating furnaces [6]. Usage of those gases in reheating furnaces and annealing lines with radiant tube burners was briefly analyzed [7]. It was found that there are no significant constraints for application of those gases, although cleaning the gas has to be done prior usage to avoid damaging the equipment. Researchers [8] investigated the influence of the syngas impurities on scale formation on steel slabs in the reheating furnaces, and found that they can cause corrosion and slagging.

Usage of other alternative gases (such as biogenic syngas fuels) has not been extensively explored, especially in the preheating furnaces where the temperatures are significantly lower and the conditions for complete combustion are not favorable. Moreover, the biogenic syngas may contain a significant amount of tars, which can either require gas cleaning (inherently connected with exergy losses) or cause difficulties in process equipment selection and operation in temperatures above the tars dew point.

Other contaminants which could be present in the biogenic syngas are halogen species (Cl, Br) [9] and, to a smaller extent, the alkali metals (Na, K) [10] which can cause operational problems [11]. Taking into account the above mentioned, there are no studies of the application of the syngas coming from the biomass gasification in the preheating furnaces.

One of the possible methods for low-emission combustion is partial substitution of natural gas with gaseous biofuels, whose CO₂ emission factor, according to the European Commission regulations, is equal to 0 [12]. An example of such gas is syngas obtained from the solid biomass gasification process.

There is a noticeable interest in the issue of replacing natural gas as a source of heat in the industry with renewable gas fuels. The possibility of reducing CO₂ emissions by co-firing syngas in gas turbines [13] and coal-fired boilers [14] has been studied. Research has been done on emission levels of nitrogen oxides (NO_x), carbon monoxide (CO), polycyclic aromatic hydrocarbons (PAH), and volatile organic compounds (VOC) accompanying the combustion of syngas [15]. Partial replacement of natural gas by biogas has been proven to be a sensible approach for implementation in the glass processing industry as no negative effects in product quality have been observed [16]. There have been no studies investigating the impact of hot biogenic syngas co-firing on heat treatment process parameters in steel preheating furnaces. The preliminary study preceding this work has shown that the use of low-calorific alternative fuels (specifically: basic oxygen furnace gas and biogenic synthesis gas) does not excessively change the course of the heating process, and that the introduction of dedicated syngas burners is a preferred option of organizing co-firing in the considered furnace [17].

The goal of this study is to analyze the effects of partial substitution of natural gas with biomass-derived synthesis gas on temperature of a typical load treated in an exemplary steel sector preheating furnace. The potential of introducing carbon-neutral low-calorific syngas to the process sector has not yet been studied. The results are to be compared with the ones gathered from the furnace fired in standard operation mode (leaning on natural gas only) in order to assess the possibility of applying this method of carbon dioxide emission reduction to other industrial units without worsening thermal parameters of the process.

2. Materials and Methods

2.1. Model Setup

2.1.1. Furnace

The numerical model is based on the existing preheating furnace BOSIO 1 located in Store, Slovenia. For this study a medium-size preheating furnace was selected. This particular furnace was chosen because it is a representative example of thousands of similar, simple operation units installed around the world. The characteristic batch loading (using bogie hearth) enables high flexibility for thermal treatment of loads of different sizes and shapes. The obtained results should be extrapolated with ease to furnaces of similar type.

This gas-fired unit is equipped with four burners combusting natural gas (NG) able to operate with power up to 400 kW each, four independent recuperators preheating the air from room temperature to 60 °C (333 K), and a doubled chimney with the natural draft. During the heat treatment a vortex-like flow structure inside the furnace is created, and direct contact between streams of flue gas and the load is avoided (Figure A1). For co-firing purposes, an addition of two burners dedicated to combust syngas (SG) was proposed—their operating power is 360 kW each, and they are located in the vicinity of NG burners to ensure complete combustion of syngas. The geometry of the furnace model is presented in Figure 1. The load is a 4.1 m long steel cylindrical mold with an outer diameter of 1.8 m. It was assumed that its material density is 7700 kg/m³, specific heat is 502.5 J/(kg·K), and thermal conductivity is 50 W/(m·K).

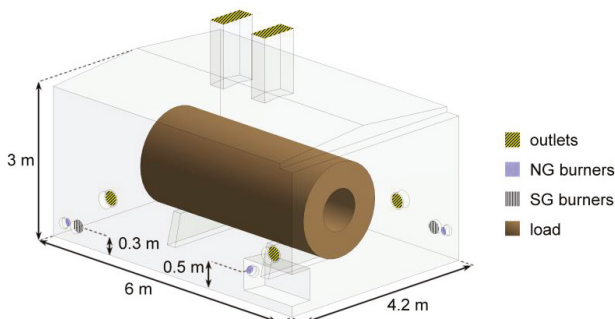


Figure 1. Geometry of the furnace model (NG—natural gas, SG—synthesis gas).

Numerical domain of the furnace was discretized with a hybrid mesh—structured elements form the load, chimneys, and part of the syngas burners interior, and the rest of the geometry was filled with polygonal elements (total number of cells: 875,119).

Figure 2 shows the NG and SG burners' primary (17% of comburent air, marked blue) and secondary (83% of burner air, marked red) preheated air inlets separated by the inlet of the respective fuel (green for syngas, yellow for natural gas). The secondary air swirl angle is 30°. The air consists of 77.45% nitrogen, 20.59% oxygen, and 1.96% water vapor by volume, what is an exemplary value corresponding to air at 85% relative humidity at 20 °C. The heat leaves the furnace to ambient at 20 °C (293 K) through convection: heat transfer coefficient at the outer walls of the furnace was specified as 25 W/m²·K, and with exhaust gas through the chimney outlets. Thermal insulance of the walls was estimated as 0.1 m²·K/W (0.2 m²·K/W for the walls surrounding NG burner no. 1 (the closest to the viewer in Figure 1) due to their reduced thickness of 0.1 m). Emissivity was 0.9, regardless of the temperature level and the material type.

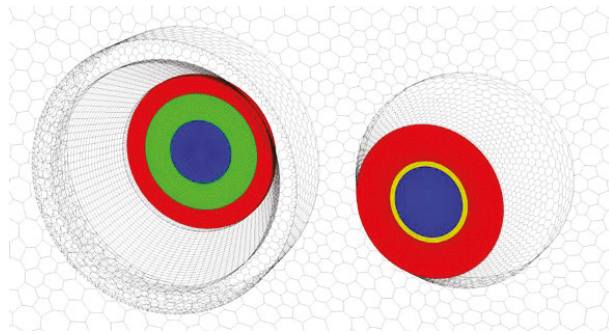


Figure 2. Discretization of surfaces near syngas (left) and natural gas (right) burners—colors mark respective air and fuel inlets (blue—core air, yellow—NG, green—SG, red—secondary air).

Total power of the considered furnace is limited to 1440 kW. The same power was fed in fuel in the numerical model. The influence of the recuperators extracting a fraction of the exhaust gases from the inside of the furnace on the gas flow was represented by assigning fixed velocity (1.33 m/s) to the recuperator outlets. In cases where no syngas is fed into the system, inlets of the SG burners were treated as adiabatic walls.

2.1.2. Fuels

The chemical composition of both considered fuels was specified by the furnace operator. Natural gas available in the facility contains the following combustible species: 97.97% methane, 0.76% ethane, and 0.38% other hydrocarbons (by volume)—the rest consists of carbon dioxide, nitrogen, and oxygen (<0.1%). NG is fed to the furnace at 20 °C (293 K).

The alternative fuel is generated by the located on-site fluidized bed gasifier, in which air is used as a gasification agent. The gasifier produces up to 1 MW power in gaseous fuel (ca. 0.7 MW on average). The lower heating value of a typical syngas produced by this type of gasifiers fluctuates in the range of 3–7 MJ/m³_N [18]. As one of the adopted objectives to achieve higher efficiency of the co-firing system is to preserve the initial high temperature of syngas, it was assumed that the SG produced by the gasifier is not cooled down on the way to the furnace, and it enters the dedicated burners at 600 °C (873 K). Hot syngas is not cleaned from tars—SG temperature should not drop below 350 °C (633 K) to avoid tar condensation and contamination of the installation. The amount of energy contained in tars (below 0.04 MJ/m³_N of SG, as tars concentration in the considered syngas is lower than 1 g/m³_N) is insignificant for the course of the heat treatment.

Presence of species with concentrations lower than 0.5% vol. was neglected. The composition of the gasification product is variable over time and estimated average values were chosen for the calculations (Table 1). Lower heating values for natural gas and synthesis gas are 50.05 and 4.52 MJ/kg, respectively. The fuels were considered in a dry state.

Table 1. Chemical composition of natural gas (NG) and syngas (SG) adopted for simulations.

Component	Natural Gas (% vol.)	Syngas (% vol.)
O ₂	0	1
CO ₂	0	12
CO	0	21
CH ₄	98	3
C ₂ H ₆	2	0
H ₂	0	14
N ₂	0	49
H ₂ O	0	0

Despite the content of CH₄, CO, and CO₂, syngas is regarded as carbon-neutral because of its biomass origin. This means carbon dioxide emission factor for SG is 0 kg CO₂/GJ, instead of 135 kg CO₂/GJ as its gas composition would indicate. NG emission factor is 55 kg CO₂/GJ.

2.2. Operation Modes

To evaluate the influence of NG-SG co-firing on the quality of the heat treatment, nine different furnace powering scenarios were developed and implemented in the furnace model—the test matrix showing the case numeration and respective substitution rates, NG burner power, and air supply levels is shown in Figure 3. For each case the furnace power is equal to the initial one, i.e., 1440 kW. Three main factors that can affect the process course were identified and tested:

- Mode of work (NG only or co-firing)—to value the impact of SG presence, e.g., two additional flames, on the heat treatment;
- Air–fuel equivalence ratio at natural gas burners λ_{NG} (2.0, 3.0, or resulting from feeding 1980 m³_N/h (at normal conditions ca. 0.71 kg/s) of air to the natural gas burners, i.e., the amount supplied in the original BOSIO 1 furnace—to check the correlation between the amount of air fed to the furnace, the resulting change in gas motion, and the heat transfer;
- Power distribution among the corners of the furnace (even or uneven)—to determine the effect of balancing the power outcome of the NG-SG burner pair and the two NG burners without adjacent SG burner, accomplished by adjusting the power of NG burners so at every corner of the furnace 360 kW of heat is released.

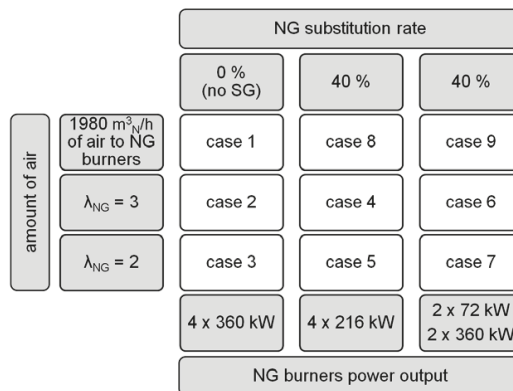


Figure 3. Parameters of the considered furnace operation modes.

The air–fuel equivalence ratio for SG burners λ_{SG} is fixed to 1.15, because syngas as a low calorific fuel is considered more prone to incomplete combustion or flame blowout [19], and as such needs conducive conditions to avoid it.

The first 2 h of the process were simulated—during that time the burners are turned on continuously, and the tracked indicators, i.e., average temperature and maximum temperature difference of the load are expected to increase. At the beginning of the heat treatment ($t = 0$ s), the load and the air inside the furnace are 20 °C (293 K). Case 1 (no syngas, 1980 m³_N/h of air) serves as the reference case.

2.3. Calculation Method

CFD tools are widely used to simulate and optimize the processes of heat transfer [20] and energy release from various fuels [21]. A transient 3D model was prepared and used to determine the changing conditions inside the furnace over time. The model based on URANS approach covers turbulent gas flow by solving three-dimensional Reynolds-Averaged Navier-Stokes equations with realizable $k-\epsilon$ turbulence model applied to solve the Reynolds stresses. Gravitational forces were included. The solver is pressure-based and because adaptive time step sizes (0.1 s for the first 1 s of the process, 1 s for the period between 1 s and 15 s of the process, and 15 s for the rest of the process) were used in the simulations, the coupled algorithm for calculating pressure was chosen.

The gas is a multicomponent single-phase mixture composed of CO₂, CO, CH₄, C₂H₆, H₂, O₂, H₂O, and N₂, whose local mass fractions are predicted through solving the conservation equations for each species (except for nitrogen, which is the balancing species), and both density (following the incompressible ideal gas law) and specific heat of each compound are temperature dependent. Species can participate in the volumetric chemical reactions Equations (1)–(4), which are the source of thermal energy in the system.



The rate of these chemical reactions is controlled by turbulent mixing, that is an acknowledged approach used for modelling non-premixed combustion (eddy-dissipation model) [22].

The numerical model allows the heat to be transferred by convection, conduction (within the load's volume), and radiation mechanisms. Radiative heat transfer is calculated using discrete ordinates method with the weighted-sum-of-grey-gases model included. Temperature is obtained through solving the energy equation. The CFD simulations were performed in Ansys Fluent 19.0.

2.4. Discretization Error

In order to evaluate the accuracy of the numerical model, the influence of the meshing method on the results was evaluated. Ten different discretization grids were analyzed—all of them consist of structured and polygonal elements. Two examples of the tested meshes are presented in Figure 4.

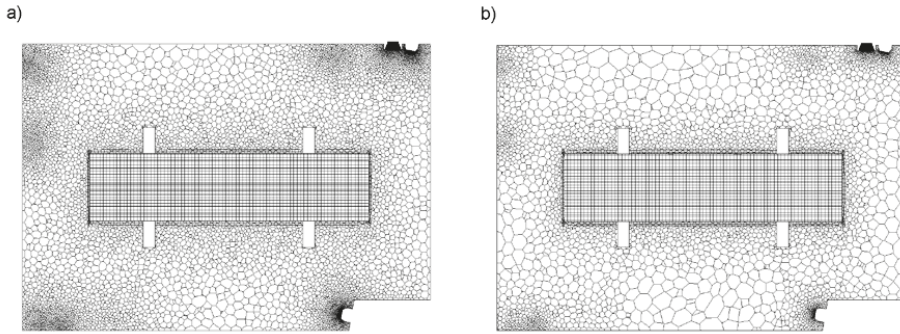


Figure 4. Examples of discretization mesh located 0.5 m above the furnace bogie level consisting of (a) 875,119 and (b) 533,386 elements.

The volume average temperature of the load (ALT) was chosen for an indicator of the discretization error. Case 1 was simulated using the same model settings and the same time step sizes, and the obtained results of ALT after 2 h of the process were compared (Figure 5). The black point on the chart marks the mesh used for performing the calculations for cases 1–9.

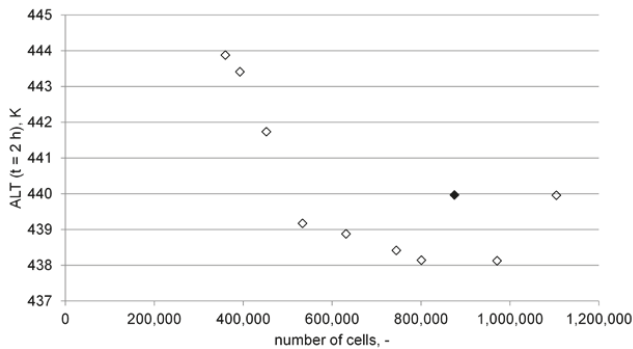


Figure 5. Convergence study results—volume average load temperature after 2 h of the heat treatment for different discretization meshes.

One can see that enhancing the grid resolution keeps the values of ALT within the 2 K range, what appears to be an acceptable value of error, i.e., less than 2% when compared to the value change of average load temperature (Δ ALT).

3. Results

The results of the numerical calculations contain information about, among others, temperature field in the gas and solid domains. Exemplary visualization of the obtained temperature results for case 7 is shown in Figures 6 and 7.

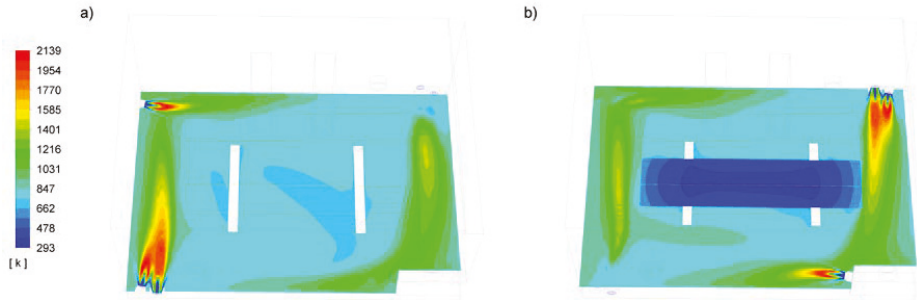


Figure 6. Temperature contours after 2 h of the heat treatment (a) 0.3 m and (b) 0.5 m above the furnace bogie level—case 7.

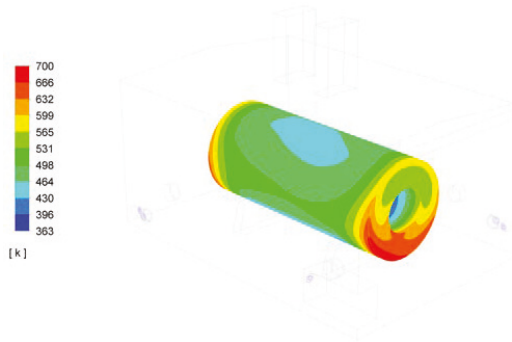


Figure 7. Temperature of the load surface after 2 h of the heat treatment—case 7.

In this study the focus was on the mold temperature levels, especially after 2 h of the treatment. Acquisition of the data took place at every time step, therefore at least every 15 s of the simulated process time. The results for the two analyzed cases (1—the reference one, and 7—the SG co-firing scenario with the results most similar to case 1) are presented in Figure 8.

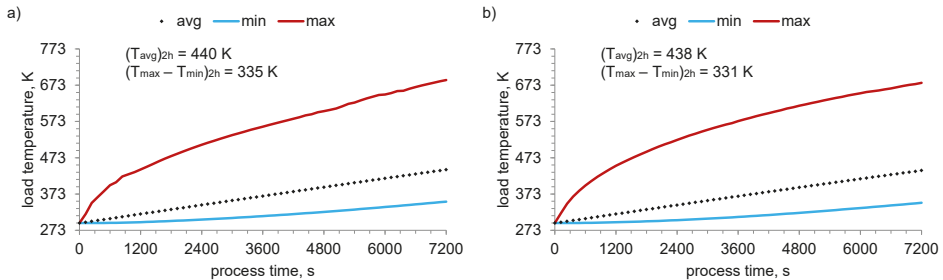


Figure 8. Volume average (avg), minimum (min), and maximum (max) temperatures of the load during the first 2 h of the heat treatment: (a) case 1, (b) case 7.

The applicability and efficiency of each powering mode was assessed on the basis of load temperature difference (LTD) and volume average load temperature (ALT), respectively. Value of LTD is defined as the temperature difference between the hottest (T_{max}) and the coldest (T_{min}) point of the load—lower LTD means better thermal uniformity. ALT is an indicator of thermal efficiency, i.e., the

ratio of the energy fed in fuel to the energy received by the load—higher values of this measure denote improved usage of heat.

Substituting 40% of NG by low-calorific SG with a constant amount of air supplied to the NG burners has a negative or no effect on thermal uniformity of the load, depending on whether the power among the furnace corners has not or has been equated, respectively (cases 8, 9; Figure 9a). Introducing syngas, while maintaining λ_{NG} at 2.0, increases the maximum load temperature difference up to the level noted in the reference case (cases 5, 7; Figure 9a), for which λ_{NG} is 1.42. Adjusting the natural gas burners’ power in cases where λ_{NG} is equal to 2.37 or 3.0 is noticeably beneficial from the LTD perspective (cases 4, 6, 8, and 9).

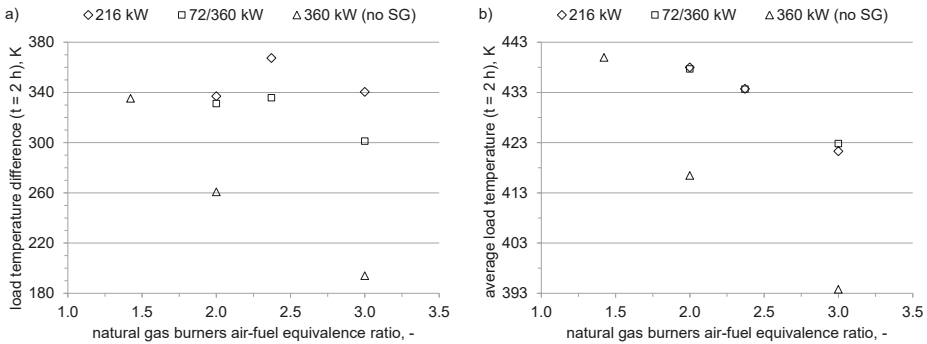


Figure 9. Load temperature difference (a) and average load temperature (b) values for different ways of supplying power (number of kW represents the power of NG burners).

Use of different NG burners power outputs has no impact on average load temperature, regardless of λ_{NG} applied (cases 4, 6 and 5, 7 and 8, 9; Figure 9b). Reducing the air–fuel equivalence ratio is correlated with elevation of the heating efficiency, especially in case of no syngas addition. Implementation of co-firing significantly raises the amount of heat absorbed by the load—for λ_{NG} equal 3.0 by $28.1\% \pm 0.7\%$, and for λ_{NG} equal 2.0 by $17.3\% \pm 0.1\%$, reaching $98.5\% \pm 0.2\%$ (cases 5 and 7) of the reference case heating efficiency.

Within 1 h the furnace powered conventionally (cases 1–3) consumes ca. 103.6 kg of natural gas and emits 285.5 kg of CO₂ (under the assumption of complete fuel combustion). When 40% of NG is replaced by SG (cases 4–9), the amount of fossil carbon dioxide added to the atmosphere drops by 40% as well—in that case the emission is 171.3 kg CO₂/h.

4. Discussion

The results of numerical simulations for the considered cases (Figure 3, Section 2.2) are compared in Figure 10. The value of change of average load temperature (ΔALT), calculated as the difference between ALT after 2 h of the process and the initial temperature of the system (i.e., 20 °C), is proportional to the amount of energy transferred to the load. ΔALT for case 1 serves as the reference value.

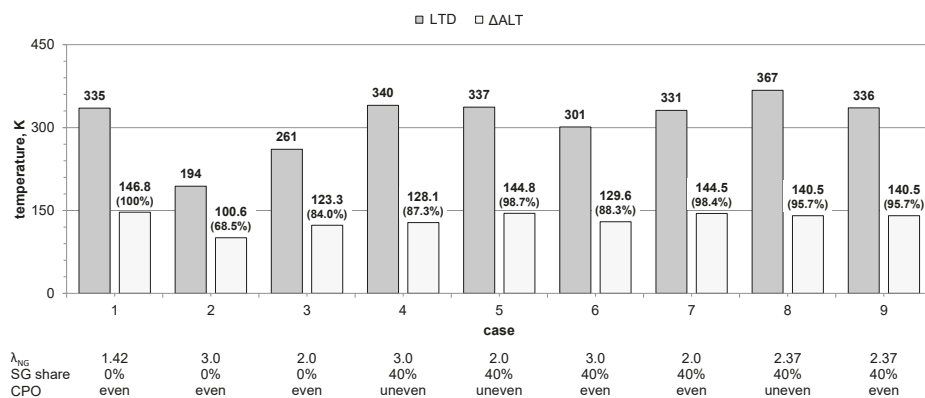


Figure 10. Load temperature difference (LTD) and change of average load temperature from initial temperature (Δ ALT) after 2 h of the heat treatment (CPO—furnace corner power output).

Conducted CFD calculations show that equalization of the power output in each of the corners has a positive effect on the load temperature difference, especially in case of increased air–fuel equivalence ratio for natural gas burners and the resulting reduction of exhaust gas temperature. Replacing natural gas with biogenic syngas in the tested co-firing setup proved to achieve satisfactory efficiency of the heat treatment process—in four out of six analyzed co-firing scenarios the amount of heat transferred to the load exceeds 95% of the heat delivered to the load in the reference case (case 1). This effect is correlated with the lower SG flame temperature (Figure 6), and the fact that the streams of hot flue gases do not directly hit the load.

Analysis of the simulations results revealed a promising way of substituting 40% of natural gas in the preheating furnace with the considered biomass-derived renewable fuel, which leads to significant reduction of CO₂ emissions, thus, smaller environmental impact. This is especially prominent in case 7, in which natural gas burners operate at $\lambda_{NG} = 2.0$ on two power levels: 72 kW (the ones near the syngas burners) and 360 kW (the other two burners), so in each of the furnace corners 360 kW of heat is generated. An important advantage of case 7 over cases 9 and 6 (especially the latter one) is that lower air-to-fuel ratio at the NG burners prevents the creation of strong stream of flue gas flowing out of natural gas burners operating at 360 kW (Figure A6), that could potentially disturb the combustion in the SG burners, which are inclined to less stable operation. Aggravation of this effect, caused by enhancing the stream of flue gas leaving the NG burners can also be noticed by comparing the gas flow patterns available in the Appendix A for the following sequences of cases: 1-3-2, 7-9-6, and 5-8-4 (Figures A1–A9).

Simultaneously, the temperature results show that the co-firing method assuming low air-to-fuel equivalence ratio and uneven distribution of power among the furnace corners (corner without SG burner: 216 kW, corner with SG burner: 504 kW) can still lead to satisfactory results (case 5). Analysis of the streamlines and temperature profiles for cases 5 and 7 shows that power equalizing on the one hand reduces the risk of local load overheating (Figure A5), but on the other hand promotes creation of strong jet-like flows, which hit and locally heat up inner walls of the furnace (Figure A7). It is likely that the optimal power balance between the furnace corners, where the scale of both phenomena is reduced and the efficiency achieves its maximum, lies between the analyzed values.

Based on these results, further work to evaluate the possibility of partial replacing natural gas consumption with alternative fuels (e.g., biomass-derived gaseous fuels or off-gases) can be done, especially for other types of furnaces (e.g., the ones continuously heating and melting stream of material). It is possible that in some cases, depending on the limits on LTD values, it may be necessary

to increase the air–fuel equivalence ratio for syngas burners in order to lower SG flame temperature and improve thermal uniformity of the load.

Author Contributions: Conceptualization, P.J., A.K. and J.H.; methodology, P.J.; validation, P.J.; formal analysis, P.J.; investigation, P.J.; writing—original draft preparation, P.J.; writing—review and editing, P.J., J.H., A.K., K.B. and D.O.; visualization, P.J.; supervision, J.H.; project administration, J.H.; All authors have read and agreed to the published version of the manuscript.

Funding: This research was funded by European Union’s Horizon 2020 research and innovation programme, grant number 723803. The APC was funded by the Institute of Power Engineering.

Acknowledgments: The authors would like to thank Jernej Mele (CPPE d.o.o.) and Matej Drobne (Valji d.o.o.) for support and providing process data.

Conflicts of Interest: The authors declare no conflict of interest.

Appendix A

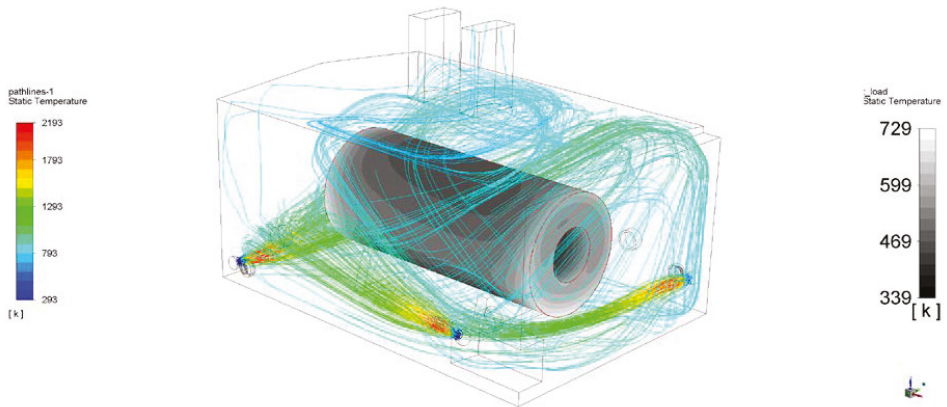


Figure A1. Gas path lines and load surface temperature after 2 h of the heat treatment—case 1.

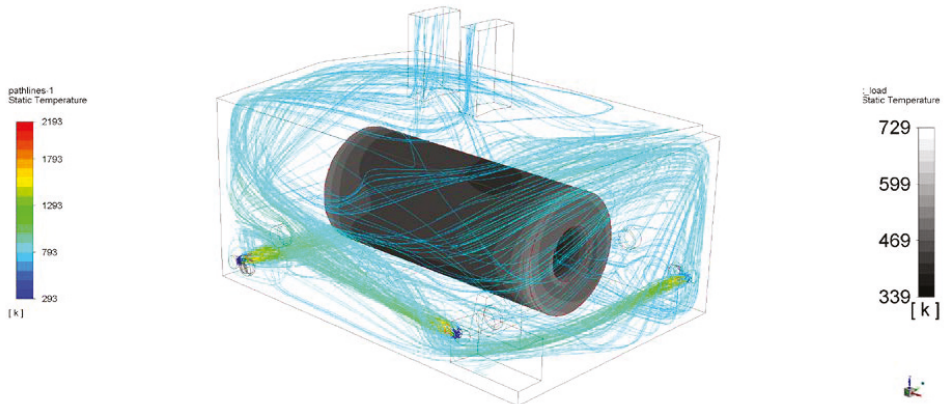


Figure A2. Gas path lines and load surface temperature after 2 h of the heat treatment—case 2.

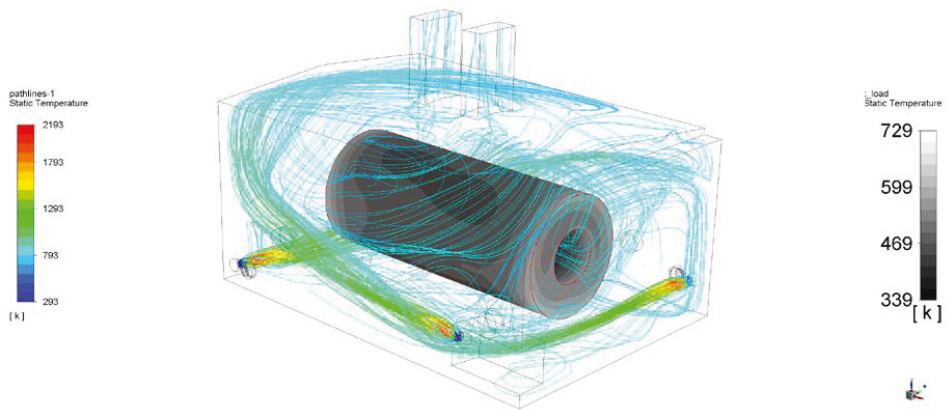


Figure A3. Gas path lines and load surface temperature after 2 h of the heat treatment—case 3.

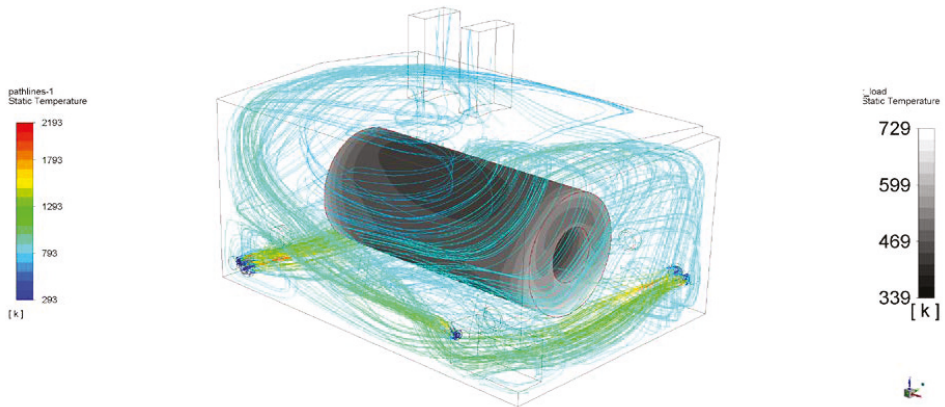


Figure A4. Gas path lines and load surface temperature after 2 h of the heat treatment—case 4.

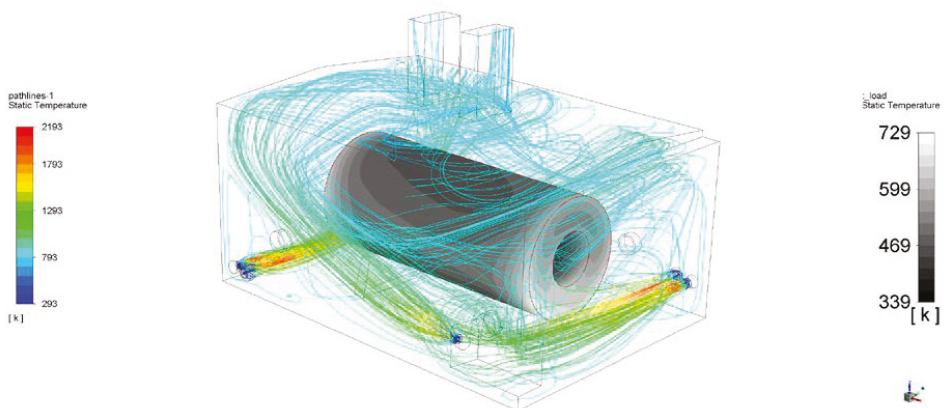


Figure A5. Gas path lines and load surface temperature after 2 h of the heat treatment—case 5.

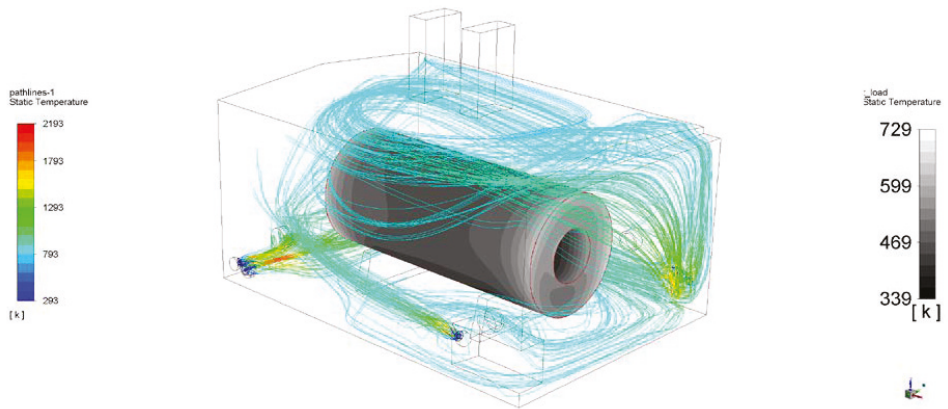


Figure A6. Gas path lines and load surface temperature after 2 h of the heat treatment—case 6.

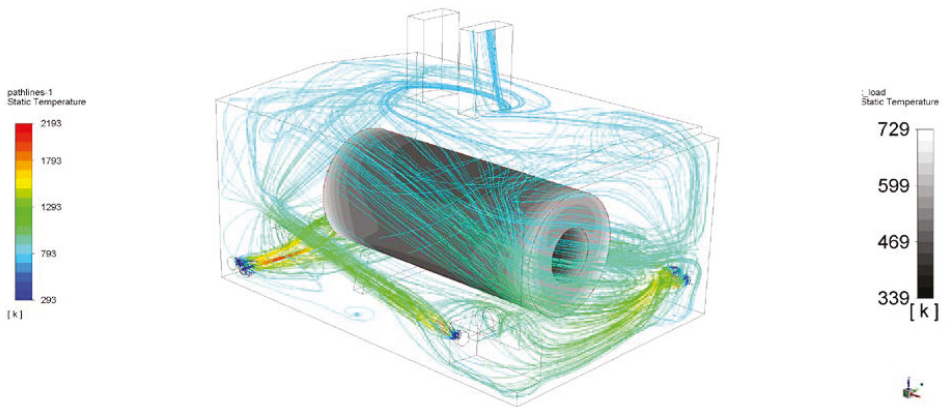


Figure A7. Gas path lines and load surface temperature after 2 h of the heat treatment—case 7.

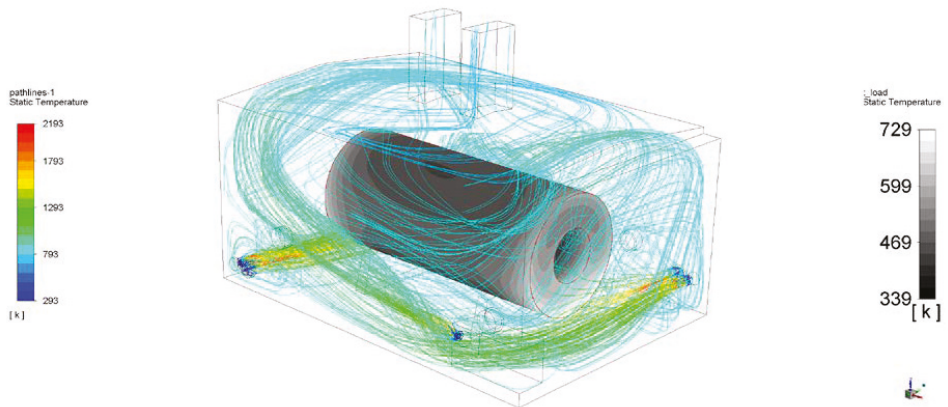


Figure A8. Gas path lines and load surface temperature after 2 h of the heat treatment—case 8.

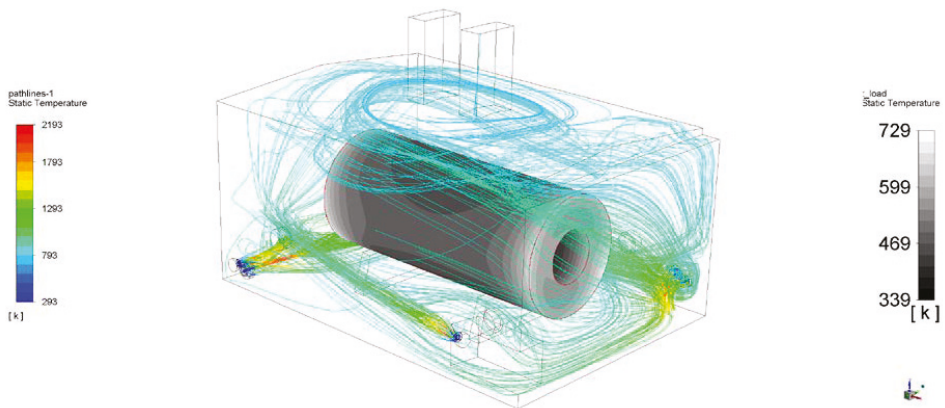


Figure A9. Gas path lines and load surface temperature after 2 h of the heat treatment—case 9.

References

1. AGEBA. *Energy Consumption in Germany in 2018*; Ziesing, H.-J., Ed.; AGEBA Arbeitsgemeinschaft Energiebilanzen e.V.: Berlin, Germany, 2019; Available online: https://ag-energiebilanzen.de/index.php?article_id=29&fileName=ageb_jahresbericht2018_20190503_engl.pdf (accessed on 29 February 2020).
2. Berent, G.; Peryt, S.; Kacprowska, J.; Gilecki, R.; Boczek, R.; Żarek, E.; Brasse, J.; Stosio, M. *Consumption of Fuels and Energy Carriers in 2018*; Walkowska, K., Ed.; Główny Urząd Statystyczny: Warsaw, Poland, 2019. Available online: <https://stat.gov.pl/obszary-tematyczne/srodowisko-energia/energia/zuzycie-paliw-i-nosnikow-energii-w-2018-roku,6,13.html> (accessed on 29 February 2020).
3. Yue, X.-L.; Gao, Q.-X. Contributions of natural systems and human activity to greenhouse gas emissions. *Adv. Clim. Chang. Res.* **2018**, *9*, 243–252. [[CrossRef](#)]
4. Tello, P.; Weerdmeester, R. *SPIRE Roadmap 2030*; A.SPIRE Asbl: Brussels, Belgium, 2013.
5. Pinera, V.C.; Riesgo, D.C.; Battaglia, V.; Fantuzzi, M.; Rocca, A.D.; Ageno, M.; Rensgard, A.; Wang, C.; Niska, J.; Ekman, T.; et al. *High Efficiency Low NOX BFG Based Combustion Systems in Steel Reheating Furnaces (HELNOx-BFG)*; Publications Office of the European Union: Luxembourg, 2017. [[CrossRef](#)]
6. Battaglia, V.; Malfa, E.; Zanusso, U.; Arribas Ramirez, J.J.; Ekman, T.; Adler, W.; Dapper, M.; Filippini, E.; Magni, F.; Niska, J.; et al. *CO₂ Reduction in Reheating Furnaces (CO2RED)*; Publications Office of the European Union: Luxembourg, 2011. [[CrossRef](#)]
7. Caillat, S. Burners in the steel industry: Utilization of by-product combustion gases in reheating furnaces and annealing lines. *Energy Procedia* **2017**, *120*, 20–27. [[CrossRef](#)]
8. Liu, H.; Saffaripour, M.; Mellin, P.; Grip, C.-E.; Yang, W.; Blasiak, W. A thermodynamic study of hot syngas impurities in steel reheating furnaces—Corrosion and interaction with oxide scales. *Energy* **2014**, *77*, 352–361. [[CrossRef](#)]
9. Simell, P.; Stahlberg, P.; Solantausta, Y.; Hepola, J.; Kurkela, E. Gasification gas cleaning with nickel monolith catalyst. In *Developments in Thermochemical Biomass Conversion*; Bridgwater, A.V., Boocock, D.G.B., Eds.; Springer: Dordrecht, The Netherlands, 1997; pp. 1103–1116. [[CrossRef](#)]
10. Nielsen, H.P.; Frandsen, F.J.; Dam-Johansen, K.; Baxter, L.L. The implications of chlorine-associated corrosion on the operation of biomass-fired boilers. *Prog. Energy Combust. Sci.* **2000**, *26*, 283–298. [[CrossRef](#)]
11. Niska, J.; Grip, C.E.; Mellin, P. Investigating potential problems and solutions of renewable fuel use in steel reheating furnaces. In Proceedings of the Finnish-Swedish Flame Days 2013, Jyväskylä, Finland, 17–18 April 2013; Available online: <http://kth.diva-portal.org/smash/get/diva2:681855/FULLTEXT01.pdf> (accessed on 28 February 2020).
12. European Commission. Commission Regulation (EU) No 601/2012 of 21 June 2012 on the monitoring and reporting of greenhouse gas emissions pursuant to Directive 2003/87/EC of the European Parliament and of the Council. *Off. J. Eur. Union* **2012**, *L181*, 30–104. Available online: <https://eur-lex.europa.eu/eli/reg/2012/601/oj> (accessed on 29 February 2020).

13. Fiaschi, D.; Carta, R. CO₂ abatement by co-firing of natural gas and biomass-derived gas in a gas turbine. *Energy* **2007**, *32*, 549–567. [[CrossRef](#)]
14. Kalisz, S.; Pronobis, M.; Baxter, D. Co-firing of biomass waste-derived syngas in coal power boiler. *Energy* **2008**, *33*, 1770–1778. [[CrossRef](#)]
15. Whitty, K.J.; Zhang, H.; Eddings, E.G. Emissions from Syngas Combustion. *Combust. Sci. Technol.* **2008**, *180*, 1117–1136. [[CrossRef](#)]
16. Fiehl, M.; Leicher, J.; Giese, A.; Görner, K.; Fleischmann, B.; Spielmann, S. Biogas as a co-firing fuel in thermal processing industries: Implementation in a glass melting furnace. *Energy Procedia* **2017**, *120*, 302–308. [[CrossRef](#)]
17. Józwiak, P.; Hercog, J.; Kiedrzyńska, A.; Badyda, K. CFD analysis of natural gas substitution with syngas in the industrial furnaces. *Energy* **2019**, *179*, 593–602. [[CrossRef](#)]
18. You, S.; Ok, Y.S.; Tsang, D.C.W.; Kwon, E.; Wang, C.-H. Towards practical application of gasification: A critical review from syngas and biochar perspectives. *Crit. Rev. Environ. Sci. Technol.* **2018**, *48*, 1165–1213. [[CrossRef](#)]
19. Lieuwen, T.; McDonell, V.; Santavicca, D.; Sattelmayer, T. Burner development and operability issues associated with steady flowing syngas fired combustors. *Combust. Sci. Technol.* **2008**, *180*, 1169–1192. [[CrossRef](#)]
20. Echi, S.; Bouabidi, A.; Driss, Z.; Abid, M.S. CFD simulation and optimization of industrial boiler. *Energy* **2019**, *169*, 105–114. [[CrossRef](#)]
21. Silva, J.; Teixeira, J.; Teixeira, S.; Preziati, S.; Cassiano, J. CFD Modeling of Combustion in Biomass Furnace. *Energy Procedia* **2017**, *120*, 665–672. [[CrossRef](#)]
22. Kassem, H.I.; Saqr, K.M.; Aly, H.S.; Sies, M.M.; Wahid, M.A. Implementation of the eddy dissipation model of turbulent non-premixed combustion in OpenFOAM. *Int. Commun. Heat Mass Transf.* **2011**, *38*, 363–367. [[CrossRef](#)]



© 2020 by the authors. Licensee MDPI, Basel, Switzerland. This article is an open access article distributed under the terms and conditions of the Creative Commons Attribution (CC BY) license (<http://creativecommons.org/licenses/by/4.0/>).

Article

Isomerization of n-C₅/C₆ Bioparaffins to Gasoline Components with High Octane Number

Jenő Hancsók ^{1,*}, Tamás Kasza ² and Olivér Visnyei ¹

¹ Department of MOL Hydrocarbon and Coal Processing, University of Pannonia, 10 Egyetem Street, H-8200 Veszprém, Hungary; visnyei.oliver@almos.uni-pannon.hu

² MOL Plc., 2 Olajmunkás Street, H-2440 Százhalombatta, Hungary; tkasza@mol.hu

* Correspondence: hancsokj@almos.uni-pannon.hu

Received: 13 March 2020; Accepted: 27 March 2020; Published: 3 April 2020

Abstract: The thermal and catalytic conversion processes of alternative feedstocks (e.g., waste and biomass) to different engine fuels can result in the formation of a significant amount of light hydrocarbons as by-products in the boiling range of gasoline. The properties of these C₅/C₆ hydrocarbons need to be improved due to many reasons, e.g., their benzene content, and/or poor oxidation stability (high olefin content) and low octane number (<60). The aim of the research work was to increase the octane number of benzene containing C₅/C₆ bioparaffin fractions by catalytic isomerization. These by-products were obtained from special hydrocracking of waste cooking oil to hydrocarbons in the boiling range of aviation turbine fuels (JET fuels)/diesel fuels. Experiments were carried out in a reactor system containing down-flow tubular reactors over Pt/Al₂O₃/Cl and Pt/H-Mordenite/Al₂O₃ catalysts at 115–145 °C and 230–270 °C, respectively. Based on the results obtained at different process parameter combinations, it was concluded that the hydrogenation of benzene was complete over both catalysts, and the liquid yields were higher (ca. 98% > ca. 93 %) in the case of Pt/Al₂O₃/Cl. In addition, the octane number was also enhanced (ca. 32 > ca. 27 unit) in the products compared to the feedstock. This was because a higher isoparaffin content can be obtained at a lower operating temperature. Moreover, cracking side reactions take place to a lesser extent. The utilization of these isomerized bio-origin light fractions can contribute to the competitiveness of second-generation biofuels.

Keywords: waste-originated feedstock; isomerization; biogasoline; benzene-free; increased octane number

1. Introduction

The energy demand of the world is continuously increasing due to new industrial developments and population growth [1]. Internal combustion engines with different operation principles will remain the main form of propulsion for terrestrial, air, and maritime transportation in the next 20–30 years. Accordingly, hydrocarbons as engine fuels for internal combustion engines will continue to play an important role as demonstrated in Figures 1 and 2a,b [2]. The proportion of gasoline will decrease slightly, but will still account for a one-third share in 2040. This decrease is due to the better fuel economy and the spread of electric vehicles [3] (Figure 3). However, contrary to forecasts, electric vehicles cannot spread as rapidly as expected, due to reasons such as availability of raw materials, recycling, sustainability, etc.

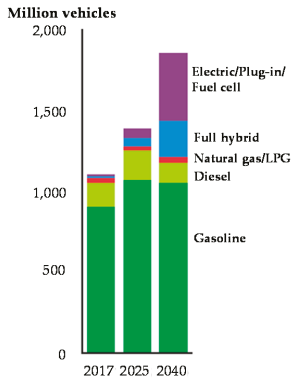


Figure 1. Light-duty vehicles by fleet type.

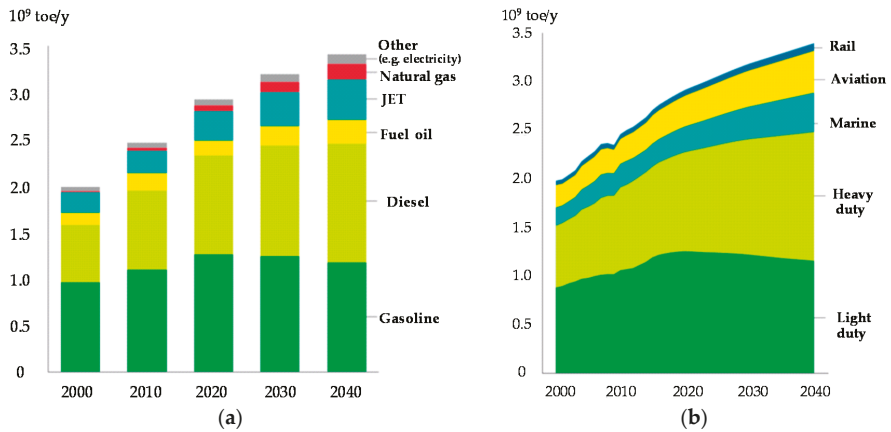


Figure 2. (a) Global energy mix by engine fuels. (b) Energy demand by type of transportation.

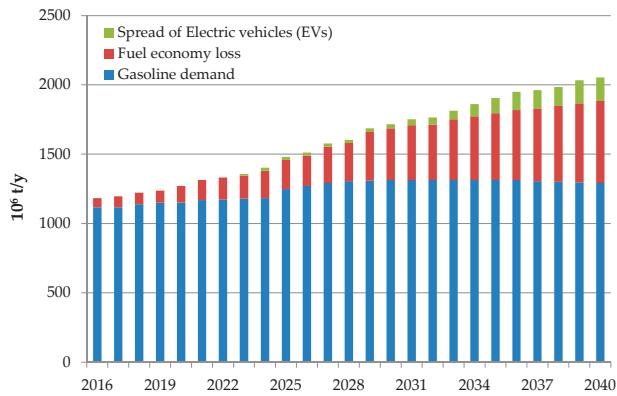


Figure 3. Expected gasoline demand taking into account to better fuel economy and the spread of electric vehicles.

Sustainable production of alternative engine fuels is a big challenge. Accordingly, different biofuels presently play a significant role for many countries in the world. The foreseen decrease of fossil reserves, global protection of the environment, and sustainability of mobility are the main driving forces for the research into renewable alternative energy sources [4]. The latest directive of the European Union requires the production of fuels from non-edible, renewable, or waste feedstocks [5]. Currently, the main bio-component of gasoline is bioethanol [6], which is also a molecular constituent in ethyl-tert-butyl-eter (bio-ETBE), an important gasoline blending component [7]. Despite the numerous advantages of ethanol, it has also many disadvantages, such as high solubility in water, increase of vapor pressure in gasoline, lower energy content, corrosion effects, high ozone producing potential, and high atmospheric reactivity [8]. Moreover, it is mainly produced from food-based plants, e.g., corn. As a result of persistent research and development in the last few years, the construction of plants using lignocellulose as feedstock has already begun [9]. However, their technological efficiency and reliability need to be proven [10].

The conversion processes of alternative feedstocks, such as biomass and waste, to different fuels result in the formation of a significant amount of light hydrocarbons (e.g., C₅-C₇ fractions), mainly as by-products in the boiling range of gasoline. The following processes can result in light hydrocarbons from alternative sources:

- From waste or biomass-derived syngas by Fischer–Tropsch (F–T) synthesis via direct synthesis, which results in the so-called C₅-C₇ fraction, F–T light gasoline [11], or, eventually, via indirect route by F–T synthesis combined with the hydrocracking of heavy F–T wax [12]. The oligomerization and hydrogenation of light olefins (C₂=–C₃=) obtained from F–T synthesis can also yield light hydrocarbons [13].
- From the oligomerization of fuel gas rich in light olefins such as ethylene, propylene, or butylene obtained from bio-oil or other bio-originated feedstock, e.g., rice straw biomass [14]. The obtained iso-olefins need to be hydrogenated to iso-alkanes.
- Another possibility is the oligomerization and subsequent hydrogenation of light gasoline fractions having a high olefin content obtained from thermal/catalytic cracking of waste polyolefins with different structures, such as polyethylene or polypropylene [15].
- Gasoline-range hydrocarbons can be produced from sorbitol, a sugar-based compound from lignocellulosic biomass, via hydrodeoxygenation over Zr-phosphate-supported Pd-bimetallic (Pd+ Pt/Ru/Ni/W etc.) catalysts [16]. The product mixture contains a large number of individual components with very different structures, e.g., corrosive acids and compounds in the aqueous phase. The treating and separation of the products could require complex and expensive solutions.
- In the so-called renewable power-to-paraffin hydrocarbons process, hydrogen produced via water electrolysis can be used for the hydrogenation of carbon monoxide/carbon dioxide to get alkanes [17,18].
- Alkanes can be obtained from bioethanol via dehydration, oligomerization, and hydrogenation of olefinic double bounds [19].
- N-alkanes can be manufactured through simple sugars from lignocellulose applying a very complex and expensive production process: acid-catalyzed dehydration, Aldol condensation (base catalyst), hydrogenation on metal catalyst, dehydration, and hydrogenation (acid and metal catalysts). Such products have very a low octane number, which should be increased by the catalytic process [20].
- Paraffins can be obtained from long-chain fatty aldehydes by oxidative reformylation [21].
- Liquid alkanes (\leq C₁₃) can be produced from CO₂ and H₂O on Co/TiO₂ catalyst by the Solar Photothermochemical Alkane Reverse Combustion (SPARC) method [22].
- Alkanes can be obtained from C₅-C₆ sugars through hydroxymethylfurfural, levulinic acid, and gamma-valerolactone.

- The simplest reaction pathway for the production of C₅-C₇ paraffins is the special hydrocracking of natural/waste fatty acids as a by-product and/or natural/waste fatty acid esters, e.g., waste cooking oil [23] or waste lards [24] from protein processing industry [25].

Based on the results of the presented publications it was concluded that by-products containing mainly C₅-C₇ paraffins can be obtained from different alternative sources. These by-products have very low octane numbers (<55–65) and contain undesirable components, such as olefins, aromatics, oxygenates, and other corrosive compounds; therefore, they are not suitable as gasoline blending components (“drop in fuel”). Isomerization and dehydrocyclization (aromatization) are the main chemical processes for the quality improvement of n-paraffins to enhance their octane number. Via isomerization the products are iso-paraffins, and via the dehydrocyclization process the obtained products are aromatics. Aromatics, including benzene, have very high octane numbers, e.g., the research octane number (RON) of benzene is 101. However, they are carcinogenic, therefore their concentration in gasoline must be reduced. Gasoline standards strictly limit the concentration of benzene, e.g., in California, USA, the limit is 0.62 v/v%, and in the EU this value is 1.0 v/v% [4].

No experimental results were provided in the publications about quality improvement, e.g., increasing the octane number of light gasoline fraction obtained from alternative sources. Based on the aforesaid reasons, the main research target of this paper was to investigate the quality improvement of benzene containing light hydrocarbons (rich in n-paraffins), from alternative sources via hydroisomerization. The main goal was also to convert the n-paraffins to branched paraffins with a higher octane number via hydrogenation, i.e., saturation of benzene to cyclo-hexane and its isomerization to methyl-cyclo-pentane.

2. Experimental Part

The aim of the research work was the investigation of quality improvement, mainly the octane number increasing possibilities of C₅/C₆ bioparaffin fractions by isomerization and the hydrogenation of benzene and oxygenates (e.g., methyl-/ethyl-formate, methyl-acetate, and 2-butanone) in one catalytic step. These light hydrocarbons were obtained as side products by the special hydrocracking of waste cooking oil to hydrocarbons in the boiling range of JET fuels/diesel fuels. The aim of the study was also the determination of favorable process parameters, such as temperature, liquid hourly space velocity, pressure, and hydrogen/feedstock ratio, for the conversion of C₅/C₆ fractions to hydrocarbons with a high octane number in different catalytic systems. In addition, the activity and selectivity of the two applied catalysts with different composition were compared during the experiments.

2.1. Apparatus

The catalytic experiments were carried out in an experimental apparatus (Figure 4) containing all the important equipment that can be found in the reactor system of a modern industrial hydrogenation/isomerization plant, e.g., dryer, compressor, pumps, feed vessel, pre-heater, reactor, cooler, separator, and flow meters, etc.. The composition of the products can be measured by gas chromatograph connected to the reactor system. It is important to emphasize that the reactors can be operated in parallel or serial. The length and diameter of the fixed bed reactors are 470 and 25 mm, respectively.

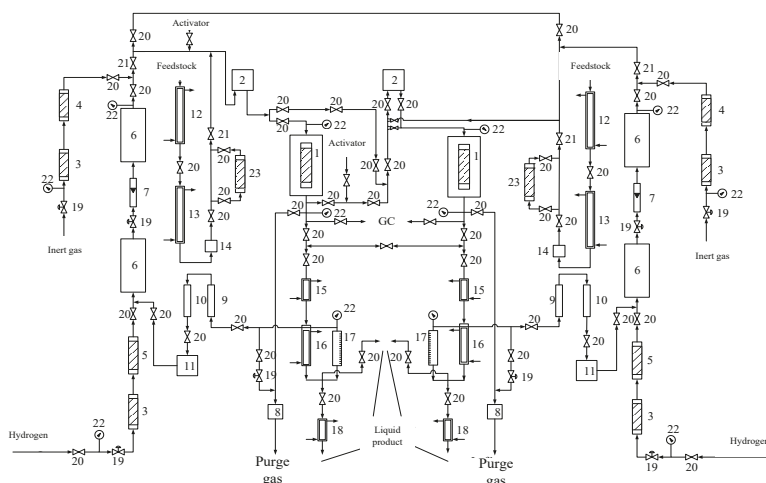


Figure 4. Simplified scheme of the experimental apparatus (1 reactor; 2 pre-heater; 3 oxygen transformer; 4, 5 gas dryer; 6, 10 gas-filter; 7 gas-flow meter; 8 gas-flow meter; 9 drop-holder; 11 compressor; 12, 13 feedstock vessel; 14 pump; 15, 18 cooler; 16 separator; 17 level detector; 19 controlling valve; 20 blocking valve; non-return valve; 22 pressure indicator; 23 feedstock dryer.

2.2. Materials and Methods

2.2.1. Feedstock

The main characteristics of alternative-origin biogasoline fractions used in the catalytic experiments are summarized in Table 1. Feedstock “A” was obtained from feedstock “B” by decreasing the water content, and removing sulfur and oxygen-containing compounds using Molecular Sieve 4A and 13X, respectively. This was because one of the chosen catalysts (Pt/Al₂O₃/Cl) for the experiments is very sensitive to the water and sulfur content of the feedstock.

Table 1. The main characteristics of light biogasoline fractions.

Characteristics	Feedstock	
	A	B
Composition, %		
C ₁ -C ₄	0.2	0.2
i-C ₅	3.9	4.0
n-C ₅	48.6	48.1
2,2-dimethylbutane (2,2-DMB)	<0.01	<0.01
2,3-dimethylbutane (2,3-DMB)	0.2	0.3
2-methylpentane (2-MP)	4.1	3.9
3-methylpentane (3-MP)	2.7	2.6
n-C ₆	36.8	37.3
methyl-cyclopentane	0.3	0.2
cyclohexane	1.0	1.1
benzene	1.3	1.4
ΣC ₇	0.9	0.9
Oxygen-containing compounds, mg/kg	n.d.	41
Sulfur content, mg/kg	<1.0	2.5
Water content, mg/kg	<1.0	14
C ₅ paraffin hydrocarbons in feedstock, %	52.5	52.1
Research octane number (RON)	48.4	48.6
Motor octane number (MON)	47.3	47.5
Sensibility (RON-MON)	1.1	1.1
Paraffin hydrocarbons, %	98.7	98.6
Total liquid i-, c-paraffin content, %	12.2	12.1

2.2.2. Catalysts and Adsorbents

Based on the preliminary experimental results with various kinds of catalysts, Pt/Al₂O₃/Cl and Pt/H-Mordenite/Al₂O₃ catalysts were selected for quality improvement of feedstock “A” and “B”, respectively. The main properties of the catalysts are summarized in Table 2.

Table 2. The main properties of catalysts used in the experiments.

Properties	Pt/Al ₂ O ₃ /Cl	Pt/H-Mordenite/Al ₂ O ₃
Pt-content, %	0.28	0.38
Pt-dispersion, %	84	89
Specific surface area (BET), m ² /g	426	448
Si/Al molar ratio	-	19.5
Chlorine content, % (Reactor I/Reactor II)	3.1/7.6	-
Length/diameter of catalyst extrudates (average, mm)	3.9/1.8	4.8/2.4

During the pre-selection of the catalysts, Pt/Al₂O₃/Cl showed the highest isomerization activity at favorably low temperatures. However, this catalyst is very sensitive to the water and sulfur content of the feedstock; thus, these impurities were removed from feedstock “B” to obtain feedstock “A” by commercial Molecular Sieves 4A and 13X purchased from Sigma-Aldrich. Hydrogenation and isomerization of feedstock “A” over the Pt/Al₂O₃/Cl catalyst were carried out in the reactor system where both reactors were operated in serial. Halogen content of the Pt/Al₂O₃/Cl in case of Reactor I was lower than that of Reactor II to ensure sufficiently available active sites for the hydrogenation of benzene and for the isomerization reactions. The catalyst volume in Reactor I (40 cm³) was half of the volume used in Reactor II (80 cm³) to avoid significant increases in temperature in Reactor I. This heat releases during the fast hydrogenation reaction of benzene to cyclohexane, and during isomerization reactions, which are also exothermic.

The catalytic isomerization of feedstock “B” over Pt/H-Mordenite/Al₂O₃ was carried out on one side of the same catalytic test apparatus. Compared to the commercial light gasoline isomerization catalysts (Pt-content: 0.30–0.34 %) used in industry, platinum content was slightly increased to 0.38%; this value was determined in previous experiments. Higher platinum content increases the number of available active metal sites of the catalyst for the hydrogenation of benzene, as well as the other hydrogenation/dehydrogenation reactions. A volume of 80 cm³ of catalyst was placed in the middle of the reactor and treated before the experiments as follows: dried at 150 °C for 2 h in nitrogen, heated to 300 °C at 25–30 °C/h in hydrogen atmosphere (40 dm³/h), temperature was held for 3 h, and then increased to 400 °C and held for 1 h.

2.2.3. Process Parameters

The process parameters of the systematic technological experiments over two different catalysts were varied in different ranges (Table 3).

Table 3. The process parameters of the experiments.

Process Parameters	Pt/Al ₂ O ₃ /Cl	Pt/H-Mordenite/Al ₂ O ₃
Temperature, °C	115–145	220–270
LHSV ¹ , h ⁻¹	1.0–3.0 ²	1.0–3.0
Pressure, bar	30	30
H ₂ /feedstock molar ratio	0.15:1.0	1.0:1.0

¹ Liquid hourly space velocity. ² for the total catalyst volume.

2.2.4. Analytical and Calculation Methods

Hydrocarbon composition of the feedstock and products was determined according to ASTM D 5134-13(2017) standard. Octane numbers of the feeds and products were calculated from their hydrocarbon composition and by blending octane numbers of the individual components. In order to evaluate the efficiency of isomerization and the yields of iso- and cyclo-paraffins, the thermodynamic equilibrium concentration (ATEC_T) was calculated according to Equation (1).

$$\text{ATEC}_T = \frac{(c_{i-Cx})_T}{(C_{i-Cx})_{ThT}} * 100 \quad (1)$$

where $(c_{i-Cx})_T$ is the concentration of the isomer at the actual temperature in the C₆ fraction of product, and $(C_{i-Cx})_{ThT}$ is the equilibrium concentration of the isomer.

The Pt content of the catalysts was determined by the inductively coupled plasma (ICP) method; the platinum dispersion of catalysts was determined by CO pulse chemisorption, and CO consumption was detected by a thermal conductivity detector. The Al and Si contents of H-Mordenite were also determined by the ICP method. The specific surface areas were determined by the Brunauer–Emmett–Teller (BET) method from the corresponding nitrogen adsorption isotherm. The chlorine content of catalysts was measured by the Volhard method [26]; the sample was dissolved in concentrated sulfuric acid and Cl ions were precipitated with silver nitrate solution. Excess silver solution was back titrated with a thiocyanate solution to give the amount of chlorine in the original sample. The chlorine contents of products were determined according to the ASTM D4929–19 (Standard Test Method for Determination of Organic Chloride Content in Crude Oil). The oxygen-containing compounds were detected by GC-MS. The water contents of the feedstock and products were determined by Coulometric Karl Fischer titration.

3. Results and Discussion

Catalysts and the optimal process parameter combinations for the quality improvement of biogasoline fractions were determined based on preliminary experimental results to obtain the most favorable experimental results.

The yield of gas and liquid product mixtures obtained from the two different catalysts differed in the function of process parameters. The yield of the gas products obtained in Reactor I from feedstock “A” over the Pt/Al₂O₃/Cl catalyst was higher than 99.3% in every case. This was due to the low chlorine content of the catalyst, the high liquid hourly space velocity (LHSV), and the low experimental temperature applied in Reactor I. The low chlorine content of the catalyst results in lower acidity, and thus lower cracking activity. The yields of products obtained from Reactor II decreased up to 2.1%, which was higher than in the case of Reactor I. This was due to the higher chlorine content, and thus higher acidity and cracking activity of the catalyst.

According to the above, the yields of the liquid products varied from 97.2% to 99.4% in the function of process parameters, as shown in Table 4. These yield values are high even from an industrial perspective. The lowest acceptable yield value for a light naphtha isomerization unit is 92%. Data in Table 4 illustrate well that the gas production was low (0.6–2.8 %), due to the reasons mentioned above.

The yield of gas phase products (C₁–C₄) obtained from feedstock “B” on the Pt/H-Mordenite/Al₂O₃ catalyst was below 5% up to 250 °C at every LHSV. At higher temperatures and lower LHSV the yield of gas products sharply increased because the cracking reactions took place to a greater extent (Table 5). About 45% of the gas phase product was i-butane, which can be utilized for alkylate production or as an LPG (propane-butane gas) blending component.

Table 4. Yield of the liquid products in the function of process parameters (catalyst: Pt/Al₂O₃/Cl, feedstock: "A").

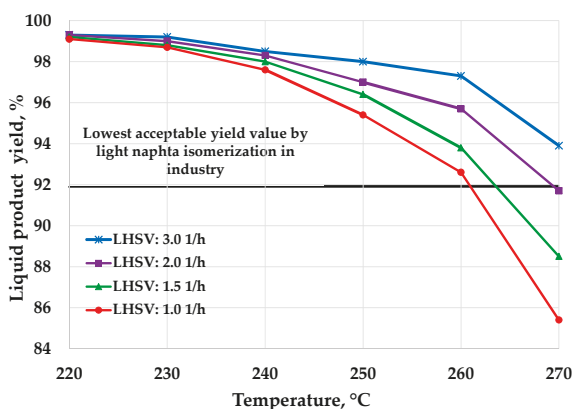
Liquid Hourly Space Velocity ¹ , h ⁻¹	Yield of Liquid Products, %			
	115 °C	125 °C	135 °C	145 °C
1.0	98.6	98.1	97.6	97.2
1.33	98.8	98.3	97.9	97.4
1.66	99.1	98.6	98.2	97.7
2.0	99.4	98.9	98.5	98.0

¹ LHSV values for the total catalyst volume of Reactor I and II.

Table 5. Yield of the gas products as a function of process parameters (catalyst: Pt/H-Mordenite/Al₂O₃, feedstock: "B").

LHSV, h ⁻¹	Yield of Gas Products, %					
	220 °C	230 °C	240 °C	250 °C	260 °C	270 °C
1.0	0.9	1.3	2.4	4.6	7.4	14.6
1.5	0.8	1.2	2.0	3.6	6.2	11.5
2.0	0.7	1.0	1.7	3.0	4.3	8.3
3.0	0.7	0.8	1.5	2.0	2.7	6.1

According to the yield data of gas products, the yield value of the liquid products changed in opposite tendency due to the above-mentioned cracking reactions (Figure 5). The yield of liquid products changed between 85.4% and 99.3%. The lowest values were obtained under the strictest process parameters, at high temperature (T: 270 °C) and high residence time (LHSV: 1.0 h⁻¹) in the catalytic system. Curves in Figure 5 illustrate well that iso-paraffins can be obtained with high yield from high n-paraffin containing biogasoline fractions for a wide range of process parameters.

**Figure 5.** Change of liquid product yields as a function of temperature and LHSV (catalyst: Pt/H-Mordenite, feedstock: "B").

Based on the gas and liquid product yields obtained from the different catalysts, it was concluded that the liquid yield obtained from Pt/Al₂O₃/Cl was significantly higher than in the case of Pt/H-Mordenite/Al₂O₃. The reason for this was because the cracking reactions took place to a lesser extent due to the lower isomerization temperature.

In order to evaluate the isomerization reaction results, the thermodynamic equilibrium concentration (ATEC) was determined for the individual components in the C₅ and C₆ fractions

as a function of process parameters. The isomerization activity of the catalyst was monitored by the concentration of 2-methyl-butane (2-MB in C₅ fraction) and 2,2-dimethyl-butane (2,2-DMB in C₆ fraction). Only 2-MB can be formed from n-pentane during isomerization; 2,2-dimethyl-propane (2,2-DMP) cannot be formed due to the steric and reaction mechanism reasons. The 2,2-DMB component has the lowest reaction rate among the hexane isomers; its formation is the rate-determining step of the isomerization of n-hexane, and its equilibrium concentration depends mainly on the reaction temperature [27].

Figure 6a,b demonstrate the ATEC values of 2-MB and 2,2-DMB in the liquid products obtained from feedstock “A” on the Pt/Al₂O₃/Cl catalyst as a function of process parameters.

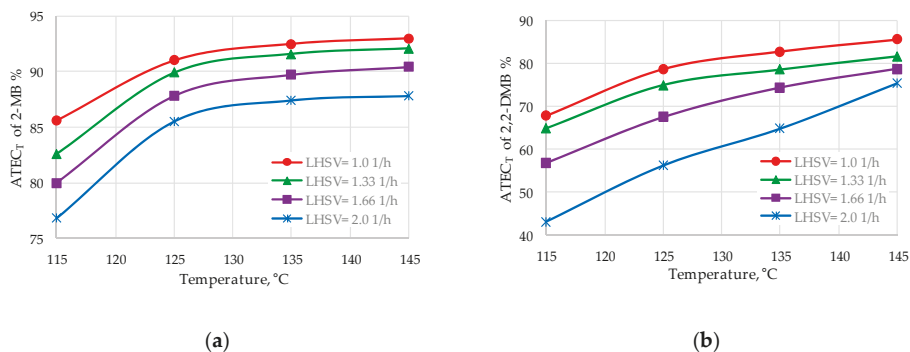


Figure 6. ATEC of 2-MB (a) and 2,2-DMB (b) as a function of temperature and LHSV (catalyst: Pt/Al₂O₃/Cl, feedstock: “A”).

As a comparison, ATEC values of 2-MB and 2,2-DMB in the liquid products obtained from feedstock “B” on the Pt/H-Mordenite/Al₂O₃ catalyst as a function of process parameters are shown in Figure 7a,b.

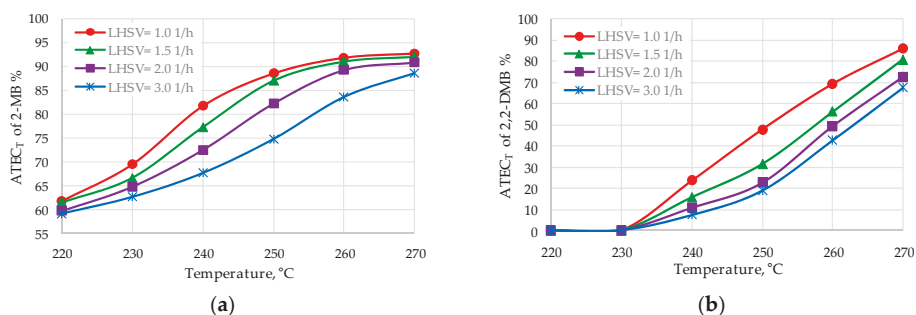


Figure 7. ATEC of 2-MB (a) and 2,2-DMB (b) as a function of temperature and LHSV (catalyst: Pt/H-Mordenite/Al₂O₃, feedstock: “B”).

Curves in Figure 6a,b and Figure 7a,b demonstrate well that the concentrations of the two emphasized isomers increasingly approach the thermodynamic equilibrium concentrations by increasing the reaction temperatures and decreasing the LHSV. However, the extent of the increase in ATEC values lessened by increasing the temperature, especially at 125–145 °C and 250–270 °C, respectively, at lower LHSV. The reason for this is that the process parameters have less impact on the reaction rate near to the equilibrium concentrations. This is also supported by the fact that in case of the Pt/Al₂O₃/Cl catalyst, the ATEC values of 2-MB at the temperature of 125–145 °C and LHSV

of 1.0–1.66 h⁻¹ were 87.8–93.0%, with an absolute difference of 5.2%, while, in the case of 2,2-DMB, these values changed between 67.5% and 85.6%, with an absolute difference of 18.1%. However, in the case of the Pt/H-Mordenite/Al₂O₃ catalyst, the ATEC values of 2-MB at a temperature of 250–270 °C and LHSV of 1.0–1.5 h⁻¹ were 87.0–92.8%, with an absolute difference of 5.8%, while, in the case of 2,2-DMB, these values changed between 32.1% and 86.8%, with an absolute difference of 54.7%.

Based on the results of a previous publication [28] it was shown that among the C₆ i-paraffins obtained, the ATEC value of 2,3-dimethylbutane (2,3-DMB), 2-methylpropane (2-MP), and 3-methylpropane (3-MP) were significantly higher than in the case of 2,2-DMB. To prove this phenomenon in the present study, ATEC values of 2-MP obtained from both feedstocks on the applied catalysts are illustrated in Figure 8a,b.

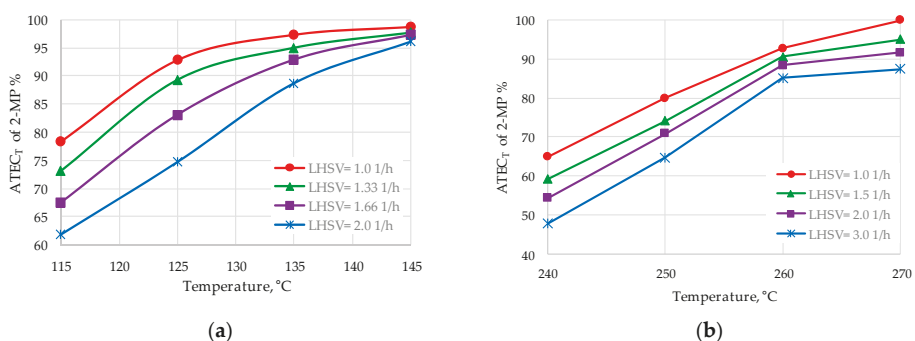


Figure 8. ATEC values of 2-MP (a) (catalyst: Pt/Al₂O₃/Cl, feedstock: "A"); and 2-MP (b) (catalyst: Pt/H-Mordenite/Al₂O₃, feedstock: "B") as a function of temperature and LHSV.

The highest ATEC values of the individual i-paraffins presented in the figures were obtained at 145 °C (Pt/Al₂O₃/Cl) and at 270 °C (Pt/H-Mordenite/Al₂O₃) at LHSV of 1.0 h⁻¹. However, the liquid yields were the lowest due to the high hydrocracking activity of catalysts at these process parameters. It is also important to emphasize that the highest possible equilibrium concentrations of 2-MB and 2,2 DMB at the highest experimental temperature are the lowest, because these values are decreasing approximately exponentially with increasing temperature due to the exothermic skeletal isomerization reactions [4].

Based on the results obtained from the two different catalysts, the most favorable process parameter combinations for the isomerization of benzene containing bio-originated C₅–C₆ fractions are the following: temperature, 125–135 °C; LHSV, 1.0–1.33 h⁻¹ (Pt/Al₂O₃/Cl); and temperature, 260 °C; LHSV, 1.0–1.5 h⁻¹ (Pt/H-Mordenite/Al₂O₃). The benzene content of the target products was <0.05 mg/kg, and oxygenate content was not detected, thus the hydrogenation was complete. The main properties of the liquid products obtained over both catalysts at favorable process parameter combinations are summarized in Table 6. From the results, it was concluded that in the case of the Pt/Al₂O₃/Cl catalyst the yield of the liquid products and their research octane number was higher with ca. 5% and 4–5 units, respectively, compared to the results obtained on Pt/H-Mordenite/Al₂O₃. When the n-paraffins and the mono-methyl pentanes having low octane number were recirculated with 95%, the RON of the products could reach 92. This is a good result taking into account that the feedstock was benzene free. It is noted that benzene has a high research octane number (101), and its hydrogenation to cyclohexane results in a lower octane number (84). This decrease in octane should be compensated for by the production of isomers having a very high RON. These i-paraffins are free of sulfur and aromatics; consequently, during their application in internal combustion engines compared to current engine fuels, the pollutant emission is lower and contains less harmful pollutants.

Table 6. Main characteristics of liquid products obtained over Pt/Al₂O₃/Cl and Pt/H-Mordenite catalysts at favorable process parameters (respectively: temperature, 125–135 °C; LHSV, 1.0–1.33 h⁻¹; and temperature, 260 °C; LHSV, 1.0–1.5 h⁻¹).

Characteristics	Products	
	Pt/Al ₂ O ₃ /Cl	Pt/H-Mordenite
Liquid yield, % (0 % recirculation)	97.6–98.3	92.9–93.8
ATEC, %		
2-MB	89.9–92.5	90.5–91.8
2,2-DMB	75.0–82.8	57.6–70.4
2-MP	89.3–97.3	90.5–92.7
RON/MON (0 % recirculation)	79.4–80.9/78.1–79.5	74.9–76.4/73.9–75.4
Sensibility (RON-MON)	1.3–1.4	1.1–1.0
ΔRON/ΔMON (product-feedstock)	30.8–32.3/29.5–32.0	24.7–28.0/24.7–28.1
Liquid yield, % (95 % n-Cx recirculation)	75.4–78.1	68.1–69.3
RON/MON (95 % n-Cx recirculation)	87.1–88.8/85.3–86.7	84.1–85.3/83.0–84.3
Sensibility (RON-MON)	1.8–2.1	1.1–1.0
Liquid yield, % (95 % n-Cx, 2-MP, 3-MP recirculation)	57.6–60.4	52.7–54.8
RON/MON (95 % n-Cx, 2-MP, 3-MP recirculation)	91.7–92.3/90.0–90.7	88.7–90.0/87.5–88.9
Sensibility (RON-MON)	1.7–1.6	1.2–1.3

4. Conclusions

The catalytic isomerization process applying Pt/Al₂O₃/Cl and Pt/H-Mordenite/Al₂O₃ catalysts at favorable process parameters (respectively: temperature = 125–135 °C, LHSV = 1.0–1.33 h⁻¹; and temperature = 260 °C; LHSV = 1.0–1.5 h⁻¹; P = 30 bar; H₂/feedstock molar ratio = 0.15:1.0) is suitable to enhance the octane number of light biogasoline fractions containing benzene and oxygenates. The increase in octane number compared to the feedstock was ca. 32 and ca. 27 units, respectively. The yield of liquid products was high (ca. 98% and ca. 93%) and contained only paraffin hydrocarbons, primarily i-paraffins depending on the extent of recirculation of components having a low octane number. The thermodynamic equilibrium concentration values of these i-paraffins was around 75–95% and 56.1–92.7%. These light biogasoline blending components produced from renewable feedstocks by the presented catalytic hydroisomerization process with Pt/Al₂O₃/Cl and Pt/H-Mordenite/Al₂O₃ catalysts have lower pollutant emissions during their application. Unlike Pt/H-Mordenite/Al₂O₃, the Pt/Al₂O₃/Cl catalyst is very sensitive to water, sulfur, and oxygen-containing compounds; thus, feedstock needs to be pre-treated. However, the isomerization process at lower temperatures is energy and feedstock efficient (cracking reactions take place to a lesser extent). Moreover, the octane number of the products is higher by ca. 5 units. These factors more than compensate for the costs of the feedstock pre-treatment.

Author Contributions: Conceptualization, J.H.; methodology, J.H. and O.V.; validation, J.H. and T.K.; formal analysis, O.V.; investigation, J.H., T.K. and O.V.; resources, T.K.; data curation, O.V.; writing—original draft preparation, J.H. and O.V.; writing—review and editing, J.H., T.K. and O.V.; visualization, O.V.; supervision, J.H.; funding acquisition, J.H. All authors have read and agreed to the published version of the manuscript.

Acknowledgments: The authors acknowledge the financial support of the project of the Economic Development and Innovation Operative Programme of Hungary, GINOP-2.3.2-15-2016-00053: Development of liquid fuels having high hydrogen content in the molecule (contribution to sustainable mobility) and the project of Széchenyi 2020 under the EFOP-3.6.1-16-2016-00015: University of Pannonia's comprehensive institutional development program to promote Smart Specialization Strategy. The Project is supported by the European Union and co-financed by Széchenyi 2020.

Conflicts of Interest: The authors declare no conflict of interest.

References

1. BP Statistical Review of World Energy. Available online: <https://www.bp.com/content/dam/bp/business-sites/en/global/corporate/pdfs/energy-economics/statistical-review/bp-stats-review-2019-full-report.pdf> (accessed on 9 March 2020).
2. ExxonMobil, Outlook for Energy 2019: A Perspective to 2040. Available online: https://corporate.exxonmobil.com/-/media/Global/Files/outlook-for-energy/2019-Outlook-for-Energy_v4.pdf (accessed on 5 March 2020).
3. Be Future Forward, Honeywell UOP. Available online: https://www.digitalrefining.com/article_1002373.pdf (accessed on 6 January 2020).
4. Srivastava, S.P.; Hancsók, J. *Fuels and Fuel-Additives*; John Wiley & Sons: Hoboken, NJ, USA, 2014; p. 374.
5. European Parliament, 2018, Directive of the European Parliament and of the Council cast, 2016/0382 (COD). Available online: <http://data.consilium.europa.eu/doc/document/PE-48-2018-INIT/en/pdf> (accessed on 5 February 2020).
6. Mansouri, A.; Rihani, R.; Laoufi, A.N.; Özkan, M. Production of bioethanol from a mixture of agricultural feedstocks: Biofuels characterization. *FUEL* **2016**, *185*, 612–621. [[CrossRef](#)]
7. Abdellatif, F.H.H.; Babin, J.; Arnal-Herault, C.; Nouvel, C.; Six, J.-L.; Jonquieres, A. Bio-based membranes for ethyl-tert-butyl-ether (ETBE) bio-fuel purification by pervaporation. *J. Membr. Sci.* **2017**, *524*, 449–459. [[CrossRef](#)]
8. Manzetti, S.; Andersen, O. A review of emission products from bioethanol and its blends with gasoline. Background for new guidelines for emission control. *FUEL* **2015**, *140*, 293–301. [[CrossRef](#)]
9. Toor, M.; Kumar, S.S.; Malyan, S.K.; Bishnoi, N.R.; Mathimani, T.; Rajendran, K.; Pugazhendhi, A. An overview on bioethanol production from lignocellulosic feedstocks. *Chemosphere* **2020**, *242*, 125080. [[CrossRef](#)] [[PubMed](#)]
10. Padella, M.; O’Connell, A.; Prussi, M. What is still Limiting the Deployment of Cellulosic Ethanol? Analysis of the Current Status of the Sector. *Appl. Sci.* **2019**, *9*, 4523. [[CrossRef](#)]
11. Sauciu, A.; Abosteif, Z.; Weber, G.; Potetz, A.; Rauch, R.; Hofbauer, H.; Schaub, G.; Dumitrescu, L. Influence of operating conditions on the performance of biomass-based Fischer-Tropsch synthesis. *Biomass. Convers. Bior.* **2012**, *2*, 253–263. [[CrossRef](#)]
12. Ershov, M.; Potanin, D.; Guseva, A.; Abdellatif, T.M.M.; Kapustin, V. Novel strategy to develop the technology of high-octane alternative fuel based on low-octane gasoline Fischer-Tropsch process. *FUEL* **2020**, *261*, 116330. [[CrossRef](#)]
13. Atashi, H.; Dinarvandi, K. Determination of selectivity equations heavy and light product of petroleum on iron based catalysts in Fischer-Tropsch synthesis. *Petrol. Sci. Technol.* **2019**, *37*, 2035–2042. [[CrossRef](#)]
14. Wang, T.; Zhang, Q.; Ding, M.; Wang, C.; Li, Y.; Zhang, Q.; Ma, L. Bio-gasoline production by coupling of biomass catalytic pyrolysis and oligomerization. *Energy Proced.* **2017**, *105*, 858–863. [[CrossRef](#)]
15. Fehér, C.; Tomasek, S.; Hancsók, J.; Skoda-Földes, R. Oligomerization of light olefins in the presence of a supported Brønsted acidic ionic liquid catalyst. *Appl. Catal. B-Environ.* **2018**, *239*, 52–60. [[CrossRef](#)]
16. Kwon, E.E.; Kim, Y.T.; Kim, H.J.; Lin, K.Y.L.; Kim, K.H.; Lee, J.; Huber, G.W. Production of high-octane gasoline via hydrodeoxygenation of sorbitol over palladium-based bimetallic catalysts. *J. Environ. Manage.* **2018**, *227*, 329–334. [[CrossRef](#)] [[PubMed](#)]
17. Herz, G.; Reichelt, E.; Jahn, M. Design and evaluation of a Power-to-Liquid process for the production of valuable hydrocarbons from CO₂ and H₂O. *DGMK Tag.* **2017**, *2*, 181–186.
18. Mesfun, S.; Sanchez, D.L.; Leduc, S.; Wetterlund, E.; Lundgren, J.; Biberacher, M.; Kraxner, F. Power-to-gas and power-to-liquid for managing renewable electricity intermittency in the Alpine Region. *Renew Energy* **2017**, *107*, 361–372. [[CrossRef](#)]
19. Mohsenzadeh, A.; Zamani, A.; Taherzadeh, M.J. Bioethylene Production from Ethanol: A Review and Techno-economical Evaluation. *Chem. Bio. Eng. Rev.* **2017**, *4*, 75–91. [[CrossRef](#)]
20. Huber, G.W.; Chedda, J.N.; Barre, C.J.; Dumestic, J.A. Production of liquid alkanes by aqueous-phase processing of biomass-derived carbohydrates. *Science* **2005**, *308*, 1446–1450. [[CrossRef](#)] [[PubMed](#)]
21. Shokri, D.; Que, L. Conversion of Aldehyde to Alkane by a Peroxoiron(III) Complex: A Functional Model for the Cyanobacterial Aldehyde-Deformylating Oxygenase. *J. Am. Chem. Soc.* **2015**, *137*, 7686–7691. [[CrossRef](#)]
22. Chanmanee, W.; Islam, M.F.; Dennis, B.H.; MacDonell, F.M. Solar photothermochemical alkane reverse combustion. *PNAS* **2016**, *113*, 2579–2584. [[CrossRef](#)]

23. Bezergianni, S.; Kalogianni, A. Hydrocracking of used cooking oil for biofuels production. *Bioresour. Technol.* **2009**, *100*, 3927–3932. [[CrossRef](#)]
24. Rosson, E.; Sgarbossa, P.; Pedrielli, F.; Mozzon, M.; Bertani, R. Bioliquids from raw waste animal fats: An alternative renewable energy source. *Biomass Conv. Bioref.* **2020**. [[CrossRef](#)]
25. Baladincz, P.; Hancsók, J. Fuel from waste animal fats. *Chem. Eng. J.* **2015**, *282*, 152–160. [[CrossRef](#)]
26. Jeffery, G.H.; Bassett, J.; Mendham, J.; Denney, R.C. *Vogel's Textbook of Quantitative Chemical Analysis*, 5th ed.; Longman Scientific & Technical: New York, NY, USA, 1989; pp. 355–356.
27. Hancsók, J.; Holló, A.; Debreczeni, É.; Perger, J.; Kalló, D. Benzene saturating isomerization. *Stud. Surf. Sci. Catal.* **1999**, *125*, 417–424.
28. Holló, A.; Hancsók, J.; Kalló, D. Kinetics of hydroisomerization of C₅–C₇ alkanes and their mixtures over platinum containing mordenite. *Appl. Catal. A-Gen.* **2002**, *229*, 93–102.



© 2020 by the authors. Licensee MDPI, Basel, Switzerland. This article is an open access article distributed under the terms and conditions of the Creative Commons Attribution (CC BY) license (<http://creativecommons.org/licenses/by/4.0/>).

Article

Nonlinear Finite Element Analysis-Based Flow Distribution and Heat Transfer Model [†]

Tomáš Létal *, Vojtěch Turek, Dominika Babička Fialová and Zdeněk Jegla

Institute of Process Engineering, Faculty of Mechanical Engineering, Brno University of Technology, Technická 2, 61669 Brno, Czech Republic; turek@fme.vutbr.cz (V.T.); Dominika.Fialova@vutbr.cz (D.B.F.); zdenek.jegla@vut.cz (Z.J.)

* Correspondence: letal@fme.vutbr.cz

[†] This paper is an extended version of our paper presented at the 22nd Conference on Process Integration for Energy Saving and Pollution Reduction-PRES'19, Agios Nikolaos, Crete, Greece, 20–23 October 2019, and published in Chem. Eng. Trans. 2019, 76, 157–162, doi:10.3303/CET1976027.

Received: 27 February 2020; Accepted: 27 March 2020; Published: 2 April 2020

Abstract: A new strategy for fast, approximate analyses of fluid flow and heat transfer is presented. It is based on Finite Element Analysis (FEA) and is intended for large yet structurally fairly simple heat transfer equipment commonly used in process and power industries (e.g., cross-flow tube bundle heat exchangers), which can be described using sets of interconnected 1-D meshes. The underlying steady-state model couples an FEA-based (linear) predictor step with a nonlinear corrector step, which results in the ability to handle both laminar and turbulent flows. There are no limitations in terms of the allowed temperature range other than those potentially stemming from the usage of fluid physical property computer libraries. Since the fluid flow submodel has already been discussed in the referenced conference paper, the present article focuses on the prediction of the tube side and the shell side temperature fields. A simple cross-flow tube bundle heat exchanger from the literature and a heat recovery hot water boiler in an existing combined heat and power plant, for which stream data are available from its operator, are evaluated to assess the performance of the model. To gain further insight, the results obtained using the model for the heat recovery hot water boiler are also compared to the values yielded by an industry-standard heat transfer equipment design software package. Although the presented strategy is still a “work in progress” and requires thorough validation, the results obtained thus far suggest it may be a promising research direction.

Keywords: flow distribution; process and power industry equipment; finite element analysis

1. Introduction

During design, operation, and troubleshooting of various process and power equipment-containing tube bundles, it often is important to know the velocity and temperature fields in both the tube and the shell sides. These are obtained predominantly using Computational Fluid Dynamics (CFD) models and, therefore, articles covering a wide range of such applications are available. For example, Wei et al. [1] discussed a coupled CFD-Lagrange multipliers optimization method for flow distribution adjustments to prevent freezing of power generation natural draft cooling systems during winter operation. Chien et al. [2], on the other hand, presented a coupled CFD-surrogate-based optimization of flow distribution in a heat exchanger inlet header. Zhou et al. [3] focused on CFD investigation and optimization of a compact heat exchanger comprising a single row of tubes, and Łopata et al. [4] published an article covering the experimental investigation of flow distribution in a similar cross-flow heat exchanger, but with a tube bank consisting of elliptical tubes. CFD evaluation and optimization of solar collectors, commonly also using a single row of risers, were discussed, for instance, by García-Guendulain et al. [5], who aimed to improve the collector performance by changes of riser-to-header cross-sectional area

and diameter ratios. Karvounis et al. [6] carried out a numerical and experimental study of the flow field in a forced circulation Z-type flat plate solar collector. Articles focusing on two-phase flow are also common. Li et al. [7] studied flow reversal in vertically inverted U-tube steam generators used in marine nuclear power plants, whereas Klenov and Noskov [8] investigated the effect of two-phase flow pattern in an inlet duct on flow distribution in the upper part of a trickle bed reactor. As for dispersion headers, which are often used in flue gas cleaning equipment, a CFD investigation of the impacts of inlet flow rate, hole diameter, and downstream distance on the flow distribution in an annular multi-hole header was presented by He et al. [9]. Other frequent research areas where the knowledge of flow distribution is critical are fuel cells and micro-channel heat exchangers. One might mention, e.g., the CFD and laser Doppler velocimetry investigation of flow distribution in a polymer electrolyte membrane fuel cell stack by Bürkle et al. [10], the CFD evaluation of pressure and flow distribution effects on the performance of polymer electrolyte membrane fuel cells by Heck et al. [11], or the CFD optimization of a liquid cooling system of a power inverter in an electric vehicle presented by Hur et al. [12]. Various studies involving liquid-cooled micro-channel heat sinks for electronics are quite common as well. See, e.g., the article by Li et al. [13] discussing the optimization of the micro-channel topology.

Studies not utilizing CFD are much less common and, typically, focus on evaluations of the respective equipment via physical experiments. To name just a few, one could mention the experimental investigation of flow distribution and its effect on the performance of a plate-fin heat exchanger by Zhu et al. [14], the study of two-phase refrigerant distribution in a finned-tube evaporator by Tang et al. [15], or the article by Quintanar et al. [16] covering natural circulation flow distribution in a multi-branch manifold. Micro-channel equipment was discussed, e.g., by Yih and Wang [17], who carried out an experimental investigation of the thermal-hydraulic performance of a micro-channel heat exchanger for waste heat recovery, or by Lugarini et al. [18], who focused on the evaluation of flow distribution uniformity in a comb-like micro-channel network. On the other end of the size spectrum are heat exchanger networks, in which Ishiyama and Pugh [19] studied thermo-hydraulic channeling in the individual parallel branches. In their paper, they also presented a model for prediction of flow distribution in the branches for the case when no flow control was implemented. Similarly, Novitsky et al. [20] discussed multilevel modeling and optimization of large-scale pipeline systems using specialized software tools. In these two studies, however, modelling of pressure drop was only done in a simplified manner. Korelstein [21], on the other hand, discussed mathematical properties of classical hydraulic network flow distribution problems which included pressure-dependent closure relations. An essentially identical problem can also be encountered when it comes to the design of water distribution networks. Still, proper inclusion of pressure drop in the respective models is rare because they generally focus on layout optimization while meeting the local water demands (see, for instance, the article by Cassiolato et al. [22], who proposed a Mixed-Integer Nonlinear Programming (MINLP) model for this purpose), identification of sources of contamination (as done, e.g., using a convolutional neural network by Sun et al. [23]), detection of leakage points (see, for example, the article by Fang et al. [24]), evaluation of the network performance and reliability (as discussed, e.g., in the Hanoi case study by Jeong and Kang [25]), etc.

To the best of the authors' knowledge, there currently is no semi-accurate but fast Finite Element Analysis-based model of fluid flow other than [26] that would properly include the pressure drop. This model, however, does not consider heat transfer and, thus, is of limited practical value to the designers of process and power equipment. Consequently, CFD models, because of their significant computational cost, are being employed for evaluations of fluid flow distribution and heat transfer only if absolutely necessary. As a result, the corresponding temperature fields, which, to a large degree, depend on mass flow rates through individual tubes, are also unknown. This may not pose significant problems if thermal stress is relatively even throughout the tube bundle in question. Nonetheless, mechanical failures of bundles, stemming from improper design procedures which a priori assume uniform flow distribution, are not uncommon when it comes to heat exchangers featuring large changes

in stream temperatures. The present paper, therefore, introduces a significantly extended version of the flow-only, adiabatic model discussed in [26]. This includes heat transfer between the fluids in the tube and the shell sides of a cross-flow tube bank heat exchanger (e.g., an economizer) as well as various other improvements. Shell-side flow was modelled as unidirectional. As test cases, a simple cross-flow tube bundle heat exchanger from the literature and an existing heat recovery hot water boiler, for which the necessary data had been provided by its operator, were considered. These were compared to the results obtained using the present model and, to gain further insight, also to the data from an industry-standard heat exchanger design software package. A good agreement among the data sets was observed.

2. Materials and Methods

The original model discussed in [26] assumed adiabatic flow, that is, no heat transfer was allowed on the walls of the parallel flow channels in the distribution system. The model was shown in the same article to provide data with relative errors of at most 4% compared to detailed transient CFD simulations even in the case of highly turbulent flows. Such accuracy was achievable due to the relative simplicity of the flow systems for which the respective model has been intended (e.g., tube bundles in heat recovery steam generators). The overall conclusion, therefore, was that, in terms of application in preliminary analyses of selected heat transfer equipment or for shape optimization of the mentioned equipment, the model was suitable for engineering practice.

Because of the nature of the model, its performance in case of laminar flow was a priori expected to be acceptable. Although several tests were carried out earlier even with low total mass flow rates to make sure this really was the case, no example was given in [26]. To remedy this, let us mention, for instance, one of the test flow distribution systems (see Figure 1) used in the original article and the respective laminar flow distribution data and relative errors. For convenience’s sake, parameters of the flow system are listed in Table 1. The obtained mass flow rates are compared in Figure 2a, while Figure 2b shows the corresponding relative errors. It can be seen that the error values generally were in a $\pm 1\%$ band with only two of them being at around 1.2%. Relative errors obtained using other test flow systems were of similar magnitudes. Thus, one could conclude that, in the case of laminar flow, the accuracy was even better than when the flow was highly turbulent.

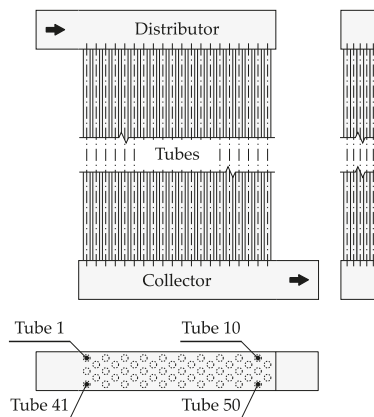


Figure 1. Schematic of the flow distribution system from Table 1.

Table 1. Parameters of the flow distribution system used to obtain the laminar flow-related data shown in Figure 1.

Parameter	Value
headers (W × H × L)	55 × 55 × 280 mm
tube bundle	5 rows with 10 tubes each, tube layout: 60°
tubes	straight, inner diameter: 10 mm, length: 2000 mm
fluid	water, 0.5 kg s ⁻¹ , 300 K
flow regime	laminar, average tube Re ≈ 1500

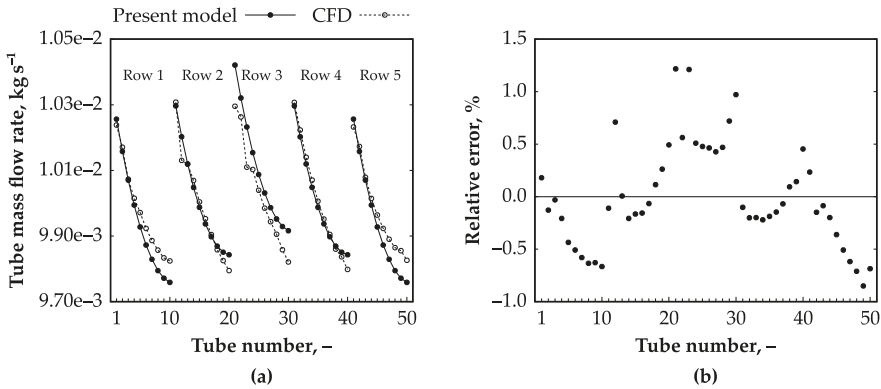


Figure 2. (a) Tube mass flow rates obtained for the flow system from Table 1 using the model based on Finite Element Analysis (FEA) discussed in [26] and a transient Computational Fluid Dynamics (CFD) simulation. Average tube Reynolds number was ca. 1500. (b) The corresponding relative tube mass flow rate errors (FEA vs. CFD simulation). Tube numbers correspond to Figure 1. For the details regarding the CFD model, the reader is kindly referred to [27].

2.1. Inclusion of Heat Transfer into the Model

The main shortcoming of the original, flow-only version of the Finite Element Analysis (FEA)-based model was its inability to properly evaluate tube bundles in which heat transfer could not be neglected. Given the intended purpose of the model (that is, usage in engineering practice), this functionality had to be implemented.

Please note that heat transfer was not, strictly speaking, evaluated using FEA. However, the temperature fields in the tube side and the shell side were still obtained using a system of linear equations generated as shown in the following text, and this system was then solved in the usual manner. It was assumed that the temperature profile between two end nodes of an edge was continuous and was given by the mean temperatures on control volume cross-sections, which were perpendicular to the corresponding edge. The iterative solver then worked similarly to any other segregated solver. First, the fluid flow (FEA-based) submodel was solved under the assumption of a constant temperature field. Next, the heat transfer submodel was solved under the assumption of a constant velocity field. This was followed by the update of the fluid physical properties and other necessary post-iteration tasks, and then the fluid flow submodel was solved again. This iterative procedure was repeated until convergence was reached.

Even though the heat transfer submodel was not using FEA, the corresponding mesh on which the temperature field was calculated can be constructed in a similar manner. In the fluid flow mesh, the field to be calculated was described by total pressures in the nodes. The temperature field can be described analogously with the difference being that every edge had its own temperature in the node. Figure 3 shows the two meshes and the differences between meshes.

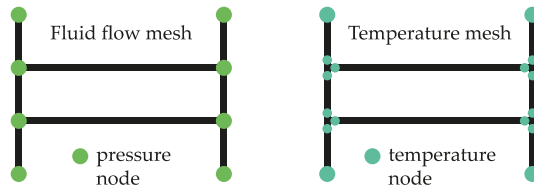


Figure 3. Comparison of the fluid flow mesh (left) and the temperature mesh (right). The fluid flow mesh consists of 8 edges with 8 nodes total, and there are 8 unknown pressures (in the green nodes, some of which are shared between edges); in the temperature mesh, there are $2 \times 8 = 16$ nodes and, therefore, 16 unknown temperatures.

As mentioned before, the temperatures were calculated using a set of linear equations. From Figure 3 it is clear that a flow system consisting of n edges will feature $2n$ node temperatures and, therefore, $2n$ linear equations were required. There were three classes of temperature-related equations that were used in the model:

- Flow mixing and splitting,
- Heat transfer through channel walls, and
- Boundary conditions.

2.1.1. Flow Mixing and Splitting

When, in an arbitrary mesh node, streams q_1, q_2, \dots, q_m are mixed into a single stream j , we can write

$$\sum_{q \in \{q_1, q_2, \dots, q_m\}} \dot{m}_q c_{p,q} (T_j - T_q) = 0. \tag{1}$$

Here, \dot{m}_q denotes the mass flow rate of the q th stream, $c_{p,q}$ the specific heat capacity, and T_j and T_q the corresponding stream temperatures. Each specific heat capacity should be taken as the mean value obtained for the corresponding temperature range $[T_j, T_q]$.

If, on the other hand, a single stream j is split into streams r_1, r_2, \dots, r_n , the outflow temperature is the same for all these streams, and the respective n equations are

$$T_r = T_j, \quad r \in \{r_1, r_2, \dots, r_n\}. \tag{2}$$

In some systems, there may be blind edges with zero mass flow rate. The temperatures in the nodes of these edges are calculated as if the edges were of the regular type featuring outflow (see also the schematic in Figure 4).

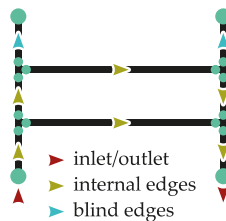


Figure 4. Internal flows in a system vs. flow mixing; there are 4 locations (the T-joints) for which the flow mixing/splitting equations must be present in the final linear system.

In a general case with streams q_1, q_2, \dots, q_m being mixed and then split into streams r_1, r_2, \dots, r_n , one will get one Equation (1) governing the resulting outflow temperature T_j and $(n - 1)$ Equation (2),

that is, $(n - 1)$ identities for the remaining outflow temperatures. The total number of equations governing the mixing/splitting in the node will, therefore, be equal to number of outflow streams.

2.1.2. Heat Transfer through Channel Walls

Let us have two meshes representing the tube and the shell sides of a heat exchanger and focus on an arbitrary pair of adjacent control volumes representing a portion of the tube side (i.e., a tube segment) and the enclosing portion of the shell side (see Figure 5). Let $\dot{m}_t, c_{p,t}, T_{t,1}$, and $T_{t,2}$ denote the tube side mass flow rate, mean specific heat capacity at constant pressure, and inlet and outlet temperatures and $\dot{m}_s, c_{p,s}, T_{s,1}$, and $T_{s,2}$ the corresponding shell-side quantities.

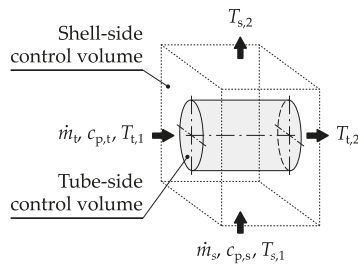


Figure 5. A pair of adjacent control volumes representing a portion of the tube side and the enclosing portion of the shell side.

Should, e.g., the hot fluid be placed in the shell side, then the overall heat balance could be written as

$$\dot{m}_t c_{p,t} (T_{t,2} - T_{t,1}) = \dot{m}_s c_{p,s} (T_{s,1} - T_{s,2}). \tag{3}$$

Let us for a moment assume that the temperature of the fluid in the shell-side control volume is constant and is equal to the shell-side inlet temperature, $T_{s,1}$. Let us also assume that the tube-side inlet temperature, $T_{t,1}$, is known. Additionally, let L denote the length of the tube-side mesh edge and U the cumulative overall heat transfer coefficient. The heat flux for a small portion of this edge having the length dx can then be expressed as

$$d\dot{Q} = \dot{m}_t c_{p,t} (T_t(x + dx) - T_t(x)) = U \frac{dx}{L} (T_{s,1} - T_t(x)). \tag{4}$$

This can be modified, rearranged, and written in integral form,

$$\int_{T_{t,1}}^{T_t(x)} \frac{1}{T_{s,1} - T_t(x)} dT_t(x) = \int_0^x \frac{U}{\dot{m}_t c_{p,t} L} dx, \tag{5}$$

which yields

$$T_t(x) = T_{s,1} + (T_{t,1} - T_{s,1}) \exp\left(-\frac{U}{\dot{m}_t c_{p,t}} \frac{x}{L}\right), \quad x \in [0, L]. \tag{6}$$

From Equation (6), we immediately see that the temperature at the end of the edge can be obtained using

$$T_{t,2} = T_{s,1} + (T_{t,1} - T_{s,1}) \exp\left(-\frac{U}{\dot{m}_t c_{p,t}}\right). \tag{7}$$

Equation (7) must be linearized for it to be used in a matrix solver. This is done in a straightforward manner by taking

$$C_U = \exp\left(-\frac{U}{\dot{m}_t c_{p,t}}\right) = \text{const.}, \tag{8}$$

where the necessary cumulative overall heat transfer coefficient, U , is computed from the tube-side and shell-side heat transfer coefficients. These, in turn, are calculated using equations from literature (e.g., [28] in the case of plain tubes or [29] if the tubes are finned) depending on the actual bundle geometry and flow conditions. Additional information regarding validation of the commonly used empirical equations for estimation of heat transfer coefficient in the case of plain and serrated fins can be found, for instance, in [30]. One could also use the correlations from [31], which have been obtained via the machine learning technique. If U-shaped or helical fins of various types are employed, then the two-part article by Hofmann and Heimo [32,33] can be recommended to the reader. The final, linearized equation for a single edge, therefore, is

$$C_U T_{t,1} - T_{t,2} = (C_U - 1) T_{s,1}. \tag{9}$$

Considering the shell-side outlet temperature, for cross-flow with $T_{s,1} = \text{const.}$ on the entire inlet face of the control volume, we have

$$d\dot{Q} = U \frac{dx}{L} (T_{s,1} - T_t(x)) = \dot{m}_s c_{p,s} \frac{dx}{L} (T_{s,1} - T_{s,2}(x)). \tag{10}$$

Just as before, this can be modified and rearranged to yield

$$T_{s,2}(x) = T_{s,1} + \frac{U}{\dot{m}_s c_{p,s}} (T_{s,1} - T_{t,1}) \exp\left(-\frac{U}{\dot{m}_t c_{p,t}} \frac{x}{L}\right), \quad x \in [0, L]. \tag{11}$$

The mean shell-side outlet temperature then is

$$T_{s,2} = \frac{1}{L} \int_0^L T_{s,2}(x) dx = T_{s,1} + \frac{\dot{m}_t c_{p,t}}{\dot{m}_s c_{p,s}} \left(\exp\left(-\frac{U}{\dot{m}_t c_{p,t}}\right) - 1 \right) (T_{s,1} - T_{t,1}), \tag{12}$$

which corresponds to the shell-side outlet temperature obtained using the respective set of linear equations.

One could also simplify the model even further by using a one-dimensional shell-side mesh (i.e., a mesh such that each cross-section of the shell along the general flow direction is spanned by just one cell). With a row of n tubes being present in a specific shell-side cell, Equation (3) would simply become

$$\sum_{i=1}^n \dot{m}_{t,i} c_{p,t,i} (T_{t,i,2} - T_{t,i,1}) = \dot{m}_s c_{p,s} (T_{s,1} - T_{s,2}), \tag{13}$$

while Equation (7), still necessary for each of the n tubes, would remain almost identical:

$$T_{t,i,2} = T_{s,1} + (T_{t,i,1} - T_{s,1}) \exp\left(-\frac{U_i}{\dot{m}_{t,i} c_{p,t,i}}\right), \quad i = 1, 2, \dots, n. \tag{14}$$

There also is a special case of no heat transfer, which can be treated similarly. The necessary equation can easily be obtained by setting the heat transfer coefficient in Equation (14) to zero, which results in the equation being reduced to the equality between the temperatures in the end nodes of an edge. This is important because the number of linear equations describing heat transfer is always constant no matter if heat transfer occurs or not.

2.1.3. Boundary Conditions and the Complete System of Linear Equations

Up to this point, every equation was simply describing some relationship between the node temperatures. For a steady state problem to be completely specified, some temperatures must be known. However, let us first analyze the number of equations available thus far. For a fluid flow system with n edges and m inflow streams, there are $2n$ unknown temperatures. We can get n equations from the heat transfer. The following $n - m$ equations can be obtained from stream mixing in the nodes. The remaining m equations must be provided via boundary conditions, i.e., inlet temperatures must be specified for each of the inflow stream (other arrangements may be possible in selected cases). When there are multiple fluid flow systems connected by heat transfer equations, the number of available equations remains the same.

2.1.4. Coupling of the Flow Distribution and Heat Transfer Submodels

Each major iteration of the FEA-based solver consists of two steps. The first step is a fixed temperature field analogy of the adiabatic model (as described in [26]; robustness of the model can be improved by carrying out this first step repeatedly until the respective residual falls below a predefined threshold). New estimates of the temperature fields for both the tube and the shell sides are then obtained in the second step. Here, the necessary values of C_U are updated using edge mass flow rates from the first step and the corresponding new estimates of cumulative overall heat transfer coefficients. To solve the respective combined linear system for the tube-side and the shell-side temperatures, one boundary temperature must be provided for each stream (for instance, at the inlet of each tube in the bundle and for each inlet cell in the discretized shell side). The resulting temperature matrix could look, for example, like the one in Figure 6. Even though linear systems represented by such matrices can be solved quite easily, it is obvious from the figure that implementation of a reordering algorithm would be necessary should one want to improve performance via preconditioning in case of much larger linear systems.

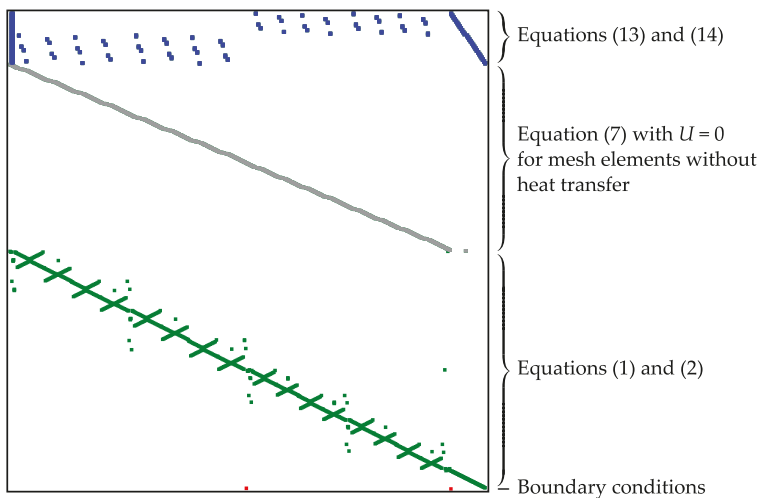


Figure 6. Non-zero values in the sparse temperature field matrix used in the second step of the FEA solver. Please note that, for the sake of clarity, only a small matrix with the rank slightly below 800 is shown here, which originates from a flow distribution system with two bundles consisting of just four tubes each.

As the convergence criterion, the fluid flow submodel used the scaled norm of the difference between the solutions from the predictor step and the corrector step. The corresponding scaled residual

limit was 10^{-5} . In the case of the heat transfer submodel, if we denote the original linear system $\mathbf{Ax} = \mathbf{b}$, then the scaled residual norm is computed from $\mathbf{b} - \mathbf{Ax}$ just before the heat transfer submodel is solved. (If it were done after the respective solution process, the norm would be equal to zero.) The same residual limit, that is, 10^{-5} , was used here.

All physical property data (mean specific heat capacity, dynamic viscosity, etc.) are always taken for the current conditions from the IAPWS [34] or the CoolProp [35] physical property libraries, or, in special cases (e.g., flue gas), are computed using various interpolation functions or tabulated data depending on the actual compositions. Thermal properties of the tube and fin materials are always obtained using tabulated data from literature (for example, from the technical standard [36]).

2.2. Shell-Side Pressure Drop

Similarly to heat transfer coefficients, pressure drop in the shell side cross-flow tube bundle is calculated via well-known empirical equations from, e.g., [37]. The actual formula to be used depends on the bundle geometry, possible presence of fins, etc.

2.3. The Developed Computer Code

The computer code was developed in Python [38] and utilized NumPy [39] to carry out the necessary matrix computations. The Visualization Toolkit (VTK) [40] and meshio [41] libraries were used to export solution data to Kitware ParaView [42] for visualization. Although no graphical user interface (GUI) is available yet, the authors plan to add it in the future, for example, via the Django web framework [43]. Please note that the code is not publicly available.

Apart from the inclusion of heat transfer, many additional improvements of the code have been made since the publication of the initial article discussing the FEA-based model [26]. The most important one probably is parallelization of the mass flow rate corrector step (please see [26] for details). As the correction algorithm was carried out independently for each mesh edge, a set of asynchronous workers was created using the standard Python multiprocessing library, and the correction tasks were processed in batches on all available CPU cores. This then results in much shorter computational times. Parallelization of the internal matrix computations, however, was not implemented because, given the numbers of elements in the simplified meshes, the matrices were rather small. In other words, the CPU time saved by parallel solution would be wasted on auxiliary operations needed to split the task to multiple cores, thus rendering the net improvement either negligible or even negative.

3. Results

In this section, two test cases are discussed to demonstrate the capabilities of the present version of the developed model. First, a simple cross-flow tube bundle heat exchanger from the literature is evaluated in Section 3.1. Section 3.2 then focuses on a heat recovery hot water boiler in an existing combined heat and power plant, for which stream data have been provided by its operator.

3.1. Simple Cross-Flow Tube Bundle Heat Exchanger from the Literature

The example discussed here was taken from [44] and involves an air-to-water heat exchanger from Figure 7. Its parameters are listed in Table 2 together with the data obtained using the present model and HTRI Xchanger Suite 8.0.1 [45]. The computational time needed by the present model to automatically create the necessary meshes, reach in 46 major iterations the results mentioned below, and export all the solution data into Kitware ParaView for visualization purposes was ca. 15 s on an average desktop computer with the Intel Core i-5 2500K CPU. The ranks of the matrices used in the model were ca. 800 and ca. 1600 in case of fluid flow and heat transfer, respectively.

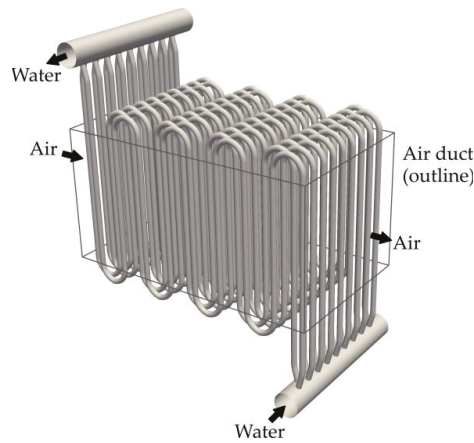


Figure 7. The evaluated air-to-water heat exchanger (please note that the tubes are shown as unfinned for clarity even though the exchanger used rolled helical fins in the heated portion of the bundle). The dimensions of the air duct were $0.56 \times 0.5 \times 1.0$ m (width \times height \times length).

Table 2. Parameters of the air-to-water heat exchanger (for the remaining construction data, etc., please see [44]) and the corresponding results obtained using the present model and HTRI Xchanger Suite (“HTRI XS”).

Parameter	Literature [44]	Present Model	HTRI XS
TS ¹ inlet conditions		3.0 kg s ⁻¹ , 25 °C, 500 kPa	
TS outlet temperature	37.0 °C	37.5 °C	36.3 °C
TS pressure drop	2.24 kPa	3.01 kPa	1.9 kPa
SS ² inlet conditions		2.7 kg s ⁻¹ , 95 °C, 200 kPa	
SS outlet temperature	40.0 °C	37.6 °C	42.8 °C
SS pressure drop	1.40 kPa	1.38 kPa	1.2 kPa
heat duty	150.3 kW	156.6 kW	143.0 kW

¹ Tube side (water); ² Shell side (air).

In order to minimize the number of sources of discrepancies, the necessary heat transfer coefficients were calculated by the present model using the equations mentioned in the literature [44]. The results should, therefore, have been identical, yet they were not. The reason for the difference became clear once one noticed that, in [44], the iterative computation was stopped while the difference between the hot and the cold heat duties was still relatively large. In fact, should one carry out the heat balance for the data from the literature, one would get the actual water heat duty of 150.3 kW (as listed among the results) while for air the duty would be 149.9 kW. There may also be another reason for the discrepancies in the data, namely the fact that, in [44], the computation was done using average temperatures, average fluid physical properties, etc. for the entire tube side and shell side.

Considering the differences between the values provided by the present model and the data yielded by HTRI Xchanger Suite, these most likely stemmed from the software package using much more accurate equations for obtaining the heat transfer coefficients. It, therefore, is entirely possible that with different equations the results obtained using the present model would be much closer to the data from HTRI Xchanger Suite. In any case, this supports the notion that any such tool or model can only be as good as the equations internally utilized by it.

To demonstrate the level of detail of the solution data provided by the developed software, the water and air temperatures were exported (together with the respective geometry, which used only

plain tubes to improve clarity) into Kitware ParaView. The resulting combined plot is shown in Figure 8.

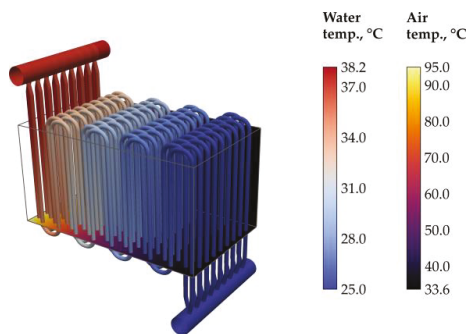


Figure 8. Visualization generated in Kitware ParaView of the bundle in the air duct (some faces are culled). These were colored by the tube-side (water) and the shell-side (air) temperatures obtained using the FEA-based model.

3.2. Heat Recovery Hot Water Boiler in an Existing Plant

A heat recovery hot water boiler with nominal thermal power of 53.3 MW in an existing combined heat and power (CHP) plant was selected as the second test case. The boiler contained two counter-flow tube bundles which were mounted in the vertical portion of the flue gas duct (i.e., the tubes are horizontal, see Figure 9). Both bundles consisted of several passes, and each pass was composed of four staggered tube rows with 48 tubes per row. In the bottom bundle, the first pass was unfinned, the second pass used plain round fins, and serrated fins were utilized in the third pass. The top bundle contained solely tubes enhanced with serrated fins. The built-up area of the heated portion of each bundle was ca. 7.6×4.0 m. All stream-related data presented in this article were obtained by the operator of the boiler in the course of a guarantee test.

The boiler was driven by flue gas exiting from a gas turbine. Because the temperature field (see the measurement array shown in Figure 9) was almost uniform, the corresponding boundary condition was specified in both the models discussed further as a constant. The outlet temperature of flue gas was estimated by the operator because the respective quantity had not been measured during the guarantee test. All the necessary data are summarized in Table 3.

Table 3. Data provided by the operator of the heat recovery hot water boiler.

Parameter	Value
tube side fluid	water
tube side inlet conditions	141.7 kg s^{-1} , $48.0 \text{ }^\circ\text{C}$, $1,071.7 \text{ kPa}$
tube side outlet temperature	$139.3 \text{ }^\circ\text{C}$
tube side pressure drop	32.15 kPa
shell side fluid	flue gas
shell side inlet conditions	124.5 kg s^{-1} , $453.9 \pm 3.6 \text{ }^\circ\text{C}^1$, 101.31 kPa
shell side outlet temperature	ca. $70 \text{ }^\circ\text{C}^2$
shell side pressure drop	1.61 kPa
heat duty	53.3 MW

¹ Calculated from time-dependent data obtained using the measurement array shown in Figure 9; ² Estimated (not measured during the guarantee test).

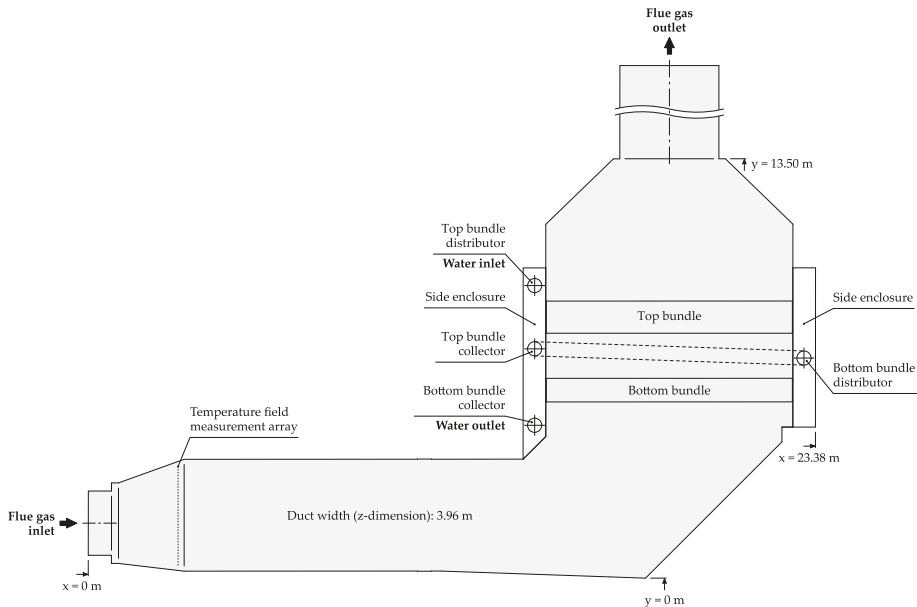


Figure 9. Schematic of the investigated boiler. Top bundle collector was connected to the bottom bundle distributor via an external duct as indicated using the dashed lines. The temperature field measurement array, consisting of 12 (4×3) sensors, was only installed in the duct during the guarantee test.

The simulation carried out using the developed computer code mentioned in Section 2.3 included both water distribution in the tube side and heat transfer between the flue gas and water. To assess the accuracy of the predicted temperatures, the boiler was also analyzed using an industry-standard tool, namely, HTRI Xchanger Suite. Please note that, with respect to the requests of the manufacturer of the boiler and the operator of the CHP plant, no other data regarding the apparatus can be explicitly specified in this article. For the same reason, neither the HTRI Xchanger Suite case files nor the simplified 3-D CFD model of the flue gas duct discussed in the following sections can be made available.

3.2.1. Simulation in HTRI Xchanger Suite

Compared to a full-scale CFD simulation of the boiler, which would rarely be done in the case of equipment of such size, the actual computational time required by HTRI Xchanger Suite was negligible (units of seconds). Unlike CFD, however, the software generally focuses on the thermal side of the apparatus design, i.e., its primary goal is to provide as accurate stream temperatures as possible while the flows in both the tube and shell sides are assumed to be uniformly distributed (unless the user specifies the distribution explicitly). Moreover, one cannot directly set tube inner and outer surface roughnesses, which may significantly influence the predicted pressure drops.

Results obtained using the discussed software package are listed in Table 4 together with the data provided by the operator of the heat recovery hot water boiler. The table also mentions the absolute and relative errors. From these, one can see that the predictions of both the outlet temperatures and the tube-side pressure drop were quite accurate. The predicted shell-side pressure drop, however, was markedly lower than the measured value. It also was a notable disadvantage that no detailed information was given by HTRI Xchanger Suite regarding the actual flow distributions in the bundles and the shell.

Table 4. Results obtained using HTRI Xchanger Suite and the corresponding errors compared to the data from the operator of the boiler. It is apparent that the temperatures and the tube-side pressure drop were predicted quite accurately, but the shell-side pressure drop was markedly below the measured value.

Parameter	Value	Error
tube side outlet temperature	136.9 °C	−2.4 °C (−1.7%)
tube side pressure drop	32.33 kPa	+0.18 kPa (−0.6%)
shell side outlet temperature	59.3 °C	ca. −10.7 °C (−15%)
shell side pressure drop	0.93 kPa	−0.68 kPa (−42%)
heat duty	53.1 MW	−0.2 MW (−0.4%)

3.2.2. Assessment of the Shell-Side Flow Behavior

In order to verify whether the assumption of uniform velocity distribution over the flue gas duct cross-section was appropriate in the FEA-based computation discussed in the next section, a simplified 3-D CFD model of the duct was created in ANSYS Fluent [46]. Parameters of the model are listed in Table 5. To keep computational demand at a reasonable level, the bundles were replaced by porous zones. Additionally, the entire duct was split into several parts, and hexahedral cells were used whenever possible to further lower the cell count while maintaining acceptable mesh quality. After the necessary mesh adaptation, the final cell count was ca. 3.3 M (see the y^+ histogram in Figure 10). As for cell equiangle skewness, only 1231 cells (ca. 0.04% of the total number of cells) featured skewness greater than 0.6, of which 1227 fell between 0.6 and 0.7. The obtained contour plot of velocity magnitude just below the bottom bundle is then shown in Figure 11. This indicates that, although the velocity distribution was not entirely uniform (see also the pathlines in Figure 12), the non-uniformity was still at a reasonable level, which should not lead to significant inaccuracy in the calculated overall heat transfer rate.

Table 5. Parameters of the simplified 3-D CFD model of the flue gas duct.

Parameter	Value
solver	pressure-based, transient
pressure-velocity coupling	SIMPLE
transient formulation	2nd order implicit, time step: 0.01 s
active equations	flow, turbulence
turbulence model	Realizable $k-\epsilon$, Scalable Wall Functions
discretization	2nd order (pressure), 2nd order upwind (other quantities)
inlet/outlet types	mass flow inlet, pressure outlet

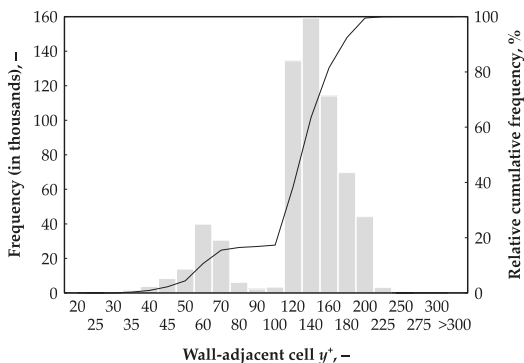


Figure 10. Histogram of y^+ values of wall-adjacent cells in the model from Table 5. There were 275 cells with $y^+ \leq 30$ (all of these but 12 were between 25 and 30, ca. 0.04% of the total number of wall-adjacent cells) and no cells with $y^+ > 300$.

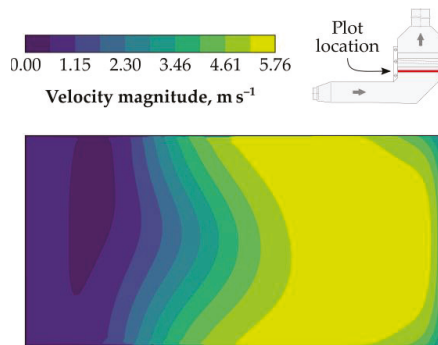


Figure 11. Contour plot of velocity magnitude just below the bottom bundle, which was obtained using the CFD model from Table 5. The velocity distribution was not uniform (due to the flue gas duct being bent) and fluctuated in time.

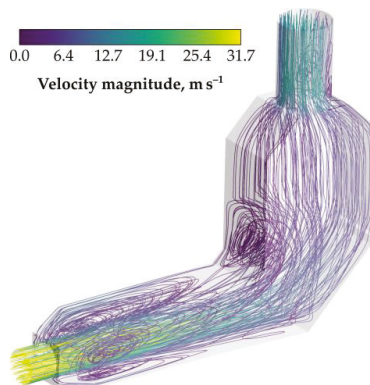


Figure 12. Pathlines in the flue gas duct, which were colored by velocity magnitude. One can see that the flow behind the bend is pushed to one side as indicated in Figure 11 and that there are relatively large recirculation zones present.

3.2.3. Present Model

The data yielded by the present, FEA-based model are listed in Table 6 together with the values provided by the operator of the boiler. Here, the accuracy was slightly lower than that of HTRI Xchanger Suite, but it still was acceptable. The computational time needed to automatically create the meshes, reached in 39 major iterations the solution, and export the necessary solution data into Kitware ParaView for visualization purposes was ca. 240 s on the same average desktop computer used in the previous example. The ranks of the matrices were ca. 9000 and ca. 18,500 in case of fluid flow and heat transfer, respectively.

As mentioned before, the present model uses a one-dimensional mesh to represent the shell side. This means that the predicted temperature distribution was, too, only one-dimensional, while flow distribution across the shell-side cannot be predicted at all. In the tube side, on the other hand, the mass flow rate was known for each individual tube, and the predicted temperature distribution was spatially as fine or as coarse as the utilized tube bundle mesh. Figure 13 shows the predicted shell-side temperature distribution along the portion of the flue gas duct enclosing the two bundles, which was obtained using the present model, and the corresponding temperatures provided by the operator of the boiler and yielded by HTRI Xchanger Suite. The temperature curve yielded by the model matches the

point values reasonably well with the discrepancies being most likely caused by the usage of different equations for the calculation of the necessary heat transfer coefficients.

Table 6. Results obtained using the present model and the corresponding errors compared to the data from the operator of the boiler. The accuracy was not as good as in the case of HTRI Xchanger Suite, but, in terms of fast, approximate analyses of process and power equipment, it was sufficient.

Parameter	Value	Error
tube side outlet temperature	136.1 °C	−3.2 °C (−2.3%)
tube side pressure drop	30.33 kPa	−1.82 kPa (−5.7%)
shell side outlet temperature	62.9 °C	ca. −7.1 °C (−10%)
shell side pressure drop	1.14 kPa	−0.47 kPa (−29%)
heat duty	52.6 MW	−0.7 MW (−1.3%)

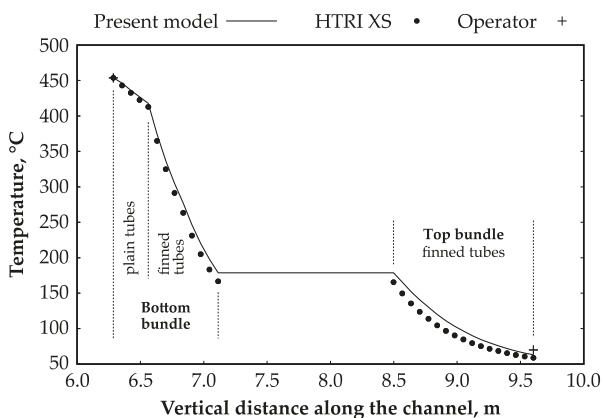


Figure 13. Comparison of the temperature distribution in the portion of the flue gas duct enclosing the two bundles, which was obtained using the present model, and the corresponding temperatures provided by the operator of the boiler and yielded by HTRI Xchanger Suite (“HTRI XS”). Vertical distance along the channel corresponds to the distance from the point denoted “y = 0 m” in Figure 9.

Similarly as before, a combined plot of water and flue gas temperatures was generated using Kitware ParaView. This is shown in Figure 14.

The obtained tube mass flow rates were distributed quite uniformly in both bundles. The actual relative standard deviations from uniform flow distribution computed using

$$\delta = \frac{100}{\dot{m}_{id}} \sqrt{\frac{1}{n} \sum_{i=1}^n (\dot{m}_i - \dot{m}_{id})^2}, \tag{15}$$

where \dot{m}_{id} denotes the ideal mass flow rate through one tube of the bundle, n the number of tubes therein, and \dot{m}_i the mass flow rate through the i th tube, were 0.3% and 0.4% in case of the top bundle and the bottom bundle, respectively.

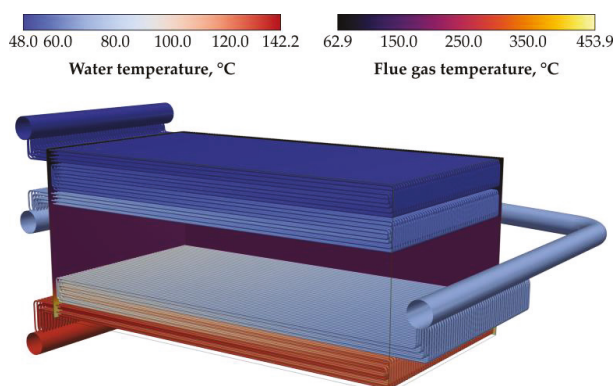


Figure 14. Visualization generated in Kitware ParaView of the bundles and the surrounding portion of the flue gas duct (front faces are cullled). These were colored by the tube-side (water) and the shell-side (flue gas) temperatures obtained using the FEA-based model.

4. Discussion

The results yielded by the present model and by HTRI Xchanger Suite for the air-to-water heat exchanger from the literature have shown that even though an apparatus can be decomposed into parts for which correlations or calculation procedures for heat transfer coefficients and pressure losses may exist, successfully applying them may not be straightforward. The main reason is that such procedures require local fluid and material properties, and these generally depend on the temperature and pressure, that is, quantities which the designer is trying to calculate. This is where the present model steps in. The data have also highlighted the facts that the accuracy of any model depends to a large degree on the quality of equations utilized for the calculation of the various coefficients and that further research in this area is, therefore, necessary. Additionally, one can draw the conclusion that using averaged values for the entire tube side and shell side can lead to notable differences. In the case of the outlet temperatures in this air-to-water heat exchanger, it was up to ca. $\pm 7\%$.

As for the heat recovery hot water boiler, the most important stream parameters are listed in Table 7. It can be seen that the tube-side outlet temperature and pressure drop were better predicted by HTRI Xchanger Suite, while the accuracy of the shell-side outlet temperature and pressure drop predictions was higher in the case of the present model. Overall, the accuracy of the model was deemed acceptable concerning its intended purpose.

Table 7. Summary of the main results obtained using the two discussed approaches alongside the data provided by the operator of the boiler.

Parameter	Present Model	HTRI Xchanger Suite	Operator
TS ¹ outlet temperature	136.1 °C	136.9 °C	139.3 °C
TS pressure drop	30.33 kPa	32.33 kPa	32.15 kPa
SS ² outlet temperature	62.9 °C	59.3 °C	ca. 70 °C ³
SS pressure drop	1.14 kPa	0.93 kPa	1.61 kPa
heat duty	52.6 MW	53.1 MW	53.3 MW

¹ Tube side (water); ² Shell side (flue gas); ³ Estimated (not measured during the guarantee test).

A significant advantage of the model over the industry-standard design package offered by HTRI (or other commonly used heat transfer equipment design packages) lies in the fact that it provides detailed data on the tube-side fluid flow and temperature distributions. This information can be of great value when trying to prevent certain types of operating problems (e.g., excessive thermal loading

of the tubes in the bundle and the subsequent mechanical failures). Another advantage is that in the case of cross-flow tube bundles (the primary target application of the present model), HTRI Xchanger Suite assumes that mixing of tube streams occurs after each pass, even if this may not actually be true. Such a simplification may increase convergence, but it also may diminish local effects and, therefore, introduce errors into the data.

5. Conclusions

The point of this research was not to develop a replacement to the universally applicable, commercial heat transfer equipment design packages, such as HTRI Xchanger Suite. On the contrary, the goal was to create a simplified model for heat exchangers representable using sets of interconnected 1-D meshes, which are typically used in high-temperature (i.e., heat recovery) industrial applications and are prone to suffer from operating problems. The model, once finished, should be fast, yet accurate enough, and should provide estimates of not only the flow distribution in the bundle and the tube- and shell-side temperature fields but also the resulting mechanical stress field in the bundle caused by uneven thermal loading. In other words, the aim was to have a supplementary tool which would enable the designer to evaluate in advance, and without any significant effort or time spent, the thermal-hydraulic behavior of the mentioned heat exchangers as well as the likelihood of them suffering mechanical failures under the design operating conditions. In this regard, the FEA-based modelling approach seems to be promising, but a lot of work, as well as a thorough validation, are still needed before it is ready for production use.

The comparison with HTRI was mentioned in this paper solely to present the current capabilities of the model in terms of heat transfer prediction. The discrepancy (or at least a part of it) was very likely caused by the heat transfer coefficients and the hydraulic resistance coefficients being calculated differently. However, the model was designed in such a way that it can easily incorporate any standard method for calculating these coefficients for the simple 1-D mesh elements. More complex flow systems can then be built from these simple elements and the solution strategy remains the same, which ensures scalability of the model.

Considering the fact that shell-side flow velocity fields commonly are not uniform, one of the possible future improvements of the FEA-based model could lie in strictly using a grid of cells in the shell side (in the plane perpendicular to the general direction of flow) instead of only one cell. Another enhancement, which the authors plan to implement, is to make it possible to interface the current computer code with other simulation codes. This would enable the evaluation of flow systems in which some parts are more complex and, therefore, not directly compatible with the simplified mesh elements used by the FEA-based model.

Author Contributions: Conceptualization, T.L. and V.T.; methodology, T.L. and V.T.; software, T.L.; validation, V.T. and T.L.; investigation, T.L., V.T., and D.B.F.; resources, Z.J.; writing—original draft preparation, V.T.; writing—review and editing, V.T.; visualization, V.T. and T.L.; supervision, V.T. All authors have read and agreed to the published version of the manuscript.

Funding: This research was funded by the Czech Ministry of Education, Youth, and Sports/EU Operational Programme Research, Development and Education, grant No. CZ.02.1.01/0.0/0.0/16_026/0008413 “Strategic partnership for environmental technologies and energy production”.

Conflicts of Interest: The authors declare no conflict of interest.

Nomenclature

Roman Symbols:

c_p	specific heat capacity, $\text{J kg}^{-1} \text{K}^{-1}$
C_U	constant in the linearized equation governing temperature change in a tube-side mesh edge, –
k	turbulent kinetic energy, $\text{m}^2 \text{s}^{-2}$
L	mesh edge length, m
m	number of inbound streams, –
\dot{m}	mass flow rate, kg s^{-1}
n	number of edges in a system, number of tubes, number of outbound streams, –
\dot{Q}	heat flux, W
Re	Reynolds number, –
T	temperature, $^{\circ}\text{C}$
U	cumulative overall heat transfer coefficient, W K^{-1}
x	length coordinate, m
y^+	dimensionless wall distance, –

Greek Symbols:

δ	relative standard deviation from uniform flow distribution, %
ε	rate of dissipation of turbulent kinetic energy, $\text{m}^2 \text{s}^{-3}$

Subscripts:

1	at the inlet of the control volume
2	at the outlet of the control volume
i, j, q, r	summation indices
id	ideal value
s	in the shell side
t	in the tube side

References

- Wei, H.; Yang, X.; Ge, Z.; Yang, L.; Du, X. Anti-freezing of natural draft dry cooling system of power generation by water re-distribution during winter. *Int. J. Heat Mass Transf.* **2020**, *149*, 119194. [[CrossRef](#)]
- Chien, N.B.; Linh, N.X.; Jong-Taek, O. Numerical optimization of flow distribution inside inlet header of heat exchanger. *Energy Procedia* **2019**, *158*, 5488–5493. [[CrossRef](#)]
- Zhou, J.; Ding, M.; Bian, H.; Zhang, Y.; Sun, Z. Characteristics of flow distribution in central-type compact parallel flow heat exchangers with modified inlet and header. *Appl. Therm. Eng.* **2020**, *166*, 114636. [[CrossRef](#)]
- Łopata, S.; Ocloń, P.; Stelmach, T. Investigation of flow non-uniformities in the cross-flow heat exchanger with elliptical tubes. *E3S Web Conf.* **2019**, *108*, 01009. [[CrossRef](#)]
- García-Guendulain, J.M.; Riesco-Ávila, J.M.; Picón-Núñez, M. Reducing thermal imbalances and flow nonuniformity in solar collectors through the selection of free flow area ratio. *Energy* **2020**, *194*, 116897. [[CrossRef](#)]
- Karvounis, P.; Koubogiannis, D.; Hontzopoulos, E.; Hatziapostolou, A. Numerical and experimental study of flow characteristics in solar collector manifolds. *Energies* **2019**, *12*, 1431. [[CrossRef](#)]
- Li, M.; Hao, J.; Chen, W.; Li, W. Experimental and theoretical investigations on reverse flow characteristics in vertically inverted U-tube steam generator under transient condition. *Prog. Nucl. Energy* **2020**, *120*, 103216. [[CrossRef](#)]
- Klenov, O.P.; Noskov, A.S. Influence of input conditions on the flow distribution in trickle bed reactors. *Chem. Eng. J.* **2020**, *382*, 122806. [[CrossRef](#)]
- He, Y.; Sun, Z.; Shen, B.; Guo, F.; Yang, Y.; Zhan, X.; Li, X. CFD study on the flow distribution of an annular multi-hole nozzle. *Can. J. Chem. Eng.* **2020**, *98*, 590–606. [[CrossRef](#)]
- Bürkle, F.; Moyon, F.; Feierabend, L.; Wartmann, J.; Heinzl, A.; Czarske, J.; Büttner, L. Investigation and equalisation of the flow distribution in a fuel cell stack. *J. Power Sources* **2020**, *448*, 227546. [[CrossRef](#)]
- Heck, J.D.; Vaz, W.S.; Koylu, U.O.; Leu, M.C. Decoupling pressure and distribution effects of flow fields on polymer electrolyte fuel cell system performance. *Sustain. Energy Technol. Assess.* **2019**, *36*, 100551. [[CrossRef](#)]

12. Hur, D.-J.; Jeong, S.-H.; Song, S.-I.; Noh, J.-H. Optimization based on product and desirability functions for flow distribution in multi-channel cooling systems of power inverters in electric vehicles. *Appl. Sci.* **2019**, *9*, 4844. [[CrossRef](#)]
13. Li, H.; Ding, X.; Jing, D.; Xiong, M.; Meng, F. Experimental and numerical investigation of liquid-cooled heat sinks designed by topology optimization. *Int. J. Therm. Sci.* **2019**, *146*, 106065. [[CrossRef](#)]
14. Zhu, J.; Zhang, W.; Li, Y.; Ji, P.; Wang, W. Experimental study of flow distribution in plate-fin heat exchanger and its influence on natural gas liquefaction performance. *Appl. Therm. Eng.* **2019**, *155*, 398–417. [[CrossRef](#)]
15. Tang, H.; Zhang, T.; Liu, X.-H. Experimental study on refrigerant maldistribution in a fin-and-tube evaporator for a direct expansion air-conditioning system. *Energy Build.* **2020**, *208*, 109638. [[CrossRef](#)]
16. Quintanar, N.R.; Nguyen, T.; Vaghetto, R.; Hassan, Y.A. Natural circulation flow distribution within a multi-branch manifold. *Int. J. Heat Mass Transf.* **2019**, *135*, 1–15. [[CrossRef](#)]
17. Yih, J.; Wang, H. Experimental characterization of thermal-hydraulic performance of a microchannel heat exchanger for waste heat recovery. *Energy Convers. Manag.* **2020**, *204*, 112309. [[CrossRef](#)]
18. Lugarini, A.; Franco, A.T.; Errera, M.R. Flow distribution uniformity in a comb-like microchannel network. *Microfluid. Nanofluid.* **2019**, *23*, 44. [[CrossRef](#)]
19. Ishiyama, E.M.; Pugh, S.J. Effect of flow distribution in parallel heat exchanger networks: Use of thermo-hydraulic channeling model in refinery operation. *Heat Transf. Eng.* **2020**, *41*, 189–198. [[CrossRef](#)]
20. Novitsky, N.N.; Alekseev, A.V.; Grebneva, O.A.; Lutsenko, A.V.; Tokarev, V.V.; Shalaginova, Z.I. Multilevel modeling and optimization of large-scale pipeline systems operation. *Energy* **2019**, *184*, 151–164. [[CrossRef](#)]
21. Korelstein, L. Hydraulic networks with pressure-dependent closure relations, under restrictions on the value of nodal pressures. Maxwell matrix properties and monotonicity of flow distribution problem solution. *E3S Web Conf.* **2019**, *102*, 01005. [[CrossRef](#)]
22. Cassiolo, G.; Carvalho, E.P.; Caballero, J.A.; Ravagnani, M.A. Optimization of water distribution networks using a deterministic approach. *Eng. Optim.* **2020**. [[CrossRef](#)]
23. Sun, L.; Yan, H.; Xin, K.; Tao, T. Contamination source identification in water distribution networks using convolutional neural network. *Environ. Sci. Pollut. Res.* **2019**, *26*, 36786–36797. [[CrossRef](#)] [[PubMed](#)]
24. Fang, Q.-S.; Zhang, J.-X.; Xie, C.-L.; Yang, Y.-L. Detection of multiple leakage points in water distribution networks based on convolutional neural networks. *Water Supply* **2019**, *19*, 2231–2239. [[CrossRef](#)]
25. Jeong, G.; Kang, D. Hydraulic uniformity index for water distribution networks. *J. Water Resour. Plan. Manag.* **2020**, *146*, 04019078. [[CrossRef](#)]
26. Létal, T.; Turek, V.; Fialová, D. Nonlinear finite element analysis-based flow distribution model for engineering practice. *Chem. Eng. Trans.* **2019**, *76*, 157–162. [[CrossRef](#)]
27. Fialová, D. Flow Distribution in Equipment with Dense Tube Bundles. Master's Thesis, Brno University of Technology, Brno, Czech Republic, 2017. (In Czech).
28. Gnielinski, V. Heat Transfer in cross-flow around single rows of tubes and through tube bundles. In *VDI Heat Atlas*, 2nd ed.; Part, G., Stephan, P., Kabelac, S., Kind, M., Martin, H., Mewes, D., Schaber, K., Eds.; Springer: Berlin, Germany, 2010; pp. 725–730. [[CrossRef](#)]
29. Webb, R.L.; Kim, N.-H. Externally finned tubes. In *Principles of Enhanced Heat Transfer*, 2nd ed.; Taylor & Francis Group: New York, NY, USA, 2005.
30. Lindqvist, K.; Naess, E. A validated CFD model of plain and serrated fin-tube bundles. *Appl. Therm. Eng.* **2018**, *143*, 72–79. [[CrossRef](#)]
31. Lindqvist, K.; Wilson, Z.T.; Naess, E.; Sahinidis, N.V. A machine learning approach to correlation development applied to fin-tube bundle heat exchangers. *Energies* **2018**, *11*, 3450. [[CrossRef](#)]
32. Hofmann, R.; Heimo, W. Experimental and numerical investigation of the gas side heat transfer and pressure drop of finned tubes—Part I: Experimental analysis. *J. Therm. Sci. Eng. Appl.* **2012**, *4*, 041007. [[CrossRef](#)]
33. Hofmann, R.; Heimo, W. Experimental and numerical investigation of the gas side heat transfer and pressure drop of finned tubes—Part II: Numerical analysis. *J. Therm. Sci. Eng. Appl.* **2012**, *4*, 041008. [[CrossRef](#)]
34. Python Implementation of the IAPWS Standard. Available online: <https://github.com/jjgomerai/iapws> (accessed on 21 January 2020).
35. Bell, I.H.; Wronski, J.; Quoilin, S.; Lemort, V. Pure and pseudo-pure fluid thermophysical property evaluation and the open-source thermophysical property library CoolProp. *Ind. Eng. Chem. Res.* **2014**, *53*, 2498–2508. [[CrossRef](#)] [[PubMed](#)]

36. European Committee for Standardization. *EN 12952-2:2011. Water-Tube Boilers and Auxiliary Installations—Part 2: Materials for Pressure Parts of Boilers and Accessories*; European Committee for Standardization: Brussels, Belgium, 2011.
37. Ganapathy, V. Finned tubes. In *Waste Heat Boiler Deskbook*; The Fairmont Press, Inc.: Lilburn, GA, USA, 1991; Appendix A; pp. 275–306.
38. Python Language Reference, Version 3.8.1. Available online: <https://www.python.org> (accessed on 21 January 2020).
39. Oliphant, T.E. *A Guide to NumPy*; Trelgol Publishing: Spanish Fork, UT, USA, 2006.
40. Schroeder, W.; Martin, K.; Lorensen, B. *The Visualization Toolkit*, 4th ed.; Kitware, Inc.: Clifton Park, NY, USA, 2006.
41. I/O for Mesh Files. Available online: <https://github.com/nschloe/meshio> (accessed on 21 January 2020).
42. Ayachit, U. *The ParaView Guide: A Parallel Visualization Application*; Kitware, Inc.: Clifton Park, NY, USA, 2015.
43. Django, Version 3.0.2. Available online: <https://djangoproject.com> (accessed on 21 January 2020).
44. Pismennyi, E.; Polupan, G.; Carvajal-Mariscal, I.; Sanchez-Silva, F.; Pioro, I. Examples of calculations. In *Handbook for Transversely Finned Tube Heat Exchanger Design*; Academic Press: Cambridge, MA, USA, 2016; Chapter 7; pp. 83–106. [[CrossRef](#)]
45. Heat Transfer Research, Inc. *HTRI Xchanger Suite User's Guide, Version 8.0.1*; Heat Transfer Research, Inc.: Navasota, TX, USA, 2019.
46. ANSYS, Inc. *ANSYS Fluent User's Guide, Version 2019 R3*; ANSYS, Inc.: Canonsburgh, PA, USA, 2019.



© 2020 by the authors. Licensee MDPI, Basel, Switzerland. This article is an open access article distributed under the terms and conditions of the Creative Commons Attribution (CC BY) license (<http://creativecommons.org/licenses/by/4.0/>).

A Framework for Flexible and Cost-Efficient Retrofit Measures of Heat Exchanger Networks

Christian Langner ^{1,*}, Elin Svensson ² and Simon Harvey ¹

¹ Department of Space, Earth and Environment, Chalmers University of Technology, 412 96 Gothenburg, Sweden; simon.harvey@chalmers.se

² CIT Industriell Energi AB, 412 58 Gothenburg, Sweden; elin.svensson@cit.chalmers.se

* Correspondence: christian.langner@chalmers.se; Tel.: +46-(0)31-772-5255

Received: 24 February 2020; Accepted: 17 March 2020; Published: 20 March 2020

Abstract: Retrofitting of industrial heat recovery systems can contribute significantly to meeting energy efficiency targets for industrial plants. One issue to consider when screening retrofit design proposals is that industrial heat recovery systems must be able to handle variations, e.g., in inlet temperatures or heat capacity flow rates, in such a way that operational targets are reached. Consequently, there is a need for systematic retrofitting methodologies that are applicable to multi-period heat exchanger networks (HENs). In this study, a framework was developed to achieve flexible and cost-efficient retrofit measures of (industrial) HENs. The main idea is to split the retrofitting processes into several sub-steps. This splitting allows well-proven (single period) retrofit methodologies to be used to generate different design proposals, which are collected in a superstructure. By means of structural feasibility assessment, structurally infeasible design proposals can be discarded from further analysis, yielding a reduced superstructure. Additionally, critical point analysis is applied to identify those operating points within the uncertainty span that determine necessary overdesign of heat exchangers. In the final step, the most cost-efficient design proposal within the reduced superstructure is identified. The proposed framework was applied to a HEN retrofit case study to illustrate the proposed framework.

Keywords: heat exchanger network (HEN); retrofit; flexibility; optimization; critical points; multi-period

1. Introduction

After the Paris Agreement 2015, decarbonization of industry and energy-intensive industrial processes has been proposed as one of the key measures to limit the increase of the global average temperature well below 2 °C. Within decarbonization of industry, waste heat recovery is dedicated to play a major role.

Systematic approaches to design and synthesize heat recovery systems, especially heat exchanger networks (HENs), have been subject to research since the early 1980s with the introduction of the graphical Pinch analysis method [1]. In addition to the graphical Pinch analysis method, mathematical programming has been well established as a complementary approach to HEN synthesis. Both sequential approaches [2] and simultaneous approaches [3], where targeting and network synthesis are performed separately and simultaneously, respectively, have been developed and reported in the literature. In addition, hybrid methods, which combine graphical methods and mathematical programming [4], have been suggested. Among others, Axelsson et al. [5], Bengtsson et al. [6], as well as Escobar and Trierweiler [7] have applied graphical and mathematical methods to case studies, including industrial applications, and reported results and comparisons.

The above-mentioned methods do not account for the variation and uncertainty in operating data that often occur in industrial applications. One example is the variation of input conditions for

HENs, i.e., temperatures and flowrates, but also uncertainty in design characteristics, such as heat transfer coefficients of heat exchangers (HEXs). The consequences of neglecting these variations and uncertainties as well as using average or nominal values for design purposes can be increased utility demand (see, e.g., [8]). Additionally, more severe operability issues may occur, e.g., the controllability of target values may not be guaranteed. In order to face these challenges, different strategies have been proposed and a good overview is provided by Kang and Liu [9] in their recent review paper on the synthesis of flexible HENs. Some literature is mentioned here. Kotjabasakis and Linnhoff [10] developed an approach to mitigate the unwanted response of a HEN to variations based on sensitivity tables and systematic utilization of downstream paths. Hafizan et al. [11] utilized the plus-minus principle, introduced by Linnhoff and Vredeveld [12], to visualize the impact of process modifications on the minimum utility target, to derive heuristics for HEN design synthesis based on graphical methods if the respective HEN is subject to disturbances in inlet temperatures.

In addition to graphical approaches (e.g., Pinch-based), mathematical programming has great potential when dealing with variations and uncertainty in operating data. Floudas and Grossmann [13] introduced a multi-period approach to the HEN synthesis problem, which was automated [14] and developed further in the late 1980s [15]. More recently, the multi-period approach has been developed further by a number of authors. In this context, Aaltola [16] extended the SYNHEAT model of Yee and Grossmann [3] to multiple periods. Additionally, Verheyen and Zhang [17] as well as Short et al. [18] improved the model of Aaltola [16] by considering more specific HEX design data. The multi-period HEN synthesis strategy was further applied by Tveit et al. [19] to industrial applications.

Compared to the synthesis of HENs for greenfield problems, the rearrangement of an existing HEN (retrofitting problem) is a different problem. In contrast to greenfield design situations, a retrofitting problem is often characterized by additional constraints and limitations. Extensive work exists on retrofitting methodologies based on graphical insights (e.g., Lai et al. [20], Kamel et al. [21], Bonhivers et al. [22]), mathematical programming (e.g., Ciric and Floudas [23], Asante and Zhu [24], Athier et al. [25]), and those methodologies that can be characterized as hybrid methodologies combining graphical analysis and mathematical programming (e.g., Smith et al. [26], Jiang et al. [27], Akpomemie and Smith [28]). A comprehensive overview on different retrofitting methodologies can be found in [29].

The above-mentioned retrofit methodologies for HENs do not account for variations and uncertainties in operating data, e.g., in inlet temperatures or heat capacity flowrates. Usually, steady-state or average values are considered, i.e., the reported methodologies are suited for retrofitting single-period HENs, only. However, the capability to account for variations and uncertainties is essential in certain industry applications. Persson and Berntsson [8] showed that considering annual average values to calculate the steam savings potential of a retrofit heat integration project in a pulp mill can lead to an overestimation of 15% compared to the steam savings potential calculated with monthly average values. Persson and Berntsson further concluded in [30] that the steam savings potential decreases even further if it is calculated with average values of shorter time periods (e.g., daily or 10-min periods). In contrast to the results reported by Persson and Berntsson as well as the excessive amount of methodologies available for retrofitting single-period HENs, little attention has been paid to HEN retrofit methodologies that account for variations and uncertainties in operating data. It is worth mentioning that this imbalance between only a few methodologies for multi-period HEN retrofit in comparison with the reported methodologies for single-period HEN retrofit was observed by authors previously publishing in the field (see, e.g., [31]). In fact, to our knowledge, only two systematic retrofitting methodologies for multi-period HENs are reported in the literature. These two retrofitting methodologies are described in the following paragraph.

Papalexandri et al. [32] developed a multi-period Mixed Integer (Non-)Linear Program (MI(N)LP) model, which is based on multi-period hyperstructures, including the considered retrofit alternatives. Furthermore, Papalexandri et al. [32] proposed an iterative scheme between the developed multi-period MI(N)LP and a flexibility analysis subproblem to identify the retrofit alternative, which is operable

over a priori defined variations and yields the minimum total annualized cost. Another retrofitting methodology was reported by Kang and Liu [31], who introduced a two-step method to achieve retrofit design proposals that can operate cost efficiently at multiple periods. In a first step, the multi-period HEN synthesis model as it is used in greenfield design problems is employed. In the second step, existing exchangers are relocated in order to meet the required area demands identified in step one.

Although the above-mentioned retrofit approaches account for variations and uncertainty in operating data, there are several reasons why these approaches are not easily applied to large and complex industrial applications. Commonly, complexities, such as splitting or recirculation of streams, are present in industrial heat recovery systems, which cause nonlinearities in the mathematical formulation of these systems. Therefore, the resulting multi-period MINLP, including retrofit design proposals incorporated as hyper structures as proposed in [32], becomes complex, which inevitably leads to difficulty in finding feasible solutions. Additionally, the flexibility analysis subproblem for large and complex industrial applications is difficult to solve even with state-of-the-art global MINLP solvers. Moreover, depending on the problem complexity itself, the solution produced by common multi-period HEN synthesis formulations and the current network layout may differ essentially. Consequently, relocating existing exchangers to meet identified area demands as proposed in [31] can easily result in inefficient trial and error procedures.

The above reported methodologies are based on mathematical programming, which coincides with the benefits of mathematical programming when dealing with variations in operating data. However, in comparison to these methodologies, graphical insights-based methods have great potential to be applied to large and complex applications due to their beneficial user interaction. Recently, different strategies have been reported in the literature to utilize approaches based on graphical insights in the design process of multi-period HEN retrofitting case studies. A common strategy to deal with variations in operating conditions from a Pinch analysis perspective is to develop different retrofit proposals for a number of selected sets of operating conditions (e.g., annual, seasonal, and monthly average values) [8]. The different design proposals are then evaluated and may be combined to achieve an, over all considered operating points, operable and energy-efficient retrofit proposal. Another strategy is to develop different retrofit proposals by employing graphical insights-based retrofitting methods (e.g., Bridge analyses [22] or advanced composite curves [33]) for a specific nominal point and analyze the network's response to variations to obtain insights and identify the best performing retrofit design proposal [34]. Additionally, Langner et al. [35] proposed to decouple the design and analysis steps in retrofitting processes. By means of this decoupling, well-proven (single period) retrofit design methodologies can be utilized to generate different design proposals, which thereafter are evaluated and adjusted in a trial and error manner with respect to flexibility and energy efficiency [35]. In conclusion, approaching a retrofit problem subject to variations in operating data from a Pinch analysis perspective relies to a large extent on trial and error procedures as different design proposals must be evaluated and manually combined. Good results can be obtained, but the design process itself is often very inefficient due to the trial and error character of the respective strategies.

As pointed out, systematic methodologies for retrofitting industrial HENs subject to variation in operating data are needed, but the available methodologies fulfill this demand only partly. Therefore, we propose a new framework in this paper to achieve flexible and cost-efficient retrofit measures by combining the beneficial designer interaction of graphical approaches (e.g., Pinch based) at an early stage in the design process with the efficiency of mathematical programming. By means of this combination, inefficient trial and error procedures can be avoided. The proposed framework is based on single-period (e.g., Pinch based) retrofit methodologies, (structural) flexibility analysis, critical point analysis, and multi-period optimization. The proposed framework is outlined in Section 3 of this paper. In the following section, the theoretical background of (structural) flexibility analysis and critical point analysis is provided.

2. Theoretical Background

2.1. (Structural) Flexibility Analysis

Flexibility analysis of HENs has been subject to research since the early 1980s. In 1982, Marselle et al. [36] first introduced the concept of resilient HENs with respect to a certain disturbance range in the inlet conditions. In 1985, Saboo et al. [37] introduced a resilience index to quantify the resilience of HENs. In the same year, Swaney and Grossmann [38] extended the concept of the resilience index to a flexibility index, which is applicable not only to HENs but also to chemical processes in general. Both the resilience and the flexibility index indicate the maximum disturbance range in which inlet conditions may vary while at the same time achieve feasible operation. This maximum disturbance range can be interpreted as a hyperrectangle in the space of the varying inlet conditions. In this context, both indices are defined as the ratio between the largest scaled hyperrectangle within the feasible region and the hyperrectangle defined by an expected disturbance range. Therefore, feasibility is achieved if the respective index is larger or equal to 1. For two varying inlet conditions, this can be visualized as in Figure 1. The largest scaled rectangle within the feasible region can mathematically be expressed by the following set of equations (δ corresponds to flexibility/resilience index):

$$T_{1,N} - \delta \cdot \Delta T_1^- \leq T_1 \leq T_{1,N} + \delta \cdot \Delta T_1^+, \tag{1}$$

$$T_{2,N} - \delta \cdot \Delta T_2^- \leq T_2 \leq T_{2,N} + \delta \cdot \Delta T_2^+. \tag{2}$$

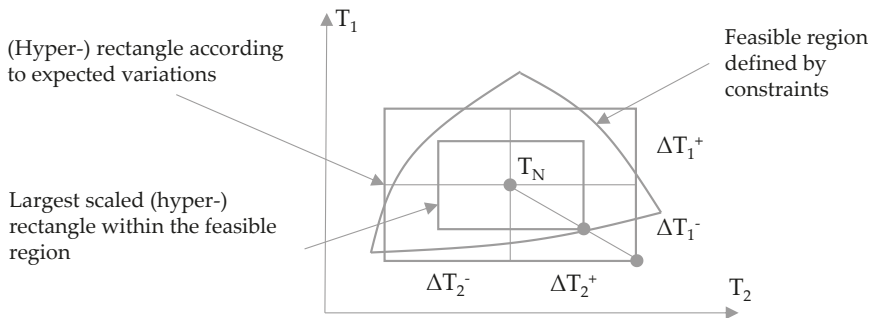


Figure 1. (Hyper-)rectangle with respect to expected variations and maximum scaled (hyper-)rectangle inscribed within the feasible region in the space of the varying inlet temperatures of a heat exchanger network [38].

In Figure 1, the largest scaled rectangle within the feasible region is smaller than the rectangle according to the expected variations. Thus, feasibility with respect to the expected variations is not achieved (flexibility or resilience index is smaller than 1). In both index formulations, the physical performance of the HEN or the chemical process is described by the following set of constraints:

$$h_i(d, x, z, \Theta) = 0; i \in I, \tag{3}$$

$$g_j(d, x, z, \Theta) \leq 0; j \in J, \tag{4}$$

where d is the vector of design variables, x corresponds to the state variables, z is used for the control variables, and the varying inlet conditions or uncertain parameters are depicted by Θ (see [37,38]). In HENs, typical design variables are the area values of HEXs while typical uncertain parameters are the inlet temperatures or heat capacity flow rates of process and/or utility streams. State and control variables correspond to the internal network temperatures and duties of HEX. Furthermore, the operational equality constraints of HENs are heat and mass balances while operational inequality

constraints ensure a minimum temperature difference as well as that heat transfer is only possible from hot to cold streams. Additionally, design constraints of HEXs (in form of heat transport equations) may also be considered as operational inequality constraints.

Feasibility is achieved when all constraints $i \in I$ and $j \in J$ are satisfied at the point of operation. With both formulations, it is possible to describe the resilience or flexibility for convex problems in which the solution lies at a vertex point of the largest scaled (hyper-)rectangle within the feasible region (see Figure 1). In 1987, Grossmann and Floudas [39] developed an active set approach to guarantee a global solution of the flexibility index problem also for some non-convex problems. More recently, Li et al. [40] suggested a framework to calculate the flexibility index by means of an alternating direction matrix embedded in a simulated annealing algorithm. Furthermore, Zhao and Chen [41] proposed to explicitly calculate the shape of the uncertainty space via cylindrical algebraic decomposition and quantifier elimination.

In the context of flexibility analysis of HENs, the term structural flexibility is used to define the set of constraints that are included in the flexibility analysis. Often, it is distinguished between structural constraints (e.g., heat and mass balances) and design constraints (e.g., heat transport equations of HEX). Marselle et al. [36] distinguished, for example, between a resilient network structure and a resilient network itself. Marselle et al. [36] further suggest that a network structure is resilient if it remains feasible for the specified disturbance range independent of the HEX areas (i.e., HEX areas are not specified). A resilient network structure is, thus, the premise for a resilient network, which remains feasible for the specified disturbance range for specified HEX areas [36]. This definition of structural resilience was later used by Li et al. [42] to describe the structural flexibility of HENs. In accordance with the literature, our work distinguishes between the structural feasibility of a design and the (general) feasibility of a design. Both can be assessed by solving the flexibility index problem. In the case of structural feasibility assessment, design constraints are discarded, and only structural constraints are considered, i.e., the heat transferred by HEXs is not limited by design characteristics. In the case of (general) feasibility assessment, design constraints are included, i.e., the heat transferred by HEXs is limited by design characteristics (i.e., the installed surface area and the overall heat transfer coefficient of exchangers).

2.2. Multi-Period Design Problem and Critical Point Analysis

In a multi-period design problem, independently of the chosen approach, sufficiently many sets of operating points need to be considered to guarantee the flexibility and cost efficiency of the achieved solution. However, with an increasing number of sets of operating points, the complexity of the problem increases. Especially for large-scale industrial applications, the computational capacity can be a limiting factor. To overcome these difficulties, different works in the literature deal with the reduction of the sets of operating points, e.g., by sensitivity analyses [43] or by the identification of critical operating points [44] of a given design proposal. The main idea of these approaches is to identify those variations (within a given uncertainty span) of the uncertain parameters, which require the largest equipment size and are, thus, critical for the design and operation of the HEN. This implies that the HEN itself must be structurally feasible and the feasibility may only be limited by design characteristics, i.e., HEX surface area and heat transfer coefficients (see Section 2.1). The identified critical operating points can be utilized to find the necessary overdesign of HEXs in a fixed HEN structure. By including the identified critical points in the design problem, feasibility for the entire uncertainty span can be achieved. Additionally, representative operating points/scenarios may be identified, e.g., by the screening of historical data, and included in the design problem to achieve a cost-efficient solution (cost optimal for the set of critical points and representative operating points/scenarios). In conclusion, the design problem subject to critical and representative operating points/scenarios can be expressed as the following multi-period MI(N)LP optimization problem:

$$\begin{aligned}
 \min_{x,z,d} \text{TAC} &= \sum_{s \in S} [w_s * c_{\text{operating},s}] + c_{\text{investment}} * \text{CRF} \\
 \text{s.t.} & \\
 & \left. \begin{aligned}
 h_i(x, z, d, \theta_{\text{op}}) &= 0; i \in I \\
 g_j(x, z, d, \theta_{\text{op}}) &\leq 0; j \in J \\
 g_d(x, z, \theta_{\text{op}}) - d &\leq 0; d \in \text{DV} \\
 d &\geq 0 \\
 x, z, d, \theta_{\text{op}} &\in \mathbb{R}, \theta_L \leq \theta_{\text{op}} \leq \theta_U
 \end{aligned} \right\} \text{op} \in (S \cup \text{CP}).
 \end{aligned} \tag{5}$$

In (5), TAC represents the total annualized cost of the HEN design, which is described by the annual operating cost $c_{\text{operating}}$ in €/year (utility cost) of a number of defined representative operating points/scenarios $s \in S$, which are weighted with their normalized duration factor w_s (time period represented by operating point divided by entire time period), and the investment cost $c_{\text{investment}}$ in € (e.g., HEX investment cost), which are annualized with a given capital recovery factor CRF. The set of equality constraints is depicted by h_i with $i \in I$ (heat and mass balances) and the set of inequality constraints is represented by g_j with $j \in J$ (temperature and other operational restrictions). The set of design constraints g_d depends on the set of the non-negative design variables d with $d \in \text{DV}$. In h_i , g_j , and g_d , x is the vector of the state variables, z corresponds to the control variables, and the varying inlet conditions or uncertain parameters are depicted by θ . Consequently, in order to find the optimal value for TAC (for the respective operating points), the degrees of freedom of the optimization problem are the non-negative design variables d with $d \in \text{DV}$ and the control variables (of the HEN) z . The set of constraints must be satisfied at all representative operating points/scenarios $s \in S$ and at all identified critical operating points $c \in \text{CP}$, i.e., for certain, previously identified, fixed combinations of values for the uncertain parameters. In (5), the set of constraints must be satisfied at each operating point present in the union of the two sets S and CP : $\text{op} \in (S \cup \text{CP})$. This way, a flexible and cost-efficient design is achieved.

To identify those variations (within a given uncertainty span) that require the largest equipment size, sensitivity analyses can be used if monotonic correlations between uncertain parameters and design variables exist. One example is the correlation between the uncertain heat transfer coefficient and the surface area of a HEX—the maximum area of the HEX is obtained at the smallest value of the heat transfer coefficient within the uncertainty span [45]. However, it can be assumed that not many parameters follow these clear correlations and critical operating points can be determined following the procedure introduced by Pintarič and Kravanja in [44], which is based on the following idea:

“The main idea is to identify points with the largest values of design variables at optimum objective function. This may be achieved by maximizing design variables one by one, while allowing uncertain parameters to obtain any value between the specified bounds, and simultaneously minimizing cost function.” [44] (p. 1607)

This implies a max-min problem for each design variable $d \in \text{DV}$, i.e., maximizing the design variable of interest d_i while minimizing the cost function $C(x, z, d, \theta)$, which is stated in problem (6). Compared to the cost function in (5) (TAC), in the cost function of (6) ($C(x, z, d, \theta)$), the operating cost of the representative operating points is not included:

$$\begin{aligned}
 \max_{\theta} d_i &= \min_{x,z,d} C(x, z, d, \theta) = c_{\text{operating}} + c_{\text{investment}} * \text{CRF} \\
 \text{s.t.} & \\
 & \left. \begin{aligned}
 h_i(x, z, d, \theta) &= 0; i \in I \\
 g_j(x, z, d, \theta) &\leq 0; j \in J \\
 d &= g_d(x, z, \theta); d \in \text{DV} \\
 x, z, d, \theta &\in \mathbb{R}, d \geq 0, \theta_L \leq \theta \leq \theta_U.
 \end{aligned} \right\} \tag{6}
 \end{aligned}$$

To solve the max-min problem, Pintarič and Kravanja [44] developed different formulations:

- The Karush–Kuhn–Tucker (KKT-) formulation;
- The two-level formulation; and
- The approximate one-level formulation.

By means of these formulations, possible candidates for critical points are identified. In a second step, a set covering algorithm is applied to the identified candidates to merge them into a final set of critical points. Both the two-level and the approximate one-level formulation approximate the solution of the KKT-formulation. Moreover, the approximate one-level formulation is dependent on a heuristically chosen Big-M parameter and solutions can be very sensitive to this parameter. Additionally, if the system is convex, all critical points are vertices of the uncertain space. These critical vertices can be identified by solving problem (5), excluding the representative operating points, sequentially at all vertices. Those vertices at which the maximum values for each design variable are obtained are critical [44].

3. Methodology

In order to achieve retrofit design proposals that can operate cost efficiently at multiple operating points, a framework was developed. The framework is shown in Figure 2 and will be outlined in the following subsections. The proposed framework utilizes single-period and well-proven retrofit design methodologies but also “experience-based” retrofit design proposals can be considered. Design proposals that are structurally infeasible are discarded after a structural feasibility assessment. To avoid suboptimal solutions due to unnecessary overdesign of equipment, the proposed framework is based on the identification of critical points. Cost efficiency for the entire operating period is ensured, by considering representative operating points besides the identified critical points when solving the eventual design problem. A final feasibility check is performed to ensure that all critical points have been identified (i.e., the set of critical points is complete); otherwise, the new critical point, which is identified during this check, is added to the set of critical point(s) and the design problem is solved again.

3.1. HEN Retrofit Design Proposals for Single Operating Point—Generation of Superstructure

In a first step, retrofit design measures are derived using single-period and well-proven retrofit design methodologies. Additionally, “experience-based” design proposals may be considered, which can be based on, e.g., already known operability issues. By means of this, the designer is actively involved in the design process, which can be beneficial in industrial applications. The derived design changes are collected in a superstructure, which eventually represents all design proposals that are considered.

3.2. Structural Feasibility Assessment—Reduction of Superstructure

In the next step, the structural feasibility of the identified proposals is analyzed. As outlined in Section 2.1, this can be done by calculating the flexibility index discarding all design constraints and considering only structural constraints. The flexibility index can be calculated using the active set approach developed by Floudas and Grossman [39]. However, the active set approach may result in impractical large problem formulations as industrial applications are often complex. Alternative formulations exist, such as the calculation of the flexibility index via the direction matrix [40] or via cylindrical algebraic decomposition and quantifier elimination [41]. However, the first alternative relies on the simulated annealing algorithm, which means that the global solution may not be found in a reasonable period of time. Moreover, applying cylindrical decomposition to industrial applications (which typically involve more than four HEXs and uncertain parameters) requires excessive computational capacity, which may not be available. An alternative is Monte Carlo network simulations with random variations within the uncertainty span while degrees of freedom are utilized to control operational targets and minimize utility cost in a similar way as it was proposed by

Kachacha et al. in [46]. With an increasing number of uncertain parameters and complexity of the problem, computational capacity is the limiting factor for this approach. Although all listed methodologies for (structural) feasibility assessment have known drawbacks, it is assumed that structural feasibility assessment of HENs (also in more complex industrial applications) is possible. To reduce the probability of faulty results, the authors suggest applying several of the proposed methods and compare the achieved results. If design proposals can be identified that are structurally infeasible for at least some operating points within the uncertainty span (i.e., flexibility index smaller than 1), these design proposals are excluded from the superstructure, yielding a reduced superstructure.

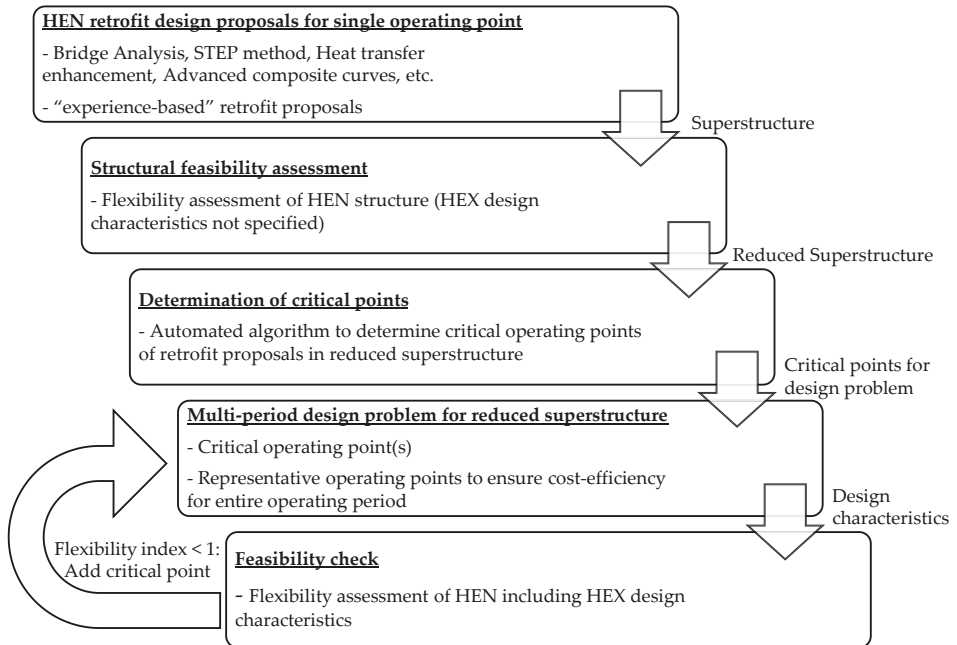


Figure 2. Retrofitting framework to achieve flexible and cost-efficient retrofit measures of heat exchanger networks (HENs).

3.3. Determination of Critical Points

In the next step, critical operating points for each design proposal are identified using the different strategies for the identification of candidates for critical points and the set covering algorithm introduced by Pintarič and Kravanja [44]. The determination of critical operating points has been implemented in a methodology for synthesis of HENs with large numbers of uncertain parameters [45]. However, it has not yet been implemented in a retrofitting framework. The main difference in a retrofitting framework is that besides the investment cost of new HEXs, investment in existing equipment can also be considered, e.g., heat transfer enhancement or an increase of the area of existing HEXs, as well as structural changes, such as resequencing and repiping of existing HEXs. However, structurally, problems (5) and (6) are similar for a HEN synthesis and a HEN retrofitting problem.

It is worth mentioning that for the critical point analysis, each design proposal (which is present in the reduced superstructure) is considered individually, i.e., for each design proposal, this step yields an individual set of critical points. To allow a fast evaluation of the different design proposals, the different strategies for the identification of candidates for critical points and the set covering algorithm proposed

in [44] were automated in this work in order to be applicable to a superstructure-based approach and industrial applications (see Supplementary Material).

3.4. Multi-Period Design Problem for Reduced Superstructure

With all critical points obtained, the multi-period design problem for the reduced superstructure and the representative operating points can be formulated. This problem is very similar to problem (5), with the exception that each design proposal $p \in P$ may include a not generalizable number of individual equality constraints $i \in I_p$, inequality constraints $j \in J_p$, and design constraints/variables $d \in DV_p$ as well as an individual set of critical points $c \in CP_p$, which results in an individual set of operating points $op_p \in (S \cup CP_p)$ at which the set of constraints of the respective design proposal must be satisfied. Therefore, problem (5) is reformulated:

$$\begin{aligned}
 \min \text{TAC} &= \sum_{p \in P} y_p * \left\{ \sum_{s \in S} [w_s * C_{\text{operating},s,p}] + C_{\text{investment},p} * \text{CRF} \right\} \\
 \text{s.t.} & \\
 & \left. \begin{aligned}
 & y_p * h_i(x, z, d, \theta_{op,p}) = 0; i \in I_p \\
 & y_p * g_j(x, z, d, \theta_{op,p}) \leq 0; j \in J_p \\
 & y_p * [g_d(x, z, \theta_{op,p}) - (d_{\text{existing}} + d)] \leq 0; d \in DV_p \\
 & d \geq 0 \\
 & x, z, d, \theta_{op,p} \in R, \theta_L \leq \theta_{op,p} \leq \theta_U \\
 & \sum_{p \in P} y_p = 1 \\
 & y_p \in \{0, 1\}; p \in P.
 \end{aligned} \right\} op_p \in (S \cup CP_p) \tag{7}
 \end{aligned}$$

In problem (7), the set of individual design proposals of the reduced superstructure is represented by $p \in P$. Each design proposal is expressed via a binary variable y_p and one and only one of these binary variables is forced to be 1, which will be the design proposal, which performs most cost efficiently at the representative operating points (and critical operating points). Instead of solving problem (7) simultaneously, it may also be solved proposal-wise, setting one y_p to 1 and eventually comparing the TAC of all proposals to identify the most cost-efficient proposal of the reduced superstructure. In this context, it should be noted that all costs that can be associated with the respective retrofit design proposal must be included in the respective cost functions $C_{\text{operating},p}$ and $C_{\text{investment},p}$. This is especially important for retrofitting projects of industrial HENs, which are often very interconnected, and which may cause increased cost in other operational units.

3.5. Feasibility Check

In a final step, the feasibility is checked by means of the methodologies presented in Section 3.2. This step is necessary to ensure that all critical points have been identified (i.e., the set of critical points is complete). As outlined in Section 2.1, the previously derived HEX design characteristics are included, i.e., design constraints and solution obtained by solving the multi-period design problem. Since including design characteristics is likely to increase the complexity of the problem, solutions obtained by the methodologies presented in Section 3.2 should be analyzed and it is advisable to compare the achieved results of different methodologies to reduce the probability of failures. If feasibility for the respective design cannot be guaranteed, the result of the feasibility check can provide useful insights. Besides the flexibility index, the feasibility check provides a point in the space of the uncertain parameters, which limits the flexibility. The vector between this point and the average operating point (see Figure 1) can be used to generate candidates of critical points, which can be added to the multi-period design problem. If the newly generated design is feasible, the critical point has been successfully identified; otherwise, the new flexibility limit is analyzed, and the step is repeated until a feasible design is obtained.

4. Illustrative Example

The methodology described in Section 3 is illustrated using a four-stream example. The example was adapted from Lal et al. [34] with some modifications for demonstration purposes and was used as an initial network in a retrofitting process. In Figure 3, the initial network, the average stream data, and six different retrofit proposals are presented. These retrofit proposals are partly inspired by design proposals obtained by applying the Bridge analysis methodology presented in [34]. The main objective of the different retrofit proposals was to reduce the utility consumption in the heaters of the HEN. Table 1 shows the hot utility demand of the initial network as well as the hot utility demand and the hot utility savings of the six retrofit proposals.

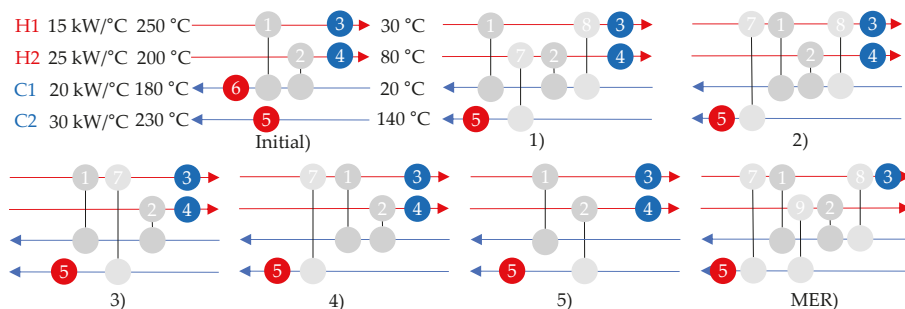


Figure 3. Initial network with average stream data and six different retrofit proposals.

Table 1. Hot utility demand for the initial heat exchanger network (HEN) and the different retrofit proposals as well as the potential savings for average operating conditions.

Proposal Number	Hot Utility Demand [kW] (at Average Conditions)	Hot Utility Savings [kW] (at Average Conditions)
Initial	2700	-
1)	1450	1250
2)	1900	800
3)	2000	700
4)	2000	700
5)	1450	1250
MER)	750	1950

The initial network consists of two process-to-process HEX and four utility HEXs. In Table 2, the design characteristics of the existing process-to-process HEX are listed. For simplicity, it was assumed that the utility HEXs are not limited by size, i.e., any possible duty can be satisfied. For process-to-process HEX, a constant overall heat transfer coefficient (i.e., U-value) of 0.523 kW/(m² °C) was assumed.

Table 2. Design characteristics of the initial network.

HEX	UA Value [kW/°C]	A [m ²]
1	33.68	64.4
2	12.71	24.3

4.1. Structural Feasibility Assessment

The proposed retrofit designs can be considered as different pathways in a superstructure, and in a next step, the structural feasibility of the different proposals was evaluated. For the evaluation,

variations in the four inlet temperatures and heat capacity flow rates were assumed. The variations are shown in Table 3.

Table 3. Variations of the average stream data.

Stream	ΔT^+ [°C]	ΔT^- [°C]	ΔF_{cp}^+ [kW/°C]	ΔF_{cp}^- [kW/°C]
H1	5	10	5	5
H2	10	10	5	5
C1	1	1	0.8	0.8
C2	25	20	2	2

The structural feasibility was evaluated by calculating the flexibility index using the active set approach developed by Floudas and Grossman [39]. Since all constraints $i \in I$ and $j \in J$ (see Section 2.1) are linear, the active set approach guarantees the globality of the solution [39]. In Table 4, the structural flexibility index for each retrofit proposal is listed.

Table 4. Results of the structural feasibility assessment of the different retrofit proposals.

Proposal Number	Structural Flexibility Index
1)	1.47
2)	1.47
3)	1.0
4)	1.0
5)	0.07
MER)	1.18

The flexibility analysis revealed that retrofit proposal 5 is structurally infeasible, i.e., the structural flexibility index is smaller than 1 (see Table 4), meaning that for some operating points within the uncertainty span, the target temperature of at least one stream cannot be reached. This retrofit proposal was therefore removed from the initial superstructure of retrofit proposals, yielding a reduced superstructure.

4.2. Economic Data and Identification of Critical Points

In order to identify the critical points of the different retrofit design proposals, design variables were defined. These design variables could be modified in order to achieve feasibility for the entire range of operating conditions. It was assumed that the area of the two existing units could be increased while new units could be designed freely. Furthermore, the structure of the objective function of the overall design problem was specified. All in all, the total annualized cost (TAC) of the design should be minimized. Consequently, different cost functions were specified:

- Investment cost for a new HEX: $Inv.cost_{new}$;
- Investment cost for increasing an existing HEX: $Inv.cost_{increase}$;
- Operational cost for utility cooling: p_{CU} ; and
- Operational cost for utility heating: p_{HU} .

Additionally, representative operating points $s \in S$, their normalized duration factor w_s , the capital recovery factor CRF, and the annual operating time $t_{operating}$ were specified, in order to achieve cost efficiency for the entire operating period. The structure of the objective function for the retrofit design proposals is given in Equation (8):

$$\min TAC = \sum_{s \in S} [w_s (p_{CU} Q_{CU,s} + p_{HU} Q_{HU,s})] * t_{operating} + (Inv.cost_{increase} + Inv.cost_{new}) * CRF. \quad (8)$$

As mentioned in Section 2.2, the cost function, which is minimized in problem (6) to identify critical points, does not include the operating cost of the representative operating points. The cost function that was used for determining the critical points is given in Equation (9):

$$\min C = (p_{CU}Q_{CU} + p_{HU}Q_{HU}) \cdot t_{operating} + (Inv.cost_{increase} + Inv.cost_{new}) \cdot CRF. \tag{9}$$

For simplicity, it was assumed that the increase of the two existing HEX units could be described by the same cost function. The cost for increasing a HEX in € is given in Equation (10) (A in m^2):

$$Inv.cost_{increase} = 4000 + 2000 \cdot A_{increase}. \tag{10}$$

For new HEX units, it was also assumed that the same cost function is applicable for all possible new HEX units. The cost of a new HEX in € is given in Equation (11) (A in m^2):

$$Inv.cost_{new} = 40,000 + 2000 \cdot A_{HEX}. \tag{11}$$

A capital recovery factor of 0.1 (e.g., 15 years lifetime and an interest rate of 7%) and an annual operating time of 8200 h were assumed. Furthermore, for the operating cost, the data in Table 5 were used. It was further assumed that no additional costs are associated with the retrofit proposals.

Table 5. Cost data for operational cooling and heating.

Utility	Price [€/MWh]
Cooling (p_{CU})	1.7×10^{-3}
Heating (p_{HU}):	15

For each of the five retrofit design proposals, which together constitute the reduced superstructure, one set of critical points was identified. These sets of critical points are listed in Table A5 in Appendix B. The sets of critical points listed in Table A5 are complete, i.e., the designs based on these sets were proven to be feasible by means of flexibility analysis (see Section 4.3). To avoid numerical difficulties, the logarithmic mean temperature difference in the design constraints of the HEXs was approximated using Paterson’s approximation (see, e.g., [47]). As the determination of the critical points was connected to difficulties that were neither reported in the literature nor have been experienced when the results of the available literature examples of critical point analysis of HENs (see [44,45]) were reproduced, a description and a discussion on the determination of the critical points can be found in Appendix A. In this context, modifications on the existing methodologies were suggested to be able to determine critical points for more complex HEN structures but also for retrofit studies of HENs. For more information, see Appendix A.

4.3. Solution of the Multi-Period Design Problem and Final Feasibility Check

In the final step, the multi-period design problem was solved. In order to calculate the TAC of the different design proposals, representative operating points and their respective normalized duration factors were defined. For the illustrative example, 11 representative operating points were assumed. Furthermore, it was assumed that each operating point had the same normalized duration factor. The different representative operating points and their normalized duration factors are given in Table A4 in Appendix B. As can be seen in Table A4, extreme values (which can be calculated with the values given in Table 3) were not considered as representative operating points since these values represent extreme situations, which are usually not representative for longer operating periods.

To reduce the computational complexity, the multi-period design problem was solved individually for each retrofit proposal. The problems were solved using the global solver BARON. Table 6 shows the TAC for the proposals in the reduced superstructure, the annual net savings (difference between the annual operating cost of the initial HEN and the TAC of the proposals), and the flexibility index.

The annual operating cost of the initial HEN was used as a benchmark for the TAC of the different retrofit proposals and was calculated considering the cost data presented in Section 4.2. The annual operating cost of the initial network is 314,600 €/y. Additionally, the derived design values of the process-to-process HEXs of the different retrofit design proposals are shown in Tables A6–A10 in Appendix B. The results in Table 6 indicate that proposal MER is the most cost efficient.

Table 6. Total annualized cost, annual net savings, and flexibility index of the different retrofit design proposals in the reduced superstructure.

Proposal Number	Total Annualized Cost [€/y]	Net Savings [€/y]	Flexibility Index [-]
1)	228,000	86,600	1.00
2)	237,300	77,300	1.19
3)	250,000	64,600	1.00
4)	262,900	51,700	1.00
MER)	223,100	91,500	1.00

The flexibility index was calculated using the active set approach developed by Floudas and Grossman [39] and the results were verified by searching for the minimum direction matrix using simulated annealing as it is reported in [40]. In contrast to [40], the subproblem to find the maximum value for δ (maximum feasible variation of the uncertain parameters) in a given direction was obtained by utilizing BARON. The parameters that were used for the simulated annealing algorithm are shown in Table A11 in Appendix B.

Introducing different representative operating points to the problem increases the problem size and complexity, which may cause longer CPU times to guarantee the globality of the obtained solution. The solutions presented above were obtained on an Intel i7-6600 2.6 GHz processor with 16.0 GB RAM in 1800 s. It is worth mentioning, that globality (within default EpsA range of BARON: $1e-6$) could be achieved in the case of proposals 2, 3, and 4. However, it should be mentioned that the optimality gap for proposal 1 was less than 500 €/y while the largest remaining optimality gap was 37,000 €/y in case of proposal MER. Although the remaining optimality gap of the proposal MER is considerable in comparison to the possible savings, the found local solution was considered satisfactory as it indicates that proposal MER is the most cost efficient.

4.4. Discussion of the Results of the Illustrative Example

As mentioned previously, a discussion around the determination of the set of critical points for the different retrofit proposals of the illustrative example can be found in Appendix A.

Based on the results presented in Table 6, the proposal MER performs the most cost efficiently. This, however, relates to the used cost functions. Different cost functions will certainly lead to different results and another proposal may be most cost efficient. The influence of the cost functions can be illustrated by a comparison of the solutions of proposals 1 and MER. An analysis of the results of the multi-period design problem of proposals 1 and MER revealed that the TAC of proposal 1 consists of 23% annualized capital cost (and 77% operating cost) while the TAC of proposal MER consists of 56% annualized capital cost (and 44% operating cost). Thus, the used cost functions favor design proposals that allow more utilization of the HEX surface area. However, if the cost for the area is increased (e.g., increased parameters in investment cost functions), it can be assumed that design proposals that allow more utilization of utilities will be more cost efficient.

From Table 6, it can be seen that design proposal 2 has a significantly higher flexibility index than 1, which indicates overdesign of the HEX units. This overdesign results from the consideration of the chosen representative operating points. When the multi-period design problem for proposal 2 was solved considering only the identified set of critical points (and discard all operating cost), the flexibility index of the achieved design was calculated as 1. To check the influence of the representative operating periods and thereby the completeness of the identified sets of critical points, similar calculations were

also made for the other design proposals in the reduced superstructure and the results are shown in Table 7. The results in Table 7 indicate that the sets of critical points shown in Table A5 are complete as it was possible to achieve feasible design characteristics (flexibility index is 1) respecting only the sets of critical points. As all operating costs were discarded, the objective function of these design problems represented only the total annualized capital cost of a certain design.

Table 7. Total annualized (capital) cost and flexibility index of the different retrofit design proposals in the reduced superstructure without considering the representative operating points.

Proposal Number	Total Annualized (Capital) Cost [€/y]	Flexibility Index [-]
1)	19,600	1.00
2)	19,600	1.00
3)	37,200	1.00
4)	37,200	1.00
MER)	95,600	1.00

5. Conclusions

In this work, a novel framework for retrofitting multi-period HENs was developed and presented. The proposed framework divides the retrofit design process into five sub-steps, which allows for the combining of the beneficial designer interaction of graphical approaches (e.g., Pinch based) at an early stage in the design process with the efficiency of mathematical programming to derive flexible and cost-efficient retrofit measures. In this context, inefficient trial and error procedures are avoided. Additionally, by means of splitting the design process in five different sub-steps, the complexity of the sub-problems is decreased compared to the overall problem.

The proposed framework utilizes the designer interaction of graphical approaches to derive different design proposals, which can be very beneficial for large and complex HENs usually found in industrial heat recovery systems. Well-proven, single-period retrofit design methods, such as Bridge analysis, but also “experience-based” retrofit design proposals may be employed. As the single-period character of graphical retrofitting methodologies does not ensure the flexibility and cost-efficiency of the generated proposals for the entire operating period, different mathematical evaluation strategies are incorporated in the proposed framework. By means of structural feasibility assessment based on the calculation of the flexibility index, structurally infeasible design proposals can be identified and discarded from further analysis. Additionally, critical point analysis was suggested to identify those operating points within the uncertainty span that determine necessary overdesign of the HEXs to ensure feasibility of the HEN retrofit proposals for the entire operating range. In order to identify the most cost-efficient proposal, a multi-period MI(N)LP optimization problem was formulated, which considers the identified critical points (for feasibility) as well as representative operating points (for cost-efficiency). A final feasibility check was suggested to ensure that the complete set of critical points has been identified.

The determination of critical points based on [44] was automated and the achieved results were discussed. Compared to the available literature examples, the HEN examples included in this study are more complex, which caused difficulties when determining critical points. Modifications of the existing methodologies (see Appendix A) were suggested in order to identify the complete set of critical points for the HEN retrofit example presented in this study. It is worth mentioning that by means of the above-mentioned final feasibility check, an incomplete set of critical points is recognized. Additionally, by means of the obtained results of the final feasibility check, the missing critical point(s) can be identified to be included in the multi-period MI(N)LP design problem.

The framework presented in this paper yields opportunities to increase heat recovery in applications operating at multiple periods, e.g., industrial applications. As decarbonization of industry is essential to limit the increase of the global average temperature well below 2 °C, systematic approaches to successfully retrofit industrial heat recovery systems are in demand more than ever.

In comparison to existing approaches for retrofitting multi-period HENs, the presented framework splits the design process in five different sub-steps, which decreases the complexity of the sub-problems. The decreased complexity can be the decisive factor for a successful retrofit project when large and complex industrial applications are addressed. The novel contributions of this paper are summarized in the following list:

- Development of a novel framework to achieve flexible and cost-efficient retrofit measures for HENs operating at multiple periods;
- Implementation of critical point analysis in a retrofitting framework to achieve flexible retrofit solutions of HENs;
- Possibility to employ well-proven, single-period retrofit design methods, e.g., advanced composite curves, Bridge analysis, etc., but also “experience-based” retrofit design proposals in a framework that guarantees flexibility and cost efficiency (with respect to investment and operating cost) for the entire operating period;
- Possibility to compare design proposals of different single-period retrofit design methods in a superstructure-based mathematical program ensuring flexibility and cost efficiency with respect to investment and operating cost;
- Automatization of the KKT-formulation, the two-level formulation, and the set-covering algorithm initially suggested by Pintarič and Kravanja [44] to identify critical points of different design proposals (see Supplementary Material); and
- Extension of the set covering algorithm suggested by Pintarič and Kravanja [44] in order to handle more complex network structures (see Appendix A).

Supplementary Materials: The following are available online at <http://www.mdpi.com/1996-1073/13/6/1472/s1>: Directory with source code of the automated determination of critical points including the following files: `Main_KKT.py`, `Main_2_level.py`, `CalcA.py`, `ExtendedSetCovAlgorithm.py`, `Lower_Control_Design.py`, `SetCovAlgorithm.py`, `Upper_Uncertainty.py`. Additionally, model instances are provided to test the automated KKT-formulation and two-level formulation on each of the 5 different design proposals (in the reduced superstructure) discussed in Section 4 (see e.g., Figure 3 and Table 6).

Author Contributions: Conceptualization, C.L. and E.S.; methodology, C.L. and E.S.; software, C.L.; validation, C.L.; formal analysis, C.L.; investigation, C.L.; resources, S.H.; data curation, C.L.; writing—original draft preparation, C.L.; writing—review and editing, E.S. and S.H.; visualization, C.L.; supervision, E.S.; project administration, S.H.; funding acquisition, E.S. and S.H. All authors have read and agreed to the published version of the manuscript.

Funding: This research was funded by the Swedish Energy Agency, grant number P42326, and the Södra Foundation for Research, Development and Education.

Acknowledgments: We would like to thank Gulnara Shavaliyeva, Holger Wiertzema, Paraskevi Karka, Sofie Marton and Stavros Papadokostantakis for interesting discussions and useful suggestions. Furthermore, we would like to acknowledge three anonymous reviewers for their valuable comments.

Conflicts of Interest: The authors declare no conflict of interest. The funders had no role in the design of the study; in the collection, analyses, or interpretation of data; in the writing of the manuscript, or in the decision to publish the results.

Appendix A. Discussion on the Determination of Critical Points

As mentioned in Section 4, the determination of critical points for the illustrative example was connected to difficulties. These difficulties are described in the following subsections and explanation attempts, and future work is proposed. This section of the appendix is intended for the interested reader and concerns specific issues related to the mathematical formulation of the critical point analysis.

For the determination of critical points, the three different strategies and the set covering algorithm presented by Pintarič and Kravanja in [44] were considered. As previously mentioned, the approximate one-level formulation depends on a heuristically chosen Big-M parameter and solutions can be very sensitive to this parameter [44]. For this reason, the approximate one-level formulation was discarded from this study. It was identified that depending on the chosen strategy, different aspects need to be considered, which may relate to the structure of the HEN under investigation.

Appendix A.1. Two-Level Formulation

The two-level formulation approximates the solution of the KKT-formulation and may be impractical for large industrial applications since an iterative scheme is involved. The main idea of the two-level formulation is to decompose the max-min problem ((6) in Section 2.2) into two subproblems, which can be solved separately in an iterative procedure. The two subproblems are:

- The lower (control-design) level problem; and
- The upper (uncertainty) level problem.

At iteration k , in the lower (control-design) level problem, the solution of the minimization problem ($\min_{x,z,d} C(x, z, d, \theta)$) is approximated for fixed values of the uncertain parameters (obtained from upper (uncertainty) level problem in iteration $k-1$). In the upper (uncertainty) level problem, the solution of the maximization problem ($\max_{\theta} d_i$) is approximated by fixing the control variables to the values obtained by the lower (control-design) level problem while the uncertain parameters are relaxed to continuous variables within their respective bounds. The iteration procedure is stopped if the values obtained for the design variable d_i at the lower and upper level problem are within a previously defined range. By means of the two-level formulation, the operating point in the uncertainty span is obtained at which the maximum value for the design variable d_i is achieved while the cost function $C(x, z, d, \theta)$ is minimized (i.e., a potential critical point). For further details concerning the iterative procedure, see [44].

The iterative scheme can be tedious for large-scale industrial problems with many design variables, control variables, and uncertain parameters. To overcome this problem, the iterative scheme was automated as part of this study (see Supplementary Material). In this automation, the lower (control-design) level problem was solved using BARON and the upper (uncertainty) level problem was solved using the GAMS interface of CONOPT or IPOPT to obtain marginal values. In order to apply the two-level formulation, control variables need to be determined. Industrial systems may be complex and very interconnected, which results in many different and complex control strategies.

A mathematical analysis of the model equations (h_i with $i \in I$) of the design proposals, which form the reduced superstructure of the illustrative example, revealed that the proposals demand either two (proposals 3 and 4) or three control variables (proposals 1, 2, and MER). This allows different combinations of control variables and it is worth mentioning that the obtained sets of critical points were not equivalent with respect to the solution of the final design problem. This will be explained at the example of design proposal 3. If the control variables are limited to the duties of the utility exchangers (Q3, Q4, and Q5 in Figure 3), three control variable combinations are possible. When using these different combinations to obtain the critical points through the two-level formulation and the set covering algorithm described in [44], different sets of critical points were obtained. These different sets, the TAC of the designs based on the different sets, and the corresponding flexibility index are shown in Table A1. As can be seen in Table A1, with only one of the tested control variable combinations, it was possible to achieve a feasible design.

Table A1. Results of the two-level formulation for design proposal 3.

Control Variables	Critical Points (Read as Follows)	Total Annualized Cost [€/y]	Flexibility Index [-]
	[$T_{in,H1}, T_{in,H2}, T_{in,C1}, T_{in,C2}, F_{CPH1}, F_{CPH2}, F_{CP C1}, F_{CP C2}$] with T in [$^{\circ}C$] and F_{cp} in [$kW/^{\circ}C$]		
Q3, Q4	[240.0, 190.0, 19.0, 165.0, 20.0, 20.0, 20.8, 28.0]	221,400	0.69
	[255.0, 190.0, 21.0, 165.0, 20.0, 30.0, 19.2, 28.0]		
Q3, Q5	[240.0, 190.0, 21.0, 120.0, 10.0, 0, 20.8, 32.0]	218,600	0.5
	[255.0, 190.0, 21.0, 165.0, 20.0, 0, 20.8, 28.0] [0, 190.0, 21.0, 120.0, 20.0, 0, 20.8, 32.0]		
Q4, Q5	[240.0, 190.0, 21.0, 120.0, 10.0, 30.0, 19.2, 32.0]	250,000	1.00
	[240.0, 190.0, 19.0, 120.0, 10.0, 20.0, 20.8, 32.0]		

It was identified that in order to be applicable to HEN retrofitting problems, including the possibility to increase the size of existing HEX units, the lower (control-design) level problem of iteration k (A1) of the two-level formulation (compare [44]) needs to be modified. For a selected design variable d_i , the lower (control-design) problem is relaxed the following way:

$$\begin{aligned}
 & \min_{x,z,d} C(x, z, d, \theta^{k-1}) \\
 & \text{s.t.} \\
 & h_i(x, z, d, \theta^{k-1}) = 0; i \in I \\
 & g_j(x, z, d, \theta^{k-1}) \leq 0; j \in J \\
 & g_d(x, z, \theta) - (d_{\text{existing}} + d) \leq 0; \forall d \in DV \setminus \{d_i\} \\
 & g_{d,i}(x, z, \theta) - (d_{i,\text{existing}} + d_i) = 0; d_i \in DV \\
 & x, z, d \in R, d \geq 0.
 \end{aligned} \tag{A1}$$

Physically, this reformulation implies that existing HEX units can be bypassed, which may be necessary to ensure the feasibility of the lower (control-design) level problem for given values of the uncertain parameters (obtained by the upper (uncertainty) level problem of the previous iteration).

As mentioned previously, the two-level formulation approximates the solution of the KKT-formulation, which would explain discrepancies between the sets of critical points identified with the two-level and the KKT-formulation. However, to the authors’ knowledge, the influence of differently chosen control variables on the sets of critical points (and thereby on the flexibility index of the corresponding design) when applying the two-level formulation was not yet reported in the literature. It is worth mentioning that similar observations were made for proposal 4, although the values for the TAC and the flexibility index were different compared to Table A1.

Furthermore, it was observed that with more complex network structures, additional difficulties may occur if the two-level formulation is applied. This will be explained at the example of proposal 1. In the case of proposal 1, three control variables need to be defined, which are fixed when solving the upper (uncertainty) level problem. Again, different combinations were tested, and the flexibility indices of the derived designs were calculated (see Table A2). For explanation of the variable names of the control variables, refer to Figure A1 in Appendix B. As can be seen from the flexibility indices in Table A2, with none of the tested combinations of control variables, a feasible design could be derived. It is worth mentioning that depending on the choice of the control variables, convergence between the lower (control-design) level problem and the upper (uncertainty) level problem could not be achieved for at least some of the design variables of proposal 1. Similar observations were made when the two-level formulation was used to identify the sets of critical points for proposals 2 and MER.

Table A2. Results of the two-level formulation for design proposal 1.

Control Variables	Critical Points (Read as Follows)	Total Annualized Cost [€/y]	Flexibility Index [-]	Convergence between Upper and Lower Problem
	[$T_{in,H1}, T_{in,H2}, T_{in,C1}, T_{in,C2}, F_{CPH1}, F_{CPH2}, F_{CPC1}, F_{CPC2}$] with T in [°C] and Fcp in [kW/°C]			
Q4, Q5, Q6	[240.0, 190.0, 19.0, 120.0, 20.0, 30.0, 20.8, 32.0] [240.0, 190.0, 19.0, 120.0, 20.0, 20.0, 20.8, 32.0] [255.0, 190.0, 21.0, 120.0, 20.0, 0, 19.2, 32.0]	227,200	0.92	Not converged (30 iterations) for some design variables
Q4, Q6, T8	[240.0, 190.0, 19.0, 120.0, 20.0, 20.0, 20.8, 32.0] [255.0, 190.0, 19.0, 120.0, 20.0, 20.0, 19.2, 32.0]	227,200	0.92	converged
Q6, T2, T8	[240.0, 190.0, 21.0, 120.0, 20.0, 0, 20.8, 32.0] [255.0, 190.0, 21.0, 120.0, 20.0, 0, 19.2, 32.0]	227,200	0.92	converged
T1, T4, T7	[240.0, 210.0, 19.0, 165.0, 10.0, 30.0, 20.8, 28.0] [255.0, 210.0, 19.0, 165.0, 20.0, 30.0, 20.8, 28.0]	227,200	0.92	converged

These observations could have several explanations: Another, not tested, combination of control variables must be chosen, the calculation of the marginal values of GAMS is not sufficiently accurate, the set covering algorithm is not globally valid, or the approximative character of the solution of the two-level formulation is too strong. When analyzing the complete set of critical points of proposal 1, which is shown in Table A5 in Appendix B, it was found that the actual critical point is [240.0, 190.0,

19.0, 120.0, 10.0, 20.0, 20.8, 32.0] (i.e., this point is sufficient to derive a feasible design for proposal 1). An indication for a not valid set covering algorithm would be if this critical point can be found as a combination of one of the above presented points, i.e., if a “0” element in one of the points could be replaced with another value to achieve the critical point. This, however, is not possible. This is not proof that the set covering algorithm is globally valid. It indicates, however, that in the case of proposal 1, the set covering algorithm is not responsible for missing the critical point and one of the other above listed reasons must be responsible. Future work should focus on identifying strategies or guidelines for the application of the two-level formulation to HENs.

As mentioned previously, the difficulties experienced with the two-level formulation are not reported in the literature. These difficulties did not appear when the results reported in the literature (application of two-level formulation to the HEN example; see [44]) were reproduced. It was assumed that the experienced difficulties are related to structural differences. Compared to the structure of the HEN example in the literature, the structure of the examples presented in Section 4 differs. In the literature example, the respective HEN consists of more streams (seven) while the number of process-to-process HEX (four) is similar to (some of) the presented examples in Section 4. Consequently, it was observed that the distribution of HEXs is different in the literature example. For example, in the literature example, only one process stream is connected to two process-to-process HEXs while all other streams are connected to one process-to-process HEX, only. Additionally, the literature example demands only one control variable. Therefore, it can be assumed that the control structure of the literature example is simpler as the HEN itself is less interconnected compared to the HEN examples in this study. A preliminary conclusion drawn from this is that with increasing structural complexity of the HEN of interest, the risk for failure of the two-level formulation increases. Possible assessment criteria for the structural complexity of a HEN are:

- Ratio between the number of process streams and the number of process-to-process HEX: The higher this number, the less complex the HEN; and
- Number of process-to-process HEX connected to a single process stream: The higher this number, the more complex the HEN.

In this context, it is worth mentioning that it was possible to derive the complete set of critical points by means of the two-level formulation for the structurally less complex design proposals 3 and 4 while it was not possible for the more complex design proposals 1, 2, and MER.

Appendix A.2. A Karush–Kuhn–Tucker (KKT-)Formulation

The main idea of the KKT-formulation is to apply the KKT conditions to the minimization problem of problem (6) ($\min_{x,z,d} C(x,z,d,\theta)$) and then solve the remaining single-level optimization problem ($\max_{\theta} d_i$) for each design variable $d_i \in DV$ individually. Similar to the result of the two-level formulation, the result of the KKT-formulation is the operating point in the uncertainty span at which the maximum value for d_i is obtained while the cost function $C(x,z,d,\theta)$ is minimized (i.e., a potential critical point) [44]. If one is able to solve the KKT-formulation globally, the solution represents the global solution of problem (6). In contrast to the two-level formulation, the solution process of the KKT-formulation does not involve an iterative procedure. However, a global NLP solver is necessary to solve the resulting problem, which may cause difficulties for large industrial applications. Additionally, as global solvers usually do not provide marginal values, an (local) NLP solver needs to be applied afterwards to obtain marginal values, which are necessary to identify the influencing uncertain parameters (compare [44]).

In order to obtain marginal values, in this study, the KKT-formulation was first solved using BARON and the found solution was used as an initialization for IPOPT in GAMS. However, the calculation of BARON was interrupted after 300 s and the best (local) obtained solution was used for the initialization of IPOPT. In all tested cases, IPOPT returned the same value as BARON and marginal values were provided. The KKT-formulation was solved for the five different design

proposals. For design proposals 1, 2, 3, and 4, the sets of critical points which are shown in Table A5 in Appendix B (i.e., the complete sets of critical points) were obtained by solving the KKT-formulation and applying the set covering algorithm as it was reported by Pintarič and Kravanja in [44]. However, the situation was different for the design proposal MER. The set of critical points that was obtained by the KKT-formulation and the set covering algorithm for proposal MER together with the corresponding TAC and flexibility index are shown in Table A3.

Table A3. Results of the Karush–Kuhn–Tucker (KKT)-formulation of design proposal MER.

Proposal Number	Critical Points (Read as Follows)	Total Annualized Cost [€/y]	Flexibility Index [-]
	[$T_{in,H1}$, $T_{in,H2}$, $T_{in,C1}$, $T_{in,C2}$, F_{cpH1} , F_{cpH2} , F_{cpC1} , F_{cpC2}] with T in [°C] and F_{cp} in [kW/°C]		
MER	[240.0, 190.0, 21.0, 120.0, 20.0, 0, 20.8, 32.0] [255.0, 0, 21.0, 165.0, 20.0, 30.0, 19.2, 28.0] [240.0, 210.0, 21.0, 120.0, 0, 30.0, 19.2, 32.0] [0, 190.0, 19.0, 120.0, 10.0, 20.0, 20.8, 32.0]	202,000	0.75

Comparing the TAC and the flexibility index shown in Table A3 to the results for the proposal MER shown in Table 6 indicates that the set of critical points (shown in Table A3) is incomplete. A first solution attempt was to investigate the influence of the uncertain parameters that have “0” elements in the set of critical points (e.g., F_{cpH2} in the first identified critical point of the set shown in Table A3). These “0” elements result from the calculation of the marginal values of the uncertain parameters, meaning that the corresponding uncertain parameter was discovered to have no influence on at least one of the design variables when solving the KKT formulation (compare [44]). When solving the design problem, the uncertain parameters corresponding to these “0” elements are defined as variables for the respective critical point, i.e., these uncertain parameters can obtain any value within the uncertainty span at the solution of the design problem. As the identified sets were incomplete, it seemed that the influence of one or several uncertain parameters was not correctly detected. This was investigated by extending the set covering algorithm. In addition to the three steps reported in the appendix of [44], a fourth step was added. In this step, each “0” element present in the set of critical points, obtained after the first three steps, was replaced with all possible combinations with respect to the other points in the set and the set covering formulation (AP6 in [44]) is solved.

Example: If a set consists of the following three points [1,2,1,1], [1,1,3,1] and [2,0,0,1], the third point is replaced by all possible combinations with respect to elements of the first two points. For each of the two “0” elements of the third point (second and third element), the nonzero values in the other two points are considered to replace the 0: (1,2) for the second element and (1,3) for the third element. Eventually, four additional candidates to replace the third point are found: [2,1,1,1], [2,1,3,1], [2,2,1,1], and [2,2,3,1]. After applying the previously mentioned set covering formulation, one candidate point remains: [2,2,1,1]. This candidate point replaces the third point of the initial set.

With this additional step in the set covering algorithm, the set of critical points shown in Table A3 was transformed to the set of critical points that is shown in Table A5 in Appendix B. Eventually, with the additional step in the set covering algorithm, the complete set of critical points was found, and the feasible design for the proposal MER was achieved (see Table 6).

Obviously, the KKT-formulation is easier to solve for less complex HENs as the different HEX units are less dependent on each other. This is reflected in the achieved results as the extended set covering algorithm was only necessary to identify the complete set of critical points for proposal MER. In all other cases, the extra step in the extended set covering algorithm was not necessary. It was further investigated if increasing the maximum calculation time of BARON would result in different solutions for proposal MER. However, even an increase to 1000 s did not have any impact on the results. Actually, for several design variables, the best (local) solution was found before BARON started iterating, i.e., during the local search before the iteration scheme of BARON is executed. This implies that different starting points could have an impact. However, the influence of different starting points was not studied.

The achieved results indicate that more complex HEN structures can be handled by means of the KKT-formulation compared to the two-level formulation. Future work should focus on rather complex HEN structures and investigate if modifications of the KKT-formulation are necessary to ensure that, in combination with the extended set covering algorithm, the complete set of critical points can be identified.

Appendix A.3. Adding Critical Points via Flexibility Assessment

If it is not possible to identify the critical points of the HEN by following the strategies described in [44] and the above suggested modifications and investigations (e.g., different combinations of control variables when applying the two-level formulation), the results of the feasibility check may be utilized. Although it was possible to identify the complete sets of critical points for all design proposals of the reduced superstructure, this step is demonstrated on the example of the proposal MER. Utilizing the KKT formulation, the set of critical points shown in Table A3 were identified. The operating point that limits the flexibility was obtained and the normalized vector between the limiting point and the average operating point (see stream data in Figure 3) was calculated. As the obtained vector was a direction of the corner point [240.0, 210.0, 21.0, 165.0, 10.0, 30.0, 19.2, 28.0], this corner point was added to the set of critical points and the multi-period design problem was solved again. The solution obtained was similar to the feasible design of the proposal MER shown in Table 6. Consequently, in this example, one iteration was necessary to achieve the complete set of critical points and thereby a feasible design. There is, however, no guarantee that one iteration would be sufficient for any other example. It is assumed that especially for examples with one or several critical points that are not corner points, more iterations (and probably trial and error evaluations) are necessary.

Appendix B.

In the following appending section, different tables and figures are shown, which are referred to in previous sections of the article.

Table A4. Representative operating points for the illustrative example.

$T_{in,H1}$ [°C]	$T_{in,H2}$ [°C]	$T_{in,HC1}$ [°C]	$T_{in,C2}$ [°C]	F_{cpH1} [kW/°C]	F_{cpH2} [kW/°C]	F_{cpC1} [kW/°C]	F_{cpC2} [kW/°C]	W_s [-]
243.65	208.10	19.59	155.49	15.44	23.23	20.14	28.60	1/11
249.72	202.83	20.29	156.26	16.14	21.22	19.87	29.51	1/11
246.41	202.73	20.34	162.06	16.50	28.27	20.49	29.59	1/11
248.81	194.63	20.04	133.91	16.40	25.15	20.23	31.24	1/11
249.82	202.35	20.76	136.65	12.00	27.33	19.72	31.40	1/11
247.16	200.40	19.21	124.26	14.96	25.44	19.88	30.61	1/11
248.18	200.50	20.56	158.58	19.83	24.80	20.51	28.78	1/11
242.30	206.05	19.89	157.40	11.83	22.99	19.61	30.97	1/11
244.50	207.36	19.13	160.11	14.09	25.36	19.99	30.75	1/11
248.71	204.38	20.02	140.01	13.03	20.93	20.18	30.28	1/11
253.53	191.07	19.39	127.44	12.99	27.18	20.29	30.82	1/11

Table A5. Sets of critical points for the different design proposal of the reduced superstructure.

Proposal Number	Critical Points (Read as Follows)
	$[T_{in,H1}, T_{in,H2}, T_{in,C1}, T_{in,C2}, F_{cpH1}, F_{cpH2}, F_{cpC1}, F_{cpC2}]$ with T in [°C] and Fcp in [kW/°C]
1)	[240.0, 190.0, 21.0, 120.0, 10.0, 20.0, 20.8, 32.0]
	[255.0, 210.0, 19.0, 120.0, 10.0, 30.0, 20.8, 32.0]
	[240.0, 190.0, 19.0, 120.0, 10.0, 20.0, 20.8, 32.0]
2)	[240.0, 190.0, 19.0, 120.0, 10.0, 20.0, 20.8, 32.0]
	[240.0, 190.0, 19.0, 120.0, 20.0, 20.0, 20.8, 32.0]
	[255.0, 190.0, 19.0, 165.0, 20.0, 20.0, 19.2, 28.0]
	[255.0, 190.0, 19.0, 165.0, 0, 20.0, 20.8, 28.0]
3)	[240.0, 190.0, 21.0, 120.0, 10.0, 20.0, 20.8, 28.0]
	[240.0, 190.0, 19.0, 120.0, 10.0, 20.0, 20.8, 28.0]
	[255.0, 190.0, 0, 120.0, 20.0, 20.0, 20.8, 28.0]
4)	[240.0, 190.0, 21.0, 120.0, 20.0, 20.0, 20.8, 32.0]
	[240.0, 190.0, 19.0, 0, 10.0, 20.0, 20.8, 0]
	[255.0, 190.0, 0, 165.0, 20.0, 20.0, 19.2, 28.0]
MER)	[255.0, 190.0, 21.0, 165.0, 20.0, 30.0, 19.2, 28.0]
	[255.0, 190.0, 19.0, 120.0, 10.0, 20.0, 20.8, 32.0]
	[240.0, 190.0, 21.0, 120.0, 20.0, 20.0, 20.8, 32.0]
	[240.0, 210.0, 21.0, 120.0, 10.0, 30.0, 19.2, 32.0]
	[255.0, 210.0, 21.0, 165.0, 20.0, 30.0, 19.2, 28.0]
	[240.0, 190.0, 21.0, 120.0, 20.0, 30.0, 20.8, 32.0]
	[240.0, 210.0, 21.0, 120.0, 20.0, 30.0, 19.2, 32.0]
	[240.0, 190.0, 19.0, 120.0, 10.0, 20.0, 20.8, 32.0]

Table A6. Design characteristics for design proposal 1.

HEX	ΔUA [kW/°C]	ΔA [m ²]
1	13.58	25.97
2	1.02	1.95
7	77.81	148.77
8	9.94	19.01

Table A7. Design characteristics for design proposal 2.

HEX	ΔUA [kW/°C]	ΔA [m ²]
1	0.0	0.0
2	26.5	50.67
7	26.59	50.84
8	19.35	37.0

Table A8. Design characteristics for design proposal 3.

HEX	ΔUA [kW/°C]	ΔA [m ²]
1	74.87	143.16
2	39.71	75.93
7	57.59	110.11

Table A9. Design characteristics for design proposal 4.

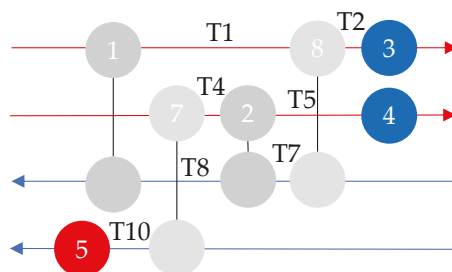
HEX	ΔUA [kW/°C]	ΔA [m ²]
1	74.87	143.16
2	20.04	38.32
7	24.69	47.21

Table A10. Design characteristics for design proposal MER.

HEX	ΔUA [kW/°C]	ΔA [m ²]
1	26.71	51.07
2	103.96	198.78
7	33.22	63.51
8	9.57	18.30
9	89.36	170.85

Table A11. Parameters for simulated annealing algorithm.

Parameter	Value
Initial temperature	10 K
Final temperature	2×10^{-20} K
Annealing of temperature	$0.974 * T$
Stop criterion	No improvement after 2000 iterations

**Figure A1.** Internal network temperatures of design proposal 1.

References

- Linnhoff, B.; Hindmarsh, E. The pinch design method for heat exchanger networks. *Chem. Eng. Sci.* **1983**, *38*, 745–763. [\[CrossRef\]](#)
- Floudas, C.A.; Ciric, A.R.; Grossmann, I.E. Automatic synthesis of optimum heat exchanger network configurations. *AIChE J.* **1986**, *32*, 276–290. [\[CrossRef\]](#)
- Yee, T.F.; Grossmann, I.E. Simultaneous optimization models for heat integration. II. Heat exchanger network synthesis. *Comput. Chem. Eng.* **1990**, *14*, 1165–1184. [\[CrossRef\]](#)
- Jiang, N.; Bao, S.; Gao, Z. Heat Exchanger Network Integration Using Diverse Pinch Point and Mathematical Programming. *Chem. Eng. Technol.* **2011**, *34*, 985–990. [\[CrossRef\]](#)
- Axelsson, E.; Olsson, M.R.; Berntsson, T. Heat integration opportunities in average Scandinavian kraft pulp mills: Pinch analyses of model mills. *Nord. Pulp Pap. Res. J.* **2006**, *21*, 466–475. [\[CrossRef\]](#)
- Bengtsson, C.; Nordman, R.; Berntsson, T. Utilization of excess heat in the pulp and paper industry—A case study of technical and economic opportunities. *Appl. Therm. Eng.* **2002**, *22*, 1069–1081. [\[CrossRef\]](#)
- Escobar, M.; Trierweiler, J.O. Optimal heat exchanger network synthesis: A case study comparison. *Appl. Therm. Eng.* **2013**, *51*, 801–826. [\[CrossRef\]](#)
- Persson, J.; Berntsson, T. Influence of seasonal variations on energy-saving opportunities in a pulp mill. *Energy* **2009**, *34*, 1705–1714. [\[CrossRef\]](#)

9. Kang, L.; Liu, Y. Synthesis of flexible heat exchanger networks: A review. *Chin. J. Chem. Eng.* **2019**, *27*, 1485–1497. [[CrossRef](#)]
10. Kotjabasakis, E.; Linnhoff, B. Sensitivity tables for the design of flexible processes (1)—How much contingency in heat exchanger networks is cost-effective? *Chem. Eng. Res. Des.* **1986**, *64*, 197–211.
11. Hafizan, A.M.; Klemeš, J.J.; Alwi, S.R.W.; Manan, Z.A.; Hamid, M.K.A. Temperature disturbance management in a heat exchanger network for maximum energy recovery considering economic analysis. *Energies* **2019**, *12*, 594. [[CrossRef](#)]
12. Linnhoff, B.; Vredeveld, D.R. Pinch Technology Has Come of Age. *Chem. Eng. Prog.* **1984**, *80*, 33–40.
13. Floudas, C.A.; Grossmann, I.E. Synthesis of flexible heat exchanger networks for multiperiod operation. *Comput. Chem. Eng.* **1986**, *10*, 153–168. [[CrossRef](#)]
14. Floudas, C.A.; Grossmann, I.E. Automatic generation of multiperiod heat exchanger network configurations. *Comput. Chem. Eng.* **1987**, *11*, 123–142. [[CrossRef](#)]
15. Floudas, C.A.; Grossmann, I.E. Synthesis of flexible heat exchanger networks with uncertain flowrates and temperatures. *Comput. Chem. Eng.* **1987**, *11*, 319–336. [[CrossRef](#)]
16. Aaltola, J. Simultaneous synthesis of flexible heat exchanger network. *Appl. Therm. Eng.* **2002**, *22*, 907–918. [[CrossRef](#)]
17. Verheyen, W.; Zhang, N. Design of flexible heat exchanger network for multi-period operation. *Chem. Eng. Sci.* **2006**, *61*, 7730–7753. [[CrossRef](#)]
18. Short, M.; Isafiade, A.J.; Fraser, D.M.; Kravanja, Z. Two-step hybrid approach for the synthesis of multi-period heat exchanger networks with detailed exchanger design. *Appl. Therm. Eng.* **2016**, *105*, 807–821. [[CrossRef](#)]
19. Tveit, T.M.; Aaltola, J.; Laukkanen, T.; Laihanen, M.; Fogelholm, C.J. A framework for local and regional energy system integration between industry and municipalities—Case study UPM-Kymmene Kaukas. *Energy* **2006**, *31*, 2162–2175. [[CrossRef](#)]
20. Lai, Y.Q.; Manan, Z.A.; Alwi, S.R.W. Simultaneous diagnosis and retrofit of heat exchanger network via individual process stream mapping. *Energy* **2018**, *155*, 1113–1128. [[CrossRef](#)]
21. Kamel, D.A.; Gadalla, M.A.; Abdelaziz, O.Y.; Labib, M.A.; Ashour, F.H. Temperature driving force (TDF) curves for heat exchanger network retrofit—A case study and implications. *Energy* **2017**, *123*, 283–295. [[CrossRef](#)]
22. Bonhivers, J.C.; Srinivasan, B.; Stuart, P.R. New analysis method to reduce the industrial energy requirements by heat-exchanger network retrofit: Part 1—Concepts. *Appl. Therm. Eng.* **2017**, *119*, 659–669. [[CrossRef](#)]
23. Ciric, A.R.; Floudas, C.A. A comprehensive optimization model of the heat exchanger network retrofit problem. *Heat Recovery Syst. CHP* **1990**, *10*, 407–422. [[CrossRef](#)]
24. Asante, N.D.K.; Zhu, X.X. An automated and interactive approach for heat exchanger network retrofit. *Chem. Eng. Res. Des.* **1997**, *75*, 349–360. [[CrossRef](#)]
25. Athier, G.; Floquet, P.; Pibouleau, L.; Domenech, S. A mixed method for retrofitting heat-exchanger networks. *Comput. Chem. Eng.* **1998**. [[CrossRef](#)]
26. Smith, R.; Jobson, M.; Chen, L. Recent development in the retrofit of heat exchanger networks. *Appl. Therm. Eng.* **2010**, *30*, 2281–2289. [[CrossRef](#)]
27. Jiang, N.; Shelley, J.D.; Doyle, S.; Smith, R. Heat exchanger network retrofit with a fixed network structure. *Appl. Energy* **2014**. [[CrossRef](#)]
28. Akpomimie, M.O.; Smith, R. Retrofit of heat exchanger networks with heat transfer enhancement based on an area ratio approach. *Appl. Energy* **2016**. [[CrossRef](#)]
29. Sreepathi, B.K.; Rangaiah, G.P. Review of Heat Exchanger Network Retrofitting Methodologies and Their Applications. *Ind. Eng. Chem. Res.* **2014**, *53*, 11205–11220. [[CrossRef](#)]
30. Persson, J.; Berntsson, T. Influence of short-term variations on energy-saving opportunities in a pulp mill. *J. Clean. Prod.* **2010**, *18*, 935–943. [[CrossRef](#)]
31. Kang, L.; Liu, Y. Retrofit of heat exchanger networks for multiperiod operations by matching heat transfer areas in reverse order. *Ind. Eng. Chem. Res.* **2014**, *53*, 4792–4804. [[CrossRef](#)]
32. Papalexandri, K.P.; Pistikopoulos, E.N. A Retrofit Design Model for Improving the Operability of Heat Exchanger Networks. In *Energy Efficiency in Process Technology*; Pilavachi, P.A., Ed.; Springer: Dordrecht, The Netherlands, 1993; pp. 915–928.
33. Nordman, R.; Berntsson, T. Use of advanced composite curves for assessing cost-effective HEN retrofit I: Theory and concepts. *Appl. Therm. Eng.* **2009**, *29*, 275–281. [[CrossRef](#)]

34. Lal, N.S.; Atkins, M.J.; Walmsley, T.G.; Walmsley, M.R.W.; Neale, J.R. Insightful heat exchanger network retrofit design using Monte Carlo simulation. *Energy* **2019**, *181*, 1129–1141. [[CrossRef](#)]
35. Langner, C.; Svensson, E.; Harvey, S. Combined Flexibility and Energy Analysis of Retrofit Actions for Heat Exchanger Networks. *Chem. Eng. Trans.* **2019**, *76*, 307–312. [[CrossRef](#)]
36. Marselle, D.F.; Morari, M.; Rudd, D.F. Design of resilient processing plants—II Design and control of energy management systems. *Chem. Eng. Sci.* **1982**, *37*, 259–270. [[CrossRef](#)]
37. Saboo, A.K.; Morari, M.; Woodcock, D.C. Design of resilient processing plants—VIII. A resilience index for heat exchanger networks. *Chem. Eng. Sci.* **1985**, *40*, 1553–1565. [[CrossRef](#)]
38. Swaney, R.E.; Grossmann, I.E. An index for operational flexibility in chemical process design. Part I: Formulation and Theory. *AIChE J.* **1985**, *31*, 621–630. [[CrossRef](#)]
39. Grossmann, I.E.; Floudas, C.A. Active constraint strategy for flexibility analysis in chemical processes. *Comput. Chem. Eng.* **1987**, *11*, 675–693. [[CrossRef](#)]
40. Li, J.; Du, J.; Zhao, Z.; Yao, P. Efficient Method for Flexibility Analysis of Large-Scale Nonconvex Heat Exchanger Networks. *Ind. Eng. Chem. Res.* **2015**, *54*, 10757–10767. [[CrossRef](#)]
41. Zhao, F.; Chen, X. Analytical and triangular solutions to operational flexibility analysis using quantifier elimination. *AIChE J.* **2018**, *64*, 3894–3911. [[CrossRef](#)]
42. Li, J.; Du, J.; Zhao, Z.; Yao, P. Structure and area optimization of flexible heat exchanger networks. *Ind. Eng. Chem. Res.* **2014**, *53*, 11779–11793. [[CrossRef](#)]
43. Pintarič, Z.N.; Kasaš, M.; Kravanja, Z. Sensitivity Analyses for Scenario Reduction in Flexible Flow Sheet Design with a Large Number of Uncertain Parameters. *AIChE J.* **2013**, *59*, 2862–2871. [[CrossRef](#)]
44. Pintarič, Z.N.; Kravanja, Z. Identification of critical points for the design and synthesis of flexible processes. *Comput. Chem. Eng.* **2008**, *32*, 1603–1624. [[CrossRef](#)]
45. Pintarič, Z.N.; Kravanja, Z. A methodology for the synthesis of heat exchanger networks having large numbers of uncertain parameters. *Energy* **2015**, *92*, 373–382. [[CrossRef](#)]
46. Kachacha, C.; Zoughaib, A.; Tran, C.T. A methodology for the flexibility assessment of site wide heat integration scenarios. *Energy* **2018**, *154*, 231–239. [[CrossRef](#)]
47. Pettersson, F. Heat exchanger network design using geometric mean temperature difference. *Comput. Chem. Eng.* **2008**, *32*, 1726–1734. [[CrossRef](#)]



© 2020 by the authors. Licensee MDPI, Basel, Switzerland. This article is an open access article distributed under the terms and conditions of the Creative Commons Attribution (CC BY) license (<http://creativecommons.org/licenses/by/4.0/>).

Article

Simultaneous Synthesis of Heat Exchanger Networks Considering Steam Supply and Various Steam Heater Locations

Yao Sheng ¹, Linlin Liu ^{1,*}, Yu Zhuang ², Lei Zhang ¹ and Jian Du ¹

¹ School of Chemical Engineering, Institute of Chemical Process Systems Engineering, Dalian University of Technology, Liaoning, Dalian 116024, China; shengyao@mail.dlut.edu.cn (Y.S.); kelez@dlut.edu.cn (L.Z.); dujian@dlut.edu.cn (J.D.)

² Key Laboratory of Liaoning Province for Desalination, School of Energy and Power Engineering, Dalian University of Technology, Liaoning, Dalian 116024, China; zhuangyu@mail.dlut.edu.cn

* Correspondence: liulinlin@dlut.edu.cn

Received: 10 February 2020; Accepted: 17 March 2020; Published: 20 March 2020

Abstract: In process industries, the heating gap in heat exchanger networks (HENs) is normally compensated by the steam generated from a utility system, thus these two mutually influencing systems should be designed as a whole through establishing structural interrelationships. In this work, an improved stage-wise superstructure of HENs is proposed to integrate with a Rankine cycle-based utility system. Inner- and inter-stage heaters are considered in the new structure. Furthermore, the selection of steam in different levels is also investigated, extending the possibilities of steam utilization in HENs and generation in utility systems. The presented methodology is able to realize the optimal design of HENs by considering the supply and utilization of steam. Heaters' allocations, matches of streams, steam distribution and utilization are optimized accompanying with the trade-off amongst equipment investment, fuel consumption and power generation in objective, which is highly related to the final structure of the system. The optimization problem is formulated into a mixed-integer non-linear programming (MINLP) model and solved towards the lowest total annual cost (TAC) of the entire system. Finally, a case study with two scenarios is studied. The detailed results are given and analyzed to demonstrate the benefit from structural improvement.

Keywords: improved superstructure; HENs; utility system; steam heater; MINLP

1. Introduction

With the continuous increase of energy consumption in industrial processes, the energy crisis has further intensified on account of the limited fossil energy reserves. Energy prices are also on the rise at the same time, which drives the pursuit of energy-saving technologies and methods. Heat exchanger networks (HENs) are an inevitable part in processing enterprises for heat recovery. Hot process streams that need to be cooled down and cold process streams that need to be heated up widely exist in process enterprises. Synthesis of HENs is able to obtain HEN structures with reasonable matches between these hot and cold process streams and recover waste heat to the greatest extent. Thus the additional utility consumption will be greatly reduced. On the other hand, utility systems based on steam power cycles are one of the major sources which can export multi-level steam and power to industrial enterprises from a single primary energy source. Energy consumption in utility systems accounts for a large proportion of total industrial energy consumption, which makes it meaningful to improve energy efficiency of utility system. These two parts, the HEN and the utility system, are involved the whole process of energy supply, energy consumption and energy saving. While in implementation, the utility system is usually designed independently with its connections with the processes ignored, so the simultaneous synthesis and optimization of HENs and utility systems should be improved.

Determining the use of utilities is always one important content in HEN synthesis, either within a sequential synthesis method or a simultaneous synthesis method. In pinch technology [1] and the trans-shipment model-based method [2], the consumption of cold and hot utilities is targeted by monitoring of pinch point locations, before designing the network structure in terms of pairing hot and cold streams; in the superstructure-based simultaneous method [3], utility consumption is optimized by the trade-off with the capital costs of heat exchangers. Although the study of HEN synthesis has been developed for decades, there are still deficiencies. For example, most previous works on HEN synthesis only used one type of utility at the stream end and assumed that the temperatures of these utilities are able to satisfy all the hot and cold demands, while the fact is that the utility can be in many forms, such as flue gas, steam with different temperatures and hot water. Thus, studies have been launched to investigate the reasonable use of these utilities in HEN synthesis. Costa and Queiroz [4] introduced an extension of the problem table algorithm to optimize and analyze multiple utilities selection and utilization instead of using a grand composite curve. Although the advantages of multi-level utility selection are not analyzed, it is an effective way to optimize multi-level utility utilization with a table algorithm. Salama [5] developed a simple and direct numerical geometry-based technique to target optimal assignment of multiple utilities, but only the heat load was optimized without considering the equipment investment. Shenoy et al. [6] presented a cost-optimal targeting methodology considering the trade-off between energy consumption and equipment investment simultaneously. Optimal selections and loads for multiple utilities were determined based on pinch analysis and the cheapest utility principle. In essence it was still a sequential method, which makes it impossible to achieve a real trade-off between energy and equipment costs. Isafiade and Fraser [7] studied an interval-based MINLP superstructure where the intervals were defined according to the supply and target temperatures of hot or cold process streams. The superstructure model was then applied to HEN synthesis with multi-level available utilities, trading off operating and capital costs for each type of utility. Many nonlinear terms were ignored by mixing split streams at equal temperature, which made the obtained results improvable. Ponce-Ortega et al. [8] developed a stage-wise superstructure that allowed existence of intermediate placement of multiple utilities within each stage. Load and placement of multiple utilities were treated as optimization variables by employing disjunctive programming formulation, rather than regarding utilities as process streams and setting their capacity flowrates as optimization variables. Na et al. [9] proposed a modified superstructure that contained utility sub-stages between adjacent stages. Series utility locations were fixed to facilitate convergence. These studies greatly expanded the design space of the HEN structure and utilization of multiple utilities, but the selection of multiple utilities was mainly based on their price, and the interactions with other systems was not investigated in depth. Zhang et al. [10] explored a new HEN superstructure presentation named the stage-wise chessboard model for management of feasible research regions. A random walk algorithm was employed to lower the calculation load. The problem can be solved faster, but many possible matches are not included in the proposed superstructure because it was equivalent to a stage-wise superstructure with only one stage. Pavão et al. [11] considered the solving difficulty of complex mathematical models resulting from an enhanced stage-wise superstructure which includes the use of multiple utilities at single stream branches. An enhanced meta-heuristic solution method was presented to handle the complex mathematical model, and the superstructure had no difference from the superstructure in Ponce et al. [8] mentioned above. Ma et al. [12] launched multi-objective optimization of interplant HENs operated for multi-periods, which used steam as the heat transfer medium. This research analyzed the conflict between environmental impacts and exchanger investment according to the trade-off between utility consumption and exchanger areas in a case study, but the influence of multi-level steam distribution on the environmental and economic objectives was ignored. Besides, power generation in the utility system was not included in the objective function either, thus the HEN and utility system were not globally integrated.

HENs have been further integrated with utility systems based on their close interactions. Klemeš et al. [13] studied the simultaneous synthesis of a production process and a utility system

based on pinch analysis methodology in a total site integration, but the optimization was carried out after integration within a single plant was completed in advance. Thus the heat recovery and utility system were not optimized simultaneously. Liew et al. [14] optimized the design and operation of a centralized utility system to adapt to shutdowns or process upsets, making a trade-off between operational adaptability and operating costs. Detailed synthesis of the HEN was not included either. Chen and Lin [15] proposed a MINLP model to design a steam network and heat recovery network simultaneously. Hot and cold utilities were only placed at the stream ends, while steam can be generated within an inner-stage to promote energy synergy among plants. Different from previous total site integrations, the heat demand of the HEN is unknown before the design stage, but this research did not consider the utilization of multiple types of utilities within the inner-stage. Hipólito-Valencia et al. [16] combined an organic Rankine cycle with HEN and converted waste heat into mechanical energy, which provided more inspiration for the combination of HEN and other processes. Goh et al. [17] synthesized a HEN and utility system simultaneously, but the minimum operating cost, hot and cold utility demands were determined in advance through multiple cascade automated targeting, without realizing the overall optimization. Luo et al. [18] integrated a HEN with a utility system, using the sensible heat of steam condensate to heat cold process streams. Besides, waste heat of the hot process streams was recovered to preheat boiler feedwater, but the combination was allocated at stream ends, which limited the optimization space compared with the superstructure considering inner-stage utility utilization. Martelli et al. [19] developed a two-stage sequential synthesis algorithm to solve the nonconvex MINLP problem derived from the simultaneous synthesis of HEN and utility systems. An isothermal mixing assumption was made and the utility systems were set as process streams, which will increase the problem-solving complexity. Elsidio et al. [20] have worked on the simultaneous synthesis of utility systems, Rankine cycles and heat exchanger networks. However, their mathematical model was established based on a p - h superstructure but not a stage-wise superstructure. The main purpose was proposing an ad hoc bilevel decomposition method to improve solution efficiency but not optimizing the utility utilization through improving the superstructure. The simultaneous optimization of multi-plant heat integration using steam as intermediate fluid described in Chang et al. [21] reflected the utilization of energy within the inner-stage, but the steam used within the inner-stage was generated from process streams, and the utility system was not considered completely here. Huang et al. [22] extended their research to the simultaneous optimization of a heat exchanger network, steam Rankine cycle and organic Rankine cycle, but the steam utilization and ORC evaporator were placed at stream ends, and inner- and inter-stage improvements were not considered in the superstructure.

Research about HEN synthesis and utility system is summarized here. On one hand, improvements have been made to provide more matching possibilities in HENs and obtain HEN configurations closer to an optimal solution. On the other hand, utility systems and HENs were considered simultaneously to strengthen the heat integration. In total site heat integration using the sequential method, the utility system was usually designed after the determination of heating demand, making it unable to obtain the optimal trade-off between equipment investment and operating cost. As for the mathematical programming method which can perform the design of HENs while optimizing the operation of the utility system, either the heaters were placed at stream ends, or the operating parameters and power generation of utility system were not included, even though the utilization of utilities was considered within the inner-stage. Thus, in order to achieve a better network management, an improved superstructure considering multiple utilities utilization within the inner- and inter-stage is presented and integrated with the utility system based on a Rankine cycle. Multiple utilities (steam in different pressure levels) are produced in cascade in the utility system with concurrently power generation. The structure of the HEN and the operation of the utility system are simultaneously influenced by the placement and distribution of multiple utilities, leading to a trade-off among capital costs, fuel costs and power generation profits. It should be noted that steam is not regarded as process stream but rather as an additional heating source in this study, so the established mathematical model corresponding to the special HEN superstructure including inner- and inter-stage heaters is different from previous

formulations, by which the steam in any alternative level can be selected as long as the temperature difference demand is met. Finally, cases are illustrated to show the goals of this paper, demonstrating that multi-level steam selection and utilization within the inner- and inter-stage will provide a larger optimization space for steam distribution, power generation and fuel consumption of the utility system, achieving better economic performance of the whole system.

2. Problem Statement

A synthesis of HEN involving the optimization of steam supply and utilization is desired in this study, and the entire problem can be described as follows: a set of hot and cold process streams which must be cooled and heated are given with their heat capacity flowrates, supply temperatures, target temperatures and heat transfer coefficients. To compensate the heating gap, a utility system is optimized to produce appropriate steam, in terms of multiple paralleled mains/levels with different pressures and as well temperatures. These steam branches are usually classified as high pressure steam, medium pressure steam, and low pressure steam (HPS, MPS, LPS), etc. In this study, a set of steam alternatives with certain pressures and temperatures are given for selection. The utility system follows the basic process of a Rankine cycle, but the properties and quantity of generated steam must be optimized towards the best benefit of the whole system. Additionally, all the cost-related parameters are also given in order to assess cold utility cost, fuel cost, equipment investment (for heat exchangers, boilers and turbines) and the profit from selling power. The integration problem aims at achieving the most cost-efficient configuration of steam supply HEN, by making trade-offs amongst the contribution of the mentioned economic sectors in the total annualized cost. For this purpose, the interaction between the two sub-systems must be comprehensively explored and the network details, such as fuel consumption, steam generation and allocation, generated power, stream matches, heat loads, operating temperatures, and area of heat exchangers must be optimized. In order to alleviate the solving difficulties caused by a complicated mathematical presentation, it is assumed that: (1) the heat capacity and heat transfer coefficient are constant throughout the whole process; (2) the heat exchange task is completed in a countercurrent heat exchanger; (3) all operations are adiabatic, ignoring the heat loss and mass loss; (4) transportation problems are not taken into account; (5) only the primary units in the utility system are considered, ignoring the auxiliary devices.

3. Method Overview

To solve the mentioned synthesis problem, an optimization-based method is developed and presented in this study. Since a synthesis solution is characterized by two aspects: the network structure (referring mainly to where to exchange heat and whether generate the steam) and the network parameters (which should be quantified, such as flowrate, temperature, heat exchange areas), a superstructure embedding all potential network configurations is introduced as the first step of the method, to offer decision options for the network structure, then a mathematical model is formulated to perform the optimization, making an automatic determination for both network structure and network parameters. Although this method is developed from the general concepts of HEN and utility systems, the major contribution of this work is still worth mentioning, that is, the utilization of steam in the HEN is extended by considering various locations along streams, being in series or/and parallel with stream-stream heat exchange, and meanwhile not only with the given utility steam but having the generation and allocation of steam integrated, such that the interaction between HEN and utility system can be explored with more space. It is believed that better design solutions will be obtained by using this method. For clarity, the superstructure is described in Section 4, followed by the mathematical model presentation in Section 5.

4. Superstructure

Figure 1 presents the superstructure of the proposed integration problem. All potential configuration alternatives of the HEN are displayed by considering the utilization of steam. For the

HEN side, two hot process streams and two cold streams are used to exhibit the features of the stage-wise superstructure. Since the heaters involving steam could be before, after and in parallel with stream-stream heat exchangers, new stages are introduced in the superstructure to fully explore the utilization of steam. It should be noticed that the stages are divided into two types—the inner-stage and the inter-stage—which are alternately arranged. Within each inner-stage, a cold process stream can be split into multiple branches to perform the heat exchange with hot process streams and steam simultaneously. After that, the branches are mixed non-isothermally into a main stream and go into the inter-stage, where only steam is allowed to heat the cold streams. Inter-stage heaters are allowed at both the start and end of cold streams, so the inter-stage number is one more than that of inner-stages. This arrangement could provide much more matching options between cold process streams and steam with limited stages, enriching the configurations of the superstructure. Hot streams are operated in the traditional manner, cooled down by cold process streams within inner-stages and cooling water at stream ends.

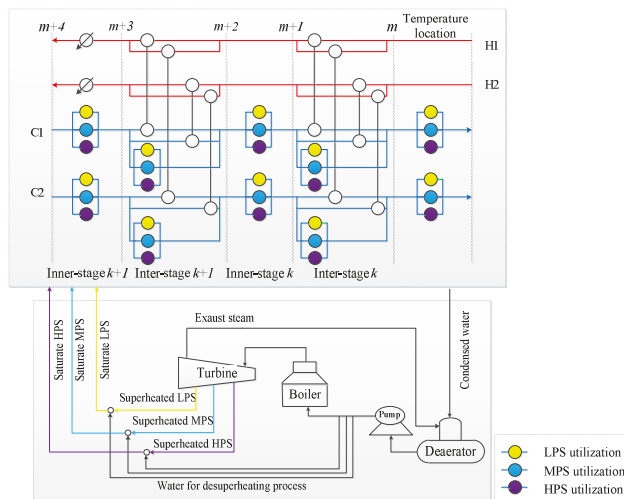


Figure 1. Superstructure for combined HEN and utility system.

The operation of utility system is in typical Rankine cycle: the highest pressure superheated steam is generated in a boiler through combusting fuel, and then sent into a turbine to generate multi-level superheated steam with turbine condensed steam extracted and condensed at the end, producing power at the same time. The superheated steam needs to be desuperheated by mixing with water from the deaerator before being sent to the HEN as saturated steam. After heating the process streams, the condensed water returns to the deaerator, and splits into two parts after the operation, part is sent to the boiler and evaporated into superheated steam, and the residue is mixed with multi-level superheated steam to obtain saturated steam, finishing a cycle. Although the flowsheet of the utility system is quite certain, the possibilities of steam generation and utilization in the HEN need to be determined within the design.

Based on the presented superstructure, a mathematical model can be formulated to determine the optimal network structures and network parameters. In this work, considering the deaerator is an energy-consuming unit, another system without deaerator is also investigated, e.g., using a chemical deaeration technique. The resultant variation in structure is that part of the condensed water is mixed with the corresponding superheated steam, while the rest flows back to the boiler directly.

5. Mathematical Formulation

The synthesis of the overall network is performed with a mathematical model in MINLP. The mass balances, heat balances, feasibility constraints, and formulas for device related and cost related calculations are all given to describe the characteristics contained in the superstructure. The model is decomposed into three parts for understanding: model for HEN synthesis, constraints for the utility system, and the objective function. Implementation of the model is also introduced.

As mentioned in problem statement, the given parameters in the model contain:

- (1) Stream parameters: supply and target temperatures, flowrates, heat transfer coefficients;
- (2) Cost-related parameters: unit price of cold utility, fuel and power; cost parameters for heat exchanger, boiler and turbine;
- (3) Parameters of the steam options: enthalpy of saturate steam, superheated steam, condensate, and water from deaerator.

The notation for these parameters is listed in the Nomenclature section. The rest of the notations in the model indicate the variables that should be determined within model implementation. The binary variables ($z_{i,j,k}$, zcu_i , $zhu_{j,k,n}$, $zhus_{j,k,n}$) indicate the existences of heat exchangers, determining the structure of the network, and the continuous variables (including inlet and outlet temperatures, stream flowrate, heat load, heat exchange area of each exchanger, quantity of generated steam and power, and cost results) refer to the operation and assessment aspects of the obtained network.

5.1. Model for HEN Synthesis

The model of the HEN is formulated to determine the existences of heat exchangers, operating parameters of heat exchangers, required heat transfer area, capital cost and utility cost. The model formulation presented below consists mainly of mass and energy balance equations. Temperature feasibility constraints are also included. Several sets are defined to assist the expression of involved parameters and variables: $i \in I$, $j \in J$ denote hot and cold process streams, $k \in K$ denotes temperature interval of inner- and inter-stage, $m \in M$ is the order of temperature location which is corresponding to stage k , $n \in N$ denotes the steam levels in different pressures.

Heat balances of hot and cold process streams are defined by Equations (1) and (2), wherein FH_i and FC_j denote the total heat capacity flowrates of a hot process stream i and a cold process stream j ; $thin_i$, $thout_i$, $tcin_j$, $tcout_j$ denote supply and target temperatures of streams; $q_{i,j,k}$ represents the heat load of a heat exchanger between hot and cold streams; $qhu_{j,k,n}$ and $qhus_{j,k,n}$ are the heat satisfied by steam n within inter-stage and inter-stage, respectively. $qhu_{j,0,n}$ is the heat satisfied by steam n at the end of cold stream j . Equation (1) is used to ensure each hot stream is cooled from its supply temperature to target by performing adequate heat exchanges with cold streams and cold utility. Analogously, Equation (2) is involved to guarantee that the required heat of each cold stream is satisfied by inner-stage stream-stream exchange, inter-stage stream-steam exchange (including the matching at stream end) and inner-stage stream-steam exchange:

$$\sum_j \sum_k q_{i,j,k} + q_{c_i} = FH_i(thin_i - thout_i) \quad (1)$$

$$\sum_i \sum_k q_{i,j,k} + \sum_k \sum_n qhu_{j,k,n} + \sum_k \sum_n qhus_{j,k,n} + \sum_n qhu_{j,0,n} = FC_j(tcout_j - tcin_j) \quad (2)$$

Equations (3)–(6) present the energy balances of hot and cold process streams within inner- and inter-stage. $ti_{i,m}$ and $tj_{j,m}$ are temperature locations of process streams corresponding to stage k . Equation (3) shows that, within inner-stage, hot streams only exchange heat with cold streams. Equation (4) defines that cold process streams can be heated up by hot process stream and steam n in parallel form within inner-stage k , and more than this, the inter-stage heating from steam is also available, as indicated in Equation (5). The relationship of temperature location m and stage k is worth

mentioning here. In view of the existence of inner- and inter-stage, the presentation of temperature location becomes complicated. In order to enhance the universality of the model, constraints are employed to determine the relationship of m and k . For inner-stage k , the left temperature location m of process stream corresponds to $2k-1$, right temperature location m of process stream corresponds to $2k$. While for inter-stage k , its left temperature location is the same as right temperature of inner-stage k , so its left temperature location is $2k$, and the right temperature location corresponds to $2k+1$:

$$FH_i(t_{i,m-1} - t_{i,m}) = \sum_j q_{i,j,k} \quad m = 2k \tag{3}$$

$$FC_j(t_{j,m-1} - t_{j,m}) = \sum_i q_{i,j,k} + \sum_n q_{hus_{j,k,n}} \quad m = 2k \tag{4}$$

$$FC_j(t_{j,m} - t_{j,m+1}) = \sum_n q_{hu_{j,k,n}} \quad m = 2k \tag{5}$$

$$FC_j(tc_{out_j} - t_{j,m}) = \sum_n q_{hu_{j,0,n}} \quad m = 1 \tag{6}$$

Equations (7)–(9) express the mass balances of hot and cold process streams within the inner- and inter-stages. A hot stream must be split into branches to perform the potential heat exchanges with cold streams within each inner-stage (Equation (7)), but for a cold stream, there are two kinds of matches within inner-stage k , with hot process streams and with steam (Equation (8)). For inter-stages, split branches can only match with steam (Equation (9)):

$$FH_i = \sum_j fhs_{i,j,k} \tag{7}$$

$$FC_j = \sum_i fcs_{i,j,k} + \sum_n fcsp_{j,k,n} \tag{8}$$

$$FC_j = \sum_n fcsk_{j,k,n} \tag{9}$$

The characteristics of an exchanger include its location, inlet and outlet temperatures, hot and cold stream (branch) flowrates, heat load and heat transfer area. Due to the variety of the exchangers in the presented superstructure, the models for exchangers are presented in five sets: inner-stage stream-stream exchangers, inter-stage stream-steam exchangers, inner-stage stream-steam exchangers, heaters at end of cold process streams, and coolers at the end of hot streams. All these exchangers are expressed with similar heat balances and area equations in the modeling.

Equations (10)–(16) are used to calculate the heat load $q_{i,j,k}$ and heat transfer area $A_{i,j,k}$ of heat exchangers between hot and cold streams within inner-stage k . Heat balance Equations (10) and (11) are used to constraint the inlet and outlet temperatures of the unit that, the released heat from hot stream i equals to that obtained by the pairing cold stream j . $dtij1_{i,j,k}$ and $dtij2_{i,j,k}$ in Equations (12) and (13) denote the temperature difference at the two sides of the heat exchanger. In order to circumvent the presence of logarithm and the resultant difficulty in model solving, the logarithmic mean temperature difference used for transfer area calculation (Equation (15)) is approximated by Equation (14) [23]. In the model, binary variable $z_{i,j,k}$ is employed to indicate the existence of heat exchangers, that is, $z_{i,j,k} = 1$ means the heat exchanger exists, otherwise the exchanger is not involved. Heat loads are highly related to the locations of exchangers, so Equation (16) is used by defining sufficiently large constant Q_{max} to assist with the constraint:

$$q_{i,j,k} = fhs_{i,j,k}(t_{i,m-1} - th_{i,j,k}) \quad m = 2k \tag{10}$$

$$q_{i,j,k} = fcs_{i,j,k}(tc_{i,j,k} - t_{j,m}) \quad m = 2k \tag{11}$$

$$dtij1_{i,j,k} \leq ti_{i,m-1} - tc_{i,j,k} + T_{max}(1 - z_{i,j,k}) \quad m = 2k \tag{12}$$

$$dtij2_{i,j,k} \leq th_{i,j,k} - tj_{j,m} + T_{max}(1 - z_{i,j,k}) \quad m = 2k \tag{13}$$

$$\Delta Ti_{j,i,k} = (dtij1_{i,j,k} \times dtij2_{i,j,k} \times (dtij1_{i,j,k} + dtij2_{i,j,k}) \times 0.5)^{1/3} \tag{14}$$

$$A_{i,j,k} = q_{i,j,k} / (h \times \Delta Ti_{j,i,k}) \tag{15}$$

$$q_{i,j,k} \leq z_{i,j,k} \times Q_{max} \tag{16}$$

In similar way, Equations (17)–(23) are included to describe the steam heaters within each inner-stage. It is stipulated that steam, at most one type, is allowed for each possible stream-steam match, so Equation (22) is introduced into the model, by using $zhus_{j,k,n}$ to denote the existences of the heaters:

$$qhus_{j,k,n} = fcsp_{j,k,n}(tcsp_{j,k,n} - tj_{j,m}) \quad m = 2k \tag{17}$$

$$dths1_{j,k,n} \leq thus_{j,k,n} - tcsp_{j,k,n} + T_{max}(1 - zhus_{j,k,n}) \quad m = 2k \tag{18}$$

$$dths2_{j,k,n} \leq thus_{j,k,n} - tj_{j,m} + T_{max}(1 - zhus_{j,k,n}) \quad m = 2k \tag{19}$$

$$\Delta Thus_{j,k,n} = (dths1_{j,k,n} \times dths2_{j,k,n} \times (dths1_{j,k,n} + dths2_{j,k,n}) \times 0.5)^{1/3} \tag{20}$$

$$Ahus_{j,k,n} = qhus_{j,k,n} / (h1 \times \Delta Thus_{j,k,n}) \tag{21}$$

$$\sum_n zhus_{j,k,n} \leq 1 \tag{22}$$

$$qhus_{j,k,n} \leq zhus_{j,k,n} \times Q_{max} \tag{23}$$

Equations (24)–(30) are formulated to determine the steam heater within each inter-stage. $zhu_{j,k,n}$ denotes the existence of the heater having steam n involved. Equation (29) is employed to ensure that a cold process stream can only be heated up by one steam at most within each inter-stage:

$$fcsk_{j,k,n}(tj_{j,m} - tj_{j,m+1}) = qhu_{j,k,n} \quad m = 2k \tag{24}$$

$$dth1_{j,k,n} \leq thu_{j,k,n} - tj_{j,m} + T_{max}(1 - zhu_{j,k,n}) \quad m = 2k \tag{25}$$

$$dth2_{j,k,n} \leq thu_{j,k,n} - tj_{j,m+1} + T_{max}(1 - zhu_{j,k,n}) \quad m = 2k \tag{26}$$

$$\Delta Thu_{j,k,n} = (dth1_{j,k,n} \times dth2_{j,k,n} \times (dth1_{j,k,n} + dth2_{j,k,n}) \times 0.5)^{1/3} \tag{27}$$

$$Ahu_{j,k,n} = qhu_{j,k,n} / (h1 \times \Delta Thu_{j,k,n}) \tag{28}$$

$$\sum_n zhu_{j,k,n} \leq 1 \tag{29}$$

$$qhu_{j,k,n} \leq zhu_{j,k,n} \times Q_{max} \tag{30}$$

Equations (31)–(37) are employed to determine the size of the heaters at the end of cold process streams. As mentioned in the superstructure section, the number of inter stages is one more than that of inner stages, so the exchange for this stage is expressed with the subscript '0':

$$fcsk_{j,0,n}(tcout_j - tj_{j,m}) = qhu_{j,0,n} \quad m = 1 \tag{31}$$

$$dth1_{j,0,n} \leq thu_{j,0,n} - tcout_j + T_{max}(1 - zhu_{j,0,n}) \tag{32}$$

$$dth2_{j,0,n} \leq thu_{j,0,n} - tj_{j,m} + T_{max}(1 - zhu_{j,0,n}) \quad m = 1 \tag{33}$$

$$\Delta Thu_{j,0,n} = (dth1_{j,0,n} \times dth2_{j,0,n} \times (dth1_{j,0,n} + dth2_{j,0,n}) \times 0.5)^{1/3} \tag{34}$$

$$Ahu_{j,0,n} = qhu_{j,0,n} / (h1 \times \Delta Thu_{j,0,n}) \tag{35}$$

$$\sum_n zhu_{j,0,n} \leq 1 \tag{36}$$

$$qhu_{j,0,n} \leq zhu_{j,0,n} \times Q_{max} \tag{37}$$

Equations (38)–(44) present the calculation of heat load qc_i and heat transfer area Acu_i of the cooler at i th stream end. tcu_{in} and tcu_{out} are the specified inlet and outlet temperatures of cold utility. zcu_i denotes the existence of a cooler:

$$FH_i(t_{i,m} - thout_i) = qc_i \quad m = M \tag{38}$$

$$Acu_i = qc_i / (h \times \Delta Tcu_i) \tag{39}$$

$$dtku1_i \leq t_{i,m} - tcu_{out} + T_{max}(1 - zcu_i) \quad m = M \tag{40}$$

$$dtku2_i \leq thout_i - tcu_{in} + T_{max}(1 - zcu_i) \tag{41}$$

$$\Delta Tcu_i = (dtku1_i \times dtku2_i \times (dtku1_i + dtku2_i) \times 0.5)^{1/3} \tag{42}$$

$$qc_i \leq zcu_i \times Q_{max} \tag{43}$$

5.2. Constraints for the Utility System

The utility system consists of a boiler, turbine and deaerator. Steam at different pressure levels is extracted from the turbine as a utility. Equation (44) presents the required heat load of steam n , $qsteam_n$, equaling to that consumed in inter-stage steam-steam exchanges and inner-stage steam-steam exchanges. The mass flow is deduced from Equation (45), wherein $lheat_n$ is the latent heat of saturated steam n :

$$qsteam_n = \sum_j qhu_{j,0,n} + \sum_j \sum_k qhu_{j,k,n} + \sum_j \sum_k qhus_{j,k,n} \tag{44}$$

$$msteam_n = qsteam_n \times ahour \times 3600 / lheat_n \tag{45}$$

Superheated steam extracted from the turbine is desuperheated by boiler feedwater from the deaerator. Equations (46)–(48) give the mass and heat balances for this process, according to the model of Luo et al. [18]. Saturated steam is obtained after mixing superheated steam and the boiler feed water which comes from the deaerator. Equations (46) and (47) describe the mass and heat balances of this desuperheating process, wherein $enth$ denotes the enthalpy of each involved stream/steam. As all condensate water of saturated steam is mixed with exhaust steam in the deaerator at the specified operating temperature of the device, the flow rate of the exhaust steam must be constrained by the balance of the deaerator as indicated in Equation (48), wherein m_{ext} denotes the mass flow of exhaust steam from turbine.

$$msteam_n = msteam_{superheated,n} + mw_{deaerator,n} \tag{46}$$

$$msteam_n \times enth_n = mw_{deaerator,n} \times enth_{deaerator,n} + msteam_{superheated,n} \times enth_{superheated,n} \tag{47}$$

$$\sum_n msteam_n \times enth_{condensate,n} + m_{ext} \times enth_{ext} = \left(\sum_n msteam_n + m_{ext} \right) \times enth_{deaerator} \tag{48}$$

Equations (49)–(52) are used to calculate economy-related factors. Equation (49) gives the power generation model of the steam turbine, wherein $msteam_z$ is the total mass flow through subsection z of the turbine, equaling the sum of the steam at lower pressure level. As shown, the quantity of generated power is determined by the enthalpy difference of the inlet and outlet superheated steam as well as the steam flow rate through each section. The costs of fuel, turbine and boiler, which are highly-related to steam distribution and power generation, are obtained through Equations (50)–(52) [15], respectively. Fuel cost is calculated in Equation (50), wherein the required heat load for generating steam from condensate to superheated state is determined by steam flow rate, $\sum_n msteam_{superheated,n}$, and unit enthalpy

difference of the material in and out the boiler, $(enth_{boil,out} - enth_{boil,in})$. Accordingly, the consumption of fuel can be calculated based on the heat content of fuel, $heatcap$, and boiler efficiency, eff_{boil} . As shown in Equations (51)–(52), the capital cost of the turbine is determined by the quantity of generated power and the capital cost of the boiler depends on the amount of steam generated:

$$wt^{total} = \sum_z msteam_z \times (enth_{superheated,z}^{in} - enth_{superheated,z}^{out}) \times eff_{turb} / 3600 \tag{49}$$

$$C_{fuel} = \left((enth_{boil,out} - enth_{boil,in}) \times \sum_n msteam_{superheated,n} \right) \times cfuel / (eff_{boil} \times heatcap) \tag{50}$$

$$C_{tur} = a_{tur} + b_{tur} \times wt^{total} / \text{ahour} \tag{51}$$

$$C_{boil} = a_{boil} + \left(b_{boil} \times \left(\sum_n msteam_{superheated,n} + m_{ext} \right) \right) / \text{ahour} \tag{52}$$

5.3. Objective Function

The aim the study is to obtain an integrated system with the minimum total annual cost (TAC). As presented in the objective function of Equation (53), the TAC equals the total economic cost minus the profit from selling power. Economic cost is composed by the capital cost for exchangers, turbine, boiler, and the operating cost for fuel and cold utility consumption. The exchangers are assessed in general form $CF + CE \times A^\beta$, in which CF , CE and β denote the fixed charge of heat exchanger, coefficient of area cost and exponent for area cost, respectively. $lheat_{condenser}$ is latent heat of exhaust steam from turbine end. The costs of turbine, boiler and fuel are obtained according to Equations (50)–(52). The quantities of consumed cold utility and generated power are determined by Equations (38) and (49), then the corresponding cost and profit are calculated by multiplying the unit prices C_{cu} and C_{pow} :

$$\begin{aligned} \min TAC &= \sum_i (CF_{cu,i} \times zcu_i) + \sum_i \sum_j \sum_k (CF_{i,j,k} \times z_{i,j,k}) + \sum_j \sum_n (CF_{hu,j} \times zhu_{j,0,n}) \\ &+ \sum_j \sum_k \sum_n (CF_{hu,j} \times (zhus_{j,k,n} + zhu_{j,k,n})) + \sum_i (CE_{cu,i} \times Acu_i^\beta) \\ &+ \sum_i \sum_j \sum_k (CE_{i,j,k} \times A_{i,j,k}^\beta) + \sum_j \sum_n (CE_{hu,j} \times A_{hu,j,0,n}^\beta) + \sum_j \sum_k \sum_n (CE_{hu,j} \times (A_{hu,j,k,n}^\beta + A_{hus,j,k,n}^\beta)) \\ &+ C_{cu} \times \left(\sum_j qc_j + m_{ext} \times lheat_{condenser} \right) + C_{fuel} + C_{tur} + C_{boil} - C_{pow} \times wt^{total} \end{aligned} \tag{53}$$

5.4. Model Implementation

The formulated model is in MINLP presentation, containing a large number of continuous variables, binary variables and non-linear terms. The former kind refers to operational aspects, such as designed load, flowrate, temperature, fuel consumption, steam quantity, generated power and device size, while the later kind account for structure aspect, related to the existence of heat exchange matches and the utilization of steam. Non-isothermal mixing, heat exchange area calculation and cost calculation contribute to the non-linear terms. The model is programmed in the general modeling software GAMS and solved by the solver BARON [24], within the Windows 10 computing environment using an Intel(R) Core(TM) i7-8700k CPU @ 3.70 GHz, 32.0 GB RAM. Here it should be noted that the global optimum cannot be always guaranteed if handling big size problems, but appropriate initial values of the variables will facilitate the search to improve the quality of solutions.

6. Case Study

6.1. Case Description

A case is studied in this section to illustrate the proposed synthesis method. The most cost-saving network solution is expected. The case comprises four hot and four cold process streams, for which the characteristics, including heat capacity flowrates, supply temperatures and target temperatures are given in Table 1. Supply and target temperatures of cooling water utility are 25 °C and 35 °C. Three pressure levels of steam in low, medium and high pressure levels (LPS, MPS, HPS) are defined as 170.4 °C, 198.3 °C and 263.9 °C with the corresponding pressure, so the production and utilization of the steam should be optimized according to the performance the entire system. Turbine exhaust steam condensate is 45.8 °C [18]. Overall heat transfer coefficients are fixed at 1.0 and 0.5 kW·m⁻²·°C⁻¹ for steam heating and non-steam heating, respectively. The prices of boiler fuel natural gas and generated power are 0.227 \$·kg⁻¹ and 0.076 \$·kWh⁻¹ [18], respectively. Efficiencies of boiler and turbine are set to be 0.9 and 0.7 [17]. Annual operation time is 8000 h·y⁻¹. Minimum heat transfer temperature difference is set to be 10 °C. Coefficients for turbine cost a_{tur} and b_{tur} are 81,594 \$·y⁻¹ and 18.52 \$·kWh⁻¹·y⁻¹ [18]. Coefficients for boiler cost a_{boil} and b_{boil} are 101,840 \$·y⁻¹ and 3.441 \$·h·kg⁻¹·y⁻¹ [15].

Table 1. Process data of the case study.

Hot Stream	T _{in} (°C)	T _{out} (°C)	FC(kW/°C)	Cold Stream	T _{in} (°C)	T _{out} (°C)	FC(kW/°C)
1	315	159	167	1	30	255	190
2	238	195	220	2	49	219	100
3	230	60	80	3	59	185	50
4	200	143	130	4	117	134	150

It is believed that the structure of HEN and the operation of utility system will impact the entire system greatly. Thus, two design schemes with two scenarios of each are investigated within the synthesis. The schemes are defined according to different condensate recovery manners. In the first scheme, condensates of exhaust steam and multi-level steam (HPS, MPS, LPS) are collected in the deaerator which works at a certain operating temperature [18], and then sent to the boiler. In the other scheme, condensates of multi-level steam are recovered without flowing through the deaerator, and exhaust steam at the turbine end is no longer needed to maintain the operating temperature of the deaerator. For each scheme, two scenarios are studied according to different HEN superstructures. In the first scenario, steam utilities are only used at stream ends. While in the second scenario, the proposed structure is adopted, as using the steam not only within inner-stage but also within inter-stage. Therefore, four situations for the whole system are studied and compared to demonstrate the method.

6.2. Results and Discussion

6.2.1. Scheme 1: Deaerator is Involved in the System

In this scheme, steam is only used at stream ends, while the deaerator is employed as cited in [18], maintaining its operating temperature at 158 °C. Figure 2 presents the structure result of Scenario 1, which features the TAC of 3,599,059 \$·y⁻¹. As shown, cold process stream C1 is heated by hot process streams H1, H2 and H3, C2 is heated by H2 and H4, three heaters are needed at stream ends of C2, C3 and C4. In total, 2550 kW LPS, 6300 kW MPS and 3228 kW HPS are generated from utility system and sent to HEN. Besides, exhaust steam is extracted and condensed at turbine end, mixing with condensates in deaerator and maintaining its operating temperature.

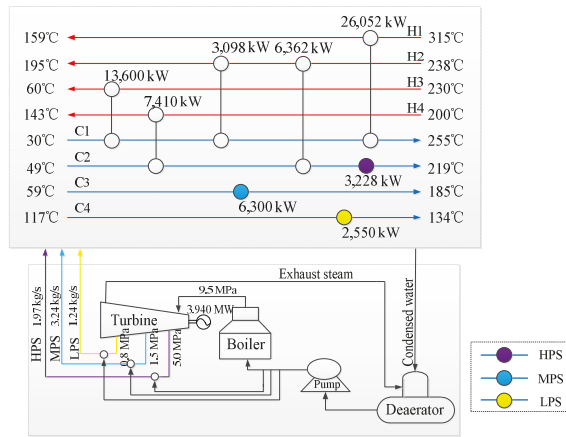


Figure 2. Structure with minimum TAC of Scenario 1.

Figure 3 shows the solution of Scenario 2, discarding the location limit on steam heaters. The TAC of the solution is 2,866,637 $\text{\$}\cdot\text{y}^{-1}$.

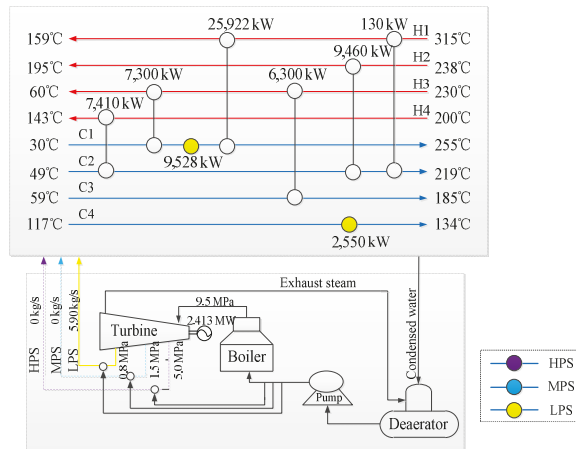


Figure 3. Structure with minimum TAC of Scenario 2.

As shown, C1 is heated by H1 and H3, C2 is heated by H2 and H4, C3 is heated by H3. It is worth noting that the originally required higher pressure steam in Figure 2 is replaced by lower pressure steam with the load of 12,078 kW of LPS. One heater of the two is located within the inter-stage of C1. This illustrates that the appropriate use of steam considering the inner- and inter-stage location is able to enhance the use of lower pressure steam.

The cost composition of the two scenarios is summarized in Table 2. As indicated, fuel cost of Scenario 2 (3,240,049 $\text{\$}\cdot\text{y}^{-1}$) is 32.2% lower than that of Scenario 1 (4,782,431 $\text{\$}\cdot\text{y}^{-1}$). This is because only higher pressure steam can be used at stream ends in Scenario 1 due to the temperature constraints, so the resultant high temperature condensate needs additional extracted and condensed exhaust steam to maintain the operating temperature of deaerator, leaning to the greater fuel consumption. Accordingly, the boiler cost (212,203 $\text{\$}\cdot\text{y}^{-1}$) and turbine cost (152,718 $\text{\$}\cdot\text{y}^{-1}$) of Scenario 1 are both higher than Scenario 1, while for heat exchanger investment, higher pressure steam is replaced by low pressure steam, increasing the heat transfer temperature difference and increasing heat exchanger area,

so by adding all concerned components, equipment investment of the two scenarios make nearly no difference. In spite of the decreased power generation profit in Scenario 2, fuel costs account for most of the investment, thus finally, TAC of Scenario 2 presents a 20.4% lower than Scenario 1. Conclusion can be made that the improved HEN superstructure provides more possibilities for the selection of multiple utilities and lower pressure steam is more economical in this system.

Table 2. Results of Scheme 1.

	Scenario 1	Scenario 2	-	Scenario 1	Scenario 2
Cost of fuel(\$·y ⁻¹)	4,782,431	3,240,094	Heat exchangers investment(\$·y ⁻¹)	699,045	748,222
Boiler investment(\$·y ⁻¹)	212,203	176,611	Profit of selling power(\$·y ⁻¹)	2,395,504	1,467,250
Turbine investment(\$·y ⁻¹)	152,718	125,158	TAC(\$·y ⁻¹)	3,599,059	2,866,637

6.2.2. Scheme 2: Deaerator is not Involved in the System

In Scheme 2, condensates of the steam in different levels are recovered without flowing through the deaerator. Superheated steam is desuperheated by the corresponding condensates. Two scenarios with different HEN superstructures (Scenario 3 and Scenario 4) are studied.

Figure 4 presents the obtained configuration of Scenario 3, with TAC of 2,774,184 \$·y⁻¹. As indicated, HPS, 3228 kW, MPS, 6300 kW and LPS, 2550 kW are used at stream ends of C2, C3 and C4 respectively. Figure 5 is the configuration solution of Scenario 4, which costs 2,670,969 \$ per year. As shown, totally 10,848 kW of LPS and 1230 kW of MPS are extracted from utility system. Besides being used within inner-stage of C1, LPS is also allocated sequentially after MPS on C2 within the inter-stage. That is to say, partial MPS is replaced by LPS in this scenario. From the resulted configuration it is implies that lower pressure steam are located within inner- and inter-stage in the improved HEN superstructure.

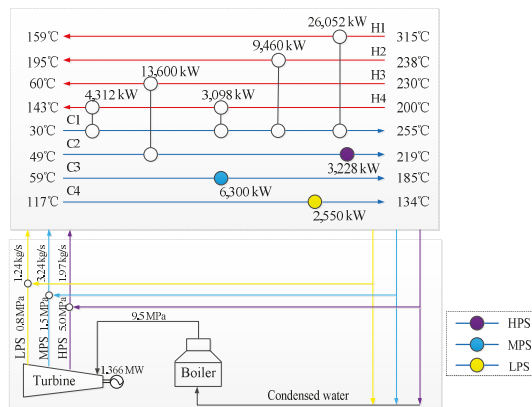


Figure 4. Structure with minimum TAC of Scenario 3.

Table 3 summarized the cost composition of Scenario 3 and 4. Fuel cost of Scenario 4 (2,852,680 \$·y⁻¹) is increased by 5.5% compared to Scenario 3 (2,704,636 \$·y⁻¹). As for the equipment investment, utilization of lower pressure steam in Scenario 4 results in a 10.6% higher heat exchanger cost (690,124 \$·y⁻¹) than that of Scenario 3 (624,017 \$·y⁻¹). Boiler and turbine investments of the two scenarios are nearly the same. However, more power is generated when producing lower pressure steam through the turbine in Scenario 3, due to which the profit of power generation in Scenario

4 (1,156,928 \$·y⁻¹) is 39.3% higher. Combining all the above costs, the improved HEN structure gains lower TAC in total, about 3.7% decrease. It can also be concluded that lower pressure steam is more economical.

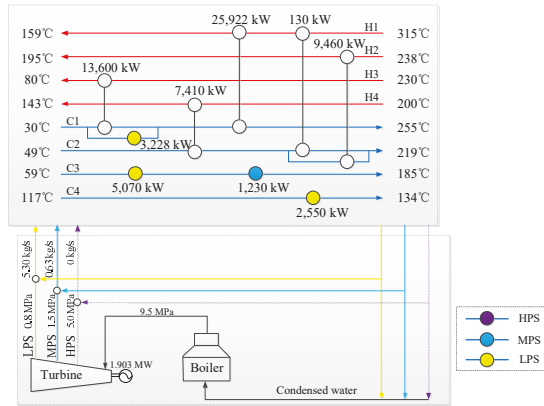


Figure 5. Structure with minimum TAC of Scenario 4.

Table 3. Results of Scheme 2.

	Scenario 3	Scenario 4		Scenario 3	Scenario 4
Cost of fuel(\$·y ⁻¹)	2,704,636	2,852,680	Heat exchangers investment(\$·y ⁻¹)	624,017	690,124
Boiler investment(\$·y ⁻¹)	169,897	169,149	Profit of selling power(\$·y ⁻¹)	830,622	1,156,928
Turbine investment(\$·y ⁻¹)	106,256	115,944	TAC(\$·y ⁻¹)	2,774,184	2,670,969

The two schemes demonstrate that the generation and utilization of utilities have great effects on the HEN structure and equipment investment. In the design where the deaerator is employed in the utility system as cited, more exhaust steam needs to be extracted and condensed to guarantee the operating temperature by mixing with condensed water when higher pressure steam is extracted from the turbine. This will result in more fuel consumption and higher TAC because of the expensive fuel expense. Thus, using lower pressure steam is more economical. In the structure where condensed water is recovered without a deaerator, more power is generated and less heat is supplied when producing lower pressure steam with the same fuel consumption compared with higher one. It is proved that lower pressure is more economical when supplying the same amount of heat to the HEN, although with lower temperature grade. From the above analysis, it is demonstrated that, on the one hand, allowing heaters within inner- and inter-stages is able to generate a better management for utility utilization than the case of only having heaters at stream ends, because steam selections are less restricted by temperature difference constraints and more LPS can be used, which is conducive to the use of energy cascade utilization. On the other hand, a better trade-off among equipment investment, power generation and fuel consumption can be made through the optimization of the whole system with the TAC target.

7. Conclusions

An improved superstructure for HENs synthesis which contains the utilization of multiple utilities within inner- and inter-stages has been presented to integrate with the utility system. The coupling relationship between HENs and Rankine cycle-based utility systems is investigated and extended by

considering various locations of steam heaters. The HEN structure has an impact on steam distribution and accordingly determines the operation of the utility system, thus in the study, the stream matches and heat transfer area of HEN, as well as the multi-level steam distribution, fuel consumption and power generation in utility system are all optimized to minimize the TAC of the whole system. Results are discussed and analyzed with case studies. The obtained economic benefits, 20.4% and 3.7% cost cuts for the cases separately, have demonstrated the method very well. It is concluded that the thermal property and quantity of steam have great effect on fuel consumption, power generation and heat transfer area, leading to an economic trade-off; relieving the location limit on steam heaters could create better solution, in terms of using more lower pressure steam not only at stream ends. Future research will be launched to develop this method to deal with the simultaneous synthesis problem of industrial park HEN and utility system with considering the selection of primary energy sources, e.g., fuel, solar, nuclear, wind, etc.

Author Contributions: Methodology, Y.S. and L.L.; validation, Y.S., L.L., Y.Z., L.Z. and J.D.; writing—original draft preparation, Y.S.; writing—review and editing, L.L., Y.Z., L.Z. and J.D.; visualization, Y.S.; supervision, L.L.; project administration, L.L.; funding acquisition, L.L. All authors have read and agree to the published version of the manuscript.

Funding: This research was funded by Natural Science Foundation of China (No.21878034 and 21776035) and the Fundamental Research Fund for Central Universities of China (DUT18LAB11).

Conflicts of Interest: The authors declare no conflict of interest.

Nomenclature

Indices and sets

i	hot stream
j	cold stream
n	steam level
m	temperature location
k	stage
M	total number of temperature location

Parameters

FH_i	heat capacity flow rate of hot stream
FC_j	heat capacity flow rate of cold stream
$thin_i$	inlet temperature of hot stream
$thout_i$	outlet temperature of hot stream
$tcin_j$	inlet temperature of cold stream
$tcout_j$	outlet temperature of cold stream
$tcuin$	inlet temperature of cold utility
$tcuout$	outlet temperature of cold utility
$thu_{j,k,n}$	temperature of hot utility n within inter-stage k
$thus_{j,k,n}$	temperature of hot utility n within inner-stage k
$h1$	heat transfer coefficient for hot utility
h	heat transfer coefficient for process streams
γ	a sufficiently large constant number
ef_{fturb}	efficiencies of turbine
ef_{fboil}	efficiencies of boiler
$ahour$	8000 hours per year
$heatcap$	heat content of boiler fuel
C_{cu}	cost coefficient for cold utility
C_{pow}	cost coefficient for power
$cfuel$	cost coefficient for boiler fuel
CE, CF, β	parameters for cost of heat exchanger

Binary variables

$z_{i,j,k}$	the existence of matching between hot and cold process streams
zcu_i	the existence of matching between hot process streams and cold utility
$zhu_{j,k,n}$	the existence of matching between cold process streams and hot utility n within inter-stage k
$zhus_{j,k,n}$	the existence of matching between cold process streams and hot utility n within inner-stage k

Continuous variables

$q_{i,j,k}$	heat load between hot and cold process streams within inner-stage k
qc_i	heat load between hot stream i and cold utility
$qhu_{j,k,n}$	heat load between cold stream j and hot utility n within inter-stage k
$qhus_{j,k,n}$	heat load between cold stream j and hot utility n within inner-stage k
$qc_{condenser}$	cold utility requirement for exhaust steam
$t_{i,m}$	temperature of hot stream
$t_{j,m}$	temperature of cold stream
$th_{i,j,k}$	outlet temperature of split branch of hot stream matching with cold stream j
$tc_{i,j,k}$	outlet temperature of split branch of cold stream matching with hot stream i
$tcsp_{j,k,n}$	outlet temperature of split branch of cold stream matching with utility n
$fhs_{i,j,k}$	heat capacity flow rate of split branch of hot stream matching with cold stream j
$fcs_{i,j,k}$	heat capacity flow rate of split branch of cold stream matching with hot stream i
$fcs_{j,k,n}$	heat capacity flow rate of split branch of cold stream matching with utility n within inner-stage k
$fcsk_{j,k,n}$	heat capacity flow rate of split branch of cold stream matching with utility n within inter-stage k
$A_{i,j,k}$	area of heat exchanger for cold and hot process streams
Acu_i	area of heat exchanger for hot stream i and cold utility
$Ahu_{j,k,n}$	area of heat exchanger for cold stream j and hot utility n within inter-stage k
$Ahus_{j,k,n}$	area of heat exchanger for cold stream j and hot utility n within inner-stage k
$qsteam_n$	total heat demand of steam n
$msteam_n$	total mass demand of steam n
m_{ext}	mass flow rate of exhaust steam
wl^{total}	power generation of utility system
C^{fuel}	fuel cost
C_{tur}	turbine cost
C_{boil}	boiler cost

References

1. Linnhoff, B.; Hindmarsh, E. The pinch design method for heat exchanger networks. *Chem. Eng. Sci.* **1983**, *38*, 745–763. [[CrossRef](#)]
2. Papoulias, S.A.; Grossmann, I.E. A structural optimization approach in process synthesis I: Utility systems. *Comput. Chem. Eng.* **1983**, *7*, 695–706. [[CrossRef](#)]
3. Yee, T.F.; Grossmann, I.E. Simultaneous optimization models for Heat Integration-II. Heat exchanger network synthesis. *Comput. Chem. Eng.* **1990**, *14*, 1165–1184. [[CrossRef](#)]
4. Costa, A.L.H.; Queiroz, E.M. An extension of the problem table algorithm for multiple utilities targeting. *Energy Convers. Manag.* **2009**, *50*, 1124–1128. [[CrossRef](#)]
5. Salama, A.I.A. Optimal assignment of multiple utilities in heat exchange networks. *Appl. Therm. Eng.* **2009**, *29*, 2633–2642. [[CrossRef](#)]
6. Shenoy, U.V.; Sinha, A.; Bondyopadhyay, S. Multiple utilities targeting for heat exchanger networks. *Chem. Eng. Res. Des.* **1998**, *76*, 259–272. [[CrossRef](#)]
7. Isafiade, A.J.; Fraser, D.M. Interval-based MINLP superstructure synthesis of heat exchange networks. *Chem. Eng. Res. Des.* **2008**, *86*, 245–257. [[CrossRef](#)]
8. Ponce-Ortega, J.M.; Serna-González, M.; Jiménez-Gutiérrez, A. Synthesis of heat exchanger networks with optimal placement of multiple utilities. *Ind. Eng. Chem. Res.* **2010**, *49*, 2849–2856. [[CrossRef](#)]

9. Na, J.; Jung, J.; Park, C.; Han, C. Simultaneous synthesis of a heat exchanger network with multiple utilities using utility substages. *Comput. Chem. Eng.* **2015**, *79*, 70–79. [[CrossRef](#)]
10. Zhang, H.; Cui, G.; Xiao, Y.; Chen, J. A novel simultaneous optimization model with efficient stream arrangement for heat exchanger network synthesis. *Appl. Therm. Eng.* **2017**, *110*, 1659–1673. [[CrossRef](#)]
11. Pavão, L.V.; Costa, C.B.B.; Ravagnani, M.A.S.S. An enhanced stage-wise superstructure for heat exchanger networks synthesis with new options for heaters and coolers placement. *Ind. Eng. Chem. Res.* **2018**, *57*, 2560–2573. [[CrossRef](#)]
12. Ma, J.; Chang, C.L.; Wang, Y.F.; Feng, X. Multi-objective optimization of multi-period interplant Heat Integration using steam system. *Energy* **2018**, *159*, 950–960. [[CrossRef](#)]
13. Klemeš, J.J.; Dhole, V.R.; Raissi, K.; Perry, S.J.; Puigjaner, L. Targeting and design methodology for reduction of fuel, power and CO₂ on total sites. *Appl. Therm. Eng.* **1997**, *17*, 993–1003. [[CrossRef](#)]
14. Liew, P.Y.; Alwi, S.R.W.; Varbanov, P.S.; Manan, Z.A.; Klemeš, J.J. Centralised utility system planning for a total site heat integration network. *Comput. Chem. Eng.* **2013**, *57*, 104–111. [[CrossRef](#)]
15. Chen, C.L.; Lin, C.Y. Design of entire energy system for chemical plants. *Ind. Eng. Chem. Res.* **2012**, *51*, 9980–9996. [[CrossRef](#)]
16. Hipólito-Valencia, B.J.; Rubio-Castro, E.; Ponce-Ortega, J.M.; Serna-González, M. Optimal integration of organic rankine cycles with industrial processes. *Energy Convers. Manag.* **2013**, *73*, 285–302. [[CrossRef](#)]
17. Goh, W.S.; Wan, Y.K.; Tay, C.K.; Ng, R.T.L. Automated targeting model for synthesis of heat exchanger network with utility systems. *Appl. Energy* **2016**, *162*, 1272–1281. [[CrossRef](#)]
18. Luo, X.; Huang, X.; El-Halwagi, M.M.; Ponce-Ortega, J.M. Simultaneous synthesis of utility system and heat exchanger network incorporating steam condensate and boiler feedwater. *Energy* **2016**, *113*, 875–893. [[CrossRef](#)]
19. Martelli, E.; Elsidio, C.; Mian, A.; Marechal, F. Minlp model and two-stage algorithm for the simultaneous synthesis of heat exchanger networks, utility systems and heat recovery cycles. *Comput. Chem. Eng.* **2017**, *106*, 663–689. [[CrossRef](#)]
20. Elsidio, C.; Martelli, E.; Grossmann, I.E. *A Bilevel Decomposition Method for the Simultaneous Synthesis of Utility Systems, Rankine Cycles and Heat Exchanger Networks, Proceedings of the 28th European Symposium on Computer-Aided Process Engineering (ESCAPE28), Graz, Australia, 10–13 June 2018*; Friedl, A., Klemeš, J.J., Radl, S., Varbanov, P.S., Wallek, T., Eds.; Elsevier: Kidlington, UK, 2018; Volume 43, pp. 373–378.
21. Chang, C.; Chen, X.; Wang, Y.; Feng, X. Simultaneous optimization of multi-plant Heat Integration using intermediate fluid circles. *Energy* **2017**, *121*, 306–317. [[CrossRef](#)]
22. Huang, X.; Lu, P.; Luo, X.; Chen, J.; Yang, Z.; Liang, Y.; Wang, C.; Chen, Y. Synthesis and simultaneous MINLP optimization of heat exchanger network, steam Rankine Cycle, and organic Rankine Cycle. *Energy* **2020**, *195*, 116922. [[CrossRef](#)]
23. Chen, J. Comments on the improvements on a replacement for the logarithmic mean. *Chem. Eng. Sci.* **1987**, *42*, 2488–2489. [[CrossRef](#)]
24. Rosenthal, R.E. GAMS-A user's guide. *GAMS Dev. Corp.* **2010**, *49*, 397–400.



© 2020 by the authors. Licensee MDPI, Basel, Switzerland. This article is an open access article distributed under the terms and conditions of the Creative Commons Attribution (CC BY) license (<http://creativecommons.org/licenses/by/4.0/>).

Article

Techno-Economic and Environmental Evaluations of Decarbonized Fossil-Intensive Industrial Processes by Reactive Absorption & Adsorption CO₂ Capture Systems

Ana-Maria Cormos, Simion Dragan, Letitia Petrescu, Vlad Sandu and Calin-Cristian Cormos *

Department of Chemical Engineering, Faculty of Chemistry and Chemical Engineering, Babes—Bolyai University, Arany Janos 11, RO-400028 Cluj-Napoca, Romania; cani@chem.ubbcluj.ro (A.-M.C.); sdragan@chem.ubbcluj.ro (S.D.); letitiapetrescu@chem.ubbcluj.ro (L.P.); vcrcsandu@chem.ubbcluj.ro (V.S.)

* Correspondence: cormos@chem.ubbcluj.ro; Tel.: +40-264593833

Received: 17 January 2020; Accepted: 6 March 2020; Published: 9 March 2020

Abstract: Decarbonization of energy-intensive systems (e.g., heat and power generation, iron, and steel production, petrochemical processes, cement production, etc.) is an important task for the development of a low carbon economy. In this respect, carbon capture technologies will play an important role in the decarbonization of fossil-based industrial processes. The most significant techno-economic and environmental performance indicators of various fossil-based industrial applications decarbonized by two reactive gas-liquid (chemical scrubbing) and gas-solid CO₂ capture systems are calculated, compared, and discussed in the present work. As decarbonization technologies, the gas-liquid chemical absorption and more innovative calcium looping systems were employed. The integrated assessment uses various elements, e.g., conceptual design of decarbonized plants, computer-aided tools for process design and integration, evaluation of main plant performance indexes based on industrial and simulation results, etc. The overall decarbonization rate for various assessed applications (e.g., power generation, steel, and cement production, chemicals) was set to 90% in line with the current state of the art in the field. Similar non-carbon capture plants are also assessed to quantify the various penalties imposed by decarbonization (e.g., increasing energy consumption, reducing efficiency, economic impact, etc.). The integrated evaluations exhibit that the integration of decarbonization technologies (especially chemical looping systems) into key energy-intensive industrial processes have significant advantages for cutting the carbon footprint (60–90% specific CO₂ emission reduction), improving the energy conversion yields and reducing CO₂ capture penalties.

Keywords: fossil-intensive industrial processes; decarbonization technologies; reactive absorption/adsorption CO₂ capture systems; modeling; simulation; and process integration; techno-economic and environmental assessments

1. Introduction

Global warming and climate change are fundamental issues nowadays. In order to significantly reduce global warming for long-term sustainable development, the greenhouse gas emissions (especially the fossil ones) need to be significantly cut and decoupled from economic growth [1]. Along this line, the industrial and transport sectors are facing important modifications and restructuring with the aim of reducing the fossil energy sources as required for the development of an economy with a low carbon footprint. Among industrial applications with significant greenhouse gas emissions, the heat, and power generation, iron and cement production, and various fossil-based chemical systems are the biggest contributors. To illustrate the major importance of these industrial sectors and to consider the global greenhouse gas emissions one can mention that the coal-based power generation is responsible

by more than 10 Gt CO₂ from the 33.1 Gt CO₂ emitted globally in 2018 [2], production of iron and steel counts for about 6% of global CO₂ emissions [3], and the cement production counts for 5% of global CO₂ emissions [4]. Accordingly, the fossil-intensive industrial processes need significant changes in forthcoming years to efficiently contribute to the global effort of reducing carbon emissions.

As possible technical and scientific options to cut the fossil carbon emissions, a broad range of measures can be applied, ranging from promoting renewable ene.g., increasing the energy conversion, and utilization yields too large scale deployment of carbon capture, utilization and storage (CCUS) technologies [5]. These technologies are seen as important options for the medium time horizon to allow a smoothly transition from the current fossil-based economy to a future low carbon one. For the integration of the CO₂ capture process into various energy-intensive applications, several conceptual options are already available and widely evaluated in the literature, e.g., pre-, post- and oxy-fuel combustion methods [6]. Once captured, CO₂ can be used as raw material for various processes (e.g., production of various chemicals and fuels), stored in appropriate geological formations (e.g., saline aquifers) or used for increasing the oil/gas recovery yields [7].

This work is assessing some key fossil fuel-intensive industrial applications in view of energy and cost-effective process decarbonization. The selected industrial applications are power generation, iron and steel production, cement production, as well as producing chemicals which can also be used as decarbonized energy carriers (e.g., hydrogen). The chemical absorption (scrubbing) method [8] and the innovative chemical/calcium looping cycles based on reactive adsorption systems [9] were evaluated as decarbonization technologies. Apart from the carbon footprint reduction, the overall energy conversion yields, as well as other techno-economic and environmental performance indicators, represent important elements in the present evaluations. Similar non-carbon capture plants are also assessed to quantify the various penalties imposed by decarbonization (e.g., ene.g., raw materials, and utility consumptions, overall energy efficiency, main economic factors). The decarbonized plant concepts have a 90% CO₂ capture rate, a value which is in line with assessment methodology of CO₂ capture technologies presented in relevant literature sources, e.g., International Energy Agency Greenhouse Gas Programme (IEAGHG) reports for decarbonization of iron and steel production [3] or cement production [4]. In addition to technical and environmental indicators, the economic impact of process decarbonization is also presented considering key performance indexes.

The selected industrial applications were subject to various technical investigations ranging from the conceptual design of decarbonized plants and evaluation of CO₂ capture unit mass and energy integration analysis, usage of computer-aided tools for process design, and integration to the evaluation of main plant performance indexes based on industrial and simulation results. The key novelty aspect of the presented work is to provide an integrated in-depth techno-economic and environmental evaluation methodology of decarbonized industrial processes.

2. Carbon Capture Technologies for Efficient Decarbonization of Industrial Applications

As decarbonization technologies, two carbon capture methods were assessed in view of integration into fossil-intensive industrial applications. The first option considers a mature technology based on chemical scrubbing employing alkanolamines [10]. This technology represents the conventional option when acid gas removal (e.g., CO₂, sulfur compounds, etc.) is required in various chemical industrial processes (e.g., natural gas reforming for ammonia synthesis, sulfur removal from oil refinery, etc.). For this main reason, the reactive gas-liquid absorption technology was considered as potential decarbonization process for the evaluated energy-intensive industrial applications. To illustrate this decarbonization technology, Methyl-DiEthanol-Amine (MDEA) was selected as a chemical solvent. The selection of the MDEA solvent was based on the following key advantages over more conventional Mono-Ethanol-Amine (MEA): higher CO₂ loadings (1 mole CO₂/mole MDEA vs. up to 0.5 mole CO₂/mole MEA), higher solution concentration (50% vs. 30%), lower degradation, corrosion and toxicity,

better thermal stability, etc. [11]. The overall chemical reaction for MDEA-based decarbonization is presented below:



For this decarbonization technology, the above global chemical reaction is used in a cycle, as presented in Figure 1. The gas to be decarbonized is treated in the absorption column being put in contact with an MDEA aqueous solution (50% wt.). The loaded (rich) solvent is pumped in a separate column where using heat, the CO_2 is desorbed, and thus, the solvent regenerated. The regenerated (lean) solution is pumped back in the absorption column (some make-up being necessary to cover the solvent losses). The CO_2 is treated for moisture removal and compressed to the final delivery pressure (120 bar) prior to storage/utilization. A key element of this decarbonization technology represents the heat consumption (at the bottom of the desorption column) for CO_2 desorption and solvent regeneration. Currently, for the post-combustion CO_2 capture configurations applied to fossil-based power generation plants (10–15 volumetric percentages of CO_2 content in the gas to be treated), this heat duty is about 3 GJ/t CO_2 [12]. For pre-combustion capture configurations, the heat consumption for solvent regeneration is significantly reduced to about 0.6–0.8 GJ/t due to pressure reduction [13].

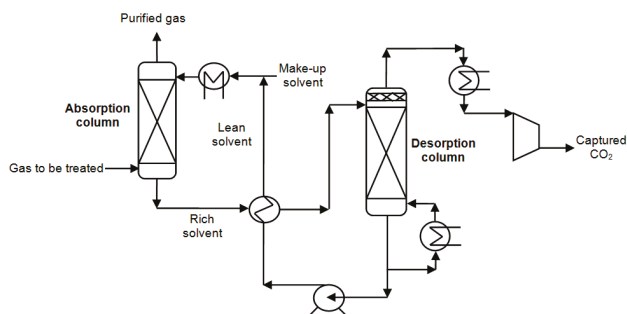


Figure 1. CO_2 capture by chemical scrubbing via an absorption-desorption cycle.

The second evaluated decarbonization option makes use of an innovative reactive system based on calcium adsorption (Calcium Looping—CaL). Similar with chemical scrubbing option presented above, the chemical looping cycle can also be used for pre- and post-combustion decarbonization configurations. This technique uses two separate reactors for decarbonization as follow [9]:

The carbonation reactor where the gas to be decarbonized is put in contact with the calcium sorbent for CO_2 capture. The reactions for pre- and post-combustion decarbonization are exhibited below:



Calcination reactor when CaCO_3 is thermally disintegrated to CaO and CO_2 according to the next chemical reaction:



The innovative calcium looping method was selected as decarbonization technology for the fossil-intensive industrial applications based on the following reasons: it represents a promising technology in reducing the CO_2 capture energy and cost penalties, possibility to use the spent sorbent (deactivated calcium sorbent) within the main process, sorbent lower cost and large availability, etc. [14]. For this decarbonization technology, the conceptual design is presented in Figure 2. As for gas-liquid absorption decarbonization technology, the calcium looping cycle requires an additional energy input (for the calcination reactor). In the calcination reactor, some sort of fuel (e.g., natural gas, syngas,

coal, etc.) is to be oxy-combusted for providing the required energy input for the calcium carbonate decomposition. Oxygen must be used for combustion in order not to dilute the CO₂ captured stream with nitrogen. Different for gas-liquid decarbonization technology, the CaL cycle is operating at significantly higher temperatures: carbonation (CO₂ fixation) reactor to 500–650 °C and calcination reactor to about 850–1000 °C [15]. These operating conditions enable high-temperature heat recovery with positive consequences on the overall energy conversion yield [16].

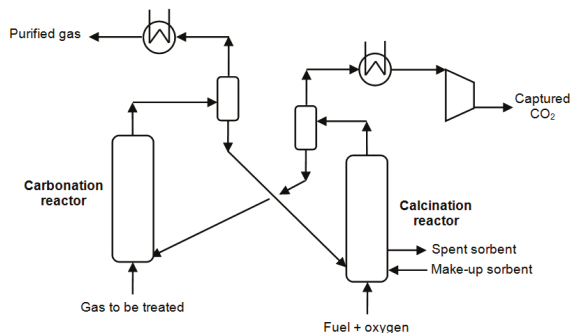


Figure 2. CO₂ capture by the calcium-based sorbent looping cycle.

3. Conceptual Designs, Main Design Assumptions, and Process Integration Elements

To illustrate the influence of plant decarbonization over the most relevant techno-economic and environmental indexes, some key fossil-intensive industrial applications were considered as follow:

- Cases 1: Coal-based gasification power plants;
- Cases 2: Coal-based super-critical power plants;
- Cases 3: Integrated iron & steel plants;
- Cases 4: Cement production plants.

The evaluated gasification plants consider both pre- and post-combustion decarbonization scenarios is based on the Integrated Gasification Combined Cycle (IGCC) design [17]. The conventional gasification-based power plant design without carbon capture involves a partial oxidation process (with oxygen and steam) of the solid fuel to syngas (mainly a mixture of hydrogen and carbon monoxide). Further, the syngas is treated for sulfur removal in an acid gas removal unit, and the clean gas is used for power generation in a combined cycle gas turbine unit [18].

For the pre-combustion capture, the syngas is decarbonized either by gas-liquid absorption or calcium looping, and the hydrogen-rich stream is then used for power generation (in a combined cycle gas turbine unit) or hydrogen and power co-generation. For the post-combustion capture, the flue gases from the syngas-fueled gas turbine are treated for decarbonization with the same two carbon capture technologies (MDEA-based gas-liquid absorption and calcium looping). The conceptual plant layouts of decarbonized IGCC power plants are shown in Figure 3.

The evaluated coal-based super-critical power plants are based on the conventional state of the art design [19]. The combustion-based power plants involve total oxidation of solid fuel with air. The hot flue gases are then used for steam generation. The steam cycle parameters were selected in line with industrial standards: live steam at 290 bar/582 °C also having two steam reheats at 75 bar/580 °C, and 20 bar/580 °C. The cooled flue gases are treated for particulate matter, NO_x, and SO_x removal prior to decarbonization. The two decarbonization technologies analyzed in this paper (MDEA-based chemical scrubbing by gas-liquid absorption and calcium-based gas-solid looping cycle) were evaluated in a post-combustion capture configuration. The conceptual plant layout of the decarbonized super-critical power plant, is presented in Figure 4.

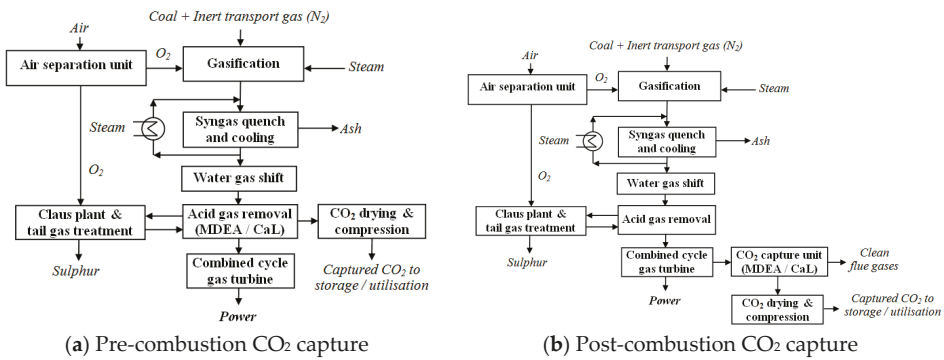


Figure 3. Decarbonized Integrated Gasification Combined Cycle (IGCC) power plant options.

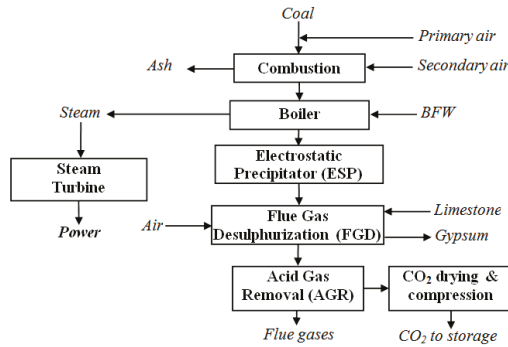


Figure 4. Decarbonized super-critical power plant.

The evaluated decarbonization scenario for iron and steel production considers an integrated steel mill in accordance with the current state of the art [20]. The iron and steel production involve sinter production, iron production (a blast furnace), desulphurization plant, steel production (basic oxygen furnace), and various metallurgical steps. Within an integrated steel mill, there are numerous CO₂ emission sources; this analysis considers the carbon capture for the main ones: captive power and heat (steam) plant, blast furnace and hot stoves, lime and coke production systems [21]. The two decarbonization technologies (MDEA-based chemical scrubbing by gas-liquid absorption and calcium-based gas-solid looping cycle) were evaluated in a post-combustion configuration. The conceptual plant layout of decarbonized iron and steel production system is presented in Figure 5.

The evaluated decarbonization scenario for cement production considers the current conventional design [22]. The cement production involves raw meal production, preheating, calcination (clinker production), and grinder (cement production) steps. The generated CO₂ within the cement production process has two main sources—one from the fuel to be combusted in the calcination step and one from the calcium carbonate decomposition [23]. The two decarbonization technologies (MDEA-based chemical scrubbing and calcium-based gas-solid looping cycle) were evaluated in a post-combustion capture configuration. The conceptual plant layout of the decarbonized cement plant is presented in Figure 6.

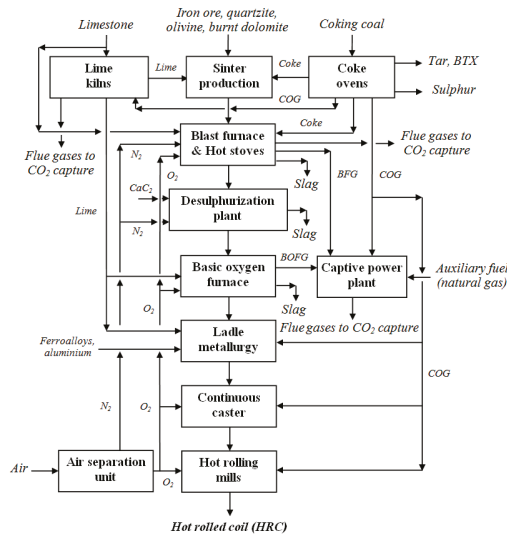


Figure 5. Decarbonized integrated steel mill.

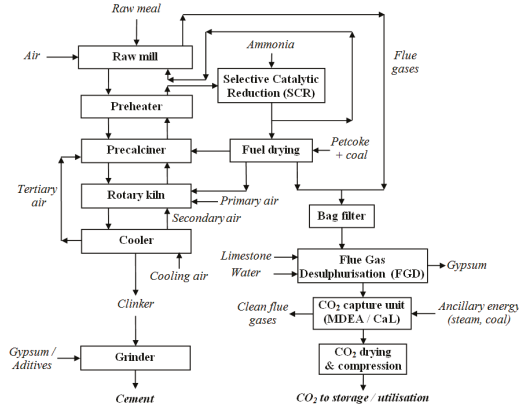


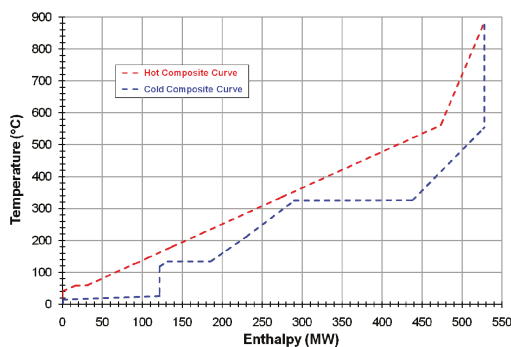
Figure 6. Decarbonized cement plant.

Table 1 shows the most important design assumptions of evaluated fossil-intensive industrial applications (power generation, iron, steel, and cement production) to be decarbonized as well as the two CO₂ capture technologies (reactive gas-liquid absorption and calcium looping cycle). More detailed specifications are provided in the reference sources indicated in Table 1. Assumptions were furthermore used for modeling and simulation of assessed case studies. In this respect, ChemCAD software was used as a process flow modeling tool. Then the simulation results were employed to evaluate the most important plant performance indexes (e.g., fuel consumption, ancillary ene.g., and raw materials consumption, plant decarbonization rate, carbon footprint, etc.).

Table 1. Main design elements of evaluated decarbonized industrial processes.

Unit	Design Assumptions
Fossil fuel (coal) specifications [22]	Ultimate analysis (dry weight percentages): 72.30% carbon, 4.11% hydrogen, 1.69% nitrogen, 7.45% oxygen, 0.56% sulfur, 13.89% ash; Moisture: 8%; Lower heating value: 25.17 MJ/kg
Gasification power plant [12]	Entrained-flow gasifier with syngas quench Separate H ₂ S and CO ₂ removal by absorption and adsorption systems Combined cycle power using one M701G2 gas turbine
Super-critical power plant [17]	290 bar/582 °C and two reheats at 75 bar/580 °C and 20 bar/580 °C 95% NO _x removal yield by selective catalytic reduction unit 98–99% SO _x removal yield by wet desulphurization unit
Integrated steel mill [3]	Plant capacity: 4 Mt/y hot-rolled coil (HRC) Decarbonization of power plant, hot stoves, lime and coke production Natural gas-based heat and power unit for ancillary consumptions Captive heat and power plant: subcritical boiler and combined cycle
Cement plant [4]	Plant capacity: 1 Mt/y cement 95% NO _x removal yield by selective catalytic reduction unit 98–99% SO _x removal yield by wet desulphurization unit Coal-based heat and power unit for ancillary energy consumptions
Decarbonization unit employing a chemical scrubbing system [19]	Methyl-diethanol-amine (MDEA) aqueous solution 50% wt. Absorption/desorption columns: 42–55 °C/115–125 °C 90% flue gas decarbonization rate (pre- and post-combustion) Solvent regeneration: thermal using LP steam at 140–150 °C
Decarbonization unit employing a Ca-based sorbent system [19]	Natural limestone as calcium-based sorbent Carbonation/calcination reactors: 540–615 °C/825–975 °C 90% flue gas decarbonization rate (pre- and post-combustion) Oxy-fuel combustion system to provide heat for sorbent regeneration Power consumption for oxygen production unit: 200 kWh/t
CO ₂ conditioning unit [14]	Four compression stages with 120 bar final pressure at plant gate Moisture removal by gas-liquid absorption using Tri-Ethylene-Glycol (TEG) CO ₂ composition (volume percentages): >95% CO ₂ , <2000 ppm CO, <200 ppm H ₂ O, <50 ppm H ₂ S, <4% other gases

The evaluated carbon capture designs were assessed in view of heat and power integration analysis for optimization of overall energy conversion yield [24]. In this respect, Pinch Analysis was used for Heat Integration of hot and cold streams within the plant. The main focus of Heat Integration analysis of the two carbon capture technologies was to enhance heat recovery potential by process-to-process heat exchange and to reduce external hot and cold utility consumptions [25]. To show the fundamental advantage in terms of high-temperature heat recovery of calcium-based gas-solid looping cycle over the chemical scrubbing option, Figure 7 presents the Hot and Cold Composite Curves for CaL cycle used for super-critical power plant decarbonization [16].

**Figure 7.** Calcium looping cycle Heat Integration analysis.

In contrast with the calcium looping cycle, the reactive gas-liquid absorption cycle has low-temperature hot streams (40–60 °C); therefore, the available heat cannot be used in an

energy-efficient manner (e.g., for steam generation) but only to be taken by cooling water (external cooling utility) [11]. It can be observed that the high-temperature heat recovery capacity of the CaL unit significantly improves the overall energy conversion yield. In fact, the CaL unit can be seen not only as a carbon capture system but also as an energy conversion system since additional fuel (coal) is oxy-combusted with the goal to provide the heat input for CaCO₃ decomposition.

4. Techno-Economic and Environmental Assessment Methodology

This section of the paper is dedicated to present the overall techno-economic and environmental plant performance indicators. All evaluated decarbonized energy-intensive industrial concepts were mathematically modeled and simulated using ChemCAD software. The most important simulation data (as mass and energy balances, fuel conversion yields, overall plant decarbonization rate, etc.) were benchmarked against industrial data for model validation; e.g., for the gasification [18] and combustion [19] power plant concepts, for the integrated steel plants [3], for the cement production plants [4], for the alkanolamines-based carbon capture processes [26] and for the calcium looping-based carbon capture [27] and its integration into various energy systems [28]. No significant differences between simulation results and literature data were noticed/registered.

After validation of the simulation results, the most relevant techno-economic and environmental plant performance indexes were calculated using the following equations:

Gross/net power conversion efficiencies show the energy conversion rates for the gasification and combustion power plants:

$$\eta_{gross/net} = \frac{Gross \ / \ net \ electricity \ output \ [MW_e]}{Thermal \ energy \ of \ used \ fuel \ (coal) \ [MW_{th}]} \times 100 \quad (5)$$

Ancillary power consumption was calculated considering all electricity consumptions of various plant sub-systems:

$$Ancillary \ power \ consumption = \sum Plant \ units \ power \ consumption \quad (6)$$

Plant decarbonization rate (noted as CO₂ Capture Rate—CCR) takes into account the percentage of feedstock carbon that was captured:

$$CCR = \frac{Sequestered \ carbon \ molar \ flow \ [kmole/h]}{Carbon \ molar \ flow \ of \ coal \ [kmole/h]} \times 100 \quad (7)$$

Specific emission of CO₂ (*SE*_{CO₂}) quantifies the vented CO₂ quantity when 1 MW of power or 1 ton of steel/cement is produced:

$$SE_{CO_2} = \frac{Emitted \ CO_2 \ mass \ flow \ [kg/h]}{Net \ power \ output \ [MW_e] / Steel \ or \ cement \ output \ [t]} \times 100 \quad (8)$$

Specific consumption of primary energy for CO₂ avoided (*SPECCA*) takes into accounts both non-carbon capture and carbon capture power plant concepts using the following equation:

$$SPECCA = \frac{Heat \ rate \ Capture \ [\frac{MJ_{LHV}}{MWh_e}] - Heat \ rate \ No \ capture \ [\frac{MJ_{LHV}}{MWh_e}]}{Specific \ emissions \ No \ capture \ [\frac{kg \ CO_2}{MWh_e}] - Specific \ emissions \ Capture \ [\frac{kg \ CO_2}{MWh_e}]} \quad (9)$$

Specific capital investment (*SCI*) calculates the capital investment required for production of 1 kW of net power or 1 ton of steel/cement:

$$SCI = \frac{Capital \ investment \ [MEuro]}{Net \ power \ output \ [kW_e] / Steel \ or \ cement \ output \ [t]} \cdot 100 \quad (10)$$

Levelized costs of decarbonized power, steel, and cement were calculated according to the International Energy Agency-Greenhouse Gas R&D Program methodology [29] using the net present value method. This method was translated into in-house developed calculation routines.

CO_2 avoided cost was calculated considering the levelized cost of electricity (or steel/cement) and specific CO_2 emissions in both plant conditions with and without carbon capture:

$$CO_2 \text{ avoided cost} = \frac{LCOE_{\text{Capture}} - LCOE_{\text{No capture}}}{\text{Specific } CO_2 \text{ emissions}_{\text{No capture}} - \text{Specific } CO_2 \text{ emissions}_{\text{Capture}}} \quad (11)$$

The above-mentioned performance indicators, as well as others (e.g., fuel and raw material consumptions, ancillary energy consumptions, etc.) were calculated for the evaluated fossil-intensive industrial applications. Regarding environmental impact indicators, several Life Cycle Assessment (LCA) studies were performed by the authors for gasification [30], combustion [31], and iron and steel [32] but due length constraints only the carbon footprint was presented in details. The LCA results are presented in detail for one illustrative case (i.e., super-critical combustion power plant).

5. Results and Discussions

5.1. Coal-Based Gasification Power Plants

For decarbonization of gasification-based power plants, two technical options are available. The pre-combustion route when the shifted syngas is decarbonized before combustion in a combined cycle. The post-combustion route when the syngas is used for power production in a combined cycle as in any conventional IGCC design without carbon capture, and then the combustion gases are treated for CO_2 capture (see Figure 3). For gasification systems, the general opinion is that the pre-combustion configurations are more efficient than the post-combustion ones considering the partial pressure of CO_2 in the gas to be decarbonized [16]. This work is considering both pre- and post-combustion capture options to illustrate, in a quantitative manner, the advantages of the pre-combustion capture option. For post-combustion capture, only the calcium looping option was considered. This consideration was based on its higher energy efficiency compared to the chemical scrubbing option. The following gasification-based power plant concepts were evaluated:

Case 1.1—Conventional gasification-based power plant without decarbonization;

Case 1.2—Decarbonized power plant based on the pre-combustion concept using reactive gas-liquid absorption (MDEA);

Case 1.3—Decarbonized power plant based on the pre-combustion concept using reactive gas-solid system (CaL);

Case 1.4—Decarbonized power plant based on the post-combustion concept using reactive gas-liquid absorption (MDEA).

The most important techno-economic and environmental performance indicators of evaluated coal-based gasification power plants are summarized in Table 2.

As shown in Table 2, the pre-combustion capture configurations have a lower decarbonization energy penalty than the post-combustion option (9.3–9.7 vs. 11.7 net energy efficiency percentage points). This energy efficiency difference of about two net percentage points between pre-combustion and post-combustion capture cases can be explained by the significantly higher partial pressure of CO_2 in the gas subject to decarbonization (12–14 bar for pre-combustion cases vs. 0.13–0.16 bar for post-combustion cases). For the pre-combustion options, the MDEA concept (Case 1.2) shows higher net efficiency than the CaL concept (Case 1.3).

The specific consumption of primary energy for CO_2 avoided (SPECCA indicator) shows slightly better performances for the MDEA system compared to the CaL one (either prior or after combustion). In addition, CaL design (which uses a Circulated Fluidization Bed—CFB system) is more complicated to be adjusted for operation at high pressures (about 30–40 bar) as required in the pre-combustion

option [33]. Specific CO₂ emissions (carbon footprint) for all decarbonized plants are significantly reduced compared to the benchmark case without carbon capture. A full Life Cycle Analysis (LCA) reveals (as illustrated below in case of super-critical combustion-based power plants) that other environmental impact indicators increase by plant decarbonization [30]. This negative element of process decarbonization is explained by increasing the raw materials consumptions, reducing energy efficiency, and introducing new plant sub-units (CO₂ capture and conditioning units).

Table 2. Gasification power plants techno-economic and environmental performance indexes.

Performance Index	UM	Case 1.1	Case 1.2	Case 1.3	Case 1.4
Fossil fuel (coal) consumption	t/h	151.00	166.80	222.00	228.17
Coal lower heating value (LHV)	MJ/kg		25.17		
Power plant input thermal energy	MW	1055.74	1166.21	1552.15	1595.30
Power output (combined cycle)	MW	560.61	535.88	716.25	720.50
Power consumption	MW	76.25	108.91	156.18	175.01
Net power output	MW	484.36	426.97	560.07	545.49
Net power efficiency	%	45.87	36.61	36.08	34.19
Plant decarbonization rate	%	0.00	90.00	90.00	90.00
Specific power plant emissions	kg/MWh	760.25	85.48	83.02	88.95
SPECCA	MJ/kg	-	2.94	3.14	3.99
Specific capital investment	€/kW	1874.00	2620.00	2305.00	3286.00
Levelised cost of electricity	€/MWh	54.13	73.28	76.07	81.25
CO ₂ avoided cost	€/t	-	28.38	32.40	40.39

The decarbonization process of gasification-based power generation brings significant economic penalty (23–75% increase in the specific capital investment, 35–50% increase in the electricity cost). The economic indicators show that pre-combustion capture (either gas-liquid absorption or calcium looping) is definitely better than post-combustion capture in term of specific capital investment (reduced by 20–30%), levelised cost of electricity (reduced by 6–10%) and CO₂ avoided cost (reduced by 19–30%). The MDEA-based decarbonization option has slightly better electricity cost, and CO₂ avoided cost than the calcium looping option (for the technical reasons mentioned above).

One relevant element to be mentioned here in connection with gasification systems represents the ability of this partial oxidation technology to generate, in a flexible manner, various energy carriers. For instance, after syngas decarbonization in a pre-combustion capture configuration, the hydrogen-rich gaseous stream could be employed for the generation of power, hydrogen, or other synthetic carbon-based fuels (methanol, substitute natural gas, synthetic hydrocarbons via Fischer–Tropsch process). One key advantage of these systems represents high cumulative energy efficiency. This specific design characteristic of gasification-based energy conversion systems represents an important element for the future low carbon higher efficiency systems [34].

5.2. Coal-Based Super-Critical Combustion Power Plants

To quantify the techno-economic and environmental impact of the decarbonization process for the coal-based, super-critical, combustion-based, power generation using post-combustion capture systems, the next power plant concepts were used as illustrative examples in this work:

- Case 2.1—Conventional combustion-based power plant without decarbonization;
- Case 2.2—Decarbonized power plant based on reactive gas-liquid absorption (MDEA);
- Case 2.3—Decarbonized power plant based on reactive gas-solid system (CaL).

The non-capture concept (Case 2.1) is based on current industrial design having 500 MW net output [19]. For the assessed decarbonized concepts (both having the same plant decarbonization degree—90%), the additional heat and power consumptions required for CO₂ capture are covered by the main power block. The most important techno-economic and environmental performance indicators of evaluated coal-based super-critical power plants are summarized in Table 3.

Table 3. Super-critical power plants techno-economic and environmental performance indexes.

Performance Index	UM	Case 2.1	Case 2.2	Case 2.3
Fossil fuel (coal) consumption	t/h	165.00	208.50	199.13
Coal lower heating value (LHV)	MJ/kg		25.17	
Power plant input thermal energy	MW	1153.62	1457.76	1392.24
Power output (steam turbine)	MW	528.90	569.05	596.81
Power consumption	MW	28.90	69.05	96.81
Net power output	MW	500.00	500.00	500.00
Net power efficiency	%	43.34	34.30	35.92
Plant decarbonization rate	%	0.00	90.00	90.00
Specific power plant emissions	kg/MWh	800.61	89.60	77.05
SPECCA	MJ/kg	-	3.08	2.41
Specific capital investment	€/kW	1320.00	2520.00	1875.00
Levelised cost of electricity	€/MWh	45.53	84.02	68.41
CO ₂ avoided cost	€/t	-	49.09	31.34

As presented in Table 3, the decarbonization penalty for super-critical power plants lays between seven to nine net energy efficiency percentage points (for the same decarbonization rate considered in both options—90%). The post-combustion calcium looping decarbonization system shows improved values in comparison to the chemical gas-liquid absorption scrubbing system. The difference in net power efficiency points for the two decarbonization systems is about 1.62. This value is justified by the high-temperature heat recovery potential of the calcium looping cycle. The specific consumption of primary energy for CO₂ avoided (SPECCA) also shows better value for chemical looping in comparison to chemical scrubbing (gas-liquid absorption) by about 0.67 MJ/kg. All these technical and environmental benefits of the CaL-based decarbonization process translate into improved economic performance [35]. All economic indicators are in favor of the calcium looping option in comparison to the gas-liquid absorption as assessed decarbonization technologies—specific investment cost (reduced by about 25%), levelised cost of electricity (reduced by about 18%), and CO₂ avoided cost (reduced by about 36%). Also, it worth mentioning that the combustion-based power generation is cheaper than the gasification-based power generation in a non-carbon capture scenario, but when carbon capture is implemented, the economic differences are reduced significantly or even are in favor of IGCC power plants (see Tables 2 and 3).

To illustrate an in-depth environmental impact evaluation for the assessed super-critical power plants with and without carbon capture, Table 4 presents the Life Cycle Analysis (LCA) results in a cradle-to-grave approach using CML 2001 method. The full technical details of this LCA analysis are presented in the paper indicated as reference [31].

Table 4. Environmental impact indicators (Life Cycle Analysis) for super-critical power plants.

Environmental Impact Index	UM	Case 2.1	Case 2.2	Case 2.3
Global warming potential	kg CO ₂ eq./MWh	970.37	495.93	402.20
Acidification potential	kg SO ₂ eq./MWh	0.49	4.57	1.66
Eutrophication potential	kg PO ₄ ⁻³ eq./MWh	1285.44	1739.76	1121.86
Ozone depletion potential ×10 ⁸	kg R11 eq./MWh	0.59	4.07	2.63
Abiotic depletion potential	MJ/MWh	9829.28	15,231.63	13,752.06
Freshwater ecotoxicity potential	kg DCB eq./MWh	0.27	1.66	1.10
Human toxicity potential	kg DCB eq./MWh	3.41	55.27	19.84
Photochemical oxidation potential	kg Ethene eq./MWh	0.20	2.71	0.26
Terrestrial ecotoxicity potential	kg DCB eq./MWh	0.05	0.28	0.18
Marine ecotoxicity potential	kg DCB eq./MWh	6730.54	26,011.85	16,494.81

It can be noticed that the carbon footprint (noted here as Global Warming Potential—GWP) is reduced with plant decarbonization (not corresponding to 90% plant decarbonization rate but to a lower rate due to up-stream and down-stream processes). All other environmental indicators are increasing with plant decarbonization; in some cases, the increasing rate is quite high (e.g., acidification potential, indicators related to toxicity, etc.). It worth mention that for the calcium looping system, all environmental indicators have better values than for the reactive gas-liquid absorption system. The main reason for this result represents the lower environmental impact of natural-based calcium sorbent in comparison to a chemical-based solvent.

5.3. Integrated Steel Mills

To assess the techno-economic and environmental impact of decarbonization applied to iron and steel production, the next plant concepts were used as illustrative examples:

Case 3.1—Conventional steel mill without decarbonization;

Case 3.2—Decarbonized steel mill based on reactive gas-liquid absorption (MDEA);

Case 3.3—Decarbonized steel mill based on reactive gas-solid system (CaL).

As presented in Table 1, a conventional integrated iron and steel plant was considered in the assessments with 4 Mt/y hot-rolled coil (HRC) production capacity [3]. All assessed decarbonized steel concepts are not considering any import of heat and power (steel mill off-gases are used for this purpose). In this respect, natural gas was used as additional fuel to cover the ancillary energy consumptions [36]. The decarbonized steel mill concepts capture CO₂ from the most significant plant units, e.g., captive power plant, blast furnace hot stoves, and lime coke production units. The most important performances of evaluated steel plants are exhibited in Table 5.

Table 5. Integrated steel mills techno-economic and environmental performance indexes.

Performance Index	UM	Case 3.1	Case 3.2	Case 3.3
Fossil fuel (natural gas) consumption	MW	669.80	544.00	1156.80
Power output (gas turbine)	MW	-	202.31	91.06
Power output (steam turbine)	MW	224.68	107.33	366.06
Gross power block output	MW	224.68	309.65	457.12
Power consumption	MW	9.68	1.68	132.65
Net power block output	MW	215.00	307.97	324.47
Net power block efficiency	%	32.10	56.61	28.04
Decarbonization rate (power block)	%	0.00	0.00	90.00
Specific CO ₂ emissions (power)	kg/MWh	2455.42	370.02	242.32
Specific CO ₂ emissions (steel)	kg/t HRC	980.48	229.50	166.10
Decarbonization rate (capture plant)	%	0.00	90.00	90.00
Overall plant specific CO ₂ emissions	kg/t HRC	2092.50	833.55	640.00
Quantity of captured CO ₂	kg/t HRC	0.00	1615.80	1495.20
Specific capital investment	€/t HRC	955.00	1077.00	1015.00
Levelised cost of steel	€/t HRC	520.73	614.05	580.70
CO ₂ avoided cost	€/t	-	73.46	68.92

As shown in Table 5, the decarbonization of main CO₂ emitters (captive heat and power plant, blast furnace, lime and coke production units) from an integrated iron and steel production plant cut the overall carbon footprint significantly (with a reduction of about 60 to 70%). Considering the significant amount of greenhouse gas emission of this important industrial sector, this reduction is very substantial [36]. The investigated looping cycle has some important advantages in comparison to the chemical scrubbing system, e.g., higher energy conversion yield and subsequent lower decarbonization energy and cost penalties, integration of spent calcium-based sorbent in the iron and steel production process with a positive impact on plant environmental performance [37]. As for the above-presented cases (combustion and gasification-based power generation), the decarbonization process reduces carbon footprint but increases other environmental indicators [36].

Decarbonization of iron and steel production process brings an economic penalty (6–13% increase of specific capital investment, 12–18% increase of steel production cost). The economic indicators

show that the calcium looping option has slightly better economic performance than post-combustion capture in terms of specific capital investment (reduced by about 6%), steel production cost (reduced by about 5%), and CO₂ avoided cost (reduced by about 6%).

5.4. Cement Plants

To evaluate the impact of process decarbonization (in a post-combustion capture configuration) for cement production, the next plant concepts were considered as illustrative examples:

Case 4.1—Conventional cement production plant without decarbonization;

Case 4.2—Decarbonized cement production based on reactive gas-liquid absorption (MDEA);

Case 4.3—Decarbonized cement production based on reactive gas-solid system (CaL).

As presented in Table 1, a conventional cement plant was considered in the assessments with 1 Mt/y production capacity [4]. For decarbonized cement production cases by reactive gas-liquid and gas-solid systems, a coal-based combustion unit in conjunction with a steam cycle power block was used to cover the ancillary energy (heat and power) consumptions of the carbon capture plants [38]. The excess energy was exported as the power to the grid with a 520 kg/MWh as the carbon dioxide emission factor. The most relevant techno-economic and environmental performance indexes of the assessed cement plants are exhibited in Table 6.

Table 6. Cement plants techno-economic and environmental performance indexes.

Performance Index	UM	Case 4.1	Case 4.2	Case 4.3
Fossil fuel (coal) consumption	t/h	-	33.50	22.10
Coal inferior calorific value	MJ/kg	-	25.17	-
Thermal energy (decarbonization unit)	MW	-	234.22	154.51
Power output (steam turbine)	MW	-	54.40	58.12
Gross power block output	MW	-	54.40	58.12
Power consumption	MW	16.24	34.16	42.38
Net power block output	MW	-	20.24	15.74
Net power block efficiency	%	-	8.64	10.18
Plant decarbonization rate	%	0.00	90.00	90.00
Specific plant CO ₂ emissions (on-site)	kg/t cement	728.42	135.78	120.74
Specific plant CO ₂ emissions (export)	kg/t cement	42.02	-79.93	-62.35
Specific plant CO ₂ emissions (total)	kg/t cement	770.44	55.85	58.39
Quantity of captured CO ₂	kg/t cement	0.00	1214.17	962.20
Specific capital investment	€/t cement	263.00	557.00	458.00
Levelized cost of cement	€/t cement	65.60	127.68	106.73
CO ₂ avoided cost	€/t	-	86.87	57.76

As presented in Table 6, the cement plant decarbonization cut significantly the overall carbon footprint of the process (by about 92–93%). The investigated looping cycle exhibits several benefits in comparison to the chemical scrubbing system, e.g., higher energy conversion yield and subsequent lower decarbonization energy penalty. Another important element of the calcium-based reactive gas-solid system refers to the potential to reuse the spent solid material in the cement plant (clinker production). This element brings advantages in terms of reducing carbon footprint as well as improving technical and economic performance indicators [39]. As for the above-presented cases, the decarbonization process brings a positive effect in reducing the carbon footprint, but on the other hand, increases other environmental indicators [40].

Decarbonization of the cement production process brings significant economic penalty (74–112% increase of specific capital investment, 62–95% increase of cement production cost). The economic indicators show that calcium looping option has better economic performance than post-combustion capture in term of specific capital investment (reduced by about 18%), cement production cost (reduced by about 16%), and CO₂ avoided cost (reduced by about 34%).

6. Conclusions

This techno-economic and environmental analysis assessed in a quantifiable manner the decarbonization process of some important fossil-based industrial processes (electricity generation, iron, steel and cement production). As decarbonization technologies, two reactive gas-liquid (chemical scrubbing using alkanolamines—MDEA) and gas-solid (based on calcium-based sorbents) systems were assessed. The CaL decarbonization option exhibits improved performance indicators over the chemical scrubbing for the evaluated post-combustion capture configurations (higher energy conversion yields, lower carbon footprint and specific primary energy consumption, better economic indicators, etc.). In addition, for some of the evaluated processes (steel and cement production plants), the spent solid sorbent from the looping cycle can be utilized by the integration of the whole production chain with positive techno-economic and environmental results. For the pre-combustion capture configuration (evaluated here in relation to a coal gasification plant), the chemical scrubbing by gas-liquid absorption shows higher energy efficiency and more potential for future developments than CaL decarbonization option. Regarding the environmental impact of the LCA analysis, it is worth mentioning that the carbon footprint is reduced by the process decarbonization, but other environmental indicators show significant increases. To illustrate this element, the results of an LCA analysis were presented in detail for super-critical combustion-based power plant concepts.

Author Contributions: A.-M.C., L.P. and C.-C.C. did the model conceptualization of evaluated systems and proposed the assessing methodology, A.-M.C., S.D. and C.-C.C. assessed the main technical and environmental performances, V.S. and C.-C.C. were responsible with modeling, simulation and Heat Integration work as well as writing the paper. All authors have read and agreed to the published version of the manuscript.

Funding: This research received no external funding.

Conflicts of Interest: The authors declare no conflict of interest.

References

1. European Commission. *The European Green Deal*; COM(2019) 640 Final; European Commission: Brussels, Belgium, 2019.
2. International Energy Agency. *Global Energy & CO₂ Status Report 2019*. Available online: <https://www.iea.org/reports/global-energy-and-co2-status-report-2019/emissions> (accessed on 7 January 2020).
3. International Energy Agency—Greenhouse Gas R&D Programme. *Iron and Steel CCS Study (Techno-Economic Integrated Steel Mill)*; Report 2013/04; IEAGHG: Cheltenham, UK, 2013.
4. International Energy Agency—Greenhouse Gas R&D Programme. *Deployment of CCS in the Cement Industry*; Report 2013/19; IEAGHG: Cheltenham, UK, 2013.
5. European Commission. *A Policy Framework for Climate and Energy in the Period From 2020 to 2030*; COM(2014) 15 Final; European Commission: Brussels, Belgium, 2014.
6. Metz, B.; Davidson, O.; Coninck, H.; Loos, M.; Meyer, L. *Special Report: Carbon Dioxide Capture and Storage*; Intergovernmental Panel on Climate Change (IPCC); Cambridge University Press: New York, NY, USA, 2005.
7. Norhasyima, R.S.; Mahlia, T.M.I. Advances in CO₂ utilization technology. A patent landscape review. *J CO₂ Util.* **2018**, *26*, 323–335. [[CrossRef](#)]
8. Fang, M.; Yi, N.; Di, W.; Wang, T.; Wang, Q. Emission and control of flue gas pollutants in CO₂ chemical absorption system—A review. *Int. J. Greenh. Gas Con.* **2020**, *93*, 102904. [[CrossRef](#)]
9. Fan, L.S. *Chemical Looping Systems for Fossil Energy Conversions*; Wiley-AIChE: Hoboken, NJ, USA, 2010.
10. Borhani, T.N.; Wang, M. Role of solvents in CO₂ capture processes. The review of selection and design methods. *Renew. Sustain. Energy Rev.* **2019**, *114*, 109299. [[CrossRef](#)]
11. Cormos, A.M.; Dinca, C.; Cormos, C.C. Energy efficiency improvements of post-combustion CO₂ capture based on reactive gas-liquid absorption applied for super-critical circulating fluidized bed combustion (CFBC) power plants. *Clean. Technol. Environ.* **2018**, *20*, 1311–1321. [[CrossRef](#)]
12. Li, T.; Keener, T.C. A review: Desorption of CO₂ from rich solutions in chemical absorption processes. *Int. J. Greenh. Gas Con.* **2016**, *51*, 290–304. [[CrossRef](#)]

13. Cormos, A.M.; Cormos, C.C. Techno-economic assessment of combined hydrogen & power co-generation with carbon capture. The case of coal gasification. *Appl. Therm. Eng.* **2019**, *147*, 29–39.
14. Yan, Y.; Wang, K.; Clough, P.T.; Anthony, E.J. Developments in calcium/chemical looping and metal oxide redox cycles for high-temperature thermochemical energy storage. A review. *Fuel Process. Technol.* **2020**, *199*, 106280. [[CrossRef](#)]
15. Hornberger, M.; Spörl, R.; Scheffknecht, G. Calcium Looping for CO₂ Capture in Cement Plants—Pilot Scale Test. *Energy Procedia* **2017**, *114*, 6171–6174. [[CrossRef](#)]
16. Cormos, C.C. Economic evaluations of coal-based combustion and gasification power plants with post-combustion CO₂ capture using calcium looping cycle. *Energy* **2014**, *78*, 665–673. [[CrossRef](#)]
17. Hignman, C.; van der Burgt, M. *Gasification*, 2nd ed.; Gulf Professional Publishing, Elsevier Science: Burlington, MA, USA, 2008.
18. International Energy Agency—Greenhouse Gas R&D Programme. *Potential for Improvement in Gasification Combined Cycle Power Generation with CO₂ Capture*; Report PH4/19; IEAGHG: Cheltenham, UK, 2003.
19. National Energy Technology Laboratory. *Cost and Performance Baseline for Fossil Energy Plants, Volume 1: Bituminous Coal and Natural Gas to Electricity*; Report 2010/1397; NETL: Albany, NY, USA, 2010.
20. Ramírez-Santos, A.A.; Castel, C.; Favre, E. A review of gas separation technologies within emission reduction programs in the iron and steel sector: Current application and development perspectives. *Sep. Purif. Technol.* **2018**, *194*, 425–442.
21. Quader, M.A.; Ahmed, S.; Ghazilla, R.A.; Ahmed, S.; Dahari, M. A comprehensive review on energy efficient CO₂ breakthrough technologies for sustainable green iron and steel manufacturing. *Renew. Sustain. Energy Rev.* **2015**, *50*, 594–614. [[CrossRef](#)]
22. Cormos, A.M.; Dinca, C.; Petrescu, L.; Chisalita, D.A.; Szima, S.; Cormos, C.C. Carbon capture and utilisation technologies applied to energy conversion systems and other energy-intensive industrial applications. *Fuel* **2018**, *211*, 883–890. [[CrossRef](#)]
23. Garcia, M.; Berghout, N. Toward a common method of cost-review for carbon capture technologies in the industrial sector: Cement and iron and steel plants. *Int. J. Greenh. Gas Con.* **2019**, *87*, 142–158. [[CrossRef](#)]
24. Manan, Z.A.; Nawi, W.N.R.M.; Alwi, S.R.W.; Klemeš, J.J. Advances in Process Integration research for CO₂ emission reduction—A review. *J. Clean. Prod.* **2017**, *167*, 1–13. [[CrossRef](#)]
25. Perejón, A.; Romeo, L.M.; Lara, Y.; Lisbona, P.; Martínez, A.; Valverde, J.M. The Calcium-Looping technology for CO₂ capture: On the important roles of energy integration and sorbent behavior. *Appl. Energy* **2016**, *162*, 787–807.
26. International Energy Agency—Greenhouse Gas R&D Programme. *Improvement in Power Generation with Post-Combustion Capture of CO₂*; Report no. PH4/33; IEAGHG: Cheltenham, UK, 2004.
27. Sun, H.; Wu, C.; Shen, B.; Zhang, X.; Zhang, Y.; Huang, J. Progress in the development and application of CaO-based adsorbents for CO₂ capture—A review. *Mater. Today Sustain.* **2018**, *1–2*, 1–27. [[CrossRef](#)]
28. Haaf, M.; Peters, J.; Hilz, J.; Unger, A.; Ströhle, J.; Epple, B. Combustion of solid recovered fuels within the calcium looping process—Experimental demonstration at 1 MWth scale. *Exp. Therm. Fluid Sci.* **2020**, *113*, 110023. [[CrossRef](#)]
29. International Energy Agency—Greenhouse Gas R&D Programme. *The IEAGHG Power Plant Assessment Program (PPAP)*; Report 2005/7; IEAGHG: Cheltenham, UK, 2005.
30. Petrescu, L.; Cormos, C.C. Environmental assessment of IGCC power plants with pre-combustion CO₂ capture by chemical & calcium looping methods. *J. Clean. Prod.* **2017**, *158*, 233–244.
31. Petrescu, L.; Bonalumi, D.; Valenti, G.; Cormos, A.M.; Cormos, C.C. Life Cycle Assessment for supercritical pulverized coal power plants with post-combustion carbon capture and storage. *J. Clean. Prod.* **2017**, *157*, 10–21. [[CrossRef](#)]
32. Petrescu, L.; Chisalita, D.A.; Cormos, C.C.; Manzolini, G.; Cobden, P.; van Dijk, H.A.J. Life Cycle Assessment of SEWGS technology applied to integrated steel plants. *Sustainability* **2019**, *11*, 1825. [[CrossRef](#)]
33. Diego, M.E.; Arias, B. Impact of load changes on the carbonator reactor of a 1.7 MWth calcium looping pilot plant. *Fuel Process. Technol.* **2020**, *200*, 106307. [[CrossRef](#)]
34. Cormos, A.M.; Dinca, C.; Cormos, C.C. Multi-fuel multi-product operation of IGCC power plants with carbon capture and storage (CCS). *Appl. Therm. Eng.* **2015**, *74*, 20–27. [[CrossRef](#)]

35. Rolfe, A.; Huang, Y.; Haaf, M.; Rezvani, S.; McIlveen-Wright, D.; Hewitt, N.J. Integration of the calcium carbonate looping process into an existing pulverized coal-fired power plant for CO₂ capture: Techno-economic and environmental evaluation. *Appl. Energy* **2018**, *222*, 169–179. [[CrossRef](#)]
36. Chisalita, D.A.; Petrescu, L.; Cobden, P.; van Dijk, H.A.J.; Cormos, A.M.; Cormos, C.C. Assessing the environmental impact of an integrated steel mill with post-combustion CO₂ capture and storage using the LCA methodology. *J. Clean. Prod.* **2019**, *211*, 1015–1025. [[CrossRef](#)]
37. Nidheesh, P.V.; Kumar, M.S. An overview of environmental sustainability in cement and steel production. *J. Clean. Prod.* **2019**, *231*, 856–871. [[CrossRef](#)]
38. Dean, C.C.; Blamey, J.; Florin, N.H.; Al-Jeboori, M.J.; Fennell, P.S. The calcium looping cycle for CO₂ capture from power generation, cement manufacture and hydrogen production. *Chem. Eng. Res. Des.* **2011**, *89*, 836–855. [[CrossRef](#)]
39. Erans, M.; Jeremias, M.; Zheng, L.; Yao, J.G.; Blamey, J.; Manovic, V.; Fennell, P.S.; Anthony, E.J. Pilot testing of enhanced sorbents for calcium looping with cement production. *Appl. Energy* **2018**, *225*, 392–401. [[CrossRef](#)]
40. Kuramochi, T.; Ramírez, A.; Turkenburg, W.; Faaij, A. Comparative assessment of CO₂ capture technologies for carbon-intensive industrial processes. *Prog. Energy Combust. Sci.* **2012**, *38*, 87–112. [[CrossRef](#)]



© 2020 by the authors. Licensee MDPI, Basel, Switzerland. This article is an open access article distributed under the terms and conditions of the Creative Commons Attribution (CC BY) license (<http://creativecommons.org/licenses/by/4.0/>).

Article

Comparison of the Evaporation and Condensation Heat Transfer Coefficients on the External Surface of Tubes in the Annulus of a Tube-in-Tube Heat Exchanger

Weiyou Tang ¹, David John Kukulka ^{2,*}, Wei Li ¹ and Rick Smith ³

¹ Department of Energy Engineering, Zhejiang University, Hangzhou 310027, China; tangweiyu@zju.edu.cn (W.T.); weili96@zju.edu.cn (W.L.)

² Department of Engineering Technology, State University of New York College at Buffalo, New York, NY 14222, USA

³ Vipertex Division, Rigidized Metals Corporation, Buffalo, New York, NY 14203, USA; ricksmith@rigidized.com

* Correspondence: kukulkdj@buffalostate.edu; Tel.: +1-716-8784418

Received: 22 January 2020; Accepted: 17 February 2020; Published: 20 February 2020

Abstract: An experimental study was carried out to explore the heat transfer characteristics on the outside of smooth and enhanced tubes, during evaporation and condensation of R134A in the annulus of a tube-in-tube heat exchanger. The three-dimensional enhanced surface tube consisted of primary enhancement patterns and secondary patterns; results were compared to the performance of an equivalent smooth tube. The equivalent external diameter of the inside horizontal copper tubes used in this study was 19.05 mm, while the outer tube varied in size, allowing a comparison of heat transfer for different annulus dimensions. Tests were conducted with a fixed inlet/outlet vapor quality and a constant saturation temperature for varied mass velocities in the range of 30 to 100 kg/(m²·s). For condensation, the ratio of heat transfer coefficient enhancement (enhanced tube/smooth tube) was up to 1.78; this can be attributed to the turbulence increase, as well as liquid film re-distribution, produced from the dimples. Furthermore, the condensation heat transfer coefficient increased rapidly with increasing mass flux. For flow boiling in the annulus between the 1EHT tube and outer tube, the heat transfer coefficient during boiling was 11–36% higher when compared to the smooth tube at $x_{ave} = 0.35$, while the performance of the 1EHT tube was not as good as the smooth tube at $x_{ave} = 0.5$. The heat transfer deterioration can be explained by decreased effective nucleate flow boiling heat transfer area and the flow pattern transition between a slug/wavy-stratified flow to wavy-stratified flow.

Keywords: evaporation; condensation; surface-enhanced tube; heat transfer coefficient

1. Introduction

The application of heat transfer enhancement technologies provides the potential to minimize cost, produce smaller units, and increase the reliability of heat exchangers. Enhanced tubes with passive enhancement can enhance the thermal performance while producing a small increase (when compared to a smooth tube) to pressure drop for most conditions. Therefore, widely used enhancement structures (such as micro-fin, herringbone, corrugated tubes, etc.) draw considerable attention in various industrial applications (i.e., air conditioning and refrigeration applications). According to Webb and Kim [1], three-dimensional enhanced tubes are good choices for heat transfer augmentation; three-dimensional enhanced tubes are considered here. Enhancement in these tubes is achieved by (i) increasing turbulence and surface area, (ii) producing fluid mixing and secondary flows, and

(iii) interrupting boundary layers. Additionally, when compared to traditional two-dimensional enhancement techniques, the enhanced three-dimensional tubes provide better condensate drainage effects, and an increase in nucleate site densities can also be achieved using the unique characteristic structures that make up the enhancements (i.e., dimples, grooves, etc.).

Since these three-dimensional tubes are novel, only a few investigations were carried out into various condensation and evaporation heat transfer characteristics. Additional experimental, numerical, and optimization studies need to be performed in order to better understand the thermal potential of these three-dimensional enhanced tubes. Several previous investigations were conducted into the heat transfer performance of similar dimpled tubes. Wang et al. [2] experimentally studied the heat transfer and flow properties of a dimpled tube. The results showed that the Nusselt number was enhanced (when higher compared to the equivalent smooth tube) by 26.9–75% (for ellipsoidal dimpled tubes) and 32.9–92% (spherical dimpled tubes). Ellipsoidal dimples on the inner surface can lower the laminar-to-turbulent transitional Reynolds number to a value less than 1000. Li et al. conducted numerical works [3] and geometrical optimizations [4] on the dimpled tubes, and they concluded that three-dimensional surfaces enhanced by dimples can significantly promote the thermal performance of heat exchangers; furthermore, the shape, depth, and arrangement of dimples significantly influence the thermal performance. Vicente et al. [5] investigated the heat transfer and pressure drop for low Reynolds flow in dimpled tubes. Similar experimental works were also reported by Kukulka et al. [6] to investigate the thermal performance of three-dimensional surfaces during single-phase flows. An overall parametric study and optimization was carried out recently by Lei et al. [7] based on a response surface methodology and desirability approach, while a combination of CuO/water nanofluid and dimpled tubes was investigated by Suresh et al. [8]. Therefore, additional optimization studies need to be performed in order to maximize the heat transfer efficiency. When considering two-phase flow application, limited previous investigations were found for the individual enhancement structures. Guo et al. [9] performed an experimental study that compared the convective heat transfer coefficient for a herringbone tube and a three-dimensional enhanced surface tube during condensation and evaporation of R22, R32, and R410A; they found that the herringbone tube provided a heat transfer coefficient increase of 200–300% when compared to a smooth tube during condensation; the heat transfer coefficient of the 1EHT (enhanced three-dimensional surface) tube was 1.3–1.95 times larger than that of the smooth tube. In addition, the 1EHT tube provided the best heat transfer performance during evaporation for the three working fluids. Li et al. [10] conducted experimental investigations to explore tube-side condensation and evaporation characteristics of two different 2EHT (a differently structured three-dimensional surface) enhanced tubes. Although negligible area enhancements were provided by these two enhanced tubes, the heat transfer coefficient ratio (when compared to an equivalent plain tube) was in the range of 1.1–1.43. Aroonerat and Wongwises conducted a series of experiments that were performed in order to determine the thermal performance of dimpled tubes [11], and the effect of dimple depths [12], helical angle, and dimple pitches [13] on the condensation heat transfer coefficient and pressure drop of R134a flowing in dimpled tubes. The results showed that the dimpled tube with the largest depth provided the highest heat transfer coefficient, as well as the largest pressure drop penalty (an unexpected pressure drop increase up to 892% higher than that of the smooth tube was reported). Sarmadian et al. [14] measured and analyzed the condensation heat transfer coefficient and frictional pressure drop of R600a in a helically dimpled tube. Their experimental results indicated that the heat transfer coefficients of the dimpled tube were 1.2–2 times higher than those found in an equivalent smooth tube with a pressure drop penalty ranging from 58% to 195% (when compared to smooth tubes). Their visualization showed that the dimples could accelerate the transition between annular and stratified flows. Shafaei et al. [15] performed a saturated flow boiling experiment and reported that the heat transfer performance was substantially improved because of the enhancement design. Additional enhancement structure design analyses were investigated by Ayub et al. [16], and their results show that, under similar operating conditions, the enhanced tube

with a rod insert provided a three-fold higher heat transfer coefficient than the plain tube; additionally, the corresponding pressure drop penalty was even lower for low mass fluxes.

Several experimental investigations were conducted for two-phase heat transfer performance of annular (tube in tube) flows to evaluate the enhancement characteristics of two-sided, three-dimensional, dimple tubes. Li et al. [17] performed an experimental investigation on the shell-side flow condensation of R410A on horizontal tubes, at mass fluxes values in the range from 5–50 kg/(m²·s). Their results indicated that the smooth tube exhibited superior thermal performance over other enhanced tubes (herringbone and EHT tubes); this strange trend might be attributed to the liquid inundation at the lower portion in the annular, which results from surface tension effects. Tang and Li [18] carried out an experimental study on two horizontal enhanced tubes, as well as the enhanced surfaces that were made up of dimples, protrusions, and grooves. Mass flux and vapor qualities were varied in order to explore the possible mechanisms of the enhanced surfaces; results showed that the proposed enhanced tubes seemed to show a worse thermal performance than the smooth tube for $G < 150$ kg/(m²·s), while one of the enhanced tubes provided an enhanced heat transfer coefficient ratio in the range from 1.03–1.14 for $G = 200$ kg/(m²·s). All EHT tubes employed by Tang and Li [18] and Li et al. [17] had the same outer diameter of 12.7 mm; future investigations should determine the effect of tube diameter on the heat transfer performance.

In this study, the three-dimensional enhanced (1EHT) tube and an equivalent plain tube with the same outer diameter of 19.05 mm were employed for shell-side condensation and evaporation heat transfer performance evaluation. Unlike traditional enhanced tubes such as micro-fin tubes, herringbone tubes, and typical dimpled tubes (as discussed in Aroonarat and Wongwises [19]), the 1EHT tube has a composite enhancement structure, which is made up of helically arranged dimples and petal arrays. The special surface structure of the 1EHT tube is shown in Figure 1. Dorao and Fernandino [20] suggested that the improvement in enhanced surfaces is connected to the improvement observed in the single-phase flow. The same article indicated that the delta-T-dependent region is related to improved mixing at the wall. Given this theory, the primary deep dimples were designed to increase fluid turbulence, enhance fluid mixing, and produce secondary flows, while a roughness was produced from the staggered petal arrays of shallow dimples that were designed for boundary layer interruption and nucleate site argumentation. As shown in Figure 1, the primary dimples of the 1EHT tube had a height of 1.71 mm and a typical projected diameter of 4.4 mm. In addition, they were helically arranged on the external surface of tubes, with a pitch of 9.86 mm and a helical angle of 60°, and with an enhanced surface area ratio of 1.20 (internal surface area of the enhanced tube compared to that of the smooth tube). Detailed parameters of tested tubes are listed in Table 1. The objective of this study was to investigate the effect of mass flux, annulus gap, and enhancement structures on the heat transfer performance during condensation and evaporation of R134a in the annulus of a tube-in-tube heat exchanger.

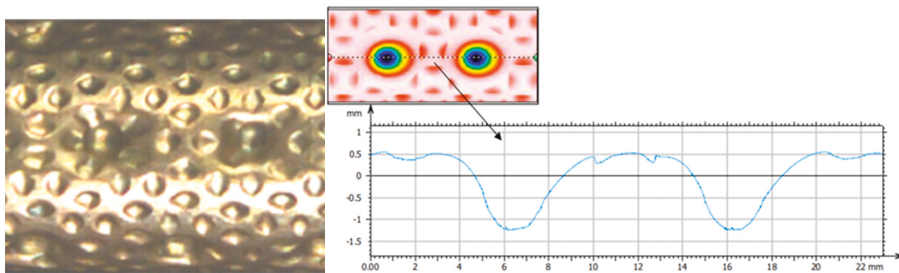


Figure 1. The external surface structure of the 1EHT tube.

Table 1. Details of the test tubes.

Tube Parameters	1EHT Tube	Smooth Tube
Internal diameter of inner tube, d_i (mm)	17.09	17.09
Outer diameter of inner tube, d_o (mm)	19.05	19.05
Average wall thickness (mm)	0.98	0.98
Height of dimple/protrusion (mm)	1.71	-
Projection diameter (mm)	4.4	-
Dimpled/protruded pitch (mm)	9.86	-
Helix angle, θ ($^\circ$)	60	-
Ratio of actual heat transfer area, A_E/A_S	1.20	1
Inside diameter of outer tube, D_i (mm)	25, 26	25, 26
Tube length, L (m)	2	2
Tube material	copper	copper
In-tube heat transfer enhancement ratio, a	1.38	-

2. Experimental Procedure

2.1. Test Apparatus

A schematic diagram of the test apparatus employed in this condensation and vaporization study is given in Figure 2a. It consisted of three fluid loops: (i) a working fluid loop containing the test section; (ii) a water circuit used for adjusting the heat input, used to regulate the vapor quality of the test section; (iii) a sub-cooled ethyl alcohol loop, used to cool the saturated two-phase refrigerant to a sub-cooled liquid at a fixed temperature.

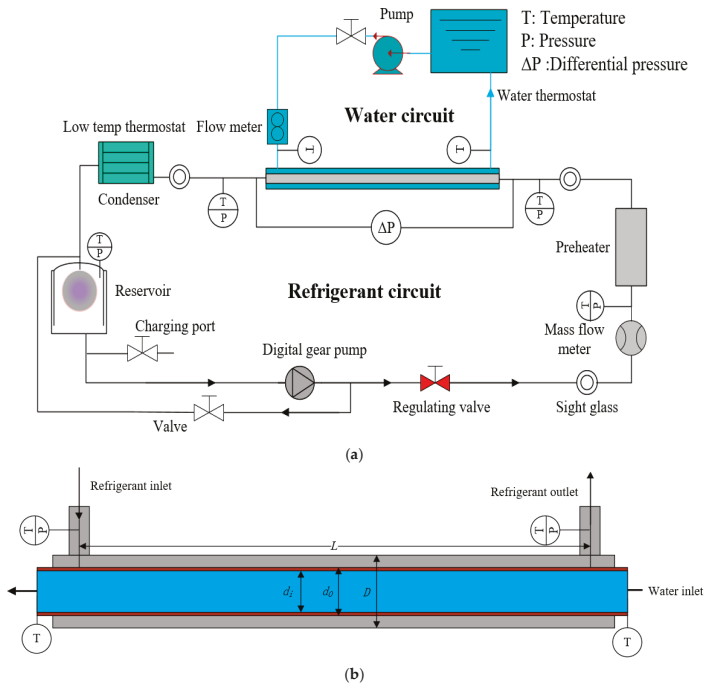


Figure 2. Schematic diagram of (a) experimental apparatus, and (b) test section.

The refrigerant loop consisted of the following components: a tube-in-tube heat exchanger (test section), condenser, reservoir, digital gear pump, flow regulator, Coriolis mass flow meter, electric

preheater, sight glasses, and valves. The test section was manufactured as a straight, horizontal counter-flow tube heat exchanger (length of 2 m). Platinum RTDs (resistance temperature detectors) were installed at the inlet and outlet of both the water side and the refrigerant side; they were able to measure the temperature with a calibrated uncertainty of ± 0.1 K. Refrigerant saturation pressure was determined by a pressure transducer (Rosemount 3051) with a range of 0–5 MPa, installed at the entrance of the test section; additionally, a differential pressure transducer was employed to measure the overall pressure drop for refrigerant flows. After leaving the test section, the refrigerant flowed into a low-temperature alcohol thermostat bath; then, the two-phase refrigerant was condensed, sub-cooled, and recirculated back into the reservoir. The sub-cooled refrigerant liquid in the reservoir was then pumped into the preheater by a gear pump; the mass flux meter (between the gear pump and the electric preheater) was utilized to ensure that the actual mass flux of the refrigerant loop was within an uncertainty of $\pm 0.2\%$ of the reading. The sub-cooled refrigerant was heated (in the preheater) by an electric heater; the electric heater was powered by a low-voltage and high-current direct current (DC) regulated power supply. The electric current varied in the range of 0–100 A with a fixed voltage of 50 V, and a maximum power of 5 kW could be supplied to heat the refrigerant in the preheater. Both the voltage and the current were collected to calculate the heating power. Therefore, the outlet vapor quality at the preheater could be controlled by the current. The enthalpy of the inlet refrigerant for the preheater was determined from the temperature and pressure, which were measured using the Platinum 100 RTD and the pressure transducer. Inlet vapor quality was calculated from the heat balance of the preheater; the electric preheater was well insulated (electrically and thermally) with a heat loss fraction lower than 5%, in order to ensure the accuracy of measurements. The water loop contained the tube side of the test section, a centrifugal pump, a thermostat bath, a magnetic flow meter, and a regulator valve. The heat input of the test section varied with the temperature of the thermostat bath and the water flow rates; in order to achieve the desired vapor quality, the refrigerant was heated or cooled in the test section. Additional details of the test apparatus can be obtained from Li et al. [21].

Figure 2b illustrates the test section employed in this work; the test section was a double-pipe heat exchanger with an effective heat length of 2 m. In this study, tubes with an inner diameter of 25 mm and 26 mm were employed as the outer tube in order to investigate the effect of annulus width; the tested tubes were used as the inner tube of the heat exchanger. In addition, the whole test section was well insulated, covered by a 40-mm-thick layer of polyurethane (thermal insulation), ensuring the accuracy of the experimental results. Before the evaporation and condensation experiments, the thermal insulation of the test section was verified using single-phase flow tests; the heat balance of the water side and refrigerant side in the test section and the preheater is given in Figure 3. The deviation in the heat balance between the water side and refrigerant side fell in an error band of $\pm 5\%$; from this analysis, it is reasonable to conclude that the test section and the preheater were well insulated.

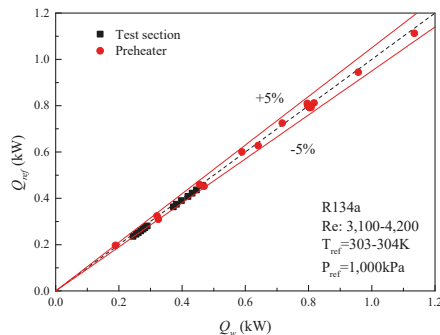


Figure 3. Heat balance measurements for single-phase flow in the smooth tube.

2.2. Test Conditions

The condensation and evaporation heat transfer characteristics of annulus flow, using R134A, were investigated. During the condensation experiments, mass velocities varied in the range of 50–120 kg/(m²·s), with a vapor quality in the range of 0.8–0.1. Heat flux increased with increasing mass velocities in order to keep a constant vapor quality variation for the test section. Mass velocities ranged from 40–80 kg/(m²·s) for the evaporation study, with the vapor quality ranging from 0.2 to 0.8. Two different annulus gaps were considered, 2.975 mm and 3.475 mm. Experimental results were sampled for a continuous period of 5 min (after the fluctuation of pressure was less than 3 kPa and the temperature variation was less than 0.1 K). A summary of the experimental conditions is given in Table 2.

Table 2. Experimental conditions.

Parameters	Range	
Refrigerant	R134A	
Experimental type	Evaporation	Condensation
Saturation temperature, T_{sat} (°C)	6	45
Refrigerant mass velocity, G (kg/m ² ·s)	30–80	50–120
Heat flux, q (kW/m ²)	9.04–15.21	9.32–19.49
Average vapor quality, x_{ave}	0.35, 0.5	0.1–0.9

3. Data Reduction and Uncertainty Analysis

3.1. Data Reduction

Experimental data were analyzed to determine the vapor quality, heat flux, and heat transfer coefficient. The overall heat transfer rate of the test section was reduced using the conservation of heat for both the water side and refrigerant side.

$$Q_w = c_{p,ts} m_{w,ts} (T_{w,ts,out} - T_{w,ts,in}) \quad a = 1, \tag{1}$$

where $c_{p,ts}$ refers to the specific heat of water taken at the average bulk temperature of the test section, $m_{w,ts}$ is the mass flow rate of tube-side water acquired by the magnetic flow meter, and $T_{w,ts,in}$ is the water temperature at the inlet and $T_{w,ts,out}$ is the water temperature at the outlet of the test section. Any heat loss in the test section was minimal because of the insulation (verified by the heat loss study). Heat flux, q , was based on the inner surface area A_i deduced from the internal diameter of the equivalent smooth tube, calculated using the following equation:

$$q = Q_w / A_o. \tag{2}$$

Inlet vapor quality (x_{in}) was determined using the energy balance of the electric preheater. Total heat measured (Q_{ph}) by the wattmeter was regarded as the heat imposed in the preheater, and it consisted of two components, sensible heat (Q_{sens}) and latent heat (Q_{lat}).

$$Q_{ph} = \lambda_{ph} \cdot VI = Q_{lat} + Q_{sens}, \tag{3}$$

$$Q_{sens} = c_{p,l,ref} m_{ref} (T_{sat} - T_{ref,ph,in}), \tag{4}$$

$$Q_{lat} = m_{ref} h_{lv} x_{in}, \tag{5}$$

$$x_{in} = \frac{\lambda \cdot VI}{m_{ref} h_{lv}} - \frac{c_{p,l,ref}}{h_{lv}} (T_{sat} - T_{ref,ph,in}), \tag{6}$$

where λ_{ph} , V , I , $c_{p,l,ref}$, m_{ref} , $T_{ref,ph,in}$, and h_{lv} refer to the heat conservation factor to account for heat loss of the preheater, electric voltage and current, specific heat of refrigerant obtained at the mean temperature of the preheater, mass flow rate, inlet temperature, and latent heat of the refrigerant, respectively. Accordingly, the vapor quality at the exit of the test section, x_{out} , was calculated as

$$x_{out} = x_{in} - Q_w / (m_{ref} h_{lv}). \tag{7}$$

Average vapor quality of the test section could be determined as

$$x_{ave} = \frac{x_{in} + x_{out}}{2}. \tag{8}$$

The logarithmic mean temperature difference between the tube side and annulus was determined from the inlet and exit temperatures of refrigerant and water.

$$LMTD = \frac{(T_{ref,ts,out} - T_{w,ts,in}) - (T_{ref,ts,in} - T_{w,ts,out})}{\ln\left[\frac{(T_{ref,ts,out} - T_{w,ts,in})}{(T_{ref,ts,in} - T_{w,ts,out})}\right]}, \tag{9}$$

where $T_{ref,ts,in}$ and $T_{ref,ts,out}$ refer to the inlet and outlet temperature of the refrigerant in the annulus, while $T_{w,ts,in}$ and $T_{w,ts,out}$ refer to the inlet and exit temperatures in the water. Assuming that there was no fouling resistance for the internal surface of the tube, the heat transfer coefficient (h_{ref}) for condensation and evaporation was deduced from the following equation:

$$h_{ref,o} = \frac{1}{A_o \left[\frac{LMTD}{Q_w} - \frac{1}{h_{w,i} A_i} - \frac{\ln(d_o/d_i)}{2\pi L k} \right]}, \tag{10}$$

where A_i and A_o refer to the tube-side and shell-side heat transfer areas, respectively, d_i and d_o are the internal and external diameters of the tested tubes, and k is the thermal conductivity of the tube wall. It is worth noting that A_i and A_o for the enhanced tubes were determined using the nominal inner and outer diameter of test tubes.

Extensive experimental investigations showed that the Gnielinski [22] correlation can accurately predict the convective heat transfer coefficients in a plain tube or annulus, and the correlation is valid in the range $3000 < Re_w < 5 \times 10^6$ and $0.5 < Pr_w < 2000$; this covers the present test conditions. Therefore, the Gnielinski [22] correlation was utilized to predict the in-tube heat transfer coefficients, h_w , for the smooth tube.

$$h_w = \frac{(f/2)(Re_w - 1000)Pr_w}{1 + 12.7(f/2)^{0.5}(Pr_w^{2/3} - 1)} \left(\frac{\mu_{bulk}}{\mu_{wall}} \right)^{0.14} \frac{k_w}{d_w}. \tag{11}$$

The ratio, $(\mu_{bulk}/\mu_{wall})^{0.14}$ accounts for the influence of viscosity at the water bulk and the internal wall temperature; thermal conductivity (k_w) values were determined at the mean temperature of the water. Fanning friction factor, f , was predicted by the Petukhov correlation [23] for plain tubes, which is applicable for $3000 < Re_w < 5 \times 10^6$, and is given by

$$f = (1.58 \ln Re_w - 3.28)^{-2}. \tag{12}$$

However, the above predictive procedures were inappropriate to use with the 1EHT tube since the inner surface of 1EHT tube was modified with enhancement patterns. Therefore, Wilson plot tests were used to calculate the water-side heat transfer coefficients h_w . The overall thermal resistance of the test section for the 1EHT tube was calculated as follows:

$$\frac{1}{h_{ts}} = \frac{d_o}{ah_w d_i} + \frac{1}{h_{ref}} + \frac{d_o \ln(d_o/d_i)}{2k}, \tag{13}$$

where h_{ts} refers to the total heat transfer coefficient of the test section, and a represents the in-tube heat transfer enhancement ratio (EHT tube compared to an equivalent plain tube). During the Wilson plot tests, the refrigerant mass flow rate was fixed at a relatively large value in order to minimize the experimental error; mass flow rate and the temperature of water were adjusted to obtain a linear relationship between the water-side thermal resistance and the overall resistance. The Wilson plot results for the 1EHT tube are given in Table 1.

All the thermal and transport properties of the refrigerant in the analysis were acquired from REFPROP 9.0, which was developed and released by NIST (National Institute of Standards and Technology). [24]; all the instruments including pressure transducers, Platinum 100 RTDs, and mass flow meters in the test apparatus were calibrated according to an NIST traceable standard.

3.2. Experimental Uncertainty Analysis

The measurement of the heat transfer coefficient depends on the test conditions and accuracy of the instruments. In this study, an uncertainty analysis was conducted according to the error propagation method given in Moffat [25]. Using this analysis, the relative uncertainty (U_R) of the dependent parameters could be calculated using the experimental uncertainty for the primary measurements, and it was estimated using the following equation:

$$U_R = \left[\sum_{i=1}^n \left(\frac{\partial R}{\partial X_i} U(X_i) \right)^2 \right]^{1/2} \quad (14)$$

The results are summarized in Table 3 for the relative uncertainties and the accuracy of various parameters. A maximum uncertainty of the heat transfer coefficient was found to be 12.12% for this study.

3.3. Experimental Validation

Single-phase heat transfer experiments were conducted for the validation of test procedures. Figure 4 depicts the relationship between the heat transfer coefficient and the Reynolds number. The single-phase experiment was conducted using R134a and R410A in the turbulent regime to validate the present test procedure. The average temperature along the test section was kept in the range of 303–304 K, and the ambient temperature was controlled at 298 K by an air-conditioner. The results were compared against the Gneilinski [22] correlation and the Dittus–Bolter correlation. All the data points could be predicted within $\pm 10\%$ by the Gneilinski [22] correlation. The EHT tube could produce a single-phase heat transfer enhancement ratio of 1.45–1.76 for the present test conditions compared to the smooth tube. In addition, a series of repetitive experiments were conducted using R410A to validate the present test procedure, and the tube-in-tube heat exchanger with $D_{it} = 6.95$ mm was employed. The same tube-in-tube heat exchanger made of the smooth tube was used for the further experiments of R134a. Two experiments were carried out on two different days for the flow boiling heat transfer performance in the annulus of the smooth tube. The inlet and the outlet vapor quality were fixed at 0.2 and 0.8, respectively. Figure 5 demonstrates a comparison of the two results, and good agreement was found between them. Therefore, it is reasonable to conclude that the results in this study have good repeatability.

Table 3. Uncertainties of measured and calculated parameters.

Measured Parameters	Accuracy
Diameter	±0.05 mm
Length	±0.5 mm
Temperature	±0.1 K
Pressure, range: 0–5000 kPa	±0.075% of full scale
Differential pressure, range: 0–50 kPa	±0.075% of full scale
Refrigerant mass flow rate, range: 0–120 kg/h	±0.2% of reading
Water mass flow rate, range: 0–600 kg/h	±0.2% of reading
Calculated Parameters	Uncertainty
Mass velocity, G (kg/m ² ·s)	±1.17%
Heat flux, q (kW/m ²)	±2.64%
Vapor quality, x	±4.12%
Heat transfer coefficient, h_{ref} (W/m ² ·K)	±12.12%

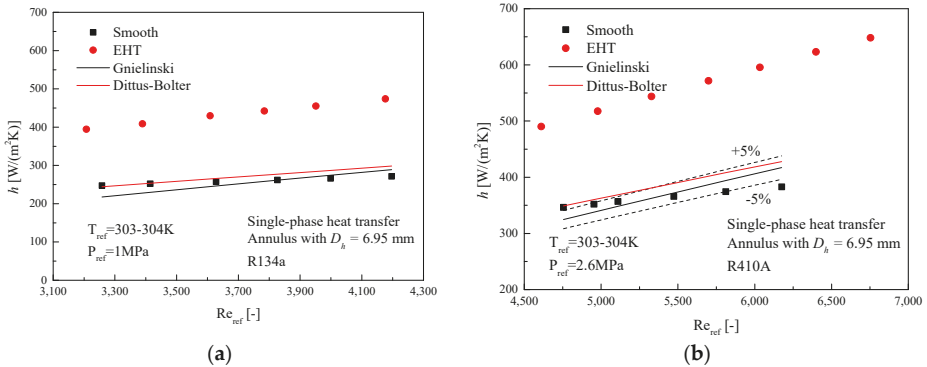


Figure 4. Variation of the single-phase heat transfer coefficient as a function of Reynolds number, and comparison against Gnielinski [22] and Dittus–Bolter correlation using work fluids: (a) R134a; (b) R410A.

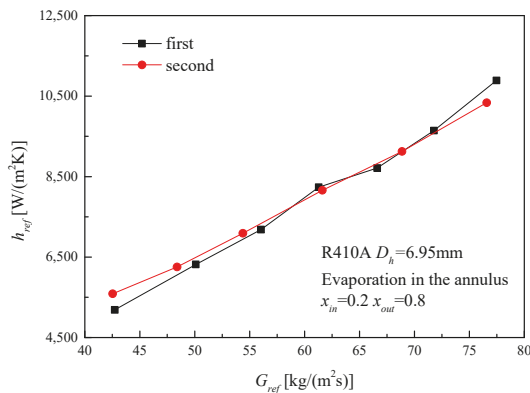


Figure 5. Repetitive experiments conducted for the flow boiling of R410A in the annulus with a hydraulic diameter of 6.95 mm.

4. Results and Discussion

4.1. Heat Transfer Characteristics of Condensation

In the condensation study, two test sections with different inner diameters of the outer tube were employed to investigate the influence of the annulus gap. The relationship of the condensation heat transfer and mass velocity is given in Figure 6a; the corresponding heat flux values are also given in Figure 6b for a comparison. These results differ from similar experimental investigations reported by Tang and Li [18] and Chen et al. [26]; the results of the present study show that the heat transfer coefficient increased with increasing mass flux, implying that the convective condensation component occupied an important role in the overall heat transfer for the present test conditions. Additionally, increased mass fluxes could also improve the interfacial shear stress and move the accumulated condensate at the bottom of the annulus to the upper part, improving the overall performance.

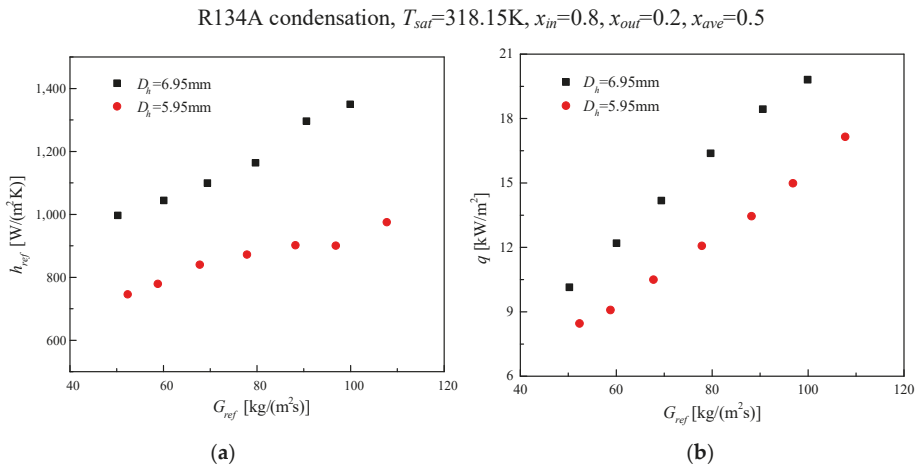


Figure 6. Variation of (a) heat transfer coefficient and (b) heat flux as a function of mass flux during condensation for a smooth tube with a different annulus spacing.

The heat transfer coefficient for the wide annulus case showed heat transfer that was approximately 33% to 50% larger than the narrow annulus case; this can be attributed to the improvement of the convective heat transfer. According to Cavallini et al. [27], the in-tube condensation flow patterns can be divided into two types: ΔT -dependent flow and ΔT -independent flow; in a horizontal tube, ΔT -dependent flow occurs when gravity is the dominant force. A similar classification can be applied to the annulus condensation cases; they all fall into the ΔT -dependent flow case due to the relatively low mass fluxes and large channel gap dimensions. For the ΔT -dependent flow case, the film condensation heat transfer component and the convective heat transfer component should be included in order to achieve an accurate prediction. Chen [28] solved the boundary layer equation for laminar film condensation of quiescent vapor on a single horizontal smooth tube; the theoretical equation for the heat transfer coefficient was given as

$$h_o = 0.728 \left[\frac{\rho_l (\rho_l - \rho_g) g h_{lv} k_l^3}{\mu_l d_o (T_{sat} - T_{wall})} \right]^{1/4}, \tag{15}$$

where the physical properties are acquired at the mean temperature between the wall and the saturation temperature of the refrigerant. Tang and Li [18] introduced a modified heat transfer equation that

could be used to predict the present data; this model added a retention angle, α , into the Chen [28] equation in order to account for the effect of vapor quality.

It should be noted that the average vapor quality along the test section was employed for the prediction of heat transfer coefficients for simplification. In addition, little difference was found between the predicted values calculated from average vapor quality and the average value in the vapor quality range. The comparison between the experimental and predicted values of Chen [28] and Tang and Li [18] correlation is illustrated in Figure 7. There was an obvious deviation between h_{exp} and h_{pre} for the Chen correlation; all these data points were overpredicted with a mean absolute deviation (MAD) of 42.5%. When using the Tang and Li [18] correlation, an acceptable prediction was given with a MAD of 7.9%; 84.6% of the data points could be predicted in an error band of $\pm 30\%$. However, neither of the above correlations could accurately predict the variation of the heat transfer coefficient versus mass flux, which would be an important contribution to the thermal performance during condensation in the annulus. Additional investigations and experimental data are demanded to explore the heat transfer mechanisms during this phenomenon.

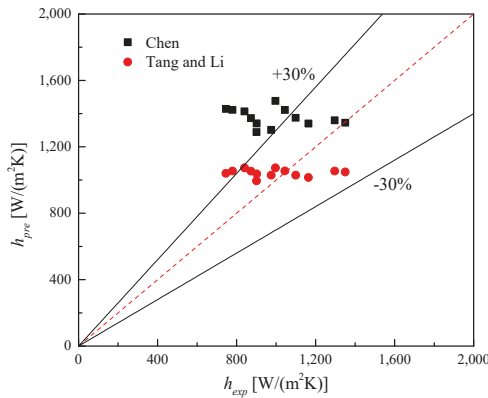


Figure 7. Prediction of Chen, and Tang and Li [18] correlation against the present data for condensation on the smooth tube.

Values of the MAD were determined as follows:

$$MAD = \frac{1}{N} \sum_1^N \frac{|h_{exp} - h_{pre}|}{h_{exp}} \times 100\%. \tag{16}$$

Figure 8a shows the variation of the heat transfer coefficient with mass flux during condensation on the outside of the 1EHT tube in the annulus; results were compared to the smooth tube. Figure 8b provides the heat flux variation for all of the test conditions. As can be seen, there was little variation between the 1EHT tube and the smooth tube; therefore, it is reasonable to compare their thermal performance under the same mass flux. It should be noted that all the results in Figure 8 were acquired for condensation in an annulus with an outer diameter $D_i = 25$ mm, with the heat flux ranging from 8–18 kW/m². The results demonstrate that the 1EHT tube provided an enhancement to the annulus condensation heat transfer performance (when compared to a smooth tube) in the range of 98–178%. According to Chen et al. [28], the superior performance of the 1EHT tube for condensation in an annulus was explained by the turbulence and flow pattern change caused by the enhanced surface structure. Additionally, surface tension might be a dominant contributor to the condensation heat transfer for $G_{ref} < 50$ kg/(m²·s). Tang and Li [18] concluded that increasing the mass flux in the annulus may change the flow pattern; two possible flow patterns are given in Figure 9. Generally, the cross-sectional liquid distribution depends on the joint actions of three forces, including gravity, surface tension, and

shear stress. At low mass fluxes, the condensate would accumulate at the bottom due to gravity being dominant; as the mass flux increases, shear stress begins to have a greater influence. In addition, the specific structures of the external tube surface can augment the convective heat transfer and begin to produce more turbulence, fluid mixing enhancement, boundary layer disruption, and creation of secondary flows.

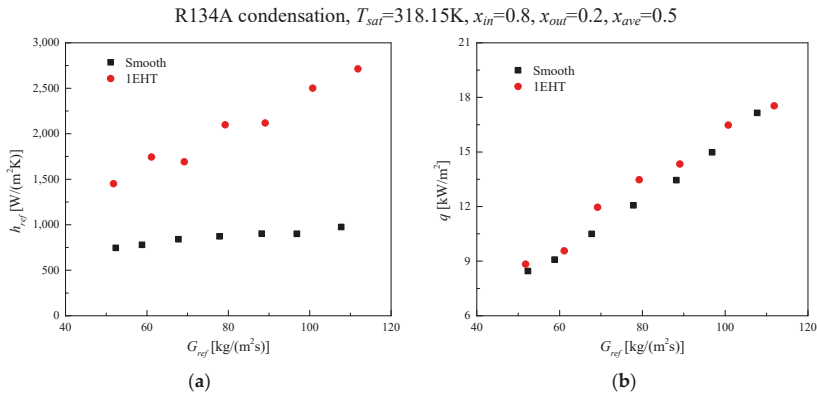


Figure 8. Variation of (a) heat transfer coefficient and (b) heat flux as a function of mass flux during condensation on the 1EHT tube in the annulus with $D_i = 5.95$ mm compared to a smooth tube.

The effect of vapor quality on the condensation characteristics in the annulus was also investigated at fixed mass velocities $G_{ref} = 80$ kg/(m²·s) and $G_{ref} = 100$ kg/(m²·s); results are given in Figure 10a. The results indicate that the heat transfer coefficient increased rapidly with increasing vapor quality, especially for the vapor quality $x_{ave} < 0.6$, and the thermal performance of the 1EHT tube at $G_{ref} = 80$ kg/(m²·s) was slightly worse than that at $G_{ref} = 100$ kg/(m²·s). The steep slope for the heat transfer coefficient versus vapor quality resulted from the increasing cross-sectional void fraction; the condensate redistributed circumferentially and produced a decrease in the average film thickness on the tube. Figure 10b shows that the heat flux was fixed in a narrow range of 3–5 kW/m². Heat transfer coefficients at $x_{ave} = 0.5$ were nearly two times higher than those data points in Figure 8a at the same mass flux. This could have been caused by the increased film thermal resistance on the external surface of 1EHT tube with the increased heat flux. The negative relationship between heat transfer coefficient and heat flux seems to have a steeper slope than predicted in the Chen et al. [28] and Tang and Li [18] correlation. The steeper slope may be attributed to the increasing condensate on the tube, and the severely flooded dimples on the surface with increasing heat flux. Generally, gravity causes the condensate on the surface to flow down the tube and accumulate at the bottom of the annulus; however, increased heat flux and dimples may increase the film thickness and degrade the thermal performance.

4.2. Heat Transfer Characteristics of Evaporation

As shown in Figure 11a, the heat transfer coefficient for evaporation of R134A in the annulus, using the smaller outer tube (inside diameter $D_i = 25$ mm), increased gradually as the mass flux increased. Different vapor quality ranges were employed for the evaporation experiments, and the average vapor quality was kept at 0.35 and 0.5. Little differences were found between the two series of results; the deviation fell within the range of experimental uncertainties. Generally speaking, the flow boiling heat transfer can be divided into two parts: (i) convective boiling and (ii) nucleate boiling heat transfer; nucleate boiling heat transfer increases with increasing heat fluxes (as detailed in Cooper [29]). For in-tube flow boiling in this study, the targeted mass velocity fell in (i) the stratified flow regimes at higher vapor qualities, and (ii) slug flow at lower vapor qualities. For relatively high

vapor qualities, gravity dominates the liquid distribution; this results in a thin liquid film or even only a gas phase on the upper part of the annulus, which decreases the effective flow boiling heat transfer area and causes heat transfer deterioration. Slug flow might exist at low vapor qualities; the transitional vapor quality between the two flow patterns is similar to the intermittent annular flow described by Wojtan et al. [30], and x_{T-A} was determined to be 0.32. The heat transfer coefficient would drop rapidly near the transitional vapor quality due to the flow pattern change. Experiments were also conducted to explore the influence of vapor quality and heat flux on the flow boiling heat transfer coefficient with an annular hydraulic diameter of $D_h = 5.95$ mm. The results were obtained by keeping the vapor quality of the test section in the ranges of 0.2–0.8 and 0.1–0.8. As shown in Figure 11b, the heat transfer coefficients for $x_{ave} = 0.5$ were slightly higher than those for $x_{ave} = 0.45$. The effect of annulus width was also investigated under similar test conditions, with a fixed average vapor quality for the test section of 0.5. The heat transfer coefficient for the narrower annulus gap seems to be a little higher than that of the wider annulus gap; little difference was found, indicating that the annulus width may be less important for flow boiling heat transfer performance than for condensation heat transfer, due to the dominance of nucleate boiling for the test conditions.

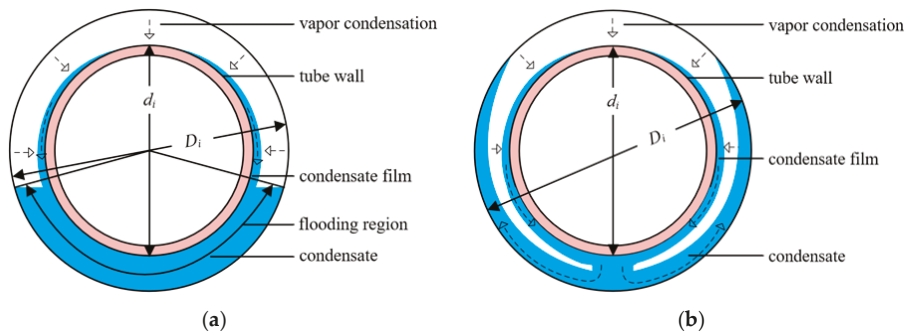


Figure 9. Schematic diagram of the possible flow pattern during condensation in the annulus for (a) low mass flux rates, and (b) large mass flux rates [18].

R134A condensation, $T_{sat}=318.15\text{K}$, $x_{ave}=0.2\text{-}0.8$

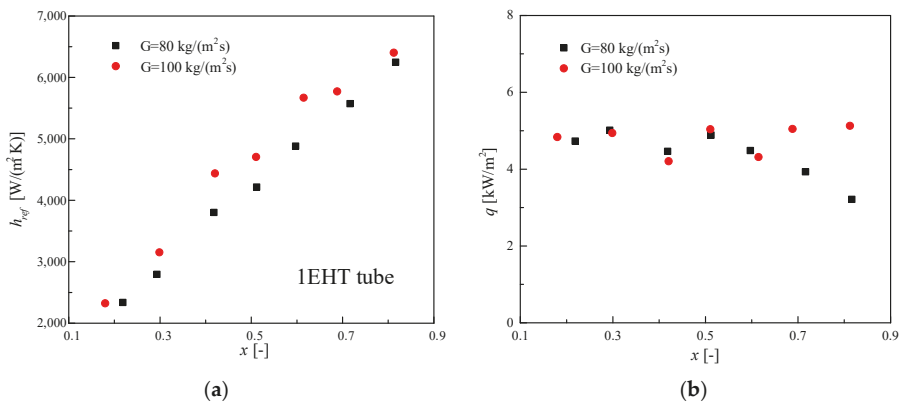


Figure 10. Variation of (a) heat transfer coefficient and (b) heat flux as a function of vapor quality for $G_{ref} = 80$ kg/(m²·s) and $G_{ref} = 100$ kg/(m²·s) with $D_h = 5.95$ mm.

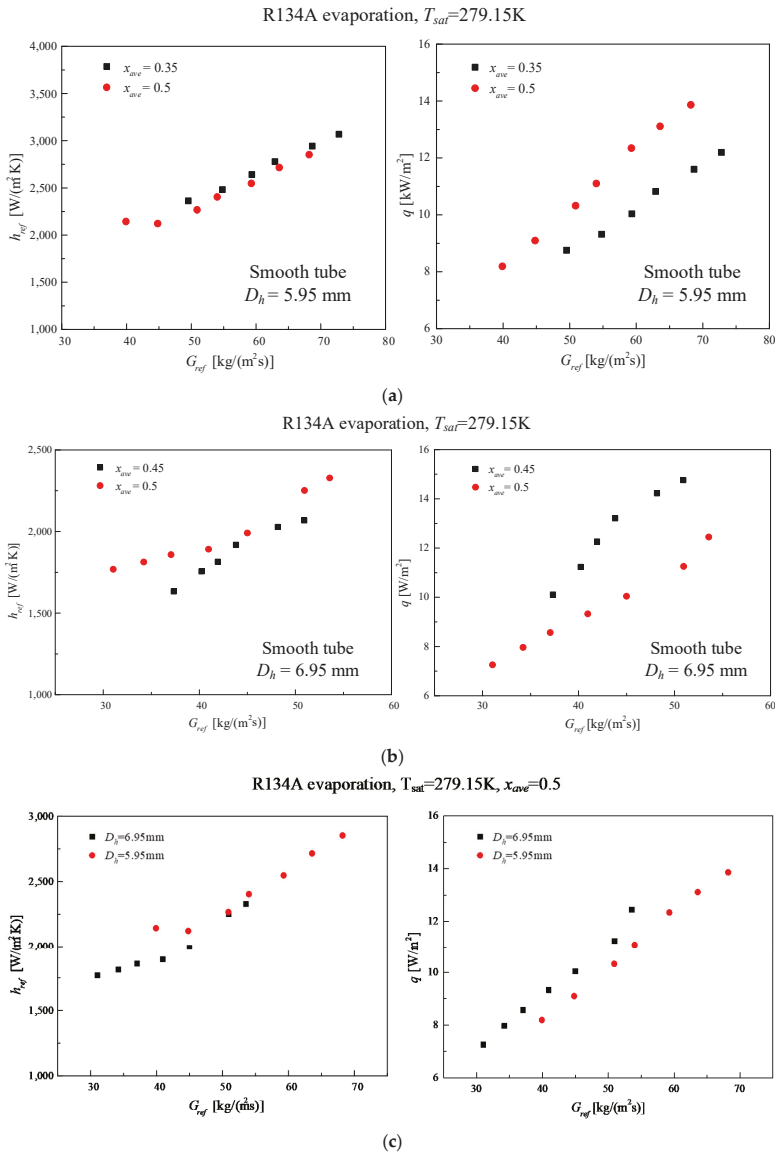


Figure 11. Variation of heat transfer coefficient and heat flux as a function of mass flux for (a) a hydraulic diameter, $D_h = 5.95$ mm with average vapor qualities of 0.35 and 0.5, (b) a hydraulic diameter, $D_h = 6.95$ mm with average vapor qualities of 0.45 and 0.5, and (c) hydraulic diameters, $D_h = 5.95$ mm and 6.95 mm.

The effect of mass velocities on the heat transfer performance was investigated with fixed average vapor qualities of 0.35 and 0.5; results are given in Figure 12. Figure 12a shows the heat transfer coefficient during flow boiling in the annulus of the 1EHT tube for $x_{ave} = 0.35$ (see Figure 12a); the heat transfer coefficient was enhanced by 11–36% when compared to the smooth tube. The heat transfer coefficient of the 1EHT tube increased with increasing mass velocities and heat flux. For $x_{ave} = 0.5$

(see Figure 12b), the performance of the 1EHT tube was not as good as the smooth tube at the tested mass velocities. The strange heat transfer performance of the 1EHT tube can be attributed to the enhanced external surface structure which consisted of depression and micro-pit arrays. The depression increases flow turbulence and enhances fluid mixing for single-phase flow; it would be reasonable to conclude that the droplet entrainment and interfacial phase mixing can be greatly enhanced by the depression. At a relatively high vapor quality, the liquid phase on the upper part of the annulus would accumulate in the large cavities; this would result in decreased film thickness for other parts of the surface without cavities. As mentioned previously, the stratified flow in the annulus may be less than the heat transfer performance of the upper part, with an accumulation of liquid phase in the large cavities. This may decrease the effective flow boiling heat transfer area for flow boiling, since nucleate flow boiling occurs only on the interface between the wall and liquid phase. A similar in-tube experimental investigation was conducted by Chen et al. [31], with their results indicating that the heat transfer coefficient decreased with increasing vapor qualities, especially when the vapor quality exceeded the transitional vapor quality between stratified-wavy flow and slug/stratified flow; the transitional vapor quality for the enhanced tubes was higher than that for the smooth tube. Similarly, the flow patterns in this study may change from slug/stratified flow to stratified-wavy flow for $x_{ave} = 0.35$ and $x_{ave} = 0.5$; the heat transfer performance can be seen to deteriorate. More experimental investigations are demanded to explore the complex interaction between enhanced structures, liquid distribution, and the flow pattern transition during flow boiling in the annulus.

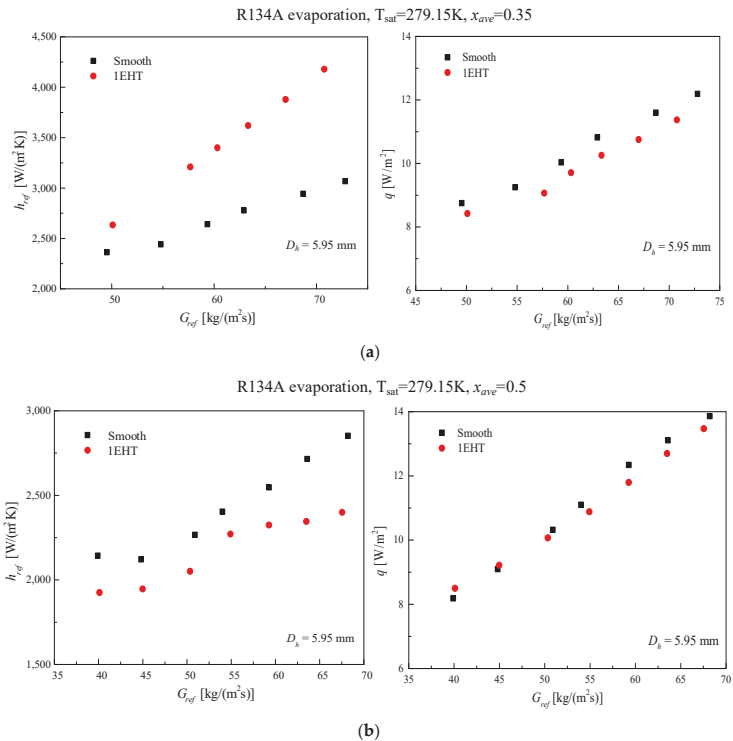


Figure 12. Variation of heat transfer coefficient and heat flux as a function of mass flux for the smooth and 1EHT tubes at (a) $x_{ave} = 0.35$, and (b) $x_{ave} = 0.5$.

5. Conclusions

An experimental investigation of the heat transfer characteristics during flow boiling and condensation of R134A in the annulus of the 1EHT tube and an equivalent smooth tube was carried out. The experiments were conducted at a constant saturation temperature of 318.15 K, and the effects of mass velocities, annulus width (gap), and vapor quality on the heat transfer coefficients were investigated and discussed. Several conclusions can be drawn, as outlined below.

1. The heat transfer coefficient increased with increasing mass velocities for both the smooth tube and the 1EHT tube. For condensation in the annulus of the smooth tube, the heat transfer coefficient in the wider annulus gap could achieve approximately 33% to 50% higher values than those found in the narrow gap; a reasonable prediction for a smooth tube was given by Tang and Li [18] correlation, with 84.6% of the data points falling in an error band of $\pm 30\%$.
2. In considering condensation in the annulus of the 1EHT tube, the 1EHT tube could greatly enhance the condensation heat transfer performance in an annulus compared to a smooth tube, and heat transfer enhancement in the range of 98–178% was seen. Furthermore, the heat transfer coefficient seemed to increase rapidly with increasing mass velocities due to the re-distribution of condensate along the circumference and the decreased liquid film thickness on the tube.
3. For flow boiling in the annulus of the smooth tube, the heat transfer coefficient for evaporation of R134A in the smaller annulus gap (for $D_h = 5.95$ mm) increased gradually with increasing mass flux; little difference was found between the heat performance of $x_{ave} = 0.35$ and $x_{ave} = 0.5$, with the latter being a little lower than the former.
4. For flow boiling in the annulus of the 1EHT tube, the heat transfer coefficient during flow boiling was enhanced by 11–36% compared to the smooth tube at $x_{ave} = 0.35$; however, the heat transfer performance of the 1EHT tube was smaller than that of the smooth tube at $x_{ave} = 0.5$. The heat transfer deterioration can be explained by a decrease in the effective nucleate flow boiling heat transfer area. This takes place because the flooded dimples are at a relatively high vapor quality, and a flow pattern transition takes place from slug/wavy-stratified flow to wavy-stratified flow. The results indicate that the unique enhancement units in this study may be inapplicable for the enhancement of wavy-stratified flow during flow boiling.

Author Contributions: Conceptualization, W.T. and D.J.K.; methodology, W.T., and R.S.; software, W.T.; validation, W.T.; formal analysis, D.J.K.; investigation, W.T.; resources, D.J.K., and R.S.; data curation, W.T.; writing—original draft preparation, W.T.; writing—review and editing, D.J.K., and W.L.; visualization, W.T.; supervision, D.J.K., R.S. and W.L.; project administration, D.J.K., and W.L.; funding acquisition, D.J.K., R.S. and W.L. All authors have read and agreed to the published version of the manuscript.

Funding: This work was supported by the National Science Foundation of Zhejiang Province (LY19E060004).

Conflicts of Interest: The authors declare no conflicts of interest.

Nomenclature

A_a	actual heat transfer area, m^2
A_i	inner surface area of test tube, m^2
A_o	outer surface area of test tube, m^2
c_p	specific heat, $J/(kg \cdot K)$
d_i	inner diameter of test tube, m
d_o	outer diameter of test tube, m
D_i	external diameter of annulus, m
D_h	hydraulic diameter of annulus, m
f	Fanning friction factor
g	gravitational acceleration, m/s^2
G	mass flux, $kg/(m^2 \cdot s)$

h	heat transfer coefficient, W/(m ² ·K)
h_{lv}	latent heat of vaporization, J/kg
I	electric current, A
k	thermal conductivity, W/(m·K)
L	tube length, m
LMTD	logarithmic mean temperature, K
m	mass flow rate, kg/s
MAD	mean absolute deviation
N	number of points
Pr	Prandtl number
Q	heat transfer amount, W
q	heat flux, W/m ²
Re	Reynolds number
T	temperature, K
U	relative uncertainty
V	electric voltage, V
x	vapor quality
<i>Greek symbols</i>	
μ	dynamic viscosity, Pa·s
θ	angle, °
ρ	density, kg/m ³
ε	void fraction
δ	liquid film thickness, m
λ_{ph}	heat balance factor of the preheater
<i>Subscripts</i>	
<i>ave</i>	average
<i>cal</i>	calculation
<i>dry</i>	dry-out
<i>e</i>	enhanced
<i>exp</i>	experimental
<i>i</i>	inner
<i>in</i>	inlet
<i>l</i>	liquid phase
<i>lat</i>	latent heat
<i>o</i>	outer
<i>out</i>	outlet
<i>ph</i>	preheating section
<i>pre</i>	predicted
<i>ref</i>	refrigerant
<i>s</i>	smooth
<i>sat</i>	saturated
<i>sens</i>	sensible heat
<i>tp</i>	two-phase
<i>ts</i>	test section
<i>v</i>	vapor phase
<i>wall</i>	tube wall

References

1. Webb, R.L.; Kim, N.-H. *Principles of Enhanced Heat Transfer*, 2nd ed.; Taylor & Francis: Abingdon, UK, 2005.
2. Wang, Y.; He, Y.-L.; Lei, Y.-G.; Zhang, J. Heat transfer and hydrodynamics analysis of a novel dimpled tube. *Exp. Fluid Sci.* **2010**, *34*, 1273–1281. [[CrossRef](#)]
3. Li, M.; Khan, T.S.; Al-Hajri, E.; Ayub, Z.H. Single phase heat transfer and pressure drop analysis of a dimpled enhanced tube. *Appl. Eng.* **2016**, *101*, 38–46. [[CrossRef](#)]

4. Li, M.; Khan, T.S.; Al Hajri, E.; Ayub, Z.H. Geometric optimization for thermal–hydraulic performance of dimpled enhanced tubes for single phase flow. *Appl. Eng.* **2016**, *103*, 639–650. [[CrossRef](#)]
5. Vicente, P.G.; García, A.; Viedma, A. Heat transfer and pressure drop for low Reynolds turbulent flow in helically dimpled tubes. *Int. J. Heat Mass Transf.* **2002**, *45*, 543–553. [[CrossRef](#)]
6. Kukulka, D.J.; Smith, R. Thermal-hydraulic performance of Vipertex 1EHT enhanced heat transfer tubes. *Appl. Eng.* **2013**, *61*, 60–66. [[CrossRef](#)]
7. Lei, X.-S.; Shuang, J.-J.; Yang, P.; Liu, Y.-W. Parametric study and optimization of dimpled tubes based on Response Surface Methodology and desirability approach. *Int. J. Heat Mass Tran.* **2019**, *142*, 118453. [[CrossRef](#)]
8. Suresh, S.; Chandrasekar, M.; Chandra Sekhar, S. Experimental studies on heat transfer and friction factor characteristics of CuO/water nanofluid under turbulent flow in a helically dimpled tube. *Exp. Fluid Sci.* **2011**, *35*, 542–549. [[CrossRef](#)]
9. Guo, S.P.; Wu, Z.; Li, W.; Kukulka, D.; Sunden, B.; Zhou, X.P.; Wei, J.J.; Simon, T. Condensation and evaporation heat transfer characteristics in horizontal smooth, herringbone and enhanced surface EHT tubes. *Int. J. Heat Mass Transf.* **2015**, *85*, 281–291. [[CrossRef](#)]
10. Li, W.; Chen, J.; Zhu, H.; Kukulka, D.J.; Minkowycz, W.J. Experimental study on condensation and evaporation flow inside horizontal three dimensional enhanced tubes. *Int. Commun. Heat Mass* **2017**, *80*, 30–40. [[CrossRef](#)]
11. Aroonrat, K.; Wongwises, S. Experimental study on two-phase condensation heat transfer and pressure drop of R-134a flowing in a dimpled tube. *Int. J. Heat Mass Transf.* **2017**, *106*, 437–448. [[CrossRef](#)]
12. Aroonrat, K.; Wongwises, S. Experimental investigation of condensation heat transfer and pressure drop of R-134a flowing inside dimpled tubes with different dimpled depths. *Int. J. Heat Mass Transf.* **2019**, *128*, 783–793. [[CrossRef](#)]
13. Aroonrat, K.; Wongwises, S. Condensation heat transfer and pressure drop characteristics of R-134a flowing through dimpled tubes with different helical and dimpled pitches. *Int. J. Heat Mass Transf.* **2018**, *121*, 620–631. [[CrossRef](#)]
14. Sarmadian, A.; Shafae, M.; Mashouf, H.; Mohseni, S.G. Condensation heat transfer and pressure drop characteristics of R-600a in horizontal smooth and helically dimpled tubes. *Exp. Fluid Sci.* **2017**, *86*, 54–62. [[CrossRef](#)]
15. Shafae, M.; Mashouf, H.; Sarmadian, A.; Mohseni, S.G. Evaporation heat transfer and pressure drop characteristics of R-600a in horizontal smooth and helically dimpled tubes. *Appl. Eng.* **2016**, *107*, 28–36. [[CrossRef](#)]
16. Ayub, Z.H.; Ayub, A.H.; Ribatski, G.; Moreira, T.A.; Khan, T.S. Two-phase pressure drop and flow boiling heat transfer in an enhanced dimpled tube with a solid round rod insert. *Int. J. Refrig.* **2017**, *75*, 1–13. [[CrossRef](#)]
17. Li, W.; Chen, X.; Chen, J.-X.; Sun, Z.-C.; Simon, T.W. Shell-Side Flow Condensation of R410A on Horizontal Tubes at Low-Mass Fluxes. *J. Heat Transf.* **2016**, *139*. [[CrossRef](#)]
18. Tang, W.; Li, W. Shell-side Condensation Characteristics of R410a on Horizontal Enhanced Tubes. *J. Heat Transf.* **2019**. [[CrossRef](#)]
19. Al-Sallami, W.; Al-Damook, A.; Thompson, H.M. A numerical investigation of the thermal-hydraulic characteristics of perforated plate fin heat sinks. *Int. J. Sci.* **2017**, *121*, 266–277. [[CrossRef](#)]
20. Dorao, C.A.; Fernandez, M. Simple and general correlation for heat transfer during flow condensation inside plain pipes. *Int. J. Heat Mass Transf.* **2018**, *122*, 290–305. [[CrossRef](#)]
21. Li, W.; Tang, W.; Chen, J.; Zhu, H.; Kukulka, D.J.; He, Y.; Sun, Z.; Du, J.; Zhang, B. Convective condensation in three enhanced tubes with different surface modifications. *Exp. Fluid Sci.* **2018**, *97*, 79–88. [[CrossRef](#)]
22. Gnielinski, V. New Equations for Heat and Mass Transfer in Turbulent Pipe and Channel Flows. *NASA Sti/Recon Tech. Rep. A* **1976**, *75*, 8–16.
23. Petukhov, B.S. Heat Transfer and Friction in Turbulent Pipe Flow with Variable Physical Properties. *Adv. Heat Transf.* **1970**, *6*, 503–564.
24. Lemmon, E.W.; Huber, M.L.; McLinden, M.O. *NIST Standard Reference Database 23: Reference Fluid Thermodynamic and Transport Properties—REFPROP, version 9.1*; Standard Reference Data Program; National Institute of Standards and Technology: Gaithersburg, MD, USA, 2010.
25. Moffat, R.J. Describing the uncertainties in experimental results. *Exp. Fluid Sci.* **1988**, *1*, 3–17. [[CrossRef](#)]

26. Chen, J.-X.; Chen, X.; He, Y.; Kukulka, D.; Li, W.; Liu, L.; Ma, L.; Smith, R.; Zhang, B. Investigation on flow condensation of refrigerant in annulus of smooth and enhanced tube-in-tube heat exchanger. *Heat Mass Transf.* **2019**, *55*, 223–234. [[CrossRef](#)]
27. Cavallini, A.; Col, D.D.; Doretti, L.; Matkovic, M.; Rossetto, L.; Zilio, C.; Censi, G. Condensation in Horizontal Smooth Tubes: A New Heat Transfer Model for Heat Exchanger Design. *Heat Transf. Eng.* **2006**, *27*, 31–38. [[CrossRef](#)]
28. Chen, J.C. Correlation for Boiling Heat Transfer to Saturated Fluids in Convective Flow. *Ind. Eng. Chem. Process Des. Dev.* **1966**, *5*, 322–329. [[CrossRef](#)]
29. Cooper, M.G. Saturation nucleate pool boiling: A simple correlation. *ICHEME Symp. Ser.* **1984**, *86*, 786. [[CrossRef](#)]
30. Wojtan, L.; Ursenbacher, T.; Thome, J.R. Investigation of flow boiling in horizontal tubes: Part I—A new diabatic two-phase flow pattern map. *Int. J. Heat Mass Tran.* **2005**, *48*, 2955–2969. [[CrossRef](#)]
31. Chen, J.; Li, W. Local flow boiling heat transfer characteristics in three-dimensional enhanced tubes. *Int. J. Heat Mass Transf.* **2018**, *121*, 1021–1032. [[CrossRef](#)]



© 2020 by the authors. Licensee MDPI, Basel, Switzerland. This article is an open access article distributed under the terms and conditions of the Creative Commons Attribution (CC BY) license (<http://creativecommons.org/licenses/by/4.0/>).

Article

Critical Analysis of Process Integration Options for Joule-Cycle and Conventional Heat Pumps

Limei Gai ^{1,*}, Petar Sabev Varbanov ¹, Timothy Gordon Walmsley ² and Jiří Jaromír Klemesš ¹

¹ Sustainable Process Integration Laboratory-SPIL, NETME Centre, Faculty of Mechanical Engineering, Brno University of Technology-VUT Brno, Technická 2896/2, 61600 Brno, Czech Republic; varbanov@fme.vutbr.cz (P.S.V.); klemes@fme.vutbr.cz (J.J.K.)

² Sustainable Energy and Water Systems Group, School of Engineering, The University of Waikato, Hamilton 3216, New Zealand; tim.walmsley@waikato.ac.nz

* Correspondence: gai@fme.vutbr.cz

Received: 27 December 2019; Accepted: 26 January 2020; Published: 3 February 2020

Abstract: To date, research on heat pumps (HP) has mainly focused on vapour compression heat pumps (VCHP), transcritical heat pumps (TCHP), absorption heat pumps, and their heat integration with processes. Few studies have considered the Joule cycle heat pump (JCHP), which raises several questions. What are the characteristics and specifics of these different heat pumps? How are they different when they integrate with the processes? For different processes, which heat pump is more appropriate? To address these questions, the performance and integration of different types of heat pumps with various processes have been studied through Pinch Methodology. The results show that different heat pumps have their own optimal application range. The new JCHP is suitable for processes in which the temperature changes of source and sink are both massive. The VCHP is more suitable for the source and sink temperatures, which are near-constant. The TCHP is more suitable for sources with small temperature changes and sinks with large temperature changes. This study develops an approach that provides guidance for the selection of heat pumps by applying Process Integration to various combinations of heat pump types and processes. It is shown that the correct choice of heat pump type for each application is of utmost importance, as the Coefficient of Performance can be improved by up to an order of magnitude. By recovering and upgrading process waste heat, heat pumps can save 15–78% of the hot utility depending on the specific process.

Keywords: Process Integration; heat pumps; Joule cycle heat pump; Pinch Analysis

1. Introduction

1.1. Background

In the 21st century, energy crises, global warming and environmental pollution are becoming more and more serious. It is urgent to improve energy efficiency, save energy and reduce emissions. One of the critical issues is to valorise low potential waste heat instead of rejecting it. Appropriate integration of heat pumps has the characteristics of efficient recovery of low-temperature heat energy, hot utility energy-saving and potentially environmental protection. Heat pumps (HP) continue to receive considerable attention and development and are becoming a critical sustainable energy technology.

Sadi Carnot [1], a French scientist in the early 19th century, first proposed the “Carnot Cycle” theory in his paper in 1824, which became the origin of HP technology. In 1912, the world’s first set of HP equipment was successfully installed in Zurich, Switzerland with river water as the low heat source for heating. HPs entered the early stage of development from the 1940s to the early 1950s. HPs used in household, and industrial buildings began to enter the market. Since the 1970s, the HP industry has advanced rapidly, and all countries have attached great importance to HP

research. Large HP development plans have been instituted by countries and organisations such as the European Community and the International Energy Agency. At present, Europe, America and Japan are competing to develop new types of HPs.

1.2. State of the Art Review

Traditional HP technologies include the vapour compression heat pump (VCHP) [2], absorption heat pump [3], and transcritical heat pump [4]. Pavlas et al. [5] developed a Process Integration methodology for an HP integrated with a biomass gasification process of a wood processing plant. Liew and Walmsley [6] adopted a Total Site targeting method to integrate open cycle VCHP for enhancing overall site energy efficiency. Walmsley [7] presented a Total Site Heat Integration (TSHI) method for integrated evaporation systems using a HP (vapour recompression) effectively with application to milk concentrating. Walmsley et al. [8] performed a Pinch Analysis of hybrid compression–absorption HP process for convective dryers by employing to simulation and optimisation tools. Stampfli et al. [9] adapted Pinch Analysis to integrating VCHP for HPs in batch processes. A hybrid method [10] that unifies the insight-based and mathematical programming approaches has been proposed for industrial HP integration in batch processes to avoid long computation times. Another criterion EPC (i.e., the coefficient of performance in exergy per total annual cost) was proposed [11] for selecting HPs, modelling diverse types of HPs for operating conditions. This criterion can both evaluate the thermodynamic and economic performances of HPs.

Urbanucci et al. [12] proposed a two-level optimisation algorithm for the high-temperature HP integration in a trigeneration system. The proposed model allowed them to analyse the HP performance for various working fluids and operating conditions. Schlosser et al. [13] developed a model for evaluation of the efficiency gains of combining HP storage and intelligent system control for integrating multiple heat sources and sinks, reporting a significant reduction in energy demand. To integrate heat-upgrading technologies in process sites, Oluleye et al. [14] developed a systems-oriented criterion for conceptual screening and selection of HPs. A Mixed Integer Linear Programming (MILP) framework has been developed [15]. The screening criterion measured the exergy degradation of technology options. However, the techniques presented in that work are only applicable to conceptual system design. Goumba et al. [16] considered the different waste heat sources and proposed the “Recov/Heat” tool, for minimising the utility demands, which makes the heat pumping task easier.

The above studies only use known models to consider the integration of VCHP and processes. Some of the older HP types used Freon as a working fluid. However, Freon is no longer used because of its negative impact on the Earth’s atmospheric ozone [17]. In addition to the improvement the Coefficient of Performance (COP) of HPs and effective utilisation of the energy input, to further improve the environmental protection, engineers are committed to the development of new working fluids and HP technologies. HP applications are also in continuous development, is widely used in air conditioning and industrial fields and playing a significant role in terms of energy-saving and environmental protection.

Another type of HP with a commercial application is the TCHP, which uses CO₂ as a working fluid. CO₂ is a natural refrigerant, commonly known under the label “R744”. It has a relatively low global warming potential (GWP) value of only 1 and does not cause damage to the ozone layer. It is non-toxic, non-flammable, low-cost and easy to obtain. At present, hot water systems with CO₂ HPs usually adopt a transcritical cycle. In the early 1990s, Lorentzen [4] proposed a transcritical CO₂ cycle based on the specific physical properties of CO₂, which significantly promoted the development of CO₂ systems in the field of refrigeration. Over the past twenty years, research institutions and enterprises in many countries around the world have done a lot of research on TCHP, which has become a research hotspot in the field of refrigeration. The exothermic process of significant temperature change (~80–100 °C) on the high-pressure side of the transcritical CO₂ system is very suitable for hot water heating. As a result, research on transcritical CO₂ HPs (TCHP) started as a hot water heater. Neksä et al. [18] built a test device for a hot water HP system. The first demonstration TCHP water heater [19] was established

for industrial use. Kim et al. [20] used a combined scroll expander–compressor unit in a two-stage compression CO₂ transcritical cycle to improve the cycle COP. Van de Bor et al. [21] compared several heat recovery technologies based on HPs and heat engines. Integration schemes with processes are not considered.

In VCHP and TCHP, the working fluid undergoes a phase change in at least one of the constituent processes, during which it absorbs or releases heat from the heat source to the heat exchanger (HX). This dependence on latent heat transfer may be a problem in some applications where average temperature variation is significant, exergy transfer efficiency is low, and COP is low. Fu and Gundersen [22] developed a HP for industrial applications based on the Joule cycle (which they called a reversed Brayton cycle). The operating parameters are investigated by thermodynamic and mathematical models, applying Pinch Analysis and Appropriate Placement rules. The provided case studies also illustrate the Heat Exchanger Network (HEN) synthesis conforming to the Heat Integration targets.

ECOP (Ecop Technologies GmbH) [23] applied a HP process based on a reverse Joule cycle (also known as Joule–Brayton or Brayton cycle) with the rotation HP implementation. Compared with the traditional HP, the Joule cycle heat pump (JCHP) features sensible heat exchange between the working fluid and process heat source/sink, which is an advantage when the process streams do not condense or evaporate or have smaller Specific Heat Capacity (CP). This provides more flexibility in accommodating process streams and achieving a higher temperature lift.

A recent work [24] has presented a system synthesis method for HP integration in the industry. The method uses a superstructure-based mathematical model, resulting in a Mixed Integer Nonlinear Programming (MINLP) formulation, achieving performance improvements over similar previous methods of up to 30%. The model considers phase-change based HPs (mainly VCHP). As is shown in this paper, the correct choice of HP type bears the significance of an order of magnitude higher than such improvements.

Many processes need heat transfer in industrial processing and power generation. Some need heating, and some need cooling or condensation. If the heat exchange network can be appropriately designed, the utility can be minimised, and the capital investment can be reduced to achieve energy saving. Pinch Analysis, pioneered by Linnhoff and Hindmarsh [25], has become a widely used method for the comprehensive design of heat exchange networks. The heat exchange network with minimum energy consumption can be obtained by optimising the heat recovery system, energy supply and process operation. Energy targeting is a powerful aid to process design and integration. Stampfli et al. [9] suggested the COP equation/curve for Process Integration with VCHP. According to the COP equation, when the condensation duty provided by the process sink is known, the evaporative duty of the HP can be obtained, and the COP curve can be drawn in Grand Composite Curve (GCC). The condensation duty can also be obtained when the process is used as a source. Gai et al. [26] extended the COP curve when the process was integrated with the JCHP. However, the COP curve for the Process Integration with a HP is derived under some assumptions or ideal conditions. Also, in the TCHP, the working fluid CO₂ is a transcritical cycle and the physical property changes substantially, so it is difficult to express the COP curve with an equation accurately.

1.3. Contributions and Novelty of This Study

A JCHP is more likely to obtain higher COP than a traditional HP under certain circumstances. However, there have been so far just a few studies on the use of JCHP and industrial processes. There is also a gap in the literature for a comparative analysis of different HP types, including the emerging JCHP. The COP equations of HP have some ideal assumptions. These results are in some deviation from the actual performance of the HP, which cannot well represent the real performance of the HP.

This study simulates and optimises the operation of the main classes of HPs in a process simulation software—Petro-SIM [27]—to get the performance of the HP, as much close to the reality as possible. These classes include the VCHP, TCHP and the JCHP.

The setting of various parameters considers possible process configurations. All COP curves and heat duties in the GCC for process and HP integration will be plotted against the actual data calculated in Petro-SIM. The choice of HP type should be performed based on the temperature–enthalpy profile of the considered industrial process for obtaining optimal performance. In this paper, the performance and application scope of three different HP systems—JCHP, VCHP, and TCHP—are discussed and compared to understand the energy-saving potential of applying the HP.

Section 2 introduces the simulation and optimisation of the considered HP types and the method of integration with the process for achieving heat recover. In Section 3, the suitability of the HP types to different temperature–enthalpy (T–H) profiles is evaluated, aiming at the minimisation of power consumption. The optimal COP of each integration case was obtained by optimising the operating parameters of the HP when given source and sink at different temperatures. In Section 4, the model is further applied to the integration of HP and different industrial process cases using Pinch Analysis, and the energy-saving potential of different types of HP is evaluated using the GCC [28].

2. Method

The main goal of heat pumping is to serve, simultaneously, part (or all) of the process heating and cooling demands, via heat upgrading from lower to higher temperatures. In Process Integration terms [28], this means taking heat from below the Pinch and returning it to the process above the Pinch. The current method has to assist engineers in the selection of the best HP type for a given process configuration. COP is the criterion indicating the quality of the solution because higher COP means serving the process at the expense of lower external energy input. The method follows the algorithm shown in Figure 1.

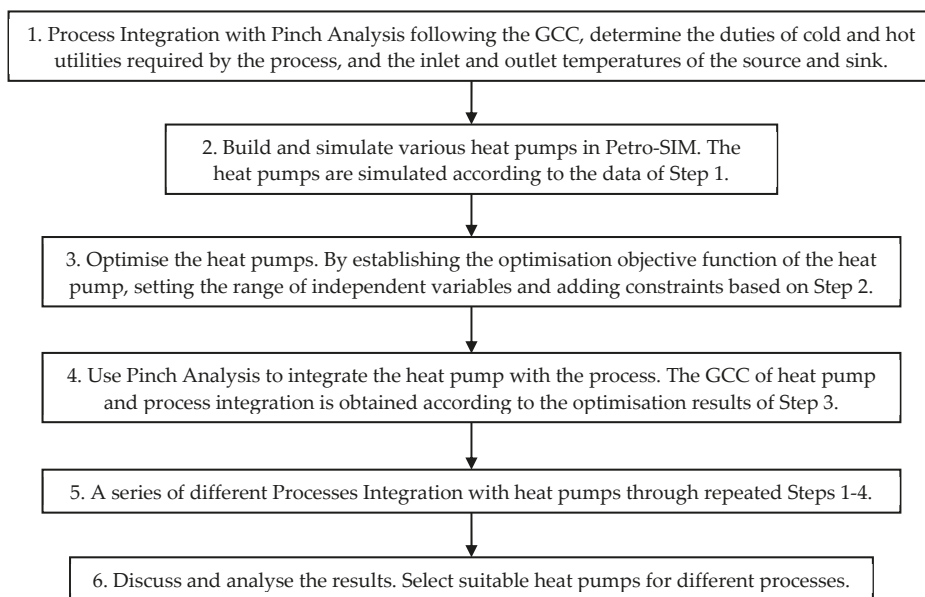


Figure 1. The method procedure.

2.1. Step 1: Process Integration with Pinch Analysis

Pinch Methodology [29] is a method to calculate thermodynamically feasible energy targets based on thermodynamic principles and analysis. The GCC [25] illustrates the difference between the heat available from hot streams and the heat required by cold streams at every temperature level, identifying

the residual heating and cooling demands of the process, to be covered by external utilities. A key property of these targets is that both loads and temperatures of the utility targets are identified. In this study, the process is firstly analysed by Pinch Analysis. The target duties of cold and hot utilities required by the process are determined, and the inlet and outlet temperatures of the heat source and heat sink for heat pumping are selected, using the GCC.

2.2. Step 2: Build and Simulate Different Heat Pumps

The HPs are simulated according to the data of the heat source and heat sink of Step 1. It takes the temperatures and the required heating or cooling duty of the process. In this work, JCHP, VCHP, and TCHP have been simulated by Petro-SIM [27], as shown in Figure 2. The use of Petro-SIM is similar to Aspen Hysys, as both are fork projects of the Hyprotech Hysys versions in the past. The main advantage of using Petro-SIM is that KBC has added dedicated modelling components for energy-related process units, such as boilers, turbines, compressors and HPs.

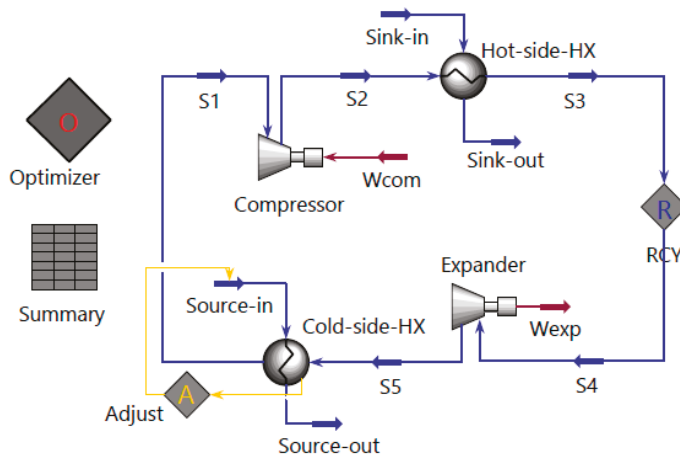
Fluid packages are based on the Peng-Robinson model [30] in combination with the Lee–Kesler Equation of State as a standard package in Petro-SIM.

Referring to the cases in Figure 2 the similarities between the three different HP cycles are as follows.

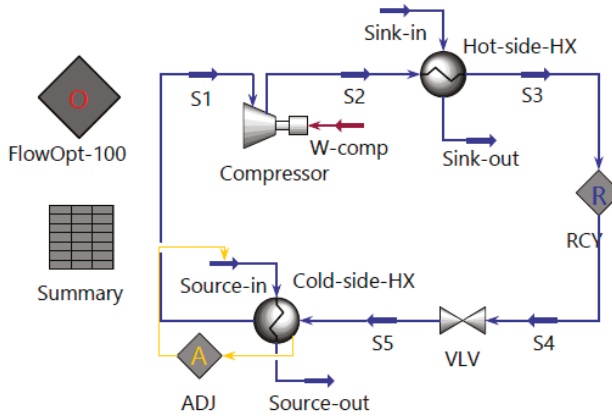
- The working fluid enters the Compressor to increase the pressure and temperature.
- The working fluid then heats the Process Heat Sink (the sink) in a heat exchanger (HX unit named “Hot-side-HX”) and is cooled down.
- Then the pressure and temperature of the working fluid are reduced through the Expander or let-down valve (VLV).
- At the next step, the working fluid absorbs heat from the Process Heat Source (the source) in a Cold-side-HX or Evaporator unit.
- The working fluid finally returns to the Compressor to complete the cycle.

A critical difference is that the working fluid of a JCHP always maintains the working fluid in a gaseous state. After being cooled by the Sink, the working fluid, generates work through the Expander in the JCHP, as shown in Figure 2a, instead of using a let-down valve as in the other two cycles. In a VCHP, the working fluid has a phase change in both heat exchangers. In the Hot-side-HX, it is condensed from a gas to a liquid phase. In the Cold-side-HX, it is heated from the liquid phase to the gas phase, as shown in Figure 2b. In a TCHP, an intermediate heat exchanger is often added, and the working fluid follows a transcritical cycle, as shown in Figure 2c.

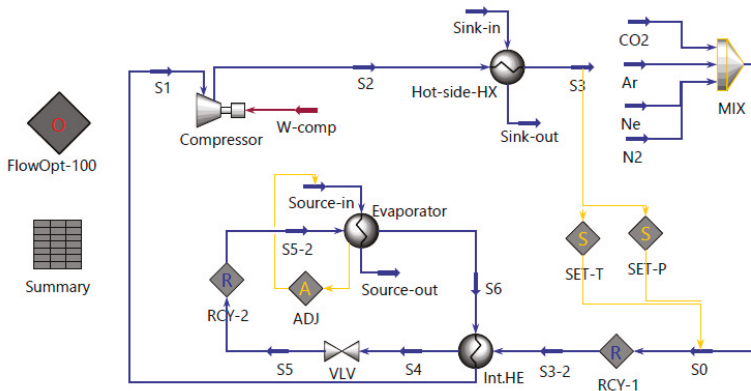
To make the simulated HP reflecting the performance of the real HP very closely, it is necessary to specify reasonable values of the device parameters in the simulation case, matching as close as possible the HP cycle and its measured indicators—mainly temperatures, pressures of the working fluid, the minimum approach temperature (ΔT_{\min}) of the heat exchangers and the isentropic efficiency of the compressor and expander. ECOP [23] has developed a special rotation HP with embedded compressor/expander that achieves high entropy efficiency for a JCHP. In this study, the JCHP model adopts the performance characteristics of that specific compressor/expander [23]. A common turbocompressor unit is used as the compressor of VCHP and TCHP, which is the most used type for industrial-scale HPs [31]. A formula for the relationship between the isentropic efficiency and compression ratio of compressors was proposed by Wang et al. [32]. It is assumed that the recoverable waste heat duty of process streams is known to recover waste heat of process in this study. This can be achieved by a “Adjust” unit (ADJ; Figure 2) to regulate the flow of the working fluid or source to fix the heat duty of the Cold-side-HX when the process stream as the source for a HP. When the process stream as the sink of a HP, this can be achieved by adjusting the flow of the working fluid or sink to fix the heat duty of the Hot-side-HX.



(a) JCHP



(b) VCHP



(c) TCHP

Figure 2. Simulation flowsheet of the heat pump as output from Petro-SIM: (a) JCHP, (b) VCHP and (c) TCHP.

2.3. Step 3: Optimise the Heat Pumps

Based on Step 2, the HP operating variables are optimised, and the optimal performance result is obtained by establishing the optimisation objective function of the HP, setting the range of independent variables and adding constraint conditions of the equation in Petro-SIM. It is necessary to optimise the HP based on the simulation to obtain its best performance. Petro-SIM has a multivariable optimiser. The optimiser can be used to optimise selected independent variables within defined ranges when a simulation converges, to minimise or maximise the objective function. The optimisation functionality of Petro-SIM can manipulate multiple process variables. It can be used for constrained optimisation expression with some flexibility, such as solving the objective function to maximise profit or minimise utility consumption. The iterative calculation method of the Optimiser in Petro-SIM is based on the IPOPT solver [27]. In this study, the HP system is optimised by adding an Optimiser unit in the Petro-SIM simulation. In the Optimiser, the independent variables, objective and constraints are defined to perform the optimisation. In this study, the optimisation independent variables were set as the outlet pressure (or temperature) of the Compressor and the outlet pressure (or temperature) of the Expander/VLV. The constraints are set as the ΔT_{\min} of the HXs. The optimisation objective function is COP of the HP. The performance of a HP is generally evaluated by the COP. The COP of a HP is defined in Equation (1) [33].

$$COP = \frac{Q_h}{W} \quad (1)$$

and

$$W = Q_h - Q_c \quad (2)$$

where: Q_h —Heat output of the heat pump, kW; W —Electrical or power consumption of the HP, kW.

The identification of the HP behaviour and best performance is performed by maximising the COP value of the HP under consideration, using the model set up in Petro-SIM [27]. The specifications of the temperatures and duties are varied within ranges expected from the considered process type, and the behaviour of the system is investigated. The procedure then provides the best HP—process configuration with the optimal values of the pressures after the compressor and the expander of the selected HP.

2.4. Step 4: Integrate the Heat Pump with the Process

At the next step, Pinch Analysis is used to integrate the HP with the process. The placement of the HP is configured following the outcomes from the previous step. When a HP is integrated with a process, the choice of a HP system depends on the operating temperature and the heat loads below and above the Pinch. In this part, the calculation results of the HPs are plotted against the GCC of the considered process, and the optimal results are linked to the GCC profiles, including the required duties and temperatures. In this way, engineers applying the method can get a better understanding of the optimal results.

The GCC of a HP and an illustrative process is shown in Figure 3. The appropriate placement of a HP means that the heat must be recovered from below the Pinch and released above the Pinch [34]. Improper placement on either side of the Pinch will result in lower energy efficiency. The figure has two lines representing each heat exchange between the HP and the process. The thick dashed lines represent the heat transfer taking place inside the HP block—absorbing and releasing heat. The thin dashed lines represent the heat exchange directly with the process. These form extra heat circuits for minimising the probability of contamination of the internal HP fluids. All other GCC figures in this paper follow the same convention.

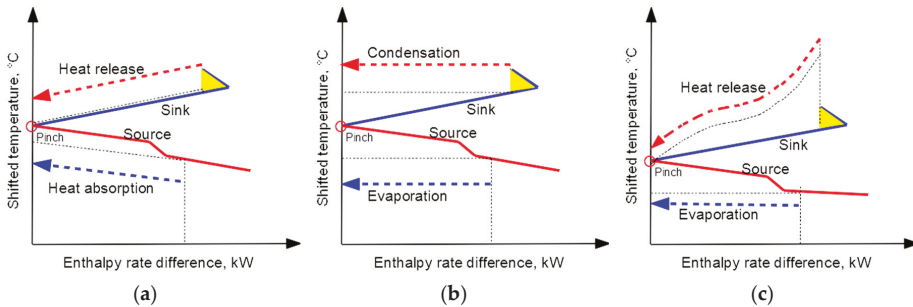


Figure 3. Grand Composite Curve (GCC) construction of a process with an integrated heat pump: (a) JCHP, (b) VCHP and (c) TCHP.

The example GCC of the JCHP is shown in Figure 3a. In the JCHP cycle, the working fluid remains in a gaseous state during the whole cycle of heat exchange with the process source and sink as well as the compression and expansion. This results in certain variations of the JCHP working fluid temperature. The heat absorption curve (blue dashed line) and heat release curve (red dashed line) are both oblique straight lines, as shown in Figure 3a. The working fluid slope of a JCHP is relatively large in GCC.

The example GCC of the VCHP is presented in Figure 3b. The working fluid of a VCHP is evaporated during heat exchange with the source and is condensed during heat exchange with the sink, so the phase transition occurs. The temperature of the working fluid of VCHP almost unchanged in exchange heat with the source or sink. The evaporation curve (blue dashed line) and condensation curve (red dashed line) are horizontal straight lines (i.e., minimal temperature change).

The GCC of the TCHP is shown in Figure 3c. The working fluid of TCHP is evaporated when the heat is absorbed from the process source. The heat release to the process sink takes place at supercritical conditions of the working fluid. This is why the working fluid temperature of TCHP remains constant during heat absorption from the source but changes significantly during the heat release to the sink. The evaporation curve (blue dashed line) is a horizontal straight line, whereas the heat release curve (red dashed line) is an oblique curve, as shown in Figure 3c.

2.5. Step 5: Evaluation of the Heat Pump Suitability to Different Process GCC Profiles

The heat duties, inlet and outlet temperatures of the heat source and sink vary among different processes. Pinch Analysis with HP placement is used, performing Steps 1–4 for a set of GCC profiles representing processes with different thermal properties. The T–H diagrams of different processes are shown in Figure 4. The configurations shown represent pairs of process heat sinks and sources of a gradual, steep and medium slope. Combinations of these are possible, but the three configurations in Figure 4 are the basic ones, which help to understand the major trends.

Each of these types of profiles implies a different degree of compatibility with the HP types considered in this work. The compatibility can be qualitatively assessed on the temperature–entropy (T–S) diagrams combining the process heat source/sink profiles with the HP profiles. Such plots are shown in Figure 5. The solid red lines represent the heat release or condensation of the working fluid in the HP, and the solid blue lines are the heat absorption or evaporation of the working fluid. The red dashed lines represent the heat release of the source, and the blue dashed lines represent the heat absorption of the sink. The performance of these three types of HPs (JCHP/VCHP/TCHP) is calculated by varying the inlet and the outlet temperatures of the process heat source and sink, and relating the results to the possible representations of temperature lifts ΔT_{in} , ΔT_{out} , or ΔT_1 , ΔT_2 (e.g., Equations (3)–(6)).

$$\Delta T_{in} = T_{sink-in} - T_{source-in} \quad (3)$$

$$\Delta T_{out} = T_{sink-out} - T_{source-out} \tag{4}$$

$$\Delta T_1 = T_{sink-in} - T_{source-out} \tag{5}$$

$$\Delta T_2 = T_{sink-out} - T_{source-in} \tag{6}$$

where: ΔT_{in} —The inlet temperature difference of the source and sink, °C; ΔT_{out} —The outlet temperature difference of the source and sink, °C; ΔT_1 —The difference between the inlet temperature of the sink and the outlet temperature of the source, °C; ΔT_2 —The difference between the outlet temperature of the sink and the inlet temperature of the source, °C.

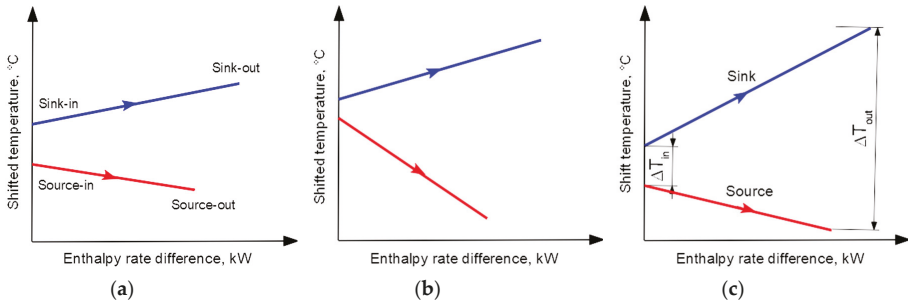


Figure 4. The T-H diagrams of different source and sink configurations for heat pump application. (a) Gradual slope; (b) Step slope; (c) Medium slope.

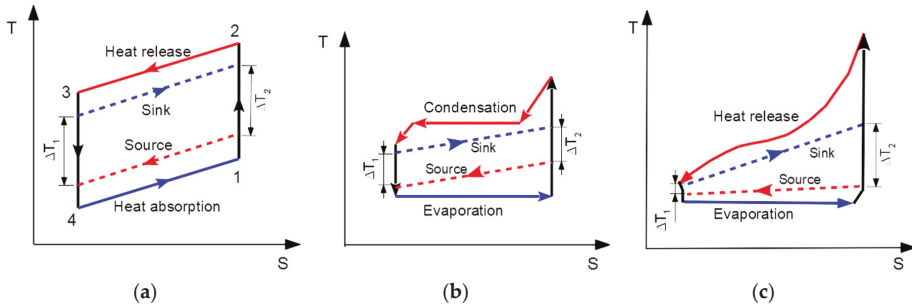


Figure 5. The ideal T-S diagram of the heat pumps (a) JCHP, (b) VCHP and (c) TCHP.

2.6. Step 6: Discuss and Analyse the Results

To select the HP suitable for each of the possible processes, the solutions obtained during Steps 1–5, provide engineers with sufficient information and understanding of why the proposed measures are appropriate and efficient. The evaluation is performed by the combined use of Pinch Analysis and Petro-SIM to simulate and optimise the HPs. The actions include constructing the GCC of the process and combining it with the plots of the considered HPs. The combined plots are then used for explaining the solutions and relating them to the process specifications—i.e., the temperatures and heating/cooling duties of the main process, plus the HP properties—i.e., working fluid and operating pressures.

3. Simulation and Optimisation of Heat Pumps

A series of simulations and optimisations were performed by changing the inlet and outlet temperatures of the source and sink to study the performance of these different HP cycles in different scenarios. The settings of parameters and variables of the HP are shown in Table 1. ΔT_{min} denotes the specifications of the minimum allowed temperature differences of the heat exchangers. The pressure

differences (ΔP) between the stream inlets and outlets of the heat exchangers in the HP are all 50 kPa. In the “Adjust” unit, the heat transfer duty of the heat exchanger Cold-side-HX is set to 10 MW by adjusting the flowrate of stream Source-in, which is the optimisation variable. The optimisation objective is to maximise the COP. Based on the simulation results, the application range of these three types of HPs is classified and can be predicted, mapping their suitability for the various process heat source and sink scenarios.

Table 1. Settings of parameters and variables.

Settings		JCHP-Ar	JCHP-CO ₂	VCHP	TCHP
Working Fluid		Argon (Ar)	CO ₂	NH ₃	CO ₂
Compressor/Expander efficiency		96%	96%	65%	65%
Variable Range	¹ P ₂ , MPa	3–8	2.5–7	1–7.5	7.5–20
	² P ₅ , MPa	0.5–5	1–4	0.2–1	2–5
constraints	ΔT_{\min} of Hot-side-HX	5–30	5–30	5–30	5–30
	ΔT_{\min} of Cold-side-HX	5–30	5–30	5–30	5–30

¹ P₂—The outlet pressure of the compressor in the HP cycle, MPa. ² P₅—The outlet pressure of the expander or expansion valve in the HP cycle, MPa.

The simulation results of the considered scenarios are shown in Figures 6 and 7. In Figure 6, the performance as a function of the temperature lifts expressed as the inlet and outlet temperature differences is evaluated. Figure 7 provides an evaluation of the COP as a function of the temperature lift expressed as ΔT_1 and ΔT_2 .

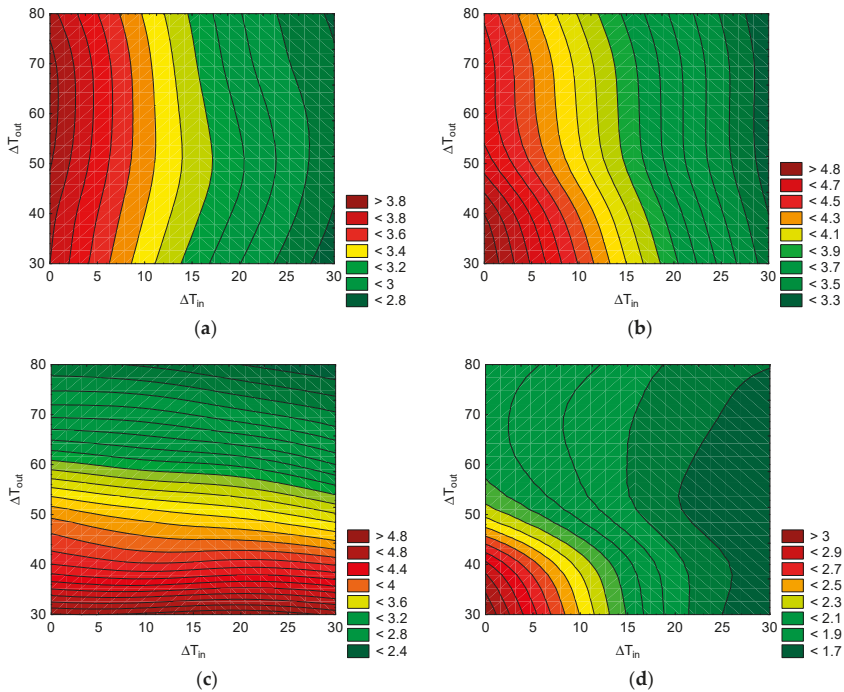


Figure 6. COP of different heat pumps varies with ΔT_{in} and ΔT_{out} : (a) JCHP-Ar, (b) JCHP-CO₂, (c) VCHP and (d) TCHP.

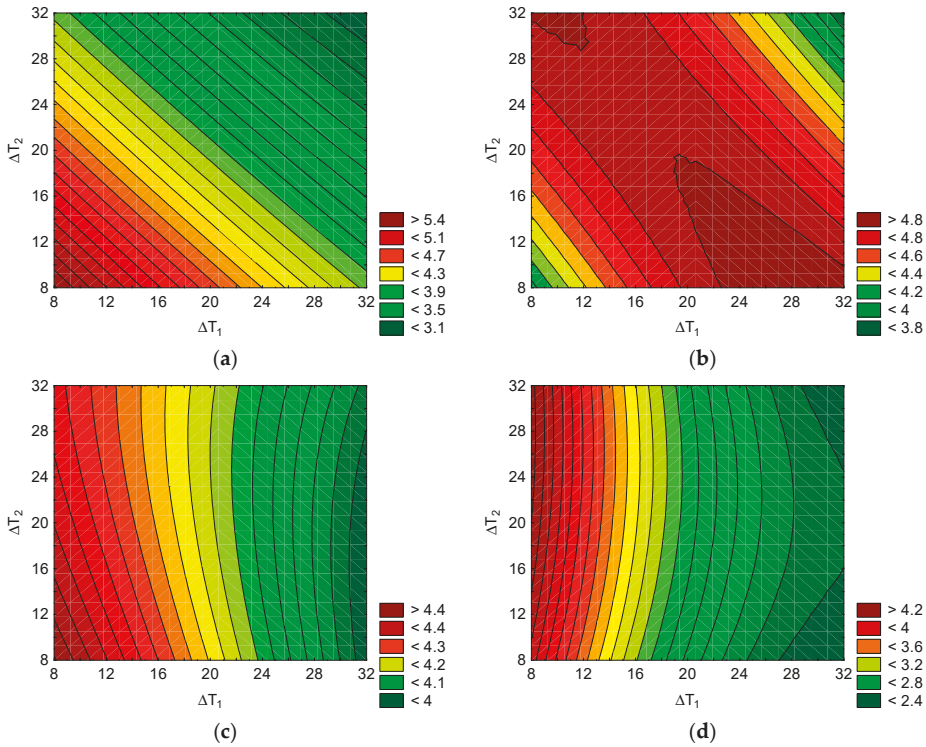


Figure 7. COP of different heat pumps varies with ΔT_1 and ΔT_2 : (a) JCHP-Ar, (b) JCHP-CO₂, (c) VCHP and (d) TCHP.

Case 1. COP modelled as a function of the temperature lift represented by ΔT_{in} and ΔT_{out}

The variation of COP of different HPs with ΔT_{in} and ΔT_{out} is shown in Figure 6. As can be seen from Figure 6a, when $0\text{ }^\circ\text{C} < \Delta T_{in} < 30\text{ }^\circ\text{C}$ and $30\text{ }^\circ\text{C} < \Delta T_{out} < 80\text{ }^\circ\text{C}$, the COP of JCHP-Ar decreased with the increase of ΔT_{in} , but did not change much with ΔT_{out} . The COP of JCHP-CO₂ decreased with the increase of ΔT_{in} but did not change much with ΔT_{out} , as Figure 6b illustrates. This indicates that, when the inlet temperature difference (ΔT_{in}) between the heat source and sink is not significant, even if the outlet temperature difference (ΔT_{out}) between the two is very large (such as ΔT_{out} increasing to $80\text{ }^\circ\text{C}$), the COP of the actual JCHP is still very high. It can be seen that the JCHP is very suitable for processes where the ΔT_{out} is massive, and ΔT_{in} is small. The smaller ΔT_{in} , the higher is the COP of JCHP.

When $0\text{ }^\circ\text{C} < \Delta T_{in} < 30\text{ }^\circ\text{C}$ and $30\text{ }^\circ\text{C} < \Delta T_{out} < 80\text{ }^\circ\text{C}$, the COP of the evaluated VCHP decreased with the increase of ΔT_{out} , but did not change much with ΔT_{in} , as can be detected from Figure 6c. Therefore, when ΔT_{out} between the source and sink is small, even if the ΔT_{in} between the two is significant (the maximum ΔT_{in} can only be equal to the ΔT_{out}), the COP of the actual VCHP is higher. The observations imply that VCHP is very suitable for processes where the temperature difference (ΔT) between the heat source and sink is not large. The smaller ΔT_{out} , the higher is the COP of VCHP.

The COP of the evaluated TCHP decreased with the increase of ΔT_{out} and ΔT_{in} when $0\text{ }^\circ\text{C} < \Delta T_{in} < 30\text{ }^\circ\text{C}$ and $30\text{ }^\circ\text{C} < \Delta T_{out} < 80\text{ }^\circ\text{C}$, as can be detected from Figure 6d. The observations imply that the application scope of TCHP is relatively narrow. TCHP is very suitable for processes where the ΔT_{in} is small and $\Delta T_{out} < 40\text{ }^\circ\text{C}$.

The variation trend of TCHP is not very regular, and the performance contours are less noticeable. This is because TCHP is a transcritical cycle, and the thermophysical properties of CO₂ in the supercritical state are nonlinear, as the substance does not behave like a gas or a liquid. This makes it necessary to model the HP behaviour also as a function of the other two temperature lift representations: ΔT_1 and ΔT_2 , by analogy with heat exchanger temperature differences and the T-S diagrams of the HP cycles.

Case 2. COP modelled as a function of the temperature lift represented as ΔT_1 and ΔT_2

The change of COP of different HPs with ΔT_{in} and ΔT_{out} is studied by fixing the outlet temperature of sink $T_{sink-out}$ to a certain level. In this study the $T_{sink-out}$ is set as 50 °C. When $T_{sink-out}$ is 50 °C, the change of COP of the different HPs with ΔT_1 and ΔT_2 is shown in Figure 7. It can be seen that the COP of JCHP-Ar decreased with the increase of ΔT_1 and ΔT_2 . The COP of JCHP-CO₂ first increased and then decreased with the increase of ΔT_1 and ΔT_2 , featuring a maximum. The COP of VCHP and TCHP decreased with the increase of ΔT_1 , but did not change much with ΔT_2 .

It can be seen from Figure 7d that when the temperature difference ΔT_1 is small, even if the temperature difference ΔT_2 is large, the COP of the TCHP is higher. The TCHP is then very suitable for a small temperature rise ΔT_1 (preferably $\Delta T_1 \leq 10$ °C) combined with a large ΔT_2 process.

In conclusion, the observations imply from Figures 6 and 7 that JCHP is very suitable for the process of steep T-H lines of the source and sink in GCC. VCHP suitable for selection when the slopes of the T-H lines of the source and sink have a relatively low gradient (closer to flat). TCHP suitable for selection when the slope of the T-H line of the source have a relatively low gradient (closer to flat) and steep T-H line of the sink in GCC.

4. Case Studies

This section analyses the integration of the different types of HPs using industrial examples to assess the practicability of the conclusion of Section 3. The optimisation objective function is the COP of the HP.

4.1. Formulation and Development: Process Integration Using JCHP, VCHP and TCHP

Four different industrial processes have been studied. The first process is a spray drying process of milk powder in a dairy factory [35], and its GCC is shown in Figure 8. The second process is also from dairy product processing [36], which uses raw milk to produce concentrated milk, pasteurised milk, cream, yoghurt and dessert. The GCC for that is shown in Figure 9. The third example is from candy processing and packaging in a candy factory [37]. The GCC is shown in Figure 10. The fourth process is a 4-column double-effect methanol distillation in a chemical plant [38]. The GCC is shown in Figure 11. The ΔT_{min} between the heat source/sink and the working fluid in the HP cycle is 5 °C. The compressors and expanders of the JCHP adopt centrifugal force rotating system structure, and their isentropic efficiency can be as high as 96%. The compressors of VCHP and TCHP are ordinary turbocompressors. In this study, isentropic efficiency is assumed to be 65%.

4.1.1. Case 1: Milk Spray Drying Process

The spray drying process of the milk powder was integrated with the HP. The stream data were only adopted the spray drying process from Atkins et al. [35], as shown in Table 2. The ΔT_{min} of the process is 20 °C.

Table 2. The stream data from a spray drying process.

Steam Name	Type	$T_s, ^\circ\text{C}$	$T_t, ^\circ\text{C}$	CP, kW/ $^\circ\text{C}$
Milk Concentrate	Cold	54	65	37.6
Dryer Inlet Air	Cold	25	200	119.2
Fluid Bed A Inlet Air	Cold	25	50	10.2
Fluid Bed B Inlet Air	Cold	25	45	14.9
Fluid Bed C Inlet Air	Cold	25	32	11.2
Air Exhaust	Hot	75	20	174.7

As can be seen from the GCC in Figure 8, the Pinch Temperature of this process is 65 $^\circ\text{C}$. The hot utility required is 17.66 MW and the cold utility required is 5.36 MW. It is assumed that all the source energy is used to heat the sink when the process is integrated with a HP. The heat duty of the heat exchanger at the source side for the HP is fixed 5.36 MW. The allowed range of the independent variables and the optimisation results of a spray dryer with an integrated HP (maximising the COP) are shown in Table 3.

Table 3. Variation settings and optimisation results of a spray drying with an integrated heat pump.

Heat Pump	Variation Ranges		Optimisation Results					
	$^1 P_2, \text{MPa}$	$^2 P_5, \text{MPa}$	COP, -	$Q_{\text{sink}}, \text{MW}$	W, MW	P_2, MPa	P_5, MPa	$^3 R, -$
JCHP-Ar	5–9	2–5	2.83	8.29	2.93	8.99	4.35	2.09
JCHP-CO ₂	4–7	1–3	2.93	8.04	2.74	6.47	1.70	3.92
VCHP	2.5–9	0.2–1	1.85	11.66	6.30	8.01	0.51	17.40
TCHP	12–20	2–5	1.77	12.11	6.83	18.65	3.03	6.27

¹ P_2 : The outlet pressure of the compressor in the HP cycle, MPa. ² P_5 : The outlet pressure of the expander or expansion valve in the HP cycle, MPa. ³ R: The compression ratio of the compressor, -.

For evaluation and interpretation, the GCC of the process integrated with different types of HPs is given, as shown in Figure 8. As can be seen from Table 3, the four HPs (JCHP-Ar, JCHP-CO₂, VCHP and TCHP) can save 47%, 46%, 66% and 69% of the hot utility by improving the waste heat quality of the process. The ranking of best COP of the HPs is JCHP-CO₂ > JCHP-Ar > VCHP > TCHP when integrating with this process. The reason can be seen in Figure 8, showing that the inlet temperature difference ΔT_{in} between source and sink is too small, while the outlet temperature difference ΔT_{out} is too large. That is, the slopes of source and sink are both steep in the GCC.

In the HP cycle, the working fluid of the JCHP does not undergo a phase change and remains in the gas phase. As a result, the ΔT between the inlet and the outlet of the working fluid in the JCHP changes significantly in the heat exchange with source or sink. The slope of the working fluid is relatively large in GCC, as shown in Figure 8a,b.

The working fluid of VCHP is evaporated during heat exchange with the source and is condensed during heat exchange with the sink, so the phase transition occurs. Therefore, in the heat exchange with the source or sink, the ΔT between the inlet and the outlet of the working fluid in the VCHP changes a little. The slope of the working fluid is small in GCC, as shown in Figure 8c. The reason for the temperature difference in the red dashed line in Figure 8c is that the working fluid becomes a superheated gas after increasing the pressure by the compressor. In the heat exchanger hot-side-HX, the working fluid is cooled to a saturated gas and then condensed to a liquid. Therefore, the red dashed line is tilted first and then becomes horizontal. However, when the working fluid is a gas that cools down from the superheated state to the saturated state, the CP is small, and the heat exchange efficiency is low. At the same time, the sink is a gas that the CP is small and the sink slope is large during the heat exchange, so the oblique part of the red dashed line is longer.

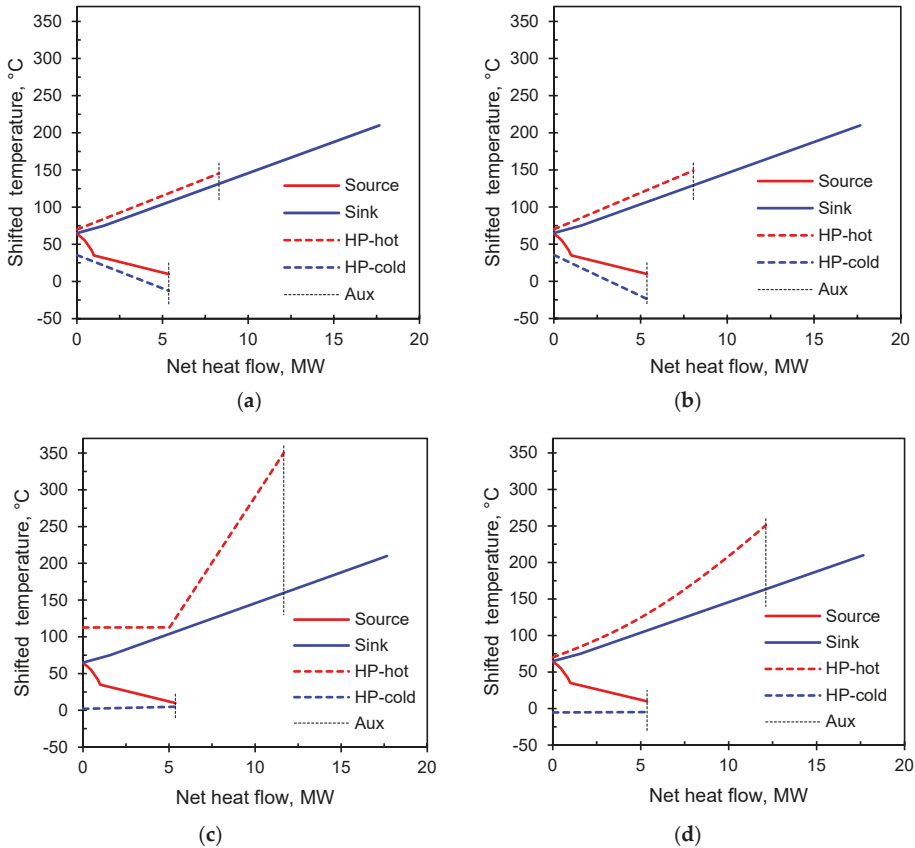


Figure 8. GCC of Case 1 and Process Integration using (a) JCHP-Ar, (b) JCHP-CO₂, (c) VCHP and (d) TCHP.

The working fluid of TCHP is evaporated during exchanging heat with the source, while is supercritical fluid during heat transfer with the sink. As the slope of the working fluid is small during the heat transfer with the source in the GCC, whereas the slope of the working fluid is significant in the heat exchange with sink in the GCC, as shown in Figure 8d. In this case, the average temperature between working fluid and source/sink in JCHP is small, so the energy loss of the heat exchangers is lower, the heat exchange efficiency is higher, and affects the COP positively. The average temperature between the working fluid and the source/sink in VCHP and TCHP is large, so the energy loss is higher, the heat exchange efficiency is smaller and affects the COP negatively. The performance of VCHP and TCHP are both weak. In addition, the compression ratio of the compressor in VCHP is 17.40 too high for a single stage. This means that multiple stages of compression would be required, resulting in a substantial increase in the cost of the compressor and a higher cost for VCHP. The outlet pressure of the compressor in TCHP is very high (18.65 MPa). This means high-pressure requirements for equipment of TCHP, with very high equipment investment costs. The economy of the VCHP and TCHP are both weak, and this process is more suitable for Heat Integration with JCHP, which is consistent with the conclusion of Section 3. It can be seen that the method proposed in this study is feasible and effective.

4.1.2. Case 2: Raw Milk Processing into Dairy Products

The stream data are taken from Wallerand et al. [36], as shown in the Appendix A (Table A1). The ΔT_{\min} of the process is 4 °C. As can be seen from the GCC in Figure 9, the Pinch Temperature of this process is 66.9 °C. The hot utility required is 2.34 MW and the cold utility required is 0.94 MW. It is assumed that the heat duty of the heat exchanger at the source side is fixed 0.71 MW. Both the process heat source and the sink undergo a phase transition. The source needs to be condensed, and the sink needs to be heated and evaporated. The pressure differences of the heat exchangers on the source side and sink sides are both set 0 kPa. The setting range of independent variables and optimisation results of HP integration into a dairy product process are shown in Table 4.

Table 4. Variable settings and optimisation results of a dairy product with an integrated heat pump.

Heat Pump	Variable Ranges		Optimisation Results					
	¹ P ₂ , MPa	² P ₅ , MPa	COP, -	Q _{sink} , MW	W, MW	P ₂ , MPa	P ₅ , MPa	³ R, -
JCHP-Ar	5–9	3–5	3.89	1.00	0.26	6.97	4.87	1.45
JCHP-CO ₂	4–8	1–4	4.52	0.92	0.20	4.37	2.56	1.74
VCHP	3.5–7	0.5–3	13.07	0.77	0.05	3.62	2.73	1.35
TCHP	14–20	2–5	1.68	1.81	1.08	17.54	3.03	5.89

¹ P₂: The outlet pressure of the compressor in the HP cycle, MPa. ² P₅: The outlet pressure of the expander or expansion valve in the HP cycle, MPa. ³ R: The compression ratio of the compressor.

The GCC of the dairy products process integrated with different types of HPs is shown in Figure 9. As can be seen from Table 4, the four HPs (JCHP-Ar, JCHP-CO₂, VCHP, and TCHP) can save 43%, 39%, 33%, and 78% of the hot utility by improving the waste heat quality of the process. The ranking of the HP COPs is VCHP > JCHP-CO₂ > JCHP-Ar > TCHP when integrating with the dairy products process.

The reason can be seen in Figure 9. The ΔT_{in} and the ΔT_{out} between the source and the sink are both too small (1.5 °C). The slopes of both the source and sink in the GCC plot are too small (flat). As the working fluid of the JCHP remains a gas across the whole HP cycle, the ΔT between the inlet and the outlet of the working fluid in the JCHP varies significantly in the heat exchange with source or sink. The slope of the working fluid is relatively large in the GCC, as shown in Figure 9a,b. As the working fluid of the VCHP is evaporated during heat exchange with the source and is condensed during heat exchange with the sink, the ΔT between inlet and outlet of the working fluid in the VCHP does not change in the heat exchange with the source or sink. The slope of the working fluid is small in the GCC, as shown in Figure 9c. The working fluid of TCHP is evaporated during exchanging heat with the source, whereas it is a supercritical fluid during the heat transfer to the sink. Therefore, the slope of the working fluid is small in the heat exchange with the source in the GCC, while the slope of the working fluid is steep in the heat exchange with sink in GCC, as shown in Figure 9d. In this case, the average temperature between the working fluid and the source/sink in VCHP is small, so the energy loss of the heat exchangers is lower, the heat exchange efficiency is higher and affects COP positively. Although the average temperature between working fluid and source/sink in JCHP and TCHP is large, so the energy loss is higher, the heat exchange efficiency is smaller, and affects negatively to the COP. The performance of JCHP and TCHP are both weak. In addition, the outlet pressure of the compressor in TCHP is too high (17.54 MPa). This means high-pressure requirements for equipment of TCHP, with very high equipment investment costs. The TCHP economy is weak. This process is more suitable for Heat Integration with VCHP, which is consistent with the conclusion of Section 3. It can be seen that the method proposed in this study is feasible and effective.

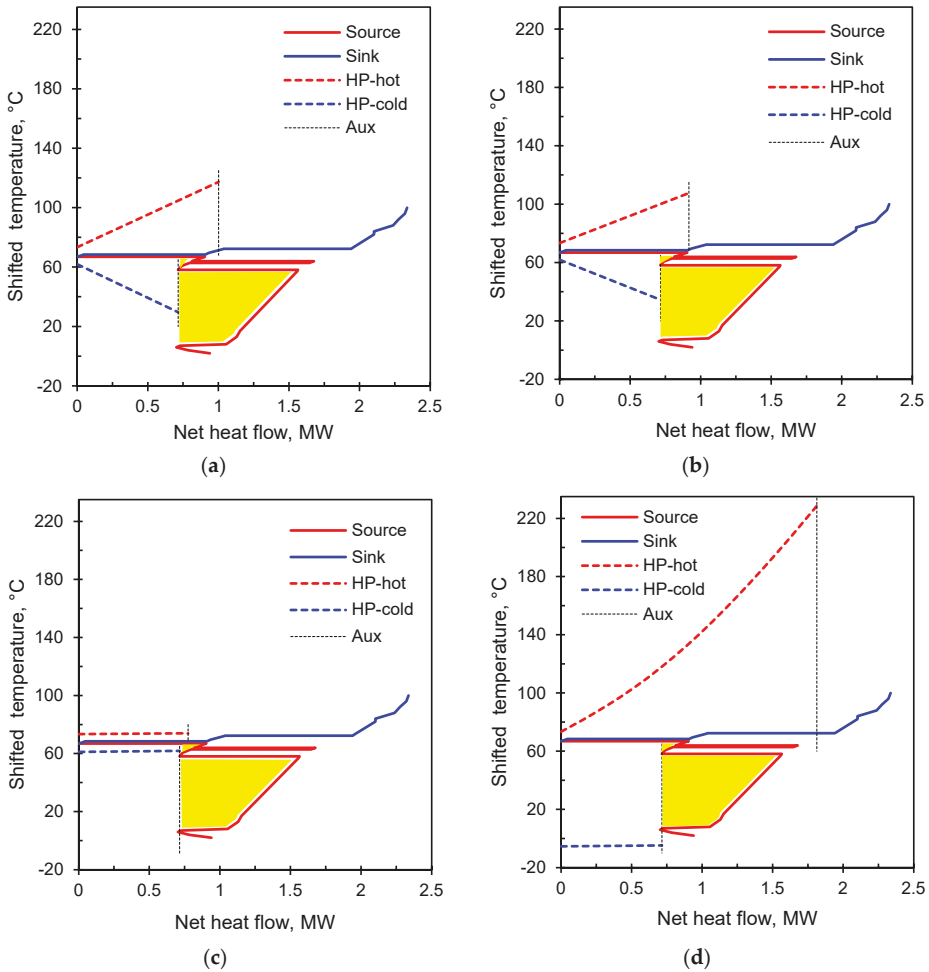


Figure 9. GCC of case 2 with integration options using (a) JCHP-Ar, (b) JCHP-CO₂, (c) VCHP and (d) TCHP.

4.1.3. Case 3: Candy Processing and Packaging

The process of candy processing and packaging was evaluated for HP integration. The stream data were taken from Miah et al. [37] and are listed in the Appendix A (Table A2). The ΔT_{min} of the process is 5 °C. As can be seen from the GCC in Figure 10, the Pinch temperature of this process is 19.5 °C. The hot utility required is 1.82 MW and the cold utility required is 0.33 MW. It is assumed that all the source energy is used to heat the sink when the process is integrated with a HP, fixing the source duty to 0.33 MW. The pressure differences of the heat exchangers on the source side and sink sides are both 50 kPa. The setting ranges of the independent optimisation variables and optimisation results of a process of candy processing and packaging integration HP are shown in Table 5.

Table 5. Variable settings and optimisation results of a process of candy processing and packaging integration heat pump.

Heat Pump	Variable Ranges		Optimisation Results					
	¹ P ₂ , MPa	² P ₅ , MPa	COP, -	Q _{sink} , MW	W, MW	P ₂ , MPa	P ₅ , MPa	³ R, -
JCHP-Ar	5–9	3–5	2.81	0.53	0.19	7.05	3.75	1.90
JCHP-CO ₂	4–7	1–4	3.55	0.46	0.13	6.13	2.65	2.36
VCHP	1.5–7	0.5–2	4.44	0.43	0.10	2.25	0.62	3.95
TCHP	9–15	2–5	1.85	0.67	0.36	10.75	3.03	3.61

¹ P₂: The outlet pressure of the compressor in the HP cycle, MPa. ² P₅: The outlet pressure of the expander or expansion valve in the HP cycle, MPa. ³ R: The compression ratio of the compressor, -.

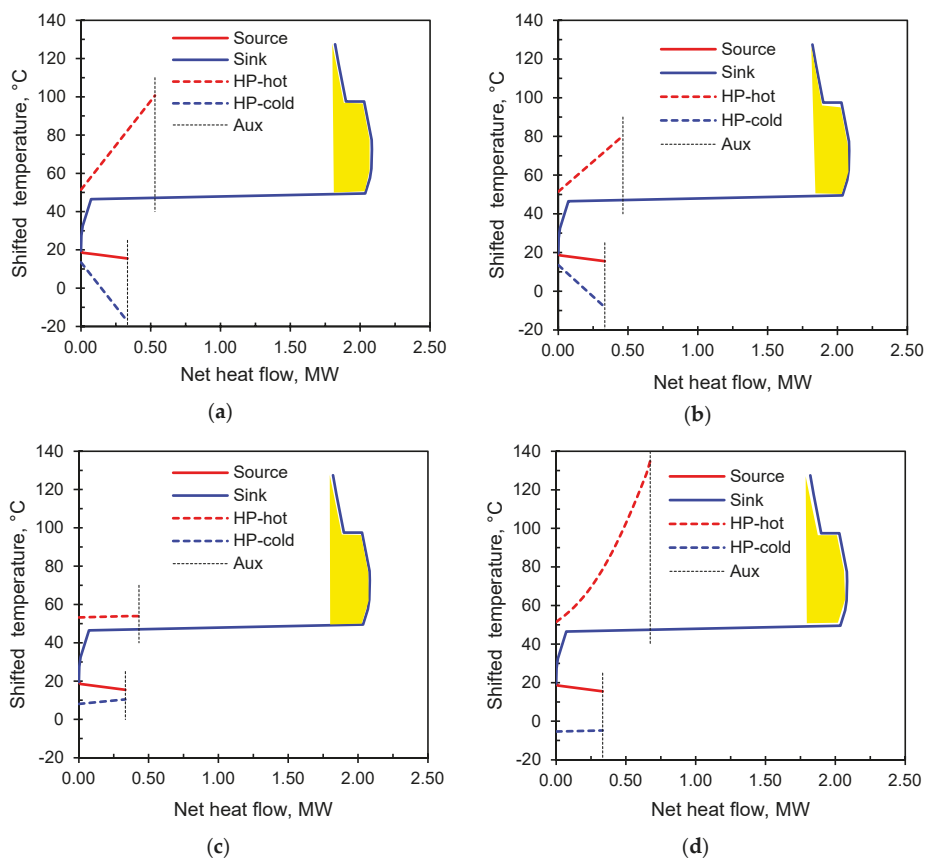


Figure 10. GCC of case 3 and integration options using (a) JCHP-Ar, (b) JCHP-CO₂, (c) VCHP and (d) TCHP.

For intuitive display of the results and analysis, the GCC of the process combined with the HPs is shown in Figure 10. As can be seen from Table 5, the four HPs (JCHP-Ar, JCHP-CO₂, VCHP and TCHP) can save 29%, 25%, 24% and 37% of the hot utility by improving the waste heat quality of the process. The ranking of the HP COPs is VCHP > JCHP-CO₂ > JCHP-Ar > TCHP when integrating with this process. The reason can be seen in Figure 10, stemming from the fact that the ΔT_{in} between the source and the sink is approximately the same as the ΔT_{out}. The slopes of source and sink are

both small in the GCC. As the working fluid of the JCHP does not undergo a phase change remaining gas, the ΔT between inlet and outlet of the working fluid in JCHP changes significantly in the heat exchange with both the source and the sink. The slope of the working fluid is relatively large in the GCC (Figure 10a,b). Due to the phase changes of the working fluid of the VCHP, the ΔT between the inlet and outlet of the working fluid in the VCHP change very little. The slope of the working fluid is small in the GCC, see Figure 10c. For the TCHP, the slope of the working fluid is small in the heat exchange with source in the GCC, whereas the slope of the working fluid is large in the heat exchange with sink in the GCC, see Figure 10d.

In this case, the average temperature between working fluid and source/sink in VCHP is small, so the energy loss of the heat exchangers is lower, the heat exchange efficiency is higher and affects the COP positively. Although the average temperature between working fluid and source/sink in JCHP and TCHP is large, and therefore the energy loss is higher, the heat exchange efficiency is smaller and affects negatively the COP. The performance of JCHP and TCHP are both weak. This process is more suitable for heat integration with a VCHP, which is consistent with the conclusion of Section 3.

4.1.4. Case 4: Methanol Distillation Process

The methanol distillation process was evaluated for HP integration based on the stream data from a 4-column double-effect methanol distillation process of a chemical plant [38]. The data are given in the Appendix A (Table A3). The ΔT_{\min} of the process is 15 °C. As can be seen from the GCC in Figure 11, the Pinch Temperature of this process is 74.26 °C. The hot utility required is 138.48 MW and the cold utility required is 139.90 MW. It is assumed that the heat duty of the heat exchanger at the sink side is fixed 20.86 MW. The pressure differences of the heat exchangers at source side are set 50 kPa, and at the sink, the side is set 0 kPa. The setting range of independent variables and optimisation results of a 4-column double-effect methanol distillation with an integrated HP are shown in Table 6. Finally, for more intuitive display the results, the GCC of a 4-column double-effect methanol distillation process integrated with different types of HPs is given, as shown in Figure 11. As can be seen from Table 6, the HPs can save 15% of the hot utility by improving the waste heat quality of the process. The ranking of the HP COPs is VCHP > JCHP-CO₂ > JCHP-Ar > TCHP when integrating with this process. The reason can be seen in Figure 11 and is related to the observation that the ΔT_{in} between source and sink is small, while the ΔT_{out} is too significant. The slopes of source and sink are both steep in the GCC.

Table 6. Variable settings and optimisation results of a methanol distillation with an integrated heat pump.

	Variable Ranges			Optimisation Results					
	¹ P ₂ , MPa	² P ₅ , MPa	³ T ₅ , °C	COP, -	Q _{source} , MW	W, MW	P ₂ , MPa	P ₅ , MPa	⁴ R, -
JCHP-Ar	4–8	1–5	–	3.23	14.40	6.46	5.49	3.50	1.59
JCHP-CO ₂	4–9	1–4	–	4.02	15.03	5.19	4.92	2.55	1.97
VCHP	2.5–8	0.2–3	–	5.67	17.18	3.64	5.28	2.40	2.24
TCHP	20–30	–	–10–25	1.50	7.09	13.92	25.71	6.07	4.27

¹ P₂: The outlet pressure of the compressor in the HP cycle, MPa. ² P₅: The outlet pressure of the expander or expansion valve in the HP cycle, MPa. ³ T₅: The outlet temperature of the expansion valve in the HP cycle, MPa. ⁴ R: The compression ratio of the compressor.

The ΔT between the inlet and outlet of the working fluid in JCHP changes significantly in the heat exchange with both the source and the sink. The slope of the working fluid is relatively large in the GCC, as shown in Figure 11a,b. For the VCHP, in the heat exchange with the source and the sink, the ΔT between the inlet and outlet of the working fluid in VCHP change very little. The slope of the working fluid is small in the GCC—see Figure 11c. The TCHP shows a different behaviour due to the transcritical nature of the heat release part. The slope of the working fluid is small in the heat exchange

with source in the GCC, while the slope of the working fluid is steep in the heat exchange with sink in the GCC, as shown in Figure 11d.

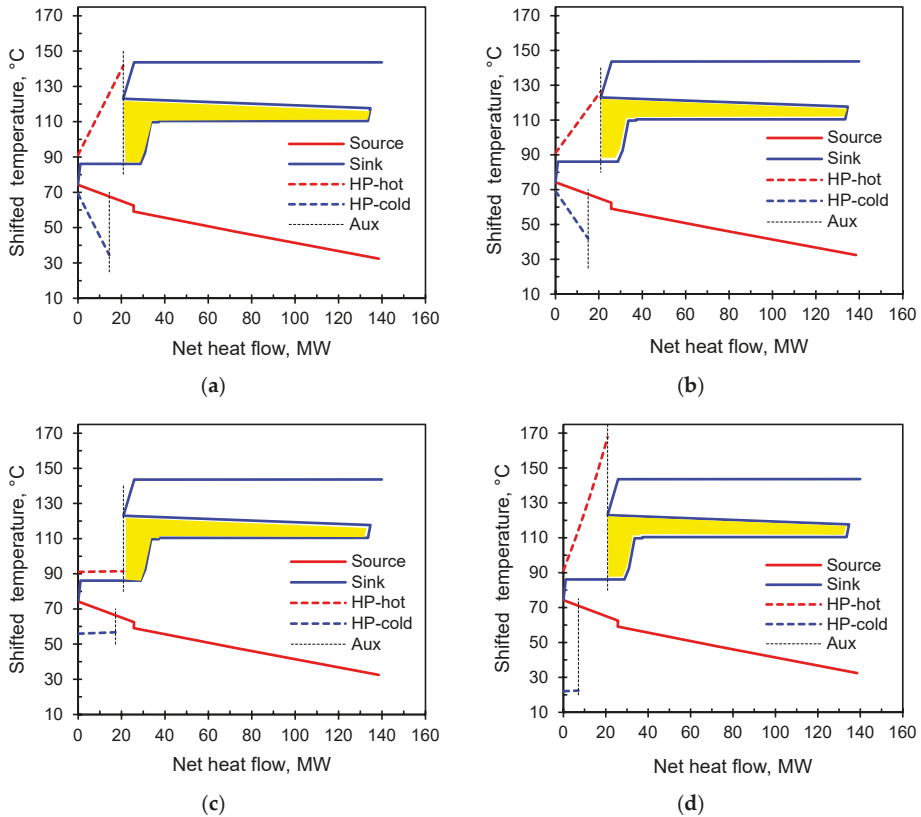


Figure 11. GCC of case 4 and integration options using (a) JCHP-Ar, (b) JCHP-CO₂, (c) VCHP and (d) TCHP.

In this case, the average ΔT between working fluid and source/sink in VCHP is small, so the energy loss of the heat exchangers is lower, the heat exchange efficiency is higher, and COP is affected positively. Although the average ΔT between working fluid and source/sink in JCHP and TCHP is massive, and thus the energy loss is higher, the heat exchange efficiency is smaller, and this affects the COP negatively. The performance of the JCHP and the TCHP are both weak. In addition, the outlet pressure of the compressor in TCHP is too high (25.71 MPa). This means high-pressure requirements for equipment of TCHP, with high equipment investment cost. The TCHP economy is likely to be poor. This process is more suitable for heat integration with VCHP, which is consistent with the conclusion of Section 3.

For the optimal COP of JCHP, the reason for the large ΔT between the working fluid and the source/sink after heat exchange can be seen in Figure 12. The figure shows the relationship between power consumption and COP of JCHP with compression ratio. In the JCHP, the heat load of the sink-side heat exchanger Q_h and the outlet pressure of the expander are fixed. By changing the outlet pressure of the compressor, a series of work required by the compressor, work produced by the expander and COP are obtained. It can be seen from Equation (1) that the COP is inversely proportional to the power consumption of the HP when Q_h is constant.

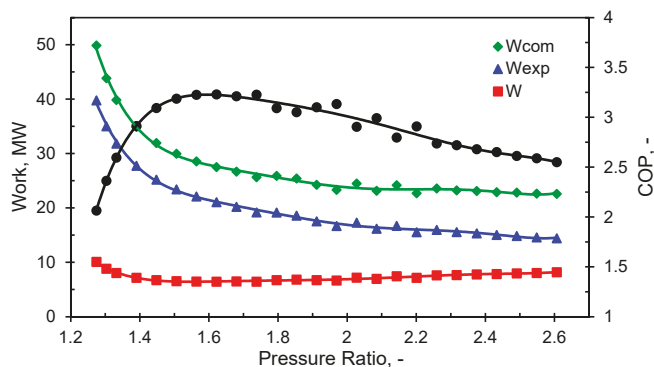


Figure 12. The relationship between power consumption and COP of JCHP with compression ratio.

As can be seen from Figure 12, with the increase of the compression ratio of the compressor (that is, the increase of the outlet pressure of the compressor compared to inlet pressure), the power consumption of the JCHP first decreases and then increases. The COP of JCHP increases first and then decreases with the increase of compressor compression ratio. That is, there is an optimal pressure for the optimal COP of the JCHP. When the outlet pressure of the compressor is lower than the optimal pressure, although the outlet temperature of the compressor decreases (that is, the inlet temperature of the working fluid exchanging heat with the source decreases and the temperature difference decreases), the COP of JCHP is not optimal. The same is true for the sink side.

4.2. Evaluation

The results of the Heat Integration of the four industrial processes with HPs are compared. They are summarised in Table 7.

Table 7. The results of different industrial Processes Integration with heat pumps.

Name	Unit	Case 1: Milk Spray Drying Process	Case 2: Dairy Product Process	Case 3: Candy Processing and Packaging	Case 4: Methanol Distillation	
GCC	T _{min}	°C	10	2	15.5	32.5
	T _{pinch}	°C	65	66.9	19.5	74.26
	T _{max}	°C	210	100	127.5	143.68
	Utility-cold	MW	5.36	0.94	0.33	138.48
	Utility-hot	MW	17.66	2.34	1.82	139.90
Source	T _{source-in}	°C	40.7	66.9	19.5	74.26
	T _{source-out}	°C	10	66.9	15.5	67
Sink	T _{sink-in}	°C	65	68.4	46.5	86.1
	T _{sink-out}	°C	-	68.4	49.5	86.1
Duty	Q _{source}	MW	5.36	0.71	0.33	-
	Q _{sink}	MW	-	-	-	20.86
COP	JCHP-Ar	-	2.83	3.89	2.81	3.23
	JCHP-CO ₂	-	2.93	4.52	3.55	4.02
	VCHP	-	1.85	13.07	4.44	5.67
	TCHP	-	1.77	1.68	1.85	1.50

For the processes with steep source and sink slopes, such as the spray drying process of the milk powder in a dairy factory in Case Study 1, the average ΔT of working fluid and source/sink in JCHP is small, resulting in a small energy loss and high heat exchange efficiency. The COP of JCHP is large, so it is appropriate to choose the JCHP.

When the source and sink slope of process is gentle or (nearly) flat, for example, as in the dairy product processing of Case Study 2 and the candy processing and packaging in Case Study 3, the VCHP is most suitable because the average ΔT of the working fluid and source/sink are small, the energy loss is small resulting in high thermal efficiency and high COP values. In Case Study 2, the ΔT_{in} is as low as 1.5 °C, and the COP of VCHP is as high as 13.07.

From Case Study 2 to Case Study 3, the ΔT_{in} increased from 1.5 °C to 11.84 °C, and the COP of the VCHP decreased from 13.07 to 4.44. Therefore, the smaller the ΔT_{in} between source and sink is, the larger is the COP of the VCHP. The COP of the VCHP decreased rapidly with the increase of ΔT_{in} between source and sink. However, the COP of JCHP decreased less with the increase of ΔT_{in} between source and sink.

The application scope of the TCHP is limited. The TCHP is more appropriate for a process with a relatively gentle source slope and a relatively steep sink slope. The best process is one which the inlet temperature of the source is less than or equal to 20 °C, and the ΔT_{in} between the source and sink is less than 10 °C.

5. Conclusions

Several main types of HPs have been critically analysed for obtaining rules and criteria on appropriate HP selection for various process configurations. In addition to the relatively recent JCHP, other HP types are in use and have been industrialised, including the VCHP and TCHP types. This paper performs a comparative evaluation of the performance of the Heat Integration scenarios of different HP types (VCHP, TCHP and JCHP) and processes, by applying the Petro-SIM process simulator and Pinch Analysis.

An answer is provided to the question of which type of HP is most suitable for a specific process. The results show that for processes with larger source and sink slopes on the T–H plot, the COP of JCHP is higher, and JCHP is more suitable. For processes with a relatively smaller and medium slope of the source and sink T–H profiles, the COP of VCHP is relatively large, and VCHP is more suitable. The scope of application of TCHP is small.

For processes with a relatively low source T–H slope and a relatively large sink T–H slope, the COP of TCHP is more substantial, and it is appropriate to select it. Because the critical temperature of CO₂ is 31.26 °C, the added constraint in this context is a process for which the source inlet temperature is lower than 20 °C, the sink temperature requires more than 40 °C, and the ΔT_{in} between the source and the sink is less than 10 °C.

By improving the waste heat quality of the process, the HPs can save 15 to 78% of the hot utility. The smaller the ΔT_{in} between source and sink is, the larger is the COP of the VCHP. The ΔT_{in} increased from 1.5 °C to 11.84 °C, and the COP of the VCHP decreased from 13.07 to 4.44. The COP of the VCHP decreased rapidly with the increase of ΔT_{in} between source and sink. However, the COP of JCHP decreased less with the increase of ΔT_{in} between source and sink.

It is shown that if an inappropriate HP is selected to integrate with the process, the COP of the HP would decline, which may lead to an increase in investment and a decrease in the economy of the HP. In the extreme cases, the differences between the most and the least suitable integration mappings can be of the order of 100% and up to tenfold. This shows the importance of performing such an analysis and making the correct choice of a HP.

For the different scenarios of Heat Integration with HPs, this study can provide guidance and suggestions for the selection of HPs, enabling a quick selection of the appropriate HPs. A simplifying assumption for the current work is the use of the COP of the HP—process combinations as the performance criterion, and considering the investment cost of HPs only qualitatively. The full analysis, relaxing this assumption and considering the investment and analysis of the economy is planned for future work. The future research will be targeted to find the balance between the COP and the economy of the HP application.

Author Contributions: L.G. has written the draft performing the complete study at the previously published idea of T.G.W. to extend the comparison of heat pump suitability to several applications. P.S.V. has consulted L.G. on the steps of the investigation and the formulation of the concepts and the procedure. P.S.V. has made a thorough refinement of the whole manuscript. J.J.K. has supervised and managed the research actions and the manuscript preparation and finalising, provided consultation to L.G. and P.S.V. on the presentation of the key concepts. T.G.W. has also provided proofreading feedback. All authors have read and agreed to the published version of the manuscript.

Funding: This research was funded by the EU project “Sustainable Process Integration Laboratory—SPIL”, project No. CZ.02.1.01/0.0/0.0/15_003/0000456 funded by EU “CZ Operational Programme Research, Development and Education”, Priority 1: Strengthening capacity for quality research under the collaboration agreement with The University of Waikato, New Zealand.

Conflicts of Interest: The authors declare no conflicts of interest. The funders had no role in the design of the study; in the collection, analyses, or interpretation of data; in the writing of the manuscript; or in the decision to publish the results.

Abbreviations

COP	Coefficient of Performance
CP	Specific Heat Capacity
GCC	Grand Composite Curve
GWP	global warming potential
HEN	Heat Exchanger Network
HP	heat pump
HX	heat exchanger
JCHP	Joule cycle heat pump
MILP	Mixed Integer Linear Programming
MINLP	Mixed Integer Nonlinear Programming
TCHP	transcritical heat pump
T–H	temperature–enthalpy
T–S	temperature–entropy
TSHI	Total Site Heat Integration
VCHP	vapour compression heat pump
VLV	let-down valve

Nomenclature

P_2	The outlet pressure of the compressor in the HP cycle, MPa
P_5	The outlet pressure of the expander or expansion valve in the HP cycle, MPa
Q_h	Heat output of the heat pump, kW
R	The compression ratio of the compressor
T_5	The outlet temperature of the expansion valve in the HP cycle, °C
T_s	supply temperature
$T_{sink-out}$	The outlet temperature of the sink, °C
T_t	Target temperature
W	Electrical or power consumption of the heat pump, kW
ΔP	The pressure difference, MPa
ΔT	temperature difference, °C
ΔT_1	The difference between the inlet temperature of the sink and the outlet temperature of the source, °C
ΔT_2	The difference between the outlet temperature of the sink and the inlet temperature of the source, °C
ΔT_{in}	The inlet temperature difference of the source and sink, °C
ΔT_{min}	minimum approach temperature
ΔT_{out}	The outlet temperature difference of the source and sink, °C

Appendix A

Table A1. The stream data of a dairy process. Data from Wallerand et al. [36].

Stream Name	$T_{s,r}$, °C	$T_{t,r}$, °C	ΔH , kW
Refrigeration	6.0	4.0	76.0
Pasteurisation 1a	4.0	66.0	2356.0
Pasteurisation 2a	66.0	86.0	676.4
Pasteurisation 1a	86.0	4.0	2773.2
Pasteurisation 1a	66.0	98.0	119.7
Pasteurisation 1a	98.0	4.0	351.6
Concentration 1	4.0	70.3	504.0
Concentration 2	70.3	70.3	904.2
Concentration 3	66.4	66.4	864.1
Concentration 4	60.8	60.8	849.8
Concentration 5	60.8	4.0	151.5
Concentration 6	68.9	68.9	904.2
Concentration 7	65.9	65.9	864.1
Concentration 9	68.9	15.0	87.8
Concentration 10	65.9	15.0	80.8
Condensates cooling 8	60.1	60.1	849.8
Condensates cooling 11	60.1	15.0	69.7
Yoghurt production 1	4.0	94.0	1026.0
Yoghurt production 2	94.0	10.0	957.6
Desert production 1	4.0	90.0	817.0
Desert production 2	90.0	70.0	190.0
Hot water	15.0	55.0	167.2
Cleaning in place 1a	58.7	70.0	188.6
Cleaning in place 1b	65.0	15.0	104.5
Cleaning in place 2a	67.5	80.0	209.5
Cleaning in place 2b	75.0	15.0	125.4
Fridge	5.0	5.0	300.0

Table A2. The stream data of a process of candy processing and packaging. Data from Miah et al. [37].

Stream Name	$T_{s,r}$, °C	$T_{t,r}$, °C	ΔH , kW
Production A			
FP-02	15.0	70.0	13.66
FP-03	15.0	70.0	16.72
FP-04	25.0	60.0	29.12
FP-05	25.0	60.0	29.12
FP-06	30.0	55.0	29.10
FP-07	30.0	55.0	29.10
FP-08	130.0	80.0	60.80
¹ FP-V	120.0	25.0	76.71
FP-08	130.0	80.0	60.80
¹ FP-V	120.0	25.0	76.71
Production B			
15 x S-S	21.0	18.0	279.00
11 x N-S	44.0	47.0	550.00
28 x S-S	44.0	47.0	1400.00
Packaging			
AHU CFP	22	18	55.52

¹ FP-V: Water, includes latent heat.

Table A3. The stream data of a 4-column double-effect methanol distillation process. Data from Cui et al. [38].

Stream Name	T _{sr} , °C	T _{tr} , °C	ΔH, MW
Crude feed preheated	40.00	85.00	8.160
PC feed preheated	78.94	135.97	13.864
LEC reboiler	78.60	78.62	27.750
PC reboiler	136.10	136.18	114.064
AC reboiler	102.90	102.92	96.267
WC reboiler	102.20	102.22	3.544
First stage condenser	81.76	70.00	26.858
Second stage condenser	70.00	40.00	1.744
PC condenser	130.50	125.19	115.115
AC condenser	66.60	40.00	107.510
WC condenser	66.60	40.00	3.584
PC top stream to tanks	125.19	40.00	7.425

References

1. Carnot, S. *Reflexions on the Motive Power of Fire: A Critical Edition with the Surviving Scientific Manuscripts*; Manchester University Press: Manchester, UK, 1986; ISBN 978-0-936508-16-0.
2. Radermacher, R.; Hwang, Y. *Vapor Compression Heat Pumps with Refrigerant Mixes*; Taylor & Francis: Boca Raton, FL, USA, 2005; ISBN 978-0-8493-3489-4.
3. Herold, K.E.; Radermacher, R.; Klein, S.A. *Absorption Chillers and Heat Pumps*, 2nd ed.; CRC Press, Taylor & Francis Group: Boca Raton, FL, USA, 2016; ISBN 978-1-4987-1434-1.
4. Lorentzen, G. Trans-Critical Vapour Compression Cycle Device. Patent Application No. WO1990007683A1, 12 July 1990.
5. Pavlas, M.; Stehlik, P.; Oral, J.; Klemeš, J.; Kim, J.-K.; Firth, B. Heat integrated heat pumping for biomass gasification processing. *Appl. Therm. Eng.* **2010**, *30*, 30–35. [[CrossRef](#)]
6. Liew, P.Y.; Walmsley, T.G. Heat pump integration for total site waste heat recovery. *Chem. Eng. Trans.* **2016**, *52*, 817–822.
7. Walmsley, T.G. A Total Site Heat Integration design method for integrated evaporation systems including vapour recompression. *J. Clean. Prod.* **2016**, *136*, 111–118. [[CrossRef](#)]
8. Walmsley, T.G.; Klemeš, J.J.; Walmsley, M.R.W.; Atkins, M.J.; Varbanov, P.S. Innovative hybrid heat pump for dryer process integration. *Chem. Eng. Trans.* **2017**, *57*, 1039–1044.
9. Stampfli, J.A.; Atkins, M.J.; Olsen, D.G.; Wellig, B.; Walmsley, M.R.W.; Neale, J.R. Industrial heat pump integration in non-continuous processes using thermal energy storages as utility a graphical approach. *Chem. Eng. Trans.* **2018**, *70*, 901–906.
10. Stampfli, J.A.; Atkins, M.J.; Olsen, D.G.; Walmsley, M.R.W.; Wellig, B. Practical heat pump and storage integration into non-continuous processes: A hybrid approach utilizing insight based and nonlinear programming techniques. *Energy* **2019**, *182*, 236–253. [[CrossRef](#)]
11. Wang, M.; Deng, C.; Wang, Y.; Feng, X.; Lan, X. Process integration and selection of heat pumps in industrial processes. *Chem. Eng. Trans.* **2018**, *70*, 1105–1110.
12. Urbanucci, L.; Bruno, J.C.; Testi, D. Thermodynamic and economic analysis of the integration of high-temperature heat pumps in trigeneration systems. *Appl. Energy* **2019**, *238*, 516–533. [[CrossRef](#)]
13. Schlosser, F.; Seevers, J.-P.; Peesel, R.-H.; Walmsley, T.G. System efficient integration of standby control and heat pump storage systems in manufacturing processes. *Energy* **2019**, *181*, 395–406. [[CrossRef](#)]
14. Oluleye, G.; Smith, R.; Jobson, M. Modelling and screening heat pump options for the exploitation of low grade waste heat in process sites. *Appl. Energy* **2016**, *169*, 267–286. [[CrossRef](#)]
15. Oluleye, G.; Jiang, N.; Smith, R.; Jobson, M. A novel screening framework for waste heat utilization technologies. *Energy* **2017**, *125*, 367–381. [[CrossRef](#)]
16. Goumba, A.; Chiche, S.; Guo, X.; Colombert, M.; Bonneau, P. Recov'Heat: An estimation tool of urban waste heat recovery potential in sustainable cities. *AIP Conf. Proc.* **2017**, *1814*, 020038. [[CrossRef](#)]

17. Sarbu, I. A review on substitution strategy of non-ecological refrigerants from vapour compression-based refrigeration, air-conditioning and heat pump systems. *Int. J. Refrig.* **2014**, *46*, 123–141. [[CrossRef](#)]
18. Nekså, P.; Rekstad, H.; Zakeri, G.R.; Schiefloe, P.A. CO₂-heat pump water heater: Characteristics, system design and experimental results. *Int. J. Refrig.* **1998**, *21*, 172–179. [[CrossRef](#)]
19. Nekså, P. CO₂ heat pump systems. *Int. J. Refrig.* **2002**, *25*, 421–427. [[CrossRef](#)]
20. Kim, H.J.; Ahn, J.M.; Cho, S.O.; Cho, K.R. Numerical simulation on scroll expander–compressor unit for CO₂ trans-critical cycles. *Appl. Therm. Eng.* **2008**, *28*, 1654–1661. [[CrossRef](#)]
21. Van de Bor, D.M.; Infante Ferreira, C.A.; Kiss, A.A. Low grade waste heat recovery using heat pumps and power cycles. *Energy* **2015**, *89*, 864–873. [[CrossRef](#)]
22. Fu, C.; Gundersen, T. A Novel Sensible Heat Pump Scheme for Industrial Heat Recovery. *Ind. Eng. Chem. Res.* **2016**, *55*, 967–977. [[CrossRef](#)]
23. Adler, B.; Mauthner, R. Rotation Heat Pump (RHP). In Proceedings of the 12th IEA Heat Pump Conference, Rotterdam, The Netherlands, 15–18 May 2017.
24. Wallerand, A.S.; Kermani, M.; Kantor, I.; Maréchal, F. Optimal heat pump integration in industrial processes. *Appl. Energy* **2018**, *219*, 68–92. [[CrossRef](#)]
25. Linnhoff, B.; Hindmarsh, E. The pinch design method for heat exchanger networks. *Chem. Eng. Sci.* **1983**, *38*, 745–763. [[CrossRef](#)]
26. Gai, L.; Varbanov, P.S.; Walmsley, T.G.; Klemeš, J.J. Process Integration Using a Joule Cycle Heat Pump. *Chem. Eng. Trans.* **2019**, *76*, 415–420.
27. KBC. *Petro-SIM*; KBC Advanced Technologies: London, UK, 2016.
28. Klemeš, J.J.; Varbanov, P.S.; Alwi, S.R.W.; Manan, Z.A. *Sustainable Process Integration and Intensification: Saving Energy, Water and Resources*, 2nd ed.; Walter de Gruyter GmbH: Berlin, Germany, 2018; ISBN 978-3-11-053536-5.
29. Klemeš, J.J.; Varbanov, P.S.; Walmsley, T.G.; Jia, X. New directions in the implementation of Pinch Methodology (PM). *Renew. Sustain. Energy Rev.* **2018**, *98*, 439–468. [[CrossRef](#)]
30. Lopez-Echeverry, J.S.; Reif-Acherman, S.; Araujo-Lopez, E. Peng-Robinson equation of state: 40 years through cubics. *Fluid Phase Equilibria* **2017**, *447*, 39–71. [[CrossRef](#)]
31. Guźda, A.; Szmolke, N. Compressors in Heat Pumps. *Mach. Dyn. Res.* **2015**, *39*, 71–83.
32. Wang, J.F.; Brown, C.; Cleland, D.J. Heat pump heat recovery options for food industry dryers. *Int. J. Refrig.* **2018**, *86*, 48–55. [[CrossRef](#)]
33. Cube, H.L.V.; Steimle, F. *Heat Pump Technology*; Elsevier: Amsterdam, The Netherlands, 2013; ISBN 978-1-4831-0247-4.
34. Klemeš, J.J. *Handbook of Process Integration (PI): Minimisation of Energy and Water Use, Waste and Emissions*; Woodhead Publishing/Elsevier: Cambridge, UK, 2013; ISBN 978-0-85709-725-5.
35. Atkins, M.J.; Walmsley, M.R.W.; Neale, J.R. Integrating heat recovery from milk powder spray dryer exhausts in the dairy industry. *Appl. Therm. Eng.* **2011**, *31*, 2101–2106. [[CrossRef](#)]
36. Wallerand, A.S.; Kermani, M.; Voillat, R.; Kantor, I.; Maréchal, F. Optimal design of solar-assisted industrial processes considering heat pumping: Case study of a dairy. *Renew. Energy* **2018**, *128*, 565–585. [[CrossRef](#)]
37. Miah, J.H.; Griffiths, A.; McNeill, R.; Poonaji, I.; Martin, R.; Leiser, A.; Morse, S.; Yang, A.; Sadhukhan, J. Maximising the recovery of low grade heat: An integrated heat integration framework incorporating heat pump intervention for simple and complex factories. *Appl. Energy* **2015**, *160*, 172–184. [[CrossRef](#)]
38. Cui, C.; Sun, J.; Li, X. A hybrid design combining double-effect thermal integration and heat pump to the methanol distillation process for improving energy efficiency. *Chem. Eng. Process. Process Intensif.* **2017**, *119*, 81–92. [[CrossRef](#)]



© 2020 by the authors. Licensee MDPI, Basel, Switzerland. This article is an open access article distributed under the terms and conditions of the Creative Commons Attribution (CC BY) license (<http://creativecommons.org/licenses/by/4.0/>).

MDPI
St. Alban-Anlage 66
4052 Basel
Switzerland
Tel. +41 61 683 77 34
Fax +41 61 302 89 18
www.mdpi.com

Energies Editorial Office
E-mail: energies@mdpi.com
www.mdpi.com/journal/energies



MDPI
St. Alban-Anlage 66
4052 Basel
Switzerland

Tel: +41 61 683 77 34
Fax: +41 61 302 89 18

www.mdpi.com



ISBN 978-3-03943-121-2